Development of organic solar cells by combinatorial methods

PhD thesis dissertation

Xabier Rodríguez Martínez

Development of organic solar cells by combinatorial methods

PhD thesis dissertation
(presented as a compendium of works)

Xabier Rodríguez Martínez

Nanostructured Materials for Optoelectronics and Energy Harvesting Group,
Instituto de Ciencia de Materiales de Barcelona (ICMAB-CSIC)

Supervisor: Mariano Campoy Quiles

Tutor: Aitor Lopeandía Fernández

PhD programme in Materials Science, Department of Physics

Universidad Autónoma de Barcelona (UAB)

Bellaterra (Barcelona), 2020

A mis abuelos

Acknowledgements

Habiendo finalizado la escritura de esta tesis doctoral me vienen a la cabeza muchos recuerdos: de mi infancia, de mi adolescencia y de mi época universitaria, junto con un gran número de personas a las que me gustaría agradecer su ayuda inestimable durante estos bonitos años de formación académica. Porque, aunque ni ellos ni ellas lo perciban, gran parte de este trabajo también es obra suya y es por ello que creo que tienen bien merecido que sus nombres aparezcan aquí reflejados como muestra de mi gratitud.

En primer lugar, me gustaría dar las gracias a mis padres, **Segun** y **Rodri**, y a mi hermana **Lu**, puesto que son los principales responsables de que hoy sea lo que soy y los que más años llevan aguantándome. Me han sabido motivar y ayudar desde el primer día para esforzarme al máximo y estar ansioso por aprender cosas nuevas cada día. Siempre me han permitido hacer lo que me gustaba, sin ponerme pegas, y se han esforzado al máximo para poder tener todas mis necesidades cubiertas, incluyendo el gran esfuerzo que sé que les supuso que me fuese a estudiar a Barcelona. Sé que puedo contar con vosotros para lo que sea bajo cualquier circunstancia, y sois una parte esencial en mi vida. Gracias por estar siempre apoyándome. Tampoco quería dejar de agradecer a mis sobrinos **Cloe** y **Eric**, que son los más majos del mundo, y también a **Berto**, por ser tan buen cuñado y siempre tan curioso por las cosas.

Agradezco también a mi abuela, **Segunda**, por lo bien que me cuidó siendo niño. Probablemente sea la otra persona con la que más tiempo he pasado en mi infancia. Siento igualmente especial aprecio por mis abuelos ya fallecidos: **Luis**, **Hortensia** y **Francisco**. Todas ellas son personas que, en mi opinión, han sabido adaptarse a circunstancias muy complicadas, y me han servido de motivación en los momentos más difíciles para seguir adelante pese a las adversidades. Gracias, esta tesis está especialmente dedicada a vosotros.

También le debo mucho a mis tíos **Carlos**, **Fran** y **José**, quienes me descubrieron a Led Zeppelin cuando era niño. Gracias a ellos, a día de hoy me basta con escuchar *How many more times* para teletransportarme veinte años atrás y ver esa

mesa caóticamente garabateada de Carlos y las montañas de CDs de la habitación de Fran. Gracias, pocas sensaciones hay más increíbles que esas y os las debo a vosotros.

Me siento igualmente afortunado de tener grandísimos amigos, con amistades que se extienden prácticamente desde el primer día de colegio en el CEIP Escultor Acuña. Es bastante impresionante y nunca dejará de sorprenderme este hecho. Muchas gracias **Alejandro**, **Iria**, **Martín**, **Andrea**, **Lois**, **Paula**, **Inés**, **Marco**… os merecéis lo mejor siempre.

De mi etapa en el IES Álvaro Cunqueiro, me gustaría mencionar a algunos profesores como **Xenaro**, **Isidoro** y **Ángel**. Creo que ellos me ayudaron a desarrollar un pensamiento crítico desde el primer día, y cada día que pasa me doy más cuenta de la suerte que tuve de encontrarme con ellos en la mejor época de aprendizaje.

Más recientemente (desde el 2012 ni más ni menos), apareció una persona en mi vida que ahora es pilar fundamental en mi día a día, como es **Marta**. A su lado la vida es fantástica, simple y llanamente. Muy pronto tendremos oportunidad de hacer realidad muchos de nuestros planes de futuro y descubrir el mundo juntos, ¡estoy seguro! Igualmente contento y afortunado me siento de que los Castroviejo sean tan majos, en especial **Chufus** y **Carmen**. Desde el primer día me han acogido como uno más y me siento con ellos ¡como en casa! Gracias.

Por último, me gustaría agradecer a los grandes compañeros que he tenido en el ICMAB: **Laura Córcoles**, **Romén**, **Bernhard**, **Enrique**, **Osnat**, **Adrián**, **Sir Perevedentsev**, **Martí**, **Pau**… ¡con esta gente trabajar en el laboratorio puede ser hasta divertido! :-) Y no me olvido de mi mentor durante los últimos 6 años, **Mariano**, que desde aquel trabajo final de grado no ha hecho más que hacerme disfrutar día tras día con nuestros progresos en ciencia combinatorial. Está claro que la *conexión galega* es un hecho, y esperamos que se mantenga por muchos años.

¡Gracias a todas y todos por tanto!

Index

1. Abstract

Organic solar cells are complex stratified devices that convert light into electricity. Therein, the photovoltaic effect takes place in the active layer, which is formed by at least two organic semiconducting materials with dissimilar electronic character: the donor or hole transporting material, and the acceptor or electron transporting material. These can be organized as a stacked bilayer or as a bulk heterojunction yet in both cases tightly bound excitons are generated upon light absorption. The excitons must split at a donor-acceptor interface before recombining to be effectively collected at the device contacts. Accordingly, the donor:acceptor mixing ratio as well as the film morphology are features subjected to optimization for every donor:acceptor pair selected. Also, the active layer thickness must be tailored to maximize the light harvesting as dictated by optical interference.

Eventually, this results in an intricate multi-dimensional landscape of device parameters to determine the final device photoconversion efficiency. The handling of this kind of problems has been traditionally performed by fabrication-intensive approaches, which rely on the massive prototyping of devices with controlled and discrete variation of each of the involved parameters individually, until building the entire multi-dimensional landscape. These methods are intrinsically inefficient regarding the use of time and resources and, as such, are considered as one of the main bottlenecks that slow down the growing of the organic photovoltaic technology.

In this thesis we develop high-throughput experimental approaches to accelerate screening of materials and optimization of organic solar cells. The methodology is based on the realization of lateral solid-state gradients on the parameters of interest, which are thought to circumvent the limitations of traditional sampling approaches by combining in a single sample the parametric variations explored by hundreds of them in discrete sampling experimentation. The photovoltaic performance is imaged throughout the gradients and spatially correlated with their parametric variations, thus moving from fabrication- to measuring-intensive screening scenarios that offer significantly higher materials screening and device optimization rates. Accordingly, the gradients require characterization techniques that provide (i) concurrent sensitivity to the varied parameters; (ii) enough lateral resolution to resolve the

smooth parametric variations; (iii) fast data acquisition; and (iv) a local probe related with the photovoltaic efficiency.

In this thesis, we demonstrate the use of Raman spectroscopy imaging to map quantitatively the thickness and mixing ratio variations of the gradients (Paper I), while light-beam induced current (LBIC) mapping is exploited to measure the photocurrent in functional devices containing the aforementioned gradients. Their joint use is demonstrated in this work to be a truly efficient screening approach to optimize organic solar cells of distinct types.

First, we study bilayer heterostructures formed by orthogonal thickness gradients and use Raman spectroscopy and LBIC to identify the thickness of each layer that results in the highest photovoltaic performance (Paper II). Then, we investigate bulk heterojunction devices made of low band gap donor polymers and fullerene acceptors and identify the optimal active layer thickness and mixing ratio of several state-of-the-art donor:acceptor binaries (Paper III). Afterwards, the work is extended to novel non-fullerene acceptors including small molecules and n-type polymers. For this latter case and in order to accommodate the particular rheology of polymeric inks, a novel deposition technique based on microfluidic dispensers and blade coating is introduced (Paper IV). Next, bulk heterojunctions of ternary organic photovoltaic blends are effectively screened following high-throughput combinatorial methods (Paper V). Finally, we perform systematic combinatorial material screening studies on polymer:small molecule binary blends to feed artificial intelligence algorithms (Paper VI). As a result, these are able to retrieve predictive models for the photocurrent space that might accelerate even further the device optimization and materials screening rate already enabled by the development of combinatorial methods in organic photovoltaics.

2. Publications

Herein, a detailed list of the six publications included in this thesis is presented, detailing my particular contributions in the co-authored works:

Paper I. "Quantifying local thickness and composition in thin films of organic photovoltaic blends by Raman scattering", X. Rodríguez-Martínez, M. S. Vezie, X. Shi, I. McCulloch, J. Nelson, A. R. Goñi, M. Campoy-Quiles, *J. Mater. Chem. C* **2017**, *5*, 7270.

My contribution: "I prepared the thin film samples and performed all the measurements. Certain compounds were synthetized by our collaborators. I developed the MATLAB coding for data fitting according to the transfer matrix model. I drafted the manuscript and prepared the figures. I am also corresponding author in this work."

Paper II. "Combinatorial optimization of evaporated bilayer small molecule organic solar cells through orthogonal thickness gradients", X. Rodríguez-Martínez, A. Sánchez-Díaz, G. Liu, M. A. Niño, J. Cabanillas-Gonzalez, M. Campoy-Quiles, *Org. Electron.* **2018**, *59*, 288.

My contribution: "I performed the measurements and analysis of the samples provided by our colleagues from IMDEA Nanociencia in Madrid (special mention to Mr. Guilin Liu as PhD student supervised by Dr. Juan Cabanillas-Gonzalez). I developed the transfer matrix coding for modelling Raman in bilayer heterojunctions. I drafted the manuscript and prepared the figures."

Paper III. "High-Throughput Multiparametric Screening of Solution Processed Bulk Heterojunction Solar Cells", A. Sánchez-Díaz, X. Rodríguez-Martínez, L. Córcoles-Guija, G. Mora-Martín, M. Campoy-Quiles, *Adv. Electron. Mater.* **2018**, *4*, 1700477.

My contribution: "I performed the Raman measurements and analysis. I matched LBIC and Raman data took at distinct setups. I prepared half of the figures

and helped Dr. Antonio Sánchez-Díaz (former postdoc in Nanopto group) in the writing of the manuscript. Special mentions to Dr. Antonio Sánchez-Díaz and Mr. Germán Mora-Martín (former MSc student supervised by Dr. Mariano Campoy-Quiles) as they entirely assumed the fabrication of devices."

Paper IV. "Microfluidic-Assisted Blade Coating of Compositional Libraries for Combinatorial Applications: The Case of Organic Photovoltaics", X. Rodríguez-Martínez, S. Sevim, X. Xu, C. Franco, P. Pamies-Puig, L. Córcoles-Guija, R. Rodriguez-Trujillo, F. J. del Campo, D. Rodriguez San Miguel, A. J. deMello, S. Pané, D. B. Amabilino, O. Inganäs, J. Puigmartí-Luis, M. Campoy-Quiles, *Adv. Energy Mater.* **2020**, DOI: 10.1002/aenm.202001308.

My contribution: "I tested the different microfluidic arrays designed over the course of this project. The initial designs that were finally only briefly mentioned in the manuscript were made by L.C.-G., R.R.-T. and F.J.C. I fabricated the graded solar cells and performed all characterization measurements and analysis. I drafted the manuscript and prepared the first version of the figures. Special mention to Mr. Semih Sevim (PhD student supervised by Dr. Josep-Puigmartí-Luis) for his valuable microfluidic knowledge during my short 3-week stay at ETH Zürich and the fabrication of the chips."

Paper V. "Efficient Exploration of the Composition Space in Ternary Organic Solar Cells by Combining High-Throughput Material Libraries and Hyperspectral Imaging", A. Harillo-Baños, X. Rodríguez-Martínez, M. Campoy-Quiles, *Adv. Energy Mater.* **2020**, *10*, 1902417.

My contribution: "I developed the transfer matrix model for the Raman in ternary blends. Mr. Albert Harillo-Baños (PhD student supervised by Dr. Mariano Campoy-Quiles) fabricated all the devices. The data analysis, writing and preparation of figures was distributed equally between both."

Paper VI. "Predicting the photocurrent-composition dependence in organic solar cells", X. Rodríguez-Martínez, E. Pascual-San-José, Z. Fei, M. Heeney, R. Guimerà, M. Campoy-Quiles, *submitted*.

My contribution: "I assumed the Raman characterization and analysis whereas Mr. Enrique Pascual-San-José (PhD student supervised by Dr. Mariano Campoy-Quiles) fabricated the devices. With the help of Dr. Roger Guimerà (Universitat Rovira i Virgili), I applied the machine learning random forest algorithm to the experimental datasets. I performed the cross-validations and feature selection procedures. I drafted the manuscript and prepared the figures."

In addition to the above list of publications, during the development of the present thesis I also contributed to other works that are partially related with the main topics of my research but are not included in the compendium:

"Dynamic disorder, phonon lifetimes, and the assignment of modes to the vibrational spectra of methylammonium lead halide perovskites", A. M. A. Leguy, A. R. Goñi, J. M. Frost, J. Skelton, F. Brivio, X. Rodríguez-Martínez, O. J. Weber, A. Pallipurath, M. I. Alonso, M. Campoy-Quiles, M. T. Weller, J. Nelson, A. Walsh, P. R. F. Barnes, *Phys. Chem. Chem. Phys.* **2016**, *18*, 27051.

My contribution: "I helped Prof. A. R. Goñi in the photoluminescence and Raman measurements performed at cryogenic temperatures. I analysed the spectra and prepared the corresponding figures."

"Defect tolerant perovskite solar cells from blade coated non-toxic solvents", Z. Bi, X. Rodríguez-Martínez, C. Aranda, E. Pascual-San-José, A. R. Goñi, M. Campoy-Quiles, X. Xu, A. Guerrero, *J. Mater. Chem. A* **2018**, *6*, 19085.

My contribution: "I performed photoluminescence and LBIC measurements on the perovskites. I did the data analysis and prepared the corresponding figure for the manuscript."

"Farming thermoelectric paper", D. Abol-Fotouh, B. Dörling, O. Zapata-Arteaga, <u>X. Rodríguez-Martínez</u>, A. Gómez, J. S. Reparaz, A. Laromaine, A. Roig, M. Campoy-Quiles, *Energy Environ. Sci.* **2019**, *12*, 716.

My contribution: "I measured the thermal conductivity of some particular samples by means of one-laser Raman thermometry and the 3ω-method. Special mention to Dr. J. Sebastián Reparaz (tenured scientist at ICMAB) who designed the corresponding characterization setups."

"Correlating the Phase Behavior with the Device Performance in Binary P3HT:NFA Blend Using Optical Probes of Microstructure", E. Rezasoltani, A. A. Y. Guilbert, J. Yan, <u>X. Rodríguez-Martínez</u>, M. Azzouzi, F. Eisner, S. M. Tuladhar, A. Wadsworth, Z. Hamid, I. McCulloch, M. Campoy-Quiles, J. Nelson, *submitted*.

My contribution: "I measured the Raman scattered spectra in the P3HT:NFA blends and performed the corresponding compositional analysis. I helped in writing that specific section of the manuscript."

3. Introduction

Mankind is currently facing one of the most challenging technological issues in modern history: the increasing energy consumption and its associated environmental impact. The global energetic demand keeps growing flawlessly as a result of the augmented consumption in developing countries and the governmental economies of the developed world countries oriented to the massive consumption of resources. Meanwhile, fossil fuels are still the main energy source worldwide,[1,2] which implies that the concentration of greenhouse gases (GHG) is expected to overcome the threshold established by the scientific community to avoid irreversible effects on Earth and its ecosystems.[3] This makes the search of novel and more environmentally-friendly energy sources a must in the following decades. In this sense, the potential that renewable energy sources have in transforming the current energy supply model is huge and they certainly constitute the future that mankind ought to pursue and develop. Within the vast field of renewable energy sources, photovoltaic technologies currently appear as the fifth most important contributor to the total power generated, a list that is led by hydroelectricity (Figure 1).[1] Nevertheless, the growing potential of the photovoltaic technology is certainly enormous as it is forecasted to cover ca. 60% of the expected growth in renewable power capacity for the next years (2019-2024 period) until becoming the major contributor by 2024 (excluding hydroelectricity).[4]

Photovoltaics (PV) aim at exploiting the ca. 89000 TW of solar electromagnetic radiation that continuously impinge on the Earth's crust.[1] Such an overwhelming digit is approximately 0.02 % of the estimated world total primary power consumption in 2018: 18.4 TW,[1] of which ca. 3 TW are destined to electricity generation according to the International Energy Agency (IEA).[2,2] The worldwide consumption model predictions also indicate that the global energy demands will

---

[1] Power estimated by considering a mean solar irradiance at the sea level of 1000 W m^{-2}, a mean net albedo of 0.3 and a mean radius of Earth equal to $6.371 \cdot 10^6$ m.

[2] According to the *BP Statistical Review of World Energy 2019*, the world total primary energy consumption in 2018 was ca. 160000 TWh, which implies an average power supply of ca. 18 TW over a full year. The *International Energy Agency World Energy Outlook 2019* also indicates that 26700 TWh were exclusively employed for electricity generation, yielding ca. 3 TW in average for such purpose over a year.

continue growing steadily between 2-3% per year as a result of the requirements of the Chinese and Indian economies.[1]
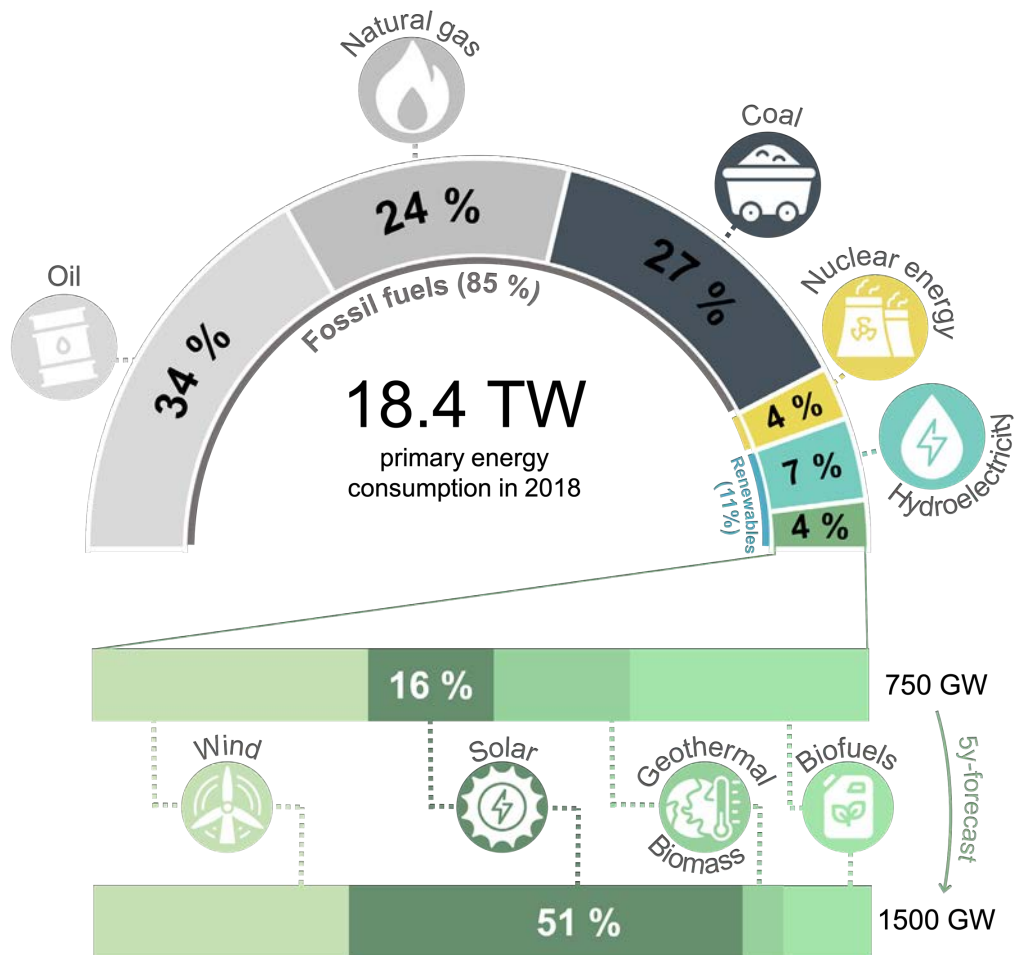
Figure 1. The world energy consumption in 2018 raised up to 18.4 TW according to the *BP Statistical Review of World Energy 2019*.[1] Accordingly, 85% of the energy generation was ascribed to fossil fuels in any of its forms (oil, natural gas and coal) whereas an 11% was produced by renewable energy sources; the remaining 4% was ascribed to nuclear energy. However, renewables (excluding hydroelectricity) are forecasted to double their installed capacity from 750 GW to 1500 GW in the next five years, mainly led by solar photovoltaics which is expected to share ca. 50% of the total generation in renewables by 2024.[2]

However, such economies are also expected to lead the solar PV capacity growth in the next years (ca. 700 GW according to the IEA)[4] guided by the distributed installation of silicon-based modules in homes, commercial buildings and industrial facilities. Silicon PV (*aka*. first generation PV) currently accounts for ca. 95% of the market share as the manufacturing scale up procedure advanced towards a more efficient use of raw material, now close to 4 g per watt peak (W_p).[5] As a result, silicon modules are set to take off with a cost per W_p as low as 0.3 €, which is an impressive figure given their lifetime (20-30 years) and power conversion efficiency (PCE, 15-20% in commercial modules).[5] Such overwhelming digit (0.30 € W_p^{-1}) encourages the silicon PV industry to lead the upcoming growth in renewable energy production capacity worldwide.

Nevertheless, first generation PV has inherent drawbacks related to their heavyweight and lack of flexibility ascribed to the need for thick devices to maximize light harvesting and to the use of thick glass encapsulants. These limitations constrain the implementation of silicon PV modules to solid rooftops, facades and dedicated solar farms, with poor aesthetical integration in the environment. Thus, silicon is not a good PV candidate for the upcoming generation of electronic devices forming the so-called *internet of things* (IoT).[6] These will require small, lightweight and off-grid energy sources to be integrated in a variety of systems, forms and shapes while being operative under indoor lighting environments, with low cost and minimal maintenance.[7] All such requirements are mostly accomplished by emerging PV technologies such as organic photovoltaics (OPV) or dye-sensitized solar cells (DSSC) modules which, in fact, have been demonstrated to surpass the 20% PCE milestone under indoor light-emitting diode (LED) lighting conditions[8] and even to exceed the performance of crystalline silicon modules.[9] The narrower and tunable light-absorption profiles of their organic photoactive materials (namely low band-gap polymers) offer improved matching with typical indoor light sources.[10] Also the optical properties of the active layer, namely its large extinction coefficient and lower refractive index in the UV-visible regime compared to silicon, aid in suppressing most of the angular dependence characteristic of silicon modules. This latter feature is quantitatively illustrated in Figure 2, which shows the reflectance obtained for non-polarized light according to transfer matrix modelling in both silicon-

based and organic PV systems. The larger angular tolerance of OPV serves to maintain high performance in cloudy or diffuse lighting environments and even to increase the photogenerated current with respect to normal incidence conditions.[11]
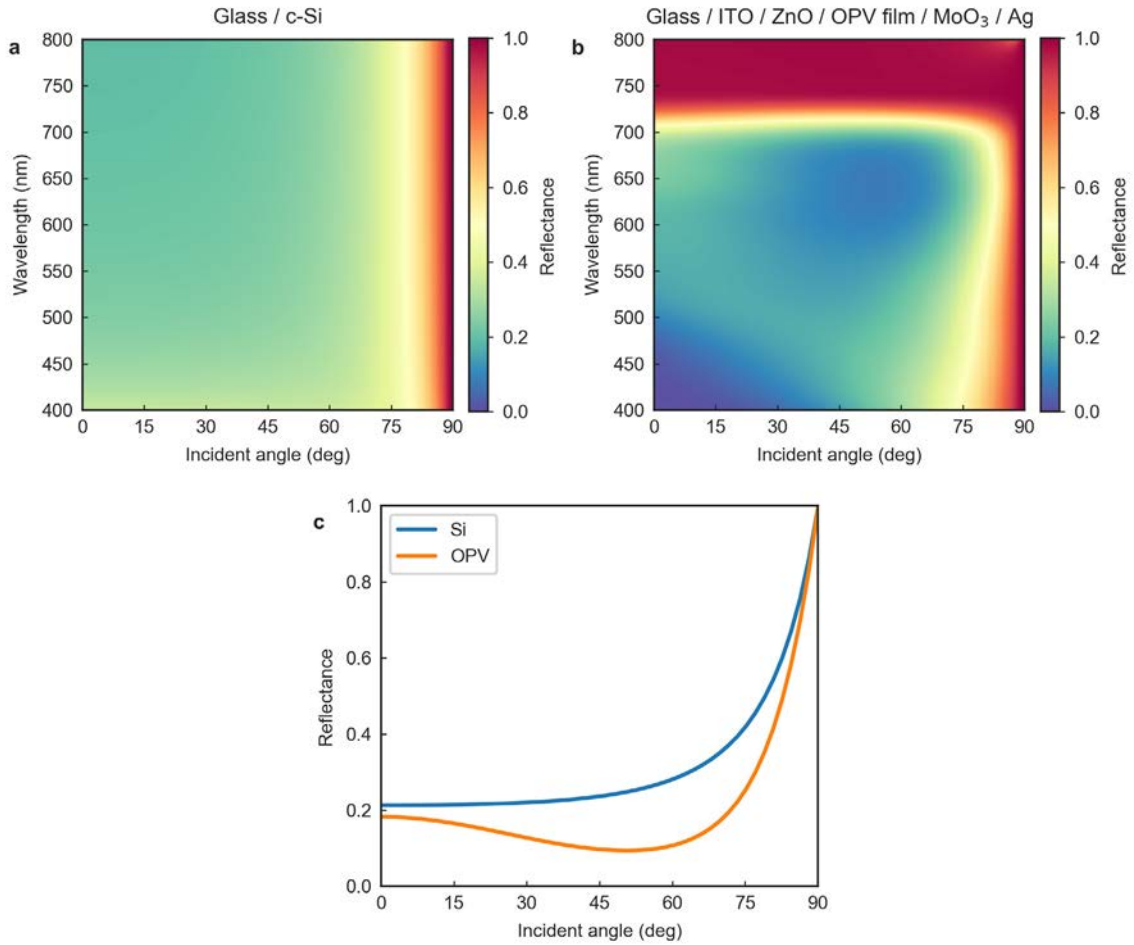
Figure 2. Transfer matrix modelling of non-polarized light showing the angular dependence of the reflectance in (a) a crystalline silicon wafer with a thick glass encapsulant; and (b) a state-of-the-art organic solar cell supported on glass. Panel (c) depicts the corresponding reflectance profiles calculated for incident monochromatic excitation at 600 nm. For the modelling of the organic solar cell in inverted geometry, the following thickness values were considered: 100 nm for the ITO; 30 nm for the ZnO; 150 nm for the active layer of PffBT4T-2OD:PC$_{70}$BM (1:1, w:w); and 5 nm for the MoO$_3$ interlayer. Visual inspection of these two panels suggests that in OPV devices the variations of the incident angle are less detrimental (and even beneficial)[11] for the reflectance, thus maintaining high PCE in cloudy or indoor environments.

Furthermore, OPV offers a unique technological advantage among its competitors, which is its compatibility with roll-to-roll (R2R) processing. Since all interlayers in organic solar cells can be entirely realized from an ink precursor, its complete manufacture can follow well-mature printing industry standards similar to those employed in press printing. Web speeds as high as 60-300 m min^{-1} are feasible, which together with low thermal energy requirements in subsequent printing and annealing steps (curing <140 °C in few minutes) result in energy payback times[3] (EPBT) of a few days only.[12] Their corresponding life cycle analysis demonstrates that OPV devices are truly efficient from fabrication to device disposal.[13] As a result, OPV positions as the most sustainable technology in terms of GHG emissions in the expected worldwide PV capacity growth.[14]

Organic solar cells are, thus, extremely versatile and aesthetically tunable.[15] They can be tailored as semi-transparent while keeping the PCE above 10%,[16] which encourages their integration into buildings or complex shapes (Figure 3). This feature includes windows, facades and greenhouses, forming the so-called building-integrated photovoltaics (BIPV) term. They are also lightweight and flexible, as the devices can be supported on plastic substrates such as polyethylene terephthalate (PET) or polyimide (PI, e.g. Kapton). Moreover, the use of nanometric films with low tensile modulus and large crack-onset strains in the device architecture prevents their malfunctioning upon bending.[17] This characteristic opens a new spectrum of unprecedented applications in textiles and foldable electronic devices that is exclusively fulfilled by OPV.

---

[3] The energy payback time (EPBT) is defined as the time invested by an energy source in generating the amount of energy required in its fabrication. Thus, the EPBT can be minimized either by increasing the efficiency of PV modules or by drastically diminishing the energy invested in their fabrication while keeping moderate efficiencies. Emerging PV technologies, and more specifically OPV, are framed in the latter case scenario.
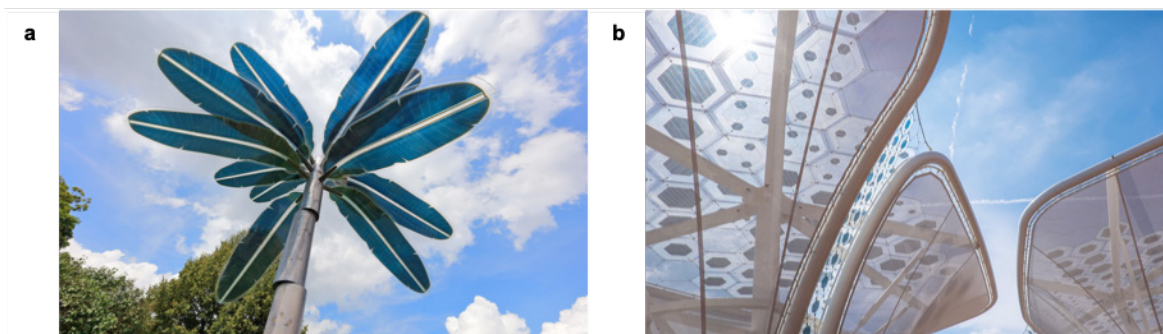
Figure 3. OPV offers the possibility to aesthetically integrate PV modules into complex curved shapes with notorious semi-transparency and colour tunability. (a) OPV Solartree ® developed by OPVIUS GmbH. (b) OPV trees in the German Pavilion at EXPO 2015 in Milan, courtesy of Merck.

Remarkably, OPV lab-scale devices have suffered a ca. 8-fold increase in photovoltaic performance over the past 20 years of research (Figure 4): starting from the 2-3% achieved in the early century for the archetypal MDMO-PPV:PC_{60}BM blend,[18] up to the current 18.2% PCE record obtained by blending low band gap co-polymers with new-generation non-fullerene acceptors (NFAs).[19] The 20% PCE milestone is yet to be achieved, albeit there are not any fundamental limits that impede overcoming such barrier and it is apparently a matter of time to be effectively realized, according to recent semi-empirical predictions.[20] On the other hand, forecasts dealing with device stability are equally encouraging, indicating that 10 years of operation in polymer:NFA blends are feasible.[21] With all that, current uses of OPV photovoltaic technology are focused on enabling off-grid energy sources in portable and lightweight electronic devices, mainly for indoor appliances. This is a particular field in which any other energy technology can nowadays compete. Concomitantly, in the upscaling of OPV modules the PCE is significantly reduced compared to lab-scale prototypes, thus the current possibilities of OPV to compete against silicon industry as the major (and massive) solar energy producer are still low. Nevertheless, OPV shows large room for improvement in both aspects: PCE and stability, and further progress is undoubtedly expected in the coming years while keeping its intrinsically low CO_2 footprint.[22]
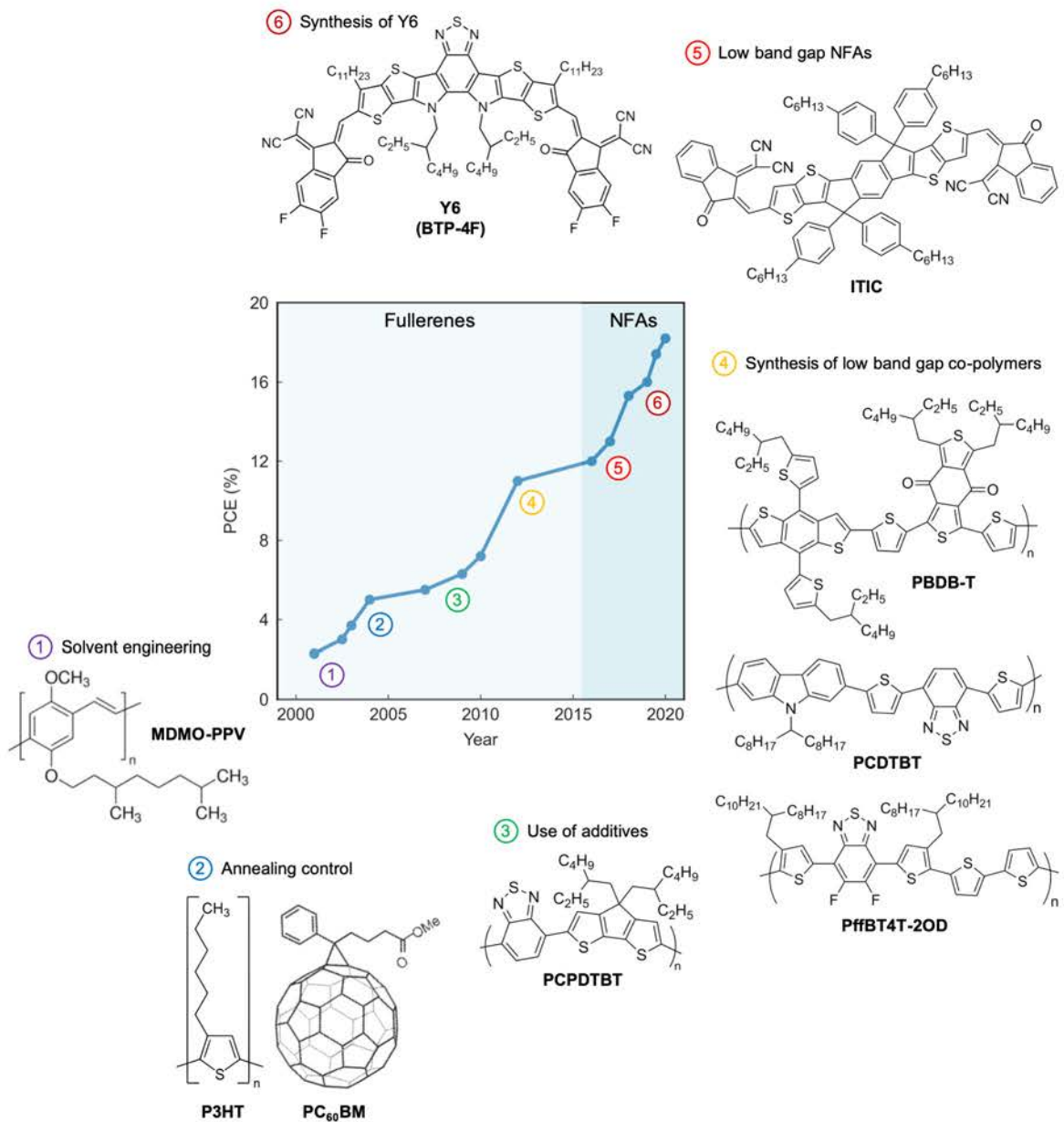
Figure 4. Record PCE chart of OPV lab-cells during the past 20 years of research. Important milestones related to processing, active layer morphology and chemical design of materials enabled the technology to keep up growing until reaching PCE figures unthinkable only ten years ago. Data adapted from NREL Best Research-Cell Efficiency Chart and reference [23].

21

3.1.   The photovoltaic effect and its derived technologies

The photovoltaic effect was first described by Becquerel in 1839 using silver chloride coated on platinum electrodes: he observed that upon illumination of such system, an electrical current and a voltage was generated.[24] Decades after, the full physical picture of the photovoltaic process was understood (Figure 5): upon interaction of an incoming photon with an electron in the valence band of a semiconductor, the electron is promoted to an excited state in the conduction band (light absorption) while leaving a hole or vacant in the valence band; such electron-hole pair is termed an *exciton*. Such exciton is then dissociated thanks to either intrinsic thermal fluctuations (in inorganic semiconductors such as silicon) or by a band offset arising at a *p-n* heterojunction, namely a donor:acceptor interface in organic semiconductor blends. The free charges are eventually collected in the corresponding electrodes thus generating an electrical current. A deeper physical picture of the photovoltaic effect reveals that for excitons to be dissociated into free charges their corresponding binding energies E_b must be overcome.[4] Otherwise, the electron-hole pairs recombine either radiatively or non-radiatively dropping the PCE.
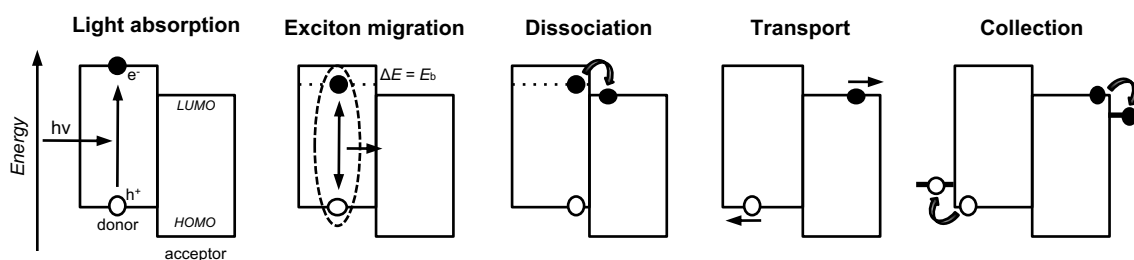
Figure 5. Energy diagram sketch of the photovoltaic process in excitonic solar cells, which can be divided into a list of sequential processes: (i) light absorption and formation of an electron-hole pair or exciton; (ii) exciton migration towards a donor-acceptor interface; (iii) exciton dissociation via charge transfer (CT) states; (iv) transport of free charges; and (v) collection at the corresponding electrodes.

---

[4] The exciton binding energy for weakly bound Mott-Wannier excitons reads $E_b = q^2 (4\pi\varepsilon_r\varepsilon_0 r)^{-1}$ in analogy to a usual Coulomb interaction between two elementary charges (q) separated by a distance r in a medium with relative permittivity ε_r, being ε_0 the permittivity of vacuum.

Historically, photovoltaic technologies have been dominated by crystalline silicon (c-Si) due to physical, fundamental and commercial reasons that facilitated the development of the technology at its early stages. From a fundamental point of view, the dielectric constant in such bulk semiconductor is large ($\varepsilon_r \approx$ 10-15), which promotes an effective screening of the Coulombic interaction between the photogenerated holes and electrons. As a result, the exciton radii are large enough to interact with the bulk crystalline lattice, which in combination with the intrinsically low effective mass for the holes and electrons in silicon makes the exciton dissociation a spontaneous process. In fact, the exciton binding energies (E_b) are well below $k_B T$ at room temperature (25 meV), which implies that the own thermal fluctuations of the system serve to efficiently separate and collect the free charges in a single-junction device. These loosely bond excitons are known as *Mott-Wannier excitons* and are characteristic of inorganic materials in general.

Other novel photovoltaic technologies that rely on thin film photoactive layers have been introduced since then, including amorphous silicon (a-Si:H), gallium arsenide (GaAs), copper indium gallium (di)selenide (CIGS) and CdTe, forming the so-called second generation PV. Thin film technologies are industrially appealing due to their inherent lower use of raw materials in the module manufacture. Still, the core materials usually require processing via vacuum deposition methods, which increase the cost-performance ratio of the commercial modules despite being the current record holders for the PCE in single-junction devices, namely GaAs with 28.8%.[25] Second generation PV devices are in general rigid, brittle and many of them include highly toxic (As, Cd) and scarce materials (Te) on their core, a fact that further limits their recyclability and long-term development. Nevertheless, notorious efforts are being drawn in transferring some of such material systems onto flexible substrates, either PI[26] or metal foils,[27] a fact which is expected to enable their compatibility with R2R manufacturing and bridge the cost-performance gap in the following years.

Inspired by photosynthetic tissues, D. Kearns and M. Calvin first observed the photovoltaic effect using organic systems in 1958.[28] Almost 30 years later, in 1986, C. W. Tang et al. introduced the two-layer organic photovoltaic cell,[29] which is

currently considered as the starting point of OPV research. Only 5 years later, O'Regan and Grätzel pioneered dye-sensitized solar cells (DSSCs) to get PCEs beyond 7%,[30] which supposed a giant leap in efficiency enhancement for organic dyes as absorbers. In 1995 an almost simultaneous publication by A. J. Heeger et al. in *Science*[31] and A. B. Holmes et al. in *Nature*[32] introduced a key milestone in the OPV field, as it substituted the pristine bi-layered, evaporated heterojunction by a solution-processed bulk heterojunction (BHJ) with enhanced photogeneration efficiencies in solar cells and photodiodes, respectively. Third generation PV had just hatched.

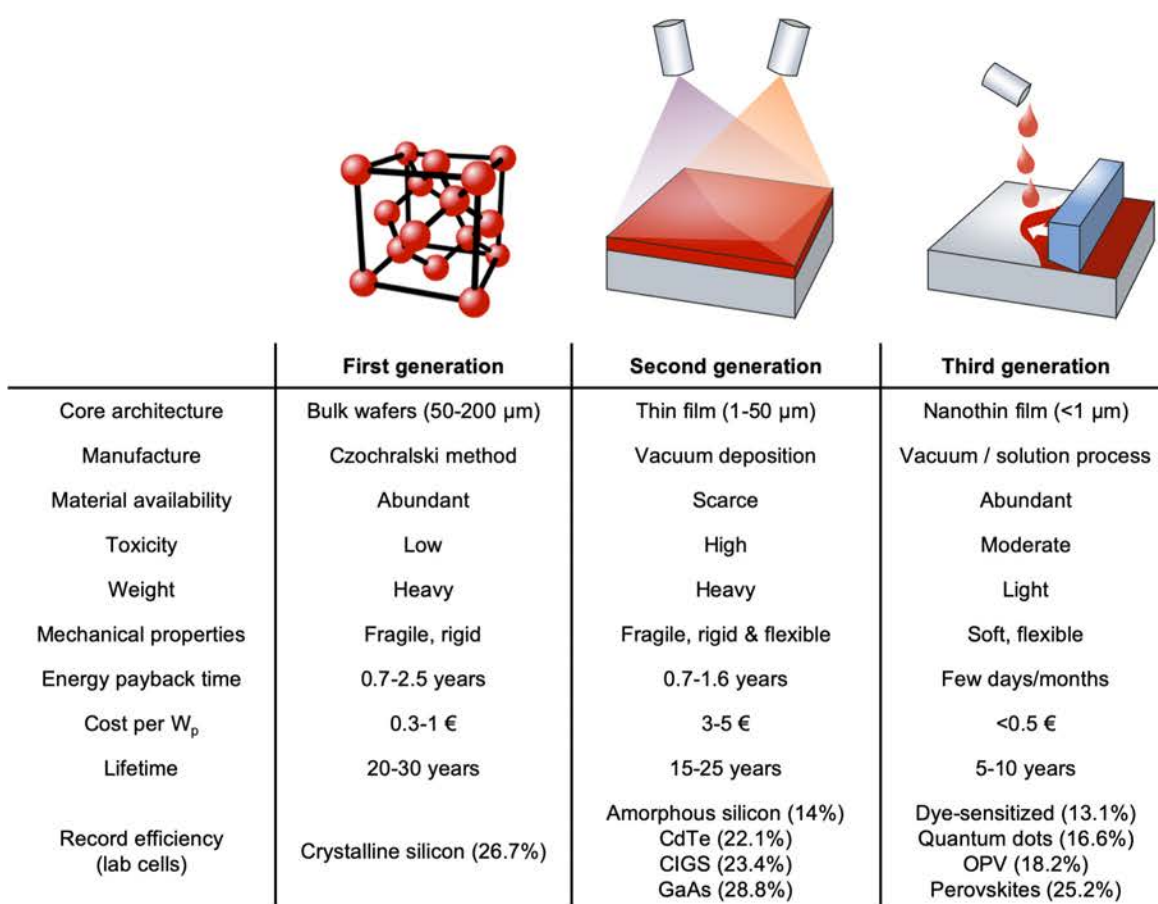|	First generation	Second generation	Third generation
Core architecture	Bulk wafers (50-200 μm)	Thin film (1-50 μm)	Nanothin film (<1 μm)
Manufacture	Czochralski method	Vacuum deposition	Vacuum / solution process
Material availability	Abundant	Scarce	Abundant
Toxicity	Low	High	Moderate
Weight	Heavy	Heavy	Light
Mechanical properties	Fragile, rigid	Fragile, rigid & flexible	Soft, flexible
Energy payback time	0.7-2.5 years	0.7-1.6 years	Few days/months
Cost per W_p	0.3-1 €	3-5 €	<0.5 €
Lifetime	20-30 years	15-25 years	5-10 years
Record efficiency (lab cells)	Crystalline silicon (26.7%)	Amorphous silicon (14%) CdTe (22.1%) CIGS (23.4%) GaAs (28.8%)	Dye-sensitized (13.1%) Quantum dots (16.6%) OPV (18.2%) Perovskites (25.2%)

Figure 6. PV technologies are historically divided into three main categories: first, second and third PV generations. First generation is a well-mature technology based on crystalline silicon PV modules of remarkable efficiency and lifetime yet too expensive and heavy for use in portable electronic devices. Second generation PV offers notorious material savings motivated by the use of thin films rather than bulk wafers; however, they require both expensive and scarce raw materials as well as vacuum or chemical vapour deposition (CVD) manufacturing approaches to be realized. Third generation PV offers unbeatable EPBTs, lightweight and flexibility due to their ease of processing from solution and minimal use of raw materials in the form of nanometric device stacks. EPBTs, cost per W_p, lifetimes and record efficiencies were taken and some of them estimated from a variety of literature references.[5,13,21,22,25]

Apart from organic solar cells and DSSCs, the term third generation PV gathers other emerging thin film technologies such as quantum dot solar cells (QDSCs) and perovskite solar cells, the latter being introduced very recently (in 2009).[33] They all share promising features compared to previous PV generations (Figure 6), such as minimal EPBT, lightweight, flexibility and large potential for low-cost manufacture in R2R setups. Despite the long-term stability and the absolute achievable PCE represent their main current limitations, the youth of such emerging thin film technologies inspires and encourages the researchers to keep on working to overcome such restrictions.

Conversely to inorganic crystals, upon light absorption the organic absorbers originate highly localized excited states and tightly bound electron-hole pairs (known as *Frenkel excitons*) due to their low dielectric permittivity ($\varepsilon_r \approx$ 3-4). In these systems the exciton binding energies are well above $k_B T$ at room temperature ($E_b \geq 0.5$ eV); this results in exciton lifetimes of the order of 1 ns and diffusion lengths below 10 nm.[34] Therefore, the exciton dissociation requires the existence of a driving force to overcome the large electrostatic interaction, and that should be precisely found within its average diffusion length.

C. W. Tang et al. first observed that such force originates at the interface between an organic absorber and a second organic species with higher electron affinity.[29] At such interface, the photogenerated electron (typically generated in the material with lowest electron affinity, i.e. the donor) is accepted by the material with larger electron affinity (i.e. the acceptor). It is precisely that difference in electrochemical potential what promotes the exciton dissociation in the vicinity of a donor-acceptor heterojunction. In the process, interfacial charge transfer (CT) states are formed prior to the charge collection at the corresponding electrodes. This sophisticated photophysics implies that finely intermixed blends of organic materials are needed to drive the exciton splitting in organic solar cells. More precisely, they ought to be blended at the nanometric scale given their limited exciton diffusion length, yet forming a continuous phase to enable the transport of the free charges to the contacts: the so called BHJ film morphology. As expected, the blending ratio

between donor and acceptor materials will largely influence the final device performance in such film architectures.

3.2. Organic semiconductors

Organic solar cells are named after the nature of their active layer components, i.e. a heterojunction of organic semiconductors. These are molecular solids whose main skeleton is formed by σ bonds established between sp^2-hybridized carbon atoms (Figure 7a). The remaining unhybridized $2p_z$ atomic orbitals interact to form the π bonds, originating the characteristic alternation of single (C-C) and double (C=C) bonds known as π-conjugation (Figure 7b). Electronically, the π-conjugation confers these materials the ability to delocalize the electronic wavefunction above and below the σ plane. This fact enables charges to easily travel along and between nearby molecules via intra- and intermolecular hopping. Structurally, the π-conjugation increases the rigidity of the molecule, which helps the backbones to self-assemble into ordered molecular crystals guided by the π-π van der Waals interactions or π-π stacking. Also the interdigitation of the side chains, which enable the solution processability of large molecular weight systems such as conjugated polymers, might drive the formation of ordered packing motifs.[35] Apart from carbon and hydrogen, organic semiconductors may contain other heteroatoms such as sulphur, nitrogen, oxygen, fluorine and chlorine, which confer them singular optoelectronic properties due to the internal redistribution of the electronic density. Such heteroatoms can, however, have a detrimental effect in the molecular ordering by disrupting the π-conjugation and altering the crystalline arrangement of the molecules.
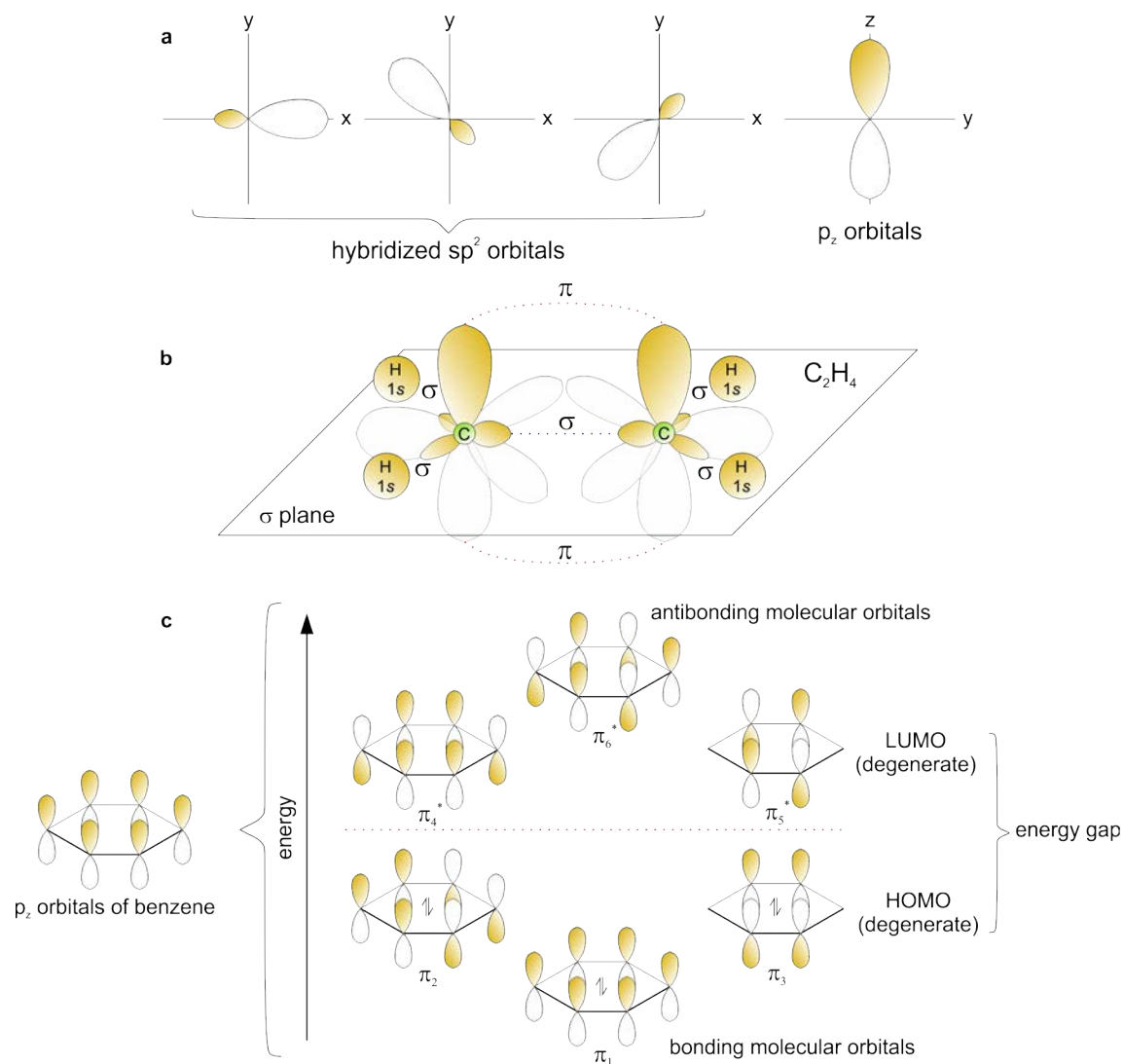
Figure 7. (a) In organic semiconductors, the four unpaired electrons of carbon atoms ($1s^2$ $2s^1$ $2p_x^1$ $2p_y^1$ $2p_z^1$) hybridize onto three sp^2 orbitals and a remaining p_z orbital ($1s^2$ $(2sp^2)^3$ $2p_z^1$). (b) The ethylene molecule (C_2H_4) represents the simplest system based on hybrid sp^2 carbon orbitals to show the formation of σ and π bonds. The π bond delocalizes the π electron at both sides of the σ plane. (c) In a benzene molecule (C_6H_6) there are six π electrons, thus three bonding (π_i) and three antibonding (π_i^*) molecular orbitals which delimit the HOMO and LUMO frontier energy levels. Between them, a forbidden energy band gap is established for the electronic states. This originates the semiconducting properties of conjugated materials.

Upon the formation of the π bonds, bonding (π) and antibonding (π^*) molecular orbitals arise originating a band gap in the density of electronic states (Figure 7c), in analogy to what occurs in inorganic crystalline semiconductors with the valence and conduction bands. In molecular crystals, the molecular orbitals substitute such bands due to the lack of long-range periodicity to apply Bloch's theorem. Consequently, the highest occupied molecular orbital (HOMO) is considered as the edge of the valence band whereas the lowest unoccupied molecular orbital (LUMO)

corresponds to the edge of the conduction band. While the HOMO is quantitatively ascribed to the ionization potential, the LUMO is identified as the electron affinity. In practice, such simplified model works to understand the main optoelectronic processes in organic semiconductors and serves to highlight the importance of the frontier energy levels alignment of a full device stack.

In Figure 8 we illustrate a selection of conjugated polymers and small molecules of frequent use in OPV. Organic semiconductors, as common inorganic semiconductors, can be classified into *p*- or *n*-type depending on the type of electrical conduction observed in the corresponding field-effect transistor (FET), forming either *p*- or *n*-channels.[36] A decade ago, however, it was generally observed that the conduction characteristics are limited by traps in the gate dielectric or in the own semiconducting layer, such as oxygen in the case of P3HT.[37] Hence, in the absence of traps, organic semiconductors are intrinsically ambipolar, which implies that they can conduct either electrons or holes depending on the device configuration and the processing or testing conditions followed (e.g. air or inert atmospheres).[36] As a result, the classification between *p*- and *n*-type organic semiconductors is often performed according to the magnitude of the measured (bulk) mobility for holes (*p*-type) and electrons (*n*-type) in hole-only or electron-only space charge limited current (SCLC) devices or time-of-flight (TOF) experiments.

The differences in charge mobilities between holes and electrons arise from the position of the Fermi energy relative to the HOMO and LUMO levels in the organic semiconductor, which determines which is the majority carrier in the material. This feature is in close relationship with the type of moieties forming the semiconductor, namely electron-withdrawing of electron-donating units (see below). Accordingly, *p*- and *n*-type organic semiconductors are usually denoted in the OPV community as electron donors and acceptors, respectively, based on the energy of their HOMO-LUMO levels. Note that for OPV applications the semiconductors are not extrinsically doped as in silicon PV; instead, the Fermi level is tuned by the structural and electronic particularities of the chemical structure, namely the choice of functional groups and substituents.[36]
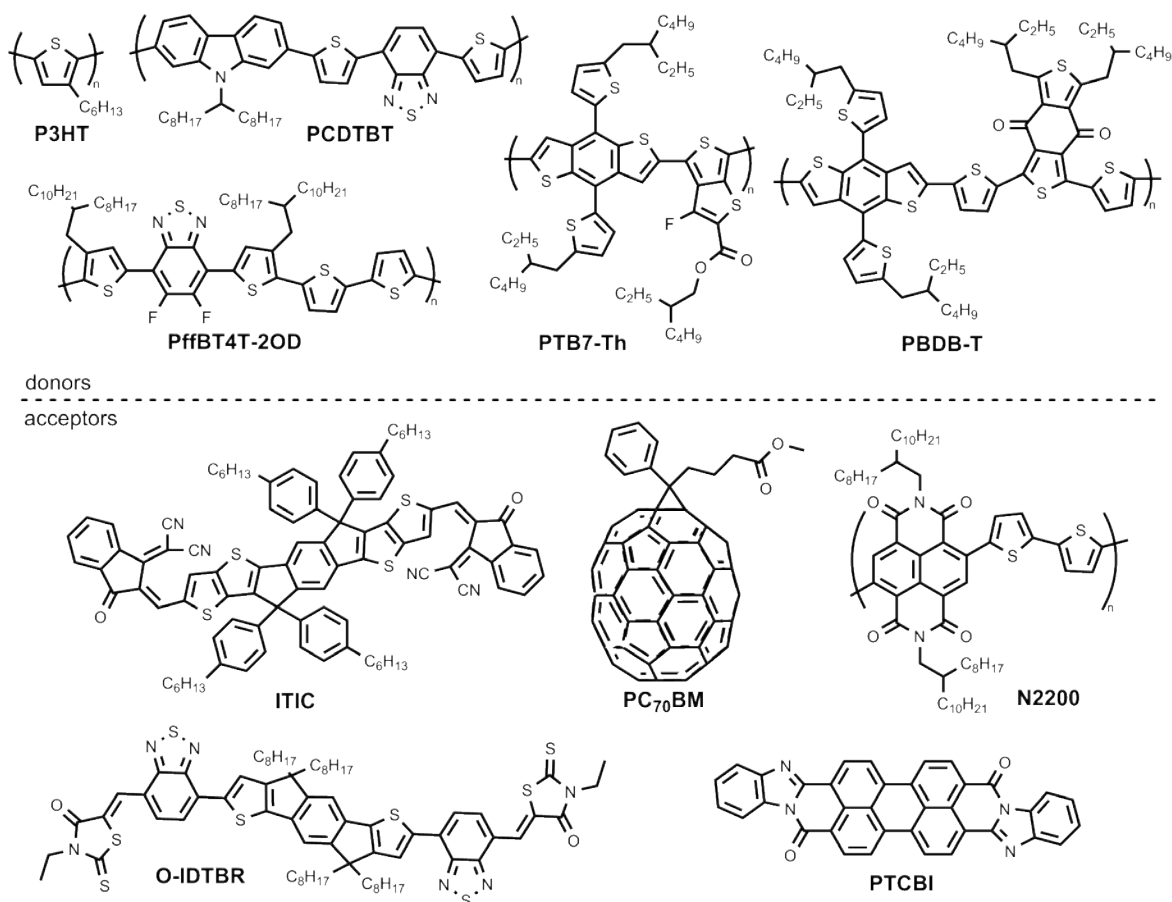
Figure 8. Organic semiconductors are characterized by a skeleton of sp²-hybridized atoms that result in an alternation of single and double bonds, a feature known as π-conjugation. Conjugated polymers such as P3HT, PCDTBT, PffBT4T-2OD, PTB7-Th and PBDB-T are typically used as electron donors in high-performing organic solar cells due to their low band gap and hole conducting properties. Conversely, conjugated small molecules such as PC$_{70}$BM, ITIC, O-IDTBR and PTCBI are characterized by high electron affinities, thus used as electron acceptors in the corresponding devices. Nevertheless, *n*-type polymers such as N2200 can also be used as acceptors in all-polymer organic solar cells.

Optically, the HOMO-LUMO energy gap is of striking importance. In most organic semiconductors such gap is of the order of the photon energies in the visible portion of the electromagnetic spectrum: ca. 400-900 nm or 3.1-1.3 eV. This fact, in combination with the acute oscillator strength of the π clouds (with extinction coefficients close to 2 in some cases, see Appendix),[38,39] leads to narrow albeit very pronounced absorption bands that match the peak photon flux of the solar emission spectrum (located at 500-600 nm), as depicted in Figure 9. Still, the long-wavelength fraction of the irradiance spectrum (900-1500 nm) is essentially wasted

and novel low band gap materials are desirable to obtain panchromatic absorption spectra in OPV devices.

In this regard, organic semiconductors offer a unique feature, which is the *à la carte* tailoring of the HOMO-LUMO energy levels to match specific requirements. Generally, the introduction of electron withdrawing moieties[5] in the conjugated backbone decreases predominantly the LUMO level of the material;[40] contrarily, electron donating groups[6] mostly increase the HOMO level. Thus, their co-polymerization into the same backbone is one of the most usual synthetic routes to obtain low band gap conjugated materials. This constitutes the so-called *push-pull effect*, or intramolecular charge transfer (ICT) between donor and acceptor moieties. Its origin can be understood from the formation of new hybridized molecular orbitals once the donor and acceptor units are covalently bonded within the backbone.[41] This strategy has been vastly followed to synthetize low band gap polymers and small molecules such as PCPDTBT or ITIC-C_2C_6, whose extinction coefficients are illustrated in Figure 9 with their maxima centred in the 600-800 nm interval.

Nevertheless, other aspects of the conjugated molecular structures might also be subjected to systematic fine-tailoring, including functional groups or atomic substituents in the main backbone; type and length of the side chains; as well as the choice of end capping groups in small conjugated molecules.

The incorporation of electron withdrawing fluorine atoms in a conjugated polymer backbone leads to a decrease in the HOMO level of the resulting material, which is an appealing feature in organic solar cells to enhance the open-circuit voltage (V_{oc}).[42]

---

[5] The electron-withdrawing moiety toolbox includes 2,1,3-benzothiadiazole (BT), thienopyrazine, thienothiadiazole, quinoxaline, thieno[3,4-*c*]pyrrole-4,6-dione (TPD) and pyrrolo[3,4-*c*]-pyrrole-1,4-dione (DPP), among many other examples.
[6] Some examples of electron-donating units are fluorene, silafluorene, carbazole, benzo[1,2-*b*:4,5-*b*]-dithiophene (BDT), cyclopenta[2,1-*b*:3,4-*b'*]dithiophene (CPDT), dithieno[3,2-*b*:2′,3′-*d*]-silole (DTS) and indacenodithiophene (IDT).
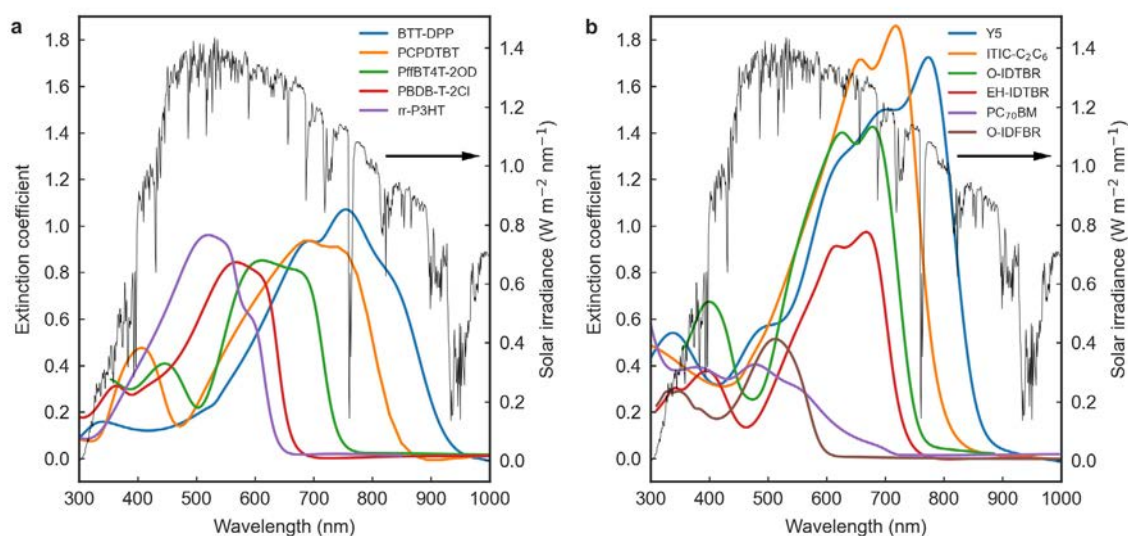
Figure 9. Extinction coefficient for a selection of organic semiconductors of typical use in OPV, namely (a) donor polymers and (b) small molecule acceptors. The materials herein plotted are intentionally selected to show the band gap tuning capability of organic semiconductors, which serves to improve their matching with the solar irradiance spectrum (illustrated as a thin solid black line in the background). The extinction coefficients of BTT-DPP, rr-P3HT and $PC_{70}BM$ are courtesy of Dr. Mariano Campoy-Quiles. The extinction coefficient of Y5 was measured by Dr. Valentina Belova (ICMAB-CSIC).

On the other hand, side chains modulate the solubility of the materials,[43] their processability and miscibility with secondary species,[44,45] and their capability to self-arrange into ordered π-stacks.[46] The latter constitutes a critical feature in organic thin-film transistors (OTFTs) to maximize the charge carrier mobility[46,47] as it enables more efficient transport pathways in the π-π direction. In this regard, also the molecular planarity, which can be enhanced by incorporating large aromatic fused-ring moieties into the backbone,[48–51] enables an efficient charge transport even in the absence of long-range ordered crystals.[52,53] Alkyl side chains, and more specifically their length and degree of branching, can have a significant effect in the optoelectronic and aggregation properties of the materials, as exemplified in Figure 9b for the extinction of O-IDTBR and EH-IDTBR films. These two small molecule acceptors structurally differ in the type of side chains only (*n*-octyl (O) and 2-ethylhexyl (EH), respectively), while a significant difference in their optical absorption onsets and absolute extinction coefficients is observed. The red-shifted absorption of O-IDTBR, which is increased even further upon annealing,[54] results

31

from the favoured tendency to crystallize of the *n*-octyl substituted indacenodithiophene (IDT) core.

Finally, end capping groups in novel small conjugated molecules such as ITIC[55] can be tailored to manipulate the extension of the intramolecular electron push-pulling effect. For instance, the incorporation of a methyl group in the pristine 2-(3-oxo-2,3-dihydroinden-1-ylidene)malononitrile end group of ITIC (ITIC-M) serves to raise its LUMO due to the weak electron-donating property of the methyl;[56] conversely, the addition of fluorine atoms (ITIC-4F) and their inherent electron-pulling effect reduces the LUMO level, thus enhancing the ICT and red-shifting the absorption spectrum.[57] These two end group modifications render critical to optimize the optoelectronic matching of the pristine ITIC with the target donor material in organic solar cells, thus significantly enhancing the final PCE with respect to the original ITIC counterpart.[56,58]
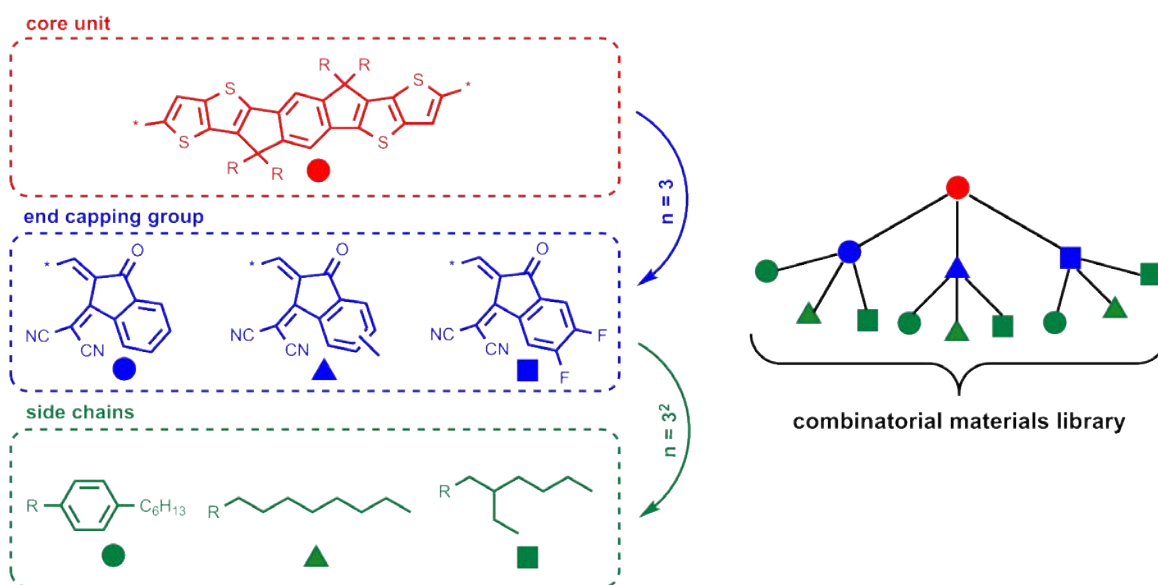

Figure 10. The structural variability of organic semiconductors, and hence the tunability of their optoelectronic properties, is enormous. In this example we select a seven-ring conjugated fused core as central unit (indacenodithieno[3,2-b]thiophene, IT, which is found in ITIC and its derivatives) and explore a combinatorial tree of materials by choosing first among three dissimilar end capping groups, and second among three different side chains. This depth-limited combinatorial tree already results in a materials library of 3^2 elements or leaves. Some of these molecules have already been synthetized, characterized and used in organic solar cells with excellent results (namely ITIC, ITIC-M, ITIC-4F, ITIC-C$_8$ and ITIC-C$_2$C$_6$); others have not been reported yet in the literature. Whether the unexplored systems are superior or not to those already known is a problem that computational screening and artificial intelligence (AI) algorithms are currently trying to unravel more systematically in combination with experimental high throughput screening approaches.

32

The multidimensionality of the structural and chemical tuning in organic semiconductors is certainly huge, and probably unfeasible to be realized systematically from an experimental point of view due to the exponential scaling of possible material combinations (Figure 10). In this regard, the use of computational approaches to pre-screen molecular motifs and select certain material candidates according to their optoelectronic properties is very useful to accelerate the discovery of novel semiconductors with improved performance. In this way, the experimentalists can concentrate their efforts on a few systems only. The Harvard Clean Energy Project exemplifies this idea as an on-going, high-throughput *in silico* screening of conjugated materials with potential use in OPV. These are classified based on their electronic properties (HOMO-LUMO levels) calculated by means of density functional theory (DFT) and the results are compared and calibrated with experimental data took from the literature. For OPV purposes, also the maximum PCEs of unknown materials are approximated using the Scharber model,[59] which was demonstrated to be a good prior in the identification of high performing polymer:fullerene combinations by using the band gap of the donor and the LUMO level of the acceptor. However, the Scharber model oversimplifies the optoelectronic processes occurring in organic solar cells and, in fact, it predicts a maximum PCE close to 15% due to intrinsic losses in the open-circuit voltage (estimated to be 0.3 V).[60] Given the current PCE record of 18.2%,[19] it is evident that the latest generation of organic semiconductors requires more advanced device models to properly match high-throughput computational and experimental screening procedures in terms of PCE predictions. In particular, a deeper understanding of the non-radiative energy losses[61–65] and charge transport dynamics[66] in organic solar cells have recently led to a famous mantra introduced by Prof. Eli Yablonovitch, who claimed that "*great solar cells have to be great LEDs*".[67] This sentence accounts for the absence of non-radiative energy losses in high-performing OPV devices, a feature which extends the lifetime of the photogenerated charge carriers. Eventually, this affects suppressing part of the recombination pathways and enhancing the V_{oc}, thus increasing the overall PCE (see below).

3.3. Organic solar cells

Organic solar cells constitute a family of electronic devices formed by a *p-n* junction of organic semiconductors that serve to generate electrical energy upon light illumination. They are, thus, light-sensitive diodes that obey the classical Shockley equation with an additional term that accounts for the photogenerated current (I_{ph}), namely

$$I(V) = I_0 \left(\exp \left(\frac{qV}{nk_BT} \right) - 1 \right) - I_{ph} = I_D - I_{ph},$$

where *I* is the current output; *V*, the voltage drop; I_0, the dark saturation current (i.e. the current flowing through the device under reverse bias in the dark); *q*, the elementary charge; *n*, the ideality factor; k_B, the Boltzmann constant; and *T*, the operating temperature. As dictated by the Shockley equation, in the dark (I_{ph} = 0) the solar cell operates as a usual diode (dotted line in Figure 11a), whereas upon illumination a photocurrent source in reverse direction to the forward bias (-I_{ph}) arises as a consequence of the photovoltaic effect (solid line in Figure 11a).
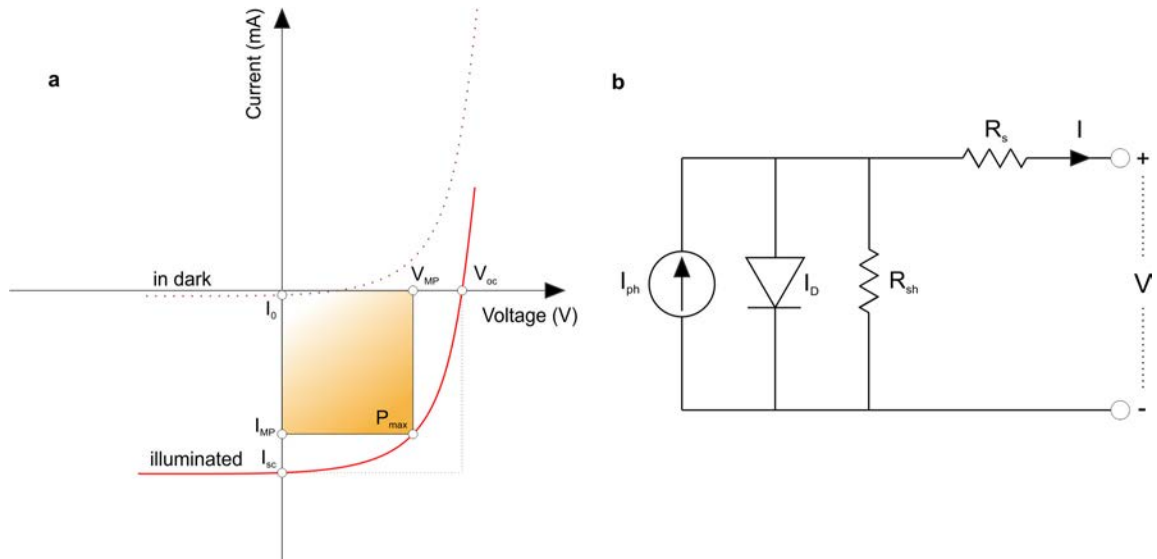

Figure 11. (a) The *IV* curve of a solar cell in the dark is equivalent to the *IV* characteristics of a *pn* junction or diode, thus showing an exponential, non-linear behaviour with *V*. Upon illumination, a photocurrent arises in reverse direction to the forward bias (-I_{sc}), thus displacing the IV curve towards the fourth quadrant. Therein, current and voltage have opposite signs, thus the diode generates net power (*P* = *VI* < 0). (b) Equivalent electric circuit of a solar cell. In an ideal behaviour, $R_{sh} \rightarrow \infty$ and $R_s \rightarrow 0$.

Nevertheless, the above Shockley equation applies in ideal devices only; in practice, the model includes a series resistance (R_s) and a shunt resistance (R_{sh}) to account for current losses at the interfaces and the bulk of the layers, as well as the existence of alternate conduction pathways (Figure 11b). Thus, the modified Shockley equation reads

$$I(V) = I_0 \left(\exp\left(\frac{q(V + IR_s)}{nk_BT} \right) - 1 \right) - I_{ph} + \frac{V + IR_s}{R_{sh}}$$

While R_s can be estimated from the slope of the *IV* curve close to the open-circuit voltage (V_{oc}) point, R_{sh} of a solar cell controls the magnitude of the slope of the *IV* curve in the vicinity of the short-circuit current (I_{sc}) point. Thus, V_{oc} is the forward voltage required to counterbalance the photogenerated current in the solar cell, and I_{sc} corresponds to the maximum photocurrent generated by the device, i.e. under no bias applied. These characteristic operating points are employed in the definition of the fill factor (FF), which reads

$$FF = \frac{P_{max}}{V_{oc}I_{sc}} = \frac{V_{MP}I_{MP}}{V_{oc}I_{sc}}$$

The FF measures the quality (or *squareness*) of the *IV* curve as a ratio of the maximum extractable power (P_{max}) with respect to the theoretical maximum power output at the V_{oc} and I_{sc} together. Finally, the power conversion efficiency (PCE) of solar cells represents the figure-of-merit used to compare the PV performance from batch-to-batch and between technologies, and it is defined as the maximum fraction of input power converted to electricity by the device:

$$PCE = \frac{P_{max}}{P_{in}} = \frac{V_{oc}I_{sc}FF}{P_{in}}$$

The above definition gathers the most characteristic device parameters provided by PV researchers during device prototyping, namely V_{oc}, I_{sc}, FF and PCE. Due to convention in the testing protocols, the air mass 1.5 global (AM1.5G) irradiance

spectrum is the most usual standard when measuring the corresponding *IV* curves under illumination and it sets P_{in} = 1000 W m^{-2}.

The device architecture of organic solar cells is formed by a stack of nanometric layers sandwiched between two electrodes, being at least one of them a semi-transparent contact. Two major device architectures are often considered: conventional and inverted structures, which can be differentiated depending on the polarity of the contacts (Figure 12). Inverted devices are industrially appealing due to their enhanced compatibility with R2R manufacturing, which is enabled by the possibility to print the silver back electrodes from nanoparticle inks or pastes. Silver also offers extra resistance against oxidation compared to aluminium electrodes (the standard in conventional architectures), thus enhanced stability. Indium tin oxide (ITO) sputtered on glass represents the most usual choice as substrate and transparent conducting front electrode, at least in lab-scale experimentation. ITO is, by far, the most expensive component in organic solar cells and it is being subjected to intense research for cheaper and solution processable substituents, such as graphite.[68]
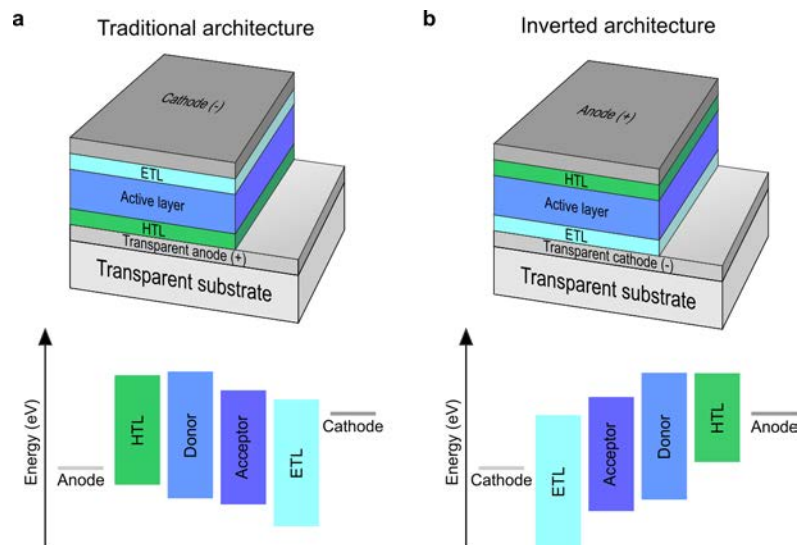

Figure 12. Organic solar cells are manufactured in either traditional (a) or inverted (b) architectures depending on the polarity of the contacts. The charge selective interlayers (either hole transport layers, HTL, or electron transport layers, ETL) are accordingly modified to tailor the electrode work function and favour the selective extraction of charges. The corresponding indicative energy level diagrams are depicted below.

The core of the device is the active layer, which is formed by a heterojunction of, at least, two organic semiconductors: an electron donating material or *p*-type semiconductor, and an electron accepting material or *n*-type semiconductor. These are commonly referred to as the donor and the acceptor, respectively. Hole- and electron-transporting interlayers are usually incorporated between the active layer and the electrodes to enhance the extraction of the photogenerated charges and the selectivity of the contacts. The choice of interlayer materials is performed according to their corresponding energy level alignment with respect to the work function of the electrodes as well as the donor's HOMO and acceptor's LUMO. The most usual solution-processed interlayers are ZnO, PEDOT:PSS, Spiro-OMeTAD and more recently transition metal dichalcogenides such as WS_2.[69] Thin evaporated interlayers such as LiF, MoO_3 and Ca are also used in lab-scale batches prior to the thermal evaporation of the metallic back electrode.

Regarding the active layer, donor:acceptor binary blends constitute the most usual selection to form the BHJ morphology. In this case, the materials are selected to maximize the driving force for efficient exciton splitting based on their HOMO-LUMO energy level alignment; as well as to widen the absorption spectrum by choosing materials with complementary absorption bands. Ternary blends, as well as quaternary blends, are currently one of the most investigated alternatives to the classical binary BHJ. Ternary BHJ blends offer the possibility to realize panchromatic absorption spectra, thus increasing the I_{sc} due to the maximized light harvesting efficiency, namely the external quantum efficiency (EQE); V_{oc} tuning via energy levels cascade alignment; and improved charge extraction in comparison with binaries.

3.4. Optimization of organic solar cells: a complex multi-parametric landscape

Organic solar cells are complex stratified devices: the simplest geometry includes a minimum of five different stacked layers. Each of them might be subjected to independent optimization in terms of thickness and composition, the latter being especially relevant in BHJ active layers. All these variables draw a complex multi-parametric landscape that eventually determines the PV performance. In the following paragraphs, we will briefly review the motivations to screen some particular device features, starting by the thickness of the layers; and how they should be optimized to reach the maximum efficiency for any OPV material system studied.

The different device interlayers of an organic solar cell are found in the nanometric scale: from 5-10 nm corresponding to the thin MoO_3 or LiF interlayers deposited prior to the metallic back electrode, to the 100-500 nm thick active layers. As a result, the whole device stack dimensions are within the visible electromagnetic spectrum regime (400-700 nm), thus it is subjected to coherent interference effects with the incoming light. This implies that the amount of light absorbed by the active layer depends on the thicknesses and complex refractive indices of the full optical device stack. Therefore, **the thickness of the active layer**, which is the major contributor to the overall device thickness, ought to be optimized for each donor:acceptor blend selected.

For organic semiconductors in general, thicker active layers result in maximized light absorption whereas thinner layers better extract charges. This is a common trade-off problem that arises when charge transport is a limiting factor for the PV performance.[66] The remaining interlayers, such as the charge-selective extracting layers, have a minor effect in the electric field distribution yet might be tuned to minimize the R_s as well as the exciton recombination.[70] Nevertheless, the effect that these interlayers have in the final device performance is minimal compared with the modulation induced by active layer thickness variations,[71–73] unless they are intentionally used as optical spacers for certain applications.[74] In this regard, transfer matrix modelling has successfully been employed to calculate the electric field distribution in the devices, using as model inputs the corresponding interlayer

thicknesses as well as their complex refractive indices.[75] Notably, transfer matrix modelling shows excellent agreement with the experimental trends observed in terms of I_{sc} as a function of the active layer thickness.[73] Typically, a rather linear increase of I_{sc} with thickness is first depicted (0-50 nm). Then, a mild oscillatory behaviour arises for moderate thickness values (50-150 nm) until a steady decrease of I_{sc} occurs for thick films (>200 nm), which results from the limited charge transport capability of organic semiconductors.

In addition to the active layer thickness, in BHJ devices **the donor:acceptor blending ratio** is critical for the device performance. Since donors and acceptors are often partially miscible substances, their corresponding multi-component mixtures can be studied in the form of phase diagrams, which are usually plotted against temperature. The blending ratio, together with the processing conditions followed to form the solid active layer (mainly temperature and carrier solvent), determine the type of thermodynamic phases that coexist once the film is dried. The resulting configuration of the solid-state mixture is usually termed as the film morphology.

Achieving optimal film morphologies for OPV applications requires having both species blended in the scale of the exciton diffusion lengths (ca. 10 nm) yet forming continuous percolating networks to the electrodes, ideally with minimal non-geminate recombination. For semi-crystalline polymers blended with fullerenes, it has been shown that slightly hypoeutectic concentrations with respect to the polymer loading result in optimal film morphologies: a two-phase arrangement of finely intermixed donor:acceptor domains together with large fullerene crystals.[76] While the intermixed regions assure high charge-transfer efficiency for the exciton dissociation, the pure fullerene domains and their inherent large electron mobility favour the charge extraction.[77] This leads, in average, to optimal donor:acceptor ratios close to 1:1 (w:w), which is the usual guess first considered by OPV researchers when exploring novel binary systems.

However, there is not any particular reason why all donor:acceptor pairs ought to have its optimal blending ratio close to the even mixture. In fact, there are examples

of donor:acceptor pairs which show acutely unbalanced optimal ratios, such as PCDTBT:PC$_{70}$BM[78] or APFO-3:PC$_{60}$BM[79] both showing its maximal performance in 1:4 weight ratios. For comparative purposes, the same fullerene acceptors blended with the workhorse semi-crystalline donor polymer P3HT yield more balanced mixing ratios, namely 1:0.7 and 1:0.9 for P3HT:PC$_{70}$BM[80] and P3HT:PC$_{60}$BM,[81] respectively. A unified model that is able to explain these compositional differences is still missing, so researchers associate the observed dissimilarities to several material-related features. These include different oscillator strengths, degree of complementary absorption with the sun irradiance and between blended species, unbalanced charge carrier mobilities or material miscibility. Thus, finding the optimal blending ratio constitutes a searching problem that must be solved individually in each donor:acceptor material system considered.

The film morphology is not exclusively controlled by the donor:acceptor ratio but there are additional processing mechanisms that have influence in the drying dynamics of the pristine inks, thus determining the type and number of thermodynamic phases obtained in solid-state. These include, among others, the choice of solvent,[82] the use of additives,[83] the casting temperature[84] and the casting methodology employed.[85,86] However, post-processing treatments such as **thermal annealing** are the most usual procedure followed to fine-tune the as-cast kinetically-trapped film morphology. Thermal annealing can sometimes drive the convergence of dissimilar film morphologies into a unique and optimal configuration in the solid-state erasing the previous processing history.[84]

Thermal annealing in binary polymer:small molecule mixtures can result in extended phase-separation due to energetic reasons: starting from a kinetically-trapped and out-of-equilibrium morphology, and given enough (thermal) energy to the system, the blend phase-separates until eventually reaching its miscibility limit. This is a typical situation encountered in blends of materials that have a strong tendency to crystallize or, alternatively, materials with low entropy of mixing such as polymer:polymer blends. In polymer:small molecule blends, the bulkier species (usually the donor polymer with respect to the acceptor small molecule) diffuses more slowly, especially if the annealing temperature is kept below the corresponding

glass transition temperature (T_g) of the polymer matrix. This leads to larger and purer acceptor domains first,[87] and eventually to a pronounced phase separation between the species (up to the miscibility limit) and device failure. Consequently, there exists an additional trade-off in terms of annealing temperature and time to tailor the film morphology and enhance the final PCE.[88] In some OPV material systems the relative performance increase with respect to unannealed devices can raise beyond 40%.[89] In overall, this complex multi-parametric optimization scenario including active layer thickness, blending ratio and annealing temperature as the main free parameters of the active layer for a given material system, requires careful exploration.

Systematic Edisonian approaches are the general choice when facing this kind of problems in the laboratory, despite being extremely expensive in terms of experimental time and resources. Edisonian experimentation relies on exploring the parametric combinations individually, sample by sample, through intensive device prototyping. In practice, the screening process is so tedious that most researchers limit their exploration to certain "typical" figures, such as the 1:1 (w:w) blending ratio or an active layer thickness close to 100 nm. Importantly, the existence of acute landforms or multi-modal distributions in the performance space might be disregarded when sticking to narrow parametric ranges, thus leading to incomplete and/or wrong conclusions when screening novel material systems. That is precisely found in the upcoming generation of ternary OPV blends, in which the compositional optimization problem contains an extra dimension hence adding complexity to the parametric landscape. In this particular case, researchers usually keep fixed the total *n*- and *p*-type loadings while varying the relative contribution of the materials with the same electronic character. In ternary blends, multimodal photocurrent landscapes have already been demonstrated (see Paper V in this thesis) indicating that the traditional optimization route employed so far is too simplistic. Therefore, extrapolating Edisonian optimization routines to the massive screening of material families such as the recently introduced NFAs and multi-component OPV blends (ternaries or quaternaries) make the optimization problem as hard as *finding a needle in a haystack*. This is accordingly envisioned as one of the major bottlenecks in the OPV progress for the following years. Thus, the development of more

advanced, time- and resources-efficient screening approaches is of high interest in the organic electronics community to speed up the growth of all its thin-film related technologies, such as OPV.

High-throughput experimentation approaches such as those based on combinatorial screening have been applied to solve multi-parametric problems in a variety of systems, including drug discovery,[90] material synthesis[91] and chemical physics.[92] The term *combinatorial screening* refers to the process of finding maxima (or minima) in certain target function, which can take finite values within a large configuration space. Experimentally, combinatorial screening routines can be based on either fabrication-intensive or measuring-intensive approaches. Fabrication-intensive protocols require the use of advanced robotics to systematically explore the multi-parametric configuration space and the design of self-driven laboratories.[93,94] This approach circumvents the technical limitations ascribed to *purely human* experimentation; however, they yet require large amounts of raw materials and devices to be fabricated or cannot be directly related with the PV performance due to processing limitations.[94]
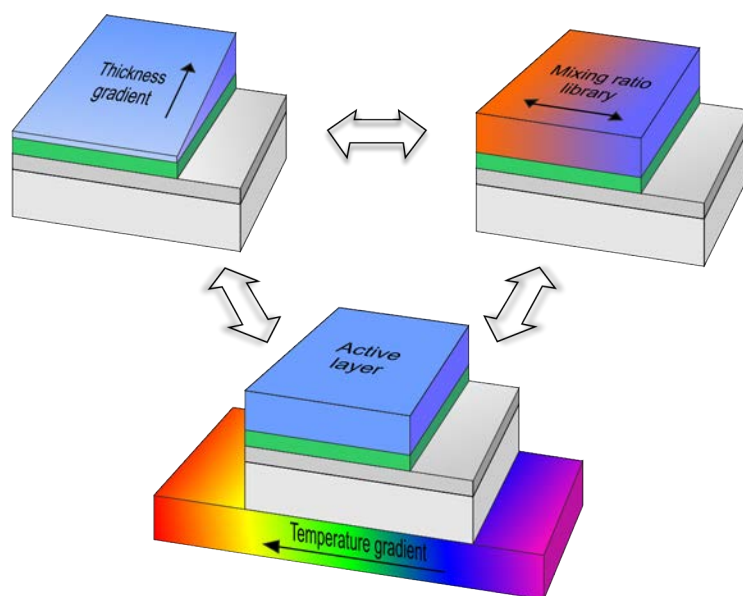

Figure 13. The generation of lateral parametric gradients enables high-throughput experimentation. In the case of organic solar cells, the active layer can be processed from solution to form thickness gradients, donor:acceptor mixing ratio libraries or thermal annealing ramps when combined with a controlled temperature stage such as a Kofler bench. Lateral parametric gradients or libraries accelerate the corresponding device screening when combined with laterally-resolving probing techniques that quantify the PV performance. Furthermore, lateral gradients can be combined orthogonally into 2D parametric libraries, a feature which doubles the screening rate and halves the resources consumption.

Conversely, measuring-intensive combinatorial approaches aim at making research *analogic*, i.e. gathering in a continuous and single sample most of the parametric variations of the target function. This serves to avoid the large demands of resources inherent to most fabrication-intensive routines. From the fabrication perspective, the continuous sampling is achieved by means of lateral gradients on the parameters of interest (i.e. parametric libraries), an approach that offers a minimal use of time and resources for the sample preparation. Time savings are particularly important when the time associated to fabrication is much longer than the time for measuring the device, as is the case in OPV. On the other hand, the parametric libraries require advanced local probing techniques having enough lateral resolution to spatially-resolve the investigated gradient. In addition, they should also be able to quantify the target function. The extrapolation of this approach to OPV is straightforward: by combining active layer thickness, composition and/or thermal annealing gradients, the corresponding multi-parametric configuration space can be explored in a high-throughput manner and minimizing experimental demands (Figure 13).

Undoubtedly, gradient-based optimization approaches can offer unbeatable exploration rates while leading to the same parametric scenario found when employing discrete approaches. This is, in fact, one of the key features of the high-throughput methodology that needs to be experimentally verified: whether Edisonian and gradient-based exploration approaches lead to the same results in terms of optimum device parameters despite following a rather different processing scheme. This aspect is especially critical in organic solar cells since the intricate morphology of the active layer is sensitive to the processing conditions and an essential feature towards the achievement of top-performing devices.

Moreover, measuring-intensive combinatorial routines are intrinsically able to generate large amounts of data points per sample, which is a consequence of the intrinsic continuity of the gradient-based parametric profiles. As example, a single organic solar cell containing a parametric library of at least two parameters on its active layer (namely thickness and blending ratio) typically results in an experimental dataset formed by 24000 dissimilar thickness-composition combinations. Such figure shapes most of the multi-parametric landscape of any

OPV blend, which apart from determining the optimal device parameters also serves to habilitate data-driven applications. In particular, the synergic combination of high-throughput screening with AI algorithms can provide material scientists novel hints in the design of next generation organic semiconductors. AI models can potentially be converted as well into artificial magnets to rapidly locate *the needle in the haystack*, pushing the screening rate of OPV materials and devices to unprecedented levels.
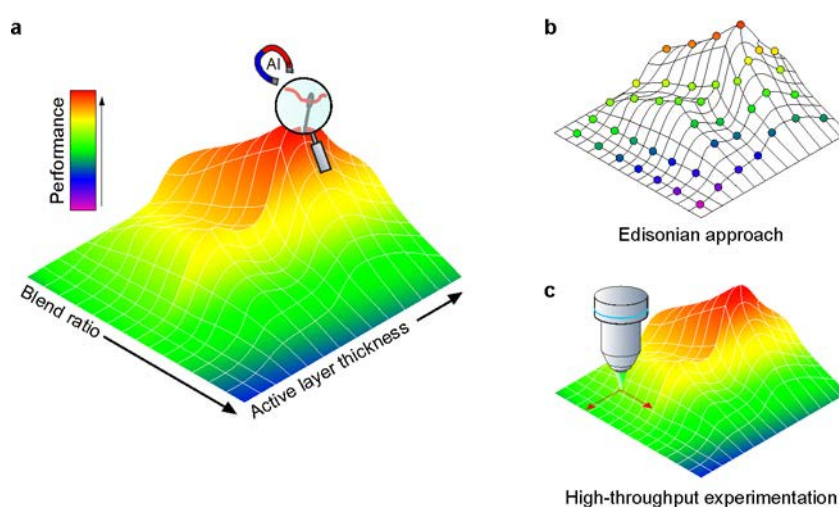

Figure 14. (a) The optimization of the device performance in organic solar cells is similar to *finding a needle in a haystack*: a complex multi-parametric energy landscape is encountered. When exploring the corresponding phase space, (b) Edisonian approaches rely on the systematic and discrete exploration of the involved parameters whereas (c) high-throughput experimentation routines are based on the combination of parametric libraries with local probing techniques. The combination of high-throughput approaches with AI algorithms can provide the researchers enough tools to build *a magnet* and quickly locate *the needle*.

4. Global summary and discussion

The work related to the core objectives of this thesis resulted in the confection of six articles, five of which have already been peer-reviewed and published in high impact factor academic journals. The remaining one has been recently submitted and is currently under peer-reviewing process. Their contents will be briefly reviewed in this short introductory section and analysed in more detail in the corresponding subsections, yet the full manuscripts and their supplementary information are attached after the main text of this thesis. A branched scheme of the papers and their topics is presented as a guideline in Figure 15 to help the reader in following the thematic distribution of the works.

The main objective of this thesis consists of developing a high-throughput fabrication and characterization methodology to be applied in the combinatorial optimization of organic solar cells. This is achieved generating lateral parametric *gradients* of the most sensitive device features as far as PV performance is concerned, namely active layer thickness, donor:acceptor ratio and thermal annealing.

Gradients or wedges comprise a continuous variation of the target parameters rather than a discretized exploration, thus forming a parametric *library*. When such library is spatially probed with enough lateral resolution and locally correlated with the PV performance, the exploration of the multi-parametric space that determines efficiency of organic solar cells can be acutely accelerated. Therefore, for the gradients to be exploited as test beds for high-throughput combinatorial screening in organic solar cells, there is a need to develop material-selective characterization techniques that can spatially resolve the lateral variations of the gradient and correlate them with the local PV performance. This is actually the seed for the ulterior growing of the high-throughput screening platform and, as such, it constitutes the first milestone pursued during the development of this thesis. For this task, Raman spectroscopy in combination with photocurrent imaging are the techniques of choice due to their unique properties in terms of material selectivity, non-invasiveness, diffraction-limited lateral resolution and high-throughput data acquisition. The development of the characterization methodology was object of a

publication in *Journal of Materials Chemistry C* (**Paper I**), which is somehow the kingpin supporting the upcoming works of the thesis.
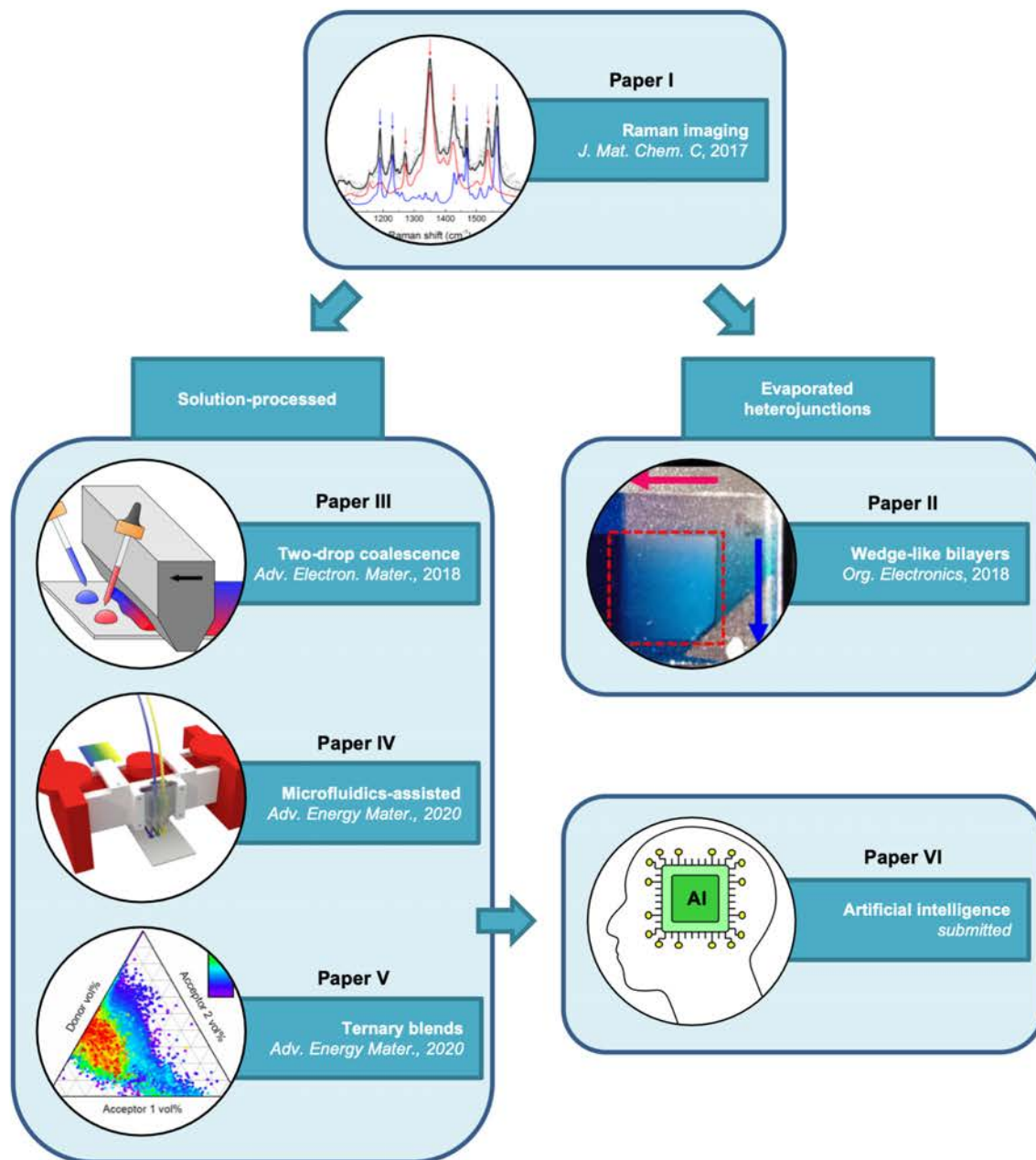

Figure 15. Branched guideline of the scientific articles developed during the present doctoral thesis and directly related to its core objectives.

For the generation of lateral gradients comprising organic semiconductors in the active layer of organic solar cells, we exploit two main processing routes, namely vacuum deposition and solution processing. Vacuum deposition is the standard manufacturing method for small molecule OPV structured as bi-layered heterojunctions. In this case, the generation of lateral gradients requires custom modifications to be implemented in the vacuum chamber, such as a movable mask to control the lateral thin film growth of the source materials. This task was developed by Dr. Juan Cabanillas-Gonzalez and his co-workers from IMDEA Nanociencia in Madrid, which provided us the full working devices comprising orthogonal gradients in their active layer. These devices served us to first test the Raman imaging methodology, ending with a publication in *Organic Electronics* (**Paper II**).

On the other hand, high-throughput experimentation based on lateral gradients is especially attractive for OPV due to the inherent solution-processability of its device interlayers. In particular, blade coating (*aka* doctor blading) is a suitable thin-film processing technique to realize thickness gradients.[95] Nevertheless, a general route for the generation of compositional gradients in solid-state films has not been reported yet and, as such, it required advanced processing approaches to be developed. For this objective, we explored two different approaches of increased complexity.

The first and simplest one is based on the coalescence of pristine donor and acceptor ink drops at the blade reservoir, which movement induces the chaotic advection of the solutions and an eventual dried film showing lateral compositional variations. This experimental approach is extremely simple to perform, resources-efficient and compatible to realize 2D parametric libraries in solid-state, as we demonstrate in our publication in *Advanced Electronic Materials* (**Paper III**) for binary OPV blends. This work was highlighted at the inside front cover of the corresponding journal issue.

However, the drop coalescence method is unsuitable for highly viscous inks such as those employed in all-polymer OPV blends. For this particular case scenario, we

developed more advanced processing setups that synergically combine microfluidics and blade coating. Microfluidics offers highly controlled, efficient and reproducible mixing in solution, which eventually results in smooth solid-state lateral compositional profiles when properly coupled with the blade coating apparatus. Importantly, this fabrication methodology can be generalized to all those solution-processable thin-film technologies that require solid-state lateral gradients, regardless the rheology of the inks employed. The manuscript of this work has been recently accepted for publication in *Advanced Energy Materials* (**Paper IV**).

High-throughput experimentation is even more demanded in ternary OPV screening than in binary blends due to the increased dimensionality of the configuration space in terms of composition. For this purpose, we introduced a general approach for the generation of ternary compositional libraries including a donor polymer and two small molecule acceptors. The approach is effective and experimentally simple to perform as it is based on the sequential deposition of the pristine inks to cover different regions of the corresponding ternary phase diagrams in several samples. This work has recently been published in *Advanced Energy Materials* (**Paper V**) and highlighted as cover picture of the corresponding journal issue.

The high-throughput screening capabilities of the here developed characterization and thin-film processing methodologies were finally exploited to perform an extensive combinatorial study of benchmark donor:acceptor binaries. This fact, jointly with the large experimental datasets generated, served us to feed AI algorithms to study the corresponding performance landscapes and their potential relationship with intrinsic features of the materials. More particularly, we focused on the existing dependence between the photocurrent, the donor:acceptor mixing ratio and the active layer thickness. As a result, we were able to draw general conclusions about them and to identify the most descriptive material features to build physically intuitive models. This enabled us to make accurate predictions out of the training materials dataset, as we detail in our recently submitted manuscript (**Paper VI**).

In the following subsections, we will review the main conclusions of each of the papers.

4.1.   Raman spectroscopy imaging of organic thin films

Since the discovery of the Raman effect in 1928 as the inelastic scattering of photons by matter, its unique properties have been extensively applied to a large range of fields: from tracking of biomarkers[96] or analysis of paintings,[97] to identification of microplastics in fish[98] or polymorphs in solid-state physics,[99] as we demonstrated for the case of methylammonium lead halide perovskites (MAPbX$_3$, X = I, Br, Cl) in a co-authored work that is not part of the compendium of the present thesis.[100]

The Raman effect takes place when an incoming monochromatic photon momentarily interacts with matter, more precisely with the electron distribution around a bond in a molecule. This promotes an electronic transition from the ground state to an excited electronic state, which can be either a *virtual* or a real energy level (Figure 16a). The photon re-emission upon electronic relaxation leads to Rayleigh (elastic) or Raman (inelastic) scattering depending on whether the emitted photon has the same energy as the incident one or not, respectively. Approximately 1 ppm of the scattered photons suffers energy losses (or gains), constituting the Stokes (or anti-Stokes) Raman scattering process. Accordingly, the energy gap (ΔE) between incident and re-emitted photons corresponds to the energy of vibrational states in the molecule. Thus, the Raman effect essentially consists of the optical activation of vibrational modes in the molecule. Nevertheless, the selection rules for a certain vibration to be Raman-active determine that the derivative of the polarizability with respect to the normal vibrational coordinate must be non-zero. This condition contrasts infrared (IR) spectroscopy, where the vibrational transition occurs when the normal mode causes a net change in dipole moment.
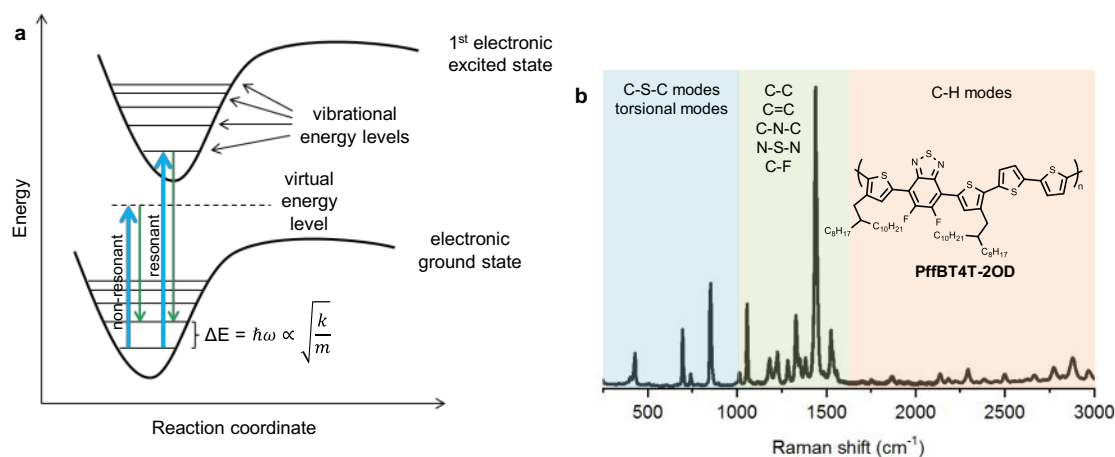
Figure 16. (a) Energy diagram of the fundamental electronic transition of a molecule along the spatial coordinate of a normal vibrational mode. (b) Raman spectrum of PffBT4T-2OD co-polymer measured at 488 nm excitation (resonant conditions). In conjugated materials at least three different energy windows are typically identified depending on the atoms involved in the vibrational modes.

The separation of the spectral components of the inelastically scattered photons by a spectrometer and the ulterior collection by a charge-coupled device (CCD) finally result in the Raman spectrum of a molecule, which is expressed in terms of wavenumbers (or Raman shift) with respect to the exciting photon energy (set as zero Raman shift, see Figure 16b). As Raman scattering is sensitive to the atomic masses (m) and electronic bond densities (k) of the molecular constituents,[7] the corresponding spectra can be exploited to identify chemical species based on their *vibrational fingerprint*, often in complementarity with IR spectroscopy. Interestingly, when the energy of the exciting photons matches a real electronic transition, the Raman process is accordingly amplified and termed as resonant Raman scattering (in contrast to non-resonant Raman scattering, Figure 16a).

Raman spectroscopy is of widespread use in organic semiconductors as a material indexing tool. This allows chemical identification in complex multi-component matrices by deconvolution of the experimental spectra according to *reference*

---

[7] The vibrational energy is quantized. Thus, in the absence of anharmonicity, the vibrational quanta can be modelled using the quantum harmonic oscillator approximation, which yields vibrational energy levels separated by an energy gap ΔE proportional to $(k/m)^{1/2}$. This expression is in close analogy with the classical harmonic oscillator problem formed by a mass (m) connected by a spring of elastic constant k. Therefore, the vibrational mode frequencies (or energies) will be accordingly increased for bonds showing higher electronic density (i.e. larger k, such that in general k(C-C) < k(C=C)) or lighter masses of the involved atoms (ΔE(C-C) < ΔE(C-H)).

vibrational libraries (see Appendix). Apart from the qualitative vibrational mode assignment (usually performed in combination with DFT calculations to aid in the indexation of modes), Raman spectroscopy has also been extensively used in the evaluation of domain order and degree of crystallinity in organic conjugated materials. This property results from fundamental studies performed in conjugated oligomers, which demonstrated that an extended conjugation length correlates with red shifted Raman mode dispersions of the characteristic C=C stretching modes.[101–103] Since domains with extended backbones and larger conjugation lengths also lead to red shifted absorption spectra,[104] resonant Raman scattering can be intentionally exploited to selectively probe the ordered or disordered counterparts depending on whether longer or shorter excitation laser wavelengths are employed, respectively; this is the so-called photoselective resonance scattering.[101,105] Since Raman band dispersion occurs also upon temperature variations, Raman spectroscopy can be employed to quantify the thermal conductivity of semi-transparent and free-standing thin films. That is precisely what we did via one-laser Raman thermometry in thermoelectric nanocomposites of bacterial cellulose and carbon nanotubes as part of a collaboration during the development of the present thesis.[106] Other uses of Raman scattering in organic thin films include probing the molecular orientation in anisotropic samples[107] as well as tracking phase transitions in neat and blended films.[100,108] This latter feature is often used to investigate the corresponding phase diagram and crystallization kinetics, which serve to properly tailor the final film morphology and match the desired optoelectronic properties (the so-called structure-property relationship). By exploiting the unique sensitivity of Raman spectroscopy against bond distortions and bending of dihedral angles, the degradation pathways of organic semiconductors such as NFAs have also been addressed.[109] This is expected to provide further insights on the operational stability of OPV materials in the upcoming years.

As a novel quantitative application of Raman scattering in organic thin films, in **Paper I** we developed a methodology that serves to quantify the film thickness and, in the case of multi-component blends, also their (volumetric) mixing ratio according to the weighted deconvolution of the overlapped, multi-component Raman spectra.

51

The approach is based on an accurate mathematical description of the Raman scattered intensity in a thin-film built using the transfer matrix method.[75] The formulation accounts for the interference of the incoming and scattered beams in multi-layered optical stacks. Film thicknesses and complex refractive indices for each layer should be known beforehand (Figure 17a). In pristine films, the quantitative analysis of the scattered intensity (I_R) as a function of thickness (d) serves to index their characteristic *solid-state Raman cross-section* (σ_R): a unique parameter that weights the absolute Raman intensity of the material and implicitly accounts for its optical constants (complex refractive index, $\eta = n + i\kappa$) at the excitation (λ) and scattered (λ_R) wavelengths. In other words, σ_R indicates how intense the Raman activity of a certain material is at the probing laser wavelength. Therefore, in BHJ multi-component mixtures of N components, $\sigma_{R,u}$ weights the reference vibrational spectra of the blended species ($I_{ref,u}$) together with their corresponding volumetric fractions (v_u), yielding

$$I_{R.BHJ}(d, v_u, \omega) \propto \int_0^d |E_R(x, v_u)|^2 \mathrm{d}x \sum_{u=1}^N v_u \sigma_{R,u} I_{ref,u}(\omega),$$

where ω is the wavenumber or Raman shift and $|E_R(x,v_u)|^2$ refers to the transfer matrix calculation of the Raman scattered intensity. The volumetric scattering fractions v_u satisfy the following sum rule: $\sum_{u=1}^N v_u = 1$. On the other hand, the complex refractive index of the multi-component film, which is implicitly included in the calculation of the Raman scattered intensity, is assumed to vary linearly according to $\eta_{mix} = \sum_{u=1}^N v_u \eta_u$. The Raman cross-sections of the organic semiconducting materials studied in this thesis are listed in the Appendix (Table I).
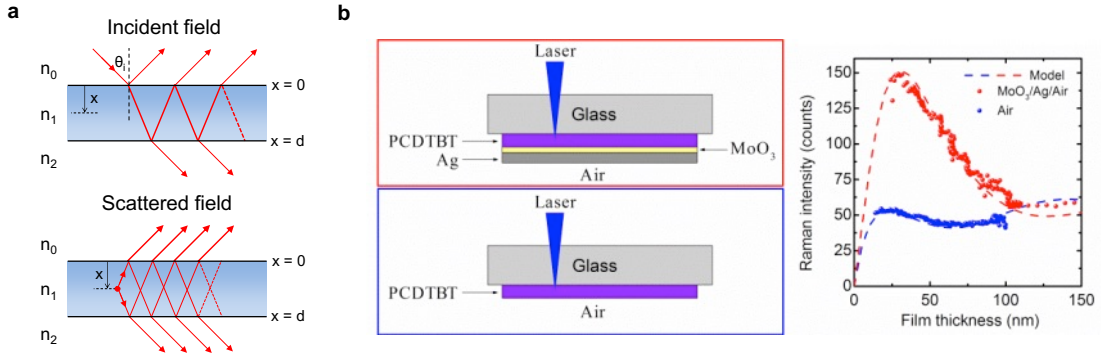
Figure 17. (a) In the transfer matrix method, the incident and Raman-scattered electromagnetic fields are modelled as plane waves. The resulting standing waves are calculated as the product of refraction and phase matrices corresponding to the interfaces and layers, respectively. (b) The transfer matrix modelling shows excellent agreement with experimental data took in distinct optical stacks, even when Raman is measured through thick glass superstrates as it occurs in organic solar cells. This fact enables the use of Raman spectroscopy as an accurate thickness probing tool.

Accordingly, the implementation of this methodology in BHJ blends first requires indexation of the corresponding pristine material Raman cross-sections as well as their vibrational fingerprint. This is a two-in-one process performed in supported neat films showing a lateral thickness gradient, since the determination of σ_R mainly requires fitting of the following relationship with a single free parameter (σ_R):

$$I_{R,\text{neat}}(d) = \sigma_R \int_0^d |E_R(x)|^2 \mathrm{d}x,$$

where $E_R(x)$ is the emergent Raman-scattered electric field amplitude due to an infinitesimal material slab located at a distance x from the film surface, and d is the thickness of the film. The integration of the scattered intensity results in mild oscillations as a function of d until reaching an asymptotic behaviour at sufficiently thick values (Figure 17b). The thickness-onset of such asymptote mostly depends on the material extinction at the probing and scattered wavelengths: the higher the extinction, the lower the thickness at which the scattered Raman intensity saturates. This implies that, in resonant conditions (i.e. $\kappa(\lambda) > 0$), Raman scattering can be employed as a reliable thickness probe below the asymptotic threshold onset. Moreover, the mild oscillations make the corresponding intensity vs. film thickness curve interpolation no longer univocal (i.e. single-valued) in the y-axis.
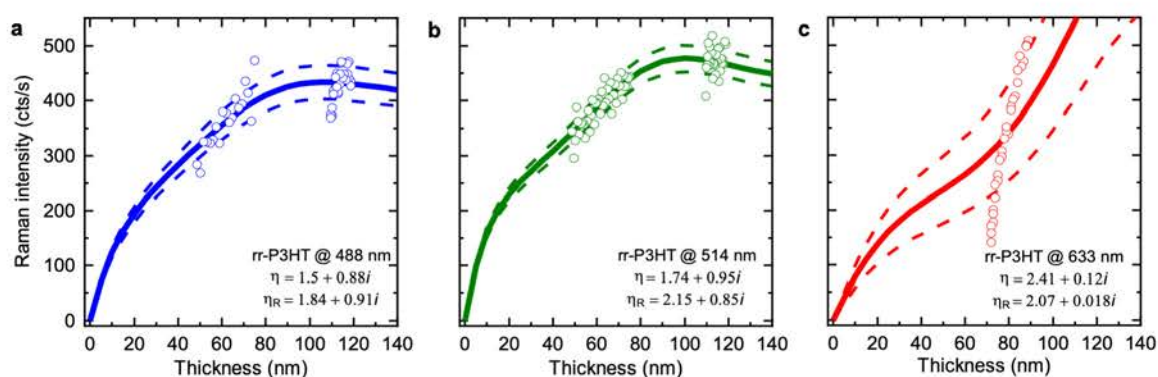
53

Figure 18. Raman intensity corresponding to the 1450 cm^{-1} C=C stretching mode in regio-regular P3HT (rr-P3HT) as a function of film thickness, measured at three different excitation wavelengths: (a) 488 nm, (b) 514 nm and (c) 633 nm. The solid lines are fits to the data using as free parameter the corresponding σ_R at each excitation wavelength. The dashed lines limit the confidence intervals of the fits (standard deviation). The complex refractive indices are included at the bottom for the incident (η) and Raman-scattered (η_R) wavelengths.

These are intrinsic limitations of the methodology when sticking to single-wavelength Raman-scattering; however, in some cases it is feasible to collect the Raman spectra of the same species under study at different excitation wavelengths, ideally in resonant and non-resonant conditions (Figure 18). Accordingly, by performing a simultaneous interpolation of the corresponding interference curves with a shared thickness parameter it is possible to widen the applicability of the methodology and extend the single-valued solutions of the (system of) equations. Nevertheless, for most organic semiconductors under resonant Raman conditions ($\kappa \approx$ 0.3-0.5), the intensity plateau is reached for thicknesses close to 100 nm or beyond, so the method still provides accurate interpolations ($\pm$10 nm) in the thickness range suitable for OPV applications.

As far as compositional analysis is concerned, the methodology was cross-validated by ellipsometry measurements and Bruggeman's effective medium approximation showing very good agreement within an experimental error of ca. 5-10 vol% depending on the blend scenario. We identified a series of requirements for the Raman analysis to reach its full potential in terms of compositional accuracy, namely: (i) largely distinguishable Raman vibrational signatures; (ii) close enough cross-section ratios between blended materials (ideally <30); and (iii) similar film morphology for the blend as that obtained in neat films. For the first two conditions,

54

a correct choice of excitation wavelength is critical albeit there are unapproachable cases in which the limitations are intrinsic to the materials selected. As an example, a hypothetic OPV ternary blend formed by a conjugated polymer and two acceptors such as ITIC and ITIC-M could be problematic to analyse due to the similarity of the vibrational fingerprints of the small molecules. Similarly, the workhorse OPV binary blend P3HT:PC$_{60}$BM cannot be successfully analysed due to the large cross-section ratio existing between the involved species, even in resonant conditions.

The third requirement, namely the obtainment of similar film morphologies in the blend films as those obtained in neat materials, originates from the distortion of the respective molecular packing when the blended species are highly miscible and semi-crystalline in their original isolated state. This fact can also lead to uncontrolled variations of the optical constants, blue-shifted absorption and anisotropy reduction.[110–112] This latter feature was demonstrated to reduce up to one third the extinction coefficient with respect to neat films.[112] Thus, there exists a collection of collateral effects upon blending that make the Raman deconvolution to be more accurate when (neat) amorphous materials are blended rather than semi-crystalline ones, especially in the case of conjugated polymers.

With all that, the diffraction-limited lateral resolution of the Raman imaging technique and its quantitative accuracy approaching ellipsometry results encourage the use of Raman spectroscopy as a bridging imaging tool between scanning probe microscopies and ellipsometry (Figure 19). Importantly, Raman imaging is especially indicated for the characterization of functional OPV devices as it allows a straightforward modelling of the scattered intensity when measuring through thick glass incoherent superstrates. Furthermore, the combination of a Raman microscope with advanced software and motorized stages enables the high-throughput spectral acquisition over large areas and in a non-invasive manner, which constitute the two main needs for the development of a truly efficient combinatorial screening platform for OPV.
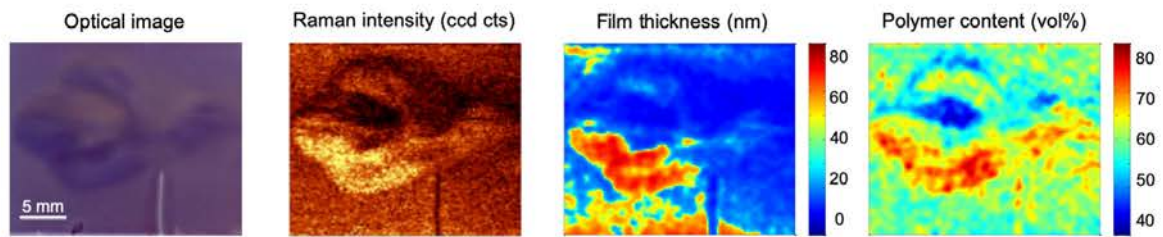
Figure 19. Raman imaging enables spatial mapping of lateral film inhomogeneities that occur during solution processing of thin layers, such as in the present case for a PCDTBT:PC$_{70}$BM thin film supported on glass.

In summary, the work presented in **Paper I** laid the foundation of the future high-throughput experimentation procedures by enabling the *in situ* quantification of key material properties in combinatorial parametric libraries. Raman imaging enables the realization of large-area thickness and compositional maps with enough lateral resolution to significantly increase the density of parametric combinations extracted from gradients as compared to discrete experimentation approaches. Eventually, this fact speeds up the overall optimization process of complex multi-parametric problems such as that found in OPV devices.

4.2. High-throughput optimization of organic solar cells

The high-throughput optimization of organic solar cells ultimately aims at combining lateral gradients on the parameters of interest with fast acquisition and large-area mapping techniques that enable a truly time- and cost-effective combinatorial screening scenario. While the mapping of parametric libraries is compatible with the aforementioned Raman imaging technique, the generation of solid-state gradients can be realized by manifold approaches. In this thesis, we explored two of the main routes typically used in the fabrication of device-oriented organic thin films, namely vacuum deposition (*aka* thermal evaporation) and solution processing. These are finally exploited to perform the high-throughput optimization of bi-layered heterojunctions and BHJ devices, respectively.

4.2.1. Evaporated bilayer organic solar cells

As detailed in the introductory section of this thesis, prior to the discovery of the BHJ active layer morphology the first generation organic solar cells consisted of bilayer heterojunction device architectures in which the donor and acceptor materials are thermally deposited between selective contacts. Herein, both donors and acceptors are insoluble conjugated small molecules due to the lack of side chains branching out of their core structure; consequently, these materials can only be deposited as thin films via thermal evaporation. In this particular type of bi-layered device architecture excitons only split at the narrow interface area between the stacked donor and acceptor layers. Therefore, careful control of their respective thickness is required in order to maximize exciton dissociation and charge collection. Typically, their thicknesses must be of the order of twice the exciton diffusion length in each of the layers (ca. 10-20 nm).

The thermal evaporation process of organic materials is particularly expensive in terms of resources. The usual setup includes ultra-high vacuum pumps and chambers as well as high energy demands to evaporate the organic raw powders. Also, because target substrates are placed one by one inside the vacuum chamber, the fabrication costs and time required to fully explore the parametric thickness space of the donor-acceptor bi-layers is huge when sticking to traditional Edisonian

experimentation approaches. Thus, the use of high-throughput and efficient optimization machineries in this particular type of device architecture is of special interest, as already demonstrated for thermally evaporated lasers and OLEDs.[113,114]

In **Paper II** we accordingly propose using a single donor-acceptor bi-layered heterojunction containing orthogonally-oriented thickness gradients to accelerate the screening and optimization of the corresponding OPV bilayer devices. The use of thermally evaporated lateral gradients in organic electronic devices has been previously exploited to build position-sensitive photodetectors by Dr. Juan Cabanillas-Gonzalez, Dr. Mariano Campoy-Quiles and co-workers.[115] They employed an advanced fabrication procedure that requires acute control of an automated shadow mask in the evaporation chamber to roll over the evaporation cone as the material sublimates. This eventually generates a thickness gradient on the target substrate (Figure 20a). The orthogonal arrangement of the donor-acceptor layers serves to enlarge the thickness library covered in a single combinatorial device (Figure 20b). Note that such orthogonal orientation, rather than the anti-parallel arrangement of the gradients, leads to a suitable parametric library for bi-layered OPV purposes as in an anti-parallel arrangement the total active layer thickness would be barely constant throughout the device. In other words, in bi-layered heterojunctions all d_{donor}, $d_{acceptor}$ and d_{total} must be optimized. The thermally evaporated devices including orthogonal gradients, as well as the reference pristine gradients for indexation purposes (σ_R and η), were entirely fabricated by Dr. Juan Cabanillas-Gonzalez and his co-workers at IMDEA Nanociencia, with a special mention to Guilin Liu as PhD student.
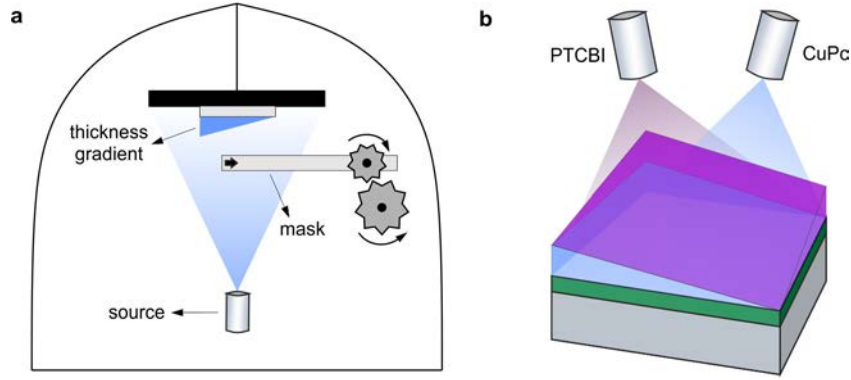
58

Figure 20. (a) Schematic drawing of the customized evaporation setup including a movable mask that allows the controlled formation of lateral thickness gradients. (b) The bilayer heterojunction with orthogonal thickness gradients of donor (CuPc) and acceptor (PTCBI) materials.

The analysis of the Raman scattered intensity in bi-layered devices accordingly requires a subtle modification of the transfer matrix modelling first presented in Paper I. According to the initial formulation provided for BHJ active layers formed by N-components, both materials appear intimately mixed below the dimensions of the laser spot, thus yielding as free parameters a single film thickness value (d) and N-1 volumetric blending ratios (v_u). However, in bi-layered devices the free parameters are the two distinct film thickness values corresponding to the donor and acceptor layers, d_1 and d_2, respectively. Therefore, the Raman scattered intensity due to the embedded layers depends simultaneously on both thickness values as

$$I_{R,BL}(d_1, d_2, \omega) \propto \sum_{u=1}^{2} \sigma_{R,u} I_{ref,u}(\omega) \int_0^{d_u} \left| E_{R,u}(x, d_{v \neq u}) \right|^2 \mathrm{d}x$$

Based on the above relationship we perform the quantitative deconvolution of the Raman spectra to map the orthogonal thickness gradients of the active layer in the combinatorial device.

In a last step, we measure the photovoltaic response of the device in the form of photocurrent maps (in short-circuit conditions) in a secondary light-beam induced current (LBIC) setup. This was jointly designed and built by current and former members of the *Nanopto* group at ICMAB.[116] By the time we developed this piece

of combinatorial work with bi-layered heterojunctions, photocurrent maps had to be sequentially measured in such secondary setup and employing monochromatic light sources only. This resulted in a laborious post-processing work to spatially match the maps acquired at different setups (namely Raman and photocurrent images) and interpolation of their measuring grids. Once the images are spatially overlapped, all three magnitudes can be easily correlated hence obtaining the actual triad of donor thickness, acceptor thickness and photocurrent dependence at a glance (Figure 21c). This approach served us to identify, within a statistically meaningful thickness-performance landscape, which are the active layer thickness values that maximize the photocurrent due to optimized absorption, exciton dissociation and charge extraction in bi-layered heterojunctions.
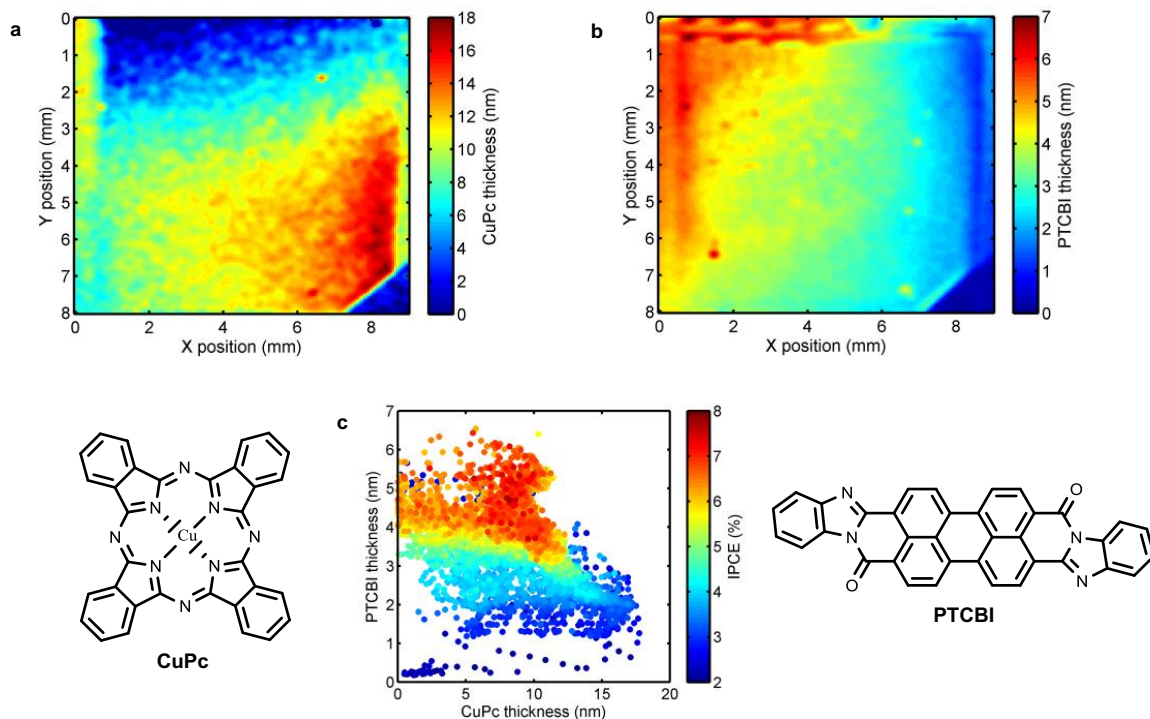

Figure 21. Lateral thickness gradients of (a) CuPc and (b) PTCBI obtained by Raman imaging at 488 nm excitation in a functional bilayer device. By spatially correlating the Raman images with the photocurrent maps extracted at 532 nm (not shown) we depict in panel (c) the incident photon-to-current efficiency (IPCE) of the CuPc-PTCBI bilayer, which enables the determination of the optimal active layer thicknesses at a glance.

Apart from demonstrating the highly efficient search of the sweet spot in device performance, the use of thickness gradients as high-throughput optimization schemes offers notable gains in terms of experimental time employed and number of samples required. Our time-savings estimate indicates that in comparison with a typical optimization routine that includes the fabrication of 20 homogeneous and discrete devices, the use of double-wedged, orthogonal devices in combination with local photocurrent measurements supposes a ca. 17-fold enhancement in the invested experimental time and resources while obtaining a ca. 100-fold increase in the number of parametric combinations explored (2000 in the present case). Concomitantly, both Edisonian and high-throughput approaches lead to the same optimized donor-acceptor thicknesses when comparing literature reports with the results obtained via combinatorial screening.

4.2.2. Blade coating parametric libraries for bulk heterojunction OPV

Undoubtedly, the major advantage of OPV is the solution processability of its constituent device layers. This unique feature protrudes among first and second PV technologies as it enables the R2R industrial manufacture of OPV modules.[117] These are expected to drop the EPBT to few days only and raise the energy return on investment (EROI) to unprecedented levels in the following years, thus contributing to turn OPV as one of the most sustainable energy technologies on the market.[12,13,22] However, prior to the massive manufacturing of certain donor:acceptor material system combination, there is a need to perform a screening of their corresponding active layer features, usually in lab-scale batches, to fully exploit the PV potential of the system. For this purpose, the development of high-throughput experimentation approaches can help in the prompt unravelling of the corresponding parametric spaces, thus accelerating the optimization of devices and discovery of novel materials. How can we generate parametric libraries in the form of solid-state films processed from solution that enable high-throughput and combinatorial experimentation studies?

Solution-processed thin films can be manufactured following a large catalogue of deposition techniques. In lab-scale, spin coating is the main choice due to its low cost, ease of use, rapid optimization and excellent film characteristics, including

homogeneity, roughness and morphology; in fact, record PCEs in OPV are achieved via spin coating of the active layer (and also interlayers).[19,20,69,118] Nevertheless, spin coating has two major drawbacks. First, it is an intrinsically low-throughput film forming technique, difficult to apply in large area devices and to scale up; and second, it offers poor control to laterally pattern films, as the coating is only based on the centrifugal spreading of the inks. Thus, the generation of combinatorial libraries by spin coating relies on intensive device prototyping, an approach that is compatible in some cases with robotized laboratories and enhanced screening rates.[93,94] Regarding film patterning, processing techniques such as blade coating offer an enhanced control of the ink wetting and drying, thus enabling the manufacture of controlled lateral gradients and parametric libraries.[95] Moreover, blade coating is natively a scalable processing approach compatible with R2R setups; however, blade coated devices generally lead to lower PCEs with respect to the spin coated champion devices due to the formation of suboptimal film morphologies upon ink drying.[85,86] In this case, the use of additives such as DIO or solvent mixtures may help in bridging and even surpass the performance gap between processing methods.[119,120]

The blade coating (*aka* doctor blading) deposition technique works by spreading ink over a target substrate with the help of an applicator and its sharp coating edge. The ink is accumulated at the blade reservoir, which is configured to leave a micrometric gap (typically 200-300 μm) between the wetting edge and the substrate. By controlling the solid content of the ink (usually 1-3 wt% or 5-20 mg mL^{-1} at most), the blade speed and the ink volume dropped at the reservoir, the dry film thickness can be tailored in nano- and micrometric scale. Interestingly, the blade speed appears as the easiest experimentally accessible parameter to control the final film thickness, as determined by phenomenological models based on Landau-Levich lubrication theory.[121] Hence, large-area and homogeneous films ranging from a few nanometres up to several micrometres in thickness can be manufactured by blade coating by simply tuning the blade speed.

Therefore, blade coating can be readily exploited to generate thickness gradients from solution, as first demonstrated by Stafford et al. in 2006.[95] Their results

suggest that a controlled accelerated movement of the blade leads to smooth and reproducible lateral thickness gradients in a single processing step, which is precisely one of the needs of high-throughput BHJ OPV optimization. Note that in Paper I we already exploited this experimental approach to explore the film thickness dependence of the Raman scattered intensity in pristine materials, a fact that notably accelerates the determination of their corresponding solid-state Raman cross-sections (σ_R).

Regarding compositional gradients, Meredith et al. first exploited knife coating to realize the high-throughput study of the phase diagram of polymer blends.[122] However, their approach was limited to high-molecular weight polymers only and consumed large amounts of raw materials, as they were progressively added, withdrawn and stirred in a single vial thus skipping the possibility to recover the pristine inks. For a binary BHJ blend, the formation of smooth lateral compositional gradients in the highest efficient manner implies the controlled mixing of the two pristine solutions only, followed by their (blade) coating. This is required to minimize the use of raw materials and recover the pristine ink solutions for future experimentations.

According to these needs, in Paper III we demonstrated for the first time the realization of organic solar cells with multi-parametric gradients of thickness, composition and annealing temperature. To enlarge the extension of the parametric libraries per combinatorial device, these gradients were mostly bidimensional, thus orthogonally-oriented. The processing scheme for orthogonal thickness-composition gradients consists of pipetting individual drops of the pristine solutions (i.e. pure donor and pure acceptor) at the blade ink reservoir, followed by the coating procedure itself (Figure 22). The coalescence of both drops as the blade travels along the substrate leads to the formation of a rather chaotic compositional library extended over the short axis, as well as a thickness gradient spanned over the long axis as the ink reservoir is depleted (or the blade decelerated). Note that we use as substrate a large aspect ratio ITO-sputtered glass substrate with its short axis (25 mm) oriented perpendicularly to the blade movement, which occurs in parallel to the long axis (75 mm). The device stack is completed by thermally evaporating a single

63

large area back electrode. Note that both device contacts can be connected with inverted symmetry at the end sides of the long axis, thus balancing and optimizing charge collection over the device active area. As a result, we obtain in a single large area device a thorough parametric library of thickness and blending ratio combinations for the selected donor:acceptor pair, which are finally mapped by means of Raman imaging and LBIC.

In our case, the development of Raman imaging (Paper I) to map thin film inhomogeneities (i.e. film thickness and donor:acceptor ratio) does not add the requirement for an acute control of the lateral composition profiles during sample manufacture (as for previous cases)[122–124] since such magnitudes are precisely determined *in situ*. The only processing requirement is, thus, the local film morphology to be equivalent to that obtained in the prototyping of homogeneous discrete devices, which assures consistency between Edisonian and high-throughput experimentation approaches (Figure 25). Note that the usual fabrication protocols of composition-controlled devices start from the prolonged overnight stirring of the raw materials in a single vial to assure their complete intermixing, whereas in the fabrication of compositional gradients by blade coating the mixing takes places *in situ* during a coating procedure that takes less than one minute.
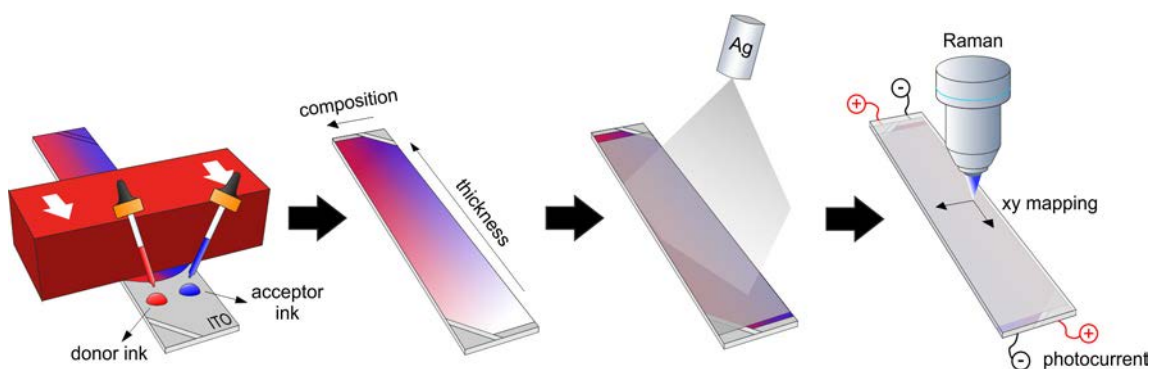

Figure 22. The high-throughput screening workflow starts by the fabrication of parametric libraries by blade coating. This is achieved by the *in situ* coalescence of pristine donor and acceptor ink drops at the blade reservoir. Then, a uniform large-area back electrode is evaporated to complete the device stack. Finally, Raman and photocurrent imaging are acquired throughout the active area. Note that Raman is acquired measuring through the thick glass substrate containing pre-patterned ITO to invert the polarity of the side contacts.

The optimization roadmap proposed in Paper III starts first by the screening of the donor:acceptor blending ratio. This is performed by fabricating a device with thickness and compositional gradients (Figure 23c and d), and correlating the local parametric variations with the photocurrent extracted in a secondary LBIC setup (Figure 23b). As a result, thickness, composition and photocurrent maps are concurrently plotted in a single graph, which enables determination of the optimal device parameters at a glance (Figure 23e). With this first combinatorial library we limit a range for optimal donor:acceptor ratios. Interestingly, this kind of figures provides a broad statistically-meaningful overview of the multi-dimensional performance landscape for the selected donor:acceptor pair. This is of special interest in an ulterior upscaling of the blend as it permits evaluation of its sensitivity upon unintentional variations of such parameters.
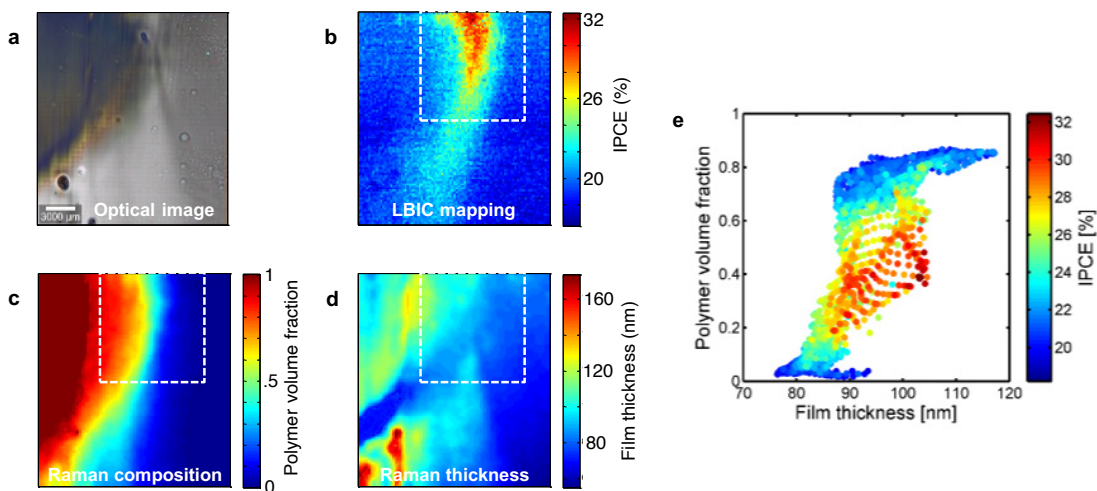

Figure 23. Example of high-throughput combinatorial screening of the thickness-composition parametric space and its dependence with photocurrent (IPCE) for the PTB7-Th:PC$_{70}$BM binary blend. (a) Optical image (in reflection) of the investigated area. (b) Photocurrent (IPCE) map extracted at 532 nm excitation. (c) and (d) panels illustrate the Raman-based images of donor polymer loading and total active layer thickness, respectively. Panel (e) depicts the existing correlation between local photocurrent maps (magnitude in colour scale) and quantitative Raman maps of thickness (x-axis) and composition (y-axis) in the high-performing area marked with dashed white rectangles. This kind of plots serves to quickly spot the active layer thickness and donor:acceptor ratio that yield optimal PV performance.

The optimization roadmap is followed then by fabricating a second device that combines in a single substrate a large area electrode as well as an array of discrete pixels (i.e. individual solar cells of small active area). In this case, the active layer is processed as a thickness gradient (typically spanning from 50 to 300 nm) with the (optimal) blending ratio kept fixed as determined in the previous step. Accordingly, the active layer thickness variations can be probed and correlated with the LBIC maps over the large area electrode whereas the discrete pixels provide the PV performance parameters (V_{oc}, FF, I_{sc} and PCE) at fixed locations along the gradient. The fabrication and characterization of this second device has, thus, two main purposes: (i) to explore the second photocurrent maximum originating from optical interference with active layer thickness; and (ii) to properly identify the active layer thickness that maximizes the overall PCE, and not exclusively the photocurrent. This is a key issue in OPV since charge transport in organic semiconductors is rather limited, thus thick films might lead to reduced FFs despite the large photocurrents observed resulting from maximized light-harvesting and optical interference. V_{oc} might also be subjected to fluctuations depending on the donor:acceptor ratio, yet the effect is more pronounced in ternary OPV blends.[125,126] Note that in the discrete pixels, all PV performance parameters are individually accessed and correlated with the lateral active layer thickness variation.

Finally, a third device is prepared including orthogonal thickness and thermal annealing gradients while keeping the donor:acceptor ratio from the previous steps (Figure 24a). In this case, the thickness gradient spans over the short axis by steeply decelerating the blade during ink spreading and setting it parallel to the blade movement direction. The thermal annealing gradient is performed by means of a calibrated Kofler bench that provides a controlled temperature profile of approximately 1 °C mm^{-1}; as a result, a maximum temperature range of 75 °C (ΔT = T_{max} - T_{min}) is achieved in a 75 mm long substrate. The annealing temperature accordingly controls the degree of phase separation as well as the crystallinity of the photovoltaic materials in the active layer, thus modifying the film morphology and having acute effects in the measured photocurrent (Figure 24b).
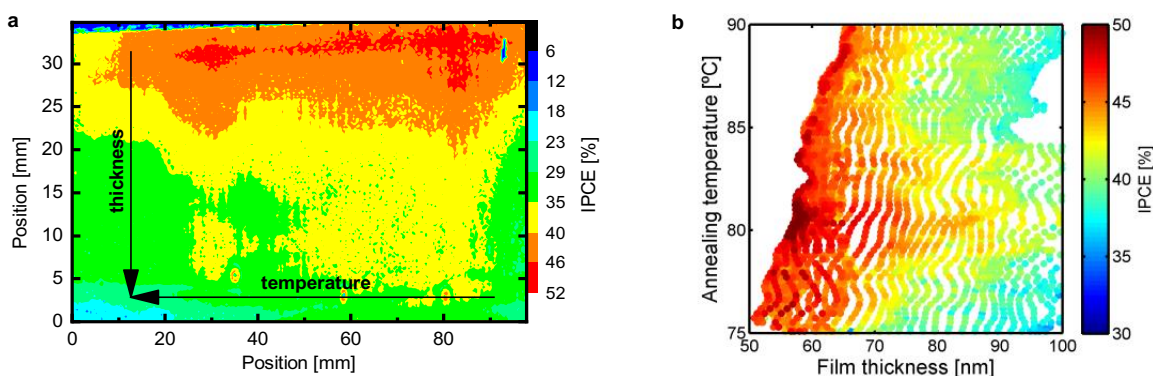
Figure 24. (a) Photocurrent map (acquired at 532 nm) of a large-area combinatorial organic solar cell of PCDTBT:PC$_{70}$BM (1:4, w:w), including orthogonal gradients of active layer thickness and annealing temperature. The donor:acceptor mixing ratio was previously optimized by thickness-composition combinatorial libraries. (b) The corresponding thickness-annealing space shows an enhancement in photocurrent when annealing is performed at 80 °C for 10 minutes.

In summary, in Paper III we demonstrate that the use of only three devices is enough to fully explore the combinatorial parametric landscape of film thickness, composition and thermal annealing for polymer:small molecule blends. This is achieved by fabricating two devices with orthogonally oriented gradients on the target parameters, as well as one device comprising both a large area electrode and an array of discrete pixels in the same substrate. In this case, the compositional libraries are simply generated by the *in situ* coalescence of the pristine inks at the blade reservoir, an approach that was demonstrated to be truly effective for most donor:acceptor material combinations.

Nevertheless, the processing requirements for the drop coalescence approach to originate smooth lateral mixing profiles are quite specific. The reason is that the processing largely depends on the rheology of the corresponding inks, more particularly on their viscosity. Neat polymer inks are characterized by a ca. 2-5-fold higher viscosity with respect to the pristine solvent, whereas small molecules barely modify the rheological properties of the original solvent, which typically shows a viscosity <1 cP. According to our experience, at least one of the pristine inks should show a viscosity ≤1 cP to yield proper mixing of the solutions and succeed with the drop coalescence method; this is, however, a general condition fulfilled in most polymer:small molecule binaries. As a result, the processing window (i.e. the casting

67

temperature and blade speed parameters) that yields successful mixing generalizes well for polymer:small molecule blends, including both fullerenes and NFAs.

In fact, the generality of the processing scheme here introduced is extensively demonstrated in Paper VI. Therein, we analyse the performance of materials families such as that formed by ITIC and some of its derivatives (ITIC-M, ITIC-4F, ITIC-C_8 and ITIC-C_2C_6), which are mixed with state-of-the-art donor polymers (PTB7-Th and PBDB-T, among others). The high-throughput experimentation enables us to perform this full screening study in a few days only while being extremely efficient regarding raw materials consumption. As a result, we build combinatorial material matrices for the photocurrent-composition space that are largely representative of the different trends and profiles obtained depending on the choice of donor:acceptor materials. Finally, we also demonstrate that high-throughput combinatorial screening and discrete devices prepared following traditional methods lead to the same overall trends and optima in terms of PV performance, even validating the existence of bimodal photocurrent distributions in some particular cases (Figure 25).

Conversely, when screening all-polymer blends and sticking to the two-drop coalescence approach, the high ink viscosities are therein detrimental for the formation of lateral mixing profiles. In fact, we normally observe the formation of an abrupt composition step rather than a smooth blending profile, which is clearly indicating the lack of intermixing during the coalescence (Figure 26). In this particular type of binary systems, more sophisticated processing schemes are required to obtain compositional libraries in solid-state.
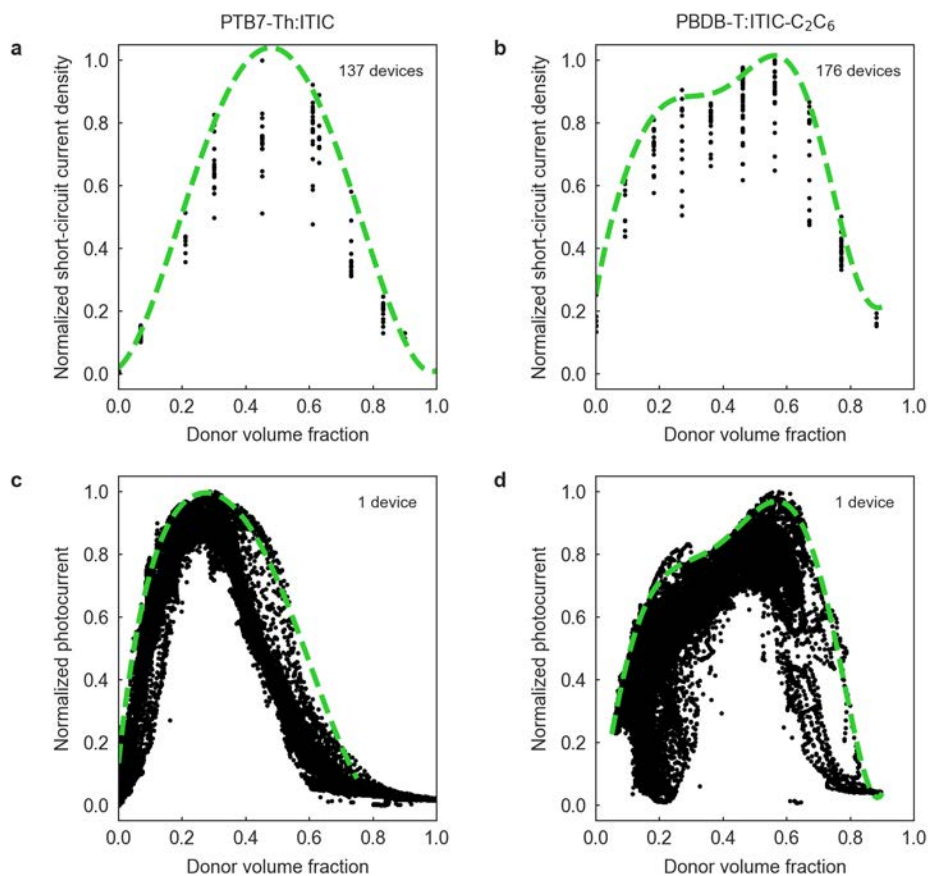
Figure 25. (a,b) Normalized short-circuit current density obtained as a function of the donor volume fraction in PTB7-Th:ITIC and PBDB-T:ITIC-C_2C_6 devices fabricated following traditional methods. In this case, the raw materials were individually weighted in controlled fractions and stirred in single vials. Note that in order to accelerate the thickness screening, the active layer was processed as a thickness gradient at each compositional step. The discrete samples were fabricated and measured by Mr. Enrique Pascual-San-José. (c,d) Photocurrent dependence obtained as a function of the donor volume fraction in the same blends using a single large-area combinatorial device processed via the two-drop coalescence method. Note the significantly reduced usage of raw materials, resources and experimental time in this latter case and the generation of statistically meaningful datasets. The combinatorial devices were manufactured by Mr. Enrique Pascual-San-José.
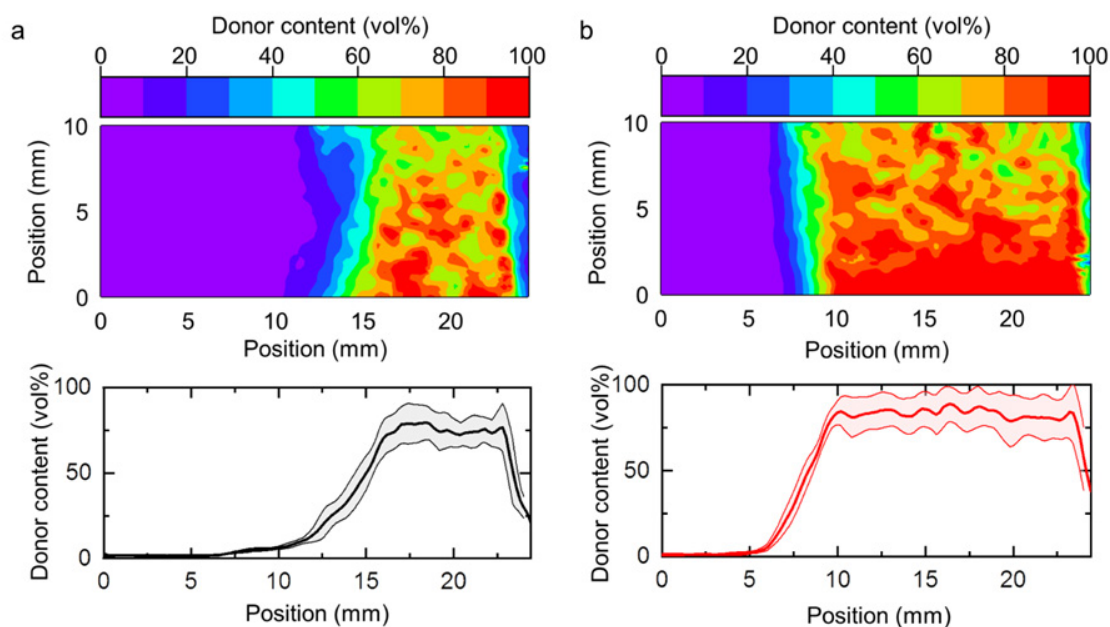
Figure 26. Composition maps and corresponding averaged lateral profiles obtained in PBDT-TPD:PNDI-T all-polymer films on glass processed according to the two-drop coalescence approach. Two 30 µL drops at a nominal concentration of 10 mg mL^{-1} in chlorobenzene were pipetted at the ink reservoir and then coated at (a) 30 mm s^{-1} and (b) 20 mm s^{-1} while holding the stage temperature at 80 °C (in both cases).

4.2.3. All-polymer compositional libraries by microfluidics-assisted blade coating

Microfluidics aims at exploiting a unique physical regime in fluid dynamics to perform highly controlled experiments in liquid state, which is known as the laminar flow regime. These conditions are achieved when employing micrometric-sized channels: the Reynolds number is accordingly lowered until the viscous forces dominate against the diffusive ones,[127] so unconventional physical processes start being feasible in the micro-scale. Also, the laminar regime enables a much deeper control of the diffusive dynamics, which for example can be used to tailor the outcomes of chemical reactions.[128,129] Accordingly, the current applications of microfluidics systems are huge and disparate: from controlled synthesis of metal-organic frameworks[130] to monitoring of 3D tumour cell cultures.[131]

In combinatorial materials science, the use of the microfluidics toolbox was first devised by G. M. Whitesides' group in the early XXI century, who pioneered the generation of controlled solution gradients in composition.[132] Their approach

consisted of a polydimethylsiloxane-based (PDMS) network of microchannels in which two pristine solutions are flowing laminarly. By controlling their diffusive mixing throughout the symmetric branched structure of the microfluidic device, G. M. Whitesides and co-workers demonstrate the confluence of the fluids in a single outlet whose profile could be laterally adjusted based on the relative selected inflow rates.

Inspired by that work, in **Paper IV** we developed a novel processing methodology that synergically combines blade coating and microfluidics to fabricate highly controllable and reproducible compositional gradients as solid-state thin films. The methodology circumvents the limitations of the two-drop coalescence approach regarding ink compatibility and reproducibility since it relies now on the *in situ* mixing by branched microfluidic dispensers coupled to the blade applicator. The microfluidic dispensers are designed so as to include two inlets (for the pristine solutions of donor and acceptor, respectively) and three nozzles as outlets, which outflow directly at the blade ink reservoir thanks to a customized poly(methyl methacrylate) (PMMA) scaffold that holds the microfluidic device in place (Figure 27). The microfluidic branched array is designed so as to pour the neat inks through the side outlets and a homogenised mixture in the central mainstream. In this way, the pristine inks (which are loaded in their respective syringes) remain unaltered and can be employed in further experimentation. Finally, the ink ejection is synchronized with the blade movement, which originates a smooth lateral solid-state gradient as a result of the now more controlled coalescence of the pristine and pre-mixed inks at the reservoir.
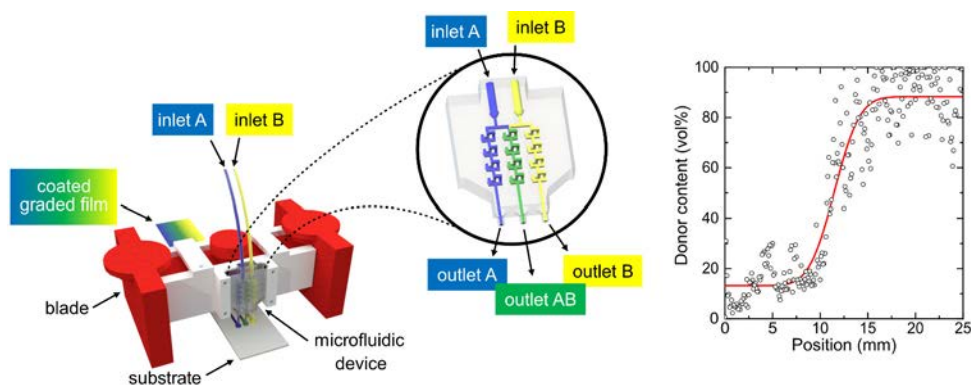
Figure 27. The microfluidics-assisted blade coating platform consists of a microfluidic dispenser coupled to the blade applicator. The microfluidic device is designed to outflow three streams, namely the pristine donor and acceptor inks and a controlled mixture in the central branch. When such three streams are merged at the blade reservoir a smooth lateral compositional gradient is generated (right panel). The compositional profile shown was measured by Raman spectroscopy and corresponds to a PCDTBT:$PC_{70}BM$ blend.

The design roadmap of the microfluidic devices was intricate and extensive due to the demanding requirements for highly efficient experimentation with OPV materials. Undoubtedly, the major bottleneck consisted of identifying suitable building materials for the microfluidic device prototyping. The reason is that the archetypal PDMS first swells and eventually tears upon exposure to chlorinated solvents, which are the typical carriers in OPV inks (chlorobenzene, 1,2-dichlorobenzene and chloroform, but also toluene and *p*-xylene as non-chlorinated). As a result, we moved to 3D printing of the microfluidic devices using UV-curable proprietary resins, a work done in collaboration with Dr. Josep Puigmartí-Luis' group settled in ETH Zürich, Switzerland.

Furthermore, for the microfluidics-assisted blade coating to be as efficient as possible in terms of raw materials consumption, we identified two extra requirements: (i) a minimal dead volume[8] and (ii) a very efficient mixing of the pristine inks. These two features were fulfilled by incorporating successive 3D mixers based on the baker's transformation[133,134] in each stream (Figure 28). These

---

[8] In microfluidics, the dead volume corresponds to the volume occupied by the microchannels themselves. In other words, once the microfluidic device is filled with liquid, the dead volume corresponds to the amount of liquid trapped in the device and that cannot be reused.

were demonstrated to be among the most efficient passive mixers ever designed in microfluidics.[135,136]

As a result of our extensive design exploration, we eventually demonstrate the formation of solid-state thin films with smooth and controllable lateral composition gradients including polymer:small molecule as well as polymer:polymer blends. In this latter case, we realize combinatorial prototypes using one of the most promising all-polymer blends in the OPV field, namely the PBDT-TPD:PNDI-T donor:acceptor pair[137] (Figure 29), which was courtesy of Prof. Olle Inganäs and his co-workers from Linköping University in Sweden. Our results performed using a minimal amount of raw materials (<10 mg) and experimental time (<4 hours, enabled by co-local Raman and photocurrent imaging) are in very good agreement with the reported literature data, indicating that a donor-enriched BHJ composition favours a photocurrent enhancement.
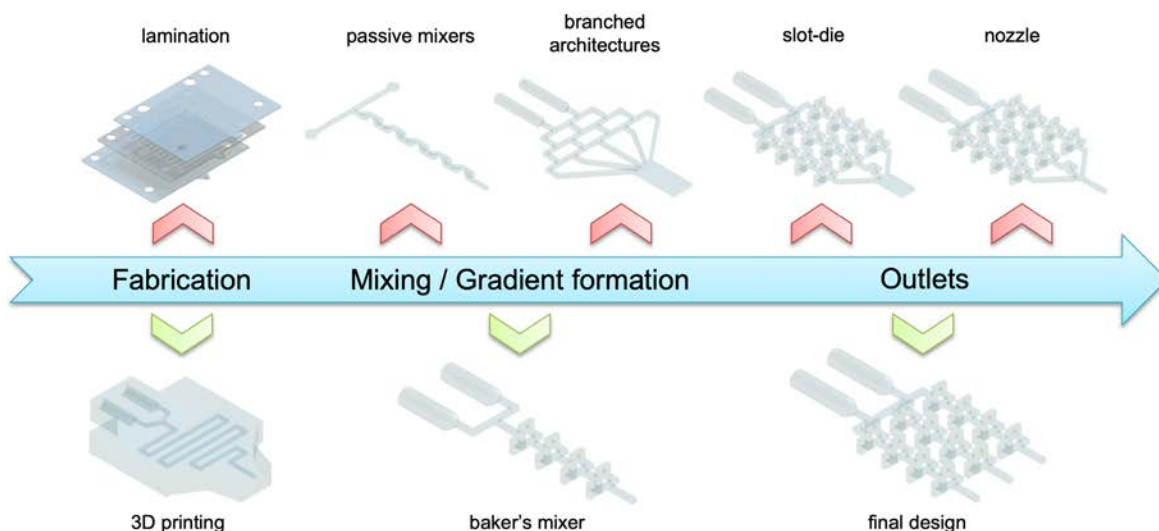

Figure 28. The design roadmap for the microfluidic device is divided into three main steps: the choice of fabrication method, the organization of branched structures for mixing and gradient formation, and the type of outlet that assures proper coupling with the blade coating apparatus. Our final design includes 3D printed microfluidic devices, with three branches including four consecutive baker's mixers each, and three nozzles as ejecting structures.
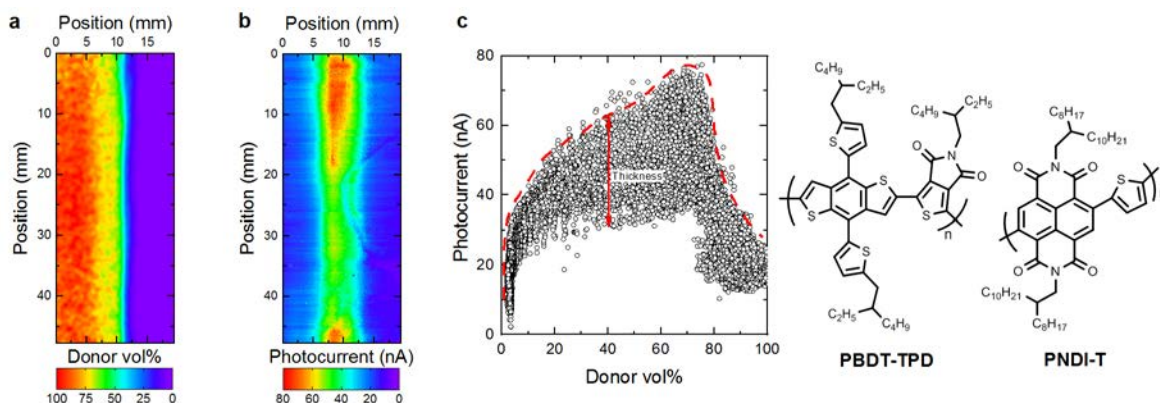
Figure 29. Characterization of the combinatorial device including the all-polymer blend formed by PBDT-TPD:PNDI-T, processed by microfluidics-assisted blade coating. (a) Compositional map extracted by means of Raman imaging. (b) Photocurrent image measured co-locally with Raman, at 488 nm excitation. (c) The corresponding photocurrent-composition space shows an optimal performance at ca. 70 vol% of donor. The vertical dispersion is ascribed to active layer thickness fluctuations as observed in panel (b). The chemical structures of the involved donor:acceptor species are depicted on the right.

Finally, while we applied the microfluidics-assisted blade coating methodology to the optimization of organic solar cells, the setup can be easily extrapolated to any application in which there is an interest in translating highly controllable liquid-state profiles to solid-state thin films.

4.3.   Ternary OPV blends: combinatorial screening at its best

Ternary blends are one of the current hot topics in the OPV field despite their long-lived existence. Some early reports dating in 2009 already indicated that ternary blending could be an efficient way to better control the film morphology and enhance the final V_{oc} and PCE with respect to the corresponding binaries.[138] Nowadays, the research on ternary blends is suffering an acute upswing mainly encouraged by the development of NFAs such as the ITIC molecule[55] or the IDTBR derivatives,[139] which overcame the lack of energy level tunability of fullerene acceptors while offering a potentially lower production cost due to their simpler synthetic routes.[140] This opened a new unprecedented path to realize panchromatic absorption spectra, energy level engineering by the formation of cascades and V_{oc} enhancement due to effective alloying effects, among other advantages.[141]

However, the addition of a third component in the active layer translates into an extra dimension in the photocurrent-composition space. Since the traditional Edisonian experimentation is accordingly scaled with that additional term, most research groups limit their screening to a fixed total donor:acceptor (D:A) ratio (typically set to 1:1 in weight) while varying the relative composition of the two materials with the same electronic character, i.e. D:(A$_{1,x}$,A$_{2,(1-x)}$) or (D$_{1,x}$,D$_{2,(1-x)}$):A. Obviously, this approach provides a constrained view of the corresponding multi-parametric landscape. Furthermore, there is not any fundamental reason why the optimal blend ratio should lie in the 1:1 total donor:acceptor trajectory. Thus, high-throughput optimization based on combinatorial libraries constitutes a particularly suitable approach to perform a broader exploration of the composition space in ternary blends with minimal experimental effort.

Such idea was accordingly developed in **Paper V** to efficiently screen the parametric space of ternary blends. For such purpose, we first adapted the characterization platform for BHJ films based on Raman imaging. In this case, the modelled Raman intensity requires adding an extra term in the summation such that

$$
I_{R.\text{ternary}}(d, v_u, \omega) \propto \int_0^d |E_R(x, v_u)|^2 \mathrm{d}x \sum_{u=1}^{3} v_u \sigma_{R,u} I_{ref,u}(\omega),
$$

where v_u is the volumetric fraction of the u-th component fulfilling that $\sum_{u=1}^{3} v_u = 1$; and $\eta_\text{ternary} = \sum_{u=1}^{3} v_u \eta_u$. In analogy to the conditions first introduced for binary blends, the model will equally reach its highest accuracy when the corresponding Raman cross-section of the blended materials are as similar as possible, and they show markedly different Raman spectra in terms of vibrational peaks, line widths and overall features.

The generation of compositional ternary libraries is more challenging than that of binaries, especially when only pristine inks are employed to avoid the massive consumption of raw materials in the preparation of premixed solutions. After trying diverse experimental approaches, we discovered that layer-by-layer (LbL) processing successfully allows the realization of such libraries. Interestingly, the

75

approach is somehow an exclusive feature of blade coating with large interest in future OPV upscaling due to its simplicity.[142–144] In LbL processing the active layer components are sequentially deposited, one on top of the other, using the pristine inks with the same carrier solvent. As a result, the layer obtained is morphologically similar to a BHJ processed in one step yet with a slight vertical segregation arising from the layer interdiffusion.[23] In fact, the PV performance attained using LbL films is comparable to or even higher than that obtained following the usual BHJ procedure with material premixing in a single vial.[144] The origin of such high PV performance is likely to be related with optimal vertical phase segregation throughout the active layer, especially when the pseudo-bilayer configuration (in the case of binaries) matches the polarity of the contacts (i.e. conventional vs. inverted device architectures).[143] For ternary blends and to the best of our knowledge, there had not been any reports on LbL coating with successful results.

Thus, in Paper V we demonstrate for the first time the fabrication of ternary blend OPV devices by LbL blade coating. Interestingly, these devices are processed in the form of combinatorial compositional libraries. They are designed to cover different regions of the corresponding phase diagram depending on the processing conditions followed but, as a rule of thumb, the polymer phase(s) should always be deposited first. Atop that polymer thin film, the acceptor material layers are subsequently deposited, being these small molecules (either fullerenes or NFAs) dissolved in the same carrier solvent as the pristine polymer. We experimentally found that it is precisely this approach what leads to large compositional combinatorial libraries in the ternary blend since performing an overcoating with a polymeric ink usually leads to complete detachment of the layers below. We hypothesize that the origin of this phenomenon is related with the ink viscosity, which in the case of polymer-based inks is high enough to detach the acceptor layer as the blade applicator spreads the solution over the substrate.
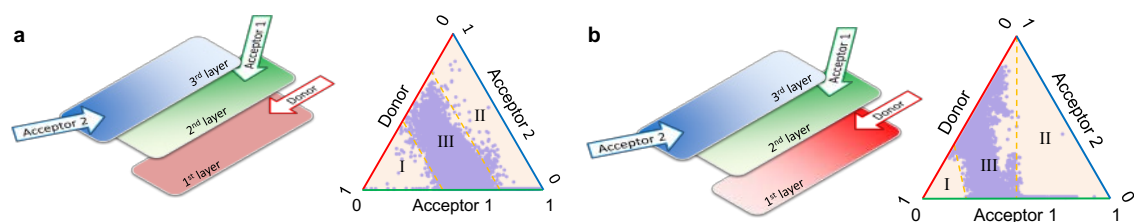
Figure 30. The realization of ternary compositional libraries relies on the LbL coating of the active layer materials, starting by the more viscous ink (i.e. the donor polymer) which can be deposited either as a homogeneous film (a) or as a thickness gradient (b). The remaining layers are deposited from the substrate corners to induce the formation of oblique gradients. Accordingly, different regions of the ternary diagrams can be explored.

In order to increase the compositional range in the ternary phase diagram, the donor layer can be processed either as a laterally homogeneous film or in the form of a gradient (Figure 30). On the other hand, the acceptor layers are systematically processed as gradients yet rotated by 45 ° with respect to the longitudinal coating direction. In this case, the thickness gradient originates from the progressive variation of substrate width available for ink spreading. Finally, we found that by alternating the coating order and the thickness of the active layer components it is possible to study different areas of the corresponding ternary diagrams. Only under special processing circumstances, we have been able to cover the entire ternary diagram using a single sample, which we still believe is an impressive finding.

A large battery of optical characterization techniques is applied onto the ternary compositional libraries, as summarized in Figure 31. Notably, in this work the photovoltaic performance is evaluated using both monochromatic light (from the laser source used to measure Raman scattering or photoluminescence, PL) as well as white light. Importantly, these data are now acquired in the same setup used to measure the Raman spectra and no longer in two different setups. This was made possible thanks to a customization of the original WITec alpha 300RA+ setup that consisted of the addition of a current amplifier, synchronized with the control software of the equipment. Accordingly, it enabled us to simultaneously collect the Raman scattered signal and the photocurrent induced in the device by the own laser spot. Thus, Raman (or PL) and photocurrent images are acquired *in situ* and co-locally in the same acquisition run. Remarkably, this constitutes a giant leap forward

in the high-throughput experimentation capabilities of the combinatorial screening approach since it *de facto* halves the time required to complete a combinatorial study when employing monochromatic light only. We also combine this new approach with PL imaging, as the PL can be correlated in some cases with the charge transfer energy as proxy of the effective *local* V_{oc}. Similarly, the PL quenching reflects efficient charge transfer and material intermixing.

Furthermore, Raman scattering is used to explore the effect that ternary blending has in the film morphology, and how this is related with the measured photocurrent. More precisely, we evaluate the disruption of the molecular order that takes place in the semi-crystalline polymer domains by looking at the Raman shift of the C=C stretching modes, such as the 1450 cm^{-1} band of P3HT (Figure 32b). These are especially sensitive to the conjugation length of the backbones,[108,145] thus serving as a probe of the degree of molecular order and chain planarity in the corresponding domains.

However, because the use of monochromatic light might lead to incomplete conclusions in terms of PV performance, a broadband excitation source is also needed to collect more *realistic* photocurrent data; this is, in fact, especially required for ternaries, where panchromatic absorption spectra are usually targeted. Therefore, we coupled the white emission of the built-in microscope lamp of the Raman setup and used it as excitation source to collect the photocurrent. In this way, we somehow mimic the standard outdoors lighting conditions and, accordingly, we termed this photocurrent imaging approach as *whiteBIC*. Nevertheless, it is worth noting that the irradiance spectrum of the white light does not match the standardized AM1.5G spectrum nor that provided by a solar simulator, which due to technical limitations cannot be coupled as excitation source in the Raman setup. Still, we found that the whiteBIC technique provides photocurrent images and absolute short-circuit current densities from batch-to-batch that are in better agreement with those reported under standard AM1.5G illumination than monochromatic excitation does. In addition, the use of white light illumination enabled us to perform absorption maps by collecting the reflectivity spectra of the full device stack, after normalization by the reflectivity of the back electrode. Notably,

all these measurements are performed in a row and in a single setup, requiring less than 3 hours per sample to be completed and generating ca. 13 million experimental data points in total, thus representing a paradigmatic example of high-throughput screening and hyperspectral imaging of OPV devices.

Finally, and as a result of our measuring-intensive ternary compositional screening, we demonstrate that ternary blends can show multimodal distributions of the PV performance. In particular, we show that distinct relative photocurrent maxima occur depending on the underlying physical processes that are more favoured in a particular blending ratio. This fact usually results from either favoured charge extraction or enhanced light harvesting, especially when fullerenes (better charge extractors in general) and NFAs (better light harvesters than fullerenes) coexist in the blend.
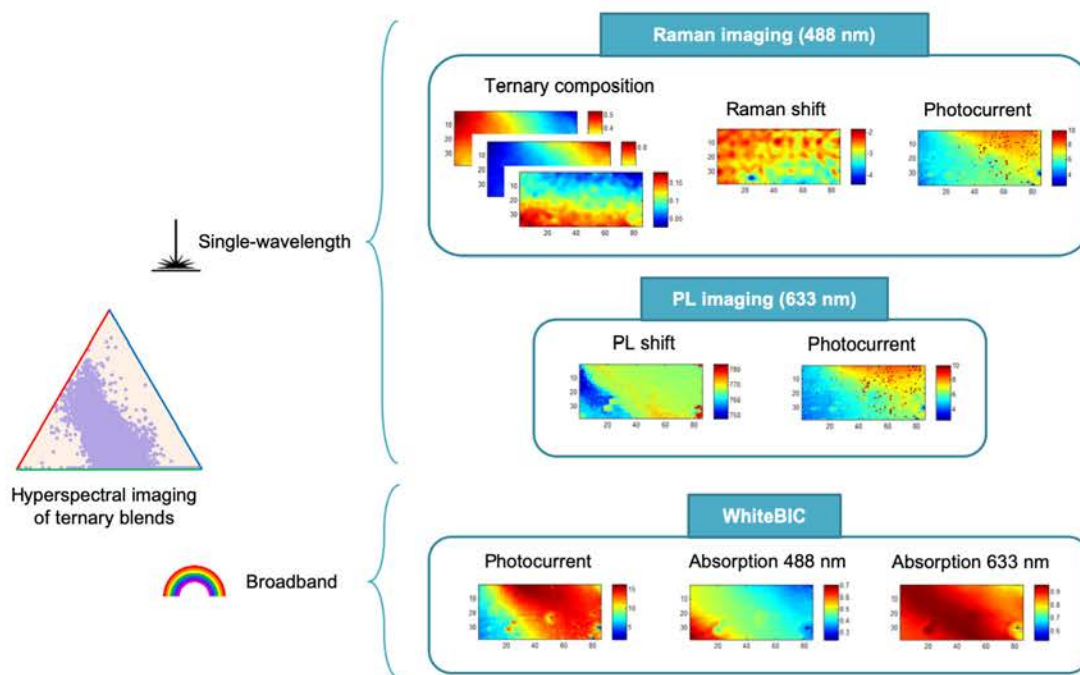

Figure 31. The hyperspectral imaging of ternary devices includes single-wavelength and broadband optical characterization techniques. Raman spectroscopy is used to retrieve the ternary composition and investigate the film morphology based on vibrational mode shifting while co-locally acquiring the photocurrent at 488 nm excitation. PL imaging is measured afterwards using a He-Ne 633 nm laser source; the photocurrent is also extracted simultaneously. Finally, a broadband illumination source is employed to measure more realistically the photocurrent dependence; at the same time, absorption maps are built based on the reflectivity of the full device stack.

In summary, by following a combinatorial screening protocol based on Raman imaging, PL imaging and (whiteBIC) photocurrent mapping we successfully explore the ternary phase diagram of several state-of-the-art blends. In our work we demonstrate the existence of a complex performance landscape as a function of composition, with multimodal distributions of the photocurrent. Our findings confirm that the 1:1 total donor:acceptor compositional trajectory does not necessarily lead to the optimal blend ratio; in fact, in some cases a performance valley is encountered precisely at that compositional range. Accordingly, the compositional space in ternary blends should be more carefully explored to find the proper balance between charge generation and extraction in the active layer. Thus, most ternary blends reported up to date with excellent PCEs might yet be partly optimized given the inherent complexity of the photocurrent-composition space. We think, however, that these are good news for ternaries since it might be indicative that there is still room for improvement in their performance.

Notably, this kind of statistically meaningful combinatorial studies including ternary blends can almost exclusively be tackled by means of high-throughput experimentation techniques (Figure 32). It is, in fact, nearly impossible to imagine tackling these experiments while sticking to traditional Edisonian approaches: the time and material requirements would be prohibitive for most research groups. Still, it is worth noting that in our high-throughput experimentation work for ternaries we have somehow skipped the optimization of the active layer thickness, since that would already add too much complexity to perform a simultaneous four-dimensional parametric screening. Instead, what we propose is to screen first the compositional space; then, and once the photocurrent hotspots are correctly located in the ternary phase diagram, the screening proceeds exploiting orthogonal thickness and annealing gradients to finally tailor the full set of device parameters. With all that, ternary blends are an example of combinatorial screening at its best.
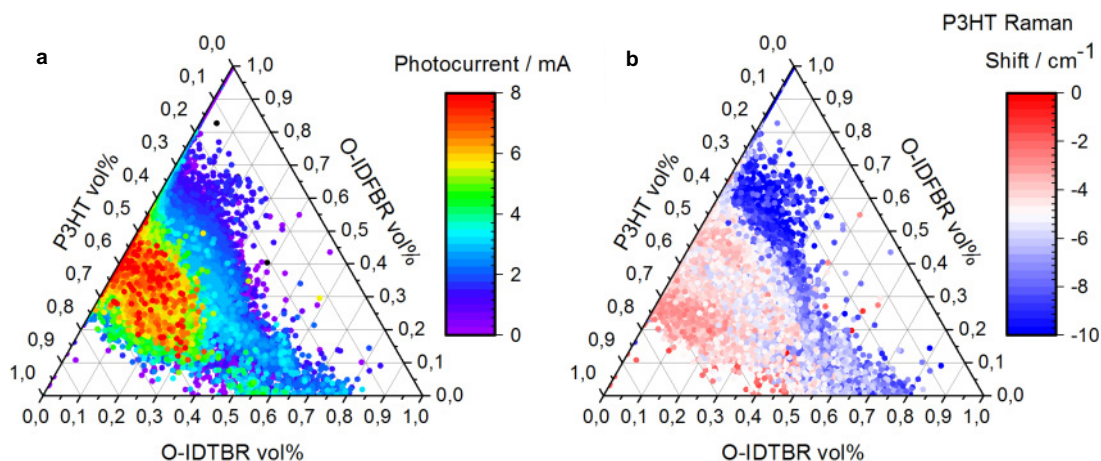
Figure 32. Example of a statistically meaningful ternary dataset composed by 150.000 experimental data points of the P3HT:O-IDFBR:O-IDTBR blend. (a) Photocurrent extracted at 488 nm excitation. (b) Raman mode dispersion of the 1450 cm^{-1} band of P3HT. We observe that the higher photocurrent occurs when the corresponding band is only moderately blue-shifted (ca. 3-5 cm^{-1}).

4.4. High-throughput experimentation and AI: the perfect pairing

High-throughput experimentation can be used to probe with minimal effort the photocurrent space in OPV blends while generating statistically meaningful datasets. These approaches literally generate millions of data points per parametric space, as we have already shown for ternary blends. An unprecedented catalogue of combinatorial studies is accordingly open, with straightforward applications into the study of material families whose molecular motifs are systematically varied, analysed and understood in terms of PV performance. Eventually, these studies might be useful to define novel design rules for the obtainment of high performing materials, as other computational[146] and data mining[147–151] studies are currently trying to introduce. In this regard, when high-throughput experimentation is used systematically to explore the PV properties of a material family, we end up immersing in a *big data* scenario. In this situation, the use of AI algorithms can notably guide researchers as far as data interpretation is concerned and also to extract predictive physical models from the observables.

AI refers to a set of computational tools with built-in learning capability. These are usually based on the classification of the data according to certain features or descriptors. The descriptors are characteristics arbitrarily chosen by the scientist

based on his/her intuition or *a priori* information collected about the target for being somehow related with it. An AI algorithm accordingly specifies how the input data is classified and which statistical magnitude is minimized at each decision node. After training of the algorithm with part of the experimental inputs and testing the resulting model in unknown data points, the accuracy of the AI model is evaluated. Finally, the AI model can be analysed to identify which are the most relevant descriptors when performing model predictions. This serves to limit the dimensionality of the complex multi-parametric spaces in which they are usually trained, thus opening the possibility to formulate more intuitive and simple models.

The current uses of AI are mostly ignored by most of us but they are certainly omnipresent in our daily life: from weather forecasting, ad recommendation and face and voice recognition, to decision making in stock markets and modelling of COVID-19 pandemic expansion, to name just a few. In the academic panorama, AI is one of the current hot topics in nearly every possible branch and it is actively encouraged by editorial boards to be exploited in combination with data mining and experiments in complex multi-dimensional parametric spaces,[152] such as those encountered in OPV. In our field, the understanding of the photocurrent-composition space is certainly a must to further accelerate the device optimization once certain potentially high-performing donor:acceptor blend is identified. So, can AI teach us something about organic solar cells and contribute in the acceleration of materials screening?
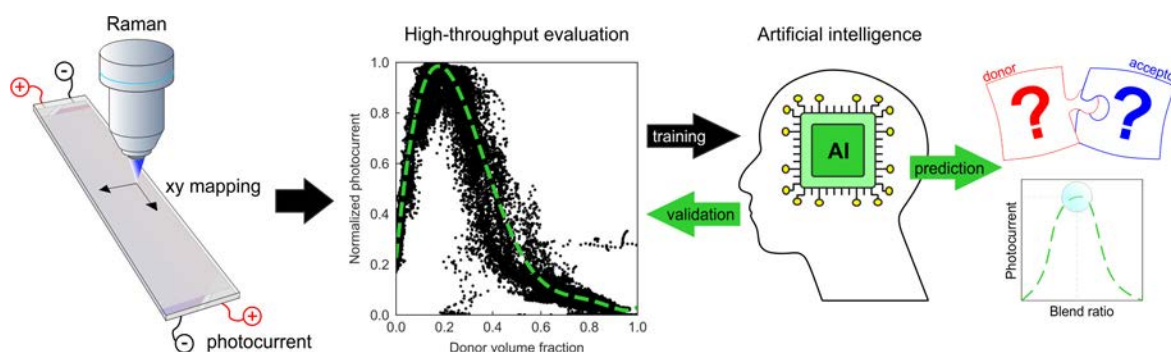

Figure 33. Illustration of the binary OPV blend screening workflow that synergically combines high-throughput experimentation with AI algorithms. The process starts by the generation of thickness-composition parametric libraries by gradient generation in blade coating, which are evaluated by combining Raman and photocurrent imaging. The large datasets generated for a broad catalogue of materials combinations are then exploited as input training sets for a series of AI ensembles. These are eventually exploited to identify the relevant descriptors that best describe the photocurrent-composition landscape and to draw accurate extrapolations in unknown donor:acceptor pairs.

Based on these needs, in **Paper VI** we synergically combine for the first time high-throughput experimentation with AI algorithms to build intuitive and powerful models for the photocurrent-composition space in binary OPV blends. The procedure (Figure 33) starts by performing a combinatorial exploration of the photocurrent-composition space in binary blends following the high-throughput experimentation approach described in Paper III, i.e. the generation of orthogonal thickness-composition libraries by the two-drop coalescence method. The high-throughput approach is systematically applied to a large collection of donor:acceptor binaries (a total of 15 dissimilar combinations are explored), including state-of-the-art low band gap polymers and NFAs.

This combinatorial grid of donor:acceptor materials served as input for the AI training of two different algorithms. On the one hand, we implemented a Bayesian machine-scientist developed by Dr. Roger Guimerà and co-workers from Universitat Rovira i Virgili (Tarragona). This algorithm is able to retrieve the most plausible mathematical relationship describing a certain set of data, which in our particular case corresponds to an analytical formula to describe the photocurrent-composition space in eight donor:acceptor blends simultaneously (Figure 34). Our results show a remarkable predictive power within the materials dataset employed for training. In fact, the algorithm is used to fill the uncharted configuration space in the studied blends. This is very useful to evaluate, for example, their potential sensitivity against unintentional thickness and/or mixing ratio fluctuations, especially when the experimental exploration is, for some reason, rather limited. Nevertheless, the model requires a large computational investment to be fitted (among 4-8 weeks of training with the 8000 experimental data points initially provided) and unfortunately it was found to provide inaccurate predictions out of the training materials set.
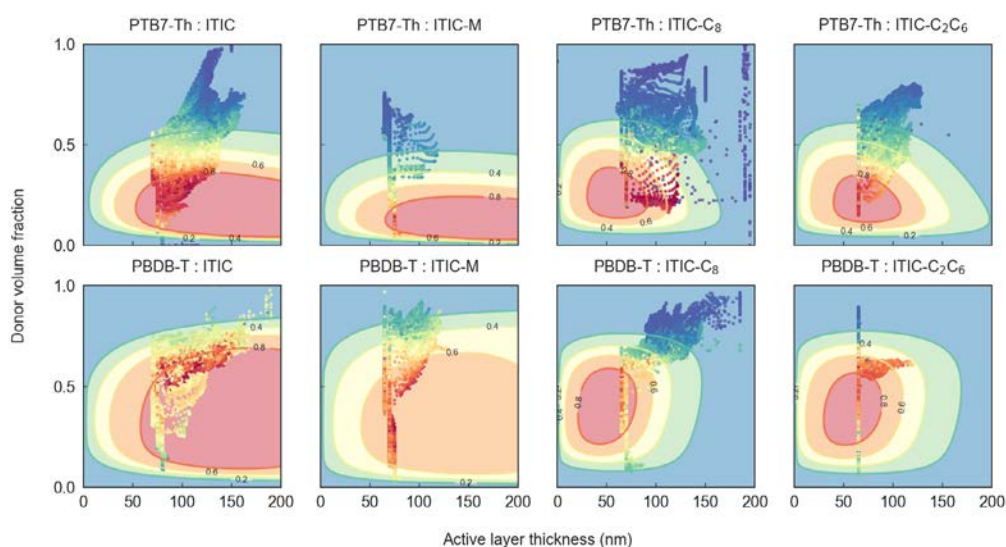
Figure 34. Contour plots for the normalized photocurrent model equation found by the Bayesian machine-scientist. The machine-scientist is trained with a full set of materials combinations formed by two donor polymers (PTB7-Th and PBDB-T) blended with four ITIC derivatives as acceptors, namely ITIC, ITIC-M, ITIC-C_8 and ITIC-C_2C_6. The algorithm identifies an 8-parameter analytical relationship to best describe the photocurrent space in all blends simultaneously, depicted as contour plots in the background of the panels. The scattered data represents the experimentally accessed data points obtained in each combinatorial donor:acceptor pair, depicted in the same colour scale as the contours.

On the other hand, we applied the workhorse machine-learning algorithm, namely a random decision forest (RF) ensemble, to build predictive models using larger datasets. RF models are based on decision trees and impurity minimization upon data classification and provide purely numerical (*black box*) solutions. Nevertheless, in this kind of models there are built-in classification magnitudes such as the feature importance (FI), which account for the importance of the descriptors according to their weight in the minimization of the impurity (i.e. the variance) at each decision node. Accordingly, when dealing with a large list of potentially influent model features, FIs can be used recursively until reaching a minimal number of parameters, thus providing more simple and intuitive models open to physical interpretation; this process is known as feature selection.
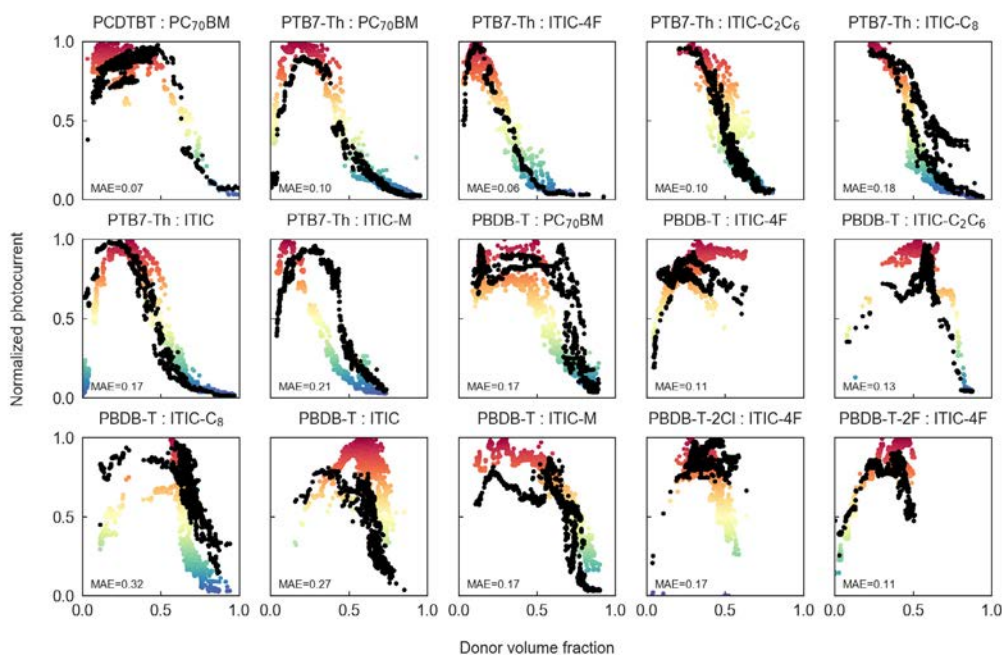
Figure 35. The leave-one-out cross-validation (LOO-cv) of the RF model provides excellent extrapolating capabilities with a mean absolute error of 0.16 (±0.07) when trained with 15 experimental datasets and two material descriptors only, namely the characteristic energy band gaps of the donor and acceptor materials. While the experimental data used for training is depicted in the background in colour scale, the RF model predictions are illustrated as scattered black dots.

Conversely to the Bayesian machine-scientist, the simpler and faster[9] RF algorithm is found to describe more accurately the experimental trends while making outstanding model predictions out of the training set. A greedy mean absolute error (G-MAE) feature selection procedure performed on the RF algorithm identifies several combinations of two descriptors only that result in successfully validated and predictive RF models. Among the parametric combinations screened, we acknowledge the one formed by the electronic (and also optical) band gaps of the donor and acceptor materials. The corresponding leave-one-out cross-validations (LOO-cv) of this model result in RF ensembles with one of the lowest mean absolute errors (Figure 35). We also observe that when our full list of optoelectronic descriptors (formed by 23 elements) is employed in the training, those parameters related with the HOMO/LUMO energy level alignment as well as some magnitudes

---

[9] The training time of a random decision forest ensemble composed by 100 decision trees and 14000 data points takes less than 10 seconds in a state-of-the-art laptop.

derived from the intrinsic charge carrier mobility of the donor (μ_d) and acceptor (μ_a) materials are distinguished among the most relevant descriptors. Particularly, the parameters related with the charge carrier mobility difference ($|\mu_a - \mu_d|$) and ratio (μ_a/μ_d) are identified as important features by the RF model (Figure 36). Interestingly, the existence of unbalanced charge mobilities for holes and electrons at the donor and acceptor phases has so far been considered as the consensual explanation for the observed disequilibrium in the photocurrent-composition space of binary OPV blends.[153] However, our RF model suggests that the observed unbalance could also be reproduced based on the degree of absorption complementarity of the donor and acceptor species and to the HOMO/LUMO energy level alignment, being both features somehow summarized in a simpler magnitude: the corresponding energy band gaps.
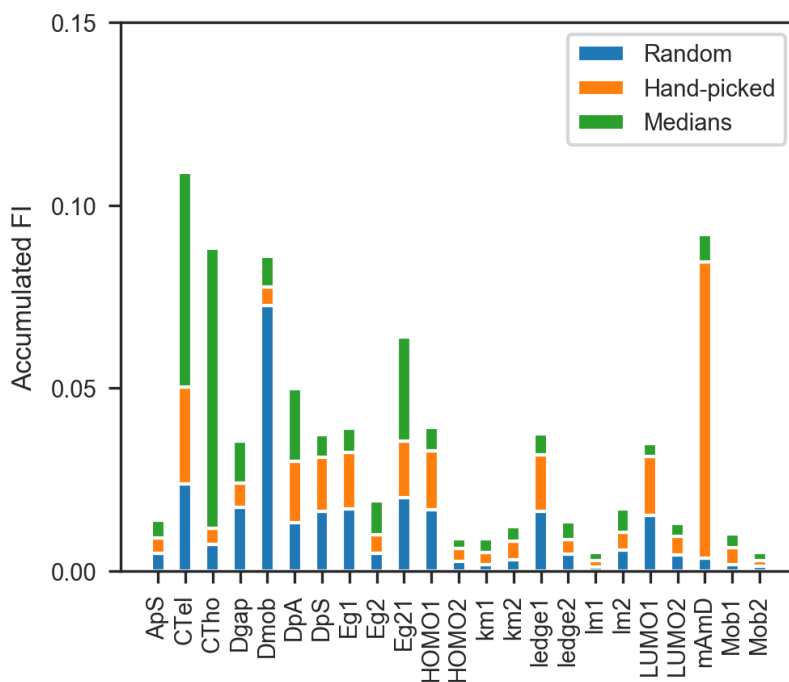

Figure 36. An analysis of the feature importance (FI) drawn by a variety of RF ensembles indicates that the most descriptive features (in overall) are related with the frontier energy level (HOMO/LUMO) alignment of the donor and acceptor materials (represented by parameters such as $CT_{el} = (|LUMO_d - LUMO_a|) / k_BT$, $CT_{ho} = (|HOMO_d - HOMO_a|) / k_BT$ or $Eg_{21} = |E_{gap,a} - E_{gap,d}|$) as well as those related with the mobility imbalance ($D_{mob} = |\mu_a - \mu_d|$, $m_Am_D = \mu_a/\mu_d$). Parameters labelled with *1* (*2*) refer to magnitudes of the donor (acceptor) material.

5. Conclusions

The conclusions of this doctoral thesis are summarized into six bullet points, corresponding to each of the articles forming the compendium:

- Raman spectroscopy can be exploited to quantify the film thickness of nanometric layers and the volumetric mixing ratio of multi-component blends. This is performed based on the transfer matrix method and the assignment of solid-state Raman cross-sections to account for interference effects and the distinct Raman activity of the materials, respectively.

- Bilayer small molecule organic solar cells can be optimized in a combinatorial manner by the orthogonal arrangement of the photoactive layers in the form of thickness gradients. Raman imaging is used jointly with LBIC to map the thickness and the photocurrent, respectively.

- Solution-processed binary bulk heterojunction devices can be subjected to high-throughput optimization by generating orthogonal thickness, composition and thermal annealing gradients. The parametric libraries are realized by blade coating pristine drop inks and laterally characterized via Raman and LBIC. This methodology renders almost 50 times faster than the conventional sample-by-sample approach while using only a small fraction (ca. 10-20%) of the semiconductor materials to complete the screening study.

- Microfluidics-assisted blade coating is introduced as a general thin film processing scheme to fabricate controllable compositional libraries onto solid-state layers. The approach enables high-throughput combinatorial screening in all-polymer binary blends.

- The complex multi-dimensional parametric space of ternary OPV blends can be efficiently screened by combining layer-by-layer blade coating for the generation of compositional libraries and hyperspectral imaging with photovoltaic and spectroscopic techniques. The emergence of multimodal performance landscapes is demonstrated.

- The systematic and high-throughput screening of the photocurrent space in binary OPV materials families generates large datasets that serve as inputs in AI algorithms. These reveal the existence of intuitive models based on

intrinsic material descriptors that can be exploited to predict the photocurrent space in any OPV binary blend. Particularly, we find that simple models of two parameters only (the donor and acceptor energy band gaps) serve to define the photocurrent vs. composition dependence with excellent accuracy.

6. Future prospects

After the research conducted throughout this doctoral thesis, we identify a series of aspects that should be addressed in the near future in order to further extend the capabilities of the high-throughput screening and combinatorial approaches herein introduced. Regarding the experimental part, we identify at least two key issues that might be reconsidered for upcoming projects.

First, the acquisition of photocurrent maps via LBIC should ideally be (re)designed to be performed with a calibrated illumination source, namely an AM1.5G solar irradiance spectrum. This feature could be exploited to obtain more standardized photocurrent values in the combinatorial devices, thus getting more robust and independent conclusions by the own high-throughput screening methodology while avoiding the fabrication of discrete devices to cross-validate the optimal parameters found.

Second, the two-drop coalescence method might be optimized to avoid the formation of minute pinholes in the active layer. Our latest explorations suggest that those are responsible for the downscaled absolute photocurrent values sometimes observed from batch-to-batch devices while sticking to certain donor:acceptor blend. For this particular reason, normalized photocurrent values were employed to feed AI algorithms in Paper VI, a fact which could be oversimplifying the models therein obtained.

On the other hand, we find remarkable potential for the high-throughput screening methodology to be adapted to different issues in the OPV panorama as well as other solution-processable thin film technologies. In particular, we find the simultaneous acquisition of composition and thickness by Raman scattering and co-local photocurrent via LBIC to be a suitable way to quickly screen the device stability, which is one of the major bottlenecks of current OPV devices. The use of *degradation gradients* or high-throughput degradation protocols, consisting in controlled annealing ramps, permeation tests against oxygen or water vapor or illumination gradients along the active layer, could be smartly exploited to track *in situ* how the active layer morphology evolves in time. This approach opens up an

interesting prospect, namely the evaluation of stability times for distinct features of the active layer in a very efficient manner, including the donor:acceptor mixing ratio, the thickness and the morphology. In fact, we have recently demonstrated that thinner active layers are significantly more stable than thicker ones for the P3HT:O-IDTBR binary blend,[84] thus encouraging us to continue with further research on that particular topic. Eventually, this could be exploited to identify which are the most resilient device parameters ranges for future upscaling as well as those which offer an extended lifetime and more economical viability. Moreover, in this latter regard the high-throughput screening methodology could be adapted for industrial purposes, namely the identification of optimal processing parametric windows for reliable industrial manufacture in R2R setups.

High-throughput experimentation could also be exploited jointly with combinatorial synthetic chemistry platforms to enable a fast and efficient screening of materials families. Historically, the development of high-performing OPV materials has been constrained to trial-and-error systematic approaches extended over more than 20 years of research (Figure 4). During that time, a constant feedback between material scientists, physicists and synthetic chemists supported the refinement of the OPV materials design rules: thousands of different combinations of conjugated moieties and side chains have been tested in co-polymers and small molecules until nailing the desired optoelectronic properties, eventually forming the current state-of-the-art of the technology. Nevertheless, would it be possible to puzzle high-throughput experimentation and combinatorial synthesis to further accelerate the materials screening in the upcoming years? This fact could end up enabling the empirical determination of novel design guidelines based on the efficient exploration of complete materials libraries (such as that depicted in Figure 10), thus going beyond the current state-of-the-art at an unprecedented pace.

Finally, we would like to remark the yet unexplored capabilities that AI algorithms have in combination with high-throughput experimental screening. The work developed in this thesis for binary OPV blends represents a significant leap forward in this regard, yet we identify further topics that could be addressed in future projects. The most natural step further could consist in applying AI to ternary blends,

which intrinsic parametric complexity often prevents a full exploration of the ternary phase diagram in terms of PV performance. Different AI algorithms could be tested to extrapolate such diagrams, thus identifying the different performance peaks and valleys with minimal effort and provide the experimentalists a first prior to nail more quickly the optimal blending ratio when facing unknown mixtures or materials. Potentially, AI algorithms could be exploited in combination with data mining in multi-component systems to understand their particular behaviour and obtain novel design rules affecting both device stability and efficiency.

7. References

[1]   BP, *BP Statistical Review of World Energy 2019, 68th Edition*, **2019**.
[2]   International Energy Agency, *World Energy Outlook 2019*, **2019**.
[3]   European Environment Agency, "Atmospheric greenhouse gas concentrations indicator (CSI 013, CLIM 052)," **2019**.
[4]   International Energy Agency, *Renewables 2019*, **2019**.
[5]   Fraunhofer Institute for Solar Energy Systems (ISE), *Photovoltaics Report, Updated 14 November 2019*, Freiburg, **2019**.
[6]   A. Al-Fuqaha, M. Guizani, M. Mohammadi, M. Aledhari, M. Ayyash, *IEEE Commun. Surv. Tutorials* **2015**, *17*, 2347.
[7]   H. Michaels, M. Rinderle, R. Freitag, I. Benesperi, T. Edvinsson, R. Socher, A. Gagliardi, M. Freitag, *Chem. Sci.* **2020**, *11*, 2895.
[8]   C. L. Cutting, M. Bag, D. Venkataraman, *J. Mater. Chem. C* **2016**, *4*, 10367.
[9]   F. De Rossi, T. Pontecorvo, T. M. Brown, *Appl. Energy* **2015**, *156*, 413.
[10]   M. Mainville, M. Leclerc, *ACS Energy Lett.* **2020**, *5*, 1186.
[11]   M. Young, C. J. Traverse, R. Pandey, M. C. Barr, R. R. Lunt, *Appl. Phys. Lett.* **2013**, *103*, 133304.
[12]   F. C. Krebs, N. Espinosa, M. Hösel, R. R. Søndergaard, M. Jørgensen, *Adv. Mater.* **2014**, *26*, 29.
[13]   N. Espinosa, M. Hösel, D. Angmo, F. C. Krebs, *Energy Environ. Sci.* **2012**, *5*, 5117.
[14]   C. J. M. Emmott, N. J. Ekins-Daukes, J. Nelson, *Energy Environ. Sci.* **2014**, *7*, 1810.
[15]   E. Pascual-San José, A. Sánchez-Díaz, M. Stella, E. Martínez-Ferrero, M. I. Alonso, M. Campoy-Quiles, *Sci. Technol. Adv. Mater.* **2018**, *19*, 823.
[16]   T. Li, S. Dai, Z. Ke, L. Yang, J. Wang, C. Yan, W. Ma, X. Zhan, *Adv. Mater.* **2018**, *30*, 1705969.
[17]   S. Savagatrup, A. D. Printz, T. F. O'Connor, A. V. Zaretski, D. Rodriquez, E. J. Sawyer, K. M. Rajan, R. I. Acosta, S. E. Root, D. J. Lipomi, *Energy Environ. Sci.* **2015**, *8*, 55.
[18]   C. J. Brabec, S. E. Shaheen, C. Winder, N. S. Sariciftci, P. Denk, *Appl. Phys. Lett.* **2002**, *80*, 1288.
[19]   Q. Liu, Y. Jiang, K. Jin, J. Qin, J. Xu, W. Li, J. Xiong, J. Liu, Z. Xiao, K. Sun, S. Yang, X. Zhang, L. Ding, *Sci. Bull.* **2020**, *65*, 272.
[20]   L. Meng, Y. Zhang, X. Wan, C. Li, X. Zhang, Y. Wang, X. Ke, Z. Xiao, L. Ding, R. Xia, H.-L. Yip, Y. Cao, Y. Chen, *Science (80-.).* **2018**, *361*, 1094.
[21]   X. Du, T. Heumueller, W. Gruber, A. Classen, T. Unruh, N. Li, C. J. Brabec, *Joule* **2019**, *3*, 215.
[22]   M. P. Tsang, G. W. Sonnemann, D. M. Bassani, *Sol. Energy Mater. Sol. Cells* **2016**, *156*, 37.
[23]   A. Colsmann, H. Röhm, C. Sprau, *Sol. RRL* **2020**, *4*, 2000015.
[24]   E. Becquerel, *Comptes Rendus* **1839**, *9*, 561.
[25]   A. Polman, M. Knight, E. C. Garnett, B. Ehrler, W. C. Sinke, *Science (80-.).* **2016**, *352*, aad4424.
[26]   A. Chirilă, S. Buecheler, F. Pianezzi, P. Bloesch, C. Gretener, A. R. Uhl, C. Fella, L. Kranz, J. Perrenoud, S. Seyrling, R. Verma, S. Nishiwaki, Y. E. Romanyuk, G. Bilger, A. N. Tiwari, *Nat. Mater.* **2011**, *10*, 857.
[27]   L. Kranz, C. Gretener, J. Perrenoud, R. Schmitt, F. Pianezzi, F. La Mattina, P. Blösch, E. Cheah, A. Chirilă, C. M. Fella, H. Hagendorfer, T. Jäger, S. Nishiwaki, A. R. Uhl, S. Buecheler, A. N. Tiwari, *Nat. Commun.* **2013**, *4*, 2306.
[28]   D. Kearns, M. Calvin, *J. Chem. Phys.* **1958**, *29*, 950.
[29]   C. W. Tang, *Appl. Phys. Lett.* **1986**, *48*, 183.
[30]   B. O'Regan, M. Grätzel, *Nature* **1991**, *353*, 737.
[31]   G. Yu, J. Gao, J. C. Hummelen, F. Wudl, A. J. Heeger, *Science (80-.).* **1995**, *270*,

1789.

[32] J. J. M. Halls, C. A. Walsh, N. C. Greenham, E. A. Marseglia, R. H. Friend, S. C. Moratti, A. B. Holmes, *Nature* **1995**, *376*, 498.

[33] A. Kojima, K. Teshima, Y. Shirai, T. Miyasaka, *J. Am. Chem. Soc.* **2009**, *131*, 6050.

[34] C. J. Brabec, N. S. Sariciftci, J. C. Hummelen, *Adv. Funct. Mater.* **2001**, *11*, 15.

[35] J. E. Northrup, *Phys. Rev. B* **2007**, *76*, 245202.

[36] J. Zaumseil, H. Sirringhaus, *Chem. Rev.* **2007**, *107*, 1296.

[37] L.-L. Chua, J. Zaumseil, J.-F. Chang, E. C.-W. Ou, P. K.-H. Ho, H. Sirringhaus, R. H. Friend, *Nature* **2005**, *434*, 194.

[38] M. S. Vezie, S. Few, I. Meager, G. Pieridou, B. Dörling, R. S. Ashraf, A. R. Goñi, H. Bronstein, I. McCulloch, S. C. Hayes, M. Campoy-Quiles, J. Nelson, *Nat. Mater.* **2016**, *15*, 746.

[39] A. Harillo-Baños, X. Rodríguez-Martínez, M. Campoy-Quiles, *Adv. Energy Mater.* **2020**, *10*, 1902417.

[40] N. Blouin, A. Michaud, D. Gendron, S. Wakim, E. Blair, R. Neagu-Plesu, M. Belletête, G. Durocher, Y. Tao, M. Leclerc, *J. Am. Chem. Soc.* **2008**, *130*, 732.

[41] C. Duan, F. Huang, Y. Cao, *J. Mater. Chem.* **2012**, *22*, 10416.

[42] Y. Liang, D. Feng, Y. Wu, S.-T. Tsai, G. Li, C. Ray, L. Yu, *J. Am. Chem. Soc.* **2009**, *131*, 7792.

[43] J.-M. Jiang, H.-K. Lin, Y.-C. Lin, H.-C. Chen, S.-C. Lan, C.-K. Chang, K.-H. Wei, *Macromolecules* **2014**, *47*, 70.

[44] W. Yue, Y. Zhao, S. Shao, H. Tian, Z. Xie, Y. Geng, F. Wang, *J. Mater. Chem.* **2009**, *19*, 2199.

[45] L. Hu, W. Qiao, X. Zhou, J. Han, X. Zhang, D. Ma, Y. Li, Z. Y. Wang, *Polym. Chem.* **2017**, *8*, 2055.

[46] T. Lei, J.-H. Dou, J. Pei, *Adv. Mater.* **2012**, *24*, 6457.

[47] J. Lee, A.-R. Han, H. Yu, T. J. Shin, C. Yang, J. H. Oh, *J. Am. Chem. Soc.* **2013**, *135*, 9540.

[48] W. Zhang, J. Smith, S. E. Watkins, R. Gysel, M. McGehee, A. Salleo, J. Kirkpatrick, S. Ashraf, T. Anthopoulos, M. Heeney, I. McCulloch, *J. Am. Chem. Soc.* **2010**, *132*, 11437.

[49] H. Bronstein, D. S. Leem, R. Hamilton, P. Woebkenberg, S. King, W. Zhang, R. S. Ashraf, M. Heeney, T. D. Anthopoulos, J. De Mello, I. McCulloch, *Macromolecules* **2011**, *44*, 6649.

[50] I. McCulloch, R. S. Ashraf, L. Biniek, H. Bronstein, C. Combe, J. E. Donaghey, D. I. James, C. B. Nielsen, B. C. Schroeder, W. Zhang, *Acc. Chem. Res.* **2012**, *45*, 714.

[51] H. Chen, M. Hurhangee, M. Nikolka, W. Zhang, M. Kirkus, M. Neophytou, S. J. Cryer, D. Harkin, P. Hayoz, M. Abdi-Jalebi, C. R. McNeill, H. Sirringhaus, I. McCulloch, *Adv. Mater.* **2017**, *29*, 1702523.

[52] X. Zhang, H. Bronstein, A. J. Kronemeijer, J. Smith, Y. Kim, R. J. Kline, L. J. Richter, T. D. Anthopoulos, H. Sirringhaus, K. Song, M. Heeney, W. Zhang, I. McCulloch, D. M. DeLongchamp, *Nat. Commun.* **2013**, *4*, 2238.

[53] R. Noriega, J. Rivnay, K. Vandewal, F. P. V. Koch, N. Stingelin, P. Smith, M. F. Toney, A. Salleo, *Nat. Mater.* **2013**, *12*, 1038.

[54] S. Holliday, R. S. Ashraf, A. Wadsworth, D. Baran, S. A. Yousaf, C. B. Nielsen, C.-H. Tan, S. D. Dimitrov, Z. Shang, N. Gasparini, M. Alamoudi, F. Laquai, C. J. Brabec, A. Salleo, J. R. Durrant, I. McCulloch, *Nat. Commun.* **2016**, *7*, 11585.

[55] Y. Lin, J. Wang, Z.-G. Zhang, H. Bai, Y. Li, D. Zhu, X. Zhan, *Adv. Mater.* **2015**, *27*, 1170.

[56] S. Li, L. Ye, W. Zhao, S. Zhang, S. Mukherjee, H. Ade, J. Hou, *Adv. Mater.* **2016**, *28*, 9423.

[57] W. Zhao, S. Li, H. Yao, S. Zhang, Y. Zhang, B. Yang, J. Hou, *J. Am. Chem. Soc.* **2017**, *139*, 7148.

[58] Y. Bai, C. Zhao, X. Chen, S. Zhang, S. Zhang, T. Hayat, A. Alsaedi, Z. Tan, J. Hou, Y. Li, *J. Mater. Chem. A* **2019**, *7*, 15887.

[59] M. C. Scharber, D. Mühlbacher, M. Koppe, P. Denk, C. Waldauf, A. J. Heeger, C. J. Brabec, *Adv. Mater.* **2006**, *18*, 789.

[60] M. C. Scharber, N. S. Sariciftci, *Prog. Polym. Sci.* **2013**, *38*, 1929.

[61] K. Vandewal, K. Tvingstedt, A. Gadisa, O. Inganäs, J. V. Manca, *Phys. Rev. B* **2010**, *81*, 125204.

[62] K. Vandewal, K. Tvingstedt, A. Gadisa, O. Inganäs, J. V. Manca, *Nat. Mater.* **2009**, *8*, 904.

[63] J. Benduhn, K. Tvingstedt, F. Piersimoni, S. Ullbrich, Y. Fan, M. Tropiano, K. A. McGarry, O. Zeika, M. K. Riede, C. J. Douglas, S. Barlow, S. R. Marder, D. Neher, D. Spoltore, K. Vandewal, *Nat. Energy* **2017**, *2*, 17053.

[64] M. Azzouzi, T. Kirchartz, J. Nelson, *Trends Chem.* **2019**, *1*, 49.

[65] M. Azzouzi, J. Yan, T. Kirchartz, K. Liu, J. Wang, H. Wu, J. Nelson, *Phys. Rev. X* **2018**, *8*, 031055.

[66] F. Deledalle, T. Kirchartz, M. S. Vezie, M. Campoy-Quiles, P. Shakya Tuladhar, J. Nelson, J. R. Durrant, *Phys. Rev. X* **2015**, *5*, 011032.

[67] E. Yablonovitch, O. D. Miller, S. R. Kurtz, **2013**, pp. 9–11.

[68] L. Liu, N. Solin, O. Inganäs, *Materials (Basel).* **2019**, *12*, 4032.

[69] Y. Lin, B. Adilbekova, Y. Firdaus, E. Yengel, H. Faber, M. Sajjad, X. Zheng, E. Yarali, A. Seitkhan, O. M. Bakr, A. El-Labban, U. Schwingenschlögl, V. Tung, I. McCulloch, F. Laquai, T. D. Anthopoulos, *Adv. Mater.* **2019**, *31*, 1902965.

[70] Z. Yin, J. Wei, Q. Zheng, *Adv. Sci.* **2016**, *3*, 1500362.

[71] A. J. Moulé, J. B. Bonekamp, K. Meerholz, *J. Appl. Phys.* **2006**, *100*, 094503.

[72] G. Li, V. Shrotriya, Y. Yao, Y. Yang, *J. Appl. Phys.* **2005**, *98*, 043704.

[73] D. W. Sievers, V. Shrotriya, Y. Yang, *J. Appl. Phys.* **2006**, *100*, 114509.

[74] S. H. Park, A. Roy, S. Beaupré, S. Cho, N. Coates, J. S. Moon, D. Moses, M. Leclerc, K. Lee, A. J. Heeger, *Nat. Photonics* **2009**, *3*, 297.

[75] L. A. A. Pettersson, L. S. Roman, O. Inganäs, *J. Appl. Phys.* **1999**, *86*, 487.

[76] C. Müller, T. A. M. Ferenczi, M. Campoy-Quiles, J. M. Frost, D. D. C. Bradley, P. Smith, N. Stingelin-Stutzmann, J. Nelson, *Adv. Mater.* **2008**, *20*, 3510.

[77] V. D. Mihailetchi, L. J. A. Koster, P. W. M. Blom, C. Melzer, B. de Boer, J. K. J. van Duren, R. A. J. Janssen, *Adv. Funct. Mater.* **2005**, *15*, 795.

[78] Z. M. Beiley, E. T. Hoke, R. Noriega, J. Dacuña, G. F. Burkhard, J. A. Bartelt, A. Salleo, M. F. Toney, M. D. McGehee, *Adv. Energy Mater.* **2011**, *1*, 954.

[79] V. Pranculis, Y. Infahsaeng, Z. Tang, A. Devižis, D. A. Vithanage, C. S. Ponseca, O. Inganäs, A. P. Yartsev, V. Gulbinas, V. Sundström, *J. Am. Chem. Soc.* **2014**, *136*, 11331.

[80] J. Y. Kim, K. Lee, N. E. Coates, D. Moses, T.-Q. Nguyen, M. Dante, A. J. Heeger, *Science (80-.).* **2007**, *317*, 222.

[81] D. Chirvase, J. Parisi, J. C. Hummelen, V. Dyakonov, *Nanotechnology* **2004**, *15*, 1317.

[82] B. Xie, K. Zhang, Z. Hu, H. Fang, B. Lin, Q. Yin, B. He, S. Dong, L. Ying, W. Ma, F. Huang, H. Yan, Y. Cao, *Sol. RRL* **2020**, *4*, 1900385.

[83] J. K. Lee, W. L. Ma, C. J. Brabec, J. Yuen, J. S. Moon, J. Y. Kim, K. Lee, G. C. Bazan, A. J. Heeger, *J. Am. Chem. Soc.* **2008**, *130*, 3619.

[84] E. Pascual-San-José, X. Rodríguez-Martínez, R. Adel-Abdelaleim, M. Stella, E. Martínez-Ferrero, M. Campoy-Quiles, *J. Mater. Chem. A* **2019**, *7*, 20369.

[85] G. Ji, W. Zhao, J. Wei, L. Yan, Y. Han, Q. Luo, S. Yang, J. Hou, C.-Q. Ma, *J. Mater. Chem. A* **2019**, *7*, 212.

[86] X. Guo, H. Li, Y. Han, Y. Yang, Q. Luo, C.-Q. Ma, J. Yang, *Org. Electron.* **2020**, *82*, 105725.

[87] B. Watts, W. J. Belcher, L. Thomsen, H. Ade, P. C. Dastoor, *Macromolecules* **2009**,

42, 8392.

[88] M. Reyes-Reyes, K. Kim, D. L. Carroll, *Appl. Phys. Lett.* **2005**, *87*, 083506.

[89] J. Liu, L. Chen, B. Gao, X. Cao, Y. Han, Z. Xie, L. Wang, *J. Mater. Chem. A* **2013**, *1*, 6216.

[90] M. Benz, M. R. Molla, A. Böser, A. Rosenfeld, P. A. Levkin, *Nat. Commun.* **2019**, *10*, 2879.

[91] F. Balkenhohl, C. von dem Bussche-Hünnefeld, A. Lansky, C. Zechel, *Angew. Chemie Int. Ed. English* **1996**, *35*, 2288.

[92] S. Matsuda, K. Nishioka, S. Nakanishi, *Sci. Rep.* **2019**, *9*, 6211.

[93] M. Kiy, R. Kern, T. A. Beierlein, C. J. Winnewisser, in *Org. Light Emit. Mater. Devices X*, **2006**, p. 633307.

[94] S. Langner, F. Häse, J. D. Perea, T. Stubhan, J. Hauch, L. M. Roch, T. Heumueller, A. Aspuru-Guzik, C. J. Brabec, *Adv. Mater.* **2020**, *32*, 1907801.

[95] C. M. Stafford, K. E. Roskov, T. H. Epps, M. J. Fasolka, *Rev. Sci. Instrum.* **2006**, *77*, 023908.

[96] X. Zhang, M. A. Young, O. Lyandres, R. P. Van Duyne, *J. Am. Chem. Soc.* **2005**, *127*, 4484.

[97] S. A. Centeno, *J. Raman Spectrosc.* **2016**, *47*, 9.

[98] O. Rodríguez-Romeu, M. Constenla, M. Carrassón, M. Campoy-Quiles, A. Soler-Membrives, *Sci. Total Environ.* **2020**, *733*, 139336.

[99] A. Francisco-López, B. Charles, M. I. Alonso, M. Garriga, M. Campoy-Quiles, M. T. Weller, A. R. Goñi, *J. Phys. Chem. C* **2020**, *124*, 3448.

[100] A. M. A. Leguy, A. R. Goñi, J. M. Frost, J. Skelton, F. Brivio, X. Rodríguez-Martínez, O. J. Weber, A. Pallipurath, M. I. Alonso, M. Campoy-Quiles, M. T. Weller, J. Nelson, A. Walsh, P. R. F. Barnes, *Phys. Chem. Chem. Phys.* **2016**, *18*, 27051.

[101] H. Kuzmany, J. Kürti, *Synth. Met.* **1987**, *21*, 95.

[102] B. Tian, G. Zerbi, K. Müllen, *J. Chem. Phys.* **1991**, *95*, 3198.

[103] B. Tian, G. Zerbi, R. Schenk, K. Mullen, *J. Chem. Phys.* **1991**, *95*, 3191.

[104] J. Rissler, *Chem. Phys. Lett.* **2004**, *395*, 92.

[105] W. C. Tsoi, D. T. James, J.-S. J. S. Kim, P. G. Nicholson, C. E. Murphy, D. D. C. Bradley, J. Nelson, J.-S. J. S. Kim, *J. Am. Chem. Soc.* **2011**, *133*, 9834.

[106] D. Abol-Fotouh, B. Dörling, O. Zapata-Arteaga, X. Rodríguez-Martínez, A. Gómez, J. S. Reparaz, A. Laromaine, A. Roig, M. Campoy-Quiles, *Energy Environ. Sci.* **2019**, *12*, 716.

[107] H. M. Liem, P. Etchegoin, K. S. Whitehead, D. D. C. Bradley, *Adv. Funct. Mater.* **2003**, *13*, 66.

[108] W. C. Tsoi, W. Zhang, J. Razzell Hollis, M. Suh, M. Heeney, I. McCulloch, J.-S. Kim, *Appl. Phys. Lett.* **2013**, *102*, 173302.

[109] J. Luke, E. M. Speller, A. Wadsworth, M. F. Wyatt, S. Dimitrov, H. K. H. Lee, Z. Li, W. C. Tsoi, I. McCulloch, D. Bagnis, J. R. Durrant, J. Kim, *Adv. Energy Mater.* **2019**, *9*, 1803755.

[110] E. J. J. Martin, N. Bérubé, F. Provencher, M. Côté, C. Silva, S. K. Doorn, J. K. Grey, *J. Mater. Chem. C* **2015**, *3*, 6058.

[111] T. Agostinelli, S. Lilliu, J. G. Labram, M. Campoy-Quiles, M. Hampton, E. Pires, J. Rawle, O. Bikondoa, D. D. C. Bradley, T. D. Anthopoulos, J. Nelson, J. E. Macdonald, *Adv. Funct. Mater.* **2011**, *21*, 1701.

[112] M. Campoy-Quiles, C. Müller, M. Garriga, E. Wang, O. Inganäs, M. I. Alonso, *Thin Solid Films* **2014**, *571*, 371.

[113] S. Klinkhammer, X. Liu, K. Huska, Y. Shen, S. Vanderheiden, S. Valouch, C. Vannahme, S. Bräse, T. Mappes, U. Lemmer, *Opt. Express* **2012**, *20*, 6357.

[114] S. Höfle, T. Lutz, A. Egel, F. Nickel, S. W. Kettlitz, G. Gomard, U. Lemmer, A. Colsmann, *ACS Photonics* **2014**, *1*, 968.

[115] J. Cabanillas–Gonzalez, O. Peña–Rodríguez, I. Suarez Lopez, M. Schmidt, M. I.

Alonso, A. R. Goñi, M. Campoy–Quiles, *Appl. Phys. Lett.* **2011**, *99*, 103305.

[116] J. Fernández-Tejero, Design and Implementation of a Photocurrent Mapping Tool for Organic Solar Cells (MSc Thesis), Universitat Autònoma de Barcelona, **2014**.

[117] M. J. Griffith, N. A. Cooling, B. Vaughan, D. C. Elkington, A. S. Hart, A. G. Lyons, S. Quereshi, W. J. Belcher, P. C. Dastoor, *IEEE J. Sel. Top. Quantum Electron.* **2016**, *22*, 112.

[118] Y. Cui, H. Yao, L. Hong, T. Zhang, Y. Tang, B. Lin, K. Xian, B. Gao, C. An, P. Bi, W. Ma, J. Hou, *Natl. Sci. Rev.* **2019**, DOI 10.1093/nsr/nwz200.

[119] J. L. Hernandez, N. Deb, R. M. W. Wolfe, C. K. Lo, S. Engmann, L. J. Richter, J. R. Reynolds, *J. Mater. Chem. A* **2017**, *5*, 20687.

[120] Z. Bi, X. Rodríguez-Martínez, C. Aranda, E. Pascual-San-José, A. R. Goñi, M. Campoy-Quiles, X. Xu, A. Guerrero, *J. Mater. Chem. A* **2018**, *6*, 19085.

[121] R. L. Davis, S. Jayaraman, P. M. Chaikin, R. A. Register, *Langmuir* **2014**, *30*, 5637.

[122] J. C. Meredith, A. Karim, E. J. Amis, *Macromolecules* **2000**, *33*, 5760.

[123] J. Carson Meredith, A. Karim, E. J. Amis, *MRS Bull.* **2002**, *27*, 330.

[124] A. Karim, E. Amis, K. Yurekli, R. Krishnamoorti, C. Meredith, *Polym. Eng. Sci.* **2002**, *42*, 1836.

[125] R. A. Street, D. Davies, P. P. Khlyabich, B. Burkhart, B. C. Thompson, *J. Am. Chem. Soc.* **2013**, *135*, 986.

[126] Y. Chen, P. Ye, X. Jia, W. Gu, X. Xu, X. Wu, J. Wu, F. Liu, Z.-G. Zhu, H. Huang, *J. Mater. Chem. A* **2017**, *5*, 19697.

[127] P. Tabeling, *Introduction to Microfluidics*, Oxford University Press, **2005**.

[128] M. Gonidec, J. Puigmartí-Luis, *Crystals* **2018**, *9*, 12.

[129] S. Sevim, A. Sorrenti, C. Franco, S. Furukawa, S. Pané, A. J. DeMello, J. Puigmartí-Luis, *Chem. Soc. Rev.* **2018**, *47*, 3788.

[130] S. Sevim, C. Franco, H. Liu, H. Roussel, L. Rapenne, J. Rubio-Zuazo, X. Chen, S. Pané, D. Muñoz-Rojas, A. J. DeMello, J. Puigmartí-Luis, *Adv. Mater. Technol.* **2019**, *4*, 1800666.

[131] A. Rodríguez-Pena, J. Uranga-Solchaga, C. Ortiz-de-Solórzano, I. Cortés-Domínguez, *Sci. Rep.* **2020**, *10*, 2779.

[132] N. L. Jeon, S. K. W. Dertinger, D. T. Chiu, I. S. Choi, A. D. Stroock, G. M. Whitesides, *Langmuir* **2000**, *16*, 8311.

[133] P. Carrière, *Phys. Fluids* **2007**, *19*, 118110.

[134] T. Yasui, Y. Omoto, K. Osato, N. Kaji, N. Suzuki, T. Naito, M. Watanabe, Y. Okamoto, M. Tokeshi, E. Shamoto, Y. Baba, *Lab Chip* **2011**, *11*, 3356.

[135] C.-Y. Lee, C.-L. Chang, Y.-N. Wang, L.-M. Fu, *Int. J. Mol. Sci.* **2011**, *12*, 3263.

[136] C.-Y. Lee, W.-T. Wang, C.-C. Liu, L.-M. Fu, *Chem. Eng. J.* **2016**, *288*, 146.

[137] X. Xu, Z. Li, W. Zhang, X. Meng, X. Zou, D. Di Carlo Rasi, W. Ma, A. Yartsev, M. R. Andersson, R. A. J. Janssen, E. Wang, *Adv. Energy Mater.* **2018**, *8*, 1700908.

[138] M. Campoy-Quiles, Y. Kanai, A. El-Basaty, H. Sakai, H. Murata, *Org. Electron.* **2009**, *10*, 1120.

[139] D. Baran, R. S. Ashraf, D. A. Hanifi, M. Abdelsamie, N. Gasparini, J. A. Röhr, S. Holliday, A. Wadsworth, S. Lockett, M. Neophytou, C. J. M. Emmott, J. Nelson, C. J. Brabec, A. Amassian, A. Salleo, T. Kirchartz, J. R. Durrant, I. McCulloch, *Nat. Mater.* **2017**, *16*, 363.

[140] N. Li, I. McCulloch, C. J. Brabec, *Energy Environ. Sci.* **2018**, *11*, 1355.

[141] T. Ameri, P. Khoram, J. Min, C. J. Brabec, *Adv. Mater.* **2013**, *25*, 4245.

[142] R. Sun, J. Guo, C. Sun, T. Wang, Z. Luo, Z. Zhang, X. Jiao, W. Tang, C. Yang, Y. Li, J. Min, *Energy Environ. Sci.* **2019**, *12*, 384.

[143] R. Sun, Q. Wu, J. Guo, T. Wang, Y. Wu, B. Qiu, Z. Luo, W. Yang, Z. Hu, J. Guo, M. Shi, C. Yang, F. Huang, Y. Li, J. Min, *Joule* **2020**, *4*, 407.

[144] S. Dong, K. Zhang, B. Xie, J. Xiao, H.-L. Yip, H. Yan, F. Huang, Y. Cao, *Adv. Energy Mater.* **2019**, *9*, 1802832.

[145] W. C. Tsoi, D. T. James, J. S. Kim, P. G. Nicholson, C. E. Murphy, D. D. C. Bradley, J. Nelson, J.-S. Kim, *J. Am. Chem. Soc.* **2011**, *133*, 9834.

[146] J. Hachmann, R. Olivares-Amaya, S. Atahan-Evrenk, C. Amador-Bedolla, R. S. Sánchez-Carrera, A. Gold-Parker, L. Vogt, A. M. Brockway, A. Aspuru-Guzik, *J. Phys. Chem. Lett.* **2011**, *2*, 2241.

[147] H. Sahu, W. Rao, A. Troisi, H. Ma, *Adv. Energy Mater.* **2018**, *8*, 1801032.

[148] H. Sahu, F. Yang, X. Ye, J. Ma, W. Fang, H. Ma, *J. Mater. Chem. A* **2019**, *7*, 17480.

[149] H. Sahu, H. Ma, *J. Phys. Chem. Lett.* **2019**, *10*, 7277.

[150] S. A. Lopez, B. Sanchez-Lengeling, J. de Goes Soares, A. Aspuru-Guzik, *Joule* **2017**, *1*, 857.

[151] W. Sun, Y. Zheng, K. Yang, Q. Zhang, A. A. Shah, Z. Wu, Y. Sun, L. Feng, D. Chen, Z. Xiao, S. Lu, Y. Li, K. Sun, *Sci. Adv.* **2019**, *5*, eaay4275.

[152] N. Huber, S. R. Kalidindi, B. Klusemann, C. J. Cyron, *Front. Mater.* **2020**, *7*, DOI 10.3389/fmats.2020.00051.

[153] Y. Firdaus, V. M. Le Corre, J. I. Khan, Z. Kan, F. Laquai, P. M. Beaujuge, T. D. Anthopoulos, *Adv. Sci.* **2019**, *6*, 1802028.

Appendix

This appendix gathers the chemical names (according to the IUPAC nomenclature), molecular structures, solid-state Raman cross-sections, Raman vibrational fingerprints (at 488 nm excitation) and refractive indices measured by means of variable-angle spectroscopic ellipsometry (VASE) for the full set of organic semiconducting materials used throughout this doctoral thesis.

All Raman spectra shown below were measured by me during the development of the thesis, yet not exclusively for OPV purposes. Regarding the complex refractive indices, data acquisition and modelling was performed by me in all cases excepting the following materials, which were courtesy of Dr. Mariano Campoy-Quiles as part of his previous investigations: rr-P3BT, rr-P3HT, rr-P3DDT, PFO, PFBT, BTT-DPP, DPP-TT-T, PTCBI, CuPc, $PC_{60}BM$, $PC_{70}BM$ and ICBA. These are included for completeness.

Abbreviations and chemical names according to IUPAC rules

rr-P3BT   Poly(3-butylthiophene-2,5-diyl) regioregular

rra-P3HT   Poly(3-hexylthiophene-2,5-diyl) regiorandom

rr-P3HT   Poly(3-hexylthiophene-2,5-diyl) regioregular

rr-P3DDT   Poly(3-dodecylthiophene-2,5-diyl) regioregular

PBTTT-C$_{14}$ Poly[2,5-bis(3-tetradecylthiophen-2-yl)thieno[3,2-*b*]thiophene]

PFO   Poly(9,9-di-*n*-octylfluorenyl-2,7-diyl)

PFBT   Poly[(9,9-di-*n*-octylfluorenyl-2,7-diyl)-*alt*-(benzo[2,1,3]thiadiazol-4,8-diyl)]

PCDTBT   Poly[*N*-9'-heptadecanyl-2,7-carbazole-*alt*-5,5-(4',7'-di-2-thienyl-2',1',3'-benzothiadiazole)]

PCPDTBT   Poly[2,6-(4,4-bis-(2-ethylhexyl)-4*H*-cyclopenta [2,1-*b*;3,4-*b*']dithiophene)-*alt*-4,7(2,1,3-benzothiadiazole)]

C$_{16}$-IDT-BT   Poly[(4,9-dihydro-4,4,9,9-tetrahexadecyl-*s*-indaceno[1,2-*b*:5,6-*b*']-dithiophene-2,7-diyl)-*alt*-(benzo[2,1,3]thiadiazol-4,8-diyl)]

TIF-BT   Dithiopheneindenofluorene-benzothiadiazole co-polymer with hexadecyl side-chains

PffBT4T-2OD   Poly[(5,6-difluoro-2,1,3-benzothiadiazol-4,7-diyl)-*alt*-(3,3'''-di(2-octyldodecyl)-2,2',5',2'',5'',2'''-quaterthiophen-5,5'''-diyl)]

BTT-DPP	Poly[(5-decylbenzo[1,2-*b*:3,4-*b*':5,6-*d*'']trithiophene-2,8-diyl)-*alt-co*-(3,6-bis(2-thienyl)-2,5-dihydro-2,5-di(2-octyldodecyl)pyrrolo[3,4-*c*]pyrrolo-1,4-dione-5,5'-diyl)]

DPP-TT-T	Poly[[2,5-bis(2-octyldodecyl)-2,3,5,6-tetrahydro-3,6-dioxopyrrolo[3,4-*c*]pyrrole-1,4-diyl]-*alt*-[[2,2'-(2,5-thiophene)bis-thieno[3,2-*b*]thiophen]-5,5'-diyl]]

PTB7-Th	Poly([2,6'-4,8-di(5-ethylhexylthienyl)benzo[1,2-*b*;3,3-*b*]dithiophene]{3-fluoro-2[(2-ethylhexyl)carbonyl]thieno[3,4-*b*]thiophenediyl})

PBDB-T	Poly[[4,8-bis[5-(2-ethylhexyl)-2-thienyl]benzo[1,2-*b*:4,5-*b*']dithiophene-2,6-diyl]-2,5-thiophenediyl[5,7-bis(2-ethylhexyl)-4,8-dioxo-4*H*,8*H*-benzo[1,2-*c*:4,5-*c*']dithiophene-1,3-diyl]]

PBDB-T-2Cl	Poly[[4,8-bis[5-(2-ethylhexyl)-4-chloro-2-thienyl]benzo[1,2-*b*:4,5-*b*']dithiophene-2,6-diyl]-2,5-thiophenediyl[5,7-bis(2-ethylhexyl)-4,8-dioxo-4*H*,8*H*-benzo[1,2-*c*:4,5-*c*']dithiophene-1,3-diyl]-2,5-thiophenediyl]

PBDB-T-2F	Poly[[4,8-bis[5-(2-ethylhexyl)-4-fluoro-2-thienyl]benzo[1,2-*b*:4,5-*b*']dithiophene-2,6-diyl]-2,5-thiophenediyl[5,7-bis(2-ethylhexyl)-4,8-dioxo-4*H*,8*H*-benzo[1,2-*c*:4,5-*c*']dithiophene-1,3-diyl]-2,5-thiophenediyl]

PBDT-TPD	Poly[(5,6-dihydro-5-octyl-4,6-dioxo-4*H*-thieno[3,4-*c*]pyrrole-1,3-diyl)[4,8-bis[5-(2-ethylhexyl)-2-thienyl]benzo[1,2-*b*:4,5-*b*']dithiophene-2,6-diyl]]

PNDI-T	Poly[[1,2,3,6,7,8-hexahydro-2,7-bis(2-octyldodecyl)-1,3,6,8-tetraoxobenzo[*lmn*][3,8]phenanthroline-4,9-diyl]-2,5-thiophenediyl]

TQ1	Poly[[2,3-bis(3-octyloxyphenyl)-5,8-quinoxalinediyl]-2,5-thiophenediyl]

N2200	Poly{[*N*,*N*'-bis(2-octyldodecyl)-naphthalene-1,4,5,8-bis(dicarboximide)-2,6-diyl]-*alt*-5,5'-(2,2'-bithiophene)}

PTCBI	3,4,9,10-perylenetetracarboxylic bisbenzimidazole

CuPc	Copper(II) phthalocyanine

PC$_{60}$BM	[6,6]-Phenyl-C$_{61}$-butyric acid methyl ester

PC$_{70}$BM	[6,6]-Phenyl-C$_{71}$-butyric acid methyl ester

ICBA	1',1'',4',4''-Tetrahydro-di[1,4]methanonaphthaleno[1,2:2',3',56,60:2'',3''][5,6]fullerene-C$_{60}$

ITIC	2,2'-[[6,6,12,12-tetrakis(4-hexylphenyl)-6,12-dihydrodithieno[2,3-*d*:2',3'-*d*']-s-indaceno[1,2-*b*:5,6-*b*']dithiophene-2,8-diyl]bis[methylidyne(3-oxo-1*H*-indene-2,1(3*H*)-diylidene)]]bis[propanedinitrile]

ITIC-M	9-Bis(2-methylene-((3-(1,1-dicyanomethylene)-6/7-methyl)-indanone))-5,5,11,11-tetrakis(4-hexylphenyl)-dithieno[2,3-*d*:2',3'-*d*']-
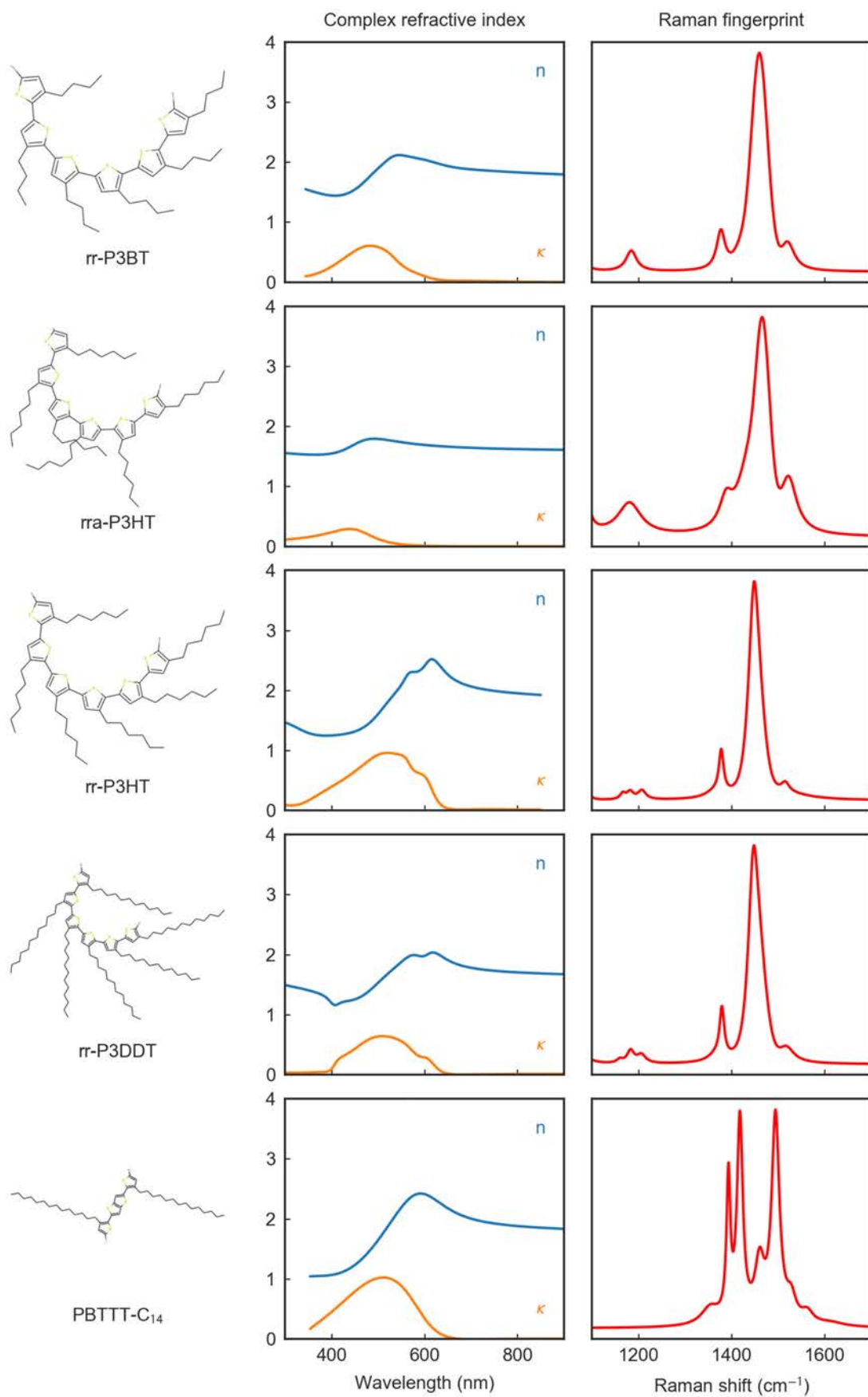
s-indaceno[1,2-*b*:5,6-*b*']dithiophene, mixture of isomers (6/7-methyl positions)

ITIC-C₈   2,2'-[[6,6,12,12-tetrakis(*n*-octyl)-6,12-dihydrodithieno[2,3-*d*:2',3'-*d*']-s-indaceno[1,2-*b*:5,6-*b*']dithiophene-2,8-diyl]bis[methylidyne(3-oxo-1*H*-indene-2,1(3*H*)-diylidene)]]bis[propanedinitrile]

ITIC-C₂C₆   2,2'-[[6,6,12,12-tetrakis(2-ethylhexyl)-6,12-dihydrodithieno[2,3-*d*:2',3'-*d*']-s-indaceno[1,2-*b*:5,6-*b*']dithiophene-2,8-diyl]bis[methylidyne(3-oxo-1*H*-indene-2,1(3*H*)-diylidene)]]bis[propanedinitrile]

ITIC-4F   9-Bis(2-methylene-((3-(1,1-dicyanomethylene)-6,7-difluoro)-indanone))-5,5,11,11-tetrakis(4-hexylphenyl)-dithieno[2,3-*d*:2',3'-*d*']-s-indaceno[1,2-*b*:5,6-*b*']dithiophene

O-IDTBR   (5*Z*,5'*Z*)-5,5'-(((4,4,9,9-tetrakis(*n*-octyl)-4,9-dihydro-*s*-indaceno[1,2-*b*:5,6-*b*']dithiophene-2,7-diyl)bis(benzo[*c*][1,2,5]thiadiazole-7,4-diyl))bis(methaneylylidene))bis(3-ethyl-2-thioxothiazolidin-4-one)

EH-IDTBR   (5*Z*,5'*Z*)-5,5'-(((4,4,9,9-tetrakis(2-ethylhexyl)-4,9-dihydro-*s*-indaceno[1,2-*b*:5,6-*b*']dithiophene-2,7-diyl)bis(benzo[*c*][1,2,5]thiadiazole-7,4-diyl))bis(methaneylylidene))bis(3-ethyl-2-thioxothiazolidin-4-one)

O-IDFBR   (5*Z*,5'*Z*)-5,5'-(((6,6,12,12-tetraoctyl-6,12-dihydroindeno[1,2-*b*]fluorene-2,8-diyl)bis(benzo[*c*][1,2,5]thiadiazole-7,4-diyl))bis(methaneylylidene))bis(3-ethyl-2-thioxothiazolidin-4-one)
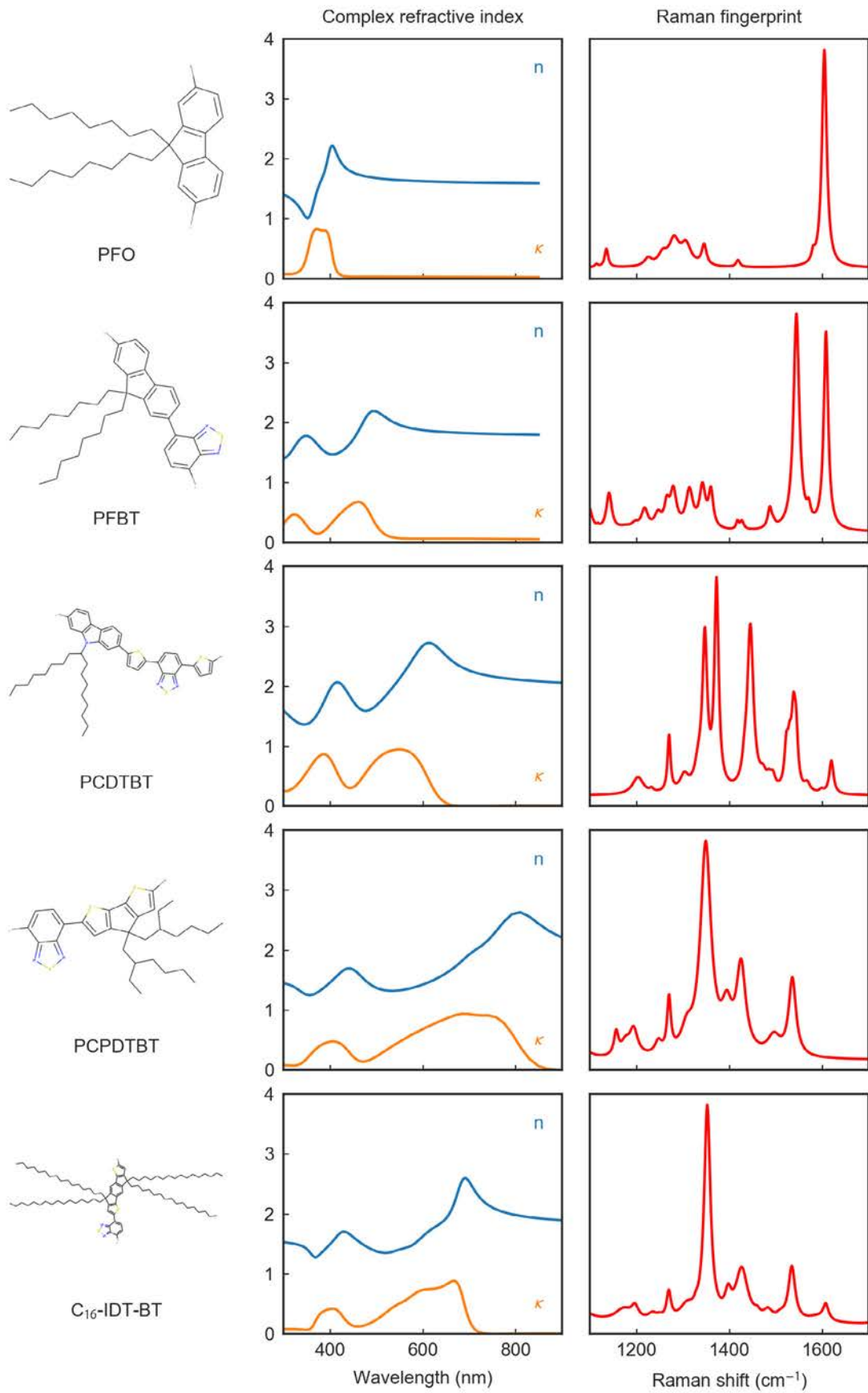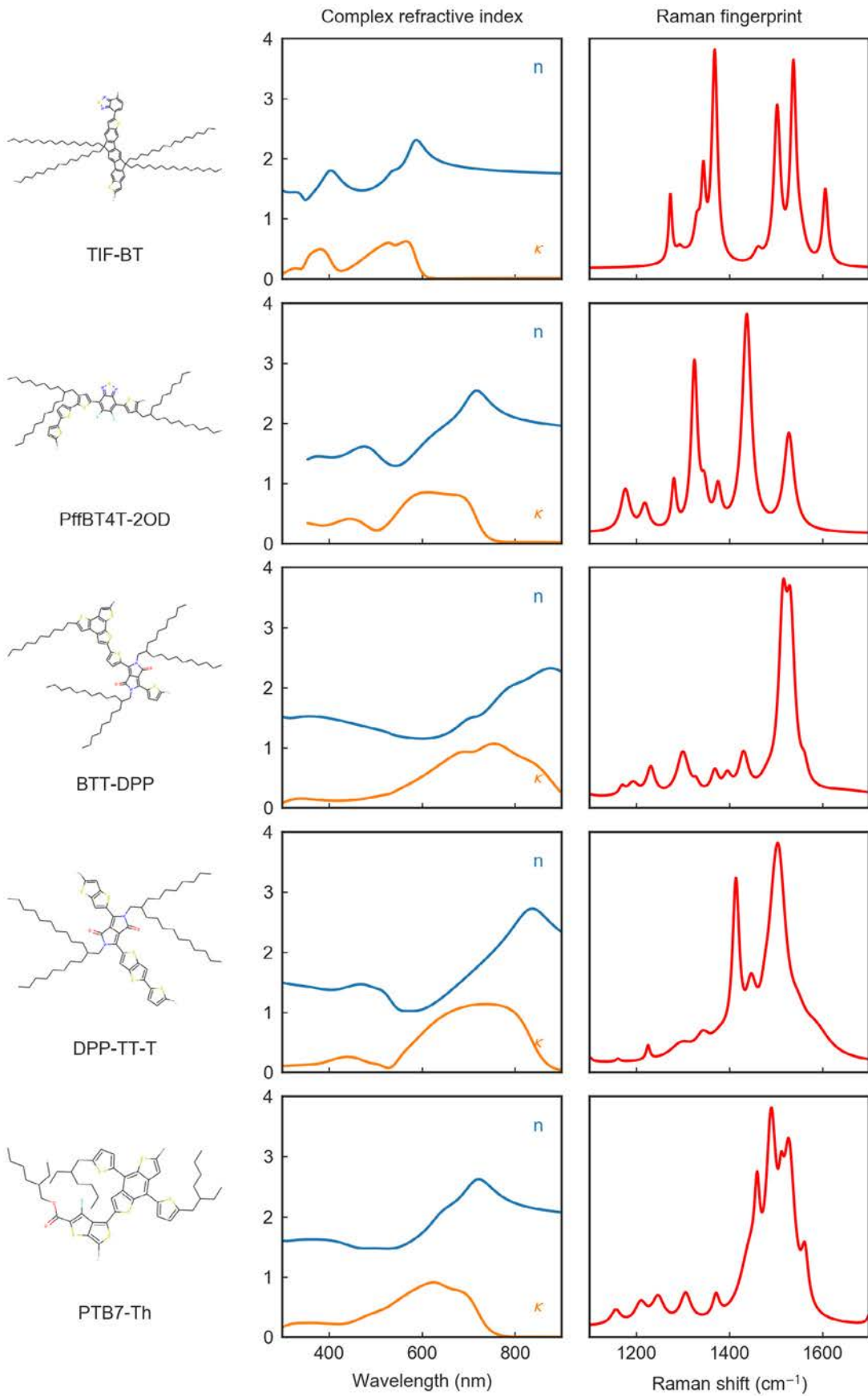
Raman cross-sections database

Table I. Solid-state Raman cross-sections measured at two different excitation wavelengths (488 nm and 514 nm) of the organic semiconducting materials used in this thesis. The Raman cross-sections are listed as ratios with respect to $PC_{70}BM$ ($\sigma_{ratio} = \sigma_{R,u} / \sigma_{R,PC70BM}$).
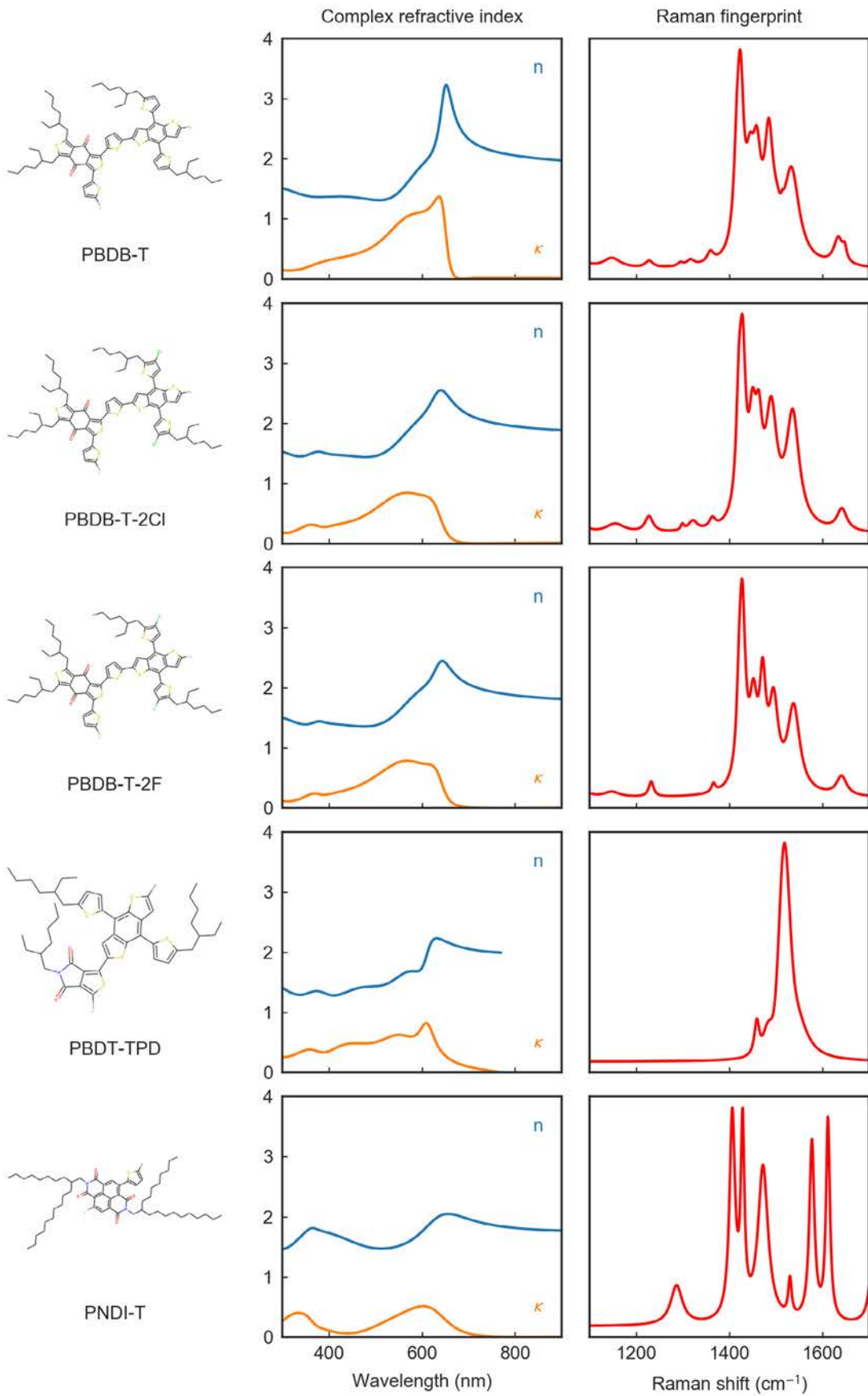
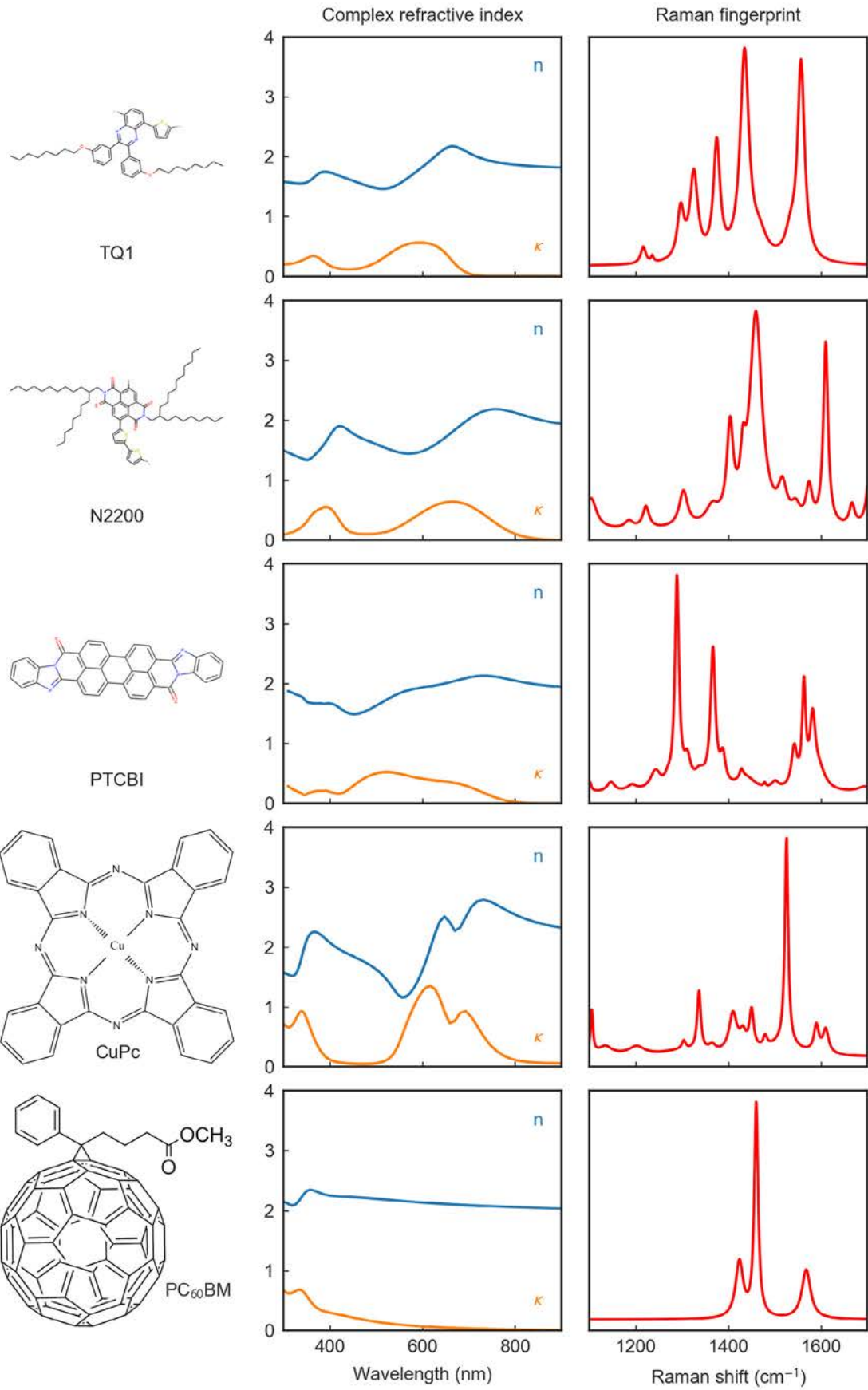| Material		488 nm				514 nm			
		σ_{ratio} (±)	n	k	Mode (cm^{-1})	σ_{ratio} (±)	n	k	Mode (cm^{-1})
Conjugated small molecules	$PC_{70}BM$	1 (NA)	2.08	0.40	1557	1 (NA)	2.14	0.35	1566
	$PC_{60}BM$	0.41 (±0.04)	2.04	0.11	1458	0.29 (±0.05)	2.03	0.09	1461
	EH-IDTBR	1.1 (±0.2)	1.48	0.20	1361		1.41	0.34	
	O-IDTBR	4 (±1)	1.44	0.29	1361		1.25	0.51	
	O-IDFBR	9 (±1)	1.59	0.46	1535		1.77	0.51	
	ITIC	1.2 (±0.3)	1.33	0.30	1540		1.25	0.47	
	ITIC-M	1.1 (±0.2)	1.28	0.33	1539		1.20	0.54	
	$ITIC-C_2C_6$	1.8 (±0.4)	1.34	0.51	1545		1.29	0.66	
	$ITIC-C_8$	1.2 (±0.3)	1.33	0.36	1545		1.30	0.49	
	ITIC-4F	0.45 (±0.09)	1.46	0.12	1344		1.39	0.14	
	CuPc	0.53 (±0.07)	1.69	0.05	1528	1.2 (±0.2)	1.53	0.08	1528
	PTCBI	10 (±1)	1.58	0.47	1290	4.6 (±0.7)	1.69	0.52	1290
Conjugated polymers	N2200	0.46 (±0.09)	1.64	0.10	1459		1.55	0.12	
	TQ1	1.34 (±0.23)	1.50	0.19	1435		1.46	0.30	
	PNDI-T	0.5 (±0.1)	1.49	0.14	1713		1.47	0.23	
	PBDT-TPD	8 (±2)	1.43	0.49	1518		1.45	0.54	
	rr-P3HT	57 (±11)	1.54	0.60	1450	51 (±5)	1.82	0.79	1450
	PCDTBT	9 (±1)	1.61	0.67	1447	18 (±2)	1.79	0.86	1445
	PCPDTBT	3.8 (±0.5)	1.42	0.17	1347	3.9 (±0.5)	1.34	0.29	1349
	C_{16}-IDT-BT	8 (±1)	1.42	0.18	1353	5.2 (±0.7)	1.35	0.31	1353
	BTT-DPP	12 (±1)	1.34	0.17	1517	12 (±1)	1.29	0.21	1517
	DPP-TT-T-1	4.3 (±0.5)	1.44	0.16	1502	1.3 (±0.1)	1.36	0.11	1502
	DPP-TT-T-3	4.4 (±0.5)	1.14	0.11	1502	1.4 (±0.1)	1.00	0.21	1502
	PTB7-Th	2.4 (±0.3)	1.47	0.38	1490		1.47	0.45	
	PffBT4T-2OD	1.3 (±0.4)	1.59	0.26	1437		1.41	0.24	
	PBDB-T	5 (±1)	1.32	0.51	1424		1.31	0.65	
	PBDB-T-2Cl	6.5 (±0.9)	1.44	0.51	1426		1.49	0.65	
	PBDB-T-2F	5 (±1)	1.36	0.47	1427		1.41	0.60	

# Complex refractive indices and Raman fingerprinting database

Complex refractive index — Raman fingerprint

rr-P3BT

rra-P3HT

rr-P3HT

rr-P3DDT

PBTTT-C$_{14}$

Wavelength (nm)

Raman shift (cm^{-1})

103

Complex refractive index

Raman fingerprint

PFO

PFBT

PCDTBT

PCPDTBT

C$_{16}$-IDT-BT

Wavelength (nm)

Raman shift (cm^{-1})

104

Complex refractive index | Raman fingerprint

TIF-BT

PffBT4T-2OD

BTT-DPP

DPP-TT-T

PTB7-Th

Wavelength (nm)

Raman shift (cm^{-1})

105

Complex refractive index   Raman fingerprint

PBDB-T

PBDB-T-2Cl

PBDB-T-2F

PBDT-TPD

PNDI-T

Wavelength (nm)   Raman shift (cm⁻¹)

106

Complex refractive index   Raman fingerprint

TQ1

N2200

PTCBI

CuPc

PC$_{60}$BM

Wavelength (nm)

Raman shift (cm^{-1})

Complex refractive index   Raman fingerprint

Complex refractive index — Raman fingerprint

ITIC-C$_2$C$_6$

ITIC-4F

O-IDTBR

EH-IDTBR

O-IDFBR

Wavelength (nm) — Raman shift (cm^{-1})

109

PAPER I

Quantifying local thickness and composition in thin films of organic photovoltaic blends by Raman scattering

X. Rodríguez-Martínez, M. S. Vezie, X. Shi, I. McCulloch, J. Nelson, A. R. Goñi, M. Campoy-Quiles, *J. Mater. Chem. C* **2017**, *5*, 7270.

Optical modeling of the Raman-scattered light enables the simultaneous quantification of thickness (d) and volumetric composition (vol%) in multi-component thin films.
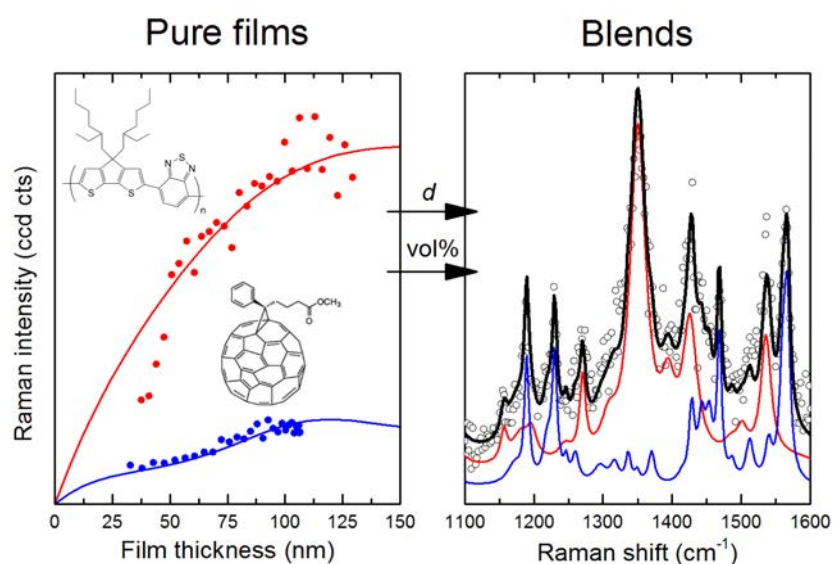
Check for updates

Quantifying local thickness and composition in thin films of organic photovoltaic blends by Raman scattering†

Xabier Rodríguez-Martínez, [iD] *[a] Michelle S. Vezie, [iD] [b] Xingyuan Shi, [iD] [b] Iain McCulloch, [iD] [cd] Jenny Nelson, [iD] [b] Alejandro R. Goñi [iD] [ae] and Mariano Campoy-Quiles [iD] *[a]

We report a methodology based on Raman spectroscopy that enables the non-invasive and fast quantitative determination of local thickness and composition in thin films (from a few monolayers to hundreds of nm) of one or more components. We apply our methodology to blends of organic conjugated materials relevant in the field of organic photovoltaics. As a first step, we exploit the transfer-matrix formalism to describe the Raman process in thin films including reabsorption and interference effects of the incoming and scattered electric fields. This allows determining the effective solid-state Raman cross-section of each material by studying the dependence of the Raman intensity on film thickness. These effective cross sections are then used to estimate the local thickness and composition in a series of polymer:fullerene blends. We find that the model is accurate within ±10 nm in thickness and ±5 vol% in composition provided that (i) the film thickness is kept below the thickness corresponding to the first maximum of the calculated Raman intensity oscillation; (ii) the materials making up the blend show close enough effective Raman cross-sections; and (iii) the degree of order attained by the conjugated polymer in the blend is similar to that achieved when cast alone. Our methodology opens the possibility of making quantitative maps of composition and thickness over large areas (from microns to centimetres squared) with diffraction-limited resolution and in any multi-component system based thin film technology.

Introduction

Conjugated polymers and small molecules offer unique optical and semiconducting properties to build functional electronic devices with appealing features, including flexibility, lightness, versatility and low manufacturing cost. Organic photovoltaics

[a] *Institut de Ciència de Materials de Barcelona (ICMAB-CSIC), Bellaterra, 08193, Spain. E-mail: xrodriguez@icmab.es, mcampoy@icmab.es*
[b] *Centre for Plastic Electronics and Department of Physics, Imperial College London, Prince Consort Road, London SW7 2AZ, UK*
[c] *Centre for Plastic Electronics and Department of Chemistry, Imperial College London, Exhibition Road, London SW7 2AZ, UK*
[d] *SPERC, King Abdullah University of Science and Technology, Thuwal 23955-6900, Saudi Arabia*
[e] *Institució Catalana de Recerca I Estudis Avançats (ICREA), Barcelona, 08010, Spain*
† Electronic supplementary information (ESI) available: Further details about the application of the methodology in different Raman setups; the multi-wavelength fitting approach in P3HT films; the sensitivity of the methodology in thin film architectures with a high refractive index contrast; and the effect of photo-degradation on the Raman intensity in some polymer:fullerene blends. See DOI: 10.1039/c7tc01472d

(OPV) is an example of an emerging technology that utilises the aforementioned properties in solar cells with good conversion efficiencies, currently exceeding 11%.[1,2] The active layer in these devices typically consists of a blend of a hole transporting conjugated polymer and an electron transporting conjugated small molecule (usually a fullerene derivative), thoroughly mixed and cast from solution as a thin film forming the so-called bulk heterojunction (BHJ).[3] The wet deposition process enables solid-state inhomogeneities to occur (*e.g.* phase segregation, thickness variations, *etc.*) that can extend up to different length scales.[4] Solubility within the solvents, miscibility between components, surface energies and drying kinetics typically govern phase separation at the nanometer to micron scale. In turn, the size and purity of domains at that scale will have a strong impact on charge generation, recombination and transport in OPV blends. The characterization of film morphology at the nanoscale is well-documented through the use of atomic force microscopy (AFM),[5] X-ray microscopy[6] and more recently through energy-filtered scanning electron microscopy (EFSEM)[7] as well as tip-enhanced optical spectroscopy (TEOS), including Raman and photoluminescence.[8] Apart from nanometric qualitative

7270 | *J. Mater. Chem. C,* 2017, 5, 7270–7282

113

This journal is © The Royal Society of Chemistry 2017

images of the film surface and topography, scanning probe microscopies such as TEOS and AFM can provide quantitative chemical maps with a lateral resolution down to 20 nm.[8–11] In the case of EFSEM this value reduces below a nanometre.[7]

A less investigated solid state inhomogeneity is that occurring at the micron to centimetre length scales. This is the result of wet solution processing without full control of the rheology of the solution (mainly viscosity and surface tension), drying kinetics and substrate energies. Typical manifestations of this include poor wettability and adhesion, thickness oscillations, coffee-ring stains, and composition profiles due to Marangoni fluxes. All these prevent the formation of uniform and smooth films with well-defined interfaces, which in turn has detrimental effects on film reproducibility and technology upscalability.[12,13] While these effects are often undesirable, it is worth noting that films exhibiting controlled lateral variations of thickness or composition (gradients) have been proposed in order to accelerate the screening of new OPV systems.[14,15] In this case, variations in film thickness and/or composition extend over a scale of a few millimetres up to several centimetres.

The aforementioned high resolution techniques such as AFM or EFSEM could, in principle, be used to characterize large scale inhomogeneities. They would, however, be unaffordably slow. On the other hand, spectroscopic techniques such as ellipsometry may be exploited to speedily infer film thickness and composition in thin films at a larger scale, being applicable even in multi-layered stacks such as functional devices if the optical constants are known beforehand.[16] The lateral resolution in ellipsometry is, however, limited by the size of the light spot used (typically greater than 200 μm), a fact that makes the study of the phase segregation on smaller length scales unfeasible. Moreover, the refractive index is only moderately selective to different materials.

Micro-Raman spectroscopy constitutes a scanning or imaging technique that can be exploited to study thin film morphology with diffraction-limited lateral resolution (ca. 300 nm in the best scenario, i.e. using 488 nm as the excitation wavelength and an objective with a numerical aperture ≥ 0.9), thus linking the two regimes explained above: nanoscale and macroscale characterization. Such resolution, in combination with the characteristic fingerprinting capability of Raman scattering, and rapid acquisition of data, enables the characterization of film inhomogeneities and phase segregation extending from a few microns up to centimetres in a single step. Raman spectroscopy also offers a series of unique advantages such as non-invasiveness and sensitivity to chemical environments.[17–22] These features make Raman spectroscopy a valuable technique to gain insights regarding structure–performance relationships in organic thin films[23] and to quantify the relative content of individual components according to their Raman fingerprint.[24]

Most studies regarding Raman measurements in π-conjugated thin films restrict themselves, with a few exceptions,[21] to a qualitative analysis of the results. While Raman shifts and peak widths are useful to identify crystalline and amorphous domains, the analysis of the Raman intensity mainly reduces to the deconvolution of the acquired spectra as weighted linear combinations of the individual components[25,26] and the relative identification of thicker or thinner regions based on a linear approximation of the measured Raman intensity.[4] As we will show below, the validity of such approximations is rather limited.

Beyond organic semiconductors, Raman scattering is currently exploited to determine the thickness of supported films[27] such as thin adsorbed layers,[28,29] graphene[30,31] and exfoliated chalcogenides[32] according to the concept of interference-enhanced Raman scattering.[33] The method is based on a detailed mathematical description of the incident and scattered electric field amplitudes in multi-layered structures, which interfere according to the optical properties of the whole stack. By properly tuning such properties as well as the thickness of the layers, the Raman intensity due to nanometric films can undergo up to a ten-fold increase compared to the bulk material.[32]

This paper extends these ideas of film thickness quantification to multi-component layers by enabling the simultaneous determination of film thickness and volumetric composition. Our methodology is based on rigorously modeling the distribution of the incoming electromagnetic field and the scattered light to account for the variations of the Raman intensity registered as a function of film thickness, in both pure materials and blends. In the latter, the raw spectra are fitted as a combination of the pure compounds using the thin film thickness and the volumetric scattering fraction as free parameters. The experimental results are in good agreement with those expected from the model and those extracted through ellipsometry provided that (i) the morphology and chemical micro-environment of the probed regions do not differ too much from those encountered for the thin film reference (pristine) materials; and (ii) the materials forming the blend show similar Raman cross-sections at the given excitation wavelengths. Moreover, the thin film thickness can be determined unequivocally if its value stays below the thickness corresponding to the first maximum of the Raman intensity oscillation predicted by the mathematical approach.

To the best of our knowledge this work constitutes the first report in which Raman scattering is used to quantify film thickness and volumetric scattering fractions (a.k.a. volumetric composition) in multi-component mixtures of conjugated materials deposited as thin films. This enables the imaging of thickness and composition with diffraction limited spatial resolution over areas from microns up to centimetres squared, thus bridging the two regimes currently addressed by other techniques (e.g. local probes for less than 25-by-25 microns squared and ellipsometry/SIMS for averaged values over cm² areas). Furthermore, the methodology itself is not restricted to a particular type of material or film architecture but it can be applied in any thin film technology which includes Raman-active chromophores: single- or multi-layered structures, free-standing or supported films, and organic or inorganic materials.

Methodology

Mathematical framework

The main scope of this work consists of developing and testing a suitable mathematical framework dictating the relationship

This journal is © The Royal Society of Chemistry 2017

114

J. Mater. Chem. C, 2017, 5, 7270–7282 | 7271

between Raman intensity, film thickness and local volumetric composition in multi-component mixtures. We first consider that the Raman scattering process is divided into three steps: (1) the excitation of the film by the incident laser beam; (2) the generation of the Raman-scattered light from the film; and (3) the collection of the Raman light. The amplitude of the incident electromagnetic field determines the probability of Raman scattering to occur within the thin film, as we consider it proportional to the probability to induce oscillating dipoles. Such a term weights the intensity of the Raman-scattered light emitted from the bulk of the film, leading to interference effects in the dependence of the Raman intensity on film thickness curve (as we demonstrate in the Experimental section).

The distribution of an incoming electromagnetic field in a multi-layered system can be described following a broad variety of formalisms, the transfer matrix method being one of the most elegant approaches.[34–36] In this case, each interface and layer is described by 2-by-2 matrices including their respective optical constants and thicknesses. Then, the electric field distribution in each layer can be calculated as a product of square matrices, assuming that the incident field is a time-independent plane wave. This methodology is strictly valid if the layers are homogeneous and the interfaces are flat within the spot size of the incident beam.

Let us consider the case of a thin film (medium 1, with optical constants n_1 and κ_1 for the refractive index and extinction coefficient, respectively) deposited on top of a glass substrate (medium 2, semi-infinite) under vacuum (medium 0, semi-infinite). In a one-dimensional case and for normal incidence, the transfer matrix method provides a simple expression for the amplitude of the electric field at a film depth x (from the vacuum interface) due to the incoming laser beam of wavelength λ_L, which reads:

$$E_L(x) = \frac{t_{01}\left(e^{i\xi_1 x} + r_{12}e^{i\xi_1(2d-x)}\right)}{1 - r_{10}r_{12}e^{2i\xi_1 d}}|E_0| = t_L|E_0| \qquad (1)$$

where i is the imaginary unit, t_{ab} and r_{ab} are the complex Fresnel transmission and reflection coefficients of the interfaces between a and b media, $\xi_1 = 2\pi(n_1 + i\kappa_1)/\lambda_L$, d is the film thickness and $|E_0|$ is the amplitude of the plane wave that describes the incoming field. For simplicity, $|E_0|$ is taken to unity. In practice, this is not a constraint as we normalize the Raman signal by the laser power arriving at the sample.

An analogous mathematical description applies also in the case of light emitted from the bulk of a film, a.k.a. the Raman-scattered light. We consider the probability of inducing oscillating dipoles in the media to be proportional to the incident electromagnetic field at the probed position of the thin film, which is then responsible for the Raman-scattered radiation according to the cross-section of the mode under study. Thus the amplitude of the scattered field E_R leaving the film towards the spectrometer can be written as

$$E_R(x) \propto \frac{t_{10}^R\left(e^{i\xi_1^R x} + r_{12}^R e^{i\xi_1^R(2d-x)}\right)}{1 - r_{10}^R r_{12}^R e^{2i\xi_1^R d}}|E_L(x)| = t_R|E_L(x)| \qquad (2)$$

where the superscript R refers to the values attained at the Raman-scattered wavelength (λ_R). Since $E_R(x)$ stands for the emergent Raman-scattered electric field amplitude due to an infinitesimal material slab located at a distance x from the film surface, the total Raman intensity I_R is given by integrating the squared modulus of the scattered field $|E_R(x)|^2$ (i.e. the scattered intensity due to such a slab) over the entire film thickness:

$$I_R(d) = \sigma_R \int_0^d |E_R(x)|^2 \, dx \qquad (3)$$

where σ_R is an empirical, solid-state effective Raman cross-section that stands for the measured Raman activity (with units of counts s^{-1} W^{-1}) of any mode under study. Eqn (3) results in an interference-like distribution for the Raman intensity as a function of film thickness. The oscillatory behaviour has the same origin as the oscillations of short circuit current as a function of film thickness observed in organic photovoltaics.[35] Note that eqn (3) also takes into account the absorption (reabsorption) of the incoming (scattered) field as indicated by the complex refractive index included in the definition of ξ_1 (ξ_1^R). Clearly, this formalism can be extended for systems comprising a larger number of layers by calculating the corresponding Fresnel coefficients of the two subsets separated by the Raman-active layer, i.e. media 0 and 2.

Eqn (3) holds for incoming and scattered s- (TE) and p-polarized (TM) waves according to their complex Fresnel coefficients.[35] This fact leads to slightly different Raman intensity distributions depending on the selected polarization combination and angle of incidence. Taking into account the polarization of the incident and scattered waves, eqn (3) can be rewritten as

$$I_R(d) = \sigma_R|E_0|^2 \int_0^d \left(\alpha|t_L^s(x)|^2 + \beta|t_L^p(x)|^2\right) \cdot \left(\alpha|t_R^s(x)|^2 + \beta|t_R^p(x)|^2\right) dx \qquad (4)$$

where α and β are the weighting factors associated with s- and p-polarizations such that $\alpha + \beta = 1$. Interestingly, we found that despite performing backscattered Raman experiments (i.e. in normal incidence) the intensity values oscillate differently with film thickness depending on the numerical aperture of the objective as well as on the type of sample geometry being measured. Microscope objectives with low magnification and numerical aperture ($10\times$, NA = 0.25) lead to data fits in which $\alpha \approx 1$, indicating that the incident electric field is mostly in normal incidence within the dimensions of the laser spot. Furthermore, $\alpha \approx 1$ when collecting the Raman-scattered light through a thick superstrate such as a glass slide ($n = 1.45$, 1.2 mm-thick) even when using objectives with larger magnification and numerical aperture ($40\times$, NA = 0.6). In this case, the refractive index contrast between air ($n = 1$) and glass ($n = 1.45$) reduces the refraction angle of the rays impinging obliquely, thus enhancing the weight of the s-component in eqn (4). For moderate magnifications and numerical apertures, and in the absence of thick incoherent superstrates, eqn (4) generally leads to fits in which $\alpha = \beta = 0.5$, thus equally mixing all incident and scattered polarizations.

7272 | J. Mater. Chem. C, 2017, 5, 7270–7282

115

This journal is © The Royal Society of Chemistry 2017

Regarding multi-component mixtures, the intensity of the acquired Raman spectra can be modeled in order to locally estimate both film thickness (d) and volumetric composition (v_u) in medium 1. To do so we assume that in a thin film of N different components the measured Raman signal corresponds to a superposition of the spectra obtained for the pure compounds forming the blend. Hence the Raman intensity at any location in the sample can be described quantitatively as a linear combination of the basis (reference) spectra for the pure compounds. Thus, accurate quantitative information can be obtained if the effective cross-sections of the individual components are known. Generalizing for a blend of N components the Raman intensity reads

$$I_{R,mix}(d, v_u, \bar{v}) \propto \int_0^d |E_R(x, v_u)|^2 dx \sum_{u=1}^N v_u \sigma_{R,u} I_{ref,u}(\bar{v}) \quad (5)$$

where $\bar{v}$ corresponds to the Raman shift; $I_{ref,u}(\bar{v})$ stands for the (reference) Raman spectrum of component u normalized at the intensity of the mode associated with the cross-section $\sigma_{R,u}$; v_u is the volumetric scattering fraction of component u (which satisfies $\sum_{u=1}^N v_u = 1$), and d refers now to the thickness of the blended thin film in the probed region. For the Raman-scattered radiation $E_R(x, v_u)$ the optical constants are assumed to vary linearly with the volumetric composition as $\varepsilon_{mix} = \sum_{u=1}^N v_u \varepsilon_u$, so we implicitly assume that they are well mixed at the λ_L-length scale. We have also tested other effective medium approximations for ε_{mix} such as Bruggeman's model and obtained results for the fit which lay within the statistical error of the linear approximation proposed (for the blends measured in this work); consequently, we adopted the latter to keep the methodology as simple as possible.

The rigorous description of the Raman-scattered radiation with the transfer matrix method presented here is compared with three simpler approaches. First, a thickness-independent approximation for the scattered light,

$$I_{mix,ind}(v_u, \bar{v}) = \sum_N v_u \sigma_{R,u} I_{ref,u}(\bar{v}) \quad (6)$$

This is a typical approximation used for bulk multi-component materials. Second, a linear dependence of the Raman intensity with film thickness,

$$I_{mix,lin}(d, v_u, \bar{v}) = d \sum_N v_u \sigma_{R,u} I_{ref,u}(\bar{v}) \quad (7)$$

This has been previously used to model blend films.[4] Finally, an exponential decay of the incoming and scattered fields within the film,

$$I_{mix,ex}(d, v_u, \bar{v}) = \int_0^d e^{-(\alpha(v_u) + \alpha_R(v_u))x} dx \sum_N v_u \sigma_{R,u} I_{ref,u}(\bar{v}) \quad (8)$$

where $\alpha(v_u) = 4\pi\kappa_1(v_u)/\lambda_L$ and $\alpha_R(v_u) = 4\pi\kappa_1^R(v_u)/\lambda_R$. This would represent the simplest (Beer–Lambert-like) model that can account for two important experimental facts, the initial increase in the Raman signal with the amount of material

(thickness) and the saturation of this behaviour for thick films (much greater than the penetration depth of the light).

Experimental validation and protocol

We experimentally validate the methodology using the following protocol:

(1) First, a thickness series of uniform, homogeneous samples containing a single, pure material is prepared. An alternative that we have extensively explored here is to use samples with a thickness gradient over relatively large lateral distances so as to be uniform within the laser spot. By scanning the laser beam across the sample, many experimental points can be obtained.

(2) Then, the Raman intensity (effective counts per second) of a particular band (usually the most intense one) is tracked as a function of film thickness.

(3) The experimental data are fitted according to eqn (4) using σ_R as a free parameter after measuring the film thickness through profilometry, AFM or ellipsometry at the same locations where Raman spectra were acquired. Thus σ_R is a material property associated with a given mode and excitation wavelength. Proper background subtraction is necessary to avoid photo-luminescence disrupting the observed trends. Note that for the calculation of eqn (4) we need the optical constants of the whole multi-layered stack as input parameters (see Table 1). They can often be taken from the literature,[16] or measured by complementary techniques such as ellipsometry.

The previous steps (1–3) are only required to experimentally verify that the oscillations of the Raman intensity with film thickness are well described by the mathematical model. When implementing the methodology to measure the Raman signal in some of the materials provided in Table 1, a few samples of the material are sufficient to measure the Raman spectrum and thickness locally. Then, by fitting the corresponding $I_R(d)$ curve, the effective Raman cross-section for that material in that particular Raman setup is extracted; the term effective refers to the fact that such a value is only valid for that setup, including optics (objective magnification and numerical aperture) and CCD yield. Finally, by using the ratiometric values provided in Table 1 the method can be implemented readily in pure or mixed films of any materials for which σ_R has been determined. These ratios remain constant regardless of the Raman setup and optics used (Fig. S1 in the ESI†). Thus once σ_R is determined for a given material (and keeping the geometrical measuring factors constant, including the numerical aperture and objective magnification), this value can be used in combination with eqn (4) to obtain an unknown thickness for pristine films on any substrate, to evaluate film homogeneity, or to monitor film thickness in-line. When extending the methodology to materials beyond those listed in Table 1, steps 1 to 3 are advised to get proper statistics and error estimations on effective σ_R values for a particular Raman setup.

When evaluating multi-component systems, the following steps need to be taken:

(4) In multi-component mixtures we first normalize every material spectrum by the intensity of the Raman mode associated with the previously estimated cross-section, σ_R, as well as by the laser power impinging at the sample. The normalization step

Table 1 Collection of ratiometric Raman cross-sections (with respect to PC$_{70}$BM) for the conjugated materials analysed in this work. The uncertainties result from the statistical error of the least squares fit for each material and they implicitly include the error in the determination of $\sigma_{R,PC70BM}$. Complex refractive indices at both the excitation wavelength and at the Raman-scattered wavelength associated with the corresponding vibrational band are also included. The film thickness corresponding to the first Raman intensity maximum serves as a reference to evaluate the single valued fitting regime of the methodology

Material	$\sigma_{R,u}/\sigma_{R,PC70BM}$		Complex refractive index at λ_L		Raman band (λ_R) cm^{-1}	Complex refractive index at λ_R		Thickness of first Raman intensity maximum	
	514 nm	488 nm	514 nm	488 nm		514 nm	488 nm	514 nm	488 nm
BTT-DPP[b]	12 ± 1	12 ± 1	1.29 + 0.21i	1.33 + 0.17i	1517	1.18 + 0.33i	1.25 + 0.23i	347 nm	>500 nm
C16-IDTBT[a]	5.2 ± 0.7	8 ± 1	1.35 + 0.31i	1.42 + 0.18i	1353	1.41 + 0.51i	1.35 + 0.36i	162 nm	500 nm
DPP-TT-T-1[b]	1.3 ± 0.2	4.3 ± 0.5	1.41 + 0.13i	1.48 + 0.17i	1502	1.16 + 0.22i	1.35 + 0.08i	>500 nm	>500 nm
DPP-TT-T-3[b]	1.4 ± 0.2	4.4 ± 0.5	1.11 + 0.27i	1.25 + 0.24i	1502	0.97 + 0.52i	1.06 + 0.33i	151 nm	>500 nm
PCBM[a]	0.15 ± 0.04	0.3 ± 0.1	2.02 + 0.09i	2.04 + 0.11i	1461	2.01 + 0.07i	2.02 + 0.09i	145 nm	135 nm
PCDTBT[a]	18 ± 2	17 ± 2	1.79 + 0.86i	1.61 + 0.67i	1445	2.18 + 0.94i	1.87 + 0.90i	103 nm	107 nm
PCPDTBT[a]	3.9 ± 0.5	3.8 ± 0.5	1.33 + 0.29i	1.42 + 0.18i	1349	1.33 + 0.48i	1.32 + 0.34i	167 nm	320 nm
rr-P3HT[a]	51 ± 5	59 ± 6	1.74 + 0.95i	1.50 + 0.88i	1450	2.15 + 0.85i	1.84 + 0.91i	103 nm	109 nm
PC$_{70}$BM[a]	1	1	2.14 + 0.35i	2.08 + 0.40i	1564	2.19 + 0.29i	2.15 + 0.33i	122 nm	116 nm

[a] Cross-sections obtained using graded films. [b] Cross-sections obtained using at least three uniform films.

implies that within the spectral region studied (usually within the range 1000–1700 cm^{-1}) the spectrum varies uniformly with film thickness and laser power as dictated by the intensity oscillation of the band associated with σ_R. This approximation is valid provided that relative Raman band intensities are constant upon variations of film thickness and/or composition. We repeat this procedure for all the materials forming the mixture to build a library of effective Raman cross-sections for each material ($\sigma_{R,u}$) in our particular setup as well as their corresponding normalized spectra ($I_{ref,u}(\bar{v})$).

Finally, we use eqn (5) to fit the raw Raman spectra of the multi-component mixtures using film thickness d and volumetric fraction v_u as free parameters. Once again, a correct background subtraction is required for proper data fitting. Note that backgrounds may be very different in pristine and blend films, since photoluminescence is often quenched by mixing.

Results and discussion

In a first set of experiments, we evaluated the Raman spectra of three soluble fullerenes and eleven different conjugated polymers; see Fig. 1. Their Raman spectra are generally feature-rich and characteristic enough so as to clearly identify their vibrational fingerprints in multi-component films. This is important as blends of conjugated polymers and fullerenes are the main material systems used as the active layer in organic solar cells. The spectral window between 1000 cm^{-1} and 1700 cm^{-1}, corresponding to modes associated with carbon single and double bonds, exhibits peaks that are both generally strong for all materials and centered at material-specific positions.

In a second series of experiments, we determined the single material effective solid-state Raman cross-sections, σ_R, for a selection of materials. For this purpose, we used films exhibiting a lateral thickness gradient (see the Experimental section) as they enable the local measurement of the Raman spectra in order to then correlate the intensity with the thickness profile obtained through profilometry, ellipsometry or AFM. A typical thickness

gradient spanned between 20 nm and 150 nm across over 5 cm in sample length. This means that over the spot size of our laser (around 20 microns) the thickness varies less than 0.06 nm and thus the sample can be considered locally homogeneous. Interestingly, with this approach we are able to combine in a single sample the equivalent information that we would have obtained by fabricating several tens of them, saving both material and time.

Fig. 2(a–d) illustrate the variation of the Raman intensity with film thickness for four conjugated materials under different excitation wavelengths: (a) PC$_{70}$BM and (b) PCPDTBT at 514 nm excitation, and (c) C16-IDTBT and (d) PCDTBT at 488 nm excitation. Additional data for these materials and P3HT can be found in Fig. S2 and S3 in the ESI.† Three of these compounds are often used as active materials in OPVs. The fourth, C16-IDTBT, is a low band gap polymer that shows a high field-effect mobility as well as a relatively insensitive polymer structure when the processing conditions are varied.[37,38] Branched side-chain analogues have been used to fabricate efficient solar cells.[39,40] The experimental data were extracted from a single graded sample supported on glass, whose thickness as a function of position was double-checked using profilometry. Marks were performed at the beginning and at the end of the measuring region, and Raman spectra were acquired at spatial intervals of 500 μm. Note that profilometric line scans are not acquired exactly at the same position where Raman was measured, but with an uncertainty of a few tenths of microns. Thus if the sample presents thickness inhomogeneities which extend over that scale, then the correlation between Raman intensity and film thickness may deviate slightly. This effect is also present if ellipsometry is used to measure the film thickness due to the difference in the diameter of the spot used in both techniques (ca. 20 μm in our Raman setup vs. >200 μm in ellipsometry). Homogeneous samples were prepared using both blade and spin coating to verify that the casting method does not have a noticeable influence on the Raman intensity of the modes under study, or the graded profile of the sample.

The general trend is that the Raman intensity slowly increases with thickness until it reaches an asymptotic maximum.
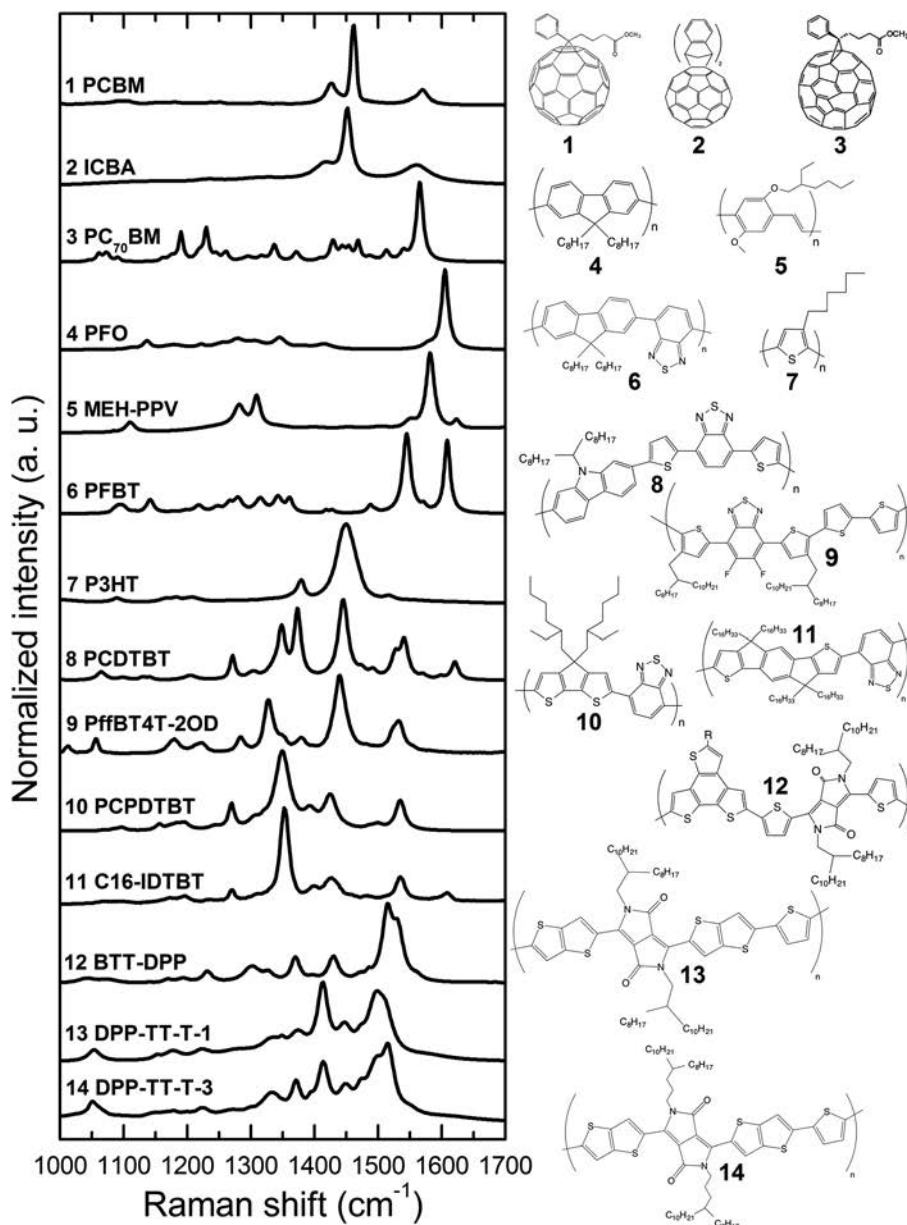
Fig. 1 Normalized Raman spectra of the conjugated polymers and fullerenes measured in this work including their chemical structure.

Additionally, there are mild oscillations of the intensity prior to reaching such an asymptote, whose amplitude and period depend on the optical constants of the whole layered stack at the excitation and scattered wavelengths. The solid lines in Fig. 2 represent a non-linear, least squares fit of the interference curve obtained by integrating eqn (4) for each material and wavelength taking $\alpha = \beta = 0.5$. For comparison, the thickness-independent (dashed-dotted line, eqn (6)), the linear (dotted line, eqn (7)) and the exponential (dashed line, eqn (8)) models are also plotted and fitted by least-squares to the experimental data (except the thickness-independent model, which matches the asymptote of the exponential model). While both the thickness-independent and the linear approximations are clearly too simple to explain the experimental trends, both the exponential and transfer matrix models fit the raw data reasonably well in most cases.

The exponential approximation, despite being such a simple approach, well reproduces the trend in most conjugated polymers given the absence of strong interference effects. Nevertheless, these are progressively more critical as the refractive index contrast between adjacent films increases, in which case the transfer matrix model provides the correct trends; see Fig. S4 in the ESI† for a detailed study of C16-IDTBT Raman mode intensities when deposited on a silicon substrate. Thus, as the complexity of the multi-layered stack increases, the accuracy of the transfer-matrix-based model is significantly enhanced compared to other simpler approximations. To demonstrate this fact we measured a PCDTBT sample showing a lateral thickness gradient in which part of its exposed surface was covered with a thermally evaporated MoO_3/Ag electrode, whose thicknesses are 12 nm and 100 nm, respectively. Since the film was supported on a glass substrate (1.2 mm thick)
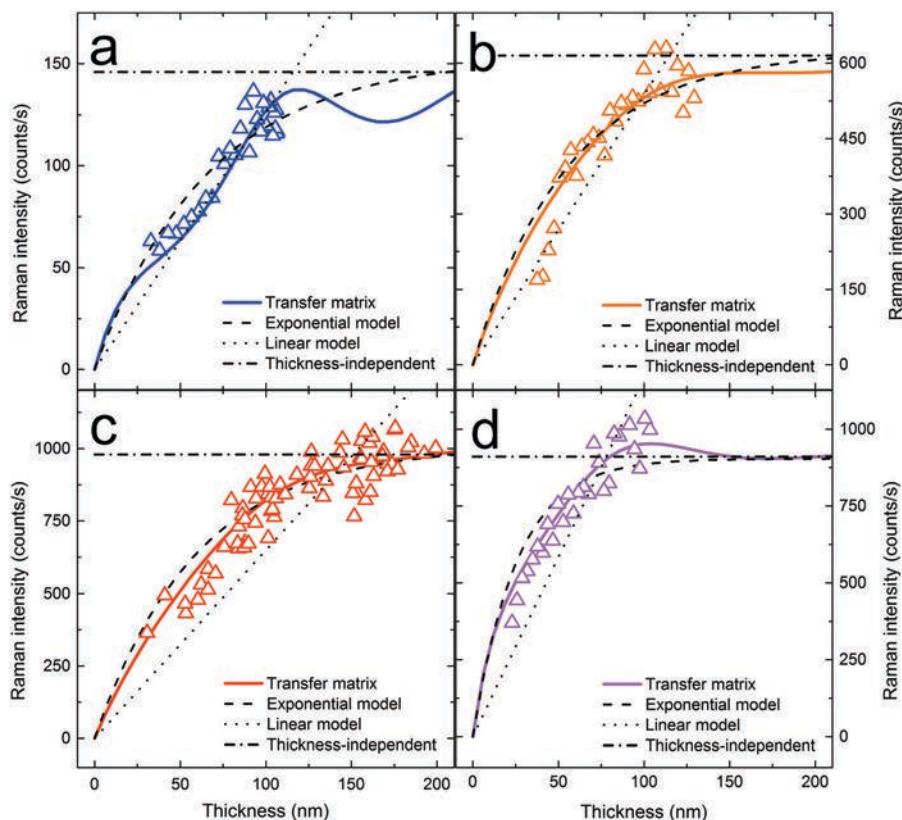
Fig. 2 Raman intensity (triangles) as a function of film thickness for (a) $PC_{70}BM$ under 514 nm excitation (1564 cm^{-1} band); (b) PCPDTBT under 514 nm excitation (1349 cm^{-1} band); (c) C16-IDTBT under 488 nm excitation (1353 cm^{-1} band); and (d) PCDTBT under 488 nm excitation (1445 cm^{-1} band). Solid lines stand for the transfer matrix modeling of the Raman process. Thickness-independent (dashed–dotted lines), linear (dotted lines) and exponential (dashed lines) models are also plotted and fitted to the experimental data to ease the comparison between approaches.

we focused the incident laser through such a thick incoherent layer, adding more complexity to the modeling of the electric field amplitudes. This structure resembles that of devices, in which the optical access is through the substrate. Fig. 3 illustrates the Raman intensity oscillations that occur in both the exposed and the covered regions using a 10× objective to focus through the glass, taking $\alpha = 1$ and assuming that the (semi-infinite) incident medium is the glass substrate ($n_0 = 1.45$). According to Fig. 3, the three-fold intensity enhancement driven by the presence of the MoO_3/Ag electrode is reproduced and the experimental data are properly fitted using the transfer matrix model in such a complex stack. Moreover, the single free-parameter used to fit the model to the experimental data, i.e. the effective Raman cross-section of PCDTBT ($\sigma_{R,PCDTBT}$), acquires equivalent values regardless of the configuration of the multi-layered stack in which the polymer film is embedded. According to Fig. 3, the effective Raman cross-section of PCDTBT at 488 nm excitation reads (2.1 ± 0.2) counts s^{-1} mW^{-1} and (2.1 ± 0.1) counts s^{-1} mW^{-1} when such a polymer film is measured through the glass (glass/polymer/air) and with a MoO_3/Ag electrode (glass/polymer/MoO_3/Ag), respectively. This experiment confirms the validity of our approach to model the Raman-scattered intensity even in model device systems as well as the generality of the effective Raman cross-sections extracted therein.

The relatively good match of the experimental data with the theoretical curves demonstrates that Raman spectroscopy can
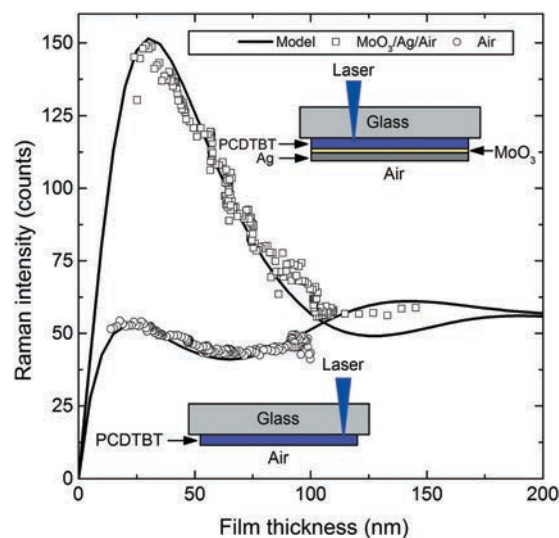
Fig. 3 Raman intensity as a function of thickness for a PCDTBT film (1445 cm^{-1} mode) deposited on a thick glass substrate (1.2 mm) in two different configurations: with (upper curve) and without (lower curve) a thermally evaporated MoO_3/Ag electrode. Data took under ambient conditions using 488 nm excitation and a 10× magnification (NA = 0.25) microscope objective to focus through the thick glass layer ($\alpha = 1$ in the modeling). The experimental data are normalized to the laser power used to measure the region without the MoO_3/Ag electrode.

also be used to rapidly determine the thickness in neat thin films, regardless of the deposition technique employed to prepare them. The accuracy of such determination is *ca.* 10 nm, which renders the method as reliable as profilometry when dealing with soft films. This accuracy corresponds to the variance in the adjustable parameters as obtained from the least squares fit. Nevertheless, a qualitative inspection of the theoretical curve shows that its oscillatory behaviour constrains the accuracy of the methodology regarding film thickness determination. As a rule of thumb, if the thin film thickness is close to the thickness of the first Raman intensity maximum (Table 1), the Raman intensity *vs.* film thickness dependence is no longer single-valued due to the oscillation of the intensity and the accuracy is lowered up to *ca.* 20 nm. Then (a) alternative measurement techniques should be performed to aid the estimation of the correct thickness; or (b) a different fitting routine should be implemented. In the latter case, we propose following a spectroscopic, multi-wavelength Raman approach in which the Raman spectra obtained at several wavelengths are fitted simultaneously with shared parameters (thickness and also composition in multi-component films). The result is then valid as long as the fitted thickness stays below the intensity saturation regime of the corresponding $I_R(d)$ curve, which occurs at different values depending on the optical constants of the material at the excitation wavelength. P3HT constitutes an example in which such an approach can be applied successfully; see Fig. S3 in the ESI.†

An important feature of the methodology presented in this work is that the values of the effective Raman cross-sections extracted from fitting eqn (4) to experimental data mainly depend on the geometry and optics of each Raman setup; in other words, their relative values are in principle constant if the same geometry (backscattering), optics and acquisition parameters at the CCD are used. This fact allows us to create a library of effective solid-state Raman cross-sections for each compound and excitation wavelength in the backscattering configuration (Table 1). In principle, if a material included in the library can be measured in a different Raman setup, Table 1 provides the general ratiometric values for the effective cross-sections of the rest of the materials listed, thus enabling the facile implementation of the methodology in a different lab. Reassuringly we have been able to verify this by extracting the effective Raman cross-sections of several materials in two different confocal Raman setups and in a variety of substrates and layered structures while using objectives with different magnifications and numerical apertures; see Fig. S1 in the ESI.† The reader is referred to steps 1 to 3 of the experimental protocol for the estimation of cross-sections for materials other than those listed in Table 1.

So far we have discussed the modeling of the Raman signal for thin films of a single component. We next discuss the application of the methodology for blends of two components. In the case of well mixed multi-component blends, we show in the Appendix that the Raman interference curve also changes as a function of composition, with the maxima varying smoothly from the thickness value that would correspond to one component, to

that of the other, following a behaviour governed by the assumed linear variation of the optical constants (see Fig. 6). There are two important requirements for the Raman signal of each component that makes the fitting of the corresponding mixture accurate. First, the Raman fingerprints of its components should be clearly distinguished through a wide range of compositions, which, according to Fig. 1, is the case for most material combinations; and secondly, the difference between Raman cross-sections cannot be too large (Table 1). For the latter our experience indicates that the ratio between Raman cross-sections should not be higher than 30 to cover the entire composition diagram (from *ca.* 5 vol% to *ca.* 95 vol%) with acceptable accuracy. In some cases this can be achieved by properly selecting the excitation wavelength so that one of the components enters in resonance while the other is not. This is applicable to materials that exhibit complementary absorption spectra over some range of the spectrum.

In the next series of experiments, the methodology for multi-component systems was tested by analysing two types of state-of-the-art polymer:fullerene blends used for OPVs. We selected two conjugated polymers, namely PCPDTBT (partially crystalline) and PCDTBT (rather insensitive to processing), and blended them with the fullerene $PC_{70}BM$ in variable weight ratios. By choosing these combinations we expected to cover two rather different cases of blending as far as morphology is concerned: while in the former case the semi-crystallinity of the polymer is likely to be partially disturbed by the presence of the fullerene,[41] in the latter case the morphology of the polymer is expected to be less sensitive to fullerene loading.[42–44] Both systems fulfil the *a priori* requirements mentioned above: they show close enough Raman cross-sections (Table 1) and clearly distinguishable Raman spectra in the region of interest (Fig. 1, 1000–1700 cm^{-1}). The accuracy of Raman scattering in determining volumetric composition is assessed by comparing the values obtained with our methodology with results from variable-angle spectroscopic ellipsometry (VASE) in the same samples and locations. For the fit of the ellipsometric data, we assumed a Bruggeman's effective medium approximation and no vertical segregation through the film. During the modeling of the Raman intensity we double-checked that the use of a linear combination rather than a Bruggeman's effective medium approximation for the optical constants of the blended film introduced an uncertainty which was within the statistical error of the subsequent fit of the spectra.

Fig. 4(a and b) illustrate the volumetric compositions extracted through both techniques (Raman and VASE) for a series of PCDTBT:$PC_{70}BM$ and PCPDTBT:$PC_{70}BM$ blends deposited as thin films. Since the Raman-based values are plotted as a function of the ellipsometric composition, a straight line of slope unity would represent perfect matching between techniques. According to Fig. 4(a and b), Raman spectroscopy matches ellipsometry when determining the composition in PCDTBT:$PC_{70}BM$ blends whereas the techniques disagree in PCPDTBT:$PC_{70}BM$ films. Fig. 4(a and b) also indicate a small mismatch between the Raman-estimated polymer fractions depending on the excitation wavelength employed, with the estimated average

This journal is © The Royal Society of Chemistry 2017

120

J. Mater. Chem. C, 2017, **5**, 7270–7282 | 7277

polymer loading being generally higher under 514 nm excitation than 488 nm.

The accuracy of the methodology in determining the film composition mainly depends on how distinguishable the Raman fingerprint spectra are as well as on the cross-section ratio of the blended materials. The optimum case would correspond to that in which the cross-section ratio is as close to unity as possible; under these circumstances, the accuracy of the Raman methodology is comparable to that of ellipsometric measurements (± 5 vol%) at moderate compositions (20–80 vol%) but is lower in the extreme cases (below 10 vol%). The former situation closely corresponds to the case of PCPDTBT:$PC_{70}BM$ blends (with a cross-section ratio of *ca.* 4), in which the statistical error bars due to the fit are of the order of $\pm 5\%$ and are lower as the content of $PC_{70}BM$ increases (which has the lowest cross-section of both). On the other hand, the large cross-section ratio between PCDTBT and $PC_{70}BM$ (*ca.* 20) lowers the accuracy in the determination of the composition as the film gets polymer-enriched. The origin of such larger uncertainty is related to the fact that as the polymer content

in the film increases the Raman fingerprint due to the fullerene is progressively hindered and the fit starts losing sensitivity to the presence of fullerene. Nevertheless, even in this adverse case the accuracy of the methodology is close to $\pm 10\%$ in volume fraction (statistically).

Regarding the disagreement between Raman spectroscopy and ellipsometry in PCPDTBT:$PC_{70}BM$ blends, we ascribe it to the structural and conformational changes that take place upon blending, with the disruption to polymer crystallinity dependent on the fullerene loading.[24,41,45] Since we have estimated the solid-state Raman cross-section of PCPDTBT using a pure graded film, the trend observed for the Raman intensity may not extrapolate perfectly well to the case of a blended film if its morphology or local density has changed significantly. At the same time, we expect variations of the optical constants to occur[23] which can explain the mismatch in the composition estimated at different excitation wavelengths. The optical constants are affected by the fullerene loading, the casting conditions (see Fig. S5 in the ESI†) and the annealing post-treatments, which modify the aggregation and crystallinity of both components.[45] This typically results in blue-shifts of the absorption and a reduction in anisotropy. It has been reported that upon blending with fullerenes, conjugated polymer chains may attain a less anisotropic orientation which eventually reduces their extinction coefficient up to one third of the value observed for pure films.[46] Moreover, since the ellipsometric data are fitted according to a Bruggeman's model using as input parameters the optical constants for the pure PCPDTBT and $PC_{70}BM$ films, slight deviations of the volumetric composition and thickness are also expected following this approach. As we show in Fig. S4 and S5 in the ESI,† variations in the optical constants can have significant effects on the resulting Raman intensity dependence on film thickness. Thus, we expect Raman spectroscopy and ellipsometry to differ in those cases in which the morphology and the optical properties of the film are noticeably affected by the blending process. Conversely, the morphology in PCDTBT:$PC_{70}BM$ blends was reported to be highly robust, with the polymer phase within the blend being as amorphous as in the neat films and $PC_{70}BM$ domains aggregating with a low degree of long-range order.[47] We have not observed any peak shifting upon blending nor variations in the relative peak intensities at any excitation wavelength even under ambient conditions, which constitutes a usual signature of robust morphology. Hence we expect the local densities and cross-sections to correlate well with those extracted for the pure films, explaining the improved matching of Raman and ellipsometry in the characterization of these samples.

We further explore the generality of the method by testing other binary blends (Table 2), including novel low band-gap co-polymers with promising power conversion efficiencies in organic solar cells, such as DPP-TT-T and BTT-DPP.[48–50] According to Table 2, DPP-TT-T blends show consistent volumetric composition and lower film thickness values between VASE and Raman, whereas both techniques disagree in BTT-DPP blends. These results suggest that some of the above-mentioned blending effects that occur in PCPDTBT:$PC_{70}BM$ films are also taking place in BTT-DPP blends, which requires a more detailed analysis of
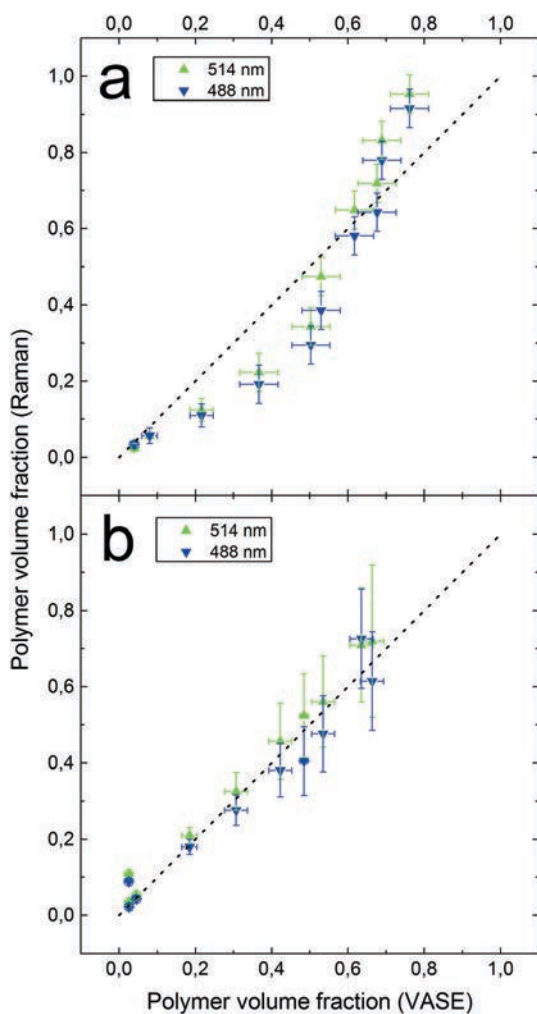

Fig. 4 Polymer volumetric fractions in (a) PCPDTBT:$PC_{70}BM$ and (b) PCDTBT:$PC_{70}BM$ blended films as extracted through Raman (Y axis) and VASE (X axis). A straight dotted line is added as a guide-to-the-eye representing perfect matching between techniques.

Table 2 Comparison of polymer volumetric composition and thin film thickness as obtained from Raman spectroscopy and extracted through VASE in a series of polymer:fullerene blends. Raman values were fitted averaging at least three spectra at random positions in the sample

Blend (w : w)	Vol% (VASE)	Vol% (Raman)		Thickness (VASE)	Thickness (Raman)	
		514 nm	488 nm		514 nm	488 nm
DPP-TT-T-1 : PC$_{70}$BM (1 : 2)	30 ± 5%	32 ± 4%	27 ± 4%	71 ± 5 nm	34 ± 5 nm	45 ± 5 nm
DPP-TT-T-3 : PC$_{70}$BM (1 : 2)	31 ± 5%	29 ± 4%	31 ± 4%	70 ± 5 nm	33 ± 5 nm	40 ± 5 nm
BTT-DPP : PC$_{70}$BM (1 : 2)	29 ± 5%	11 ± 3%	16 ± 3%	100 ± 5 nm	53 ± 5 nm	72 ± 7 nm
PCDTBT : PC$_{70}$BM (1 : 1)	49 ± 5%	50 ± 10%	50 ± 10%	27 ± 5 nm	24 ± 5 nm	26 ± 5 nm
PCPDTBT : PC$_{70}$BM (1 : 1)	53 ± 5%	47 ± 3%	39 ± 3%	63 ± 5 nm	37 ± 6 nm	60 ± 8 nm

the optical constants and degree of anisotropy that is beyond the original scope of this paper. For completeness and ease of comparison, case examples of 1 : 1 (w : w) PCDTBT : PC$_{70}$BM and PCPDTBT : PC$_{70}$BM blends are also included in Table 2.

One interesting application of the Raman methodology described in this work consists of forming Raman-based thickness and composition images of polymer:fullerene blends with a lateral resolution of a few hundreds of nanometres. As a first demonstration, we present in Fig. 5(a–c) Raman images of 1 : 1 (w : w) PCPDTBT : PC$_{70}$BM blends in which the methodology is applied to fit the acquired spectra. The images were recorded centred at a fullerene aggregate, whose thickness non-uniformity creates a visible surrounding halo [Fig. 5(a)]. Fig. 5(b and c) demonstrate how Raman is sensitive enough to accurately quantify the variation in film thickness associated with the halo, and also how the polymer content drops at the aggregate. The composition profile was calibrated according to a corrected curve extracted from

the data plotted in Fig. 4(a). Raman images suggest that the volumetric distribution of the polymer:fullerene blend is rather homogeneous throughout the sample except at the defects (aggregates).

Conclusions

We have successfully demonstrated that Raman scattering is a powerful tool for the accurate determination of film thickness and volumetric composition in polymer:fullerene blend thin films used in organic photovoltaics. The applicable thickness range extends from a few monolayers up to several hundreds of nanometres depending on the optical constants of the film and the stack in which it is embedded. To do so, we have developed a methodology which describes the dependence of the Raman intensity as a function of film thickness and composition via the transfer matrix method for the incoming and Raman-scattered light. We predicted and measured an interference-like pattern of the Raman intensity as a function of film thickness and demonstrated the capabilities of the method to infer film thicknesses below the first interference maximum within an error margin of ca. 10 nm. Regarding composition, the method returns values consistent with ellipsometry (±5 vol% in the best scenario, ±10 vol% otherwise) provided the chemical microenvironment of the different domains of the blend does not deviate too much from the neat films used to estimate reference Raman cross-sections. Hence the Raman methodology described in this work is especially suitable for those polymer:fullerene blends which include amorphous polymers or, alternatively, systems whose Raman spectrum is not very sensitive to variations of the chemical environment (structural changes, degree of order, crystallinity and miscibility). When this is not the case, a calibration curve for composition can be deduced by comparing Raman and ellipsometry.

When exploited in combination with confocal Raman imaging setups, our methodology entails a significant improvement regarding the ease and speed of characterization of thin films compared to scanning probe microscopies. In the latter case the high lateral resolution (20–30 nm) does not balance the low throughput when dealing with large film areas. The intrinsic diffraction-limited lateral resolution of the confocal Raman setup (ca. 300 nm) makes this technique appropriate for characterizing the large scale inhomogeneities that occur during wet deposition processes extending from a few microns up to centimetres. Furthermore, the present methodology can be applied to any
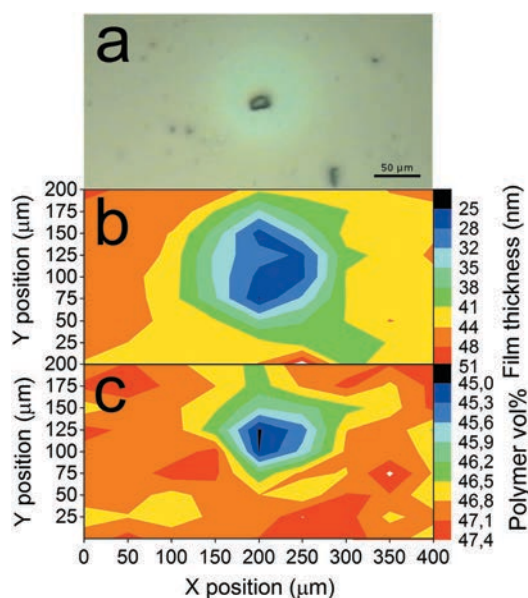

Fig. 5 Raman-based imaging of a 1 : 1 (w : w) PCPDTBT : PC$_{70}$BM blended thin film. A total of 81 spectra were taken to build the images, measured at the grid positions defined by the ticks at the axis. (a) Region analysed as seen through the optical microscope; (b) thickness in nm and (c) polymer volumetric fraction. Note that the area sampled using confocal Raman spectroscopy (400 × 200 μm²) is hundreds of times larger than the typical area covered in scanning probe microscopies (20 × 20 μm²) and close to the dimensions of the light spot in ellipsometry (200 × 200 μm²), thus linking both characterization scales.

This journal is © The Royal Society of Chemistry 2017

122

J. Mater. Chem. C, 2017, 5, 7270–7282 | 7279

thin film technology in which multiple Raman-active materials are either blended or stacked as multilayers. Some potential applications include in-line monitoring and quality control during film fabrication and optimization of optoelectronic devices in which film composition and thickness play a crucial role. In this sense, the methodology presented here offers the possibility of measuring film thickness and composition in functional (ready-to-use) devices such as organic solar cells without significant truncation of their operation. This is achieved by properly selecting the laser power to prevent photodegradation from occurring.

Experimental details

Confocal Raman spectroscopy was performed in two different setups: (1) a LabRam HR800 spectrometer (Jovin Yvon, 600 lines per mm grating) coupled to an Olympus microscope with a $20\times$ objective (NA = 0.35) in backscattering geometry; and (2) a WITec Alpha300RA (1200 lines per mm grating) with different Zeiss objectives ($10\times$, NA = 0.25; $40\times$ with correction collar, NA = 0.6; $50\times$, NA = 0.8). The excitation source corresponds to either the 633 nm line of a He–Ne laser, a 514/488 nm Ar$^+$ line or a solid-state 488 nm laser (WITec). Laser irradiances were kept below 350 W cm^{-2} to avoid photodegradation and laser-induced heating of the films.

All Raman measurements taken with the LabRam HR800 spectrometer were performed at room temperature and under vacuum, whereas those extracted using the WITec Alpha300RA were performed on-the-fly, under ambient conditions and employing low acquisition times (<500 ms). Vacuum is necessary to avoid oxygen-driven photodegradation of conjugated molecules upon laser exposure for prolonged times (>5 seconds), which has a strong influence on the Raman to photoluminescence background ratio; see Fig. S6–S9 in the ESI.† Spectra for each sample were extracted at a minimum of three different positions in the sample and averaged to account for possible inhomogeneities. The integration time and the number of integrating cycles were adjusted to avoid photodegradation. In all cases the Raman spectra were acquired focusing the laser at the film/substrate interface rather than maximizing the scattered intensity. In the latter case the experimental trends were not properly reproduced by our model. Raw data were fitted using the open-source Fityk software[51] as well as homemade fitting routines in MATLAB to automatically treat the datasets obtained as Raman maps.

Samples with thickness gradients were fabricated following a method based on accelerated blade coating.[52] In this deposition technique a controlled volume of ink (with a low solid content ranging from 20 to 40 mg mL^{-1}) containing the conjugated molecule(s) is deposited on top of a substrate and then spread over its surface employing a metallic blade or applicator. The velocity of the applicator with respect to the substrate determines the final film thickness achieved. A thickness gradient can be readily obtained accelerating/decelerating the blade during the deposition process. Chlorobenzene was used as solvent in all cases. Glass substrates were previously cleaned with acetone and

isopropyl alcohol to assure proper ink wettability and film uniformity. The temperature of the blade coater stage was kept fixed at 60 °C to ensure controlled evaporation of the solvent and drying kinetics.

The Raman characterization of samples with a thickness gradient was performed using a motorized XY stage along a straight line (LabRam HR800) or an elongated slab formed by at least three parallel lines (Alpha300RA). Alternative thickness measurements were then obtained by profilometry making use of previous localization marks made on the samples.

Variable-angle spectroscopic ellipsometry (VASE) was acquired at several angles of incidence ranging from 55 to 75 degrees using a GES-6E rotating polarizer spectroscopic ellipsometer (SEMILAB) coupled to a charge-coupled device (CCD) detector. The data were analysed using the Winelli 2 piece of software. The blends were modeled using the Bruggeman effective medium approximation for which the corresponding refractive indices of the materials have been published elsewhere.[16,53]

(6,6)-Phenyl-C$_{61}$-butyric acid methyl ester (PCBM) and (6,6)-phenyl-C$_{71}$-butyric acid ester (PC$_{70}$BM) were obtained from Solenne BV. Indene-C$_{60}$ bisadduct (ICBA), regioregular poly(3-hexylthiophene) (rr-P3HT), poly(2,7-(9,9-di-n-octylfluorene-alt-benzothiadiazole)) (PFBT), poly(9,9-dioctylfluorene) (PFO) and poly[2-methoxy-5-(2-ethylhexyloxy)-1,4-phenylenevinylene] (MEH-PPV) were purchased from Sigma Aldrich. Poly[2,6-(4,4-bis-(2-ethylhexyl)-4H-cyclopenta[2,1-b;3,4-b']dithiophene)-alt-4,7(2,1,3-benzothiadiazole)] (PCPDTBT) was purchased from Organic Nano Electronic. Poly[[9-(1-octylnonyl)-9H-carbazole-2,7-diyl]-2,5-thiophenediyl-2,1,3-benzothiadiazole-4,7-diyl-2,5-thiophenediyl] (PCDTBT) and poly[[5,6-difluoro-2,1,3-benzothiadiazol-4,7-diyl]-alt-(3,3'''-di(2-octyldodecyl)2,2';5',2'';5'',2'''-quaterthiophen-5,5'''-diyl)] (PffBT4T-2OD, also known as PCE11) were purchased from Ossila. All materials were used as received without further purification. Benzotrithiophene-diketopyrrolopyrrole copolymer (BTT-DPP), thieno[3,2-b]thiophene-diketopyrrolopyrrole copolymers (DPP-TT-T-1 and DPP-TT-T-3) and indacenodithiophene-benzothidiazole copolymer (C16-IDTBT) were synthetized at Imperial College as reported elsewhere.[38,48,54]

Appendix

The successful analysis of the Raman spectra of a binary mixture requires using both the film thickness and the volumetric fraction of one of the components as free parameters during the modeling. Since we consider that the optical constants of the blended system vary linearly with film composition ($\varepsilon_{mix} = \nu_1\varepsilon_1 + \nu_2\varepsilon_2$ and $\varepsilon_{mix}^R = \nu_1\varepsilon_1^R + \nu_2\varepsilon_2^R$), the shape of the Raman intensity curve as a function of film thickness is modified accordingly. Regarding the modeling of the scattered light, we assume that its wavelength corresponds to that of the most intense Raman band in the spectral region analyzed. In polymer:fullerene blends this approximation usually leads to a constant scattered wavelength such that $\lambda_{mix}^R = \lambda_{polymer}^R \neq f(\nu)$. This assumption is valid as (i) the high Raman cross-section of conjugated polymers compared to fullerenes implies that their characteristic Raman bands are
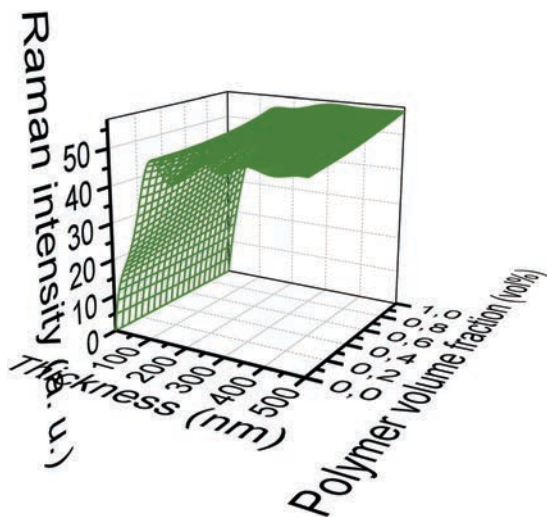
Fig. 6 Three-dimensional surface plot of the modeled Raman intensity as a function of polymer volume content and film thickness for a PCPDTBT:PC$_{70}$BM blend system under 514 nm excitation.

usually the most intense ones in the majority of composition profiles; and (ii) the spectral window we typically deal with during the fit (1000–1700 cm^{-1}) is small enough to neglect the very small variations that occur in the interference curve as a function of the scattered wavelength.

Fig. 6 illustrates how the amplitude and the film thickness associated with the Raman intensity maxima of the oscillating curve are shifted as a function of the polymer content in a PCPDTBT:PC$_{70}$BM blend under 514 nm excitation, as obtained numerically solving the following integral:

$$I_{R,mix}(d, v_u) \propto \int_0^d |E_R(x, v_u)|^2 dx \qquad (A1)$$

The general trend in this case indicates that the higher the polymer content, the more damped the intensity oscillations are as a result of the lower refractive index and the higher extinction coefficient compared to the neat fullerene film. When using a new Raman setup, we should obtain at least the effective cross-section of one of the components forming the blend to then estimate the cross-section due to the other material according to the ratios provided in Table 1 for neat films (obtained fitting eqn (4) to experimental data). Finally, the Raman spectra acquired for any blended system formed by these materials can be fitted according to eqn (5) by interpolating the film thickness and composition in the corresponding integral (eqn (A1) and Fig. 6).

Acknowledgements

Notes and references

1 Z. He, C. Zhong, S. Su, M. Xu, H. Wu and Y. Cao, *Nat. Photonics*, 2012, **6**, 593–597.

2 J. You, L. Dou, K. Yoshimura, T. Kato, K. Ohya, T. Moriarty, K. Emery, C.-C. Chen, J. Gao, G. Li and Y. Yang, *Nat. Commun.*, 2013, **4**, 1446.

3 J. Nelson, *Mater. Today*, 2011, **14**, 462–470.

4 E. Klimov, W. Li, X. Yang, G. G. Hoffmann and J. Loos, *Macromolecules*, 2006, **39**, 4493–4496.

5 H. Hoppe, M. Niggemann, C. Winder, J. Kraut, R. Hiesgen, A. Hinsch, D. Meissner and N. S. Sariciftci, *Adv. Funct. Mater.*, 2004, **14**, 1005–1011.

6 C. R. McNeill, B. Watts, L. Thomsen, H. Ade, N. C. Greenham and P. C. Dastoor, *Macromolecules*, 2007, **40**, 3263–3270.

7 R. C. Masters, A. J. Pearson, T. S. Glen, F.-C. Sasam, L. Li, M. Dapor, A. M. Donald, D. G. Lidzey and C. Rodenburg, *Nat. Commun.*, 2015, **6**, 6928.

8 N. Kumar, A. Zoladek-Lemanczyk, A. A. Y. Guilbert, W. Su, S. M. Tuladhar, T. Kirchartz, B. C. Schroeder, I. McCulloch, J. Nelson, D. Roy and F. A. Castro, *Nanoscale*, 2017, **9**, 2723–2731.

9 A. Hammiche, H. M. Pollock, M. Reading, M. Claybourn, P. H. Turner and K. Jewkes, *Appl. Spectrosc.*, 1999, **53**, 810–815.

10 F. Huth, A. Govyadinov, S. Amarie, W. Nuansing, F. Keilmann and R. Hillenbrand, *Nano Lett.*, 2012, **12**, 3973–3978.

11 F. Lu, M. Jin and M. A. Belkin, *Nat. Photonics*, 2014, **8**, 307–312.

12 I. Burgués-Ceballos, PhD thesis, Universitat Autònoma de Barcelona, 2014.

13 L. Hou, E. Wang, J. Bergqvist, B. V. Andersson, Z. Wang, C. Müller, M. Campoy-Quiles, M. R. Andersson, F. Zhang and O. Inganäs, *Adv. Funct. Mater.*, 2011, **21**, 3169–3175.

14 F. Nickel, C. Sprau, M. F. G. Klein, P. Kapetana, N. Christ, X. Liu, S. Klinkhammer, U. Lemmer and A. Colsmann, *Sol. Energy Mater. Sol. Cells*, 2012, **104**, 18–22.

15 J. Alstrup, M. Jørgensen, A. J. Medford and F. C. Krebs, *ACS Appl. Mater. Interfaces*, 2010, **2**, 2819–2827.

16 M. Campoy-Quiles, M. I. Alonso, D. D. C. Bradley and L. J. Richter, *Adv. Funct. Mater.*, 2014, **24**, 2116–2134.

17 M. D. Schaeberle, C. G. Karakatsanis, C. J. Lau and P. J. Treado, *Anal. Chem.*, 1995, **67**, 4316–4321.

18 F. Cerdeira, M. Garriga, M. I. Alonso, J. O. Ossó, F. Schreiber, H. Dosch and M. Cardona, *J. Raman Spectrosc.*, 2013, **44**, 597–607.

This journal is © The Royal Society of Chemistry 2017

124

J. Mater. Chem. C, 2017, **5**, 7270–7282 | 7281

19 P. Veerender, V. Saxena, A. K. Chauhan, S. P. Koiry, P. Jha, A. Gusain, S. Choudhury, D. K. Aswal and S. K. Gupta, *Sol. Energy Mater. Sol. Cells*, 2014, **120**, 526–535.

20 J. Razzell-Hollis, W. C. Tsoi and J.-S. Kim, *J. Mater. Chem. C*, 2013, **1**, 6235.

21 W. C. Tsoi, D. T. James, J. S. Kim, P. G. Nicholson, C. E. Murphy, D. D. C. Bradley, J. Nelson and J.-S. Kim, *J. Am. Chem. Soc.*, 2011, **133**, 9834–9843.

22 H. M. Liem, P. Etchegoin, K. S. Whitehead and D. D. C. Bradley, *Adv. Funct. Mater.*, 2003, **13**, 66–72.

23 E. J. J. Martin, N. Bérubé, F. Provencher, M. Côté, C. Silva, S. K. Doorn and J. K. Grey, *J. Mater. Chem. C*, 2015, **3**, 6058–6066.

24 W. C. Tsoi, W. Zhang, J. Razzell Hollis, M. Suh, M. Heeney, I. McCulloch and J.-S. Kim, *Appl. Phys. Lett.*, 2013, **102**, 173302.

25 U. Schmidt, S. Hild, W. Ibach and O. Hollricher, *Macromol. Symp.*, 2005, **230**, 133–143.

26 J.-S. Kim, P. K. H. Ho, C. E. Murphy and R. H. Friend, *Macromolecules*, 2004, **37**, 2861–2871.

27 K. F. McCarty, *Appl. Opt.*, 1987, **26**, 4482.

28 D. Blue, K. Helwig, M. Moskovits and R. Wolkow, *J. Chem. Phys.*, 1990, **92**, 4600–4608.

29 J. W. Ager, D. K. Veirs and G. M. Rosenblatt, *J. Chem. Phys.*, 1990, **92**, 2067–2076.

30 Y. Y. Wang, Z. H. Ni, Z. X. Shen, H. M. Wang and Y. H. Wu, *Appl. Phys. Lett.*, 2008, **92**, 43121.

31 D. Yoon, H. Moon, Y.-W. Son, J. S. Choi, B. H. Park, Y. H. Cha, Y. D. Kim and H. Cheong, *Phys. Rev. B: Condens. Matter Mater. Phys.*, 2009, **80**, 125422.

32 S.-L. Li, H. Miyazaki, H. Song, H. Kuramochi, S. Nakaharai and K. Tsukagoshi, *ACS Nano*, 2012, **6**, 7381–7388.

33 R. J. Nemanich, C. C. Tsai and G. A. N. Connell, *Phys. Rev. Lett.*, 1980, **44**, 273–276.

34 O. S. Heavens, *Optical Properties of Thin Solid Films*, Dover Publications, 1991.

35 L. A. A. Pettersson, L. S. Roman and O. Inganäs, *J. Appl. Phys.*, 1999, **86**, 487.

36 P. Peumans, A. Yakimov and S. R. Forrest, *J. Appl. Phys.*, 2003, **93**, 3693.

37 X. Zhang, H. Bronstein, A. J. Kronemeijer, J. Smith, Y. Kim, R. J. Kline, L. J. Richter, T. D. Anthopoulos, H. Sirringhaus, K. Song, M. Heeney, W. Zhang, I. McCulloch and D. M. DeLongchamp, *Nat. Commun.*, 2013, **4**, 2238.

38 W. Zhang, J. Smith, S. E. Watkins, R. Gysel, M. McGehee, A. Salleo, J. Kirkpatrick, S. Ashraf, T. Anthopoulos, M. Heeney and I. McCulloch, *J. Am. Chem. Soc.*, 2010, **132**, 11437–11439.

39 H. Bronstein, D. S. Leem, R. Hamilton, P. Woebkenberg, S. King, W. Zhang, R. S. Ashraf, M. Heeney, T. D. Anthopoulos,

J. De Mello and I. McCulloch, *Macromolecules*, 2011, **44**, 6649–6652.

40 I. McCulloch, R. S. Ashraf, L. Biniek, H. Bronstein, C. Combe, J. E. Donaghey, D. I. James, C. B. Nielsen, B. C. Schroeder and W. Zhang, *Acc. Chem. Res.*, 2012, **45**, 714–722.

41 J. T. Rogers, K. Schmidt, M. F. Toney, E. J. Kramer and G. C. Bazan, *Adv. Mater.*, 2011, **23**, 2284–2288.

42 P. A. Staniec, A. J. Parnell, A. D. F. Dunbar, H. Yi, A. J. Pearson, T. Wang, P. E. Hopkinson, C. Kinane, R. M. Dalgliesh, A. M. Donald, A. J. Ryan, A. Iraqi, R. A. L. Jones and D. G. Lidzey, *Adv. Energy Mater.*, 2011, **1**, 499–504.

43 R. B. Aïch, N. Blouin, A. Bouchard and M. Leclerc, *Chem. Mater.*, 2009, **21**, 751–757.

44 N. Blouin, A. Michaud, D. Gendron, S. Wakim, E. Blair, R. Neagu-Plesu, M. Belletête, G. Durocher, Y. Tao and M. Leclerc, *J. Am. Chem. Soc.*, 2008, **130**, 732–742.

45 T. Agostinelli, S. Lilliu, J. G. Labram, M. Campoy-Quiles, M. Hampton, E. Pires, J. Rawle, O. Bikondoa, D. D. C. Bradley, T. D. Anthopoulos, J. Nelson and J. E. Macdonald, *Adv. Funct. Mater.*, 2011, **21**, 1701–1708.

46 M. Campoy-Quiles, C. Müller, M. Garriga, E. Wang, O. Inganäs and M. I. Alonso, *Thin Solid Films*, 2014, **571**, 371–376.

47 A. J. Pearson, T. Wang, A. D. F. Dunbar, H. Yi, D. C. Watters, D. M. Coles, P. A. Staniec, A. Iraqi, R. A. L. Jones and D. G. Lidzey, *Adv. Funct. Mater.*, 2014, **24**, 659–667.

48 I. Meager, R. S. Ashraf, S. Mollinger, B. C. Schroeder, H. Bronstein, D. Beatrup, M. S. Vezie, T. Kirchartz, A. Salleo, J. Nelson and I. McCulloch, *J. Am. Chem. Soc.*, 2013, **135**, 11537–11540.

49 S. D. Dimitrov, A. A. Bakulin, C. B. Nielsen, B. C. Schroeder, J. Du, H. Bronstein, I. McCulloch, R. H. Friend and J. R. Durrant, *J. Am. Chem. Soc.*, 2012, **134**, 18189–18192.

50 Z. Chen, M. J. Lee, R. Shahid Ashraf, Y. Gu, S. Albert-Seifried, M. Meedom Nielsen, B. Schroeder, T. D. Anthopoulos, M. Heeney, I. McCulloch and H. Sirringhaus, *Adv. Mater.*, 2012, **24**, 647–652.

51 M. Wojdyr, *J. Appl. Crystallogr.*, 2010, **43**, 1126–1128.

52 C. M. Stafford, K. E. Roskov, T. H. Epps and M. J. Fasolka, *Rev. Sci. Instrum.*, 2006, **77**, 23908.

53 M. S. Vezie, S. Few, I. Meager, G. Pieridou, B. Dörling, R. S. Ashraf, A. R. Goñi, H. Bronstein, I. McCulloch, S. C. Hayes, M. Campoy-Quiles and J. Nelson, *Nat. Mater.*, 2016, **15**, 746–753.

54 S. D. Dimitrov, C. B. Nielsen, S. Shoaee, P. Shakya Tuladhar, J. Du, I. McCulloch and J. R. Durrant, *J. Phys. Chem. Lett.*, 2012, **3**, 140–144.

7282 | *J. Mater. Chem. C*, 2017, **5**, 7270–7282

125

This journal is © The Royal Society of Chemistry 2017

ELECTRONIC SUPPLEMENTARY INFORMATION

Quantifying Local Thickness and Composition in Thin Films of Organic Photovoltaic Blends by Raman Scattering

Xabier Rodríguez-Martínez,*[1] Michelle S. Vezie,[2] Xingyuan Shi,[2] Iain McCulloch,[3,4] Jenny Nelson,[2] Alejandro R. Goñi[1,5] and Mariano Campoy-Quiles*[1]

* Corresponding authors. E-mail: xrodriguez@icmab.es, mcampoy@icmab.es

[1] Institut de Ciència de Materials de Barcelona (ICMAB-CSIC), Bellaterra, 08193, Spain

[2] Centre for Plastic Electronics and Department of Physics, Imperial College London, Prince Consort Road, London SW7 2AZ, UK

[3] Centre for Plastic Electronics and Department of Chemistry, Imperial College London, Exhibition Road, London SW7 2AZ, UK

[4] SPERC, King Abdullah University of Science and Technology, Thuwal 23955-6900, Saudi Arabia

[5] Institució Catalana de Recerca I Estudis Avançats (ICREA), Barcelona, 08010, Spain

ON THE APPLICATION OF THE METHODOLOGY IN A DIFFERENT RAMAN (BACKSCATTERING) SETUP

The general applicability of the Raman methodology presented in this work was double-checked in a second setup (Alpha300RA by WITec) employing the same geometry (backscattering) although different optics (50X magnification, NA = 0.8, or 10X magnification, NA = 0.25, both objectives manufactured by Zeiss) and CCD with respect to the LabRam setup used originally (20X magnification, NA = 0.35 by Olympus). As illustrated in Fig. S-1, the Raman intensity oscillation with film thickness in C16-IDTBT at 488 nm excitation was properly reproduced on the second setup regardless the objective employed.

Interestingly, the *effective* Raman cross-section (cts s^{-1} μW^{-1}) for this material was found to be nearly one order of magnitude lower in the second setup (WITec) as compared to the first one (LabRam) if the 10X magnification objective was used (see Table S-1); on the other hand, by selecting the 50X objective at the WITec setup the effective value obtained is comparable to that extracted at the original setup (LabRam) with lower magnification (20X). These trends demonstrate that the effective values of the Raman cross-sections may deviate significantly between different setups as a consequence of the different geometrical factors, including the numerical aperture, confocality and objective magnification as well as the CCD collection yield. Nevertheless, we double-checked that the Raman cross-section ratios between dissimilar materials were within the experimental error margin in both setups (see Table S-1), thus confirming the generality of the methodology.

We have also confirmed that the effective Raman cross-sections extracted for a given setup are independent of the type of substrate employed. As an example, C16-IDTBT showed a cross-section of $(3.1 \pm 0.6) \cdot 10^{-2}$ cts s^{-1} μW^{-1} when deposited on silicon, which is a value comparable to that obtained when the film was deposited on glass substrates $(3.0 \pm 0.3) \cdot 10^{-2}$ cts s^{-1} μW^{-1}) given the error committed on thickness and laser power determination. These results indicate that the distribution of the electric field in the multi-layered stack is properly modelled by the transfer matrix method.

Table S-1 List of effective solid-state Raman cross-sections for C16-IDTBT, PCBM and PC$_{70}$BM at 488 nm excitation as extracted in two different setups with different geometrical factors and CCDs.

Raman setup	Material	Effective Raman cross-section (σ_R)	$\sigma_{R,u} / \sigma_{R,PC70BM}$
LabRam 20X, NA 0.35	C16-IDTBT	$(3.3 \pm 0.3) \cdot 10^{-2}$ cts s^{-1} μW^{-1}	8 ± 1
	PCBM	$(1.3 \pm 0.2) \cdot 10^{-3}$ cts s^{-1} μW^{-1}	0.3 ± 0.1
	PC$_{70}$BM	$(4.4 \pm 0.5) \cdot 10^{-3}$ cts s^{-1} μW^{-1}	1
WITec 50X, NA 0.80	C16-IDTBT	$(3.5 \pm 0.4) \cdot 10^{-2}$ cts s^{-1} μW^{-1}	8 ± 1
	PCBM	$(1.7 \pm 0.1) \cdot 10^{-3}$ cts s^{-1} μW^{-1}	0.41 ± 0.04
	PC$_{70}$BM	$(4.1 \pm 0.3) \cdot 10^{-3}$ cts s^{-1} μW^{-1}	1
WITec 10X, NA 0.25	C16-IDTBT	$(2.7 \pm 0.4) \cdot 10^{-3}$ cts s^{-1} μW^{-1}	-
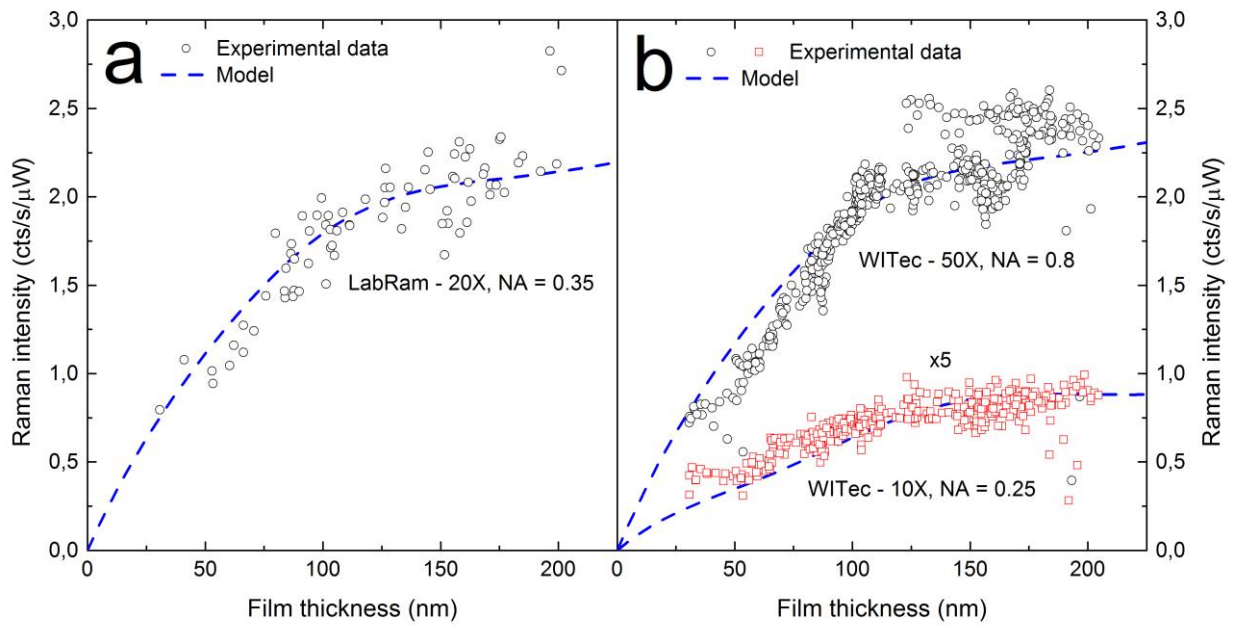
Figure S-1 Dependence of the 1353 cm^{-1} Raman band as a function of C16-IDTBT film thickness at 488 nm excitation as measured in two different setups: (a) LabRam HR800 (20X magnification, NA = 0.35) and (b) Alpha300RA by WITec (50X magnification, NA = 0.8, upper curve; and 10X magnification, NA = 0.25, lower curve with a five-fold magnification for better clarity).
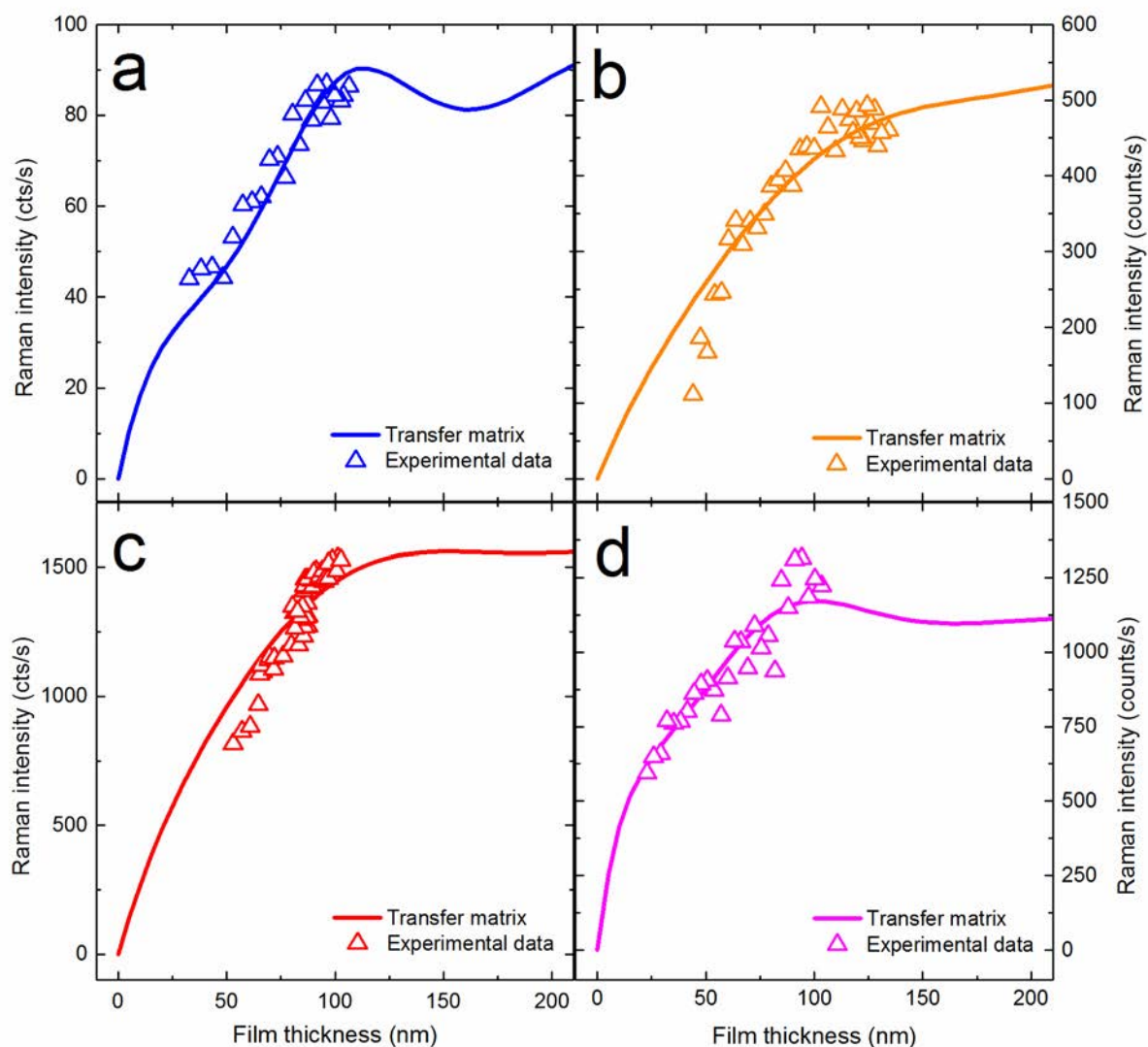
Figure S-2 Raman intensity (triangles) as a function of film thickness for (a) $PC_{70}BM$ at 488 nm excitation (1564 cm^{-1} band); (b) PCPDTBT at 488 nm excitation (1349 cm^{-1} band); (c) C16-IDTBT at 514 nm excitation (1353 cm^{-1} band); and (d) PCDTBT at 514 nm excitation (1445 cm^{-1} band). Solid lines stand for the transfer matrix modeling of the Raman process.

MULTI-WAVELENGTH FITTING APPROACH WITH SHARED PARAMETERS AS A WAY TO EXTEND THE SENSITIVITY OF THE METHODOLOGY REGARDING FILM THICKNESS DETERMINATION

The shape of the Raman interference curves is mainly determined by the optical constants at the excitation wavelength and at that shifted by the wavenumber of the mode under study. Resonant probing conditions usually lead to interference curves in which the first intensity maximum is reached for films below ca. 100 nm, given the high extinction coefficient for the material. This value is a constraint as far as the univocal determination of film thickness is concerned, without aid of secondary spectroscopic techniques. However, by changing the excitation wavelength to probe the films at non-resonant conditions, such maximum shifts to higher values (>200 nm depending on the excitation wavelength) and the Raman intensity curve starts oscillating throughout a broad thickness regime prior to saturation. Figures S-3(a)-(c) illustrate the changes in the interference curves obtained for the 1450 cm^{-1} mode in rr-P3HT under three different excitation wavelengths: (a) 488 nm, (b) 514 nm and (c) 633 nm. Whereas at 488 and 514 nm excitation resonant conditions are fulfilled, at 633 nm excitation the polymer is almost out-of-resonance as indicated by the low extinction coefficient. Consequently, if a certain rr-P3HT sample is measured using several excitation wavelengths exactly at the same locations we can perform a simultaneous fit of the Raman intensity at all wavelengths to overcome the oscillation of the intensity curves and to recover the uniqueness of the methodology. This approach is valid provided the intensity curves at all excitation wavelengths stay below their corresponding saturation regime, which location mainly depends on the magnitude of the extinction coefficient.

A similar approach can be applied in polymer:fullerene blends although the fullerene Raman cross-section is usually not high enough to identify its vibrational signature when it is excited out of resonance. Nevertheless, the signal due to the polymer will be damped by the presence of the fullerene in the scattering volume. This fact can be modelled as a lower *effective* thickness when measuring out of resonance and correlated with the volumetric fullerene fraction observed in resonance during the simultaneous fit.

In other cases the materials blended are incompatible in terms of the applicability of the methodology and alternative spectroscopic techniques must be selected instead to perform their characterization. P3HT:PCBM blends constitute an example in which neither the single-wavelength methodology nor the multi-wavelength fitting approach are successful. This is ascribed to the fact that the component Raman cross-sections are too dissimilar at all the excitation wavelengths used in this work (Table I in the manuscript) and their characteristic, most intense bands appear very close together (Fig. 1 in the manuscript). Such a difference hides the fullerene Raman signature in the measured spectra (at 488, 514 and 633 nm excitation) even in a 1:9 blend (w:w, P3HT:PCBM), hence rendering the fit inaccurate regarding film thickness and volumetric composition determination.
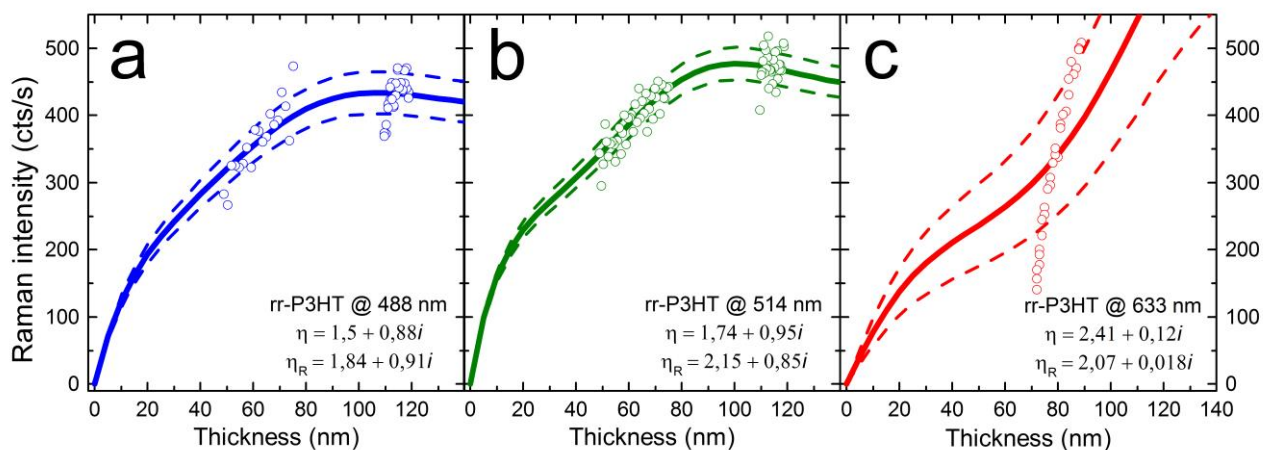
Figure S-3 Raman intensity of the 1450 cm^{-1} band in regio-regular P3HT as a function of film thickness for three excitation wavelengths: (a) 488 nm, (b) 514 nm and (c) 633 nm. The solid lines represent the best fit of the model to the experimental data with a single free parameter: the material's cross-section. The dashed lines stand for the standard deviation of the fit. The complex refractive indices attained at both the excitation wavelength (η) and the Raman-scattered light (η_R) are included at the bottom of each panel.

EVALUATION OF THE SENSITIVITY OF THE METHODOLOGY IN THIN-FILM ARCHITECTURES WITH HIGH REFRACTIVE INDEX CONTRAST

When there exists a high refractive index contrast between the Raman-active material deposited as thin film and the closest layers (usually the substrate), the electromagnetic field distribution promotes the Raman-scattered intensity to oscillate strongly at moderate film thickness values (50-300 nm). In this particular situation the accuracy in the determination of the optical constants for all layers in the multi-layered stack is critical to properly reproduce the experimental trends; in fact, Raman spectroscopy can be exploited to fine-tune the optical constants attained at a certain wavelength by fitting the Raman intensity oscillation as a function of film thickness.

As a significant example, we have explored the dependence of the 1353 cm^{-1} Raman band of C16-IDTBT deposited by blade coating as a graded film on a silicon substrate (with a native SiO$_2$ layer of ca. 5 nm). Figure S-4(a) illustrates the experimental trend obtained up to nearly 400 nm in thickness as well as the model prediction at 488 nm excitation. Clearly, the methodology cannot reproduce well the amplitude of the experimental intensity maxima although their position in terms of film thickness is the correct one. We have simultaneously studied the intensity of the silicon LO mode (520.7 cm^{-1}) as a function of polymer thickness and confirmed that the second Raman intensity maximum observed experimentally could not be successfully matched [Fig. S-4(b)].

We then proceeded to perform a fit of the experimental data using as free parameters the optical constants at 488 nm, at the silicon LO mode scattered wavelength (500.7 nm) and at the wavelength of the polymer 1353 cm^{-1} band (522 nm); see Figs. S-4(c)-S-4(d). In this case, the optical constants at 488 nm are shared in the modeling of silicon LO mode intensity and polymer band intensity. The fit results in an improved matching of the Raman intensity maxima and their location in terms of film thickness with respect to the experimental data. The optical constants obtained are experimentally acceptable given the uncertainty observed in C16-IDTBT films depending on the casting method used; see Fig. S-5. These results suggest that the accuracy of the material refractive index and extinction coefficient is critical when modeling the Raman intensity dependence in architectures with high refractive index contrast.
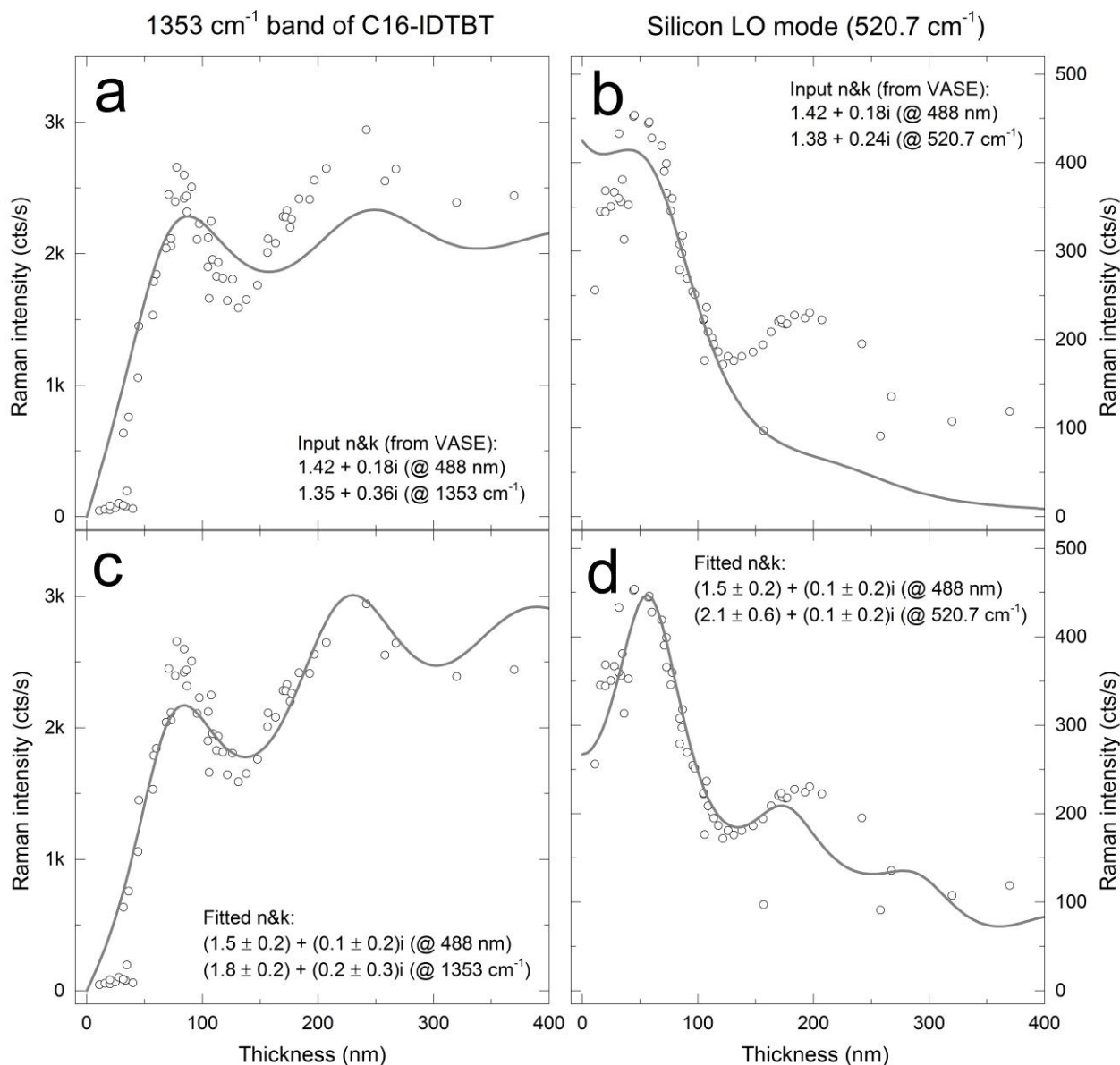
Figure S-4 Application of the methodology in a graded C16-IDTBT sample casted on a Si substrate (with a native oxide SiO_2 of ca. 5 nm, n = 1.46, k = 0). Solid lines represent the best fit to the experimental data (open circles). (a) Fit of the 1353 cm^{-1} mode intensity of C16-IDTBT using the optical constants extracted from VASE in a blade-coated, uniform sample; (b) fit of the Raman intensity of silicon LO mode (520.7 cm^{-1}) as a function of the polymer film thickness; (c) fit of the experimental data corresponding to the 1353 cm^{-1} polymer Raman mode using the optical constants as free parameters; (d) fit of the experimental data of the 520.7 cm^{-1} silicon LO mode using the optical constants as free parameters. Note that the complex refractive index at 488 nm is a shared parameter during the fit of (c) and (d) curves.
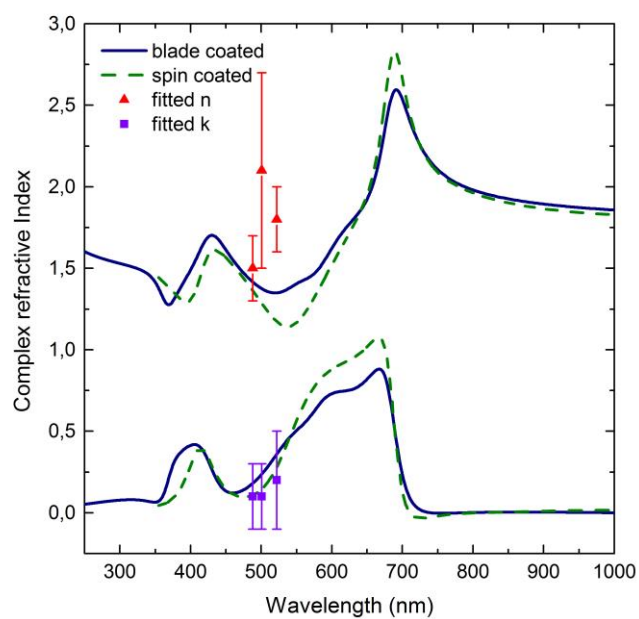
Figure S-5 Complex refractive index as obtained from VASE in C16-IDTBT samples prepared by two different methods on glass substrates: blade coating (blue solid line) and spin coating (green dashed line). The optical constants extracted from the fits in Figs. S-4(c)-S-4(d) are also included together with their corresponding error bars (standard deviations).

EFFECT OF PHOTODEGRADATION IN THE RAMAN SPECTRA OF SEVERAL CASE EXAMPLES

Conjugated materials are generally photodegraded upon exposure to a focused laser beam in an oxygen-rich atmosphere. The consequences of such degradation in terms of the vibrational Raman spectrum are mainly three: a large shift of the bands, an intensity variation and an increase of the photoluminescence background. A vast majority of the conjugated materials studied in this work follow a similar trend depending on the laser power arriving at the sample and the exposure time to the laser beam. Thus, the absence of photodegradation during the acquisition of the spectra is mandatory for the proper implementation, accuracy and reproducibility of the methodology. The rapid photobleaching in air of PCPDTBT:PC$_{70}$BM films is demonstrated in Figs. S-6 and S-7, in which the evolution of the acquired spectra is illustrated as a function of the laser exposure time. In this particular type of blend, photodegradation increases both the overall Raman intensity due to the polymer as well as the background line, eventually hiding the Raman signature of PC$_{70}$BM after 30 seconds of exposure. Thus the application of the methodology in these spectra results in an overestimation of the polymer content as the film is progressively degraded (see Fig. S-8), as well as a loss in accuracy in film thickness determination.

Photodegradation can be suppressed if the Raman experiments are performed either in vacuum (with a mechanical, rotatory pump) or in oxygen-free (inert) atmospheres. Even the blow of a nitrogen gun applied on the sample may be enough in some cases to slow down the photodegradation process (see Fig. S-8); this may be a valid option in the case of lack of suitable vacuum equipment or chambers, although it leads to poorer reproducibility than in vacuum. Apart from using inert atmospheres we have checked that if the Raman spectra are acquired in a time-scale below that in which significant photodegradation occurs, robust data can be obtained in ambient conditions. This is the case of our second setup (Alpha300RA by WITec), in which the integration time of the CCD camera can be reduced up to a few hundreds of milliseconds (30-500 ms). By exploiting this feature we can reduce the exposure time of the sample to the laser beam to harmless values in terms of photodegradation. This strategy may require an initial exploration step as the threshold exposure (and integration) time beyond which photodegradation arises. This time will depend on the power irradiance at the sample and the sensitivity of the material(s) analysed to the wavelength employed. In our setup (488 nm excitation with power values below 200 μW in free-beam conditions) we found that exposure times below 600 ms were enough to avoid the typical photodegradation signatures (peak shifting, intensity variations and increase of photoluminescence background) to disrupt the collected spectra, thus enabling the proper implementation of the methodology in air. This fact is illustrated in Fig. S-1(b) by the proper matching of the Raman intensity vs. film thickness dependence in a graded C16-IDTBT film. The data were acquired measuring on-the-fly at a constant lateral speed along the gradient direction. The integration times (and lateral speeds) were 536 ms (210 μm/s) and 336 ms (268 μm/s) for the 10X and 50X magnification objectives, respectively.

Nevertheless, there are conjugated materials in which photodegradation is not so critical, as it takes longer to manifest and to irreversibly disrupt the vibrational spectra. Neat fullerenes, as well as neat PCDTBT films and PCDTBT:PC$_{70}$BM blends constitute examples of increased robustness in terms of photobleaching. Figure S-9 shows how such polymer:fullerene blends lead to a small difference in composition (below 5 vol%) when comparing the results obtained in air or in vacuum while using moderate integration times (5-10 seconds).   However, such small mismatch in composition confirms that the exposure to the laser beam is affecting the integrity of the species in the film, although to a minor extent. Hence vacuum conditions are advised to achieve the maximum accuracy and reproducibility despite the apparent insensitivity of the materials to the laser exposure.
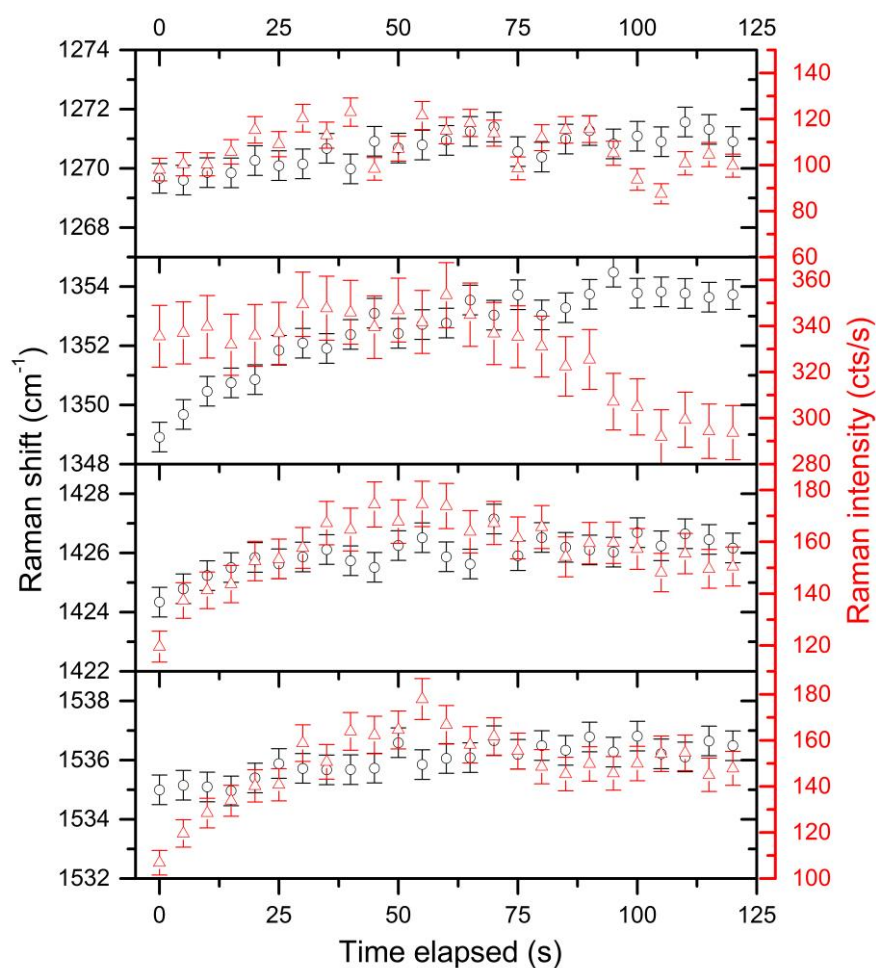
Figure S-6 Temporal evolution of the main Raman peak positions (black circles, left Y-axis) and intensities (red triangles, right Y-axis) in a pure PCPDTBT sample during exposure for two minutes to the laser beam (488 nm) in ambient conditions. Each data point corresponds to a single Raman spectrum acquired during 5 seconds of integration at the CCD. The zeroth step corresponds to the measurement performed in vacuum, which remains stable for hours.
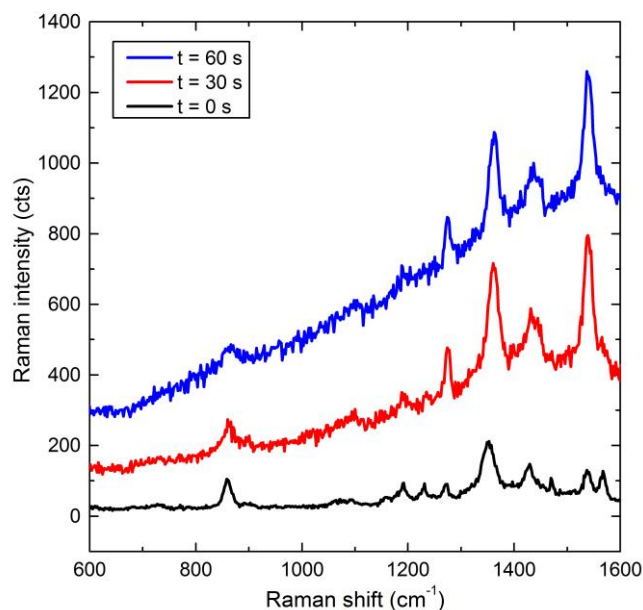
136

Figure S-7 Raman spectra due to a PCPDTBT:PC$_{70}$BM 1:1 (w:w) blend measured in air at 0 seconds (black), 30 seconds (red) and 60 seconds (blue) after laser exposure (488 nm). Note the increase on the photoluminescence background as the sample is exposed to the laser beam as well as the enhancement of the characteristic Raman modes due to the polymer, which eventually hide fullerene vibrational signature in the spectrum.
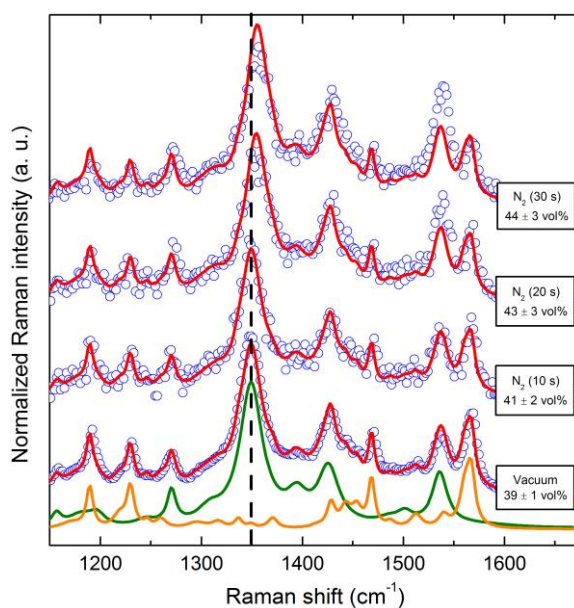
Figure S-8 Effect of photodegradation on the Raman spectrum of a 1:1 (w:w) PCPDTBT:PC$_{70}$BM blend as a function of the laser (488 nm) exposure time. Note how photodegradation is slowed down due to the blow of a nitrogen gun. The percentages refer to the polymer volume content as extracted from the fits. An extra degree of freedom is added to follow the position of the 1348 cm^{-1} band as the film is degraded. The red solid lines stand for the fit of the experimental data following the methodology described in the article, whereas the green and orange lines represent the Raman spectra due to PCPDTBT and PC$_{70}$BM, respectively.
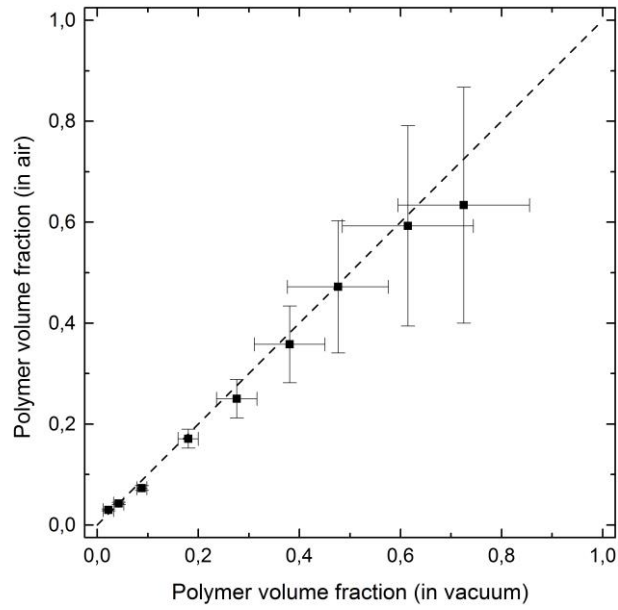
Figure S-9 The correlation between polymer volume fractions extracted in air and in vacuum with the use of Raman scattering at 488 nm excitation shows that PCDTBT:PC$_{70}$BM blends are quite robust in terms of degradation.

PAPER II

Combinatorial optimization of evaporated bilayer small molecule organic solar cells through orthogonal thickness gradients

X. Rodríguez-Martínez, A. Sánchez-Díaz, G. Liu, M. A. Niño, J. Cabanillas-Gonzalez, M. Campoy-Quiles, *Org. Electron.* **2018**, *59*, 288.

- Combinatorial optimization approach applied to heterojunction organic solar cells.
- The active layers are disposed as orthogonal wedges.
- Thicknesses are optimized combining Raman spectroscopy and photocurrent mapping.
- 20-fold reduction in the use of resources and time employing a single device.
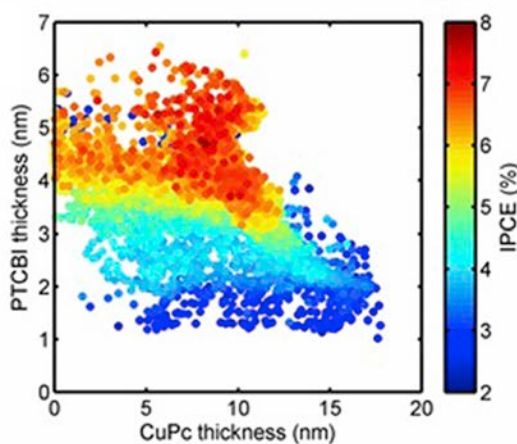
Letter

Combinatorial optimization of evaporated bilayer small molecule organic solar cells through orthogonal thickness gradients

Xabier Rodríguez-Martínez[a], Antonio Sánchez-Díaz[a], Guilin Liu[b,c,**], M.A. Niño[b], Juan Cabanillas-Gonzalez[b], Mariano Campoy-Quiles[a,*]

[a] *Institute of Materials Science of Barcelona (ICMAB-CSIC), UAB Campus, Bellaterra, 08193, Spain*
[b] *Instituto Madrileño de Estudios Avanzados en Nanociencia (IMDEA-Nanociencia), Cantoblanco, Madrid, 28049, Spain*
[c] *School of Science, Jiangnan University, Wuxi, Jiangsu 214122, China*

A B S T R A C T

We report on a combinatorial optimization procedure applied to heterojunction small molecule organic solar cells made of evaporated copper phthalocyanine (CuPc) and 3,4,9,10-perylenetetracarboxylic bisbenzimidazole (PTCBI). Our strategy consists of depositing both light harvesting compounds as orthogonally arranged wedge-shaped layers to then determine the optimum thicknesses which yield the highest photoconversion efficiency. The device performance is locally assessed by means of light-beam induced current images. A quantitative model of co-locally measured Raman images allows determining the corresponding local thicknesses of the active layers. The spatial correlation of both datasets (i.e. local photocurrent density and active layer film thicknesses) enables the rapid optimization of the photovoltaic system studied employing a single functional device, reducing in approximately 20 times the use of resources and time.

1. Introduction

Small molecule organic photovoltaics (OPV) are currently investigated as potential candidates for low-cost energy harvesting applications in large-area, flexible substrates. Copper phthalocyanine (CuPc) and 3,4,9,10-perylenetetracarboxylic bisbenzimidazole (PTCBI) constitute one of the most prominent p-type donor and n-type acceptor pair in the field, initially leading to a power conversion efficiency (PCE) of 0.95% [1]. This combination has since become a reference system for evaporated OPV. Most device architectures found in the literature including normal and inverted devices, consist of a multi-layered stack of thermally evaporated films with an embedded bilayer heterojunction of both small molecule semiconductors. Since these layers are evaporated successively, their final thickness determines the PCE of the device depending on the exciton diffusion length and extinction coefficient of each material. Thus, the optimization of this type of bilayer devices represents a paradigmatic example of multi-parametric problem, whose solution has so far been handled by systematic tests involving the fabrication of tens of devices in which some of the parameters are varied individually or simultaneously until finding the maximum device performance [2–5]. Despite the aid of photophysical models to facilitate optimization, the process remains experimentally tedious and time-

consuming so as to optimize a single photovoltaic system, not even mentioning its extrapolation to new materials that can potentially result in higher PCE. In addition, new materials are usually synthesized in small quantities constituting an extra bottleneck in the optimization process which demands an efficient use of the available resources.

In this work we follow a combinatorial approach to solve such problem with a single device and find the same optimum thicknesses as those reported elsewhere while employing significantly less time and resources. In order to achieve this, we prepare a bilayer donor-acceptor OPV in which both donor and acceptor layers are evaporated as wedges with thickness gradients varying continuously from 0 to 20 nm and arranging their thickness gradient axis orthogonally [6,7]. We then quantify the thickness of each layer at each point by means of Raman scattering directly in the functional device [8]. Finally, we measure the photocurrent as a function of position with a home-made light beam induced current (LBIC) setup, which enables the spatial correlation of CuPc and PTCBI layer thicknesses with photocurrent (proportional to the PCE) after proper matching of both datasets.

The use of wedge-shaped layers in the optimization of optoelectronic devices has already been applied to lasers [9], OLEDs [10] and solution processed photovoltaics [11]. These examples have demonstrated that the use of gradients is a very promising tool for

---

optimization and functionality. We extend the previous work beyond the one-dimensional screening of the active layer thickness to two-dimensional fabrication coupled to imaging of the local geometry and performance. The sweet spot in performance in bilayer structures is mainly determined by the donor and acceptor film thicknesses which corresponds to a trade-off between light absorption, exciton diffusion and charge generation in the functional devices. The here presented two-dimensional evaluation of evaporated bilayer small molecule organic solar cells constitutes an important advance in terms of evaluation time and material requirements.

2. Results and discussion

The studied device architecture consists of a transparent glass substrate with a 30 nm-thick, sputtered indium tin oxide (ITO) layer and a 20 nm layer of poly(3,4-ethylenedioxythiophene):polystyrene sulfonic acid (PEDOT:PSS) spin-coated on top. In order to have a well-controlled layer growth and high quality clean interfaces, organic layers were evaporated in an ultra-high vacuum (UHV) system with a base pressure of 3×10^{-9} mbar by organic molecular beam epitaxy (O-MBE). The organic layers were evaporated from Knudssen cells, calibrating the growth rate with a quartz microbalance. A combined motorized sample holder-shutter system was used to grow a double wedge structure, controlling the speed of the shutter and the growth rate in order to produce a defined thickness gradient [7,12]. A 9-mm-long wedge of CuPc was grown with a rate of 0.03 Å/s and after a 90° rotation of the sample a second wedge of PTCBI was grown with the same rate (orthogonally to the first wedge). A uniform, 5-nm-thick layer of bathocuproine (BCP) was grown on top of the double wedge serving as hole blocking layer [13]. Finally, the fabrication was completed by depositing an 80-nm-thick silver cathode by means of an e-beam evaporator using a rate of 0.05 Å/s.

Recently, Raman spectroscopy has been demonstrated to be a valuable structural probe to complement photocurrent images in OPV devices [14]. In this work, Raman measurements were performed in ambient conditions using a WITec alpha300 RA + setup with a 488 nm solid-state laser and a 633 nm He-Ne laser as excitation sources. The diffraction gratings had a density of 1200 and 600 grooves/mm, respectively. In all cases the objective employed had a $10\times$ magnification and a 0.25 numerical aperture. The Raman images shown in this work contain ca. 20,000 spectra, which were acquired in lateral steps of 50 μm employing an integration time of 136 ms per spectrum. LBIC images consisted of more than 6000 data points and were acquired in a home-made setup using lateral steps of 100 μm. The LBIC experiments were performed non-modulated and with no bias. We have estimated the beam size after focusing with a $20\times$ long working distance Mitutoyo objective to be ca. 20 μm (FWHM). The typical monochromatic power used was 44 μW for excitation with a 532 nm laser and 3,8 μW for the 630 nm monochromated light from a xenon lamp. Even though the 630 nm illumination was relatively low in our setup and thus normalization by incident power would lead to large errors in current density, we have still measured it as it corresponds to the maximum of the EQE in flat devices.

To assess the quality of the thickness gradients and for calibration purposes, single donor (acceptor) wedges were deposited on glass/ITO substrates using the same UHV techniques. The results of variable angle spectroscopic ellipsometry (VASE) and mechanical profilometry show a thickness profile which varies linearly as the light spot is displaced along the wedge (Fig. 1a). The inset in Fig. 1a confirms thicknesses ranging from ca. 20–200 nm in a 9 mm scanned length. Values obtained from single wedges were employed to extract the solid-state Raman cross-sections required to perform the quantification of film thickness in the functional device (Fig. 1c and d) [8]. The insets of Fig. 1c and d shows the Raman spectra of CuPc and PTCBI upon 488 nm excitation. For these materials, the most intense Raman bands do not overlap significantly, which facilitates their identification and ulterior thickness

quantification. The optical constants of CuPc and PTCBI extracted from VASE are plotted in Fig. 1b and also used for the Raman cross section analysis (see below).

The characterization of the layers thicknesses by Raman spectroscopy is performed according to a previously reported quantitative model of the Raman intensity which was here adapted to the bilayer device geometry [8]. The methodology exploits the transfer-matrix formalism to describe the incoming and scattered electric fields in an optical system formed by an arbitrary number of layers. This allows modelling the scattered Raman intensity as a function of the Raman-active layer thickness as well as the volumetric composition in the case of multi-component blends. Here, we have reformulated the mathematical approach of the methodology initially presented in Ref. [8] to include two film thickness values, d_1 and d_2, as free parameters for the fit of the experimental Raman spectra instead of the single thickness value, d, and a volumetric fraction, v, as occurs for an homogeneous blend. The model takes into consideration the fact that the scattered intensity of each Raman-active layer depends simultaneously on its own thickness and on the thickness of the other Raman-active layer to properly account for the filtering effect that each layer has on the incoming and scattered fields. Thus, the model function of the scattered intensity (I) reads

$$I(d_1, d_2) = \sigma_1 f_1(d_1, d_2) I_{ref,1} + \sigma_2 f_2(d_1, d_2) I_{ref,2} \tag{1}$$

where $\sigma_{1,2}$ are the effective Raman cross-sections of materials 1 and 2 in solid-state, $f_{1,2}$ describe the Raman intensity vs. film thickness dependence obtained by means of the transfer-matrix formalism for the layers containing materials 1 and 2, and $I_{ref,1,2}$ are the reference Raman spectra of materials 1 and 2 at the excitation wavelength and normalized to the Raman band to which $\sigma_{1,2}$ are referred. The n and k values of each layer are used as input parameters in the modelling (Fig. 1b). Further details on the mathematical formulation of the model and the Raman cross-sections can be found in Ref. [8]. For the present case and experimental conditions (488 nm excitation), the Raman cross-section ratio between PTCBI and CuPc was found to be PTCBI/CuPc = 18 ± 2 for their most intense vibrational bands at 1290 and 1528 cm^{-1}, respectively. The moderate value of the ratio is beneficial for the Raman characterization as it allows a good sensitivity during the fit [8].

We then used the model and calibrated cross sections to analyze the Raman signal obtained through the glass substrate of a complete device. The fits of the Raman spectra according to Eq. (1) are generally very good, as shown in Fig. 2 for three representative examples. These fits lead to film thickness maps in which both CuPc and PTCBI wedges can be visualized and quantified as illustrated in Fig. 2. According to this analysis, both wedges are not strictly orthogonal (Fig. 2a and b) but lead to a rather homogeneous total thickness of 15–20 nm (Fig. 2c). The reason for the imperfect orthogonality of the wedges is the divergence of the evaporation cone, which gives raise to thickness inhomogeneity along the axis perpendicular to the gradient. This fact can be minimized by collimating the evaporation cone (using deep crucibles with lower aperture) and reducing the distances between the evaporation source and the substrate but it is difficult to avoid completely in our current O-MBE setup.

LBIC-based photocurrent images are illustrated in Fig. 3 at two different excitation wavelengths, namely 532 nm and 630 nm. According to the absorption spectra of CuPc and PTCBI illustrated in Fig. 1b, PTCBI is the major absorber of the bilayer at 532 nm excitation, thus the variation of the photocurrent measured at such wavelength would correspond to the increased absorption of light due to the larger PTCBI thickness. This is confirmed by the general agreement between Figs. 2b and 3b, showing both images a monotonically decreasing trend in Raman intensity and 532 nm photogenerated current density, respectively, from left to right following the slope of the PTCBI wedge. Note that as the electrode of the device is continuous, the low photocurrent blue spots that appear on the left hand side in Fig. 3b do not correspond to dead pixels as such, but rather to large fluctuations in the
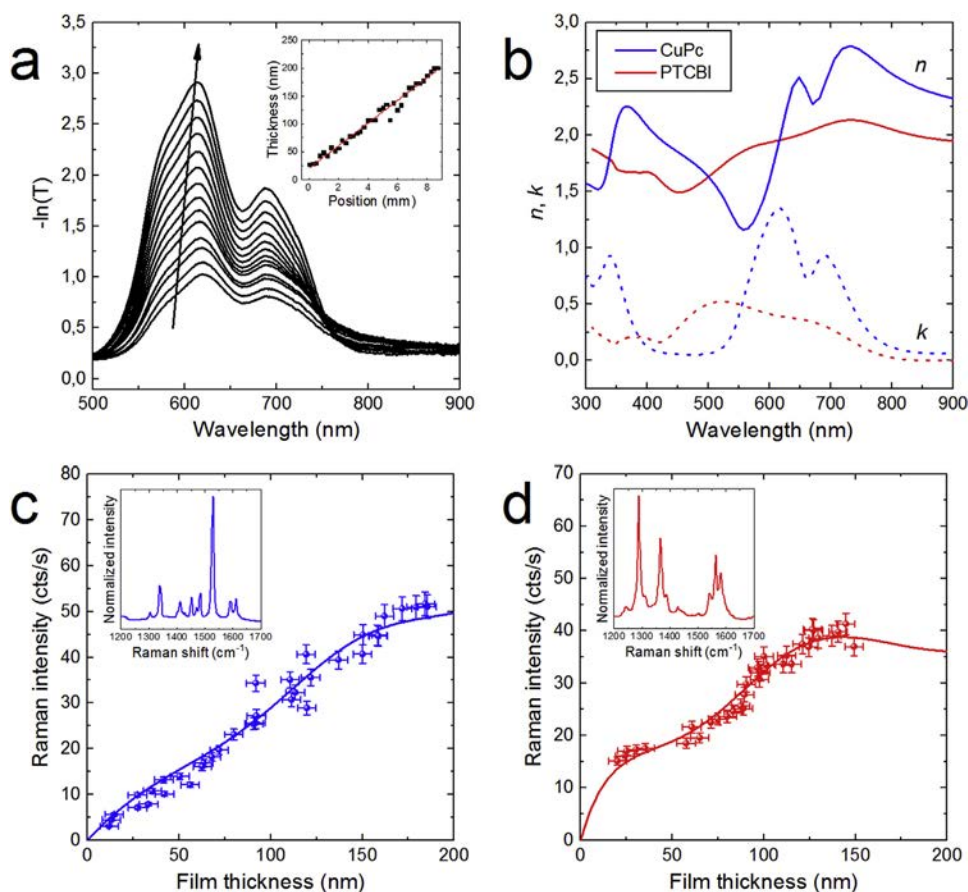
Fig. 1. (a) Single CuPc wedge layer absorbance as a function of position and (inset) thicknesses obtained by profilometry fitted to a linear equation as a guide to the eye. The arrow displayed in the absorbance spectra indicates their evolution as the thickness increases. (b) Refractive index (*n*, solid lines) and extinction coefficient (*k*, dashed lines) of CuPc (blue) and PTCBI (red) measured with VASE. (c) Intensity of the 1528 cm^{-1} mode of CuPc as a function of film thickness. The solid line stands for the fit of the model introduced in Ref. [8]. The inset shows the normalized Raman spectrum of CuPc at 488 nm excitation. (d) Intensity of the 1290 cm^{-1} mode of PTCBI as a function of film thickness and fit of the experimental data according to the transfer-matrix model in Ref. [8]. The inset shows the normalized Raman spectrum of PTCBI at 488 nm excitation. (For interpretation of the references to color in this figure legend, the reader is referred to the Web version of this article.)

photocurrent readings that have to do with the fast acquisition times for the Keithley source-meter and the home-made LabView interface developed to control the LBIC setup. We have repeatedly tested that such photocurrent spikes are not related to the sample or the excitation wavelength.

At 630 nm excitation both materials are absorbing and the
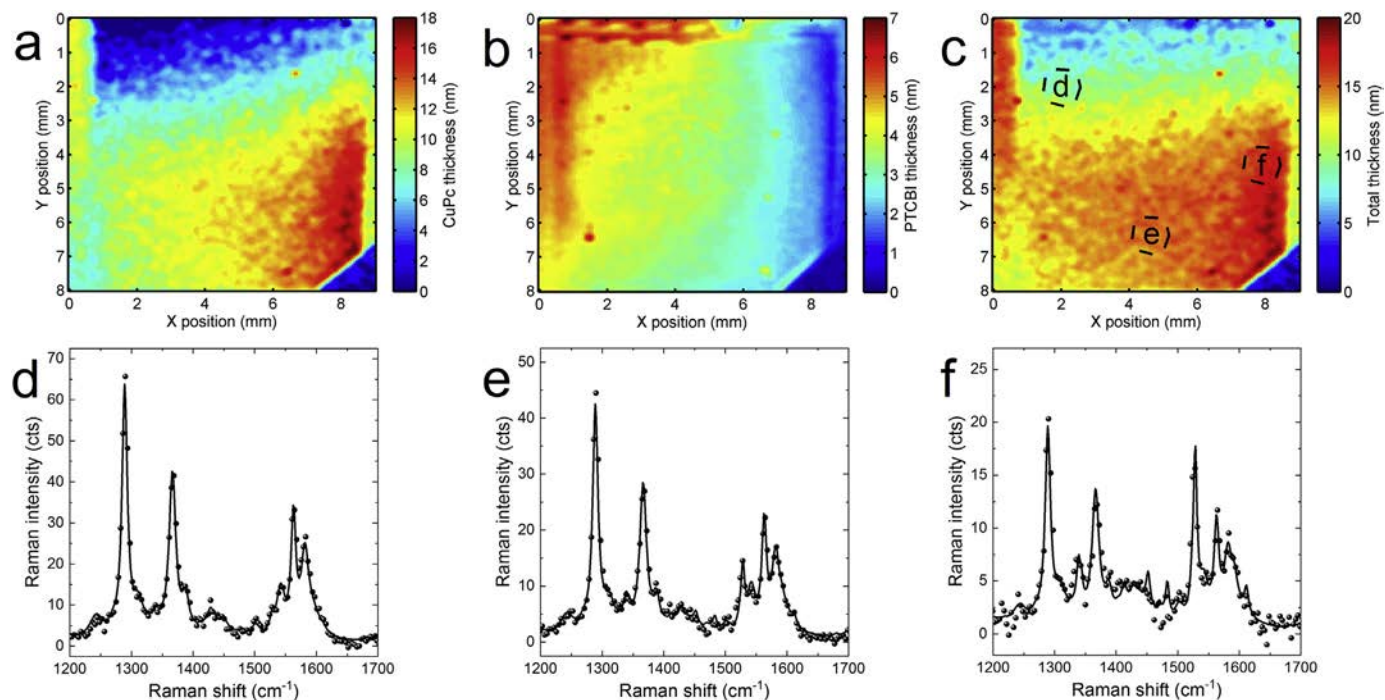
Fig. 2. Thickness spatial maps corresponding to (a) CuPc thickness, (b) PTCBI thickness and (c) total active layer thickness as extracted from Raman spectroscopy upon 488 nm excitation. (d), (e) and (f) show the experimental Raman spectra (circles) as well as the fits performed according to Eq. (1) (solid lines) at the sample locations indicated in (c).
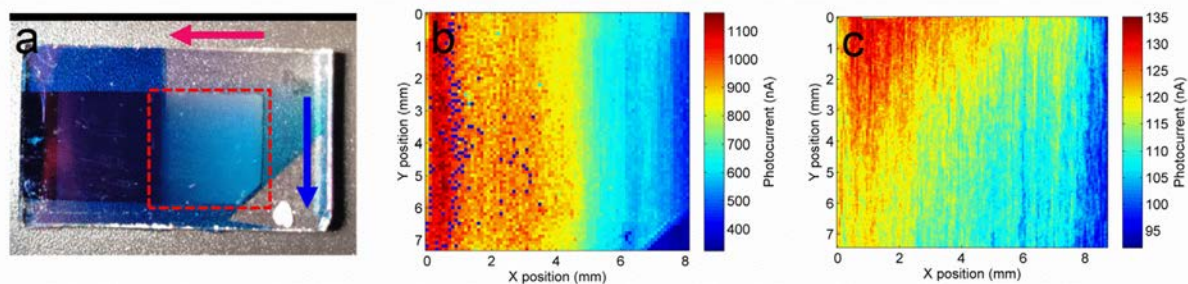
Fig. 3. (a) Photograph of the device active area. The pink and the blue arrows show the PTCBI and the CuPc gradient directions, respectively. (b) LBIC image at 532 nm excitation wavelength. (c) LBIC image at 630 nm excitation wavelength. LBIC images were taken on the area marked with a dashed line in (a). (For interpretation of the references to color in this figure legend, the reader is referred to the Web version of this article.)

photocurrent image shows a diagonal trend indicating the area where the balance between exciton diffusion and light absorption is optimized. Interestingly, the variation of CuPc thickness observed in Fig. 2a follows the same trend observed on the LBIC map at 630 nm (Fig. 3c) indicating that a small amount of CuPc is enough for good device performance. Note that while the overall photocurrent of the device cannot be extracted from a single wavelength measurement, the photocurrent contribution is expected to be the highest at 630 nm as is the case for incident photon-to-current efficiency (IPCE) measurements on flat bilayer devices.

The spatial correlation of the Raman-based thickness maps with the photocurrent images measured in the LBIC setup enables the fast combinatorial evaluation of the bilayer system. Nevertheless, since both datasets are acquired in different setups the comparison requires the proper matching of both maps by rotation and interpolation. First, using defects in the sample and sample edges, the images are slightly rotated to accommodate differences in positioning between setups. Then the pixel correlation is performed by interpolation of the map with the highest resolution. The regions showing the highest photocurrent generally correspond to those in which the light absorption, the exciton diffusion and the charge collection are optimized to yield a high IPCE in the system studied. In the here analyzed bilayer model system, the correlation between the active layer thicknesses and the photocurrent measured at 532 and 630 nm (Fig. 4a and b) indicates that a single photocurrent maximum occurs at ca. 10 nm of CuPc and ca. 5 nm of PTCBI. This thickness difference might be related to the lower extinction coefficient of PTCBI with respect to CuPc (Fig. 1b) or to difference in exciton diffusion lengths. The colored dispersion of photocurrent in Fig. 4a and b is in good agreement with previously reported works performed on devices with a similar architecture [2,4,13]. We do not observe oscillations in the photocurrent as a function of the active layer thickness as reported elsewhere and ascribed to optical interference effects [3] since we are in the very thin film thickness regime.

Typical optimization approaches in which the thickness of each

active layer is varied in discrete steps while keeping the other film thicknesses constant require fabricating a minimum of 10–20 individual samples to find the optimum solution to the multi-parametric problem [3,4,15]. In order to better visualize the advantages of our gradient-based combinatorial approach, we quantify the time saving (S) parameter according to the following expression:

$$S = \frac{N_{dev}(t_{fab} + t_{JV})}{t_{fab} + N_{pts}t_{LBIC}} \tag{2}$$

where N_{dev} is the number of discrete devices fabricated; t_{fab} is the average time required to fabricate each device which equals the time required to fabricate a single double-wedged device; t_{JV} is the time required to measure the J-V curve in a single flat device; N_{pts} is the number of photocurrent data points extracted at the LBIC setup; and t_{LBIC} is the measurement time required per LBIC data point. The optimization of the fabrication recipe can reduce t_{fab} up to ca. 3 h, whereas t_{JV} is typically not longer than 3 min per sample and t_{LBIC} equals ca. 1 s per data point. When $N_{dev} = N_{pts}$ and using the above-cited values for t_{fab}, t_{JV} and t_{LBIC}, Eq. (2) leads to $S \approx N_{dev}$, thus for a typical optimization routine using discrete samples in which the number of fabricated devices raises up to 20 units ($N_{dev} = N_{pts} = 20$), the combinatorial approach is ca. 20 times faster than the discrete approximation and also ca. 20 times more efficient in terms of use of resources and energy. Keeping $N_{dev} = 20$ but increasing N_{pts} up to 2000 results in $S \approx 17$ while having a hundred-fold increase in the number of data points available to solve the multi-parametric problem with respect to a discrete approach. Importantly, the savings in the amount of material required for the optimization is of the order of N_{dev}. Clearly, the combinatorial method presented here is significantly more efficient on the fabrication and measuring time employed for multi-parametric optimization problems.
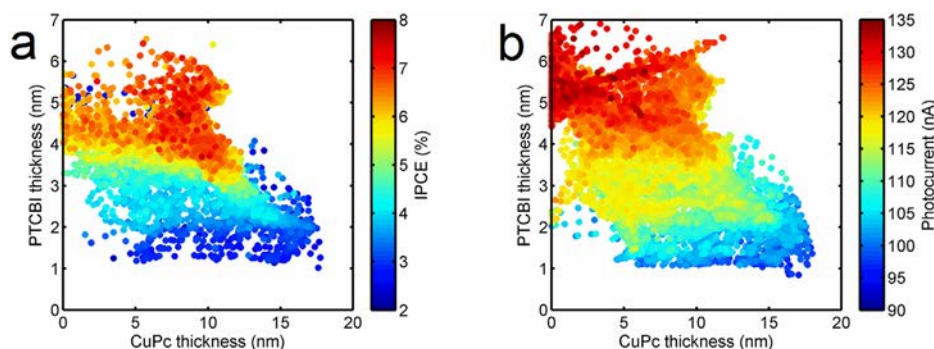

Fig. 4. (a) Incident photon-to-current conversion efficiency IPCE (%) at 532 nm excitation wavelength and (b) short circuit photocurrent at 630 nm excitation wavelength.

3. Conclusion

In summary, we have developed a combinatorial approach for the optimization of the performance of small molecule organic solar cells which implies a ca. 20-fold reduction in the consumption of resources and time with respect to a discrete optimization routine. The optimization is performed using a single functional device showing orthogonally oriented, wedged donor-acceptor layers to study the influence of their thickness on the final photoconversion efficiency. The successive local characterization with LBIC and quantitative Raman spectroscopy enables the correlation of the IPCE with the thickness of the active layers. In the case of CuPc and PTCBI heterojunction solar cells, the optimum device performance results from a trade-off between exciton diffusion and light absorption. For the device architecture studied in this work we found that the photocurrent achieved its maximum for CuPc and PTCBI layer thicknesses equal to ca. 10 nm and 5 nm, respectively. The here presented combinatorial screening methodology can be applied in any evaporated thin-film-based solar cell technology, potentially including tandem geometry and other complex multi-layered architectures such OLEDs.

References

[1] C.W. Tang, Two-layer organic photovoltaic cell, Appl. Phys. Lett. 48 (1986) 183–185, http://dx.doi.org/10.1063/1.96937.

[2] V.P. Singh, R.S. Singh, B. Parthasarathy, A. Aguilera, J. Anthony, M. Payne, Copper-phthalocyanine-based organic solar cells with high open-circuit voltage, Appl. Phys. Lett. 86 (2005) 82106, http://dx.doi.org/10.1063/1.1871347.

[3] T. Stübinger, W. Brütting, Exciton diffusion and optical interference in organic donor–acceptor photovoltaic cells, J. Appl. Phys. 90 (2001) 3632–3641, http://dx.doi.org/10.1063/1.1394920.

[4] X. Tong, R.F. Bailey-Salzman, G. Wei, S.R. Forrest, Inverted small molecule organic photovoltaic cells on reflective substrates, Appl. Phys. Lett. 93 (2008) 173304, http://dx.doi.org/10.1063/1.3005173.

[5] S.W. Hur, H.S. Oh, Y.C. Oh, D.H. Chung, J.U. Lee, J.W. Park, T.W. Kim, Organic photovoltaic effects using CuPc and C60 depending on layer thickness, Synth. Met. 154 (2005) 49–52, http://dx.doi.org/10.1016/j.synthmet.2005.07.020.

[6] J. Cabanillas-Gonzalez, M. Schmidt, O. Peña-Rodríguez, M.I. Alonso, A.R. Goñi, M. Campoy-Quiles, Effect of structure and interlayer diffusion in organic position sensitive photodetectors based on complementary wedge donor/acceptor layers, J. Nanosci. Nanotechnol. 13 (2013) 5148–5153, http://dx.doi.org/10.1166/jnn.2013.7503.

[7] M. Campoy-Quiles, V. Randon, M.M. Mróz, M. Jarzaguet, M. Garriga, J. Cabanillas-González, Continuous lateral gradients in film morphology for position sensitive detection and organic solar cell optimization, Org. Photonics Photovoltaics 1 (2013), http://dx.doi.org/10.2478/oph-2013-0002.

[8] X. Rodríguez-Martínez, M.S. Vezie, X. Shi, I. McCulloch, J. Nelson, A.R. Goñi, M. Campoy-Quiles, Quantifying local thickness and composition in thin films of organic photovoltaic blends by Raman scattering, J. Mater. Chem. C 5 (2017) 7270–7282, http://dx.doi.org/10.1039/C7TC01472D.

[9] S. Klinkhammer, X. Liu, K. Huska, Y. Shen, S. Vanderheiden, S. Valouch, C. Vannahme, S. Bräse, T. Mappes, U. Lemmer, Continuously tunable solution-processed organic semiconductor DFB lasers pumped by laser diode, Optic Express 20 (2012) 6357, http://dx.doi.org/10.1364/OE.20.006357.

[10] S. Höfle, T. Lutz, A. Egel, F. Nickel, S.W. Kettlitz, G. Gomard, U. Lemmer, A. Colsmann, Influence of the emission layer thickness on the optoelectronic properties of solution processed organic light-emitting diodes, ACS Photonics 1 (2014) 968–973, http://dx.doi.org/10.1021/ph500186m.

[11] F. Nickel, C. Sprau, M.F.G. Klein, P. Kapetana, N. Christ, X. Liu, S. Klinkhammer, U. Lemmer, A. Colsmann, Spatial mapping of photocurrents in organic solar cells comprising wedge-shaped absorber layers for an efficient material screening, Sol. Energy Mater. Sol. Cells 104 (2012) 18–22, http://dx.doi.org/10.1016/j.solmat.2012.04.026.

[12] J. Cabanillas–Gonzalez, O. Peña–Rodríguez, I. Suarez Lopez, M. Schmidt, M.I. Alonso, A.R. Goñi, M. Campoy–Quiles, Organic position sensitive photodetectors based on lateral donor-acceptor concentration gradients, Appl. Phys. Lett. 99 (2011) 103305, http://dx.doi.org/10.1063/1.3631731.

[13] P. Peumans, V. Bulović, S.R. Forrest, Efficient photon harvesting at high optical intensities in ultrathin organic double-heterostructure photovoltaic diodes, Appl. Phys. Lett. 76 (2000) 2650–2652, http://dx.doi.org/10.1063/1.126433.

[14] J. Gao, A.K. Thomas, J. Yang, C. Aldaz, G. Yang, Y. Qin, J.K. Grey, Polythienylene–vinylene structure–function correlations revealed from resonance Raman spectroscopy and photocurrent imaging, J. Phys. Chem. C 119 (2015) 8980–8990, http://dx.doi.org/10.1021/acs.jpcc.5b02166.

[15] D.W. Sievers, V. Shrotriya, Y. Yang, Modeling optical effects and thickness dependent current in polymer bulk-heterojunction solar cells, J. Appl. Phys. 100 (2006) 114509, http://dx.doi.org/10.1063/1.2388854.

PAPER III

High-Throughput Multiparametric Screening of Solution Processed Bulk Heterojunction Solar Cells

A. Sánchez-Díaz, X. Rodríguez-Martínez, L. Córcoles-Guija, G. Mora-Martín, M. Campoy-Quiles, *Adv. Electron. Mater.* **2018**, *4*, 1700477.
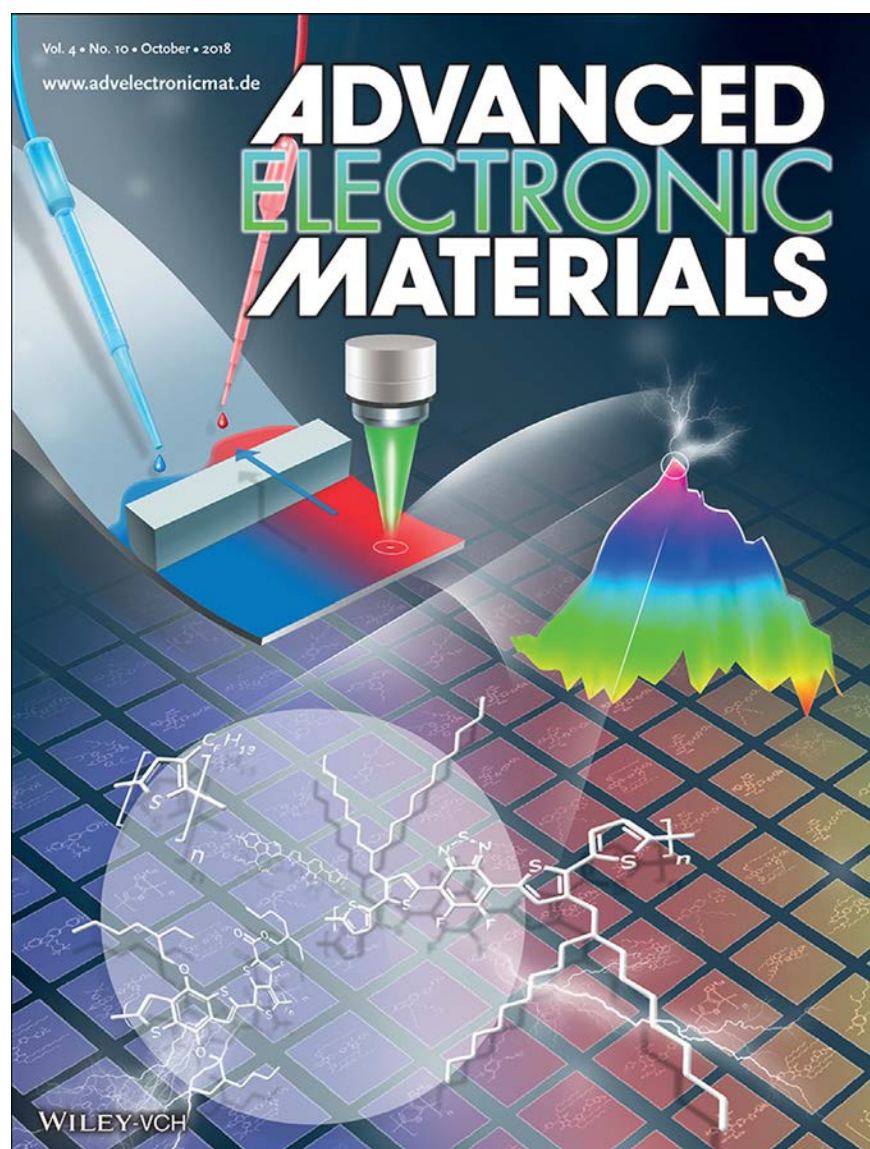
High-Throughput Multiparametric Screening of Solution Processed Bulk Heterojunction Solar Cells

Antonio Sánchez-Díaz, Xabier Rodríguez-Martínez, Laura Córcoles-Guija, Germán Mora-Martín, and Mariano Campoy-Quiles*

One of the major bottlenecks in the development of organic photovoltaics is the time needed to evaluate each material system. This time ranges from weeks to months if different variables such as blend composition, thickness, annealing, and additives are to be explored. In this study, the use of lateral gradients is proposed in order to evaluate the photovoltaic potential of a material system up to 50 times faster. A platform that combines blade coating using controllable velocity profiles (thickness gradients) with multichannel dispensers (composition gradients) and controlled lateral annealing variations (nanostructure gradients) is introduced. These samples are then analyzed using photocurrent and Raman imaging in order to correlate one to one the device performance, thickness, composition, and annealing temperature. The strength of the developed technology is shown by optimizing three different systems, namely PCDTBT:PC70BM, PTB7-Th:PC70BM, and PffBT4T-2OD:PC70BM, obtaining efficiencies ≈5%, 8%, and 9.5%, respectively, using less than 10 mg of each polymer in the process.

1. Introduction

Ever since the discovery of the conductivity of polymers[1] and their consequent application on solar light harvesting devices,[2] the scientific community has devoted a significant amount of effort to increase the performance of this technology. At early stages of the development of organic solar cells the governing principles affecting the photovoltaic performance were thoroughly investigated. Important milestones include the discovery of an effective charge transfer between donor and acceptor type compounds, the introduction of the bulk heterojunction (BHJ) concept to alleviate the compromise between charge generation and optical absorption,[3,4] and key strategies to control microstructure and optimize charge extraction.[5–7] The knowledge gained in those early steps paved the path towards the synthesis of novel materials that

resulted in improved devices presenting higher device efficiency and stability:[8] from power conversion efficiencies (PCE) in the range between 1% and 3% for workhorse materials such as poly(2-methoxy-5-(3′,7′-dimethyloctyloxy)-1,4-phenylenevinylene) (MDMO-PPV) or poly(3-hexylthiophene) (P3HT) combined with soluble fullerenes,[6,7] up to current PCE values exceeding 10% for several systems.[9–13] There is no specific fundamental limitation to organic materials that indicates that much higher values are not possible, and the number of potential candidates is nearly infinite. Indeed, the organic nature of the photoactive materials offers a myriad of possibilities to modify their chemical structure; for the case of conjugated polymers, there exists a vast assortment of combinations depending on the choice of moieties, the bridging atoms, the length and branching points of the alkyl side chains, and the molecular weight, to name but a few. Using search engines to inspect the literature, we estimate that in the last ten years ≈5000 organic conjugated materials have been tested in BHJ solar cells, albeit only a few tenths have been studied and optimized in depth. While applied quantum theory can help to select promising candidates,[14–16] the final performance often depends on a number of issues difficult to predict a priori, such as solubility, miscibility of compounds, tendency to crystallize, exact energy levels in the blend, etc. In practice, this means that for a given promising backbone, a family of systems need to be tested, including different side chains, molecular weights, donor:acceptor combinations, etc.[17] Within this large and uncharted spectrum of materials and processing variables, combinatorial screening methodologies are highly on demand to speed up their exploration while helping the technology to approach the theoretical Shockley–Queisser limit of >20% PCE.[18,19]

From the engineering point of view, three main aspects must be addressed for the evaluation of a material system for BHJ solar cells, namely the active layer thickness, the donor–acceptor (D:A) blending ratio and the nanoscale morphology (typically controlled by deposition conditions, thermal annealing, and use of additives). Ideally, those three variables can be optimized separately and to some extent it is usually an acceptable approximation; however, the full potential of a novel active layer material requires for fine tuning of the preparation conditions that take into consideration the subtle interplay between them.[20] For instance, the optimum thickness is often found close to the first interference maximum, which is governed by the refractive index of the active layer; this, on

Dr. A. Sánchez-Díaz, X. Rodríguez-Martínez, L. Córcoles-Guija,
G. Mora-Martín, Dr. M. Campoy-Quiles
Institut de Ciència de Materials de Barcelona (ICMAB-CSIC)
Campus UAB S/N, 08193 Bellaterra, Barcelona, Spain
E-mail: mcampoy@icmab.es

The ORCID identification number(s) for the author(s) of this article can be found under https://doi.org/10.1002/aelm.201700477.

**ADVANCED
SCIENCE NEWS**

www.advancedsciencenews.com

**ADVANCED
ELECTRONIC
MATERIALS**

www.advelectronicmat.de

the other hand, will be a function of the D:A ratio (fullerenes typically have higher refractive index than polymers) and the degree of crystallinity (higher crystallinity results in higher density of optical dipoles). Another example is the fact that the optimum D:A ratio will be correlated to the morphology through the phase diagram, so both need to be optimized simultaneously. This fact results in a yet unresolved evaluation conflict: on the one hand, hundreds of homogeneous samples are required for a full evaluation of the potential of a new compound, on the other, only a few tenths of milligrams are typically synthesized of each novel compound.

Most of the highest solar cell efficiencies reported in the literature are obtained with devices where the active layer is spin coated. Spin coating offers an easy option to obtain homogeneous layers over a relatively small area in a highly reproducible manner; however, the waste of material is large and changes in composition or thickness are made over several substrates. One possibility to accelerate the screening of materials with respect to the conventional method was proposed by Schubert and co-workers who used a robotic arm to inkjet print devices with combinatorial variations of parameters.[21] On top of the typical limitations of inkjet printing (such as the required fine control on ink formulation to avoid inhomogeneities derived from the coffee-ring effect and Marangoni flows, or nozzle clogging) the authors found that the fast drying of the small amounts of solution in the multi vial configuration prevented a generally successful film deposition.

An important observation that can point to new optimization avenues is the fact that the fabrication of each device takes several orders of magnitude longer than its photovoltaic evaluation. For a parallel fabrication process (say ten samples, each with several pixels), the manufacture of laboratory scale devices takes a few hours per device while taking a *JV* curve typically only takes a few minutes. Therefore, moving from a fabrication intense to a measuring intense evaluation protocol would significantly accelerate the evaluation time per compound while minimizing the material waste. The use of gradients has been suggested for this purpose. In this case, a film exhibiting a gradient of the parameters of interest is locally scanned to deduce the optimal value for the given optimization parameter. A two pump slot-die implementation has successfully demonstrated the potential of this type of gradients for the evaluation of novel compounds. Slot-die coaters integrated into roll-to-roll systems have, however, important limitations, as they require large amounts of material and the complexity of the equipment makes it very exclusive.[22,23] Thickness gradients can be easily fabricated by blade coating[24] and indeed have been employed as a demonstration for the potential of gradients in the optimization of organic photovoltaics (OPV) and organic light emitting diodes (OLEDs) at laboratory scale.[24,25]

The local evaluation of performance is typically done by using techniques such as light beam induced current (LBIC), micro-electroluminescence or lock-in thermography.[26] While these techniques are commonly employed for other types of studies, such as degradation studies, they can be equally suited for the inspection of samples intendedly fabricated with lateral inhomogeneities. It is worth noting that there have been attempts to directly monitor the characteristics of 2D composition gradients[22,23] and some of them studied the combination of thickness and temperature effects,[27] or thickness gradient screening using discrete devices.[28,29]

In this work, we advance a simple fabrication platform based on blade coating that enables the fabrication of thickness, composition, and morphology gradients. We then demonstrate its usefulness by preparing solar cells of three different systems with a composition gradient that reveals the optimum D:A blending ratio in a single substrate with minimal materials usage (<10 mg per material) and easy processing feasible with the existing infrastructure in most research laboratories in this field. With the information therein extracted, a second solar cell is prepared with the optimum D:A ratio and processed to show orthogonally oriented thickness and annealing temperature gradients. With this method, it is then possible to extract the optimum blending ratio, film thickness, and annealing conditions employing just two devices. The complete and thorough characterization of devices with gradients is done by combining only two different measurements. On the one hand, photocurrent images provide a correlation between position and photovoltaic performance. On the other hand, we use Raman scattering to elucidate the thickness and composition distributions within the active layer in functional devices, according to a recent methodology developed in our group.[30] The spatially resolved performance, composition, thickness and temperature are then correlated in order to identify the optimum preparation conditions for a specific D:A pair. In our experiments, we employed less than 10 mg of each material for their complete evaluation, a value which is within the standard amounts synthesized in the first batch of novel materials. In addition, the use of 2D gradients contemplates the interplay between the optimization variables investigated (e.g., the combination between thickness and phase segregation at certain drying conditions).

2. Results and Discussion

The evaluation process for a new material system consists of three main steps. First, the reference data for each material is taken from literature or measured. These data consist of the complex refractive index and the effective Raman cross-section, which are required to characterize the gradient. These data only need to be obtained once, and then they can be used in the analysis of the given material in combination with any other complementary material or even in multicomponent systems. The second step is the fabrication of the devices with gradients varying the parameters of interest. The third step is the measurement of the local device performance (photocurrent) and the local structure (thickness and composition). The second and third steps might be repeated for different gradients or combinations of gradients (2D gradient geometries).

In the present study, we have selected three well-known systems, namely PCDTBT, PTB7-Th, and PffBT4T-2OD combined with the electron acceptor PC70BM. Such compounds have been relatively well studied in the past and demonstrated to yield high power conversion efficiencies as well as a reasonable stability. Importantly, by using well-known polymers, we can evaluate the methodology described herein; comparing the results to previous art and thus confirm its applicability.
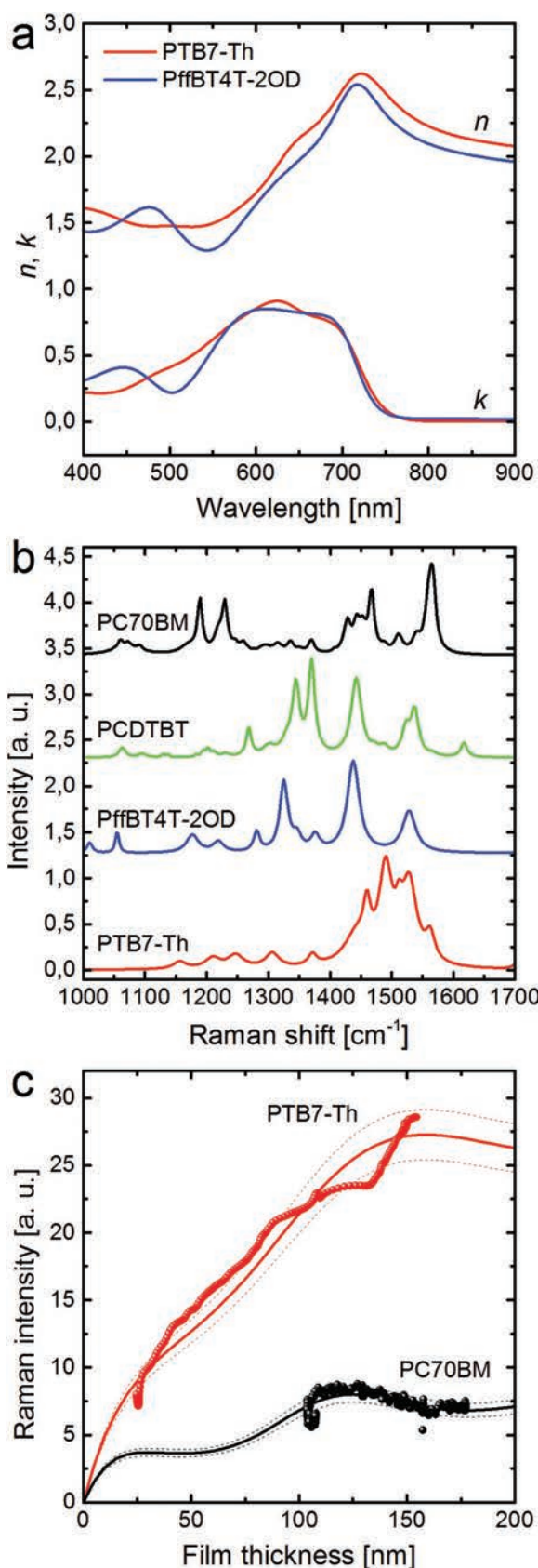
Figure 1. a) Complex refractive indices of PTB7-Th and PffBT4T-2OD.

2.1. Refractive Index and Raman Cross-Section

The optimization process proposed in this work starts by the acquisition of the complex refractive index ($n + ik$) and Raman cross-section (σ) of the materials under investigation, which then enable the characterization of the local composition and thickness by Raman scattering. By including this step in the methodology, we avoid the need for a very complicated fabrication protocol in which the composition and thickness are controlled with great accuracy. Instead, we use very simple solution fabrication tools which result in less control of the exact position and shape of the gradient, but then locally determine this gradient with good spatial resolution. Interestingly, if one is only interested in evaluating whether a parameter is important or not, this quantification might not be necessary. Moreover, in principle n, k, and σ only need to be determined once for each material, and then used in any combination with any other material (e.g., other acceptors or ternary systems).

The complex refractive index is the input parameter in the subsequent modeling of the Raman-scattering images in functional devices.[30] The optical constants were extracted by means of variable-angle spectroscopic ellipsometry. The films of the pristine materials showed a thickness gradient laterally cladded between two adjacent regions of constant thickness (the thinnest and thickest values). The same samples were used for the extraction of the corresponding Raman cross-sections, and serve as a first check of the solubility of the compound and wetting and drying properties of the solution. While in principle ellipsometry could be used to determine composition and thickness, confocal Raman spectroscopy provides (up to) diffraction-limited spatial resolution together with a much better fingerprinting capability compared to the visible absorption measured in the former. In this very first experiment, additional information is obtained such as the solubility of the material or the layer thickness derived from the concentration of the solution casted, which is mainly affected by the viscosity when working at the typical range of operating conditions in blade coating. The conditions employed to obtain thickness gradients are described in detail in the following section.

The refractive indices of PTB7-Th and PffBT4T-2OD are shown in **Figure 1**a, while those of PCDTBT and PC70BM are included in Figure S1 in the Supporting Information. These values are in the same range as the typical ones obtained for conjugated polymers and fullerenes.[31] The extinction coefficient provides information related to the band gap of the different materials, as well as the strength of absorption.[17] The thickness values obtained with ellipsometry were compared to those obtained via profilometry, so to ensure the validity of our optical description.

The same sample is then scanned using a confocal Raman scattering setup in order to obtain the Raman intensity

b) Reference Raman spectra of (from top to bottom) PC70BM, PCDTBT, PffBT4T-2OD and PTB7-Th took at 488 nm excitation in air. c) Raman intensity dependence as a function of film thickness for the 1490 cm^{-1} vibrational band in PTB7-Th and the 1557 cm^{-1} mode in PC70BM. The solid lines stand for the fitted transfer-matrix model using the corresponding Raman cross-section as fitting parameter. The dashed lines correspond to the standard deviation of the fit.

dependence on film thickness. We have recently demonstrated that this dependency can be modeled using the transfer matrix formalism[30] with the complex refractive index for the wavelengths of interest as input parameters, and the effective thin film Raman cross-section (σ) as a fitting parameter. The Raman spectra took at 488 nm excitation for the four materials used in this work are shown in Figure 1b, while the thickness dependence of the Raman intensity for PTB7-Th and PC70BM is depicted in Figure 1c. We express the Raman cross-sections as ratios with respect to σ_{PC70BM}, which constitutes the workhorse example of electron transporting small molecule in high performing organic solar cells. Therefore, the cross-section ratios found at 488 nm excitation in air read 1.9 ± 0.3, 1.3 ± 0.4, and 7 ± 1 for the 1490 cm^{-1} mode in PTB7-Th, the 1437 cm^{-1} mode in PffBT4T-2OD and the 1447 cm^{-1} mode in PCDTBT, respectively. These ratios are much lower than 30, the maximum value after which the Raman approach is not sensitive enough to quantitatively deduce the composition ratio for the whole range of compositions.[30] The use of Raman spectroscopy to characterize the photovoltaic films is also limited to thickness values below the saturation regime of the Raman intensity as well as to materials combinations which do not suffer from large variations in the degree of order and crystallinity during the blending process. In the former case the technique is mainly limited by the penetration depth of the excitation wavelength, whereas in the latter case the analysis of the scattered intensity in blends that include (semi)crystalline polymers usually results in difficulties to deduce the thickness of the thin film with enough accuracy.

2.2. Casting Methodology

We have chosen knife coating, aka blade coating, as the main technique to produce samples with parametric gradients. In this technique, a metal blade applicator is used to extend a certain volume of solution by means of the relative movement of the knife over the substrate located underneath at a given distance (gap). The movement of the blade leaves behind a wet film which, after the evaporation of the solvent, becomes a relatively homogeneous solid layer. Although blade coating is a mechanically simple deposition technique, the resulting films show a high degree of homogeneity when the experimental parameters involved are properly adjusted due to the self-metering character of the technique. These parameters include the blade velocity, the total volume of solution forming the reservoir, the gap between substrate and blade, the substrate temperature during deposition and the concentration of the solution. Following previous work,[29] we have altered our doctor blade electronics in order to control speed and acceleration of the blade throughout the coating process. The speed of the blade is typically the main factor affecting film thickness for given solution concentration and viscosity (typically increasing concentration and viscosity leads to thicker films). We observed that employing concentrations around 30 mg mL^{-1} of the blend in chlorobenzene:*ortho*-dichlorobenzene (CB:oDCB) 1:1 volume ratio and a temperature of the substrate of 100 °C yields films of similar thickness for most of the D:A materials employed. This fact is very relevant since it implies that approximate

thickness values can be predicted for new compounds without the need to severely optimize the process, minimizing the amount of blend material required for testing the deposition conditions. Typically, a thickness gradient is first performed in these conditions, using 60 µL of solution and a velocity ramp that goes from 100 to 10 mm s^{-1} within 6 cm of sample. Generally, faster speed yields thicker films, so as the blade moves decelerating, a thickness wedge is obtained. As a second order effect, the thickness also depends on the amount of solution available during the deposition itself. Below some critical liquid amount, the film becomes thinner as the blade moves since less liquid is available in front of the blade. We found that employing a decreasing speed ramp allows for steeper thickness gradients than increasing the speed as the two effects add up. When using positive speed ramps, the resulting thickness gradients are significantly less steep, a fact that could be used to effectively zoom in at specific thickness regions that are of our particular interest. Using the aforementioned conditions combined with a decreasing speed of the blade yields films that are 300 nm on the thickest part and 30 nm on the thinnest. It is worth mentioning that nonpolymeric solutions (such as small molecules) require higher concentrations to achieve such thicknesses since the viscosity is significantly lower. An example of thickness gradient for PTB7-Th is depicted in Figure S2 in the Supporting Information.

The temperature at which the substrate and blade are held during the blading process can be employed to control the drying process, which in turn can affect the morphology adopted by the D:A blend. For the solvents and viscosity ranges employed, the thickness is not significantly changed by substrate temperature as long as the film dries within a few seconds. This relatively fast drying is required to avoid liquid equilibration throughout the substrate upon passing the blade. Other factors such as the blade–substrate gap affect the final thickness in a much smaller scale thus are kept constant in our experiments being 150 µm gap a good starting point. The amount of solution is in our case mostly determined by the fact that our substrates are 7.5 cm long, the size of a typical microscope slide, and using more solution results in the unnecessary waste of material whereas using less can lead to the incomplete coverage of the area of interest. Notice that considering that each film requires 60 µL of solution with a typical solid content of 20 mg mL^{-1}, only 1.2 mg of material is needed per film, and a single film already contains most of the required information regarding thickness effects of a specific blend. Interestingly, this method can be used for other applications beyond OPV optimization, including the study of the geometrical confinement on phase transition temperatures,[32] determination of exciton diffusion lengths,[33] fabrication of position sensitive photodetectors,[34] or as miniature spectrophotometers based on microcavity resonators with a wedged active layer.[35]

We extend here this method beyond thickness gradients to also include the preparation of films with D:A composition gradients. A simple method to achieve this is by employing the aforementioned doctor blade technique and casting simultaneously two or more drops of the pristine materials. In this process, as the blade moves, the two solutions mix, and upon drying a composition gradient approximately perpendicular to the direction of movement of the blade is created. We have
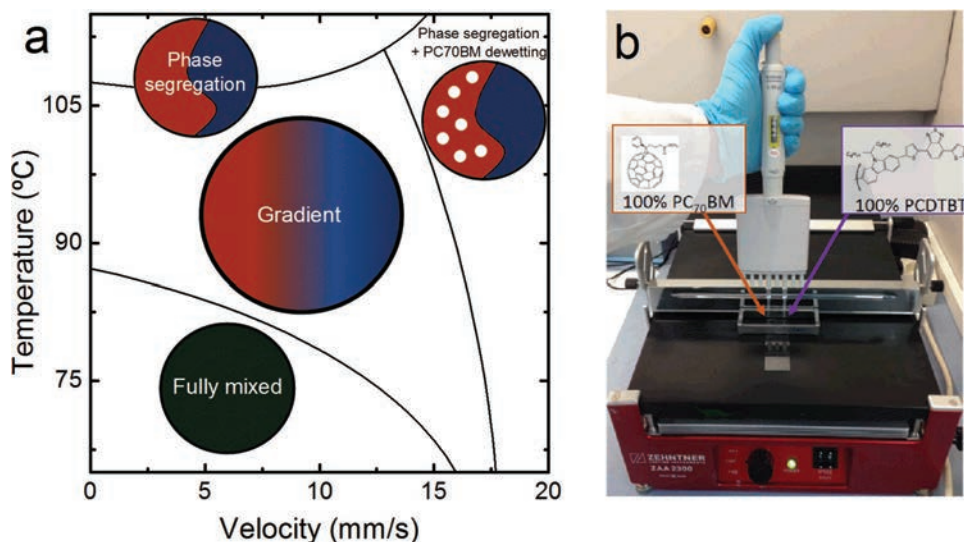
**ADVANCED
SCIENCE NEWS**

www.advancedsciencenews.com

**ADVANCED
ELECTRONIC
MATERIALS**

www.advelectronicmat.de

Figure 2. a) Phase diagram for PTB7-Th:PC70BM solar cells. At low temperatures and speeds there is a full mixture of the donor and the acceptor. At large temperatures, there is phase segregation. At large temperatures and large speeds, there is phase segregation and dewetting of PC70BM. At intermediate values of temperature and speeds, composition gradients are formed. b) Picture of the composition gradient setup prior to starting the movement of the blade.

made a systematic evaluation of blade speed and temperature to obtain the processing window that results in gradients (Figure S3, Supporting Information). Interestingly, we found that the casting conditions (substrate temperature and blade velocity) selected during the processing of the composition-graded layer determine different processing regimes that are visually depicted in **Figure 2** as a phase diagram. For a given speed, increasing temperature accelerates the drying of the solutions. For slow drying, fully mixed films are produced. When drying is too fast, no mixing is observed. There is an intermediate region of drying in which a gradient is found. The

exact conditions will clearly depend on the solution rheology, boiling point and its wettability on a given substrate. Despite being a relatively narrow range of conditions, we found them to be applicable for a large number of materials such as those presented in this manuscript and others currently under investigation like nonfullerene acceptors.

Figure 3 shows the Raman characterization of graded films for the aforementioned deposition conditions. Raman images were taken through the glass on complete devices. The Raman cross-sections deduced above were used to analyze the corresponding images in order to produce composition and thickness
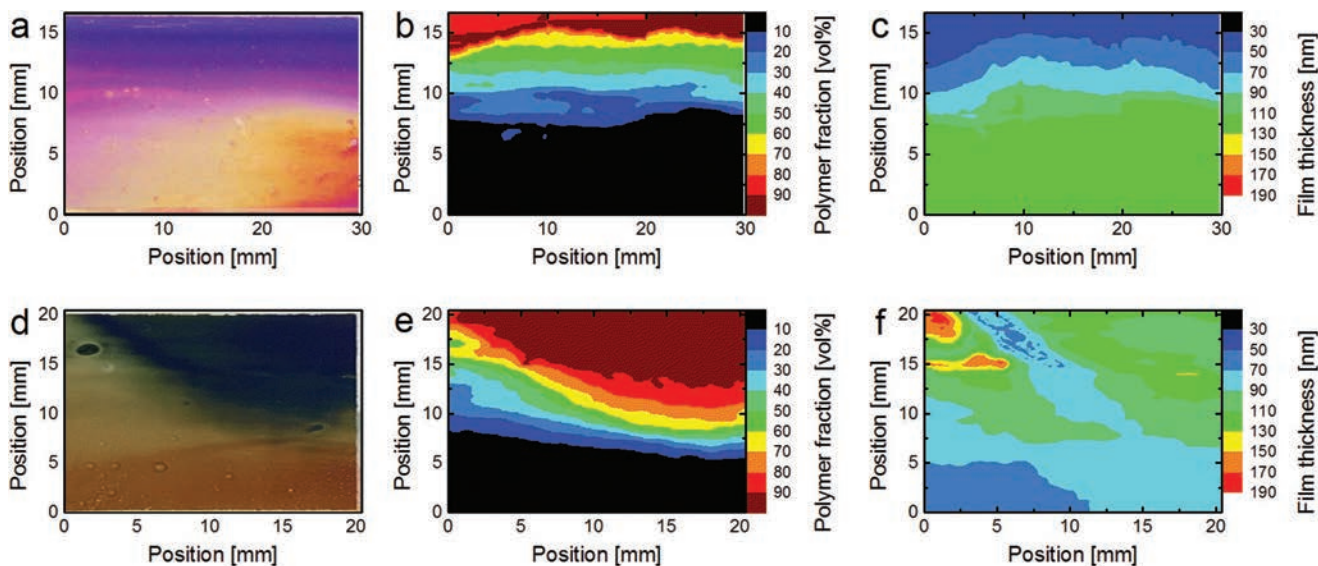
Figure 3. a) Optical image of a composition graded solar cell with a PCDTBT:PC70BM blend as active layer. b) Volumetric composition map as extracted from Raman scattering. c) Thickness map. d) Optical image of a solar cell with a composition graded active layer of PTB7-Th:PC70BM. e) Composition map of the device. f) Thickness map. All Raman data was took at 488 nm excitation in air and through the glass substrate.

ADVANCED
SCIENCE NEWS
www.advancedsciencenews.com

ADVANCED
ELECTRONIC
MATERIALS
www.advelectronicmat.de

maps.[30] The deconvolution of the local spectra according to their solid-state, effective Raman cross-sections yields the local volumetric composition while the quantitative analysis of the scattered intensity is related to the active layer film thickness. We note that aspects such as the density of Raman-active chromophores as well as their Raman susceptibility are implicitly included in the modeling of the effective Raman cross-sections, therefore making the polymer volume fraction a good estimate of the w:w blending ratios if the densities of the blended materials are known. Figure 3 shows these maps for gradients of PCDTBT:PC70BM and PTB7-Th:PC70BM. The data clearly show composition gradients spanning from 1:0 all the way to 0:1. While they are not perfectly perpendicular to the direction of the movement of the blade, the use of Raman to characterize the exact composition map enables a one-to-one correlation between device performance and composition, as we will see in the following sections. There are also some variations in film thickness which, since they can be quantified, can be used to simultaneously look at composition and thickness gradients, as we will show.

It is important to note that the colors in the optical pictures arise from both absorption and reflection due to the strong Ag reflectivity in the visible spectral range. The use of colorimetry for the identification or quantification of local composition can be misleading due to the strong interference patterns present in a metallized thin film unless rigorous optical modeling is applied. This further justifies the use of Raman and transfer matrix modeling to spatially fingerprint materials with the relevant degree of accuracy (≈5%).

The confocal Raman images analysis does not discriminate phase separation smaller than the spot of the laser (typically tenths of microns when measuring through the glass with a 10× magnification objective), and therefore, it is difficult to assess the quality of the mixing at length scales relevant to charge generation. Indeed, D:A blend solutions are often left to stir for several hours prior to using them to ensure intimate mixing. In our case, mixing is done relatively quickly during deposition: the two drops of pristine materials mix within seconds as the blade bring them together during its movement and solvent evaporates up to the point when viscosity is too large to allow molecular diffusion. (Note that diffusion is temperature dependent, so keeping the substrate above the glass transition of the polymer would enable further fullerene diffusion.) In order to evaluate possible differences coming from the very different solution mixing times, we have compared the photovoltaic performance of the described two drops method with a three drops extension, in which the central drop is a 1:1 (w:w) blend (mixed during hours) and the exterior drops are either the pristine materials or 1:9 (w:w) and 9:1 (w:w) blends if their viscosity does not allow for a good mixing within the time interval of the casting. Overall, the casting methodology we present is suitable for combinations of materials that can be dissolved and deposited using solvents with similar processing properties, including boiling point and rheology of the final solid solutions. These two parameters are critical to obtain properly mixed regions in the final film. More sophisticated mixing stages or casting conditions might be necessary for materials or solvents with strong tendency to phase-segregate. Beyond the optimization of blends for OPVs, the presented method could be used for any application in which the composition needs to be investigated, such as white OLEDs based on ternary systems with cascading energy levels[36] or determination of phase behavior and phase diagrams in multicomponent systems.[37]

2.3. Donor:Acceptor Blending Ratio Optimization

A standard protocol for optimization of the different parameters in OPV does not exist. In most research articles only the optimized parameters are given but the series of experiments leading to those optimum values is not often described. Here we choose to start by looking at the effect of composition. This is motivated by the fact that the range of optimum D:A compositions for the different materials found in literature spans between ≈1:4 to 2:1 in w:w ratios (i.e., from 80% to 33% in weight of the fullerene content). This range of potential optimum values is very broad, the cells performance often sharply depends on the exact composition, and the optimum is difficult to predict beforehand as it depends on the interplay between the absorption of each component, degree of mixing, percolating pathways, and balance of charge carrier mobilities. The optimum thickness, on the other hand, often coincides with the first interference maximum (80–120 nm) for the absorbed electric field intensity. Moreover, the derivative close to the maximum is usually very smooth, meaning that using the conditions that yield 100 nm of active layer thickness it would likely be close to the optimum solution. Some materials with good transport properties and low level of unintentional doping would exhibit a PCE maximum close to the second interference maximum (≈250 nm), so it is clearly important to look at thickness, but not to start with. The optimum thermal annealing would also be strongly linked to the exact composition through the phase diagram of the blend, and thus it makes sense to either look at it after optimizing the composition, or simultaneously within a 2D gradient.

In order to find the optimum blending ratio, a solar cell was prepared with a composition gradient ranging from pure donor to pure acceptor that includes all possible ratios in a single substrate, following the experimental protocol explained above. Optical and Raman images of the resulting layers with a composition gradient are depicted in Figure 3 for PCDTBT:PC70BM and PTB7-Th:PC70BM blends. As already mentioned, in both cases there is a composition gradient along the short axis in which the top side contains 100% polymer and the bottom 100% PC70BM. The resulting devices are characterized by means of LBIC to obtain a local photocurrent map[38–40] (**Figure 4**). The photocurrent images show that there is a central band that extends along the long axis of the substrate which corresponds to the area with the highest photocurrent generation. This result is in agreement with the Raman data that suggest that D:A mixing does occur during the casting of the active layer and that a composition gradient is obtained as indicated by the low photocurrent observed close to the substrate edges, where the composition is close to the pure cases. Since the LBIC maps illustrated in Figure 4 are corrected for excitation light intensity fluctuations, the differences in photocurrent can be ascribed to changes in composition, modulated by the small variations in
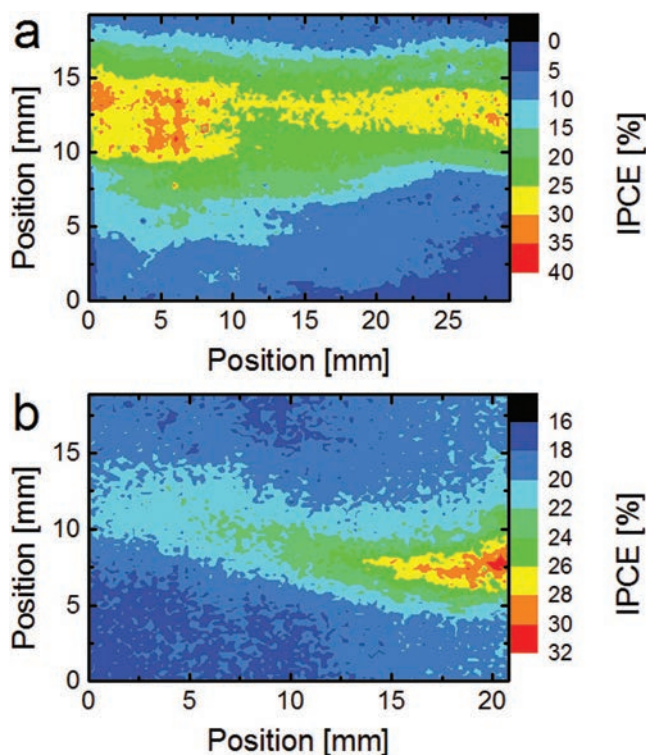
**ADVANCED
SCIENCE NEWS**
www.advancedsciencenews.com

**ADVANCED
ELECTRONIC
MATERIALS**
www.advelectronicmat.de

Figure 4. Photocurrent maps extracted by means of LBIC at 532 nm excitation in composition graded devices. a) PCDTBT:PC70BM cell. b) PTB7-Th:PC70BM cell.

film thickness. In order to separate the effect of both variables on the photocurrent, we use the quantitative Raman maps that were described in the previous section which were collected exactly on the same devices. The local photocurrent mapping from LBIC can then be spatially correlated with the thickness and composition data extracted from the Raman-based images. For visualization purposes, the results are plotted eliminating the spatial dependence, which allows for a rapid spotting of the optimum thickness and blending ratio conditions of the active layer (**Figure 5**).

As it can be observed in Figure 5, for the PCDTBT:PC70BM blend there exists an optimum active layer thickness around
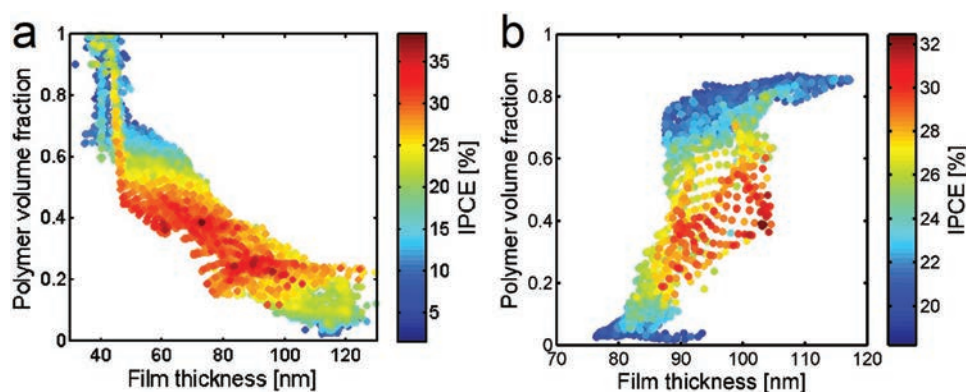
90 ± 10 nm and an optimum polymer volume fraction of around 20 ± 10 vol% which yield the highest photocurrent. The obtained polymer volume fraction corresponds to a D:A ratio of ≈1:4 (w:w) according to the reported density of the materials. Similarly, for the PTB7-Th:PC70BM blend (Figure 3b) there is an apparent optimum thickness of 100 ± 10 nm and a polymer volume fraction of around 50 ± 10 vol%, which corresponds to a D:A ratio of 1:1.5 (w:w) (considering $\rho_{PC70BM} = 1.72$ g cm^{-3}, $\rho_{PTB7-Th} = 1.17$ g cm^{-3} and $\rho_{PCDTBT} = 1.15$ g cm^{-3}).[41–43] The D:A ratio can be obtained assuming that the density of both materials is homogeneous and invariant upon the blending process. Both D:A ratios found with this methodology agree very well with the reported values in the literature, thus giving validity to the methodology.[44,45]

The uncertainty in volumetric optimum composition, partially arising from slightly different thicknesses, is of the same order than that of the accuracy of the Raman quantitative analysis.[30] Typical density values for conjugated polymers are around 1.1 to 1.3 g cm^{-3}.[41,46,47] This relatively narrow range (± 10%) of density values could be used to safely infer a reasonable density value for a new compound of yet unknown density in order to convert between volume and weight fractions.

In order to evaluate the generality of our developed technique, we have fabricated PffBT4T-2OD:PC70BM blend films with a composition gradient. The corresponding devices were measured with Raman and LBIC (Figure S4, Supporting Information). The volumetric composition was similarly extracted by means of Raman spectroscopy using the Raman cross-sections of the materials as discussed above. An optimum D:A volume ratio of 1:1 was obtained, which corresponds to a weight ratio of 1:1.5 (w/w.) considering $d_{PffBT4T-2OD} = 1.17$ g cm^{-3}. This optimum composition value is in agreement with the values reported for the best performing devices fabricated with the PffBT4T-2OD:PC70BM blend.[48] The quantitative analysis of the Raman-scattered light yields, however, inconsistent thickness values. The reason for this mismatch in the quantification of the thickness is currently under investigation but it is possibly related to variations in the refractive index upon blending, as well as the intrinsic limitations of the Raman quantification analysis detailed in the literature.[30]

The composition gradient films implicitly include the effect of the active layer thickness on the extracted photocurrent for a

Figure 5. Correlation between LBIC local photocurrent maps and quantitative Raman maps of thickness and composition in the composition graded devices shown in the previous figures. a) PCDTBT:PC70BM blend. b) PTB7-Th:PC70BM blend.

**ADVANCED
SCIENCE NEWS**

www.advancedsciencenews.com

**ADVANCED
ELECTRONIC
MATERIALS**

www.advelectronicmat.de

limited range of thickness values. A full exploration of this parameter can be performed by casting a film of constant D:A ratio, ideally using the values found in the previous experiment. This second sample allows to evaluate the photocurrent at the first two interference maxima, as well as to provide full PCE values, as we will show. Therefore, once the optimum ratio between the donor and the acceptor materials is found, such variable is kept constant while the thickness and the annealing temperature are optimized in separate substrates with their corresponding gradients.

2.4. Thickness Gradient Optimization

In order to confirm the results found in the previous experiments and validate the methodology, discrete solar cells were prepared over a thickness wedged active layer device. The specifics for the preparation of a varying thickness active layer are explained in detail in the experimental section. Discrete solar cells allow for the characterization of parameters such as open circuit voltage (V_{oc}), current density (J_{sc}), fill factor (FF), and PCE. Along the thickness gradient, a large area electrode was also deposited on the same substrate (Figure S2d, Supporting Information). This allows measuring LBIC over the whole thickness gradient with a much higher lateral resolution, in this case 100 µm as dictated by the dimensions of the laser spot. For comparison purposes, the thickness for this sample was obtained by mechanical profilometry at equidistant points along the active layer. This simple experiment reveals the profile of the active layer thickness. The combination of LBIC data over the long metallic electrode (**Figure 6**a) and JV curve scanning of discrete devices within the same substrate (Figure 6b) provides useful information about the relationship between efficiency and (LBIC) measured photocurrent.

Figure 6b summarizes the PCE and J_{sc} results extracted from the JV curves of the 12 different 8×2 mm^2 individual solar cells under 1 sun 1.5 AM-G calibrated illumination. It is important to remark that for this experiment, the indium tin oxide

(ITO)-covered substrate has a specific pattern to isolate the contacts of each individual device. The thickness gradient of the active layer covered a distance of 6 cm and spanned from ≈40 to 250 nm for both materials.

For the PTB7-Th:PC70BM binary, thickness has a relatively large effect on efficiency. The optimum thickness is found within a relatively small range, between 100 and 130 nm. Furthermore, the J_{sc} oscillates with thickness showing an absolute maximum at ≈150 nm and a second relative maximum at ≈270 nm. On the other hand, the PCDTBT:PC70BM binary shows a smooth increase in photocurrent and efficiency until ≈100 nm and then reaches a plateau up to ≈250 nm. For the D:A material systems explored in this work the values found for the optimum thickness are in agreement with previous results reported in the literature, as well as the results obtained from the composition gradient devices discussed above.[49] The procedure employed for the preparation of the reported inverted solar cells yields efficiencies in line with the values found in the literature for these D:A pairs when the optimum conditions are met.

Figure 6 indicates that in the case of the PCDTBT:PC70BM blend the photocurrent (which is directly proportional to the external quantum efficiency (EQE) in Figure 6a) measured in the continuous part of the device matches very well the discrete device performance in terms of PCE (solid green curve in Figure 6b) all over the thickness regime explored (from 50 to 250 nm). Such thickness regime covers two interference maxima in the photocurrent albeit only that occurring at ≈100 nm yields the highest PCE in the discrete devices of ≈5%. Due to limitations in charge transport, thicker films may have reduced fill factors, which means that even when the photocurrent might be high, the overall PCE may not. Although the open circuit potential is not significantly affected by film thicknesses ranging from 30 nm to several hundreds of nanometers, there exist cases in which the open circuit voltage depends on composition, such as in the recently published ternary alloys.[50,51] The proposed methodology of this manuscript which is based
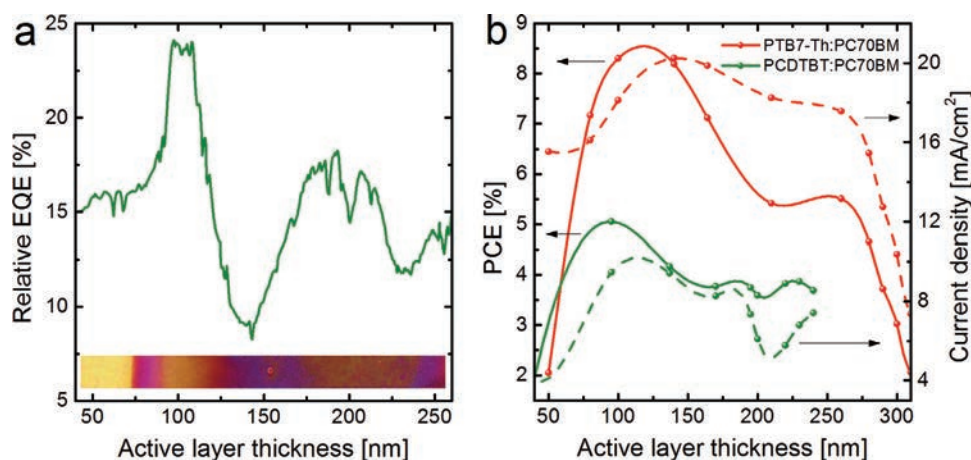

Figure 6. a) LBIC data of a single line scan along the increasing thickness active layer wedge (PCDTBT:PC70BM) compared against the thickness obtained from profilometry. The colored picture at the bottom corresponds to the area scanned with the LBIC and is adjusted to match with the thickness. Note the reflection pattern is in agreement with the photocurrent obtained. b) PCE (%) and photocurrent (J_{sc}) (mA cm^{-2}) results extracted from the JV curves measured under 1 sun 1.5 AM-G calibrated spectrum and intensity at different active layer thicknesses. The thickness was measured with profilometry.

**ADVANCED
SCIENCE NEWS**
www.advancedsciencenews.com

**ADVANCED
ELECTRONIC
MATERIALS**
www.advelectronicmat.de

on first, preparing a gradient of composition and thickness with a common electrode, and then a thickness gradient with an array of discrete pixels presents a solution for any V_{oc} discrepancies affecting the final result. Alternatively, it has been demonstrated the possibility of using a mobile top electrode, such as that proposed by Savagatrup and co-workers.[27]

One aspect that is also evident from our thickness graded samples is the fact that a Fabry–Pérot interference of the incident light between the glass and the metallic electrode occurs and has the potential to enhance light absorption within the active layer when the right conditions of layer thicknesses are achieved. Many studies have been developed to predict the exact thickness that could result in some light trapping that would enhance the incident photon-to-current efficiency; however, achieving such thicknesses typically follows a trial and error approach with spin-coating that is highly resources intensive. In our case, the natural smoothness of the gradient thickness yields all the possibilities in a single, self-referencing sample, thus allows validating the theoretical models, and vice versa. In fact, the high control of the layer gradient slope has made possible the fabrication of organic near-IR microcavity based spectrophotometers where the spectral response is strongly determined by the active layer thickness.[35]

For the PCDTBT:PC70BM thickness gradient sample an optical picture of the reflection already shows relatively strong interference patterns from white light as it can be seen in Figure 6a. When the optical image is compared to the corrected photocurrent measured along the thickness wedge, some correlation can be perceived. Apparently, the regions where the reflection is orange on the picture inset also present higher photocurrent, which could be indicative of an enhanced light trapping. This kind of interference effects are taken into account in the modeling of the Raman-scattered light in functional devices. The thickness dependent data for four different material combinations is shown in Figure S2 in the Supporting Information.

2.5. Morphology Optimization

We further tested the effect of annealing temperature over a homogenous thickness and composition active layer device. The temperature gradient was achieved with a calibrated Kofler bench that provides a controlled temperature gradient of approximately 1 °C mm⁻¹. In this experiment, the annealing process was performed prior to the metallic electrode deposition to avoid the disruption of the temperature gradient that a highly thermally conductive electrode might produce. Although ITO could have a similar effect, its thermal conductivity is lower than silver (5 vs 406 W m⁻¹ K⁻¹, respectively)[52,53] and allows keeping a controlled temperature gradient.

Figure 7 illustrates the photocurrent of 2 mm wide solar cells separated by 2 mm disposed along the temperature gradient for two PCDTBT:PC70BM devices where the active layer was cast at different temperatures and then placed on the Kofler bench for 10 min. According to Figure 7 there is not a significant dependence on the casting temperature (at least within the temperature range explored), which is indicative that morphology of the film does not strongly depend on substrate temperature
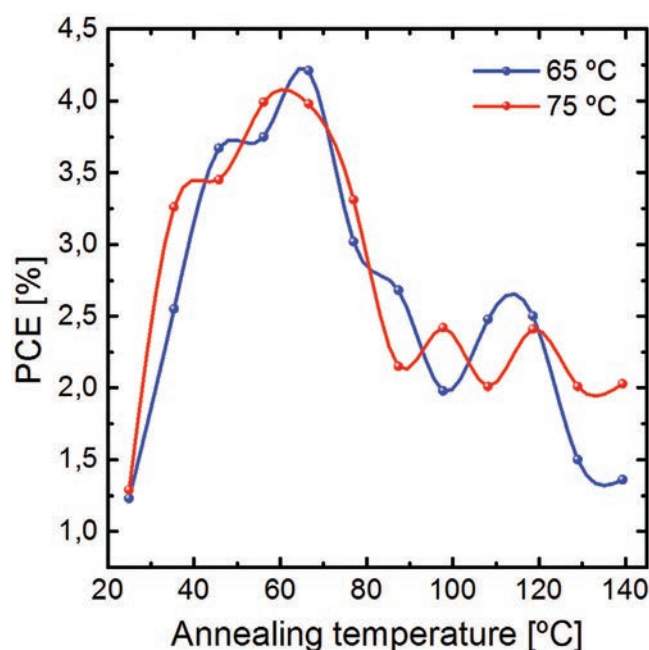

Figure 7. Effect of the annealing temperature on the PCE for solar cells with homogeneous active layer thickness of PCDTBT:PC70BM casted at 65 and 75 °C.

for this system; however, annealing beyond 75 °C results in a decrease of the photocurrent by about half compared to a mild annealing of 10 min at 70 °C where the photocurrent observed shows a maximum. This annealing study is in agreement with the results found in previous works.[54]

An alternative method to control the nanoscale morphology is the use of solvent additives. Our methodology could be used to explore if an additive has an effect on the performance of the solar cells. We have, for instance, fabricated a PTB7-Th:PC70BM sample containing a gradient of additive by depositing three drops with 0 vol%, 5 vol% and 10 vol% of 1,8-diiodooctane (DIO). The resulting LBIC is shown in Figure S5 in the Supporting Information, which clearly demonstrates a strong influence of the performance with DIO content, being the optimum in the range between 0 vol% and 5 vol%. An exact quantification cannot be made using Raman, as the additive leaves the sample and there is not a significant Raman band shift derived from variations in the film morphology. A very crude linear approximation of the additive content within the sample suggest a concentration of about 3%, which reassuringly is very close to the reported optimum. Further work needs to be carried out to find a measuring tool that allows quantifying the local amount of additive during the deposition itself.

2.6. Single Substrate Double Gradient

The here presented technique offers the possibility to generate orthogonal gradients spanned over the two axes of the substrate. In this particular case we prepared a sample showing a thickness gradient in its short axis and an orthogonally oriented thermal annealing gradient in its long axis. This approach has the added benefit of the simultaneous testing of both variables,
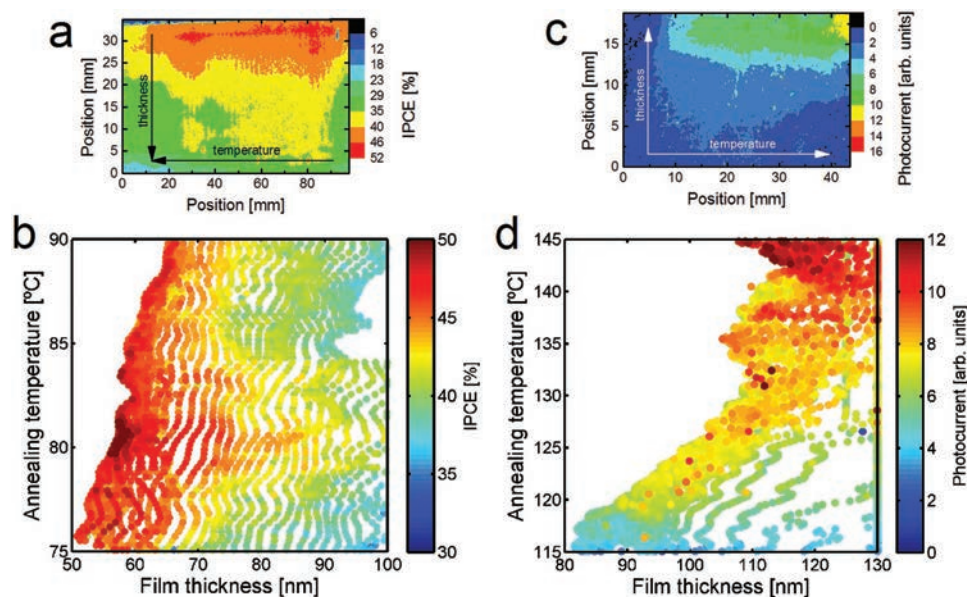
ADVANCED
SCIENCE NEWS
www.advancedsciencenews.com

ADVANCED
ELECTRONIC
MATERIALS
www.advelectronicmat.de

Figure 8. a) LBIC photocurrent map of a PCDTBT:PC70BM device with orthogonal thickness and annealing gradients. b) Correlation between the annealing temperature and the film thickness obtained by Raman scattering in the PCDTBT:PC70BM device characterized in (a). c) Photocurrent map of a PTB7-Th:PC70BM device with orthogonal thickness and annealing gradients. d) Correlation between the photocurrent and the film thickness obtained by Raman scattering in the PTB7-Th:PC70BM device shown in (c).

a type of evaluation that is very resource intense when using conventional evaluation protocols via multiple substrates with homogeneous active layers. In addition, it aids in the comparison of the effect in the performance of both variables since external fluctuations are intrinsically kept constant, e.g., differences in the interlayers or in the active layer solution occurring from batch to batch.

For this experiment, a sample was prepared by blade coating a thickness gradient along the short side of the 7.5×2.5 cm^2 substrate. The solution casted was the same employed for the previous thickness and thermal annealing isolated experiments. Before the deposition of the back contact a gradient of annealing temperature along the long side of the substrate was performed by means of a Kofler bench placed inside a glove box. Subsequently, LBIC and Raman imaging were employed to map the surface properties with a lateral resolution of 100 µm.

Figure 8a,c shows the LBIC photocurrent maps for PCDTBT and PTB7-Th based devices, respectively. It can be appreciated that the active layer thickness has a larger impact on the photocurrent than annealing for these two systems. In fact, post deposition annealing does not have any appreciable effect on PffBT4T-2OD:PC70BM blend based solar cells (Figure S4, Supporting Information), while thickness clearly has a strong influence on performance. Coming back to PCDTBT-based cells, we note that there is a nonlinear response of the films to the annealing temperature, since there is a small increase in the photocurrent at intermediate temperatures. This is in accordance to the results of discrete cells shown in Figure 7, where a small increase of performance was observed at 110 °C. This demonstrates that using temperature gradients results in high sensitivity to small temperature intervals at which there might be strong effects in performance.

The results here obtained are in agreement with the information extracted from the single gradient devices investigated above. Therefore devices based on 2D gradients open the door to further savings in time and resources.

2.7. Time and Resources Saving Analysis

The main motivation of this work deals with the development of a technique that can noticeably reduce the time and resources required to optimize novel OPV materials, thus accelerating the progress of this technology. On one hand, based on available literature, we estimate that the conventional sample-by-sample method requires at least 6 substrates with different D:A ratios to determine approximately the optimum composition window; at least 12 substrates to estimate the optimum active layer thickness; and at least 6 substrates with different annealing temperatures. On the other hand, by following the here presented combinatorial methodology we have demonstrated that the optimization can be performed using a single substrate for each variable (in the best scenario). Therefore, we estimate that using gradients instead of discrete samples reduces the usage of material by at least a factor of 5.

In terms of timesaving (S), the quantification can be performed according to the following ratio

$$S = \frac{N_{dev}\left(t_{fab} + t_{JV}\right)}{t_{fab} + N_{pts}t_{LBIC}} \tag{1}$$

where N_{dev} is the number of discrete samples fabricated (24 for the example above), t_{fab} is the average time required to fabricate each device (1.7 h per device in the best case if the fabrication is performed in batches of nine devices in parallel; see the

**ADVANCED
SCIENCE NEWS**

www.advancedsciencenews.com

**ADVANCED
ELECTRONIC
MATERIALS**

www.advelectronicmat.de

Supporting Information for details on the estimation of the fabrication time based on the authors experience working on four different international labs), t_{JV} is the time required to measure the *JV* curve in a single homogeneous device (around 5 min), N_{pts} is the number of photocurrent data points extracted at the LBIC setup and t_{LBIC} is the time spent by the LBIC setup to measure a single data point. If we would like to obtain the same amount of information from the gradients than we normally do with the homogeneous samples, then $N_{dev} = N_{pts}$, and $S \cong N_{dev} = 27$. When acquiring photocurrent maps in lateral steps of 200 µm, $N_{pts} \times t_{LBIC}$ equals ≈2 h, thus with these typical values *S* equals ≈13. This result indicates that the use of gradients instead of discrete devices as the optimization procedure in OPV devices leads to more than a 10-fold reduction in the required experimental time for evaluation.

In addition to the time and resources efficiency, the amount of information that can be obtained from gradients is much higher (denser) than the one obtained from discrete samples. On the one hand, the availability of a much larger amount of data helps to perform meaningful statistics on the relevant parameters minimizing the sample to sample variability. On the other hand, our methodology can probe combinations of parameters that would be unfeasible to consider if using a conventional sample-by-sample methodology. As an example, LBIC maps provide information coming from hundreds of active layer thickness, composition and/or annealing combinations whereas a discrete sample exclusively provides averaged information from a single combination of such parameters. For a deep optimization protocol in which 2D combinatorial arrays are made of homogeneous samples with gradual changes in the relevant parameters, N_{dev} quickly would reach ≈100, and in that case, our methodology would be almost 50 times faster than the conventional method.

3. Conclusions

In this work we have introduced a combinatorial screening methodology to optimize the performance in bulk heterojunction organic solar cells. The procedure minimizes the usage of resources and experimental time while leading to the same optimum parameters obtained following the traditional sample-by-sample methodology. Each donor:acceptor (D:A) pair explored in this work required a minimum of two graded devices (a composition gradient and an active layer thickness/annealing double gradient) to be fully optimized. The optimum values are found using a combination of a quantitative model to confocal Raman spectroscopy images with photocurrent maps. The spatial matching of both datasets serves to quickly spot the optimum window of the relevant parameters (blending ratio, active layer thickness and annealing temperature) that yield the optimum device performance. The final PCE values obtained were 5%, 8%, and 9.5% for PCDTBT:PC70BM, PTB7-Th:PC70BM, and PffBT4T-2OD:PC70BM, respectively.

We have estimated that the here presented combinatorial methodology implies a 5-fold and an ≈10–50-fold reduction in the usage of resources and time, respectively, compared with sample-by-sample methodologies, thus facilitating the fast and efficient evaluation of novel materials that are synthesized in

minimal amounts (<10 mg). This combinatorial approach will certainly accelerate the identification of highly efficient D:A pairs and contribute to the ongoing progress of the OPV technology. Interestingly, the methodology can be easily extrapolated to the optimization of other device layers or processing parameters, such as the thickness of the electron and hole transport layers as well as the content in processing additives required to maximize the device performance.

4. Experimental Section

Materials: Poly[N-9″-hepta-decanyl-2,7-carbazole-alt-5,5-(4′,7′-di-2-thienyl-2′,1′,3′-benzothiadiazole)] (PCDTBT) was obtained from Ossila, batch 1311, CB fraction. Poly[4,8-bis(5-(2-ethylhexyl)thiophen-2-yl)benzo[1,2-b;4,5-b′]dithiophene-2,6-diyl-alt-(4-(2-ethylhexyl)-3-fluorothieno[3,4-b]thiophene-)-2-carboxylate-2-6-diyl)] (PTB7-Th) was obtained from Ossila. Poly[(5,6-difluoro-2,1,3-benzothiadiazol-4,7-diyl)-alt-(3,3‴-di(2-octyldodecyl)-2,2′;5′,2″;5″,2‴-quaterthiophen-5,5‴-diyl)] (PffBT4T-2OD) was obtained from Ossila, batch M301. [6,6]-phenyl C71 butyric acid methyl ester (PC70BM) was obtained from Solenne BV. ZnO nanoparticles were synthesized following the procedure published elsewhere.[55] Patterned ITO substrates, cover slides and UV-curable epoxy were purchased from Ossila. All materials were used as received.

Sample Preparation: For the temperature and thickness gradient solar cells, PCDTBT was dissolved in CB at a concentration of 15 mg mL⁻¹ and mixed with PC70BM at a concentration of 10 mg mL⁻¹ for a total solid content of 20 mg mL⁻¹. For PTB7-Th, it was dissolved in CB mixed with PC70BM at a weight ratio 1:1.5 for a total solid content of 35 mg mL⁻¹. For PffBT4T-2OD, it was dissolved in CB:oDCB 1:1 mixed with PC70BM at a weight ratio 1:1.2 for a total solid content of 20 mg mL⁻¹, the solution was stirred overnight at 80 °C. ITO coated substrates with patterned electrodes and cut glass microscope slides were cleaned by consecutive sonication for 15 min in acetone, water with detergent and isopropanol, rinsing them with water after the detergent step. Following the solvent cleaning they were treated with ozone for 20 min. For the PCDTBT composition gradient separate solutions containing 20 mg mL⁻¹ of polymer and PC70BM were prepared in CB, then casted at a speed of 10 mm s⁻¹ with the substrate at 100 °C and using 50 µL of active layer solution. For the PTB7-Th and PffBT4T-2OD composition gradient, separate solutions containing 15 mg mL⁻¹ of the polymer and 25 mg mL⁻¹ of PC70BM were prepared in CB:oDCB 1:1 and then casted at a speed of 7 mm s⁻¹ with the substrate at 100 °C using 60 µL of active layer solution. Knife coater equipment consisted of an automatic coater Zehntner ZAA 2300 and an aluminum blade Zehntner ZUA 2000.

Light Beam Induced Current: LBIC was measured on a custom-made system. The sample was located on a motorized X, Y, and Z stage, and illuminated locally by a 532 nm laser (Thorlabs, CPS532). After passing through a multimode optical fiber and a beamsplitter (Thorlabs, EBS1), the laser was focused on the device using a long working distance 20× Mitutoyo objective. The incident light intensity was monitored with a photodiode power sensor (Thorlabs, S120VC) connected to a digital power meter (Thorlabs, PM100D). The short circuit current was monitored with a multimeter (Keithley 2400 SourceMeter). Data was acquired using custom software that allowed keeping the sample plane in focus and the diameter of the laser spot below 30 µm.

Raman imaging: Raman scattering images were acquired using a WITec alpha 300 RA+ confocal Raman setup. The samples were placed on a combined step motor/piezo stage and excited through a 10× objective using a solid state laser centered at 488 nm. Images were analyzed using WITec Project FOUR software. The quantitative modeling of the Raman-scattered light was performed using home-made fitting routines in MATLAB.

Ellipsometry: Variable angle spectroscopic ellipsometry was performed using a SEMILAB GES5 rotating polarizer ellipsometry. At least three angles of incidence were collected for each sample, and two different film thicknesses were analyzed. Fitting of the experimental data was

performed using the Standard Critical Point model implemented in the Winelli II piece of software.

Supporting Information

Supporting Information is available from the Wiley Online Library or from the author.

Conflict of Interest

The authors declare no conflict of interest.

[1] C. K. Chiang, C. R. Fincher, Y. W. Park, A. J. Heeger, H. Shirakawa, E. J. Louis, S. C. Gau, A. G. MacDiarmid, *Phys. Rev. Lett.* **1977**, *39*, 1098.

[2] C. W. Tang, *Appl. Phys. Lett.* **1986**, *48*, 183.

[3] J. J. M. Halls, C. A. Walsh, N. C. Greenham, E. A. Marseglia, R. H. Friend, S. C. Moratti, A. B. Holmes, *Nature* **1995**, *376*, 498.

[4] G. Yu, J. Gao, J. C. Hummelen, F. Wudl, A. J. Heeger, *Science* **1995**, *270*, 1789.

[5] G. Li, V. Shrotriya, J. Huang, Y. Yao, T. Moriarty, K. Emery, Y. Yang, *Nat. Mater.* **2005**, *4*, 864.

[6] F. Padinger, R. S. Rittberger, N. S. Sariciftci, *Adv. Funct. Mater.* **2003**, *13*, 85.

[7] S. E. Shaheen, C. J. Brabec, N. S. Sariciftci, F. Padinger, T. Fromherz, J. C. Hummelen, *Appl. Phys. Lett.* **2001**, *78*, 841.

[8] L. Lu, T. Zheng, Q. Wu, A. M. Schneider, D. Zhao, L. Yu, *Chem. Rev.* **2015**, *115*, 12666.

[9] H. Zhou, Y. Zhang, C.-K. Mai, S. D. Collins, G. C. Bazan, T.-Q. Nguyen, A. J. Heeger, *Adv. Mater.* **2015**, *27*, 1767.

[10] L. Zuo, C.-Y. Chang, C.-C. Chueh, S. Zhang, H. Li, A. K.-Y. Jen, H. Chen, *Energy Environ. Sci.* **2015**, *8*, 1712.

[11] J. Liu, X. Li, S. Zhang, X. Ren, J. Cheng, L. Zhu, D. Zhang, L. Huo, J. Hou, W. C. H. Choy, *Adv. Mater. Interfaces* **2015**, *2*, 1500324.

[12] J. Huang, J. H. Carpenter, C.-Z. Li, J.-S. Yu, H. Ade, A. K.-Y. Jen, *Adv. Mater.* **2016**, *28*, 967.

[13] X. Ouyang, R. Peng, L. Ai, X. Zhang, Z. Ge, *Nat. Photonics* **2015**, *9*, 520.

[14] R. Gómez-Bombarelli, J. Aguilera-Iparraguirre, T. D. Hirzel, D. Duvenaud, D. Maclaurin, M. A. Blood-Forsythe, H. S. Chae, M. Einzinger, D.-G. Ha, T. Wu, G. Markopoulos, S. Jeon, H. Kang, H. Miyazaki, M. Numata, S. Kim, W. Huang, S. I. Hong, M. Baldo, R. P. Adams, A. Aspuru-Guzik, *Nat. Mater.* **2016**, *15*, 1120.

[15] S. Few, J. M. Frost, J. Kirkpatrick, J. Nelson, *J. Phys. Chem. C* **2014**, *118*, 8253.

[16] Y. Shin, J. Liu, J. J. Quigley, H. Luo, X. Lin, *ACS Nano* **2014**, *8*, 6089.

[17] M. S. Vezie, S. Few, I. Meager, G. Pieridou, B. Dörling, R. S. Ashraf, A. R. Goñi, H. Bronstein, I. McCulloch, S. C. Hayes, M. Campoy-Quiles, J. Nelson, *Nat. Mater.* **2016**, *15*, 746.

[18] M. C. Scharber, N. S. Sariciftci, *Prog. Polym. Sci.* **2013**, *38*, 1929.

[19] D. Baran, T. Kirchartz, S. Wheeler, S. Dimitrov, M. Abdelsamie, J. Gorman, R. S. Ashraf, S. Holliday, A. Wadsworth, N. Gasparini, P. Kaienburg, H. Yan, A. Amassian, C. J. Brabec, J. R. Durrant, I. McCulloch, *Energy Environ. Sci.* **2016**, *9*, 3783.

[20] J. A. Renz, T. Keller, M. Schneider, S. Shokhovets, K. D. Jandt, G. Gobsch, H. Hoppe, *Sol. Energy Mater. Sol. Cells* **2009**, *93*, 508.

[21] A. Teichler, R. Eckardt, S. Hoeppener, C. Friebe, J. Perelaer, A. Senes, M. Morana, C. J. Brabec, U. S. Schubert, *Adv. Energy Mater.* **2011**, *1*, 105.

[22] J. Alstrup, M. Jørgensen, A. J. Medford, F. C. Krebs, *ACS Appl. Mater. Interfaces* **2010**, *2*, 2819.

[23] J. H. Lee, T. Sagawa, S. Yoshikawa, *Energy Technol.* **2013**, *1*, 85.

[24] F. Nickel, C. Sprau, M. F. G. Klein, P. Kapetana, N. Christ, X. Liu, S. Klinkhammer, U. Lemmer, A. Colsmann, *Sol. Energy Mater. Sol. Cells* **2012**, *104*, 18.

[25] S. Höfle, T. Lutz, A. Egel, F. Nickel, S. W. Kettlitz, G. Gomard, U. Lemmer, A. Colsmann, *ACS Photonics* **2014**, *1*, 968.

[26] H. Hoppe, J. Bachmann, B. Muhsin, K.-H. Drüe, I. Riedel, G. Gobsch, C. Buerhop-Lutz, C. J. Brabec, V. Dyakonov, *J. Appl. Phys.* **2010**, *107*, 14505.

[27] S. Savagatrup, A. D. Printz, T. F. O'Connor, I. Kim, D. J. Lipomi, *Chem. Mater.* **2017**, *29*, 389.

[28] C. M. Stafford, K. E. Roskov, T. H. Epps, M. J. Fasolka, *Rev. Sci. Instrum.* **2006**, *77*, 23908.

[29] F. Nickel, C. Sprau, M. F. G. Klein, P. Kapetana, N. Christ, X. Liu, S. Klinkhammer, U. Lemmer, A. Colsmann, *Sol. Energy Mater. Sol. Cells* **2012**, *104*, 18.

[30] X. Rodríguez-Martínez, M. S. Vezie, X. Shi, I. McCulloch, J. Nelson, A. R. Goñi, M. Campoy-Quiles, *J. Mater. Chem. C* **2017**, *5*, 7270.

[31] M. Campoy-Quiles, M. I. Alonso, D. D. C. Bradley, L. J. Richter, *Adv. Funct. Mater.* **2014**, *24*, 2116.

[32] M. Campoy-Quiles, M. Sims, P. G. Etchegoin, D. D. C. Bradley, *Macromolecules* **2006**, *39*, 7673.

[33] O. V. Mikhnenko, P. W. M. Blom, T.-Q. Nguyen, S. McIlroy, P. Sreearuothai, A. R. Cook, H. Jiang, J. R. Miller, K. S. Schanze, T. Aoyama, D.-W. Kim, S. Yoon, J.-Y. Bigot, J. W. Wu, J. C. Ribierre, *Energy Environ. Sci.* **2015**, *8*, 1867.

[34] J. Cabanillas–Gonzalez, O. Peña–Rodríguez, I. Suarez Lopez, M. Schmidt, M. I. Alonso, A. R. Goñi, M. Campoy–Quiles, *Appl. Phys. Lett.* **2011**, *99*, 103305.

[35] Z. Tang, Z. Ma, A. Sánchez-Díaz, S. Ullbrich, Y. Liu, B. Siegmund, A. Mischok, K. Leo, M. Campoy-Quiles, W. Li, K. Vandewal, *Adv. Mater.* **2017**, *29*, 1702184.

[36] L. Lu, M. A. Kelly, W. You, L. Yu, *Nat. Photonics* **2015**, *9*, 491.

[37] C. Müller, T. A. M. Ferenczi, M. Campoy-Quiles, J. M. Frost, D. D. C. Bradley, P. Smith, N. Stingelin-Stutzmann, J. Nelson, *Adv. Mater.* **2008**, *20*, 3510.

[38] M. T. Lloyd, C. H. Peters, A. Garcia, I. V. Kauvar, J. J. Berry, M. O. Reese, M. D. McGehee, D. C. Ginley, D. C. Olson, *Sol. Energy Mater. Sol. Cells* **2011**, *95*, 1382.

[39] J. M. Kroon, M. M. Wienk, W. J. H. Verhees, J. C. Hummelen, *Thin Solid Films* **2002**, *403–404*, 223.

[40] T. Jeranko, H. Tributsch, N.. Sariciftci, J.. Hummelen, *Sol. Energy Mater. Sol. Cells* **2004**, *83*, 247.

[41] A. J. Clulow, A. Armin, K. H. Lee, A. K. Pandey, C. Tao, M. Velusamy, M. James, A. Nelson, P. L. Burn, I. R. Gentle, P. Meredith, *Langmuir* **2014**, *30*, 1410.

[42] W. R. Mateker, T. Heumueller, R. Cheacharoen, I. T. Sachs-Quintana, M. D. McGehee, J. Warnan, P. M. Beaujuge, X. Liu, G. C. Bazan, *Chem. Mater.* **2015**, *27*, 6345.

[43] O. Dyck, S. Hu, S. Das, J. Keum, K. Xiao, B. Khomami, G. Duscher, *Polymers* **2015**, *7*, 2446.

[44] C. Cui, W.-Y. Wong, Y. Li, *Energy Environ. Sci.* **2014**, *7*, 2276.

[45] D. C. Watters, J. Kingsley, H. Yi, T. Wang, A. Iraqi, D. Lidzey, *Org. Electron.* **2012**, *13*, 1401.

[46] J. W. Kiel, B. J. Kirby, C. F. Majkrzak, B. B. Maranville, M. E. Mackay, *Soft Matter* **2010**, *6*, 641.

[47] B. A. Collins, Z. Li, J. R. Tumbleston, E. Gann, C. R. McNeill, H. Ade, *Adv. Energy Mater.* **2013**, *3*, 65.

[48] Y. Liu, J. Zhao, Z. Li, C. Mu, W. Ma, H. Hu, K. Jiang, H. Lin, H. Ade, H. Yan, *Nat. Commun.* **2014**, *5*, 5293.

[49] T.-Y. Chu, S. Alem, P. G. Verly, S. Wakim, J. Lu, Y. Tao, S. Beaupré, M. Leclerc, F. Bélanger, D. Désilets, S. Rodman, D. Waller, R. Gaudiana, *Appl. Phys. Lett.* **2009**, *95*, 63304.

[50] R. A. Street, D. Davies, P. P. Khlyabich, B. Burkhart, B. C. Thompson, *J. Am. Chem. Soc.* **2013**, *135*, 986.

[51] Y. Chen, P. Ye, X. Jia, W. Gu, X. Xu, X. Wu, J. Wu, F. Liu, Z.-G. Zhu, H. Huang, *J. Mater. Chem. A* **2017**, *5*, 19697.

[52] H. D. Young, F. W. Sears, *University Physics*, Addison-Wesley Pub. Co, Reading, MA, USA **1992**.

[53] T. Ashida, A. Miyamura, N. Oka, Y. Sato, T. Yagi, N. Taketoshi, T. Baba, Y. Shigesato, *J. Appl. Phys.* **2009**, *105*, 73709.

[54] O. Synooka, K.-R. Eberhardt, C. R. Singh, F. Hermann, G. Ecke, B. Ecker, E. von Hauff, G. Gobsch, H. Hoppe, *Adv. Energy Mater.* **2014**, *4*, 1300981.

[55] D. A. Schwartz, N. S. Norberg, Q. P. Nguyen, J. M. Parker, D. R. Gamelin, *J. Am. Chem. Soc.* **2003**, *125*, 13205.

163

**ADVANCED
ELECTRONIC
MATERIALS**

Supporting Information

High-Throughput Multiparametric Screening of Solution Processed Bulk Heterojunction Solar Cells

Antonio Sánchez-Díaz, Xabier Rodríguez-Martínez, Laura Córcoles-Guija, Germán Mora-Martín, and Mariano Campoy-Quiles*

Supporting Information

High throughput multiparametric screening of solution processed bulk heterojunction solar cells

Antonio Sánchez-Díaz, Xabier Rodríguez-Martínez, Laura Córcoles-Guija, Germán Mora-Martín, and Mariano Campoy-Quiles*

Dr. A. Sánchez-Díaz, X. Rodríguez-Martínez, L. Córcoles-Guija, G. Mora-Martín, Dr. M. Campoy-Quiles
Institut de Ciència de Materials de Barcelona (ICMAB-CSIC), Campus UAB S/N, 08193 Bellaterra (Barcelona), Spain
E-mail: mcampoy@icmab.es

Contents:

A. Refractive indices of PCDTBT and PC70BM

Figure S1. Refractive indices of PCDTBT and PC70BM as measured by means of variable-angle spectroscopic ellipsometry (VASE).

B. Characterization of films with lateral thickness gradients
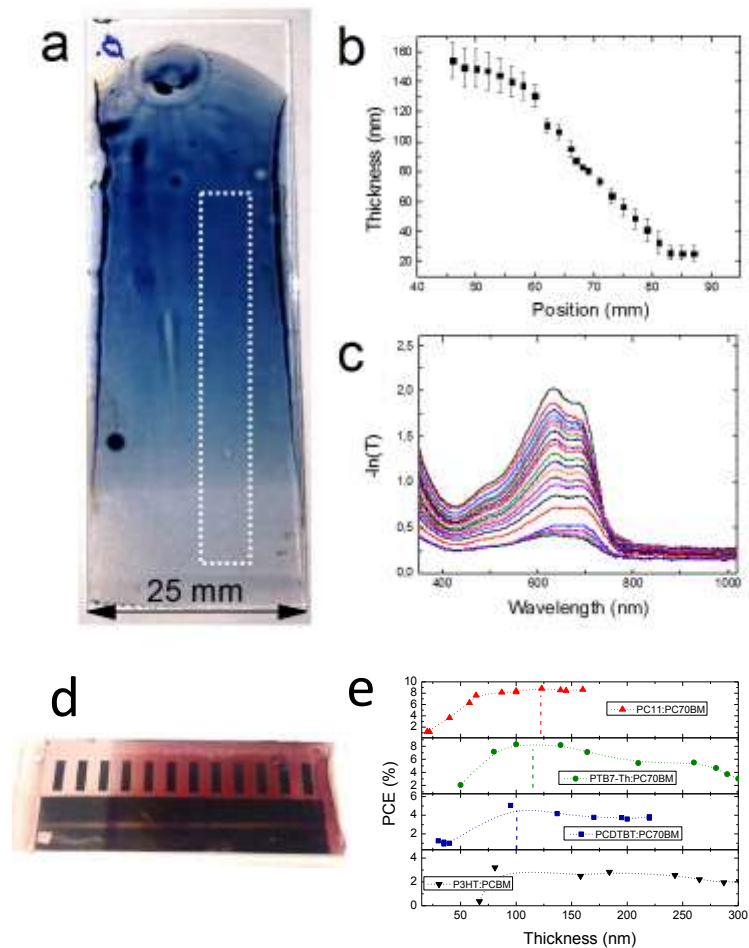
Figure S2. a) Optical image of a neat PTB7-Th film casted on glass showing a thickness

wedge increasing from bottom to top of the image. b) Quantification by means of ellipsoemtry

of the film thickness as a function of position along the area marked with a dotted white

rectangle in a). c) Transmittance as a function of position of the same area in normal

incidence. d) Photograph of a PCDTBT:PC70BM solar cell with a gradient in thickness and

two types of electrodes, pixelated electrodes (top) and continuous electrode (bottom, for

LBIC). e) Thickness dependence of solar cells prepared with different materials.

C. Exploration of the processing window to obtain films with a composition gradient

The fabrication of blade coated films using two nearby drops of dissimilar materials required an initial exploration of the experimental conditions that yielded the films with the desired properties, i.e. a smooth mixing and gradient-like variation of the composition throughout the mixing interface (in this case corresponding to the long axis of the typical 25 x 75 mm^2 glass slides). We mainly explored how the casting speed, *aka* the blade velocity, as well as the substrate temperature influenced the final film appearance and morphology as they are the two parameters that affect the most during processing. The rest of parameters including the blade gap, the pipetted volume and the concentration of the solutions were kept constant (according to the experimental details reported in the main manuscript). Figure S3 depicts the collection of samples that we prepared in order to infer the phase diagram showed in Figure 2 in the manuscript. Despite this short study was performed using the PTB7-Th:PC70BM donor:acceptor pair, the results extracted therein were readily applied to the rest of material combinations explored in this work leading to high-quality, composition graded films.
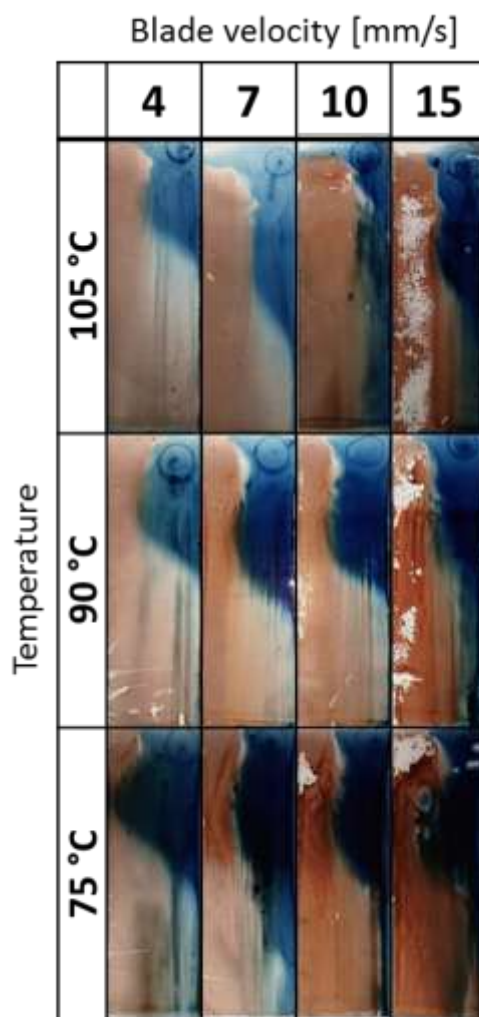
Figure S3. Optical pictures (taken in reflection with a cell phone) of the PTB7-Th:PC70BM samples prepared to explore the influence of the processing parameters on the mixing and morphology of the film. All films were casted on bare glass substrates previously rinsed and sonicated in acetone and isopropyl alcohol. Their dimensions are 25 mm width by 75 mm height.
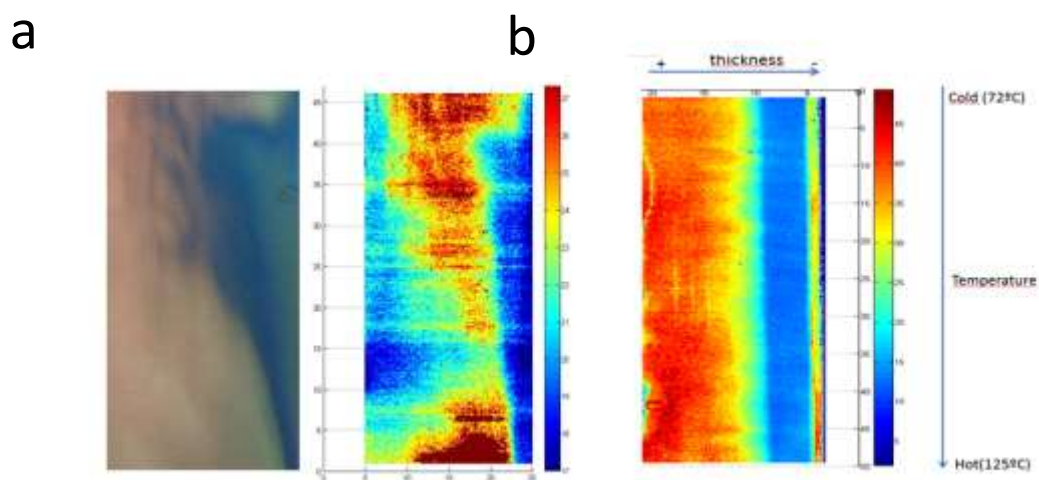
D. Solar cells based on PffBT4T-2OD:PC70BM

Figure S4. The LBIC data extracted from a PffBT4T-2OD:PC70BM solar cell showing a

lateral gradient in composition (a) and a 2D gradient in thickness and temperature (b).

E. Optimization of the processing additive (DIO) concentration in PTB7-Th:PC70BM solar cells
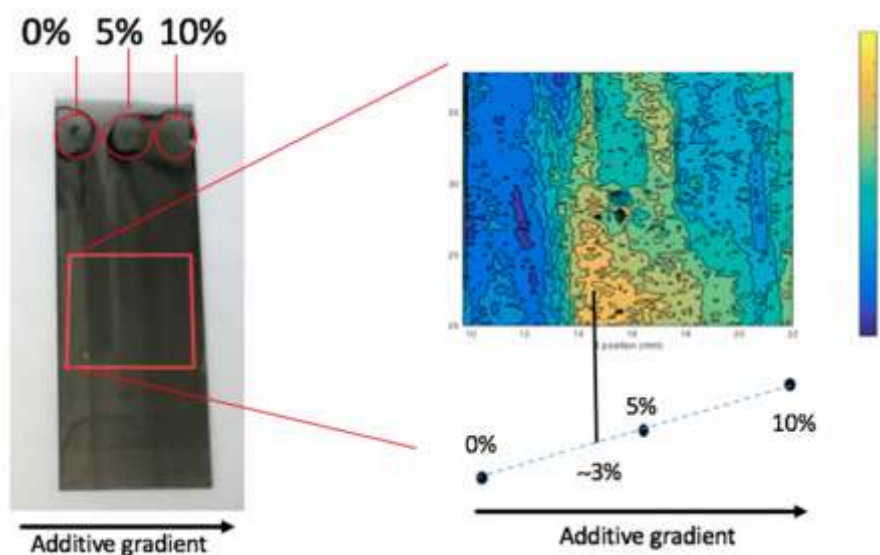
Figure S5. The LBIC data extracted from a PTB7-Th:PC70BM solar cell showing a lateral gradient in the amount of solvent additive used to process the film indicates that the optimum device performance is achieved when the content is close to 3 vol%.

F. Estimation of the fabrication time of the photovoltaic devices

The manufacture time spent in the fabrication of the solar cells comprises a series of steps which we assume to be perfectly optimized and working in their first attempt. The allocated times for each step are based on our own experience fabricating devices in four different laboratories (namely Imperial College London (UK), Japan Advanced Institute of Science and Technology (Japan), Institute of Chemical Research of Catalonia (Spain) and ICMAB-CSIC (Spain). The reader can adapt the timings below to the specific protocols used in their laboratories, which may slightly vary from lab to lab. The fabrication steps can be listed as:

- Preparation of the solutions of the materials forming the active layer, assuming we prepare solutions of different blending ratios: 1 hour + stirring overnight for at least 8 hours.

- We will assume that we use a commercial solution of ZnO (which is not our case indeed).

- Glass + ITO substrate cleaning, following the traditional protocol of consecutive sonication for 15 minutes in acetone, soap and IPA, followed by blow drying and ozone treatment for 20. We usually perform the process using tanks containing up to 9 substrates, which implies that in the best case we will spend close to 1.5 hours in the cleaning process.

- Blade coating of ZnO in 9 substrates. About 5 minutes per sample, yields 1 hour.

- Blade coating of the active layer, same conditions as ZnO leads to 1 more hour.

- The evaporation can only be done in batches of 9 substrates due to limitations of the mask. The time spent per batch can be approximated as follows: sample loading (15 minutes) + vacuum (3 hours) + evaporation of MoO_3 and Ag (30 minutes) + refill (15 minutes) = 4 hours.

- All these processes sum up nearly 15.5 hours of experimental time per batch. Assuming that we prepare 27 samples (three consecutive batches of 9 devices) we can estimate that the experimental time required per sample in the typical lab is of the order of 1.7 hours.

PAPER IV

Microfluidic-Assisted Blade Coating of Compositional Libraries for Combinatorial Applications: The Case of Organic Photovoltaics

X. Rodríguez-Martínez, S. Sevim, X. Xu, C. Franco, P. Pamies-Puig, L. Córcoles-Guija, R. Rodriguez-Trujillo, F. J. del Campo, D. Rodriguez San Miguel, A. J. DeMello, S. Pané, D. B. Amabilino, O. Inganäs, J. Puigmartí-Luis, M. Campoy-Quiles, *Adv. Energy Mater.* **2020**, 2001308.

Microfluidics and doctor blading are combined to define a novel processing scheme that enables the transfer of compositional gradients in solution to solid films. This versatile approach is exploited to generate blending ratio libraries in all-polymer organic solar cells. The method is broadly applicable to other solution-processable systems that require lateral compositional gradients for efficient, high-throughput combinatorial screening.
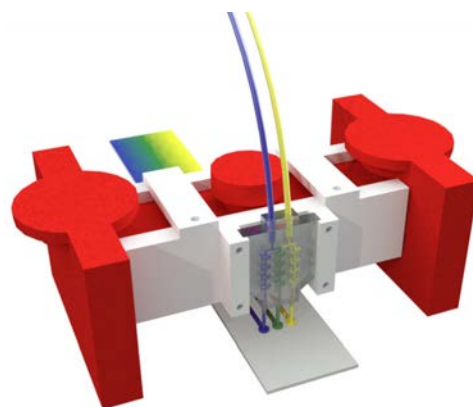
Microfluidic-Assisted Blade Coating of Compositional Libraries for Combinatorial Applications: The Case of Organic Photovoltaics

Xabier Rodríguez-Martínez, Semih Sevim, Xiaofeng Xu, Carlos Franco, Paula Pamies-Puig, Laura Córcoles-Guija, Romen Rodriguez-Trujillo, Francisco Javier del Campo, David Rodriguez San Miguel, Andrew deMello, Salvador Pané, David B. Amabilino, Olle Inganäs, Josep Puigmartí-Luis,* and Mariano Campoy-Quiles*

Microfluidic technologies are highly adept at generating controllable compositional gradients in fluids, a feature that has accelerated the understanding of the importance of chemical gradients in biological processes. That said, the development of versatile methods to generate controllable compositional gradients in the solid-state has been far more elusive. The ability to produce such gradients would provide access to extensive compositional libraries, thus enabling the high-throughput exploration of the parametric landscape of functional solids and devices in a resource-, time-, and cost-efficient manner. Herein, the synergic integration of microfluidic technologies is first reported with blade coating to enable the controlled formation of compositional lateral gradients in solution. Subsequently, the transformation of liquid-based compositional gradients into solid-state thin films using this method is demonstrated. To demonstrate efficacy of the approach, microfluidic-assisted blade coating is used to optimize blending ratios in organic solar cells. Importantly, this novel technology can be easily extended to other solution processable systems that require the formation of solid-state compositional lateral gradients.

Control of compositional gradients has been exploited in multiple materials to engineer new physical and chemical properties as well as novel functionalities. For example, gradual changes in absorption can be used to create tunable density filters,[1] and subtle variations in surface energy can drive water drops uphill.[2] Additionally, compositionally graded materials allow the investigation of the role of compositional effects on a desired property of interest. Examples in this respect include the screening of biochemical signals on cell behavior,[3] the maximization of piezoelectric coefficients,[4] the rapid exploration of material blend phase diagrams,[5] as well as the determination of the optimum composition in ternary photovoltaic devices.[6]

Material libraries are of increasing interest in printed electronics.[7] Indeed,

X. Rodríguez-Martínez, P. Pamies-Puig, L. Córcoles-Guija,
Dr. R. Rodriguez-Trujillo, Dr. M. Campoy-Quiles
Instituto de Ciencia de Materiales de Barcelona
ICMAB (CSIC)
Esfera UAB
Campus Universidad Autónoma de Barcelona
Bellaterra, Barcelona 08193, Spain
E-mail: mcampoy@icmab.es
S. Sevim, Dr. C. Franco, Dr. D. Rodriguez San Miguel, Prof. A. deMello,
Dr. J. Puigmartí-Luis
Institute of Chemical and Bioengineering
ETH Zurich
Vladimir Prelog Weg 1, Zurich 8093, Switzerland
E-mail: josep.puigmarti@chem.ethz.ch
Dr. X. Xu, Prof. O. Inganäs
Biomolecular and Organic Electronics
Department of Physics
Chemistry and Biology (IFM)
Linköping University
Linköping SE-581 83, Sweden

The ORCID identification number(s) for the author(s) of this article can be found under https://doi.org/10.1002/aenm.202001308.

DOI: 10.1002/aenm.202001308

Dr. X. Xu
Department of Materials Science and Engineering
Ocean University of China
Songling Road 238, Qingdao 266100, China
Dr. R. Rodriguez-Trujillo
Department of Electronics and Biomedical Engineering
University of Barcelona
C/Martí i Franquès 1, Barcelona 08028, Spain
Dr. F. J. del Campo
Instituto de Microelectrónica de Barcelona
IMB-CNM (CSIC)
Esfera UAB
Campus Universidad Autónoma de Barcelona
Bellaterra, Barcelona 08193, Spain
Dr. F. J. del Campo
BCMaterials
Basque Center for Materials
Applications and Nanostructures
UPV/EHU Science Park, Leioa 48940, Spain
Dr. F. J. del Campo
IKERBASQUE
Basque Foundation for Science
Bilbao, Spain

**ADVANCED
SCIENCE NEWS**

www.advancedsciencenews.com

**ADVANCED
ENERGY
MATERIALS**

www.advenergymat.de

feedback between theoretical screening studies[8–11] and high-throughput experimentation[12–14] has accelerated the discovery of new high-performing organic conjugated materials. In the case of organic photovoltaics (OPV), nonfullerene acceptors have recently emerged as promising substitutes for traditional fullerenes as *n*-type semiconductors.[15] On the other hand, polymer:polymer solar cells, which provide a range of printing and stability advantages,[16] start rivaling polymer:fullerene power conversion efficiencies.[17–20]

In a fundamental sense, each novel material combination requires an independent evaluation with regard to photovoltaic performance. The optimization of bulk heterojunction organic solar cells entails the exploration of a highly complex parameter landscape of mutually interacting variables, including the choice of solvent, solution concentration, casting temperature, donor to acceptor (D:A) ratio, film thickness, and annealing temperature.[21] The exploration of such a complex parametric space usually involves a classical sample-by-sample methodology (an Edisonian approach), which is often prohibitively costly in terms of both experimental time and resources. Indeed, discrete sampling remains the primary optimization protocol followed by most researchers in the OPV field, a fact that significantly limits the rate of materials screening and throttles the development of novel high performing devices. Accordingly, the use of combinatorial approaches based on gradients in the parameters of interest (such as film thickness,[12,22,23] morphology,[12,23] and composition[5,6,12,24–26]) represents an ideal route to accelerating such screening processes.[27,28] Whilst several approaches, based on the combination of design-of-experiments and machine-learning algorithms[29,30] as well as robotized laboratories,[31,32] have been used to address the challenges of high-throughput multiparametric screening, these methods generally require either large amounts of raw materials to fully explore the parametric space (rendering them suitable only when optimized synthetic routes or large synthetic batches are readily available)[24] or have limited reproducibility and are restricted to precise processing conditions in terms of ink rheology.[12] In this regard, more versatile experimental procedures are still needed in order to explore the entire parameters versus performance landscape in such complex optimization scenarios in a cost- and material-efficient manner.

Microfluidic technologies can be highly useful in generating compositional libraries in solution. Early reports in this regard date back to 2000,[33] with more recent studies highlighting utility in fields ranging from biology[34] to electronics.[35] In most of these investigations the generated compositional profiles are exploited directly in the liquid-state, with their transfer to solid films being far from straightforward. Microfluidic-based drop casting experiments have been used to optimize organic thin film transistors,[36] as well as transparent

Dr. S. Pané
Institute of Robotics and Intelligent Systems
ETH Zurich
Tannenstrasse 3, Zurich 8092, Switzerland
Prof. D. B. Amabilino
School of Chemistry
University of Nottingham
Nottingham NG7 2RD, UK

conductive electrodes.[37] However, these approaches are unsuitable for most applications in which large areas of nanometer-thick material films are required. Accordingly, advanced mixing and casting methodologies are urgently required to address all such demands.

Herein, we introduce a completely new microfluidic approach for the generation of solid-state thin films with lateral compositional gradients. Films are formed by blade coating of solutions delivered from the outlet channels of a microfluidic device. We show that such approach enables the efficient and large area transfer of compositional gradients generated in solution to solid state thin films onto virtually any substrate. Additionally, we show that the solid-state lateral composition profile of these microfluidically produced thin films can be finely tuned by the variation of the processing conditions, such as the total flow rate and blade coating speed. To demonstrate efficacy, we specifically optimize the chemical composition as well as the performance of polymer:polymer blend-based organic solar cells. Such systems represent a formidable challenge, due to their intrinsic high viscosities and difficult mixing dynamics.

To generate a binary compositional gradient, we utilized a microfluidic mixer incorporating two inlets (one for each of the pristine solutions) and a symmetric branched manifold that allows the distribution of the two precursor solutions into three different streams. The three streams are then directly introduced into the blade reservoir to generate a thin film (**Figure 1**a). This symmetric triple branched microfluidic device can be used to controllably generate solid state binary compositional gradients on surfaces. To ensure the efficient mixing of the two precursor solutions (the blue and yellow solutions in Figure 1a), 3D mixers, such as those based on the baker's transformation,[38] were also considered. It should be noted that these mixing units have been shown to yield the highest mixing efficiencies among passive microfluidic mixers.[39,40] In the current experiments, four interconnected baker's units were used to provide complete and homogeneous mixing at the outlet channels without the need for additional mixing units, such as extended zig-zag microfluidic channels.[41,42] Such a microfluidic design guarantees that only the middle branch generates a mixture of the two pristine precursor solutions that are flowing through the side-branched channels (inset in Figure 1a). Additionally, we systematically explored a variety of outlet configurations, including confluent and individual routing options, as well as slot-die and nozzle-like ejection models (Figures S1–S4, Supporting Information). After a thorough examination of different designs, we concluded that the solid-state compositional profiles obtained when using individual nozzles at the outlet channels were smoother and more reproducible. Moreover, it was observed that the gap between the nozzles and the substrate is key in ensuring continuous fluid ejection during the coating process, rather than a dropwise outflow. Dropwise flows eventually result in inhomogeneous films due to Marangoni flows induced in the evaporating drops (**Figure 2**).

We next evaluated the mixing performance and the composition profiles obtained in the films. The marriage of microfluidic solution processing and blade coating aims to transfer the controllable parametric profiles (compositional ratios in the present case) formed in solution (Figure 1b) to a solid-state thin

**ADVANCED
SCIENCE NEWS**

www.advancedsciencenews.com

**ADVANCED
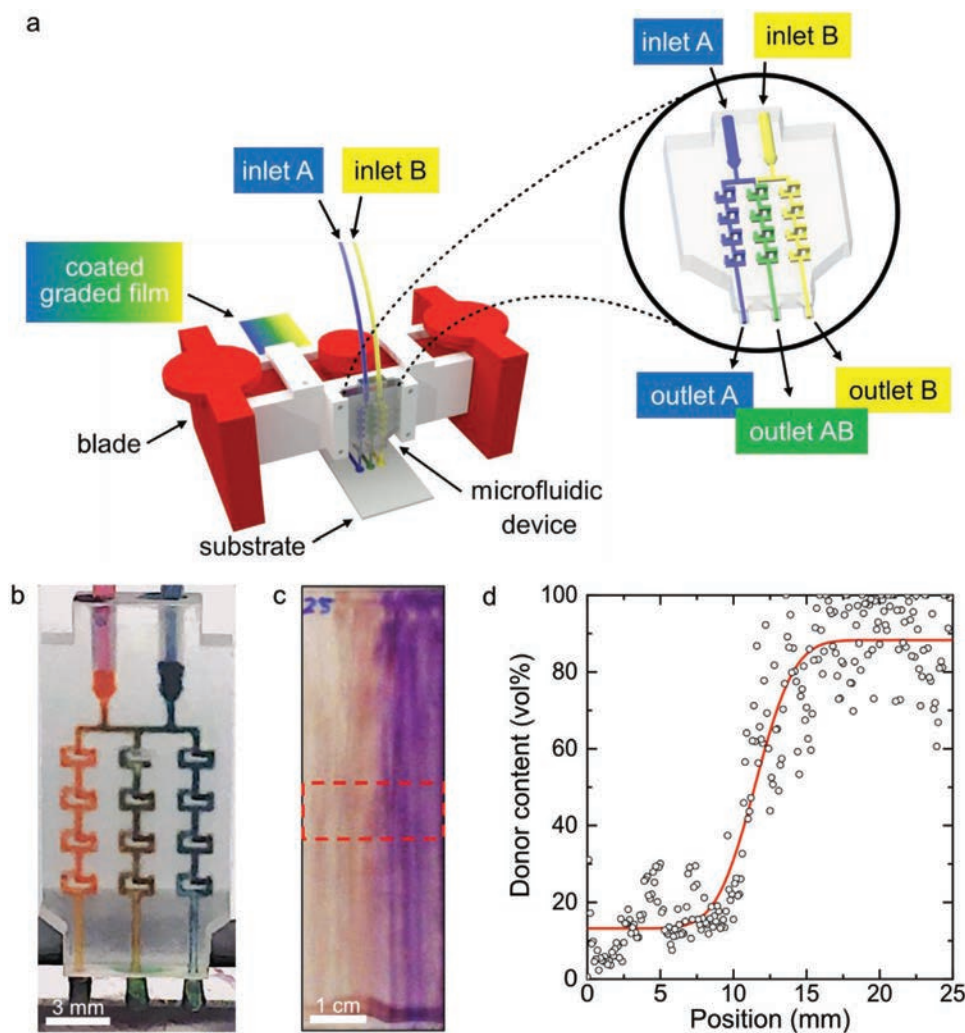ENERGY
MATERIALS**

www.advenergymat.de

Figure 1. a) Schematic of the microfluidic-assisted blade coating platform used to fabricate films containing lateral compositional gradients. The inset shows a 3D model of the microfluidic device. b) Image of the microfluidic device under operation with poly(3-hexylthiophene-2,5-diyl) (P3HT, left stream) and poly{[N,N′-bis(2-octyldodecyl)-naphthalene-1,4,5,8-bis(dicarboximide)-2,6-diyl]-alt-5,5′-(2,2′-bithiophene)} (N2200, right stream) dissolved in chlorobenzene. Note that this particular material choice was made to demonstrate generality of the method and to be able to visualize the color contrast in a simple optical image. c) A reflection image of a blade coated film on glass (25×75 mm^2) showing a lateral compositional gradient extending from pure PC$_{70}$BM (left side) to neat PCDTBT (right side). The observed longitudinal stripes parallel to the coating direction are ascribed to thickness fluctuations. d) Averaged composition profile of the dotted area marked in panel (c) obtained by means of Raman spectroscopy imaging.

film (Figure 1c). Note that a different blend is shown in each image demonstrating the generality of the method. We focused our initial experiments on polymer:fullerene blends, namely poly[N-9′-heptadecanyl-2,7-carbazole-alt-5,5-(4′,7′-di-2-thienyl-2′,1′,3′-benzothiadiazole)]: [6,6]-phenyl-C$_{71}$-butyric acid methyl ester (PCDTBT:PC$_{70}$BM), which constitutes a high performing material combination in OPV, and one which has also been recently subjected to combinatorial screening.[12] Accordingly, we characterized the quality of the mixing and the influence of experimental processing variables (blade velocity and the outflow rate) by directly probing composition in the solid-state. Characterization was performed by Raman imaging (Figure 1d) and modeling according to our previously developed methodology,[12,43] which allows extraction of both composition and photocurrent maps in a single experiment. It should be noted that modeling involved the use of previously reported values of

the complex refractive index and Raman cross-section for both materials.[12,43] A simple visual inspection (in reflection mode) of films supported on glass substrates (Figure 1c) immediately suggests the formation of lateral compositional gradients. Additionally, optically dense longitudinal stripes in the coating direction can be seen. According to Raman spectroscopy analysis these stripes can be ascribed to film thickness inhomogeneities that do not perturb the averaged lateral composition profile (Figure 1d).

Experimental investigations indicate that the film processability and the final composition profile are primarily determined by the total flow rate (Φ) and the blade coating speed (v). Φ represents the sum of the flow rates at each inlet, i.e., $\Phi = \Phi_1 + \Phi_2$. We systematically characterized the influence that both Φ and v have on the solid thin film according to the volumetric linear density (ρ) of solution poured per millimeter of

**ADVANCED
SCIENCE NEWS**

www.advancedsciencenews.com

**ADVANCED
ENERGY
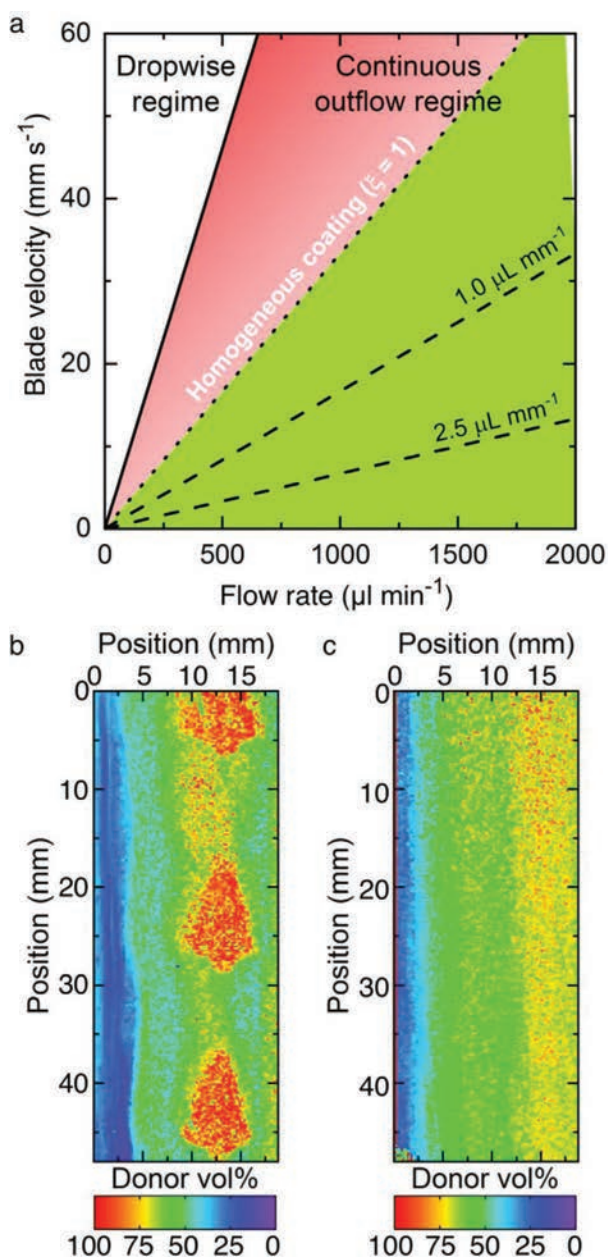MATERIALS**

www.advenergymat.de

Figure 2. a) Outflowing and coating regimes found during the micro-fluidic-assisted blade coating of films based on a phenomenological and geometrical model. b) Raman spectroscopy mapping for samples made of poly[[2,3-bis(3-octyloxyphenyl)-5,8-quinoxalinediyl]-2,5-thiophenediyl] (TQ1) as donor and N2200 as acceptor reveals that in a dropwise regime, rapid evaporation of liquid drops leads to large inhomogeneities in the solid-state. c) Conversely, when continuous outflow conditions are fulfilled, laterally homogeneous films are realized. These conditions correspond to blade velocities and outflow rates located within the green shaded area in (a). Further details of these regimes and model equations are provided in the Supporting Information.

substrate travelled by the blade, i.e., $\rho = \Phi \, v^{-1}$ [μL mm^{-1}]. In this regard, a simple geometrical model that phenomenologically delimits the required balance between Φ and v is provided in the Supporting Information. For simplicity, equal flow rates of precursor solutions (i.e., $\Phi_1 = \Phi_2$) are fixed between 600 and

900 μL min^{-1}, with a total solution volume of 50 μL injected per channel over the course of an experiment. It should be noted that prior to the generation of solid-state compositional gradients a purging step is required to realize stationary flow conditions within the branched-manifold. This step is mandatory when using differing flow rates ($\Phi_1 \neq \Phi_2$) to account for the dissimilar viscosity of the injected solutions (Figure S5, Supporting Information). Blade coating speeds were varied between 5 and 30 mm s^{-1}. It is evident that a tradeoff between Φ and v arises to successfully fabricate solid-state compositional gradients. For example, if Φ is excessively low and v excessively high, processing leads to inhomogeneous material deposition due to an insufficient supply of solution to the blade reservoir (Figure 2).

Figure 3b presents lateral composition profiles obtained for a series of PCDTBT:PC$_{70}$BM films processed at different ρ ratios. These profiles are fitted to the following model equation,

$$f(x) = \frac{a}{2} \, \mathrm{erf}\left(\frac{x-d}{b}\right) + c \tag{1}$$

which generates composition profiles (solid lines in Figure 3b) in analogy with the relationships derived from Fick's diffusion laws (vide infra). Interestingly, it can be observed that the width of the blending area (defined by b in Equation 1) linearly varies with ρ (Figure S6, Supporting Information). This finding indicates that at sufficiently high values of ρ the accumulated solution at the blade reservoir has a longer time to mix and interdiffuse during the coating process than at low ρ values, thus leading to laterally extended compositional profiles. Accordingly, besides the mixing that takes place within the baker's transformation mixers, the interdiffusion of the poured volume accumulated at the ink reservoir will also influence the solid-state compositional profiles.

It should be noted that Equation 1 is qualitatively equivalent to the relationship defined by Fick's second law for diffusion in the case of an initial release of mass at concentration c_0 (corresponding to the central outlet) that diffuses homogeneously over a finite area and with initial boundary conditions of $c_1 = 0$ (left side outlet channel) and $c_2 = 2c_0$ (right side outlet channel). In this case the spatial and temporal evolution of the concentration profile $c(x, t)$ is given by

$$c(x,t) = c_0 \left[1 + \mathrm{erf}\left(\frac{x}{\sqrt{4Dt}}\right) \right] \tag{2}$$

where D is the molecular diffusion coefficient. The comparison of Equations 1 and 2 indicates that $b \propto (4Dt)^{1/2}$, a fact that supports the observed broadening of the blending area as a function of the mixing time at the ink reservoir.

Once we had confirmed that the branched microfluidic device was able to produce solid-state compositional gradients with the well-known PCDTBT:PC$_{70}$BM pair, we demonstrated the generality of the approach with two polymers frequently used for the fabrication of OPV devices. Specifically, we fabricated large-area organic solar cells comprising a compositional gradient of poly[4,8-bis(5-(2-ethylhexyl)thiophen-2-yl)benzo[1,2-b:4,5-b']dithiophene-2,6-diyl-alt-(5-(2-ethylhexyl)-4H-thieno[3,4-c]pyrrole-4,6(5H)-dione)-1,3-diyl] (PBDT-TPD) as

**ADVANCED
SCIENCE NEWS**

www.advancedsciencenews.com
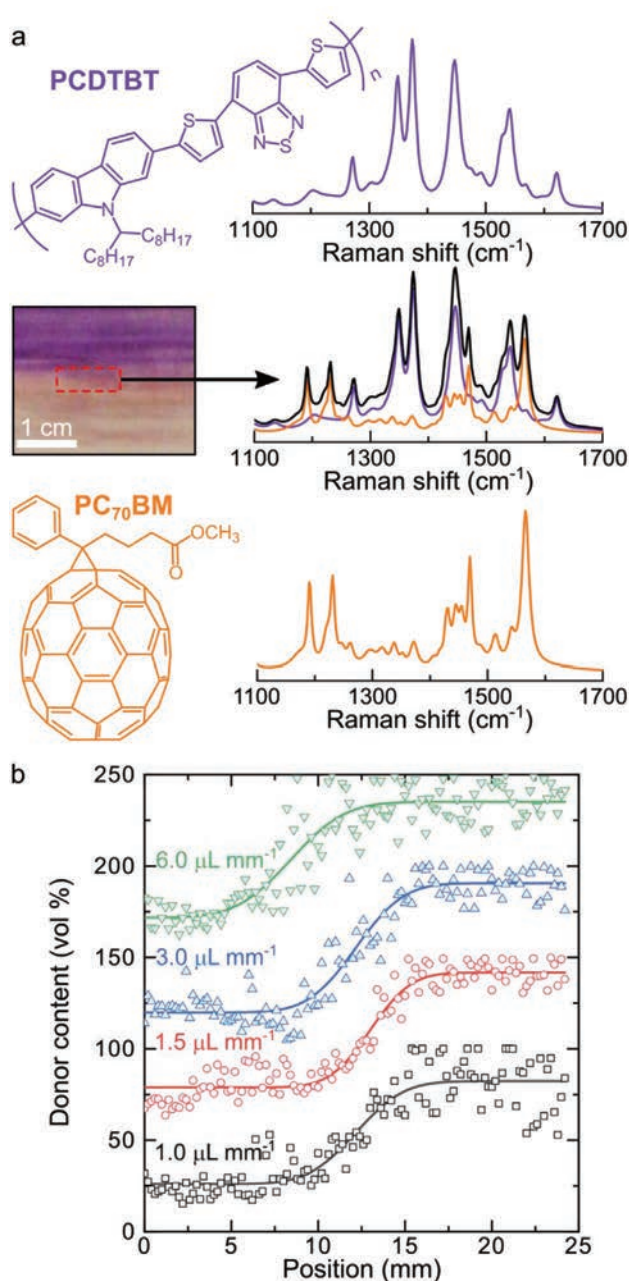
**ADVANCED
ENERGY
MATERIALS**

www.advenergymat.de

Figure 3. a) Raman spectra measured in PCDTBT:PC$_{70}$BM compositional gradient films can be deconvoluted into the corresponding vibrational fingerprint components for the polymer (purple line) and the fullerene (orange line). Accordingly, the deconvolution serves to quantify the blending ratio.[43] b) Lateral composition profiles for PCDTBT:PC$_{70}$BM films obtained at different volumetric linear densities (ρ). The datasets have been offset along the y-axis for clarity.

Figure 4. a) Molecular structures and normalized Raman vibrational fingerprints measured using 488 nm excitation of the conjugated polymers PBDT-TPD (blue, donor) and PNDI-T (red, acceptor). b) The corresponding complex refractive indices measured by means of variable-angle spectroscopic ellipsometry (VASE) on blade coated films supported on glass.

donor and poly[[N,N'-bis(2-octyldodecyl)-naphthalene-1,4,5,8-bis(dicarboximide)-2,6-diyl]-*alt*-thiophene-2,5-diyl] (PNDI-T) as acceptor (**Figure 4**a). The PBDT-TPD:PNDI-T blend constitutes one of the best performing all-polymer combinations currently used for OPV devices.[44] Such solar cells should provide for a well-controlled lateral compositional gradient in their active layer to enable fast and efficient optimization via concur-

rent Raman and photocurrent imaging.[12] As for the previous system, elucidation of composition from Raman measurements involved determination of the complex refractive index (Figure 4b) and Raman cross-section (Figures S7 and S8, Supporting Information) for the two polymers. It is important to note that the use of Raman spectroscopy in the determination of composition is particularly useful for materials with overlapping absorption features (as in the current case; Figure 4b) and when high spatial resolution is required.
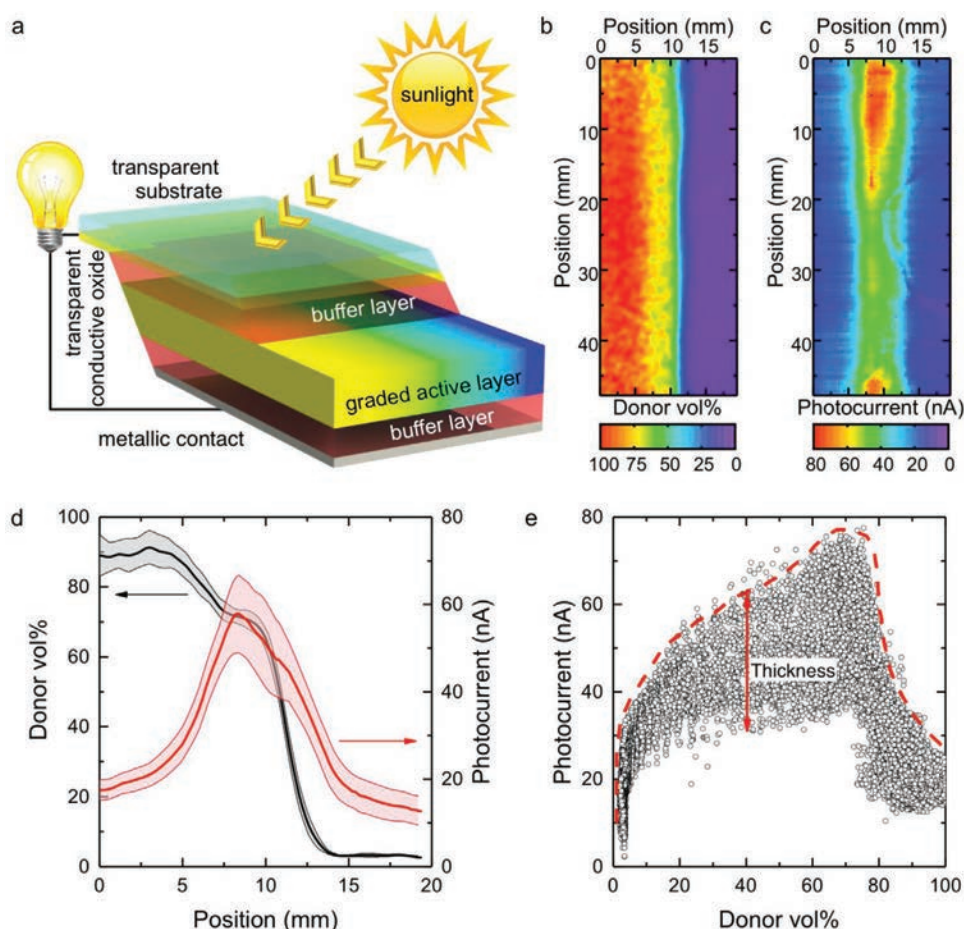
**ADVANCED
SCIENCE NEWS**

www.advancedsciencenews.com

**ADVANCED
ENERGY
MATERIALS**

www.advenergymat.de

Figure 5. a) Schematics and lay-out of an organic solar cell including a compositional gradient in the active layer. The top layers are offset for clarity. b) Composition map of a binary PBDT-TPD:PNDI-T solar cell whose active layer was processed using the microfluidic-assisted blade coating procedure. c) The corresponding photocurrent map of the device measured using 488 nm excitation. d) Averaged lateral composition and photocurrent profiles obtained along the short axis. e) Photocurrent versus donor loading data, including a guide-to-the-eye dashed line that delimits the upper shell of the top performing thickness and blending ratio combinations. The dispersion in the photocurrent axis is ascribed to active layer thickness and morphology variations, as well as to inhomogeneities in the buffer layers.

For processing, the pristine materials were dissolved in chloroform at a concentration of 9 mg mL^{-1}. In the current study, we performed a single ejection (excluding the first transient state prior to steady-state conditions) of 50 µL of solution per inlet to process a device with an area of 25×75 mm^2. This results in a raw material usage below 1 mg per polymer. In addition, the remaining solution can be used for other purposes, and the microfluidic device re-used after cleaning with a suitable solvent.

Figure 5a presents a schematic of the device with an active layer gradient. Figure 5b,c illustrates spatial maps of both composition and photocurrent, respectively, obtained after active layer processing with $\rho = 0.7$ µL mm^{-1}, $\Phi = 1200$ µL min^{-1} and $\nu = 30$ mm s^{-1}. The compositional map is obtained by quantitatively deconvoluting the corresponding Raman spectra acquired at 488 nm following a previously described methodology[43] and using the refractive index and Raman cross sections obtained from Figure 4 and Figure S8, Supporting Information. The photocurrent map is acquired concurrently using the same 488 nm laser employed as the excitation source for Raman

scattering measurements. In this way both the lateral compositional gradient and photovoltaic performance can be efficiently evaluated in a single experiment, generating ≈24 000 data points per device over a period of 2 h.

Figure 5d presents the corresponding averaged composition and photocurrent profiles. It can be seen that the blending ratio varies smoothly between the pure polymer regions, whilst following a profile that resembles those found for the PCDTBT:PC$_{70}$BM films. Conversely, the variation in photocurrent is bell-shaped, suggesting the existence of a relatively narrow optimum blending ratio for the all-polymer photovoltaic blend analyzed here.

These results suggest that beyond polymer:fullerene blends, high quality and smooth mixing gradients can be blade coated as well in a range of polymer:polymer combinations. In fact, we demonstrate that the microfluidic-assisted processing method works for distinct polymer:polymer mixtures (Figures 1b,2; Figure S9, Supporting Information) and that the compositional profiles obtained are reproducible. However, this is not the case when sticking to the simple coalescence of two drops,

which works well for low viscosity inks[12] but fails in producing controllable gradients when mixing neat polymeric solutions (Figures S10 and S11, Supporting Information).

Removal of the spatial dependence of the composition and photocurrent data allows elucidation of which blending ratios yield the highest photovoltaic performance. Figure 5e depicts ≈24 000 combinations of composition and photocurrent for the PBDT-TPD:PNDI-T binary, indicating that the optimum blending ratio is close to (70 ± 10) vol% of the donor (PBDT-TPD). Interestingly, optimal performance appears as a smooth (albeit well localized) peak in the composition diagram. Nevertheless, since photocurrent data were generated using monochromatic excitation (488 nm) the optimum D:A ratio found may not correlate perfectly with the optimum encountered under 1 Sun white light illumination, which for the present blend is close to 1.3:1 (D:A, w:w) or ≈57 wt% of donor.[44] In this regard, the higher absorption of the donor at 488 nm (Figure 4b) supports such a hypothesis. Further photocurrent mapping performed employing the built-in bulb of the Raman acquisition setup indicates as well that the photovoltaic performance peaks close to 70–75 vol% of donor (Figure S12, Supporting Information).

Additionally, it should be remembered that Raman spectroscopy imaging determines volume fractions, and there may well be small differences in density between the donor and acceptor polymers. Regardless, both the reported values and our high-throughput single sample screening consistently indicate that a donor-enriched bulk heterojunction boosts the photovoltaic performance. Conversely, the vertical dispersion observed in the photocurrent (Figure 5e) is attributed to local variations in the total active layer thickness and morphology, which are secondary parameters that require further optimization once the optimum composition has been identified. To this end, we have already demonstrated the rapid and efficient exploration of the active layer thickness dependence through the fabrication of blade-coated thickness gradients,[12] which could complement the herein presented novel optimization approach enabled by microfluidics.

In summary, we have introduced a novel processing scheme based on the combination of microfluidics and blade coating to enable the generation of solid-state compositional gradients on surfaces. This methodology is especially appealing for solution-processing organic electronic devices. More particularly, we have demonstrated the fabrication of lateral compositional gradients comprising polymer:fullerene and polymer:polymer blends that are of high current interest in bulk heterojunction OPV devices. The composition profiles achievable using our approach are both smooth and controllable in terms of lateral blending extension, as confirmed by Raman imaging. Indeed, by combining the high-throughput fabrication of lateral compositional gradients with photocurrent mapping of functional devices we have successfully shown the optimization of polymer:polymer organic solar cells with optimal use of resources and time.

Experimental Section

Materials: PCDTBT, PC$_{70}$BM, and the large-area indium tin oxide (ITO) substrates were purchased from Ossila. P3HT (regio-regular) was purchased from Sigma-Aldrich. N2200 was purchased from Polyera. TQ1 was obtained from 1-Material Organic Nano Electronic. The ZnO nanoparticle dispersion was obtained from Avantama. The polymers PBDT-TPD and PNDI-T were synthesized according to literature protocols.[44]

Sample Preparation: PCDTBT and PC$_{70}$BM were dissolved in chlorobenzene at a concentration of 10 mg mL^{-1}. The ITO substrates were cleaned by consecutive sonication in acetone, a Hellmanex 10% solution in water, isopropanol (5 min each), and sodium hydroxide 10 vol% (10 min), with rinsing in deionized water after each step. The ZnO interlayer was then deposited (50 µL and 40 °C) using an automatic Zehntner ZAA 2300 blade coater with a Zehntner ZUA 2000 aluminum applicator, in air and at a constant speed of 5 mm s^{-1}. The blade gap was set to 200 µm. The active layer was deposited using two NE-1000 pumps manually synchronized with the start of the displacement of the blade coater. A sacrificial substrate (bare glass) was placed prior to the target substrate (ITO + ZnO) until stationary flow conditions were realized at the outlets of the microfluidic array. The bottom transport layer (MoO$_3$) and the Ag electrode were thermally evaporated at a rate of 0.1 and 1 Å s^{-1}, respectively.

Optical Measurements: The optical characterization measurements performed in functional devices, including Raman scattering and light-beam induced current (LBIC), were acquired using a WITec alpha 300 RA+ confocal Raman instrument, coupled to an Olympus objective with 10× magnification (NA 0.25). A solid-state laser operating at 488 nm was employed for both Raman and LBIC measurements. Light was focused through the thick (1.1 mm), ITO-covered glass substrates and the laser power reduced to avoid photodegradation and bleaching of the active layer (3–5 mW at 488 nm in air). Samples were placed on a motorized stage and connected to a DLPCA-200 variable gain low noise current amplifier. All data were collected using WITec Project FIVE software, whilst Raman spectroscopic analysis was performed using a home-made MATLAB routine following a methodology described elsewhere.[43]

Supporting Information

Supporting Information is available from the Wiley Online Library or from the author.

Conflict of Interest

The authors declare no conflict of interest.

2001308 (7 of 8)

[1] A. Hein, C. Kortz, E. Oesterschulze, *Sci. Rep.* **2019**, *9*, 15822.

[2] S. Daniel, *Science* **2001**, *291*, 633.

[3] S. L. Vega, M. Y. Kwon, K. H. Song, C. Wang, R. L. Mauck, L. Han, J. A. Burdick, *Nat. Commun.* **2018**, *9*, 614.

[4] S. Fujino, M. Murakami, V. Anbusathaiah, S.-H. Lim, V. Nagarajan, C. J. Fennie, M. Wuttig, L. Salamanca-Riba, I. Takeuchi, *Appl. Phys. Lett.* **2008**, *92*, 202904.

[5] J. C. Meredith, A. Karim, E. J. Amis, *Macromolecules* **2000**, *33*, 5760.

[6] A. Harillo-Baños, X. Rodríguez-Martínez, M. Campoy-Quiles, *Adv. Energy Mater.* **2020**, *10*, 1902417.

[7] M. J. Fasolka, C. M. Stafford, K. L. Beers, in *Polym. Libr.*, (Eds.: M.A.R. Meier, D.C. Webster), Springer, Berlin, Heidelberg **2010**, pp. 63–105.

[8] Y. Imamura, M. Tashiro, M. Katouda, M. Hada, *J. Phys. Chem. C* **2017**, *121*, 28275.

[9] J. Hachmann, R. Olivares-Amaya, A. Jinich, A. L. Appleton, M. A. Blood-Forsythe, L. R. Seress, C. Román-Salgado, K. Trepte, S. Atahan-Evrenk, S. Er, S. Shrestha, R. Mondal, A. Sokolov, Z. Bao, A. Aspuru-Guzik, *Energy Environ. Sci.* **2014**, *7*, 698.

[10] J. Hachmann, R. Olivares-Amaya, S. Atahan-Evrenk, C. Amador-Bedolla, R. S. Sánchez-Carrera, A. Gold-Parker, L. Vogt, A. M. Brockway, A. Aspuru-Guzik, *J. Phys. Chem. Lett.* **2011**, *2*, 2241.

[11] D. Padula, J. D. Simpson, A. Troisi, *Mater. Horiz.* **2019**, *6*, 343.

[12] A. Sánchez-Díaz, X. Rodríguez-Martínez, L. Córcoles-Guija, G. Mora-Martín, M. Campoy-Quiles, *Adv. Electron. Mater.* **2018**, *4*, 1700477.

[13] C. Xie, X. Tang, M. Berlinghof, S. Langner, S. Chen, A. Späth, N. Li, R. H. Fink, T. Unruh, C. J. Brabec, *ACS Appl. Mater. Interfaces* **2018**, *10*, 23225.

[14] S. Chen, Y. Hou, H. Chen, X. Tang, S. Langner, N. Li, T. Stubhan, I. Levchuk, E. Gu, A. Osvet, C. J. Brabec, *Adv. Energy Mater.* **2018**, *8*, 1701543.

[15] C. Yan, S. Barlow, Z. Wang, H. Yan, A. K.-Y. Jen, S. R. Marder, X. Zhan, *Nat. Rev. Mater.* **2018**, *3*, 18003.

[16] A. Facchetti, *Mater. Today* **2013**, *16*, 123.

[17] H. Benten, D. Mori, H. Ohkita, S. Ito, *J. Mater. Chem. A* **2016**, *4*, 5340.

[18] G. Wang, F. S. Melkonyan, A. Facchetti, T. J. Marks, *Angew. Chem., Int. Ed.* **2019**, *58*, 4129.

[19] Y. Meng, J. Wu, X. Guo, W. Su, L. Zhu, J. Fang, Z.-G. Zhang, F. Liu, M. Zhang, T. P. Russell, Y. Li, *Sci. China: Chem.* **2019**, *62*, 845.

[20] Z. Li, X. Xu, W. Zhang, X. Meng, W. Ma, A. Yartsev, O. Inganäs, M. R. Andersson, R. A. J. Janssen, E. Wang, *J. Am. Chem. Soc.* **2016**, *138*, 10935.

[21] J. Nelson, *Mater. Today* **2011**, *14*, 462.

[22] K. Glaser, P. Beu, D. Bahro, C. Sprau, A. Pütz, A. Colsmann, *J. Mater. Chem. A* **2018**, *6*, 9257.

[23] S. Savagatrup, A. D. Printz, T. F. O'Connor, I. Kim, D. J. Lipomi, *Chem. Mater.* **2017**, *29*, 389.

[24] J. Alstrup, M. Jørgensen, A. J. Medford, F. C. Krebs, *ACS Appl. Mater. Interfaces* **2010**, *2*, 2819.

[25] A. Karim, E. Amis, K. Yurekli, R. Krishnamoorti, C. Meredith, *Polym. Eng. Sci.* **2002**, *42*, 1836.

[26] J. B. Thorstenson, L. K. Petersen, B. Narasimhan, *J. Comb. Chem.* **2009**, *11*, 820.

[27] C. M. Stafford, K. E. Roskov, T. H. Epps, M. J. Fasolka, *Rev. Sci. Instrum.* **2006**, *77*, 023908.

[28] R. L. Davis, S. Jayaraman, P. M. Chaikin, R. A. Register, *Langmuir* **2014**, *30*, 5637.

[29] B. Cao, L. A. Adutwum, A. O. Oliynyk, E. J. Luber, B. C. Olsen, A. Mar, J. M. Buriak, *ACS Nano* **2018**, *12*, 7434.

[30] H. Sahu, W. Rao, A. Troisi, H. Ma, *Adv. Energy Mater.* **2018**, *8*, 1801032.

[31] M. Kiy, R. Kern, T. A. Beierlein, C. J. Winnewisser, in *Org. Light Emit. Mater. Devices X*, (Eds.: Z.H. Kafafi, F. So), **2006**, p. 633307.

[32] S. Langner, F. Häse, J. D. Perea, T. Stubhan, J. Hauch, L. M. Roch, T. Heumueller, A. Aspuru-Guzik, C. J. Brabec, *Adv. Mater.* **2020**, *32*, 1907801.

[33] N. L. Jeon, S. K. W. Dertinger, D. T. Chiu, I. S. Choi, A. D. Stroock, G. M. Whitesides, *Langmuir* **2000**, *16*, 8311.

[34] A. G. G. Toh, Z. P. Wang, C. Yang, N.-T. Nguyen, *Microfluid. Nanofluid.* **2014**, *16*, 1.

[35] S. Cheng, Z. Wu, *Lab Chip* **2012**, *12*, 2782.

[36] C. J. Bettinger, H. A. Becerril, D. H. Kim, B.-L. Lee, S. Lee, Z. Bao, *Adv. Mater.* **2011**, *23*, 1257.

[37] S. Kustra, H. Wu, S. Basu, G. K. Rohde, C. J. Bettinger, *Small* **2012**, *8*, 3746.

[38] P. Carrière, *Phys. Fluids* **2007**, *19*, 118110.

[39] C.-Y. Lee, W.-T. Wang, C.-C. Liu, L.-M. Fu, *Chem. Eng. J.* **2016**, *288*, 146.

[40] C.-Y. Lee, C.-L. Chang, Y.-N. Wang, L.-M. Fu, *Int. J. Mol. Sci.* **2011**, *12*, 3263.

[41] A. I. Shallan, P. Smejkal, M. Corban, R. M. Guijt, M. C. Breadmore, *Anal. Chem.* **2014**, *86*, 3124.

[42] J. M. Cabot, E. Fuguet, M. Rosés, P. Smejkal, M. C. Breadmore, *Anal. Chem.* **2015**, *87*, 6165.

[43] X. Rodríguez-Martínez, M. S. Vezie, X. Shi, I. McCulloch, J. Nelson, A. R. Goñi, M. Campoy-Quiles, *J. Mater. Chem. C* **2017**, *5*, 7270.

[44] X. Xu, Z. Li, W. Zhang, X. Meng, X. Zou, D. Di Carlo Rasi, W. Ma, A. Yartsev, M. R. Andersson, R. A. J. Janssen, E. Wang, *Adv. Energy Mater.* **2018**, *8*, 1700908.

Q6

2001308 (8 of 8)

Supporting Information

Microfluidic-Assisted Blade Coating of Compositional Libraries for Combinatorial Applications: the Case of Organic Photovoltaics

Xabier Rodríguez-Martínez, Semih Sevim, Xiaofeng Xu, Carlos Franco, Paula Pamies-Puig, Laura Córcoles-Guija, Romen Rodriguez-Trujillo, Francisco Javier del Campo, David Rodriguez San Miguel, Andrew J. deMello, Salvador Pané, David B. Amabilino, Olle Inganäs, Josep Puigmartí-Luis* and Mariano Campoy-Quiles*

PART I. Design and fabrication of the microfluidic array: exploration of outlet designs and their configurations
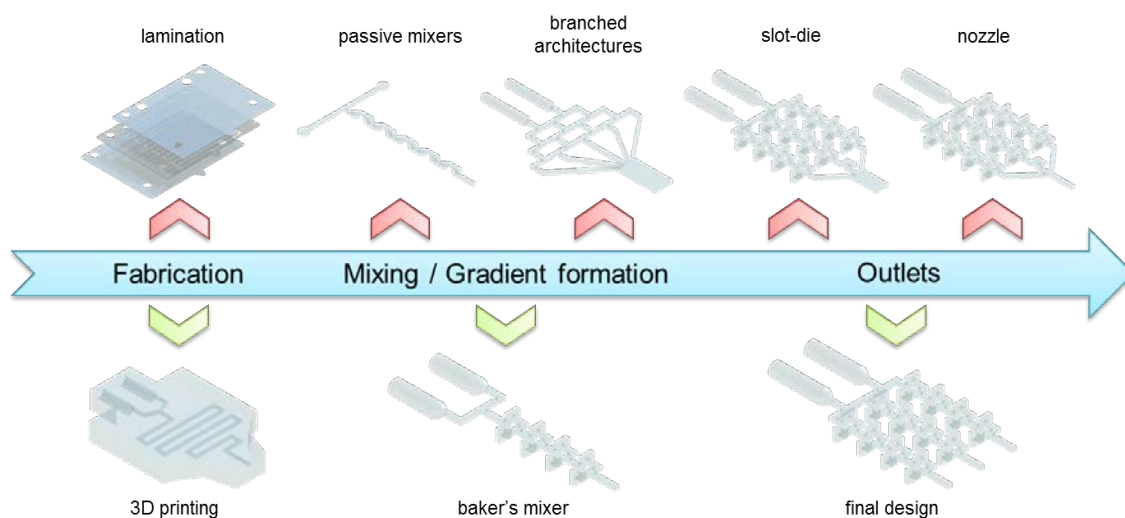

Figure S1. Design roadmap of the microfluidic device followed in this work: from choice of fabrication method to solution mixing, gradient formation and coupling of the outflows with the blade coating processing scheme.

The design of the microfluidic device (**Figure S1**) is performed according to two basic premises or requirements: (i) the ability to mix the pristine solutions very efficiently, which means minimizing the dead volume and maximizing the mixing efficiency of the pristine solutions; and (ii) to be highly resistant to chlorinated solvents.

Fabrication. Regarding the prototyping of the microfluidic devices, 3D printing is a convenient technique in terms of resolution (we employ 500 x 500 μm square section channels, see further dimensional details in **Figure S2** and **Figure S3**) and cost-effectiveness (the fabrication itself takes place in a single step). Also the realization of the topologically complex 3D architecture of the baker's units is almost exclusively tackled by the 3D printing technology as most of the usual multilevel fabrication procedures are limited to building materials such as poly(dimethylsiloxane) (PDMS),[1,2] which is unstable in chlorinated solvents. Furthermore, the large amount of resins and ink formulations developed to meet the demands of stereolithographic 3D printer users enabled us to find building materials that fulfil our requirements in terms of resistance to chlorinated solvents. The prototyping of the microfluidic devices was performed using a ProJet MJP 2500 setup commercialized by 3D Systems, Inc. together with their proprietary translucent wax VisiJet M3 Crystal, which apart from being semi-transparent, it is found to be resistant to chlorinated solvents. Two NE-1000 programmable single syringe pumps (manufactured by New Era Pump Systems, Inc.) loaded with 2 mL syringes were used for the synchronized infusion.
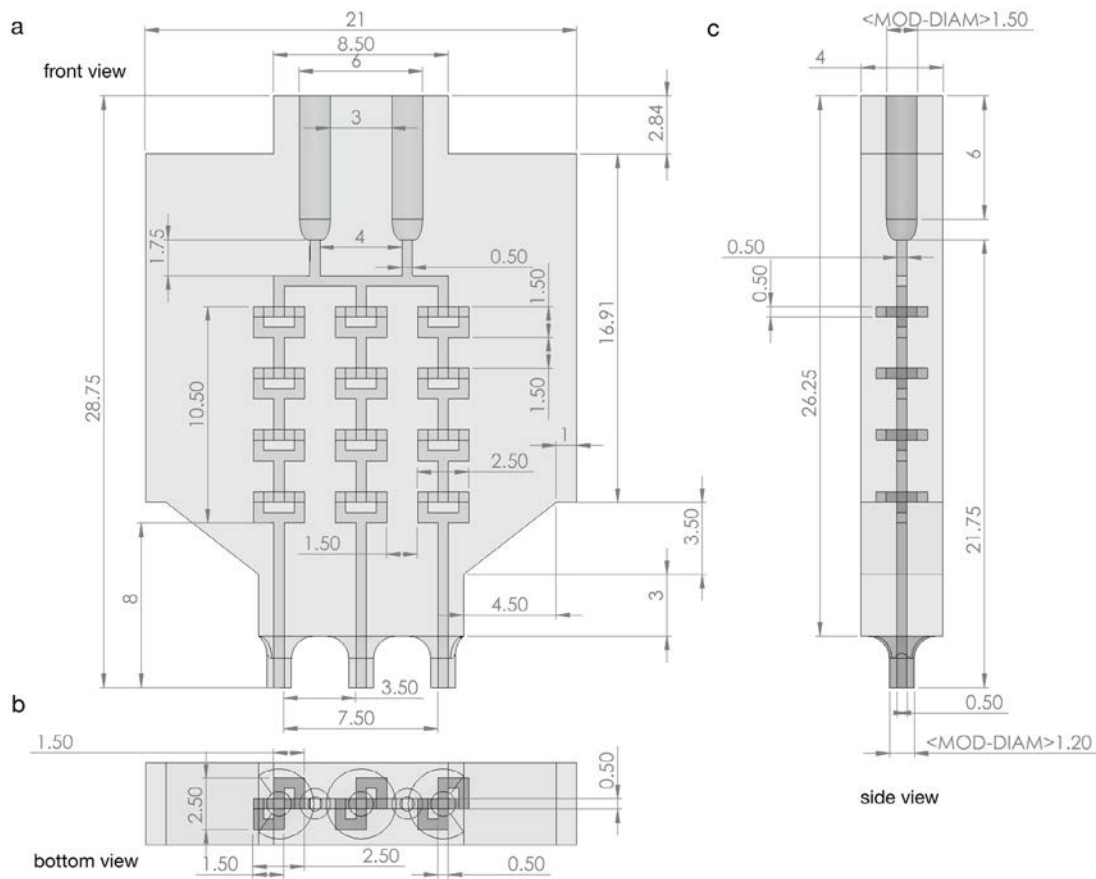
Figure S2. (a-c) Technical drawing of the microfluidic device showing the geometrical dimensions with respect to a) front view, b) bottom view and c) side view. All dimensions are in millimeter.
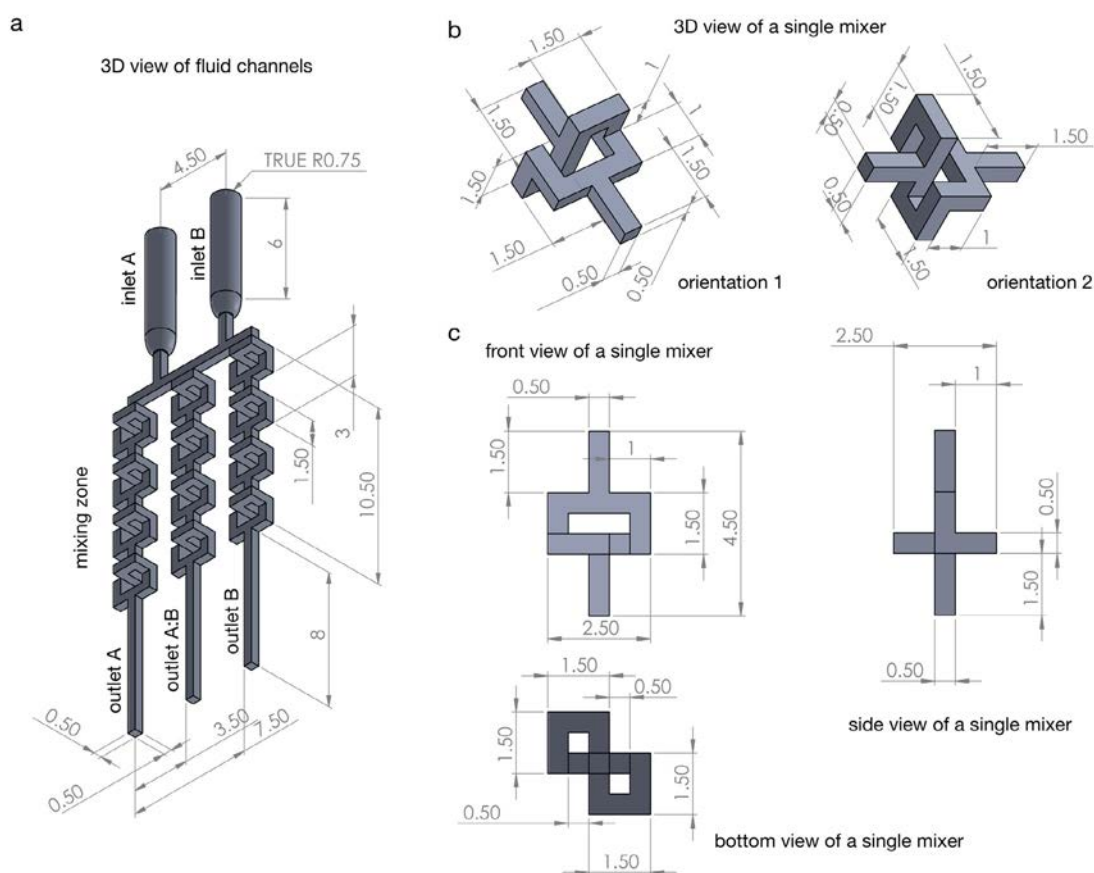
Figure S3. (a) 3D CAD drawing of fluid channels inside the microfluidic device showing the geometrical dimensions for inlets, mixing zone and outlet sections. (b) Magnified 3D views of a single mixer unit from two different orientations to give detailed information about geometry. (c) Technical drawing of a single mixer unit showing front, bottom and side views with geometrical dimensions. All dimensions are in millimeter.

Figure S4 illustrates how the 3D printed microfluidic device couples to the metallic applicator of the blade coater by using a custom computer numerical control (CNC) machined poly(methyl methacrylate) (PMMA) scaffold. Such scaffold assures that the chip can be slipped in and out and held exactly at the same position (both horizontally and vertically) in each run. The microfluidic device is located such that it pours liquid to the ink reservoir of the blade as it moves over the substrate. In this way we expect the three outflow liquid profiles to coalesce once the blade passes by while generating a smooth lateral composition wedge extending from the pure solutions to the mixture at the central region.

Mixing. A bottleneck in organic electronics is the low availability of raw materials. Frequently, in lab-scale synthetic protocols only a few tens of milligrams of a targeted molecule are available, a result that can significantly limit the amount of samples that can be produced. In this context, the unique mixing efficiency encountered in microfluidic devices could be advantageously used to generate compositional libraries where not only the sample consumption can be remarkably reduced but also a high-throughput exploration of the parametric landscape for the specific targeted material can be efficiently achieved. Therefore, efficient microfluidic-based mixing units minimizing the dead volume of the precursor solutions are highly desirable.

The mixing efficiency is mainly determined by the type of mixing units chosen as well as by their complexity. In this sense, three-dimensional mixers, such as those based on the baker's transformation,[3] have been demonstrated to yield the highest mixing efficiencies among passive mixers.[4–7] These mixing units combine the effect of chaotic advection with an accelerated diffusion due to the splitting of the mixing interfaces after each of the iterations, thus boosting up the final mixing rate per volume injected. The interconnection of just a few (4-5 iterations at most) of these baker's units has been demonstrated to yield a complete and homogeneous mixing at the outlets without the need for other types of mixing units or long zig-zag streamers.

The symmetric, triple branched structure of the final microfluidic device (Figure S1) guarantees that only the middle branch generates a mixture while the side outlets carry the pure solutions. This case corresponds to a 1:1 (v:v) blend when the injected pristine solutions have equal viscosity (μ) and inflow rates (Φ_1, Φ_2); otherwise, an unbalanced mixing ratio arises at the central mainstream which could affect the even distribution of the solid-state lateral composition profile (**Figure S5**). In each of the branches we include four baker's units to assure a proper mixing homogeneity with the smallest volume.

Recyclability. The pristine solutions should remain intact when generating compositional gradients, so they can be used for different experiments. Ideally, the microfluidic devices ought to be recyclable, which implies that they must resist subsequent immersion and sonication in chlorinated solvents (mainly chloroform and chlorobenzene as the typical solvents employed in lab-scale organic electronics).

Outlet design. The design of the outlets at the end of the branched microchannel structure was critical for obtaining good coupling between the microfluidic chip and the blade coating process. Its configuration largely affected the transfer of the liquid profiles to solid-state films in terms of both reproducibility and compositional wedge quality.

Figure S4 illustrates the 3D models of different microfluidic devices we proposed and tested in this work. Design A corresponds to the chip configuration finally selected and used in the main manuscript after thorough exploration of film quality in terms of lateral composition profiles. We also explored joint outlet configurations consisting of a single nozzle (Design B) and a single wide outlet resembling slot-die coating setups, either flat (Design C) or subtly filed to aid during the spreading process (Design D).

One of the main conclusions extracted from our exploration indicates that the use of three individual nozzles favors the generation of solid-state compositional gradients along the short axis of the substrate, i.e. perpendicularly to the blade coating movement. Conversely, the single outflow designs are suitable to fabricate composition libraries along the coating direction, especially when the inflow rates are varied accordingly during the blade coating.[8] In this sense we did not observe any inherent advantage when using wide outlet designs in the final film quality, using either flat or filed edges, albeit wide outlets could be more robust during the experimental manipulation of the chips than nozzles.
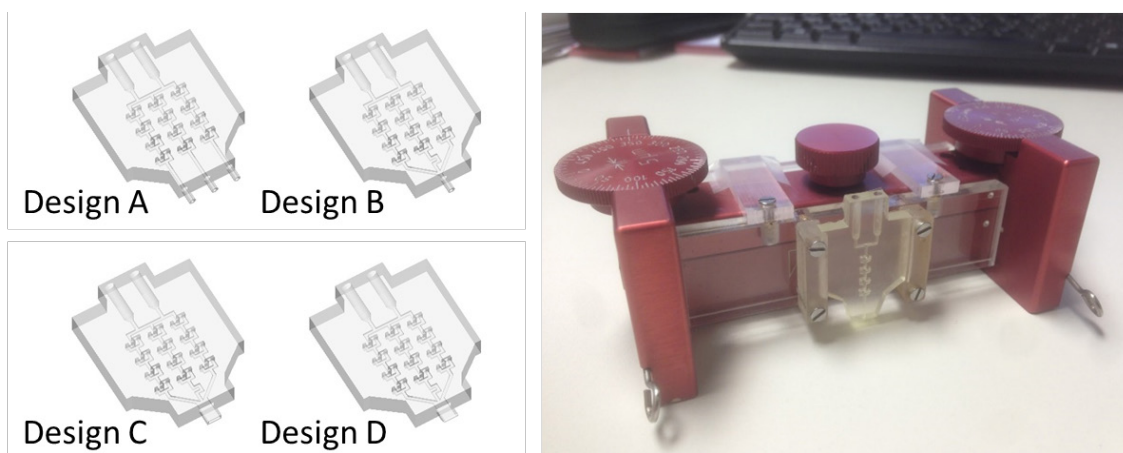
Figure S4. (Left) 3D sketches of the microfluidic devices proposed and tested in this work in terms of film quality and reproducibility. (Right) Optical picture of the home-made scaffold designed to hold the microfluidic devices in place.

PART II. Unbalanced mixing at the central mainstream

Given a certain microchannel cross-section of characteristic length L, the dynamic viscosity (μ) of the flowing solution determines its fluidic resistance (Ω), and hence the pressure drop (ΔP) according to the Navier-Stokes equation.[9] In the case of Newtonian micro-fluids at low Reynolds number, several simplifications allow rewriting such equation as a simple Ohm's law for fluidics: $\Delta P \propto \Phi \, \mu \, L^{-1}$, where Φ stands for the volumetric or mass flow rate and $\Omega \propto \mu \, L^{-1}$.

In mechanically-actuated syringe pumps the flow rates are input magnitudes. During the actuation of branched microfluidic structures the pressure drop at the microchannels is mainly determined by μ (assuming that L remains constant).[9] Therefore, a balanced distribution of the branched array requires the pressure drops at each of the mainstreams being equal; otherwise, uneven fluid distributions are attained at the outlets.

We exemplify this behavior in Figure S5, which visually compares the outflows obtained using colored inks of different viscosity in a branched microfluidic device. In Figure S5a the fluids are injected with equal flow rates (900 μL min^{-1}) and since the viscosity of the bluish

ink (3.7 cP) is approximately two times higher than that of the yellow one (1.6 cP), the outflows are noticeable unbalanced, leading either to yellowish or bluish streams. More specifically, the central stream, where the two pristine inflows mix, appears totally blue. In Figure S5b, we halved the inflow rate of the viscous blue ink and accordingly started observing a balanced, green-colored outflow through the central outlet, as a result of the paired pressure drops along the different branched channels.

Such simple experiment demonstrates that either (i) inks of similar viscosity are used during the blade coating microfluidics processing; or (ii) the inflow rates must be accordingly fine-tuned to account for their intrinsic rheological differences. However, in this latter case special care must be taken when performing the blade coating process since the fluid velocity v, which is proportional to the volumetric flow rate Φ, will be highly unbalanced and lead to a long transient state and (in the present case) yellow-enriched total outflows, a fact that could limit the blending ratio window explored in solid-state films.
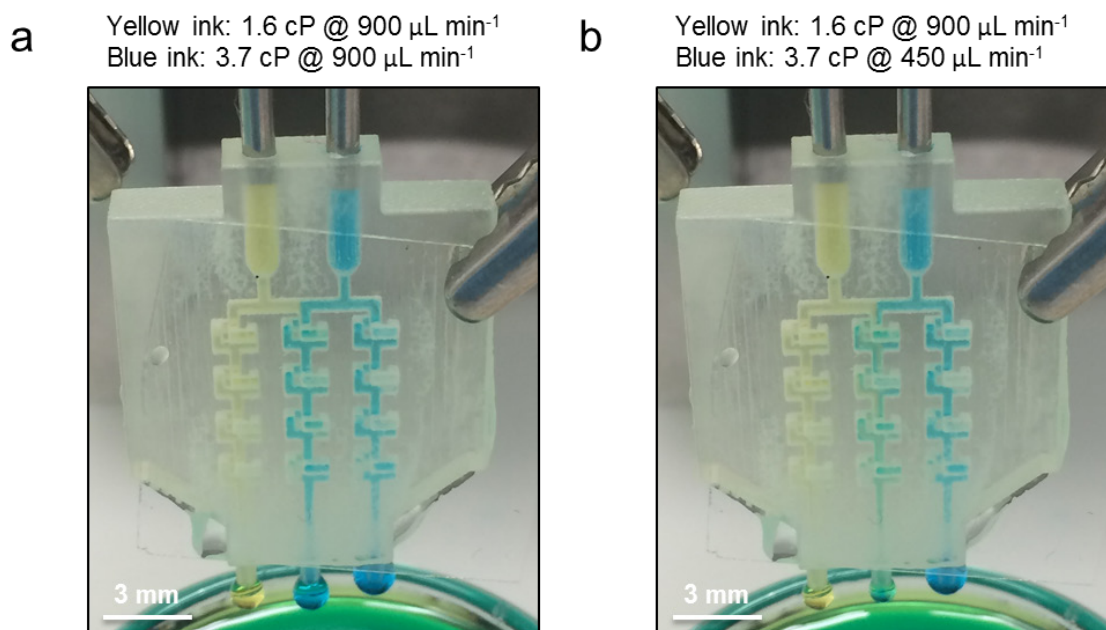
Figure S5. Optical pictures of a branched microfluidic device used to mix two inks of dissimilar viscosities: 1.6 cP (yellow ink) and 3.7 cP (blue ink). a) Case example of the outflows obtained using balanced inflow rates (900 µL min^{-1} per channel). An unbalanced outflow in the central mainstream is observed (totally blue). b) Outflows obtained when halving the inflow rate of the more viscous blueish ink (3.7 cP, 450 µL min^{-1}) to level the pressure drops. In this case the central mainstream is balanced and a green-colored outflow is observed.

In order to gain further insights about how critical the intrinsic chemical nature of the materials is for their ink rheology, we used a Modular Compact Rheometer MCR302 by Anton Paar to quantify the viscosity of a library of typical organic photovoltaic materials: from conjugated polymers such as N2200 (poly{[*N*,*N*′-bis(2-octyldodecyl)-naphthalene-1,4,5,8-bis(dicarboximide)-2,6-diyl]-*alt*-5,5′-(2,2′-bithiophene)}), PTB7-Th (poly([2,6′-4,8-di(5-ethylhexylthienyl)benzo[1,2-*b*;3,3-*b*]dithiophene]{3-fluoro-2[(2-ethylhexyl)carbonyl]thieno[3,4-*b*]thiophenediyl})), PCDTBT (poly[*N*-9′-heptadecanyl-2,7-carbazole-*alt*-5,5-(4′,7′-di-2-thienyl-2′,1′,3′-benzothiadiazole)]) and RR-P3HT (regioregular

poly(3-hexylthiophene-2,5-diyl)); to small molecules, namely PC$_{70}$BM ([6,6]-phenyl C$_{71}$ butyric acid methyl ester), PCBM ([6,6]-phenyl C$_{61}$ butyric acid methyl ester), EH-IDTBR ((5Z,5'Z)-5,5'-(((4,4,9,9-tetrakis(2-ethylhexyl)-4,9-dihydro-*s*-indaceno[1,2-*b*:5,6-*b*']dithiophene-2,7-diyl)bis(benzo[*c*][1,2,5]thiadiazole-7,4-diyl))bis(methaneylylidene))bis(3-ethyl-2-thioxothiazolidin-4-one)) and O-IDFBR ((5Z,5'Z)-5,5'-(((6,6,12,12-tetraoctyl-6,12-dihydroindeno[1,2-*b*]fluorene-2,8-diyl)bis(benzo[*c*][1,2,5]thiadiazole-7,4-diyl))bis(methaneylylidene))bis(3-ethyl-2-thioxothiazolidin-4-one)), see **Table S1**. The measurements were carried out at room temperature (23 °C) while leaving a gap of 100 μm between the stage and the rotating plate of the rheometer, which nominal diameter was φ = 39.969 mm. The inks contained chlorobenzene rather than chloroform as carrier solvent, at a typical solid loading of 10 mg mL^{-1}. Experimentally, the use of chloroform was problematic due to its quick evaporation during the acquisition of the shear stress data.

Our results (Table S1) indicate that upon fabrication of polymer:small molecule blended films their dissimilar ink viscosity could be detrimental for the successful processing. In particular, we observe that the viscosity ratio between the blended species could be as high as ca. 4.6 when mixing the bulkier and heavier polymer chains (N2200) with any of the small molecules we measured. Therefore, in these cases the rheology matters the most and requires fine tuning of the inflow rates to obtain smooth blending ratio profiles in solid state. For cases in which the viscosities are not very different, and particularly, when they are relatively low, mixing still occurs but the middle channel does not show a 1:1 (v:v) composition, which would lead to a displacement of the central part of the gradient towards one side (that of the less viscous solution) in the solid film.

Table S1. Collection of viscosities (μ) and specific viscosities ($\mu_{sp} = (\mu - \mu_s)\,\mu_s^{-1}$, being μ_s the viscosity of the neat solvent) for a library of organic photovoltaic materials including polymers and small molecules dissolved in chlorobenzene at a solid loading of 10 mg mL^{-1}.

Material (M_w)	Viscosity, μ [mPa s]	Specific viscosity, μ_{sp}	Supplier
Chlorobenzene	0.8 ± 0.1	N/A	Sigma-Aldrich
N2200 (80-120 kDa)	3.7 ± 0.4	3.8	Polyera
PTB7-Th (141 kDa)	1.6 ± 0.2	1.2	Ossila
PCDTBT (35 kDa)	1.7 ± 0.2	1.2	Ossila
RR-P3HT (20-45 kDa)	1.1 ± 0.1	0.4	Sigma-Aldrich
PC$_{70}$BM	0.8 ± 0.1	0.1	Ossila
PCBM	0.8 ± 0.1	0	Sigma-Aldrich
EH-IDTBR	0.8 ± 0.1	0	1-Material
O-IDFBR	0.9 ± 0.1	0.2	1-Material

PART III. Phenomenological modelling of the coating process

The existing gap (*g*) between the nozzles and the substrate was also found to be important during the film processing since it has a large influence on the ejection-coating regime selected: either dropwise or continuous outflow conditions.

Dropwise conditions are detrimental for film quality since they result in large inhomogeneities in film thickness; this is mainly due to the quick evaporation of the drops once on the substrate and their unbalanced coalescence at the blade reservoir.

On the other hand, continuous outflow conditions are fulfilled when the nozzles and the substrate are close enough to the substrate so that a continuous curtain flow can be formed during the ejection time. Such conditions must be met for certain coating parameters, i.e.

blade velocity (v) and outflow rate per outlet (Φ_{out}). Our CNC-machined chip holder couples to the metallic applicator of the blade coater leaving the same gap as its wetting filed edge, which is usually set to 200 μm with respect to the surface of the substrate. In order to determine which are the experimental conditions that lead to continuous outflow conditions and good film lateral homogeneity, we developed a simple, geometrical and phenomenological model for the blade coating microfluidics processing scheme (*vide infra*). During such process two phenomena take place in parallel: (i) the ejection of solution to the blade reservoir and (ii) the spreading of the ink over the substrate by the blade. Regarding the ejection of solution, we are interested in achieving continuous, curtain-like flowing conditions at the outlets in order to avoid a dropwise regime. For this to happen the requirement is that the liquid poured per outlet and per second equals the liquid required to fill up the existing volume between the outlet and the substrate surface per second. Assuming that the liquid poured by the circularly-shaped nozzle acquires a cylindrical form, then such condition reads

$$v = \frac{10^5 \Phi_{out}}{3\pi r g}, \qquad\qquad (S1)$$

where v is the blade speed in mm s^{-1}, Φ_{out} is the outflow rate per nozzle in μL min^{-1}, r is the radius of the circular outlet in μm, and g stands for the existing gap between the outlet and the substrate in μm.

During the spreading of the ink by the blade, the necessary condition is that the total amount of liquid poured per second equals the wet film volume swept by the wetting front edge of the blade per second. The wet film thickness depends on the accumulated volume in the blade front. If we assume that the wet film thickness is ca. 10% the gap regardless the accumulated volume,[10,11] then we can introduce a homogeneity factor (ξ) defined as the ratio between the ejected and swept volumes:

$$\xi = \frac{V_{ejected}}{V_{swept}} = \frac{10^2 \Phi}{6 v w d_w}, \qquad (S2)$$

where now Φ refers to the total outflow rate in µL min^{-1}, w is the width of the substrate in mm and d_w stands for the thickness of the wetting layer in µm. The threshold value for ξ that assures a homogenous coating of the entire width of the substrate corresponds to $\xi \geq 1$. Figure 2a illustrates the location of the different coating regimes in the blade speed vs. outflow rate parametric space. In this example we consider $g = 200$ µm, $w = 25$ mm and a wetting front edge of 2 mm for the metallic applicator of the blade. The solid black line in Figure 2a delimits the dropwise and continuous outflow regimes according to Equation S1. Within the continuous regime, the orange area between the solid and dotted lines corresponds to the experimental conditions in which the ink accumulated at the blade reservoir is not enough to homogeneously cover a 25 mm width substrate. Therefore, experimentally we should stick to parametric combinations of blade speed and outflow rates located within the green area in Figure 2a. As a reference, the typical volumetric linear densities (ρ) employed in the main manuscript of 1.0 and 2.5 µL mm^{-1} are depicted as dashed lines in the diagram.

PART IV. Relationship between the volumetric linear density (ρ) and the extension of the composition profile
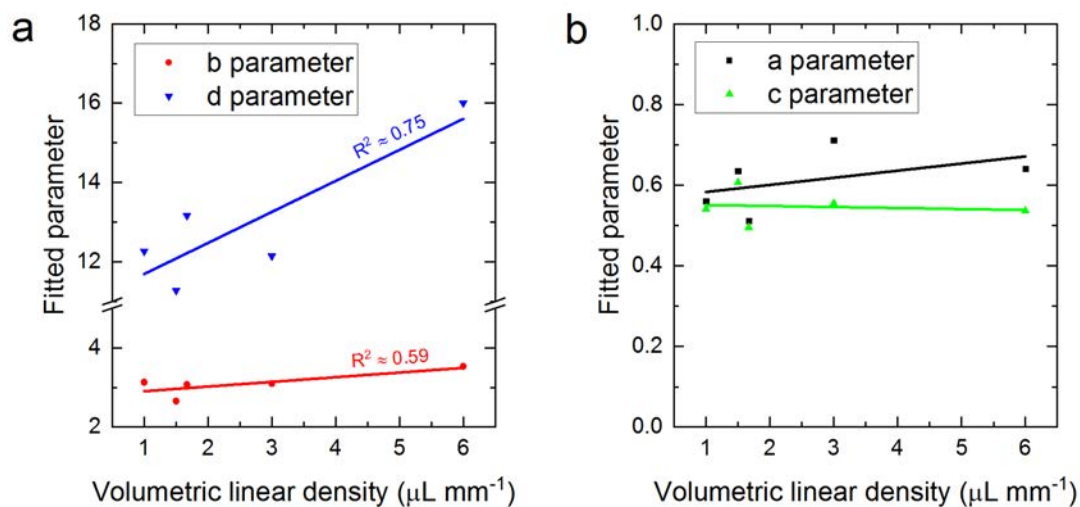

Figure S6. Parameters obtained after fitting Equation 1 in the main manuscript to the lateral composition profiles shown in Figure 3b.

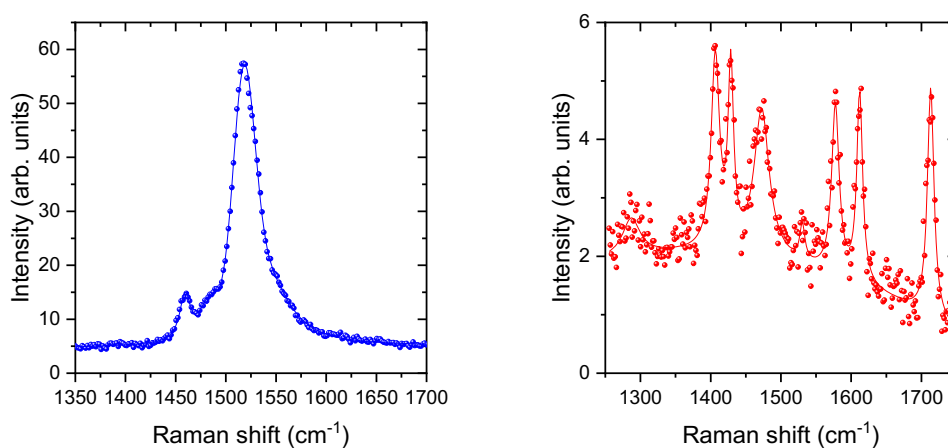**PART V. Raman cross-section analysis of PBDT-TPD and PNDI-T**

Figure S7. Characteristic vibrational Raman signature acquired at 488 nm excitation of PBDT-TPD (left panel) and PNDI-T (right panel).
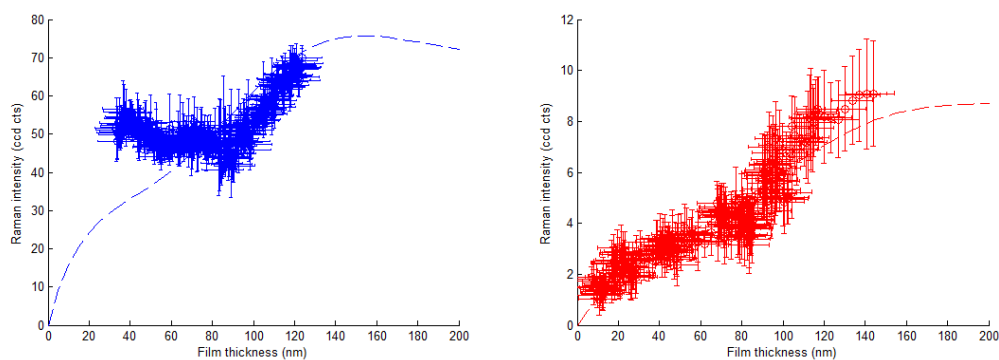
Figure S8. Raman intensity variation as a function of film thickness for PBDT-TPD (left panel, corresponding to the intensity of the 1518 cm^{-1} band) and PNDI-T (right panel, 1713 cm^{-1} band). The dashed lines correspond to the scattered intensity modulation with film thickness expected according to our transfer matrix modelling approach.[12] The scattered data corresponds to the experimental data taken on pristine films showing lateral thickness gradients.

Table S2. Raman cross-sections extracted at 488 nm excitation and ratios with respect to that of PC$_{70}$BM.

Material	σ [cts s^{-1} μW^{-1}]	Raman band [cm^{-1}]	Ratio to σ$_{PC70BM}$
PBDT-TPD	(2.7 ± 0.5) · 10^{-3}	1518	8 ± 2
PNDI-T	(1.6 ± 0.3) · 10^{-4}	1713	0.5 ± 0.1

PART VI. Reproducibility assessment of the microfluidic-based deposition technique

In order to assess the reproducibility of our method, we show in **Figure S9** the lateral compositional profiles took by Raman spectroscopy in P3HT:PCDTBT graded films. The data shown corresponds to three consecutive replicates we performed keeping constant the experimental parameters, type and orientation of substrates (bare glass slides for the present case). We appreciate experimental noise at high P3HT loadings, which is a consequence of its notably larger Raman cross-section with respect to PCDTBT (as detailed in ref. [12]), yet the overall trends observed in each of the replicates is reproduced well.
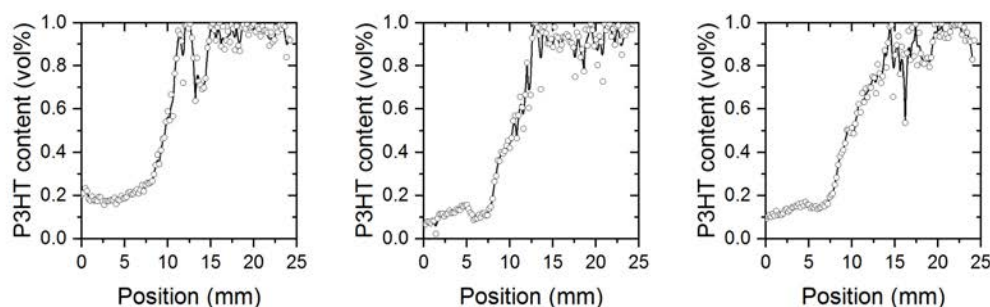

Figure S9. Lateral compositional profiles corresponding to three replicates of thin films prepared by the microfluidic-assisted blade coating platform using pre-mixed 1:9 (w:w) and 9:1 (w:w) P3HT:PCDTBT inks. The processing parameters were $\rho = 1$ µL mm^{-1}, casting temperature 70 ºC and 200 µm gap.

PART VII. Case example of polymer:polymer blends processed using two coalescent drops in blade coating

Figure S10 illustrates the composition maps and the averaged lateral blending profiles obtained in PBDT-TPD:PNDI-T all-polymer films following our previously developed method,[13] which combines conventional blade coating and two-drop coalescence at the ink reservoir. The mixing area obtained is generally very narrow and lacks reproducibility from

batch-to-batch as it is largely affected by the manual pipetting and actual drop location at the
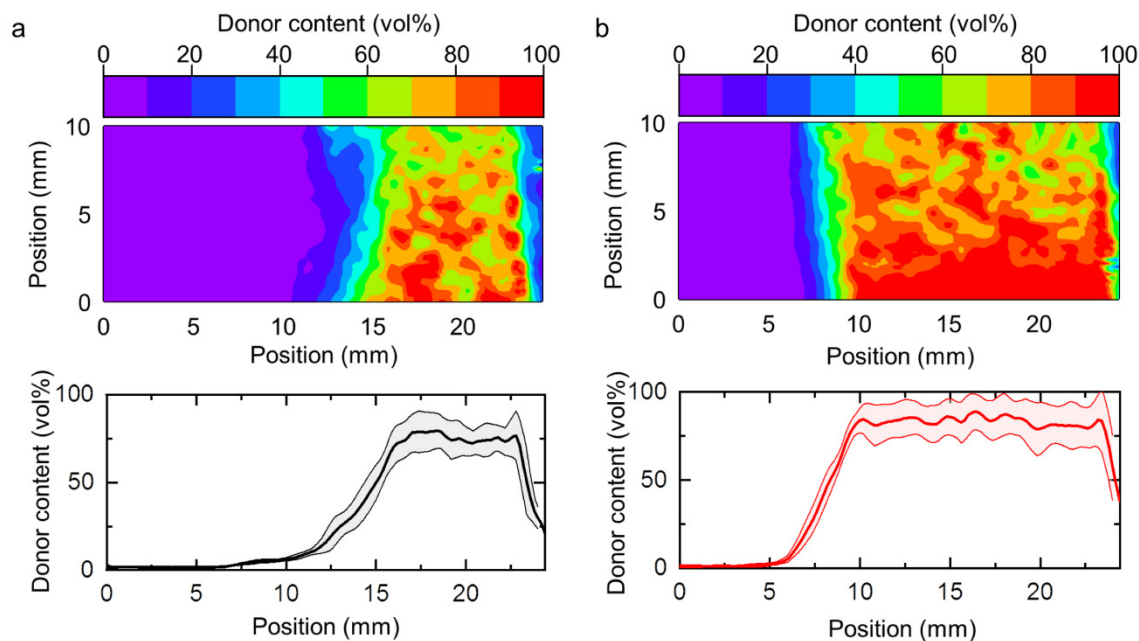
first stages of the coating.

Figure S10. Composition maps and corresponding averaged lateral profiles obtained in

PBDT-TPD:PNDI-T all-polymer films on glass processed according to the two-drop

coalescence approach in blade coating.[13] Two 30 μL drops at a nominal concentration of 10

mg mL^{-1} in chlorobenzene were pipetted at the ink reservoir and then coated at (a) 30 mm s^{-1}

and (b) 20 mm s^{-1} while holding the stage temperature at 80 °C (in both cases).

The coalescence of manually pipetted droplets at the wetting edge of the blade has two

limitations. First, the mixing is chaotic, and the film distribution of composition random,

varying each time. In the microfluidic-assisted method, the profile is controllable and can be

understood in terms of simple ink parameters (viscosity and wetting) and deposition parameters

(ink flow and blade or web speed). As an important result, the microfluidic-assisted method is

experimentally robust, producing reproducible compositional gradients, as shown in **Figure S9**.

Secondly, the two-drop coalescence method fails when dealing with highly viscous neat

solutions such as those encountered in all-polymer organic photovoltaic blends. The poor

miscibility of such inks, derived from their large viscosity and surface tension, prevents an

effective mixing when the blading process is performed by conventional drop-coalescence

methods (**Figure S11**). In this regard, we demonstrate in the main text that the microfluidic-

assisted blade coating platform constitutes a more general approach towards the fabrication of

compositional gradients. This is shown by fabricating smooth and laterally extended

polymer:fullerene as well as polymer:polymer gradients while sticking to the same processing
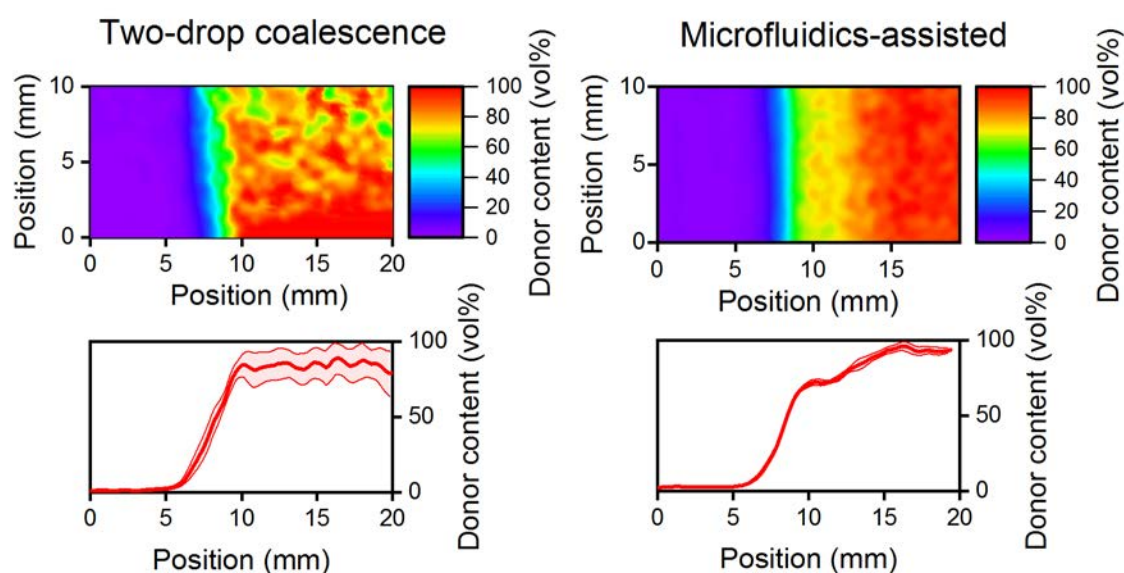
framework.

Figure S11. Here we show representative compositional profiles of a polymer:polymer film

formed by PBDT-TPD:PNDI-T obtained following two distinct methodologies. On the left-

hand side, we illustrate the outcome profile obtained by the two-drop coalescence method

introduced in 2018,[13] while the right-hand side shows the mixing profile generated via

microfluidics-assisted blade coating. In general, two-drop coalescence leads to narrow mixing

areas spanning 1 cm at most. Our advanced framework based on microfluidics enables

expanding the blending area, so that the donor:acceptor mixing ratios of larger functional

interest are better explored. The homogeneity along the coating direction is also remarkably

improved.

PART VIII. Photocurrent mapping using white-light illumination

The use of monochromatic light in the photocurrent mapping of organic solar cells provides a constrained view of the photovoltaic performance. This is especially critical for panchromatic active layers such as those found in ternary organic photovoltaic blends; in fact, we have recently shown that the photocurrent maps took using distinct excitation wavelengths show their optima at different mixing ratios, which results from the preferential absorption of light by different photoactive species in the blended active layer.[14]

In order to partly circumvent this limitation, we recently managed to couple the white bulb of the Raman microscope setup to employ it as excitation source during photocurrent imaging. This fact enables the collection of more reliable photocurrent maps since we are now spanning a broader spectral window. However, the spectral irradiance of the bulb is not standardized and shows a rather limited matching with the AM1.5G solar spectral irradiance (**Figure S12**a). Under these experimental conditions, we revisited the PBDT-TPD:PNDI-T donor:acceptor pair and still observe a sharp photocurrent peak arising at ca. 75 vol% of donor (Figure S12b). In this regard, we are currently working on further improving the photocurrent imaging setup by coupling the output of a solar simulator to our Raman setup, yet the technical issues are significant.
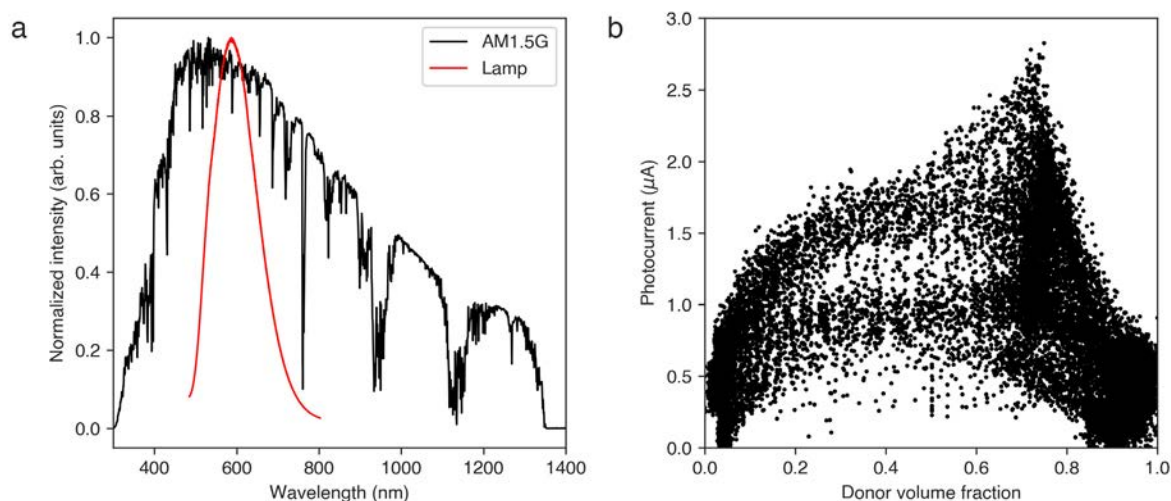
Figure S12. (a) The emission spectrum of the built-in bulb in the WITec alpha 300 RA+ microscope is compared against the standard AM1.5G irradiance spectrum. Note that the irradiance spectrum of the lamp was obtained upon reflection on a silver mirror. (b) The photocurrent measured under white light illumination in PBDT-TPD:PNDI-T solar cells shows a sharp performance peak at ca. 70-75 vol% content of donor, thus closely matching the results shown in the main text under monochromatic illumination (488 nm).

References

[1]   J. C. Love, J. R. Anderson, G. M. Whitesides, *MRS Bull.* **2001**, *26*, 523.

[2]   J. R. Anderson, D. T. Chiu, R. J. Jackman, O. Cherniavskaya, J. C. McDonald, H. Wu, S. H. Whitesides, G. M. Whitesides, *Anal. Chem.* **2000**, *72*, 3158.

[3]   P. Carrière, *Phys. Fluids* **2007**, *19*, 118110.

[4]   C.-Y. Lee, W.-T. Wang, C.-C. Liu, L.-M. Fu, *Chem. Eng. J.* **2016**, *288*, 146.

[5]   C.-Y. Lee, C.-L. Chang, Y.-N. Wang, L.-M. Fu, *Int. J. Mol. Sci.* **2011**, *12*, 3263.

[6]   A. I. Shallan, P. Smejkal, M. Corban, R. M. Guijt, M. C. Breadmore, *Anal. Chem.* **2014**, *86*, 3124.

[7]   J. M. Cabot, E. Fuguet, M. Rosés, P. Smejkal, M. C. Breadmore, *Anal. Chem.* **2015**, *87*, 6165.

[8]   J. Alstrup, M. Jørgensen, A. J. Medford, F. C. Krebs, *ACS Appl. Mater. Interfaces*

2010, *2*, 2819.

[9]   P. Tabeling, *Introduction to Microfluidics*, Oxford University Press, **2005**.

[10]   T. Wang, A. D. F. Dunbar, P. A. Staniec, A. J. Pearson, P. E. Hopkinson, J. E. MacDonald, S. Lilliu, C. Pizzey, N. J. Terrill, A. M. Donald, A. J. Ryan, R. A. L. Jones, D. G. Lidzey, *Soft Matter* **2010**, *6*, 4128.

[11]   N. Shin, L. J. Richter, A. A. Herzing, R. J. Kline, D. M. DeLongchamp, *Adv. Energy Mater.* **2013**, *3*, 938.

[12]   X. Rodríguez-Martínez, M. S. Vezie, X. Shi, I. McCulloch, J. Nelson, A. R. Goñi, M. Campoy-Quiles, *J. Mater. Chem. C* **2017**, *5*, 7270.

[13]   A. Sánchez-Díaz, X. Rodríguez-Martínez, L. Córcoles-Guija, G. Mora-Martín, M. Campoy-Quiles, *Adv. Electron. Mater.* **2018**, *4*, 1700477.

[14]   A. Harillo-Baños, X. Rodríguez-Martínez, M. Campoy-Quiles, *Adv. Energy Mater.* **2020**, *10*, 1902417.

PAPER V

Efficient Exploration of the Composition Space in Ternary Organic Solar Cells by Combining High-Throughput Material Libraries and Hyperspectral Imaging

A. Harillo-Baños, X. Rodríguez-Martínez, M. Campoy-Quiles, *Adv. Energy Mater.* **2020**, *10*, 1902417.
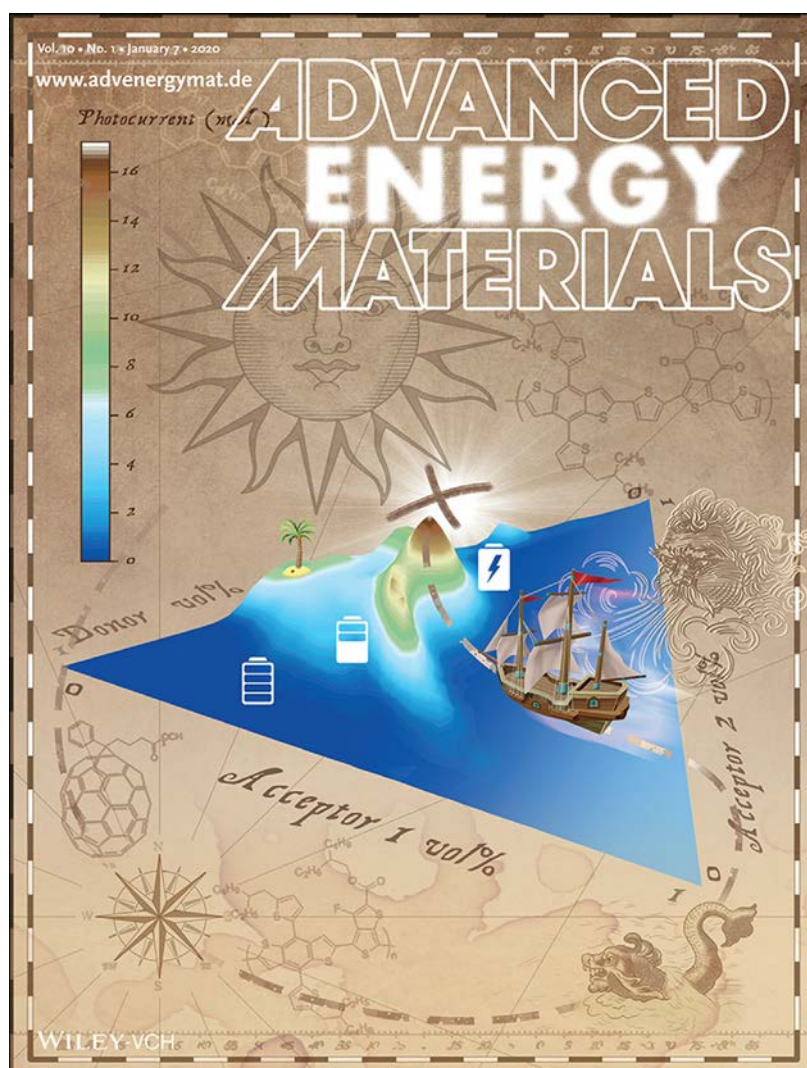
Efficient Exploration of the Composition Space in Ternary Organic Solar Cells by Combining High-Throughput Material Libraries and Hyperspectral Imaging

Albert Harillo-Baños, Xabier Rodríguez-Martínez, and Mariano Campoy-Quiles*

Organic solar cells based on ternary active layers can lead to higher power conversion efficiencies than corresponding binaries, and improved stability. The parameter space for optimization of multicomponent systems is considerably more complex than that of binaries, due to both, a larger number of parameters (e.g., two relative compositions rather than one) and intricate morphology–property correlations. Most experimental reports to date reasonably limit themselves to a relatively narrow subset of compositions (e.g., the 1:1 donor/s:acceptor/s trajectory). This work advances a methodology that allows exploration of a large fraction of the ternary phase space employing only a few (<10) samples. Each sample is produced by a designed sequential deposition of the constituent inks, and results in compositions gradients with ≈5000 points/sample that cover about 15%–25% of the phase space. These effective ternary libraries are then colocally imaged by a combination of photovoltaic techniques (laser and white light photocurrent maps) and spectroscopic techniques (Raman, photoluminescence, absorption). The generality of the methodology is demonstrated by investigating three ternary systems, namely PBDB-T:ITIC:PC$_{70}$BM, PTB7-Th:ITIC:PC$_{70}$BM, and P3HT:O-IDFBR:O-IDTBR. Complex performance-structure landscapes through the ternary diagram as well as the emergence of several performance maxima are discovered.

1. Introduction

Organic solar cells (OSCs) show increasing potential, recently achieving over 16% power conversion efficiencies (PCEs) for single-junction devices.[1] OSCs are a versatile technology due to their solution processability, compatibility with low cost roll-to-roll production, flexibility, lightweight, and aesthetically tunable properties,[2] which makes them appealing when compared to their inorganic counterparts.

Different strategies are being followed in order to improve the initially low PCE of OSCs, such as the synthesis of novel materials including low bandgap donor polymers and non-fullerene acceptors (NFAs); deeper understanding and control of the active layer morphology through side-chain engineering; improved hole- and electron-extracting interlayers;[3] multi-junction devices (tandem structures),[4] etc. Among them, the ternary bulk heterojunction (BHJ) has emerged as an efficient route to improve the photovoltaic performance of single-junction OSCs. In a ternary OSC, three materials are used in the active layer of the OSC instead of the original BHJ binary blend (donor:acceptor, D:A).[5,6] In most cases, the ternary consists of either one donor and two acceptors (D:A$_1$:A$_2$) or two donors and one acceptor (D$_1$:D$_2$:A). Ternary blends often result in improved performance of one or more of the photovoltaic parameters in the OSC compared to the corresponding binaries, thus increasing the final PCE.[7,8] While a full understanding of ternaries is yet to be developed, a number of mechanisms have been identified to contribute to this improvement. These include the increase in light harvesting by broadening of the absorption spectrum through the use of materials with complementary absorption spectra; a more efficient exciton dissociation and better charge carrier transport due to the formation of cascade energy levels; improved photocurrent due to tailored phase separation landscape and improved stability by lock-in microstructure; and enhanced open circuit voltage due to an effective alloying effect.[9–14]

Indeed, some ternary OSCs are among the best performing devices reported to date.[15] The performance of ternary OSCs depends greatly on several parameters that must be taken into account and optimized. The choice of donor and acceptor materials forming the active layer, its blending ratio and the final film thickness are just a few, and they require careful optimization to achieve the most favorable nanomorphology in the ternary BHJ layer.[12,16] The composition ratio affects the phase separation and crystallinity of the materials, ultimately modifying the electrical transport properties and the final PCE of the OSC.[17]

The most conventional optimization protocol in ternary OSCs relies on the fabrication of tens of samples, which is extremely tedious and resources-consuming. The composition

A. Harillo-Baños, X. Rodríguez-Martínez, Dr. M. Campoy-Quiles
Institut de Ciència de Materials de Barcelona (ICMAB-CSIC)
Carrer dels Til·lers s/n
Campus UAB, Bellaterra 08193, Spain
E-mail: mcampoy@icmab.es

**ADVANCED
SCIENCE NEWS**

www.advancedsciencenews.com

**ADVANCED
ENERGY
MATERIALS**

www.advenergymat.de

phase space is 2D, exponentially increasing the number of samples needed for a comprehensive study of the ternary system compared to binaries.[18] As a result, the vast majority of research done in ternary OSCs only partially explores the ternary composition phase space. Indeed, the most common strategy consists of keeping the total D:A ratio fixed (typically at 1:1), while varying the relative composition of the two materials that have the same electronic character, i.e., D:$(A_{1,x}, A_{2,(1-x)})$ or $(D_{1,x}, D_{2,(1-x)})$:A.[7,9,17] Nevertheless, there is no evidence, nor a fundamental principle, suggesting that the optimum blending ratio should be found along the 1:1 D:A composition trajectory.[12] In fact, many binary systems characterized by unbalanced transport or optical properties show optimum compositions far from the 1:1 ratio. Similar arguments could also be applicable to ternaries.[9,12,15] Moreover, since the optimization process typically performed is very limited, the absolute optimum performance might still remain unknown, which opens the possibility for an even greater improvement than what was initially thought and reported. There may even be more than one maximum in the composition phase space. The challenge, then, becomes finding a methodology that enables exploring the ternary phase space in an efficient fashion.

For the simpler case of BHJ binary blends, the optimum composition ratio lies along a 1D line, i.e., somewhere in between 1:0 and 0:1 D:A ratios. A discrete and limited exploration of the optimum blending ratio in a single binary blend requires the fabrication of several devices; the efficiency optimization requires simultaneously optimizing the active layer thickness for each composition, thus rapidly scaling up the number of samples required for evaluating a binary system. For this kind of complex multiparametric problems, we have recently proposed alternative approaches based on the high-throughput screening of BHJ binary systems and bilayered heterojunction devices.[19,20] The main concept of these methodologies is the fabrication of samples with gradients in the parameters of interest, and then imaging the performance over the gradient to locate the optimum conditions.

Inspired by the success of that work, here we present a novel methodology to perform high-throughput processing and evaluation of the performance in ternary BHJ OSCs. The methodology minimizes the use of samples and resources by fabricating large-area devices with lateral composition gradients which are equivalent to a large library of homogeneous samples. The fabrication of the samples is based on a layer-by-layer or sequential deposition of the active layer materials by means of blade coating.[21,22] All three materials are dissolved in individual solutions without the need for premixing them and deposited sequentially along different coating directions and with effective thickness gradients. The realization of orthogonal and lateral thickness gradients allows the creation of a broad library of blending ratios in a single sample, covering different regions of the ternary blend diagram. These samples are then hyperspectrally imaged by using 1) Raman imaging, which serves to quantify the local composition of the blend; 2) photoluminescence (PL) imaging, to assess the degree of mixing and infer potential V_{oc} changes; 3) absorption spectra imaging, which can be connected to the local photocurrent; 4) light beam induced current (LBIC), using monochromatic laser beams to extract the local photocurrent and being able to address the different materials

separately, at least in part, by changing the excitation wavelength when the materials exhibit non-overlapping absorption spectra; and 5) white light beam induced current (WhiteBIC) to correlate the local photocurrent with a more realistic performance in Sun operating conditions. The combination of these large datasets, which are acquired colocally using the same setup, reveals a complicated performance landscape including, in some cases, the emergence of more than one photocurrent maximum. We apply this machinery to three different D:A_1:A_2 ternary blends, namely, PBDB-T:ITIC:$PC_{70}BM$; PTB7-Th:ITIC:$PC_{70}BM$; and P3HT:O-IDFBR:O-IDTBR. Our results indicate that the usual strategies followed to optimize blending ratios in ternary blends, such as keeping fixed the total D:A ratio in the ternary blend, might lead to incomplete conclusions with underestimated performances. This finding is highly relevant for the ternary BHJ technology as it suggests that PCEs can be boosted even further by fully exploring the composition landscape.

2. Optical Characterization: Raman Imaging of Ternary BHJ Blends

2.1. General Considerations and Requirements

Currently, the realization of panchromatic active layers is feasible given the low bandgap nature of conjugated polymers (**Figure 1**c) and the bandgap tuning capability of conjugated small molecules (Figure 1d), specially the new generation of NFAs such as ITIC. Therefore, we have decided to investigate three different D:A_1:A_2 blends in the active layer: PTB7-Th:ITIC:$PC_{70}BM$; PBDB-T:ITIC:$PC_{70}BM$; and P3HT:O-IDFBR:O-IDTBR. The first two combinations are expected to maximize the absorption as they combine a low bandgap polymer (PTB7-Th or PBDB-T) with the low bandgap and highly absorbing ITIC, together with the UV-absorbing $PC_{70}BM$ which could help in harvesting shorter wavelength photons while improving the morphology of the film.[23,24] On the other hand, the ternary blend P3HT:O-IDFBR:O-IDTBR represents a paradigmatic example of complementary absorption that has recently been demonstrated to yield PCEs as high as 7.7%, which is a promising value given the low cost associated to the mass production of such active layer materials.[17]

The determination of the local composition of inhomogeneous blend films by means of Raman spectroscopy underpins our high-throughput methodology.[19,20,25] This technique enables the use of gradients produced from solution with moderate spatial control. It imposes certain restrictions, however, in the materials to be tested, which we need to pre-evaluate for the selected ternaries. First, all materials should be clearly distinguishable in terms of their vibrational fingerprint. In this sense, the heterogeneity of the conjugated backbones in organic semiconductors translates into peak-rich and characteristic vibrational spectra, mainly in the spectral window associated to C=C and C—C stretching modes (≈ 1200–1600 cm^{-1}).[25] Figure 1a depicts the vibrational Raman spectra of three different donor materials, namely PBDB-T (*aka* PCE12), PTB7-Th (*aka* PCE10), and the workhorse *p*-type polymer RR-P3HT. Figure 1b illustrates the Raman vibrational fingerprint of four different conjugated small molecules used as electron transporting materials: a fullerene acceptor, $PC_{70}BM$; and three

**ADVANCED
SCIENCE NEWS**

www.advancedsciencenews.com
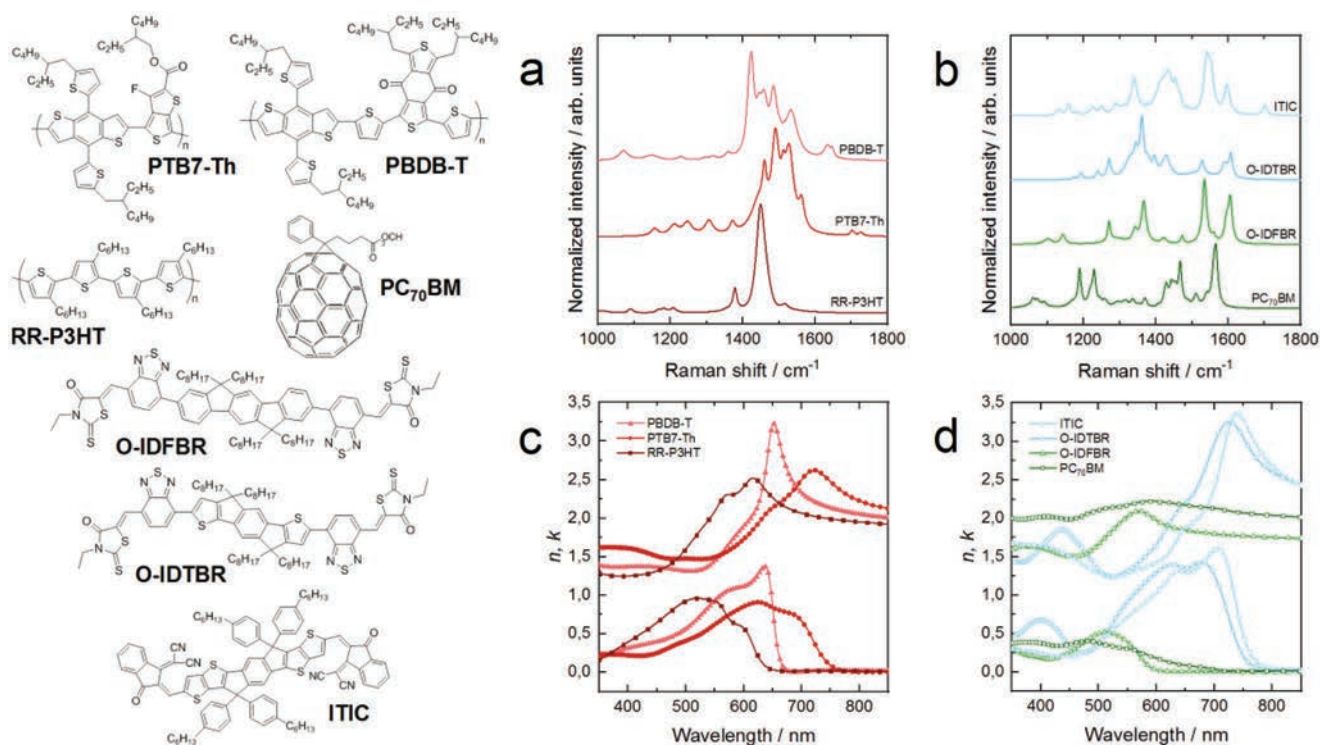
**ADVANCED
ENERGY
MATERIALS**

www.advenergymat.de

Figure 1. (Left) Chemical structures of the organic conjugated donor and acceptor materials used in this work. (Right) a) Normalized Raman spectra of donors and b) acceptors at 488 nm excitation. c) Refractive indices measured by means of variable-angle spectroscopic ellipsometry (VASE) of organic donors and d) organic acceptors.

NFAs, ITIC, O-IDTBR, and O-IDFBR. A thorough inspection of this vibrational library indicates that all possible ternary combinations should be, in principle, clearly identified. The Raman fingerprinting capability does not, hence, represent an important restriction in this sense (see also Ref. [25]).

Additionally, a successful analysis of ternary blend films requires the Raman cross-section of the materials to be similar enough to properly deconvolute the spectra and enable an accurate quantification of the composition of the film; otherwise, the large Raman intensity ratio between dissimilar materials might hinder or even impede a proper deconvolution.[20,25] **Table 1** summarizes our experimentally deduced Raman cross-section for the seven materials employed, a

Table 1. List of Raman cross-section ratios with respect to that of $PC_{70}BM$ at 488 nm excitation for the donor and acceptor materials used in this work. The Raman mode frequencies to which the Raman cross-sections are referred to and the reference spectra normalized by are also included.

Material	Raman cross-section	Raman band [cm^{-1}]
RR-P3HT	57 ± 11	1450
PBDB-T	5 ± 1	1424
PTB7-Th	2.4 ± 0.3	1490
O-IDFBR	9 ± 1	1535
O-IDTBR	4 ± 1	1361
ITIC	1.2 ± 0.3	1540
$PC_{70}BM$	1	1557

determination that requires previous knowledge of the complex refractive index of each material (see Figure 1) and the measurement of the thickness-dependent Raman signal using a sample with a thickness wedge.[25] Following our previous accuracy estimates, only those blends including RR-P3HT as donor and either ITIC or $PC_{70}BM$ as acceptor(s) would be problematic due to its cross-section ratio being larger than 30.[25] Note that the Raman cross-sections and refractive indices only need to be measured once per material, and can be also taken from literature.

2.2. Quantification of the Volumetric Composition in Ternary Blends

We have recently demonstrated that Raman spectroscopy constitutes a powerful tool for the mapping of film features such as thickness and composition by properly deconvoluting and quantifying the scattered Raman intensity.[19,20,25] The approach applies even to active layers in working devices as the thickness and complex refractive indices of the interlayers are considered in the transfer matrix modeling. So far, the methodology has been applied to binary BHJ blends as well as evaporated bilayer OSCs.[19,20] Nevertheless, the extension to BHJ ternary blends is straightforward as the third component is added as an extra term in the corresponding scattered field intensity calculations

$$I_{R,blend}(d, v_u, \omega) \propto \int_0^d |E_R(x, v_u)|^2 dx \sum_{u=1}^{3} v_u \, \sigma_{R,u} \, I_{ref,u}(\omega) \qquad (1)$$

**ADVANCED
SCIENCE NEWS**

www.advancedsciencenews.com

**ADVANCED
ENERGY
MATERIALS**

www.advenergymat.de

where d stands for the thickness of the blend film; ν_u is the volumetric fraction of the u-th component; ω refers to the frequency or Raman shift; and $I_{\mathrm{ref},u}$ represents the reference Raman vibrational fingerprint of the u-th component normalized at the intensity of the mode associated with the cross-section $\sigma_{R,u}$ (see Table 1). The transfer matrix calculation computed to get the scattered intensity term, $|E_R(x,\nu_u)|^2$, depends on both the blend film thickness and its volumetric composition. The film thickness modulates the scattered intensity, while the volumetric blending ratio is assumed to weight the complex refractive index of the film as $\varepsilon_{\mathrm{blend}} = \sum_{u=1}^{3} \nu_u\, \varepsilon_u$.

In the case of ternary blends with complementary absorption profiles the Raman scattered intensity at 488 nm excitation sharply oscillates as a function of the active layer thickness, reaching the absolute maximum at $\approx$60–70 nm of film thickness; this is a consequence of the large oscillator strength exhibited throughout the visible regime in this sort of blends and also due to the interference enhancement of the metallic back electrode encountered in the functional device.[25] This fact constrains the accessible range and reliability of thickness values characterized by means of Raman spectroscopy to a window that is usually far from the optimum in OSCs ($\approx$100–110 nm). Furthermore, the estimation of the complex refractive index in ternary blends as a weighted linear combination of the pristine indices might be too simplistic considering the morphological changes upon mixing.[26] This could be especially problematic when blending materials with large extinction coefficients in pristine films, such as PBDB-T, ITIC, or O-IDTBR (Figure 1), thus adding extra uncertainty to the transfer matrix calculations.

On the other hand, while the optical constants are highly dependent on the environment and surroundings of the embedded optical transition dipoles, we expect the Raman cross-sections, which respond to local vibrations of the conjugated backbone, to be much less affected upon blending. Based on these assumptions we simplified the Raman spectral modeling by substituting the transfer matrix integral by a free parameter, β, that weights the summation of the reference spectra, such that

$$I_{R,\mathrm{blend}}\left(\beta,\nu_u,\omega\right) \propto \beta \sum_{u=1}^{3} \nu_u\, \sigma_{R,u}\, I_{\mathrm{ref},u}\left(\omega\right) \qquad (2)$$

Equation (2) enables the determination of local composition but not thickness. Note that in Equation (2), we have implicitly calculated and measured the Raman intensity versus film thickness dependence of the pristine materials to obtain their corresponding Raman cross-sections (see Ref. [25]), so the interference nature is taken into account in part. This determination was performed using their pristine optical constants as inputs in the transfer matrix calculation.

Interestingly, we have observed that in all types of D:A_1:A_2 blends explored in this work the corresponding vibrational fingerprints are somehow shifted with respect to our tabulated and reference Raman spectra obtained in pristine films (vide infra). The (blue) shift is especially pronounced in the case of donor polymers, a fact that is related with a decrease of π-electron delocalization due to shortened conjugation length and the increase of intermolecular interactions.[27] In blended films, the blue shifting is usually related to a larger miscibility of the

materials involved and partial aggregation of the acceptor small molecules. Therefore, an extra degree of freedom is added to improve the goodness of fit, namely, a small rigid shift of the Raman peaks, δ_u, finally yielding

$$I_{R,\mathrm{blend}}\left(\beta,\nu_u,\omega,\delta_u\right) \propto \beta \sum_{u=1}^{3} \nu_u\, \sigma_{R,u}\, I_{\mathrm{ref},u}\left(\omega + \delta_u\right) \qquad (3)$$

Note that, experimentally, δ_u is < 0.5% the value of ω. We have systematically observed that for the different samples and material combinations studied here, the model summarized in Equation (3) leads to significantly improved fits of the experimental data compared to the rigorous case in Equation (1). We show in Figure S1, Supporting Information, a comparison of these three methods in the fit of a ternary sample with gradients. Equation (3) model has the virtue of making fewer assumptions regarding the similarity of the structure in the pristine materials and their corresponding blends. Indeed, we will show below that imaging δ_u for the vibrations corresponding to each material provides useful insights into the degree of mixing and/or purity of the structural domains. An additional analysis of the sources of uncertainty in the determination of compositions can be found in the Supporting Information.

3. Generation of Ternary Blend Libraries

The high-throughput screening of ternary blends requires the generation of blend composition libraries covering the largest possible area in the ternary diagram. This should be realized using the minimum number of samples (i.e., time and resources) in combination with rapid characterization techniques to be truly effective and high-throughput experimentation. We have recently demonstrated that, for binary D:A blends, it is possible to cover the entire composition range (from 1:0 to 0:1) in a single large-area solar cell by blade coating two nearby drops of the pristine solutions.[19] The processing results in films showing lateral composition and thickness gradients when combined with accelerated blade coating. Their ulterior characterization by means of Raman spectroscopy mapping and LBIC yields, in a single run, the active layer parameters (thickness and composition) which maximize the photovoltaic performance. For the generation of ternary blend composition libraries, we first tried to adapt our previous experience on the generation of binary composition gradients.[19] We explored the coating of nearby drops atop a solid dried film, which resulted in limited and localized composition ratios in the ternary diagram. We therefore, explore a number of different deposition approaches which included multiple drops and sequential deposition. Among the variety of approaches we tested, we found that the sequential (or layer-by-layer) deposition of films yielded the more complete and reproducible ternary libraries. The details of this approach are described in the following paragraphs.

Ternary blend libraries are obtained by processing the active layer as a sequential deposition of each of the pristine solutions (D, A_1, and A_2), one on top of the other, while using the same solvent and processing parameters (stage temperature and blade speed). Interestingly, the sequential deposition using non-orthogonal solvents does not lead to the detachment of

**ADVANCED
SCIENCE NEWS**
www.advancedsciencenews.com

**ADVANCED
ENERGY
MATERIALS**
www.advenergymat.de

the underneath layers but to a vertical intermixing and gradual vertical segregation in some cases. This approach is also known as layer-by-layer deposition and has recently been demonstrated to yield an optimized vertical phase segregation in some polymer:NFA binary OSCs when the devices are processed in accordance with their vertical architecture, i.e., with the donor (acceptor) layer facing the anode (cathode).[21,28]

Our exploration regarding $D:A_1:A_2$ blends indicates that the layer coating order matters to realize proper ternary active layer film libraries. The processing must start with the donor (polymer) first, followed by the acceptors (small molecules) in sequential layers. We hypothesize this requirement is related with the viscosity of the polymeric solution, which turns out to be critical when the donor is casted in second or third place. In such cases, we do not observe a significant exploration of the ternary composition diagram but the formation of either binary blends (when the polymer is deposited in second place) or even to the absence of blending (when the polymer is deposited in the last place), as evidenced from Raman scattering measurements.

The importance of viscosity is apparent for ternary combinations of the type $D_1:D_2:A$, containing two donor polymers and a small molecule acceptor. Figure S2, Supporting Information, shows the ternary phase diagram for one such sample, consisting of the $P3HT:PCDTBT:PC_{70}BM$ ternary. More than 80% of the composition space can be explored in a single sample by properly matching the ink viscosities and casting parameters.

Therefore, after first coating the donor polymer layer, we proceed with the sequential coating of the acceptor layers. These layers are processed by spreading the pristine solutions from collateral corners of the large aspect-ratio, 75 mm long by 25 mm wide, indium tin oxide (ITO) substrates we use as transparent conductive electrode (see **Figure 2**). By setting up the blade coating process to start at a sharp substrate corner we obtain a

rather controllable thickness gradient driven by the variation of the wetting front width as the blade moves over the substrate. Experimentally this is an appealing approach to obtain gradients as it simply requires rotating the substrate by 45° with respect to the coating direction to get the steepest thickness gradient. Hence, by combining in a single sample the layer-by-layer deposition consisting of a homogeneous polymer film followed by two different small molecule acceptors blade coated from collateral corners, we explore a large area of the ternary composition diagram, as depicted in Figure 2a. The region explored can be tuned, at least in part (either I, II, or III in Figure 2a) depending on the thickness of the layers, which is mainly determined by the solution weight loading and the coating speed. In fact, we checked that by blade coating the first polymer layer in the form of a lateral thickness gradient (by accelerating the blade speed) we could purposely extent the range of donor loading explored in the ternary diagram (Figure 2b).

4. Ultrafast Characterization of Ternary Libraries

Figure 3 illustrates a set of the raw mapping data extracted from a single ternary sample of $PTB7-Th:PC_{70}BM:ITIC$ processed according to the thickness gradient method depicted in Figure 2b. In this case, a PTB7-Th thickness gradient was deposited from left ([−20, y] coordinates in Figure 3a) to right ([25, y]); then a pristine solution of $PC_{70}BM$ was casted in diagonal from the top-left corner ([−20, 0]); and finally the ITIC layer was processed from the top-right corner of the sample ([25, 0]).

In order to minimize measuring time, we begin by performing a coarse (low-resolution, 45 × 25 positions) photocurrent map with white light illumination (Figure 3a) which takes less than 15 min to complete for a large area of 45 × 25 mm². This coarse photocurrent map is intended to quickly identify and locate the high performing areas of the device, thus the region of interest. This area is then zoomed in and imaged with higher resolution (Figure 3b) and several complementary techniques. During the acquisition of this high resolution photocurrent map, we simultaneously collect the reflectivity spectra of the full device stack (R_s) at each position. This reflection map, after normalization by the reflectivity of the back electrode (usually silver, R_{Ag}), yields the absorption (A) of the device as $A = 1 − R_s/R_{Ag}$ at each position. Absorption maps at selected wavelengths are shown in Figure 3f,g. We then proceed with the monochromatic characterization of the device by using a 633 nm laser to measure photocurrent (Figure 3d) and at the same time PL (Figure 3e) in a single run. While less precise than electroluminescence measurements, the energy of the PL maximum can be correlated in some cases with the charge transfer energy, and thus used as a proxy for effective *local* V_{oc} (Figure S3, Supporting Information).[29] PL quenching could also be correlated with efficient charge transfer and thus, with the degree of mixing. Finally, we colocally measure the Raman scattered spectra (which integrated intensity is depicted in Figure 3h) and the photocurrent at 488 nm excitation (Figure 3c). The selection of 488 nm as excitation wavelength in Raman scattering is related to the cross-section compatibility between materials, the fulfillment of resonant conditions and the absence of disturbing PL
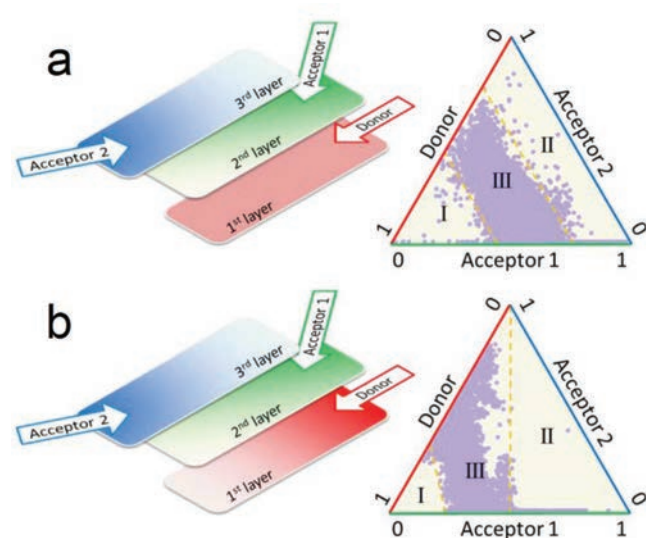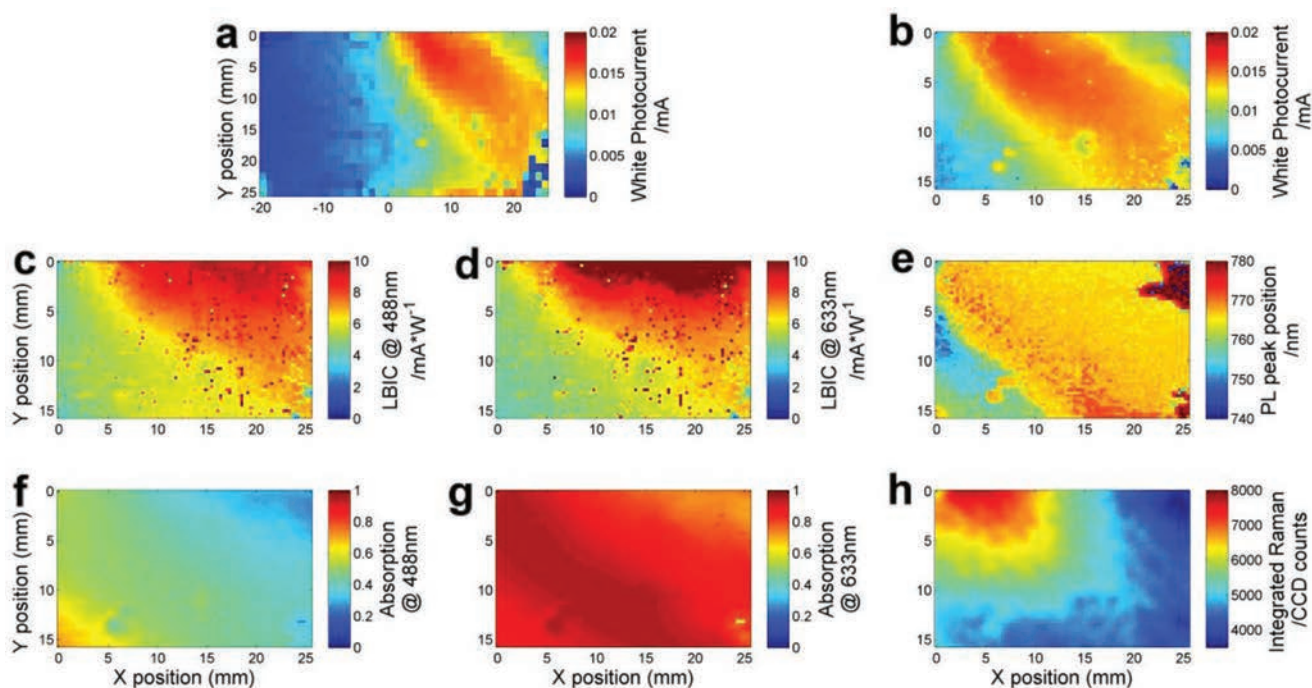
Figure 2. Sketches of the sequential blade coating deposition steps used to explore ternary blend composition diagrams for a) a homogeneous first donor layer and b) a thickness gradient as the first donor layer. The dots correspond to experimental data obtained for a RR-P3HT:O-IDFBR:O-IDTBR ternary.

**ADVANCED
SCIENCE NEWS**

www.advancedsciencenews.com

**ADVANCED
ENERGY
MATERIALS**

www.advenergymat.de

Figure 3. Full set of optical characterization maps performed in a sequentially deposited sample of PTB7-Th:PC$_{70}$BM:ITIC, with the donor layer processed as a thickness gradient. a) Coarse photocurrent map obtained with white light; b) higher resolution white light photocurrent map centered at the region of better performance; c) photocurrent map acquired at 488 nm excitation; d) photocurrent map acquired at 633 nm excitation; e) wavelength of the main PL peak measured at 633 nm excitation; f) absorption at 488 nm excitation wavelength; g) absorption at 633 nm excitation wavelength; h) integrated Raman scattered intensity from 1100 to 1600 cm^{-1} at 488 nm excitation.

backgrounds which could potentially hinder the deconvolution of the spectra.[25] The complete set of optical characterization images includes two low resolution images, three 3D images (photocurrent with typically 86 × 50 spatial points each) and three 4D images (Raman, absorption, and PL spectra (86 × 50) points × 1024 spectral points), which add up to more than 13 million experimental data points. All these measurements are performed in a row and using a single (confocal Raman) setup in less than 3 h, thus representing a paradigmatic example of high-throughput evaluation of solar cells.

The white light photocurrent maps (Figure 3a,b) are acquired using the built-in lamp in our confocal Raman scattering setup, which due to technical limitations cannot be coupled to an external illumination source, such as an AM1.5 solar simulator. Even so, the emission spectrum of the lamp spans most of the visible/NIR range (Figure S4, Supporting Information), thus we expect the corresponding photocurrent maps being qualitatively similar to what we would obtain using a dedicated light source, albeit somehow UV and NIR poor, thus slightly underestimating the photocurrent of materials that absorb strongly on those regions. The importance of using broadband illumination instead of the more standard laser is apparent when comparing the WhiteBIC (Figure 3b) and LBIC at 488 nm (Figure 3c) and 633 nm (Figure 3d). The single-wavelength photocurrent maps clearly indicate that the maximum photocurrent is generated at a different location (i.e., a different active layer thickness and blend composition) with respect to what we observe with white light illumination. We could expect this type of behavior for systems with at least partially complementary absorptions in

which all materials contribute to the photocurrent: monochromatic illumination may be indicating a region rich in a material with strong absorption at that specific wavelength, rather than the real optimum of the whole cell. This result indicates that white light should be employed in order to evaluate the performance of non-fullerene binaries and ternary devices in typical operating conditions. Furthermore, our experience suggests that the use of white light illumination focused as a large spot of ≈200 μm in diameter leads to qualitatively smoother photocurrent maps, i.e., less prone to suffering spatial photocurrent fluctuations associated to scattering by defects and dust. Despite using low magnification (10X) and low numerical aperture objectives (NA 0.25), the photocurrent maps measured using monochromatic sources of light (Figure 3c,d) generally show a larger density of photocurrent spikes. This is a result of the smaller spot size (typically 10 μm in diameter) and more pronounced focusing ability of monochromatic light, which is then more likely to scatter at the tiny defects (aggregates, scratches, dust) encountered throughout the layered device stack and the substrate. We would like to emphasize that the photocurrent images are not the result of a hidden thickness variation, as the thickness and photocurrent maps do not seem to be correlated (Figure S5b, Supporting Information).

The acquisition of monochromatic photocurrent maps is, however, useful to identify the relative contribution of the blended components to the generation of free charge carriers. For the ternary blend studied in Figure 3, we expect the absorption spectrum being largely panchromatic due to the complementary absorption of its components, PTB7-Th:PC$_{70}$BM:ITIC (Figure 1).

**ADVANCED
SCIENCE NEWS**

www.advancedsciencenews.com

**ADVANCED
ENERGY
MATERIALS**

www.advenergymat.de

According to their complex refractive index, at 633 nm excitation PTB7-Th and ITIC domains should be selectively contributing to the photogeneration of excitons, while at 488 nm excitation all three materials are absorbing. Also, the overall extinction is likely to be higher at 633 nm (Figure 3g) than at 488 nm (Figure 3f) excitation due to the noticeable larger oscillator strength of PTB7-Th and ITIC at 633 nm than $PC_{70}BM$ at 488 nm excitation. Interestingly, the 633 nm LBIC follows quite closely the ITIC composition (Figure S5, Supporting Information), which is reasonable given the very high oscillator strength of this material at these photon energies (Figure 1d). The absorption map at 633 nm shown in Figure 3g correlates well with the total volumetric fraction of PTB7-Th and ITIC obtained from the quantitative analysis of the Raman scattered intensity (Figure S5d, Supporting Information). Conversely, the spatial variations observed in Figure 3f are closely matching the measured volumetric fraction map of $PC_{70}BM$ in the ternary blend (Figure S5e, Supporting information). Examples of the raw absorption, PL and Raman spectra at selected loci are given in Figure S6, Supporting Information. Interestingly, and despite the larger absorption at 633 nm, we observe that both monochromatic photocurrent maps are quantitatively similar (Figure 3c,d). The fact that the maximum white light photocurrent is displaced with respect to the monochromatic photocurrent maps and absorption maps suggests that the optimum composition results from the fine balance between optical properties and electronic transport (facilitated with increasing fullerene content). This is, for instance, reflected by the fact that the optimum composition for samples before and after annealing is different (Figure S7, Supporting Information, and discussion below).

Finally, the PL spectra (Figure S6a, Supporting Information) vary both in peak central position (Figure 3e) and in integrated intensity (Figure S5a, Supporting Information) throughout the sample. We generally observe that the PL intensity is larger in the ITIC-rich regions that are depleted of donor; in fact, the PL intensity map resembles an inverted PTB7-Th volumetric loading image. This finding confirms that PL quenching is a good proxy for efficient charge transfer. Regarding the position of the maximum in the PL spectra we notice that it slightly redshifts as the loading ratio of ITIC (PTB7-Th) is decreased (increased); conversely, the highly enriched PTB7-Th regions appear blueshifted possibly due to the fact that the PL of the polymer becomes dominant in the therein collected spectra. The redshifted PL on the highly mixed regions may be an indicative of the contribution of the charge transfer PL to the overall sample PL. If this interpretation is correct, the small PL shift (about 20 meV) in the region where photocurrent is high (Figure 3b) would suggest that the potential changes in V_{oc} throughout the composition phase diagram are relatively small (<3%) compared to the large photocurrent changes. In other words, the PCE of the ternary will probably be dominated by photocurrent changes, and thus Figure 3b would represent well the cell efficiency.

5. Performance Phase Diagram in Ternary Systems

The colocal acquisition of the characterization maps illustrated in Figure 3 and Figure S5 (Supporting Information) enables

the removal of their spatial dependence. Therefore, the relevant parameters can be plotted in ternary composition diagrams by matching them with the composition maps extracted by means of Raman imaging spectroscopy (Figure S5, Supporting Information). **Figure 4** depicts the corresponding diagrams for two different and thermally annealed PTB7-Th:ITIC:$PC_{70}BM$ devices. In the two samples, acceptor layers were processed in different order to cover complementary areas of the diagram. Note that in these plots only the regions of highest performance were zoomed in and analyzed with increased spatial resolution.

Figure 4a depicts the local photocurrent extracted under white light illumination over the phase diagram of the ternary. We identify up to three different photocurrent maxima on a relatively smooth landscape. The first and lower one is centered at a blending ratio of PTB7-Th:ITIC:$PC_{70}BM$ 0.35:0.60:0.05 (v:v:v), which matches the single maximum we observed in the same sample prior to the annealing process (Figure S7, Supporting Information). Upon thermal annealing, a second photocurrent maximum emerges at a ratio of 0.2:0.6:0.2 (v:v:v) which is indicative of an improved film morphology motivated by the annealing process (see below). The third and markedly higher photocurrent maximum corresponds to a ratio of 0.2:0.2:0.6 (v:v:v). The first two maxima may be absorption dominated cases (ITIC exhibits high oscillator strength, see Figure 1), while the third may correspond to a ternary composition characterized by good-extraction properties. A deep minimum in performance is found for a ratio of 0.5:0.3:0.2 (v:v:v) which is observed in both samples. Interestingly, such minimum lies on the usual blending ratio scheme followed in the literature, i.e., keeping the donor loading fixed at 50%, while varying the ratio of both acceptors. We observe that the high performing areas are located in regions of low polymer loading (15–30 vol%); then, the three maxima differ in the ratio of the acceptors, being the more favorable a larger $PC_{70}BM$ loading in the present case. The reason for this dissimilar optimization blending ratios is likely to be related to the aforementioned optical versus transport compromise, together with a variable degree of phase separation and type of nanomorphology attained for each composition.[16]

In order to doublecheck the existence of two photocurrent maxima scenario in PTB7-Th:ITIC:$PC_{70}BM$ ternary blends, we have fabricated samples with fixed stoichiometry. These samples were fabricated to exhibit a thickness gradient in order to fully explore the parametric landscape. In this set of samples the donor weight fraction was kept constant at 25 wt%, while the relative acceptor loadings were varied accordingly to follow the composition trajectory that included several maxima in the ternary library (Figure 4a). The results depicted in **Figure 5**c (including two binaries and four ternary combinations) indicate that when looking at the top performing shell of devices an acute photocurrent drop occurs close to 0.25:0.35:0.40 (w:w:w) ternary ratio, resulting in two photocurrent maxima. Upon extraction of the corresponding volumetric loading ratios through Raman spectroscopy (Figure 5b) we observe that the location of the minimum and both maxima matches the previously found ratios (Figure 4a). Note that due to the dissimilar typical densities of polymers (1.0–1.1 g cm^{-3}) and small molecules (1.3–1.7 g cm^{-3}), there is a large shift between volumetric and weight loading ratios that has to be considered when interconverting such
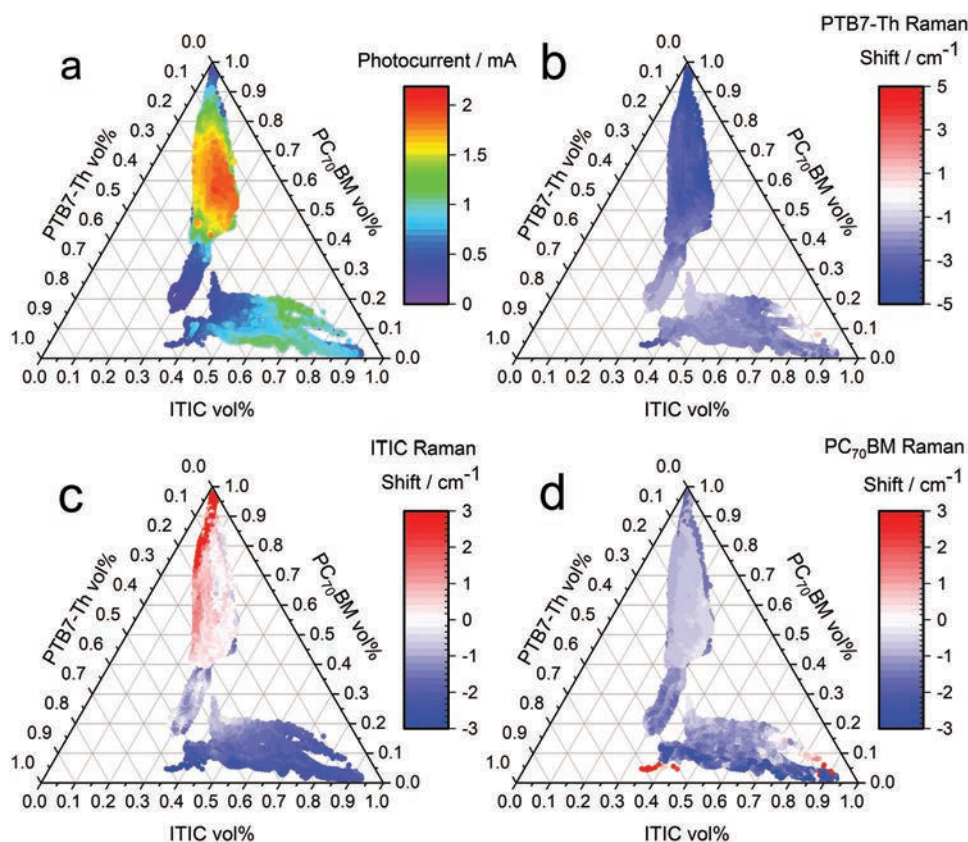
**ADVANCED
SCIENCE NEWS**

www.advancedsciencenews.com

**ADVANCED
ENERGY
MATERIALS**

www.advenergymat.de

Figure 4. Ternary composition diagrams for two ANNEALED PTB7-Th:ITIC:PC$_{70}$BM devices processed changing the coating order of the acceptor materials. The color scales refer to: a) photocurrent under white light illumination. b) Raman peak shift attributed to PTB7-Th, c) ITIC, and d) PC$_{70}$BM.

magnitudes. It is important to highlight that due to the dispersion in photocurrent induced by the active layer thickness variations (γ-axis in Figure 5c) ternary libraries might lead to incomplete performance landscapes if such parameter is not fully explored. However, this limitation can be circumvented through the complementary use of active layer thickness gradients once the optimum performance ratio is identified.

This set of stoichiometrically controlled devices serves to validate the high-throughput generation of ternary libraries as in terms of photovoltaic performance it leads to the same conclusions obtained following the traditional sample-by-sample methodology, albeit with a noticeably increased statistical meaning and reduced use of resources and time. Furthermore, we have confirmed that: i) in ternary systems multiple
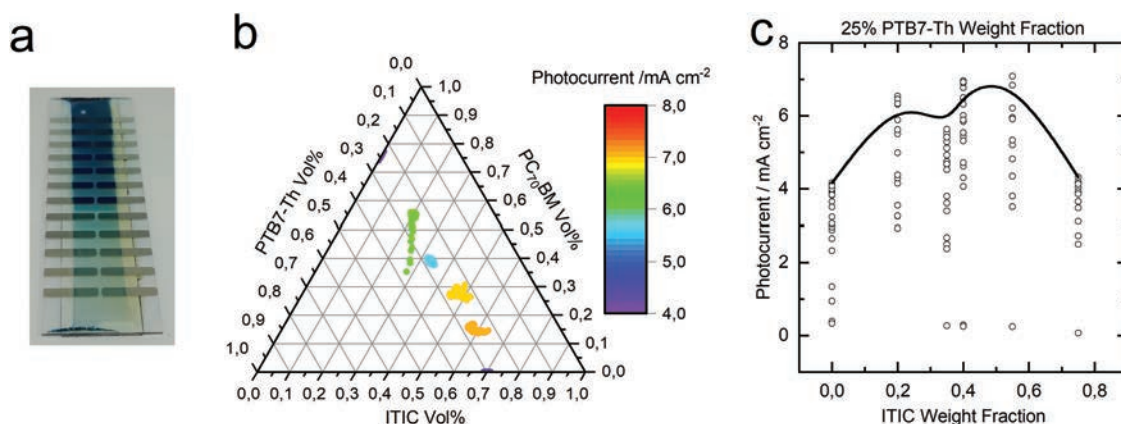
Figure 5. a) Optical image of a sample consisting of 24 different devices (12 per side) with the ternary PBT7-Th:ITIC:PC$_{70}$BM blend as active layer. The active layer was blade-coated as a lateral thickness gradient. b) Representation of the ternary composition diagram of six different samples (24 devices each, of variable thickness and fixed stoichiometric ratios), with the highest photocurrent obtained in the sample as color scale. c) Photocurrent dispersion obtained for all wedge-like samples (keeping fixed PTB7-Th loading at 25 wt%) as a function of ITIC wt%. The black line is a guide to the eye.

photocurrent maxima are feasible; ii) the thickness exploration using gradients is sufficient to capture the essence of the problem; and iii) the error in the determination of the composition using Raman is typically of the order of 5%–10%, which is an estimation based on the dispersion observed in Figure 5b for stoichiometrically controlled devices. Further details regarding the accuracy and error estimations of the Raman methodology are provided in the Supporting Information.

To gain further insights about the extent in which the film morphology is critical for the device performance, we performed further analysis of the Raman spectra, focusing now on the shifts of the corresponding vibrational modes. Raman mode shifting in conjugated polymers constitutes a phenomenon typically observed upon blending with small molecules. Depending on their degree of miscibility, the small molecules are able to intercalate throughout the polymer domains disturbing their planarity and conjugation length while affecting the intermolecular interactions. For simplicity, we perform the Raman shift analysis by assuming that the vibrational fingerprint of each material is rigidly shifted according to a corresponding δ_u parameter (see Equation (3)). In the case of PTB7-Th (Figure 4b), we notice that its vibrational bands are blueshifted with respect to the reference spectra took in pristine polymer films. Still, the shift is not as large as that observed upon degradation for the related compound PTB7,[30] thus suggesting that the observed dispersion is likely due to changes in the morphology of the film. Interestingly, the high performing areas explored in Figure 4a correlate well with large blueshifts (≈ 3 cm^{-1}) in PTB7-Th, being more pronounced at high PC$_{70}$BM loadings (≈ 5 cm^{-1}); conversely, in the low performing areas, the Raman shift of PTB7-Th vibrational bands is, in average, close to zero. These findings suggest, on the one hand, that PTB7-Th requires a thorough intermixing with the acceptors to yield an efficient splitting of the photogenerated excitons; and, on the other hand, that the miscibility of PC$_{70}$BM with PTB7-Th is larger than that of ITIC. The corresponding ternary diagrams for the Raman shift of ITIC (Figure 4c) and PC$_{70}$BM (Figure 4d) do not show a significant dispersion close to the highest photocurrent maximum, thus suggesting that purer ITIC and PC$_{70}$BM

domains coexist in this blending ratio regime. In the case of ITIC there is a moderate up shifting as its fraction in the film decreases. Consequently, the analysis of the Raman shifts in PTB7-Th:ITIC:PC$_{70}$BM blends indicates that the optimum composition corresponds to a morphology consisting of well-mixed donor:acceptor domains with about 15%–30% polymer content (large mode shifts), together with relatively pure (small mode shifts) domains of the two acceptors.

It is insightful to look at the same sample before and after annealing (Figure 4 and Figure S7, Supporting Information). A second optimum composition emerges within the phase diagram. In this case, annealing places the second optimum at higher fullerene contents, which could be a result of its more favorable steric interdiffusion through the film and subsequent improvement in the extraction of charges. An optimum composition dependent on the thermal treatment has also been observed for binary systems.

To show the generality of the high-throughput methodology, in the next series of experiments we extended the ternary blend library generation and colocal acquisition of Raman/PL/Absorption and photocurrent maps to two additional ternary blend systems, namely, PBDB-T:ITIC:PC$_{70}$BM and P3HT:O-IDFBR:O-IDTBR (see **Figure 6**). In both cases, the devices were fabricated following the procedures described above, and changing the ordering of the acceptor layers to broaden the area covered in the ternary diagrams (see the Experimental Section). The extended data for these systems can be found in Figures S8–S12, Supporting Information.

Figure 6a shows that for PBDB-T:ITIC:PC$_{70}$BM blends the highest performance corresponds to blending ratios spanning between 10 and 30 vol% of PC$_{70}$BM loading. More specifically, the photocurrent maximum locates at a blending ratio of 0.45:0.30:0.25 (v:v:v, PBDB-T:ITIC:PC$_{70}$BM). The here obtained optimum blending ratio is in very good agreement with what has been recently found in ternary spin coated devices, i.e., 0.5:0.4:0.1 (w:w:w, PBDB-T:ITIC:PC$_{70}$BM).[23] (Note that converting from volume to weight percentage can easily be done when the material densities are known) In this system, the polymer has an almost overlapping absorption with ITIC, which in turn shows in the fact that both LBIC and WhiteBIC
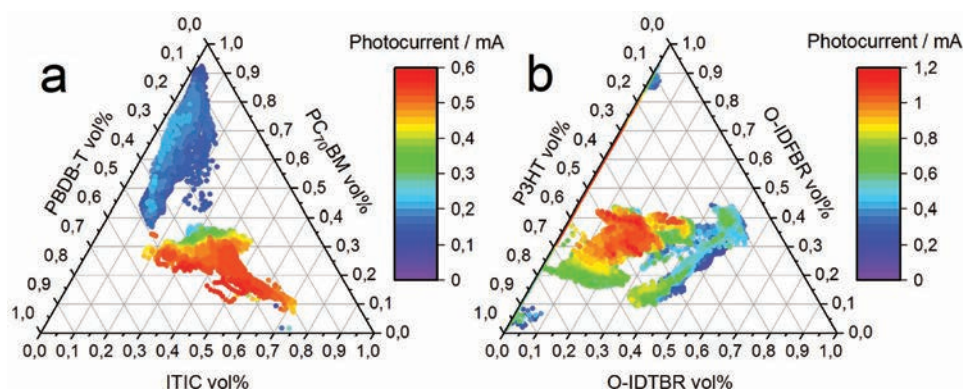

Figure 6. Ternary composition diagrams of the regions with the highest performance corresponding to a) two PBDB-T:ITIC:PC$_{70}$BM devices processed changing the coating order of the acceptor materials; and b) two RR-P3HT:O-IDFBR:O-IDTBR devices processed changing the coating order of the acceptor layers and two extra devices processed following the two-drop processing method. The color scale corresponds to the photocurrent extracted under white light illumination.
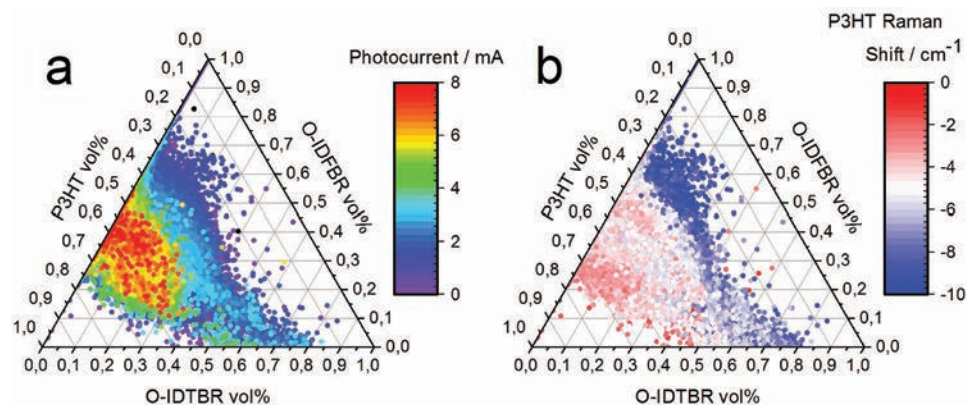
**ADVANCED
SCIENCE NEWS**
www.advancedsciencenews.com

**ADVANCED
ENERGY
MATERIALS**
www.advenergymat.de

Figure 7. Ternary composition diagrams corresponding to seven different RR-P3HT:O-IDFBR:O-IDTBR devices (≈150 000 data points per plot). The color scale corresponds to a) photocurrent at 488 nm excitation; and b) Raman peak shift of RR-P3HT.

have a similar spatial distribution (Figures S8 and S9, Supporting Information). Moreover, the contribution to the total photocurrent of relatively long wavelengths (633 nm) is larger than that of higher energies (488 nm), as seen in the corresponding LBIC maps and as expected by the corresponding absorption profiles. A series of samples with fixed stoichiometry has also been fabricated and are shown in Figure S12 (Supporting Information).

Regarding RR-P3HT:O-IDFBR:O-IDTBR blends (Figure 6b), a single white light photocurrent maximum is obtained for a ratio of 0.5:0.4:0.1 (v:v:v). This value lies relatively far from what has been previously reported for spin-coated devices, i.e., 0.5:0.15:0.35 (w:w:w).[17] P3HT has a very large Raman cross-section that can yield higher uncertainties on the composition determination compared to the other systems. The deviation from published results is, however, larger than the expected uncertainty on our composition. Therefore, we believe that the discrepancy may be related to the known factors affecting the efficiency in this system, such as molecular weight of the polymer, different attained morphologies between spin and blade coating and/or actual differences in the optimum composition depending on the specific drying kinetics associated to each processing method. Similar to the case of PTB7-Th based ternaries, which show an annealing dependence optimum composition, we believe that morphology is the most likely cause of the observed shift. Evidence supporting a strong dependence of efficiency in morphology can be extracted from the almost three times larger PL shifts (Figures S10 and S11, Supporting Information) observed in this ternary compared to the other two.

In order to gain further insights into the observed discrepancy, an additional series of RR-P3HT:O-IDFBR:O-IDTBR samples were prepared. In this case, the samples were prepared in conventional geometry (ITO/poly(3,4-ethylenedioxythiophene): poly(styrenesulfonate) (PEDOT:PSS)/ternary/LiF/Al). For this ternary, the 488 nm LBIC maps are spatially well correlated with the WhiteBIC maps (Figure S10, Supporting Information), thus both techniques should lead to the same optimum compositions. For these experiments, we chose to measure the photocurrent at 488 nm excitation as it can be measured simultaneously with the Raman image from which composition is deduced, and so is the fastest exploration possible. **Figure 7** shows the results for

a total of seven (non-annealed) RR-P3HT:O-IDFBR:O-IDTBR devices and ≈150 000 data points per plot. The large and statistically meaningful dataset included in Figure 7a yields an area of high performing blending ratios in agreement with the previous batch under white light illumination (Figure 6b). From this we conclude, first that the experiments are quite reproducible, and second, that our finding of a different maximum is not related to the sequential deposition producing large vertical phase segregation.

The Raman peak shift analysis of the RR-P3HT vibrational signature (Figure 7b) shows that the highest photocurrent occurs for moderate blueshifts (≈4–6 cm^{-1} with respect to a pristine RR-P3HT film), while both large (≈10 cm^{-1}) and small (≈0–2 cm^{-1}) blueshifts are detrimental for the device performance. Since at 488 nm excitation both crystalline and amorphous RR-P3HT domains contribute to the Raman scattered intensity,[31,32] these results indicate that the film morphology in RR-P3HT:O-IDFBR:O-IDTBR ternary blends, and more specifically the degree of crystallinity attained at the polymer domains, is critical to achieve high performance devices. Neither largely amorphous (large blueshifts) nor strongly crystalline (small blueshifts) RR-P3HT domains are favorable for the photovoltaic device performance. Instead, a tradeoff between their purity (improved percolation) and the degree of intermixing with the acceptors (improved charge separation) is needed, as suggested by the moderate blueshifts observed in the high performing areas of the phase diagram. So, it is possible that for non-annealed blade-coated devices, the degree of crystallinity of the components is hindered at the O-IDTBR rich compositions. A systematic annealing study, which goes beyond the scope of the current manuscript, would possibly help to clarify further the apparent discrepancy between our data and published data for the P3HT based ternary.

One useful observation deduced when comparing the three material systems is the fact that the high efficiency region spans over a relatively large area of the ternary phase diagram. One way to quantify this is to determine how many crossing points between composition lines are included in the red area of each sample: between two and five. In fact, the whole ternary surfaces are relatively smooth. In other words, if one explores the ternary phase diagram with 10% steps in relative composition, there are good chances to find at least two

ADVANCED
SCIENCE NEWS

www.advancedsciencenews.com

ADVANCED
ENERGY
MATERIALS

www.advenergymat.de

samples close to the absolute maximum. A rational, resource saving, approach for optimizing ternary blends would then commence by exploring the phase space in 20% steps, which would result in four samples of one binary, another four samples of the other binary, and six ternaries. The ternaries should, however, be equally spaced in the phase diagram rather than following the D:A 1:1 trajectory. This exploration would define the region of interest for a zoomed in second round with six extra devices. A total of 20 devices would then be sufficient for a first evaluation of the potential of a new ternary. While our approach, which would use around four samples to cover the whole phase space, is more accurate and statistically meaningful, the 20 devices approach has the advantage that can be implemented in most labs working on the field.

Finally, we would like to remark that, clearly, in this first manuscript we have not fully explored all the information hidden within the large amount of data points and colocal measurements. These large, self-consistent, varied and statistically meaningful datasets might be of use for data science studies, and therefore we have made it available at the CSIC repository for other researchers to use freely (http://hdl.handle.net/10261/194041).

6. Conclusion

We have introduced a solution-based methodology to produce large libraries of organic solar cells that effectively explore the ternary phase diagram. Each sample covers ≈15%–25% of the composition space with typically close to 5000 different composition/thickness values. Colocal hyperspectral images of such samples, which produced millions of data points, enables the correlation of performance with composition as well as local morphology. In particular, we show that Raman shifts are a useful tool to address the degree of mixing and purity of domains. Importantly, this broad exploration of the phase diagram enables the determination of the composition (and number) of performance maxima, which we find to sometimes lie outside the conventionally targeted D:A 1:1 trajectory. Our results were in relatively good agreement with a large series of devices fabricated with fixed composition. This type of high-throughput evaluation is, therefore, a very useful and timely contribution that will help to identify absolute performance maxima in promising multicomponent solar cells. Interestingly, the large body of data produced can open the possibility to use data science techniques in the development of solar cells through the availability of coherent and statistically meaningful data sets.

7. Experimental Section

Materials: Regioregular poly(3-hexylthiophene-2,5-diyl) (RR-P3HT) with average molecular weight of 20–45 kDa was purchased from Sigma-Aldrich, Lot# MKCD8731. Poly[(2,6-(4,8-bis(5-(2-ethylhexyl) thiophen-2-yl)-benzo[1,2-b:4,5-b']dithiophene))-alt-(5,5-(1′,3′-di-2-thienyl-5′,7′-bis(2-ethylhexyl)benzo[1′,2′-c:4′,5′-c']dithiophene-4,8-dione)] (PBDB-T), Lot# YY12062; (5Z,5′Z)-5,5′-(((4,4,9,9-tetraoctyl-4,9-dihydro-s-indaceno[1,2-b:5,6-b']dithiophene-2,7-diyl)bis(benzo[c][1,2,5]thiadiazole-7,4-diyl))bis(methaneylylidene))bis(3-ethyl-2-thioxothiazolidin-4-one)

(O-IDTBR), Lot# DW4035P; (5Z,5′Z)-5,5′-(((6,6,12,12-tetraoctyl-6,12-dihydroindeno[1,2-b]fluorene-2,8-diyl)bis(benzo[c][1,2,5]thiadiazole-7,4-diyl))bis(methaneylylidene))bis(3-ethyl-2-thioxothiazolidin-4-one) (O-IDFBR), Lot# YY12073; and 3,9-bis(2-methylene-(3-(1,1-dicyanomethylene)-indanone))-5,5,11,11-tetrakis(4-hexylphenyl)-dithieno[2,3-d:2′,3′-d']-s-indaceno[1,2-b:5,6-b']dithiophene (ITIC), Lot# YY12073, were obtained from 1-Material. Poly[4,8-bis(5-(2-ethylhexyl)thiophen-2-yl)benzo[1,2-b;4,5-b']dithiophene-2,6-diyl-alt-(4-(2-ethylhexyl)-3-fluorothieno[3,4-b]thiophene-)-2-carboxylate-2-6-diyl)] (PTB7-Th), batch M261; [6,6]-Phenyl-C71-butyric acid methyl ester (PC$_{70}$BM); as well as the indium tin oxide (ITO) substrates were purchased from Ossila. PEDOT:PSS was purchased from Heraeus. The ZnO nanoparticles dispersion was obtained from Avantama.

Sample Preparation: All materials were dissolved in chlorobenzene (CB), in a concentration range of 10–15 mg mL⁻¹ for the acceptors, and 15–20 mg mL⁻¹ for the donor polymers. Two opposite corners of the ITO coated substrates were etched with diluted HCl and solid Zn, to electrically isolate them and obtain one top and one bottom electrode per side. Then the substrates and cut glasses for encapsulation were cleaned by consecutive sonication baths in acetone, soap, isopropanol (5 min each), and sodium hydroxide 10 vol% (10 min), rinsing with DI water after each step. The top transport layer, either PEDOT:PSS or ZnO depending on the device architecture, was deposited using an automatic blade coater Zehntner ZAA 2300 with an aluminum applicator Zehntner ZUA 2000, in air conditions and at a constant speed of 5 mm s⁻¹. The drop volume used was 100 µL for PEDOT:PSS and 50 µL for ZnO. The temperature was set to 60 and 40 °C for PEDOT:PSS and ZnO, respectively. All active layer materials were deposited using a second blade coater equipment (same brand and model) that included custom-made electronics to enable speed gradients, inside a nitrogen-filled and dry glove box, at 80 °C, while setting a blade gap of 200 µm. The drop volume used was 50 µL for the donor polymer in the first layer, and 40 µL for the acceptors. The speed was set to 30 mm s⁻¹ for constant speed film processing, while a linearly decelerating speed ramp was configured from 90 to 10 mm s⁻¹ for the processing of a thickness gradient in the first layer as well as in the standard composition fixed devices. The bottom transport layer and electrode, either LiF/Al or MoO$_3$/Ag, were thermally evaporated at a rate of 0.1 Å s⁻¹ for the transport layer and 1 Å s⁻¹ for the electrode. Samples were encapsulated using a cut glass slide and epoxy resin, then cured with an UV lamp for 5 min. The annealing process, when done, was performed in the nitrogen-filled and dry glove box by placing the samples in a hot plate at 120 °C for 10 min.

Optical Measurements: Variable-angle spectroscopic ellipsometry (VASE) data were acquired at a minimum of three angles of incidence using a Sopralab GES-5E rotating polarizer spectroscopic ellipsometer (SEMILAB) coupled to a charge-coupled device (CCD) detector. The ellipsometric data were modeled using WinElli piece of software and the standard critical point model.

All the optical characterization measurements performed in functional devices (Raman scattering, PL, reflection, LBIC, and WhiteBIC) were acquired using a WITec alpha 300 RA+ confocal Raman setup, coupled to an Olympus objective with 10X magnification (NA 0.25). The built-in lamp of the setup was used for the white light measurements. Two lasers centered at 488 and 633 nm were employed for the Raman, LBIC, and PL measurements. The light was focused through the thick (1.1 mm), ITO-covered glass substrates and the laser power reduced accordingly to avoid photodegradation and bleaching of the active layer (3-5 mW at 488 nm excitation). Samples were placed in a motorized stage and connected to a variable gain low noise current amplifier DLPCA-200 manufactured by FEMTO Messtechnik GmbH. All raw data were collected using WITec Project FIVE piece of software, while the Raman analysis was performed using a home-made MATLAB routine following the methodology described elsewhere.[25]

Supporting Information

Supporting Information is available from the Wiley Online Library or from the author.

1902417 (11 of 12)

Acknowledgements

Conflict of Interest

The authors declare no conflict of interest.

Keywords

[1] Y. Cui, H. Yao, J. Zhang, T. Zhang, Y. Wang, L. Hong, K. Xian, B. Xu, S. Zhang, J. Peng, Z. Wei, F. Gao, J. Hou, *Nat. Commun.* **2019**, *10*, 2515.

[2] E. Pascual-San José, A. Sánchez-Díaz, M. Stella, E. Martínez-Ferrero, M. I. Alonso, M. Campoy-Quiles, *Sci. Technol. Adv. Mater.* **2018**, *19*, 823.

[3] Z. Zheng, Q. Hu, S. Zhang, D. Zhang, J. Wang, S. Xie, R. Wang, Y. Qin, W. Li, L. Hong, N. Liang, F. Liu, Y. Zhang, Z. Wei, Z. Tang, T. P. Russell, J. Hou, H. Zhou, *Adv. Mater.* **2018**, *30*, 1801801.

[4] G. Li, W.-H. Chang, Y. Yang, *Nat. Rev. Mater.* **2017**, *2*, 17043.

[5] G. Yu, J. Gao, J. C. Hummelen, F. Wudl, A. J. Heeger, *Science* **1995**, *270*, 1789.

[6] J. J. M. Halls, C. A. Walsh, N. C. Greenham, E. A. Marseglia, R. H. Friend, S. C. Moratti, A. B. Holmes, *Nature* **1995**, *376*, 498.

[7] Y. Sun, G. Li, L. Wang, Z. Huai, R. Fan, S. Huang, G. Fu, S. Yang, *Sol. Energy Mater. Sol. Cells* **2018**, *182*, 45.

[8] Q. An, F. Zhang, L. Li, J. Wang, Q. Sun, J. Zhang, W. Tang, Z. Deng, *ACS Appl. Mater. Interfaces* **2015**, *7*, 3691.

[9] X. Sun, J. Ni, C. Li, L. Huang, R. Xu, Z. Li, H. Cai, J. Li, J. Zhang, *Org. Electron.* **2016**, *37*, 222.

[10] P. Cheng, J. Wang, Q. Zhang, W. Huang, J. Zhu, R. Wang, S.-Y. Chang, P. Sun, L. Meng, H. Zhao, H.-W. Cheng, T. Huang, Y. Liu, C. Wang, C. Zhu, W. You, X. Zhan, Y. Yang, *Adv. Mater.* **2018**, *30*, 1801501.

[11] M. Campoy-Quiles, Y. Kanai, A. El-Basaty, H. Sakai, H. Murata, *Org. Electron.* **2009**, *10*, 1120.

[12] A. D. de Zerio, C. Müller, *Adv. Energy Mater.* **2018**, *8*, 1702741.

[13] C.-H. Chen, C.-H. Hsieh, M. Dubosc, Y.-J. Cheng, C.-S. Hsu, *Macromolecules* **2010**, *43*, 697.

[14] Y. Chen, P. Ye, X. Jia, W. Gu, X. Xu, X. Wu, J. Wu, F. Liu, Z.-G. Zhu, H. Huang, *J. Mater. Chem. A* **2017**, *5*, 19697.

[15] Z. Xiao, X. Jia, L. Ding, *Sci. Bull.* **2017**, *62*, 1562.

[16] N. Gasparini, A. Salleo, I. McCulloch, D. Baran, *Nat. Rev. Mater.* **2019**, *4*, 229.

[17] D. Baran, R. S. Ashraf, D. A. Hanifi, M. Abdelsamie, N. Gasparini, J. A. Röhr, S. Holliday, A. Wadsworth, S. Lockett, M. Neophytou, C. J. M. Emmott, J. Nelson, C. J. Brabec, A. Amassian, A. Salleo, T. Kirchartz, J. R. Durrant, I. McCulloch, *Nat. Mater.* **2017**, *16*, 363.

[18] D. Angmo, M. Bjerring, N. C. Nielsen, B. C. Thompson, F. C. Krebs, *J. Mater. Chem. C* **2015**, *3*, 5541.

[19] A. Sánchez-Díaz, X. Rodríguez-Martínez, L. Córcoles-Guija, G. Mora-Martín, M. Campoy-Quiles, *Adv. Electron. Mater.* **2018**, *4*, 1700477.

[20] X. Rodríguez-Martínez, A. Sánchez-Díaz, G. Liu, M. A. Niño, J. Cabanillas-Gonzalez, M. Campoy-Quiles, *Org. Electron.* **2018**, *59*, 288.

[21] R. Sun, J. Guo, C. Sun, T. Wang, Z. Luo, Z. Zhang, X. Jiao, W. Tang, C. Yang, Y. Li, J. Min, *Energy Environ. Sci.* **2019**, *12*, 384.

[22] Y. Cho, T. L. Nguyen, H. Oh, K. Y. Ryu, H. Y. Woo, K. Kim, *ACS Appl. Mater. Interfaces* **2018**, *10*, 27757.

[23] B. Wang, Y. Fu, C. Yan, R. Zhang, Q. Yang, Y. Han, Z. Xie, *Front. Chem.* **2018**, *6*, 1.

[24] S. Zhang, H. Shen, X. Zhang, P. Fan, B. Zhou, J. Yu, J. Huang, *IEEE J. Photovoltaics* **2018**, *8*, 171.

[25] X. Rodríguez-Martínez, M. S. Vezie, X. Shi, I. McCulloch, J. Nelson, A. R. Goñi, M. Campoy-Quiles, *J. Mater. Chem. C* **2017**, *5*, 7270.

[26] M. Campoy-Quiles, C. Müller, M. Garriga, E. Wang, O. Inganäs, M. I. Alonso, *Thin Solid Films* **2014**, *571*, 371.

[27] A. Milani, L. Brambilla, M. Del Zoppo, G. Zerbi, *J. Phys. Chem. B* **2007**, *111*, 1271.

[28] M. Granström, K. Petritsch, A. C. Arias, A. Lux, M. R. Andersson, R. H. Friend, *Nature* **1998**, *395*, 257.

[29] K. Tvingstedt, K. Vandewal, A. Gadisa, F. Zhang, J. Manca, O. Inganäs, *J. Am. Chem. Soc.* **2009**, *131*, 11819.

[30] J. Razzell-Hollis, J. Wade, W. C. Tsoi, Y. Soon, J. Durrant, J.-S. Kim, *J. Mater. Chem. A* **2014**, *2*, 20189.

[31] W. C. Tsoi, D. T. James, J.-S. S. Kim, P. G. Nicholson, C. E. Murphy, D. D. C. Bradley, J. Nelson, J.-S. S. Kim, *J. Am. Chem. Soc.* **2011**, *133*, 9834.

[32] J. Gao, A. K. Thomas, R. Johnson, H. Guo, J. K. Grey, *Chem. Mater.* **2014**, *26*, 4395.

**ADVANCED
ENERGY
MATERIALS**

Supporting Information

Efficient Exploration of the Composition Space in Ternary Organic Solar Cells by Combining High-Throughput Material Libraries and Hyperspectral Imaging

Albert Harillo-Baños, Xabier Rodríguez-Martínez, and Mariano Campoy-Quiles*

Supporting Information

Efficient exploration of the composition space in ternary organic solar cells by combining high-throughput material libraries and hyperspectral imaging

Albert Harillo-Baños, Xabier Rodríguez-Martínez and Mariano Campoy-Quiles*
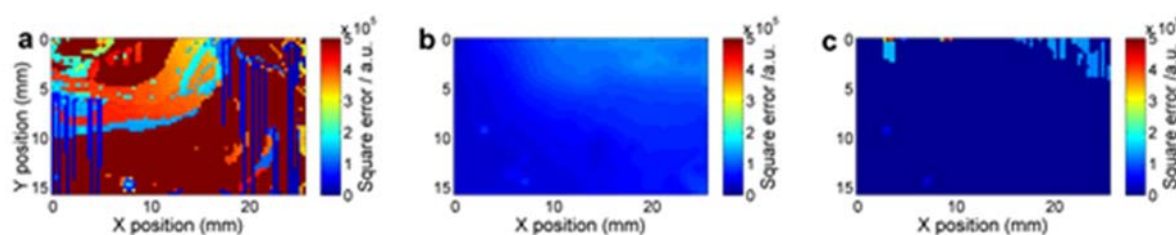
Figure S1. Squared norm of the residual for the Raman spectral modelling performed according to a) Equation 1 b) Equation 2 and c) Equation 3 as labeled in the main text. The dead regions observed in Figure S1a and S1c are ascribed to errors in the Raman model fitting, i.e. particular locations in which the algorithm is unable to find a univocal solution. This usually happens in zones where there is only one material (due to an acute loss of sensitivity) or where an imperfection of the sample causes the algorithm to drag the same result for several pixels before being able to correct. In all cases, these spikes and higher error pixels are omitted in a later step prior to plotting the ternary composition diagram.
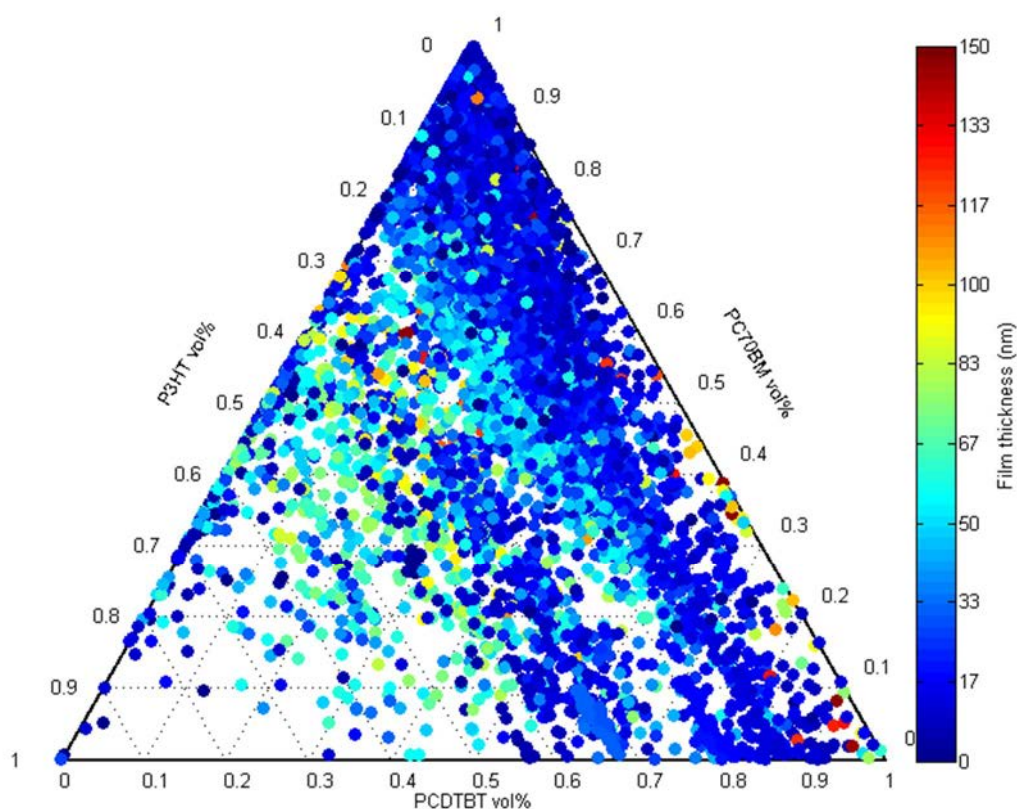
Figure S2. Ternary composition diagram for a single D_1:D_2:A blend film consisting of RR-P3HT:PCDTBT:PC$_{70}$BM.
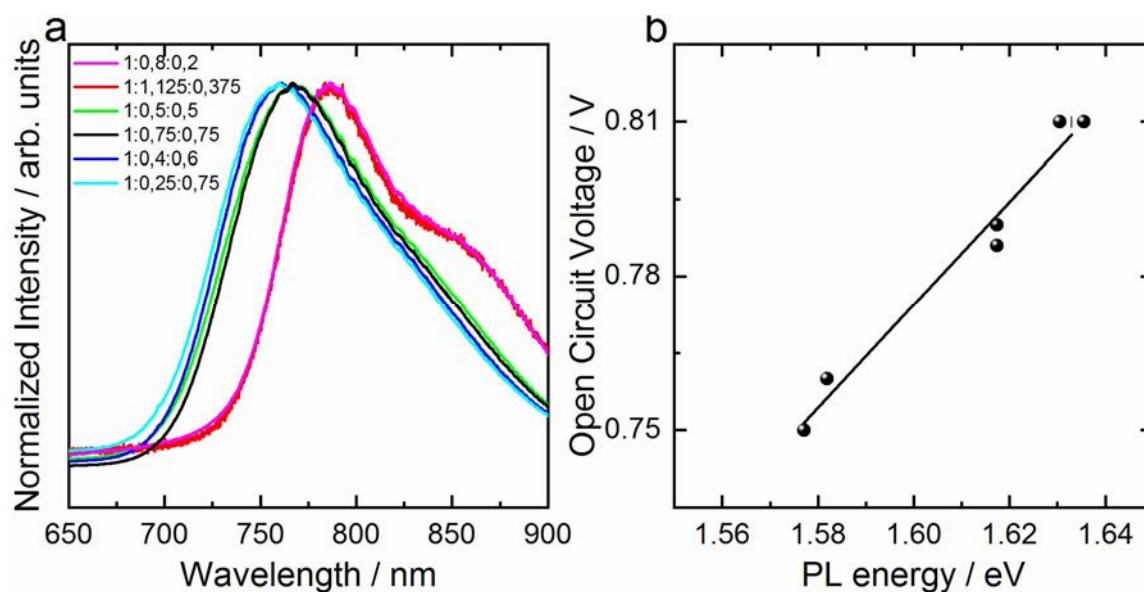

Figure S3. a) Normalized photoluminescence (PL) spectra for a series of P3HT:O-IDFBR:O-IDTBR homogeneous devices with different compositions; b) correlation between the energy

of the PL maximum (E_{PL}) for each sample and the corresponding experimental V_{oc}. The linear trend obtained can be written as
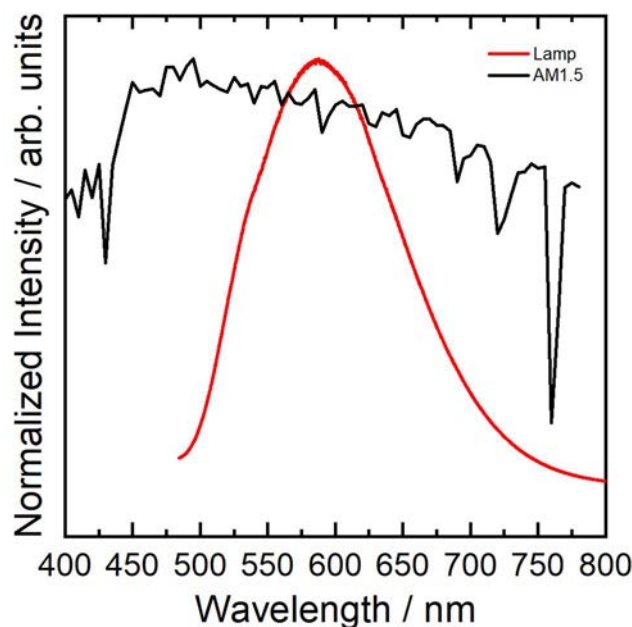
$$V_{oc}[V] = 1.003 E_{PL}[eV] - 0.830 \qquad (S1)$$

Figure S4. (Solid red line) Normalized emission spectrum of the built-in lamp in the WITec alpha 300 RA+ setup measured upon reflection on a silver mirror; (solid black line) reference AM1.5 irradiance spectrum.
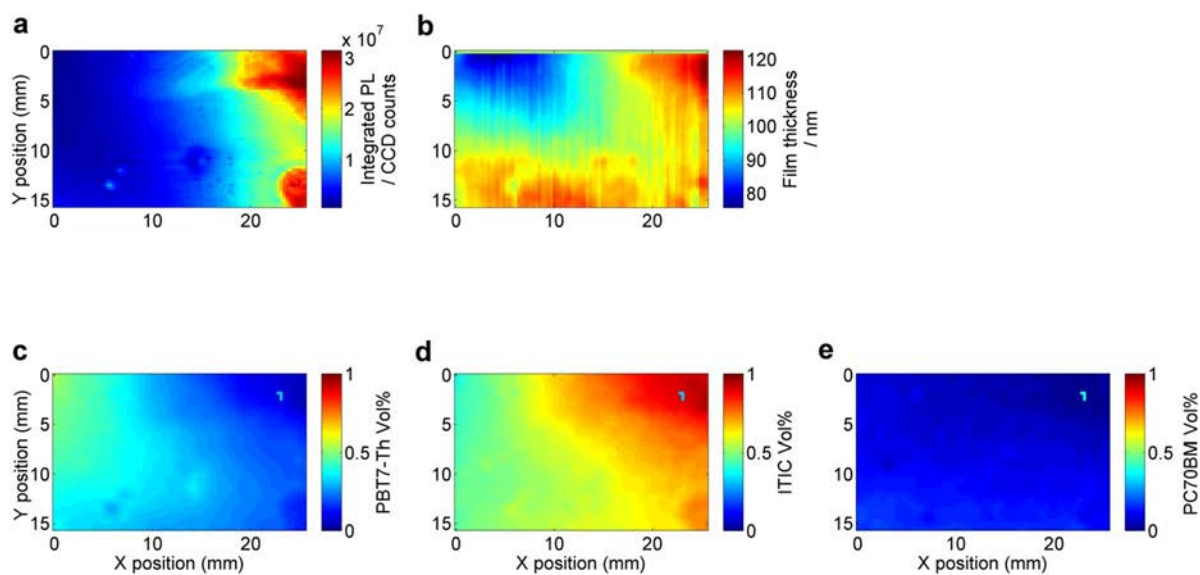

Figure S5. Additional optical characterization datasets for a PTB7-Th:PC$_{70}$BM:ITIC device showing maps of a) integrated photoluminescence spectra; b) film thickness; and volumetric

compositions of c) PTB7-Th, d) ITIC and e) $PC_{70}BM$ obtained from modelling the Raman scattered intensities and spectra.
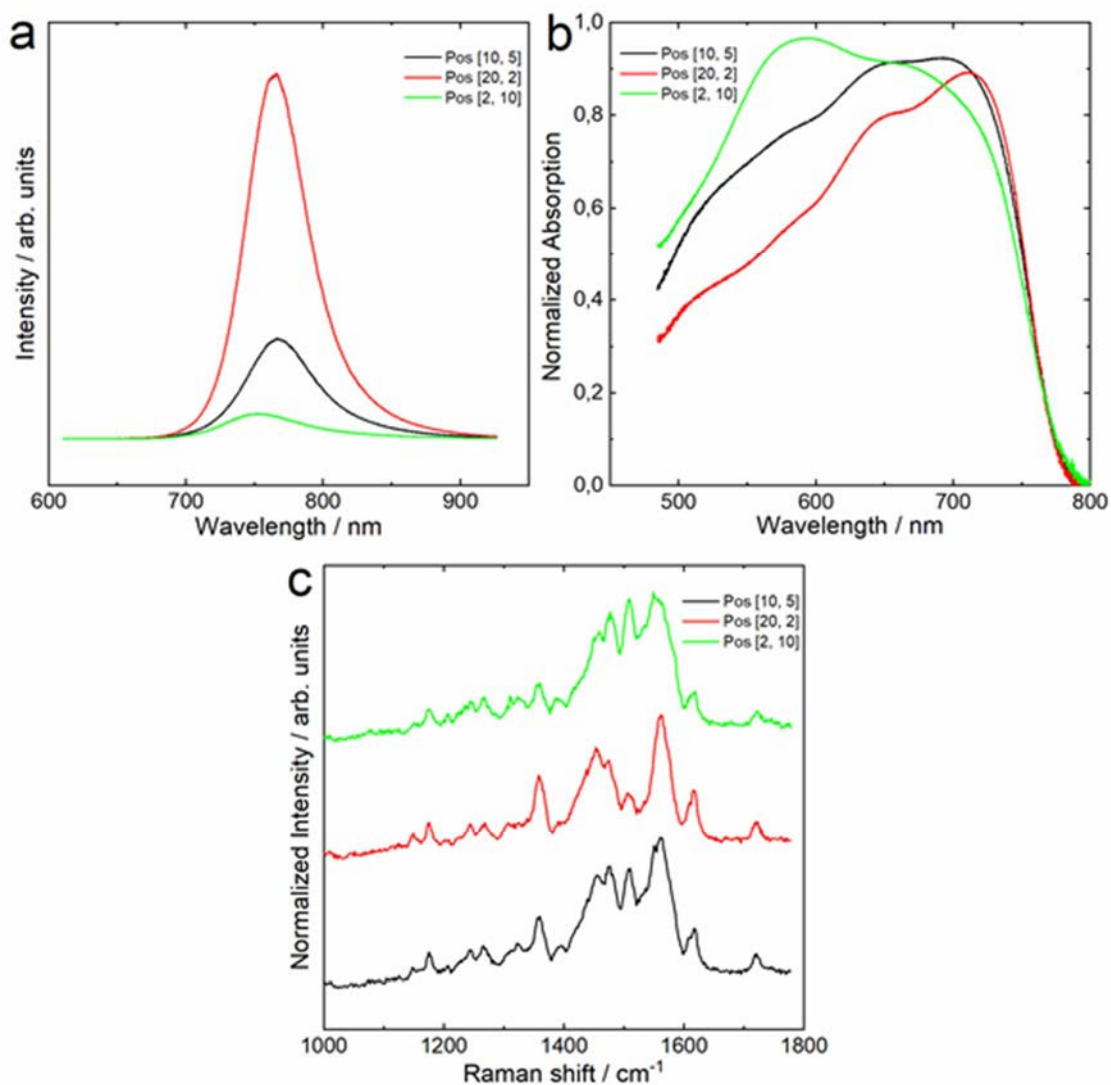

Figure S6. Representative a) photoluminescence, b) absorption and c) Raman spectra at three different XY locations of the PTB7-Th:PC_{70}BM:ITIC sample depicted in Figure S5 and Figure 3 in the main manuscript.
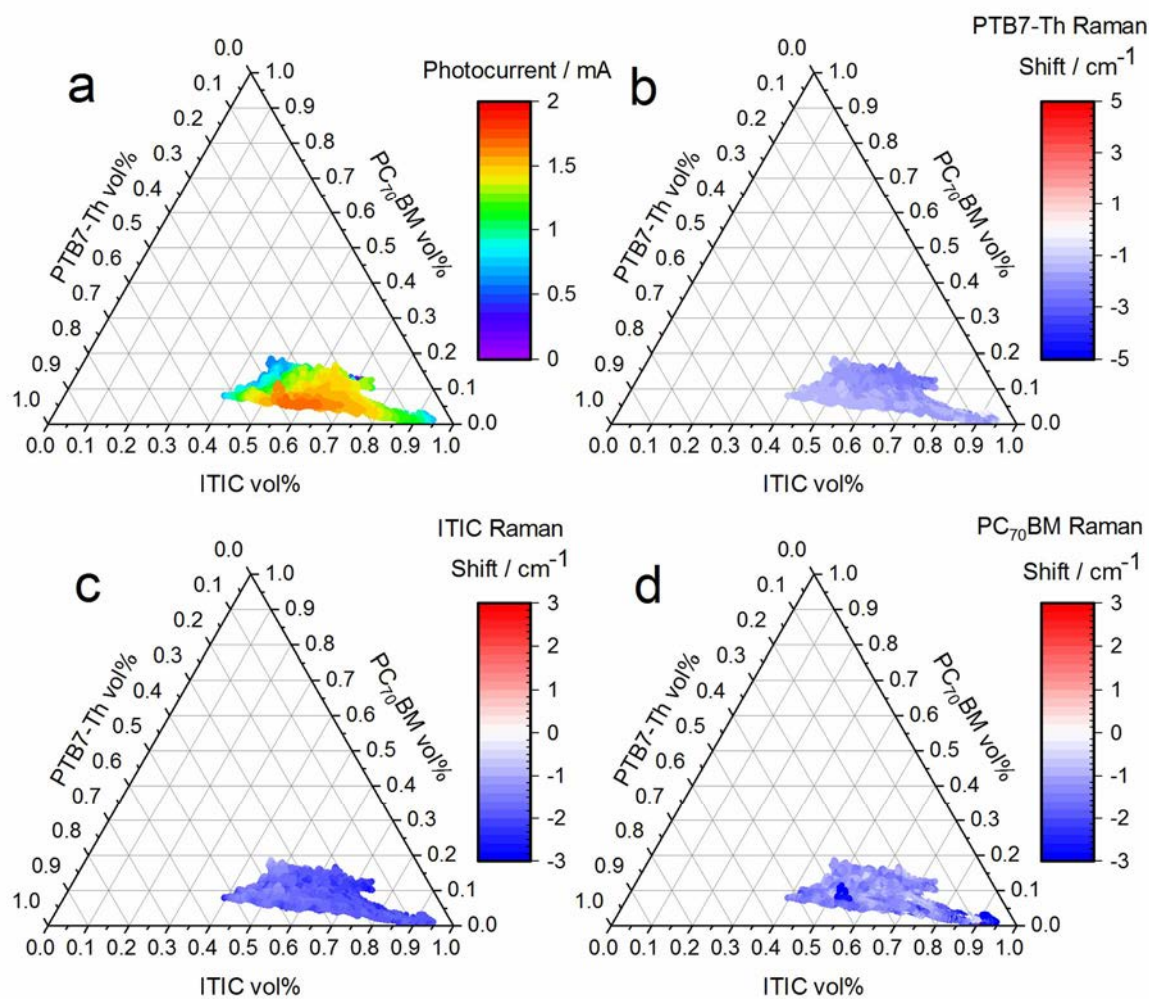
Figure S7. Ternary composition diagrams of a non-annealed PTB7-Th:ITIC:PC$_{70}$BM sample. The colour scales refer to: a) photocurrent under white light illumination; b) Raman peak shift of PTB7-Th, c) ITIC and d) PC$_{70}$BM.
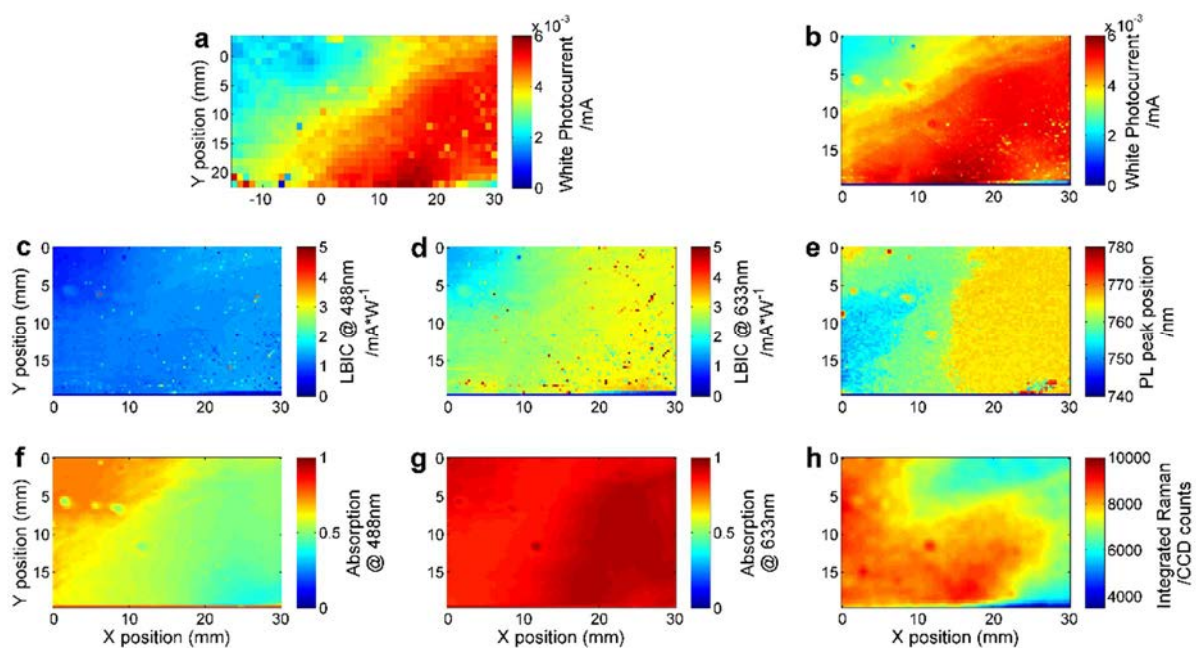
Figure S8. Full set of optical characterization maps performed in a sequentially deposited sample of PBDB-T:ITIC:PC$_{70}$BM, with the donor layer processed as a thickness gradient. a) Coarse photocurrent map obtained with white light; b) higher resolution white light photocurrent map centred at the region of better performance; c) photocurrent map acquired at 488 nm excitation; d) photocurrent map acquired at 633 nm excitation; e) wavelength of the main photoluminescence peak measured at 633 nm excitation; f) absorption at 488 nm excitation wavelength; g) absorption at 633 nm excitation wavelength; h) integrated Raman scattered intensity at 488 nm excitation.
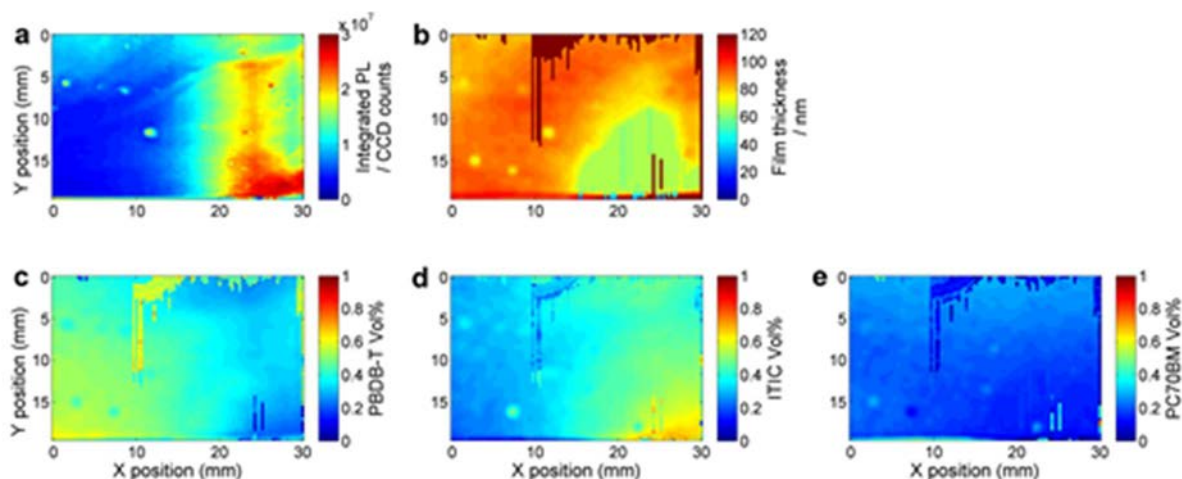
Figure S9. Additional data for a PBDB-T:ITIC:PC$_{70}$BM sample. a) Integrated photoluminescence; b) Raman-deduced thickness, and composition of c) PBDB-T, d) ITIC and e) PC$_{70}$BM.
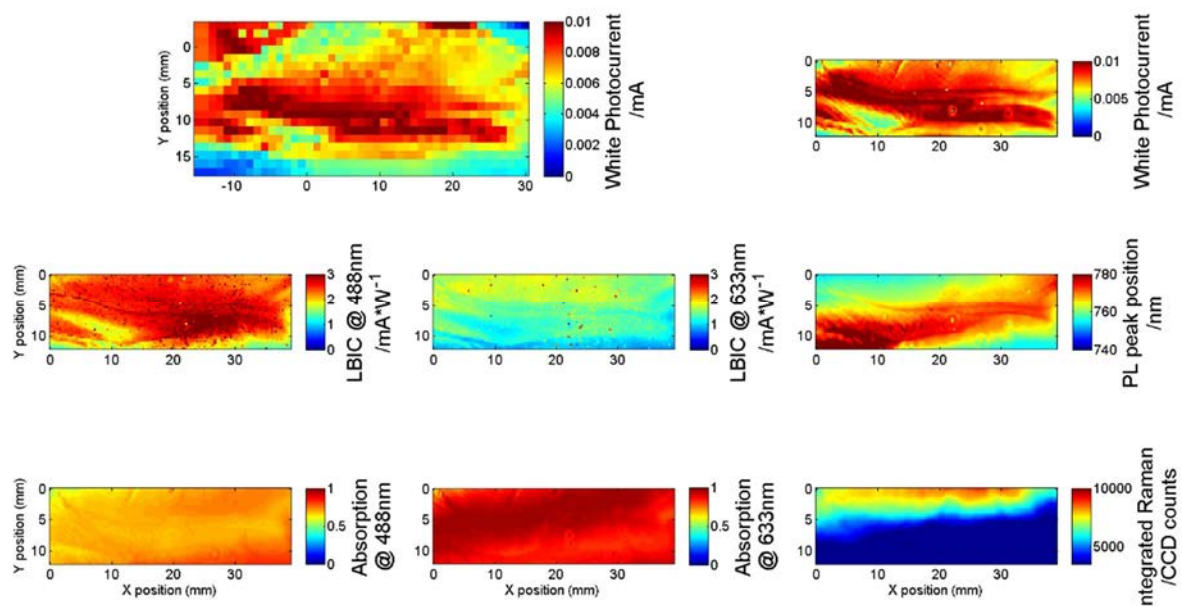

Figure S10. Full set of optical characterization maps performed in a sequentially deposited sample of P3HT:O-IDFBR:O-IDTBR, with the donor layer processed as a thickness gradient. a) Coarse photocurrent map obtained with white light; b) higher resolution white light photocurrent map centred at the region of better performance; c) photocurrent map acquired at 488 nm excitation; d) photocurrent map acquired at 633 nm excitation; e) wavelength of the

main photoluminescence peak measured at 633 nm excitation; f) absorption at 488 nm excitation wavelength; g) absorption at 633 nm excitation wavelength; h) integrated Raman scattered intensity at 488 nm excitation.
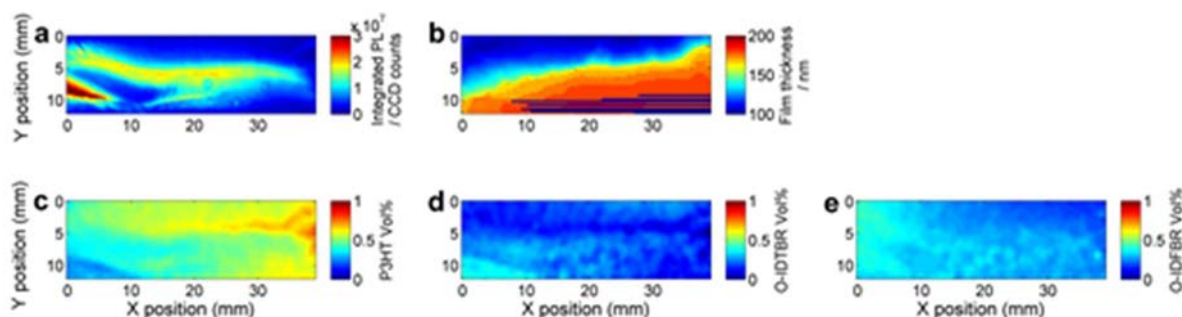

Figure S11. Additional data for a P3HT:O-IDFBR:O-IDTBR sample. a) Integrated photoluminescence; b) Raman-deduced thickness, and composition of c) P3HT, d) O-IDTBR and e) O-IDFBR.
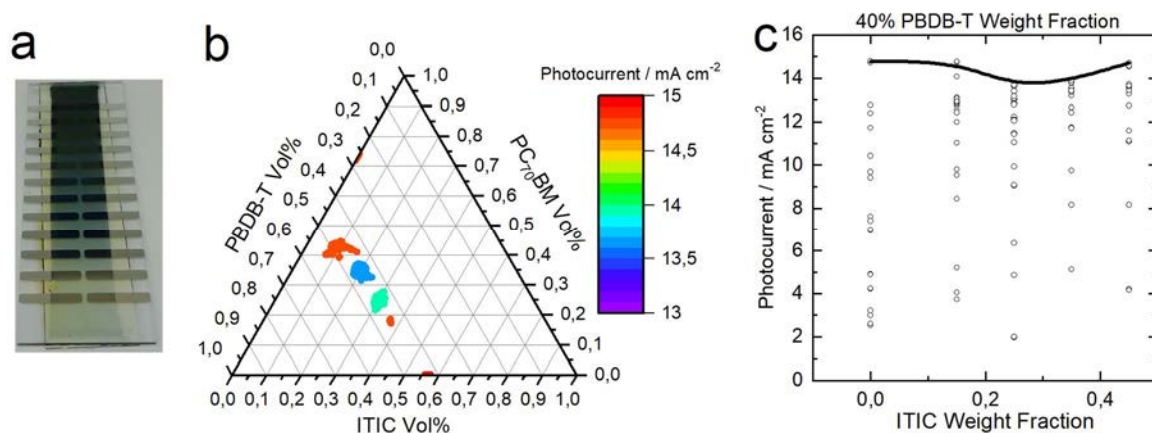

Figure S12. a) Optical image of a sample consisting of 24 different devices (12 per side) with the ternary PBDB-T:ITIC:PC$_{70}$BM blend as active layer, which was deposited as a lateral thickness gradient. b) Representation of the ternary composition diagram of 6 different samples (24 devices each, of different thickness and fixed weight blending ratios), with the highest photocurrent obtained in the sample as colour scale. c) Photocurrent dispersion obtained for all wedge-like samples (keeping fixed PBDB-T loading at 40 wt%) as a function of ITIC wt%.

Uncertainty in the determination of volumetric composition through Raman spectroscopy

The raw Raman spectra obtained experimentally in the ternary photovoltaic devices are fitted according to Equation (3) in the main manuscript, which reads

$$I_{R,\text{blend}}(\beta, v_u, \omega, \delta_u) \propto \beta \sum_{u=1}^{3} v_u \sigma_{R,u} I_{\text{ref},u}(\omega + \delta_u) \qquad \text{(S1)}$$

The six free parameters found in a ternary blend (β, v_u, δ_u) are generally fitted with large accuracy: for the here analysed ternary blends and at moderate compositions the typical standard deviation (defined with a confidence interval of 95%) of the fitted parameters is < 1% (relative error). In the worst scenario, which includes combinations of materials with large Raman cross-section ratios and blending ratios that are enriched with the most Raman active material, the fitting error can be as high as 10-20% as reported elsewhere (J. Mater. Chem. C, 2017, 5, 7270-7282). This is a consequence of the partial hindering of the characteristic vibrational fingerprints of the low Raman intensity material by the main Raman active component of the blend. Such effect can even be more pronounced if their vibrational signatures are qualitatively similar. Thus, it is important to properly choose the blended materials so as to minimize the fitting error source in the Raman modelling. The ternary blends selected in this work are all compatible in terms of Raman cross-section ratios as well as in terms of vibrational characteristics, thus the fitting error remains well below 5% in all cases.

Therefore, in the here presented case the main error source is attributed to the determination of the Raman cross-section of the materials. As described elsewhere (J. Mater. Chem. C, 2017, 5, 7270-7282), such determination is performed by fabricating films with lateral thickness gradients, then measuring the Raman intensity as a function of thickness and finally modelling and fitting the Raman scattered intensity as a function of the film thickness while using the optical constants of the sample as model inputs. This approach includes several

sources of error including the quantification of the scattered intensity, the modelling of film thickness in ellipsometry as well as the Raman intensity modelling using the experimentally determined optical constants. In our previous works we showed several examples of Raman cross-section determinations together with their standard deviation, including PTB7-Th and $PC_{70}BM$ (Figure 1c in Adv. Electron.Mater. 2018, 4, 1700477) which are used in this paper. We evaluate the effect that the error of the Raman cross-section determination has on the extracted ternary compositions by randomly adding or subtracting the corresponding standard deviation to the cross-sections and then re-fitting the raw Raman spectra. We repeat this process several times (Figure S13, panels a-e) to gain statistics and then average the datasets to obtain the corresponding relative errors in the loading of each material (Figure 13f). We observe that in the worst scenario the relative error in the composition can exceed 25% (ITIC) whereas it is close to 10% in the most favourable case ($PC_{70}BM$). In average, an error close to 10-20% is expected, matching what we previously observed in binary blends (J. Mater. Chem. C, 2017, 5, 7270-7282). This is in agreement with Raman data taken for homogeneous samples (Figure 5b in the manuscript and Figure S12b).
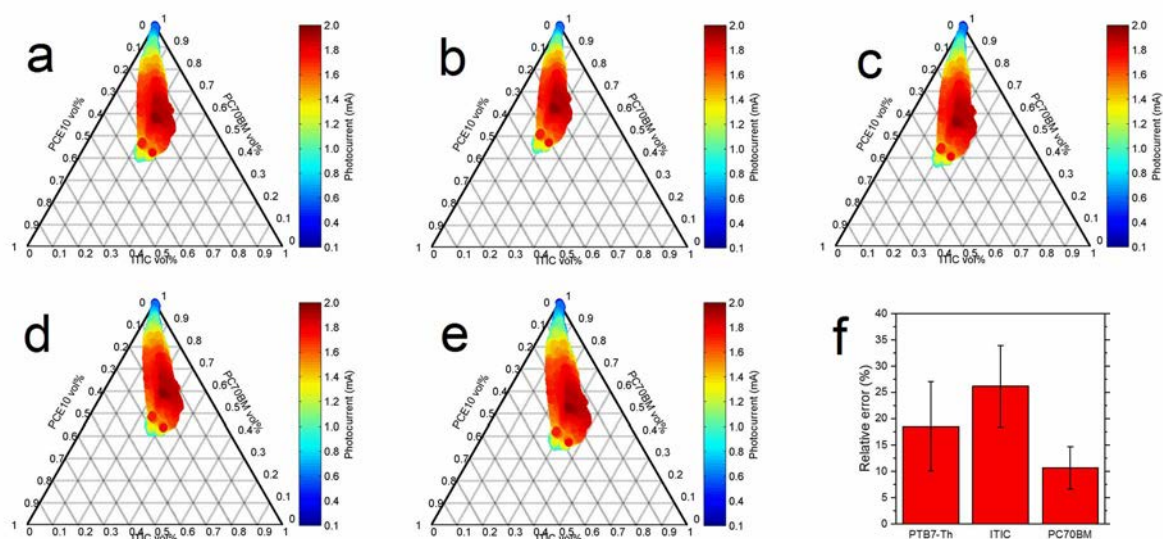

Figure S13. Panels a-e represent ternary composition diagrams of the PTB7-Th:ITIC:$PC_{70}BM$ sample analysed in Figure 4 in the main manuscript in which the

corresponding Raman cross-sections have been randomly modified within a standard deviation (either added or subtracted). Panel f shows the average relative error of the composition of each blended material.

PAPER VI

Predicting the photocurrent-composition dependence in organic solar cells

X. Rodríguez-Martínez, E. Pascual-San-José, Z. Fei, M. Heeney, R. Guimerà, M. Campoy-Quiles, *submitted*

In this manuscript, we introduce for the first time the synergic combination of high-throughput experimentation with artificial intelligence to aid in the prediction of the optimal composition in bulk heterojunction, binary OPV devices.

Predicting the photocurrent-composition dependence in organic solar cells

Xabier Rodríguez-Martínez[1], Enrique Pascual-San-José[1], Zhuping Fei[2], Martin Heeney[2], Roger Guimerà[3,4] and Mariano Campoy-Quiles[1*]

[1] Institut de Ciència de Materials de Barcelona (ICMAB-CSIC), Esfera UAB, Campus Universidad Autónoma de Barcelona, 08193, Bellaterra, Barcelona, Spain.

[2] Department of Chemistry and Centre for Plastic Electronics, White City Campus, Imperial College London, London W12 0BZ, U.K.

[3] Institució Catalana de Recerca i Estudis Avançats (ICREA), 08010, Barcelona, Spain.

[4] Department of Chemical Engineering, Universitat Rovira i Virgili, 43007, Tarragona, Spain.

* e-mail: mcampoy@icmab.es

Abstract

The continuous development of improved non-fullerene acceptors and an even deeper knowledge of the fundamental mechanisms governing performance underpin the vertiginous increase in efficiency witnessed by organic photovoltaics. While the influence of parameters like film thickness and morphology are generally understood, what determines the strong dependence of the photocurrent on the donor and acceptor fractions remains elusive. Here we approach this problem by training artificial intelligence algorithms with self-consistent datasets consisting of thousands of data points obtained by high-throughput evaluation methods. Two ensemble learning methods are implemented, namely a Bayesian machine scientist and a random decision forest. While the former demonstrates large descriptive power to complement the experimental high-throughput screening, the latter is found to predict with excellent accuracy the photocurrent-composition phase space for material systems outside the training set. Interestingly, we identify highly predictive models that only employ the materials band gaps, thus largely simplifying the rationale of the photocurrent-composition space.

1. Main text

The synthesis of novel conjugated semiconductors underpins the striking performance upswing that the field of organic photovoltaics (OPV) is currently experiencing[1]. Photoactive blends of non-fullerene acceptors[2–4] (NFAs) and low band gap donor co-polymers[5,6], have demonstrated power conversion efficiencies (PCEs) over 18%[7] in single-junction binary devices. Such figures result from an improved understanding of the donor:acceptor (D:A) material requirements in terms of extended light absorption, frontier energy level alignment and film morphology[8,9], as well as from enhanced charge transport properties[10]. Indeed, the advanced understanding of many of the fundamental working principles in OPV combined with the inherent synthetic flexibility of conjugated materials is prompting the large-scale screening of potentially high-performing OPV material candidates. Yet, for a given material system, what could we say *a priori* about its OPV potential?

At the molecular level, computational algorithms such as those developed in the on-going Harvard Clean Energy Project (CEP)[11] serve to rapidly pre-screen millions of molecular motifs and classify them according to their theoretical OPV outcome, thus motivating their ulterior synthesis. Beyond purely *in silico* screening, the development of data-driven models in the OPV field has so far been mostly restricted to data mining and training of artificial intelligence (AI) algorithms using intrinsic material descriptors[12]. This approach has been applied to make predictions in terms of novel materials[13,14] and their corresponding expected PCE[15], as well as to guide researchers in the design of potentially top-performing materials[16]. While promising, these calculations have had modest success thus far. This is due, in part, to the lack of sufficiently reproducible data in the literature; also to the difficulty to predict solid-state properties of the blend such as microstructure or gas-to-solid shifts in the optical properties and molecular energy levels; and finally, due to the fact that relevant device information is not considered in the calculations[17].

At the device level, one aspect that has been modeled very successfully is the dependence of the performance on the active layer thickness. Device modeling based on transfer matrices has been demonstrated to reproduce accurately the mild oscillations of the photocurrent found experimentally[18,19]. Further refinements based on advanced charge transport descriptions and unintentional doping effects have precisely described the thickness-dependent photocurrent[20].

Despite acutely affecting the OPV performance[21–25], predicting the optimum D:A ratio has been much more challenging due to the complexity of charge photogeneration and transport through the blend towards the electrodes. For semicrystalline polymers blended with fullerenes, optimum D:A ratios have been rationalized by the binary phase diagram[21]. In particular, slightly hypoeutectic concentrations with respect to the polymer loading were found to lead to a good compromise between charge generation and appropriate percolating pathways for charges to reach the electrodes. Also the balance of charge carrier mobilities between electrons and holes has often been considered a key feature determining the shape of the photocurrent-composition curve[26] (hereafter referred to as J_{sc}-vol%). The current OPV paradigm led by NFAs as excellent light

238

harvesters adds another ingredient to the J_{sc}-vol% dependence compared to fullerene-based devices since photocurrent generation is now fully distributed between both materials. Given the intricate optoelectronic tradeoff that sets the location of the optimum D:A ratio, novel experimental approaches and data-driven predictive models are on demand to enhance the current understanding of the J_{sc}-vol% dependence in binary OPV blends.

In this work, we synergically combine experimental high-throughput screening and AI to study the relationship between the photocurrent generation and the active layer parameters (i.e. thickness and D:A ratio) in binary OPV devices. The experimental exploration is performed by processing orthogonal parametric gradients or libraries, which in combination with local probing techniques (namely Raman spectroscopy and photocurrent imaging) serve to assess the corresponding photocurrent phase space diagrams with minimal effort[27–32]. The exploration results in a plethora of possible J_{sc}-vol% dependences: from strongly leaned bell shapes to bimodal distributions. Then, in an attempt to rationalize these complex relationships, we implement two different AI algorithms that take as input a series of intrinsic optoelectronic material descriptors. The first algorithm is a Bayesian machine scientist[33], which is found to complement the high-throughput experimental screening due to its large descriptive power while providing an analytical equation to describe the intricate J_{sc}-vol% phase spaces. Second, we use a random forest (RF) algorithm as a predictive model for the normalized J_{sc}-vol% dependences retrieving a mean absolute error (MAE) below 0.20 in untrained OPV binaries. In the RF models, we find that descriptors related with the alignment of the frontier energy levels and the mobility difference are statistically relevant in shaping the J_{sc}-vol% space. Finally, feature selection procedures reveal highly predictive models when only the donor and acceptor electronic (or optical) band gaps are employed in the training step. The RF models found herein define the J_{sc}-vol% curves in both NFA and fullerene-based binary blends with excellent accuracy.

Figure 1 illustrates the high-throughput evaluation, training, and prediction workflow used throughout the article. First, the processing of compositional libraries is accomplished by blade coating via the coalescence of pristine donor and acceptor ink drops at the blade reservoir. The blade movement induces their mixing during the coating to generate a compositional gradient perpendicularly to the displacement direction[29]. In parallel, ink depletion at the front reservoir originates a thickness gradient along the blade movement direction. Also, the dissimilar rheology of the pristine inks originates unintentional film thickness fluctuations in conjunction with the D:A ratio library (Section I, Supporting Information). Afterwards, the device is completed and a simultaneous characterization based on Raman spectroscopy and light-beam induced-current (LBIC) mapping is used to image the heterogeneous film features including thickness and composition[34], and to correlate them to the corresponding photocurrent images. This approach allows the efficient exploration of the photocurrent phase diagram of binary OPV blends in a combinatorial manner: the time and semiconductor material cost requirements can be as low as 90 seconds and 50 ng per data point, respectively (Section II, Supporting Information).
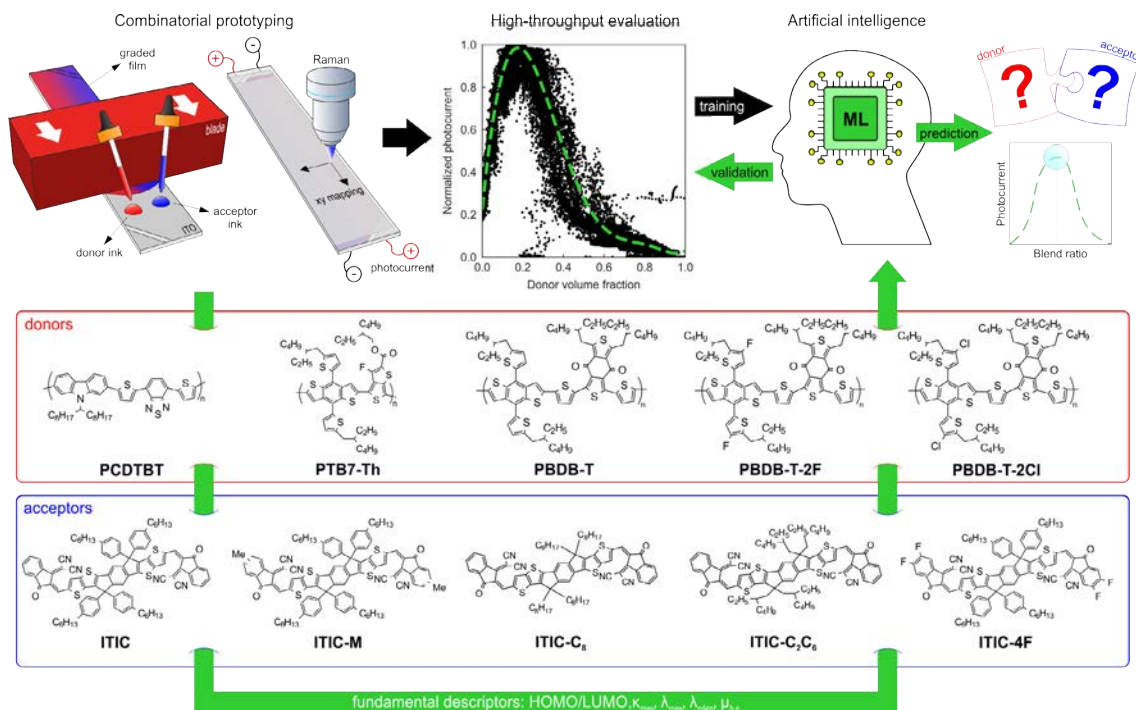
Figure 1 | The photocurrent-composition prediction workflow for binary OPV blends. The procedure is divided into three main blocks. First, the generation of parametric libraries by blade coating on functional devices in the form of lateral gradients in the active layer thickness and the D:A ratio. Second, the high-throughput photovoltaic characterization by means of co-local Raman spectroscopy and photocurrent imaging, which serves to correlate the local device performance with the variation of the target features (thickness and D:A ratio). Third, AI algorithms are trained on the experimental datasets using intrinsic fundamental descriptors of the blended materials. In the last step, the AI models are exploited to make predictions of the photocurrent-composition dependence for materials in and outside of the training dataset.

The highly efficient screening process generates large amounts of thickness-composition parametric combinations per D:A pair in the corresponding J_{sc} space (*ca.* 24,000 data points). The generated data are then employed in the training and validation of AI algorithms together with fundamental optoelectronic material descriptors such as highest occupied molecular orbital (HOMO) and lowest unoccupied molecular orbital (LUMO) energy levels, absorption coefficients (Section III, Supporting Information) and charge carrier mobilities. As detailed in Section IV, Supporting Information, those descriptors extracted from literature can be selected following distinct criteria. With these data, we first validate the ability of the AI models to reconstruct the complete J_{sc}-vol% diagram and then predict the corresponding dependence for material combinations out of the original training set. This approach is exploited to determine the optimum active layer thickness and composition in terms of photocurrent for any D:A pair (with known input descriptors).
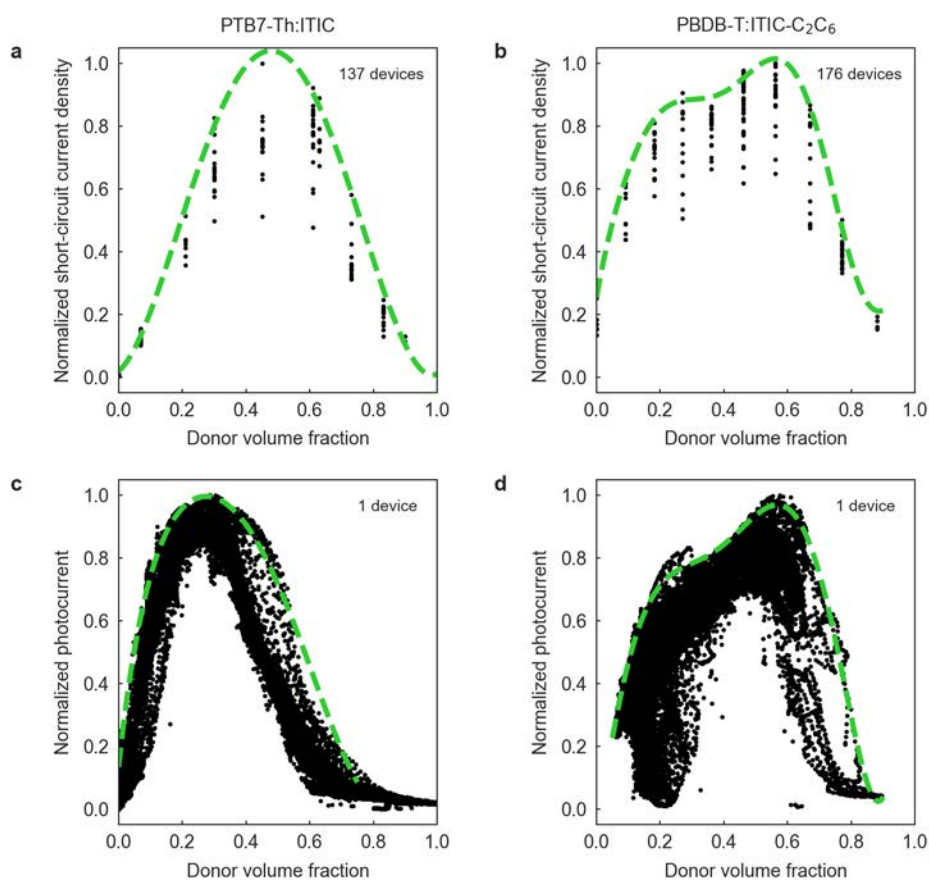
Figure 2 | Comparison of photocurrent distributions in discrete sampling and high-throughput optimization procedures. a,b, Normalized distribution of the short-circuit current density obtained in discrete devices as a function of the donor volumetric loading in PTB7-Th:ITIC and PBDB-T:ITIC-C_2C_6 blends. **c,d,** Normalized photocurrent dispersion obtained following the high-throughput optimization approach for the same blends. Green dashed lines are polynomial fits of the high-performing envelope of photocurrent values. In each case we indicate the number of devices needed to generate these plots. The reader is referred to Section I, Supporting Information, for further details on device manufacture.

Herein, the high-throughput experimentation strategy based on lateral parametric libraries substitutes the traditional sample-by-sample methodologies (*aka* Edisonian experimentation) in the screening of the J_{sc}-vol% space. Hence, we first verify that both approaches converge to the same figures in the normalized J_{sc}-vol% diagram. Figure 2 compares the J_{sc} dispersion obtained following the traditional fabrication-intensive protocol (Figure 2a and b) and the measuring-intensive strategy proposed here (Figure 2c and d). We study two high-performing OPV binary systems, namely the workhorse PTB7-Th:ITIC blend[35] as well as a novel, unreported binary formed by PBDB-T:ITIC-C_2C_6. The observed photocurrent dispersion along the *y*-axis in Figure 2a and b is mainly related to the screening of the active layer thickness as we varied the thickness at each composition in the pursuit of the optimum thickness at each blending ratio (Section I, Supporting Information). Importantly, the two systems exhibit very different J_{sc}-vol%

curves, one being a single peak centered at ca. 40 vol% of donor, while the other appears bimodal (*videinfra*).

Notably, the high-throughput methodology reproduces the unimodal and bimodal photocurrent dispersions observed as a function of the donor loading in both binaries (Figure 2c and d). Importantly, it does so with a very large statistics, strongly reducing the uncertainty with respect to the actual shape of the curve. In this approach, the vertical J_{sc} dispersion originates from both active layer thickness and morphology variations, the latter being a consequence of the *in situ* mixing of the pristine inks in the blade reservoir. Note that the high-throughput screening requires a significantly reduced amount of experimental time and resources: hundreds of discrete devices (here 137 and 176 devices in PTB7-Th:ITIC and PBDB-T:ITIC-C_2C_6, respectively) vs a single combinatorial device per binary.

The high-throughput methodology has, however, the caveat of measuring J_{sc} only rather than the full set of solar cell parameters (open-circuit voltage (V_{oc}), fill factor (FF) and PCE). Nevertheless, since V_{oc} remains fairly constant, the PCE correlates well with J_{sc} for the range of compositions of interest despite the variations observed in FF (Section II, Supporting Information). On the other hand, the use of non-standardized white light for the acquisition of the J_{sc} data and the intrinsic uncertainty of the Raman-based determination of composition[34] can explain the differences observed in the photocurrent distributions when comparing both optimization protocols; more specifically, the *ca.* 10% offset in the donor content that maximizes the photocurrent in PTB7-Th:ITIC devices. Nonetheless, these drawbacks are significantly outweighed by the rapid attainment of large experimental datasets, which serve as ideal seeds for training AI algorithms. Furthermore, the experimental approach demonstrates high reproducibility from batch-to-batch (Section II, Supporting Information).

We next examine the upper crust of the scattered photocurrent distribution observed in the combinatorial samples (dashed green lines in Figure 2c and d). These provide a large overview of the photocurrent phase space in a very efficient manner. After determining the optical properties of the D:A blends (Section III, Supporting Information) and indexing their electronic properties from the literature, we start feeding AI algorithms to elucidate the origin of the observed trends. Our tentative list of relevant descriptors contains 23 elements per D:A pair, including eight dimensionless parameters (Section IV, Supporting Information). At this stage, we did not include descriptors based on properties of the blends, such as their phase diagrams.

Our first implementation of AI is a Bayesian machine scientist[33], which includes the dimensionless descriptors as inputs to develop analytical models that explore the J_{sc}-vol% dependence (Section V, Supporting Information). For any given set of scattered data, the Bayesian machine scientist identifies the plausible and simplest mathematical models that describe the observed trends. We applied this methodology to two families of OPV binaries (Figure 3) with PTB7-Th and PBDB-T as donors, individually blended with four ITIC-based acceptors showing either distinct end groups (ITIC-M) or side-chains (ITIC-C_8 and ITIC-C_2C_6). We note that, experimentally, small but non-zero photocurrent has been measured for some pristine NFAs. A full study of this goes beyond

242

the scope of this manuscript, but it is worth noting it, even when the corresponding solar cells have comparatively low overall efficiencies.

According to the solid curves in Figure 3, which delimit the J_{sc}-vol% space encountered at different active layer thickness values, the Bayesian machine scientist reproduces well the highest-performing experimental trends. The actual model equation is provided in Section V, Supporting Information. While we would not enter in rationalizing any physical meaning, we could use it to evaluate the parameter space. Importantly, regarding the photocurrent phase space, the modeling indicates that (i) PTB7-Th binaries are characterized by sharp and unbalanced compositional optimum peaks; (ii) PBDB-T blends are more tolerant to compositional fluctuations and their maxima are more balanced in D:A ratio; (iii) binaries containing ITIC and ITIC-M show limited thickness dependence; (iv) ITIC-C_8 and ITIC-C_2C_6 blends are very sensitive to active layer thickness variations; and (v) the bimodal distribution is more or less pronounced depending on the actual thickness range. Despite the great descriptive power of the machine scientist in completing the exploration of the complex photocurrent phase space, it has some limitations arising from its computational complexity and the size of the training dataset, including: (i) month-scale times needed for training; (ii) poor predictive capability out of the training materials dataset due to the unfeasibility of sampling models for long enough time; and (iii) an uninformative utilization of the features, which makes it impossible to determine which of them are really important.
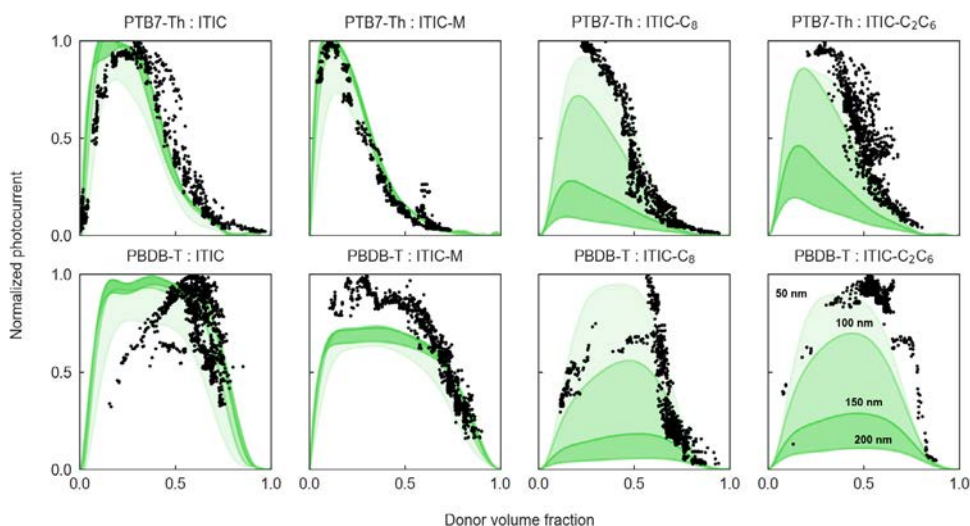

Figure 3 | A Bayesian machine scientist successfully models the photocurrent phase space in OPV binaries. The high-throughput experimental evaluation approach is first exploited to efficiently explore the corresponding photocurrent phase space as a function of the active layer thickness and the D:A ratio. Then, 1,000 high-performing photocurrent data points obtained in each of the eight different D:A combinations of PTB7-Th (upper row) and PBDB-T (lower row) blended with ITIC, ITIC-M, ITIC-C_8 and ITIC-C_2C_6, are selected to train a Bayesian machine scientist. The training results in a unified model equation including eight dimensionless parameters that can fully explore the photocurrent phase space. Such an equation enables evaluation of tolerances upon thickness and D:A ratio fluctuations as illustrated by the solid green curves and shaded areas, which delimit the high-performing shell of normalized photocurrent values at distinct active layer thicknesses: 200 nm, 150 nm, 100 nm and 50 nm.
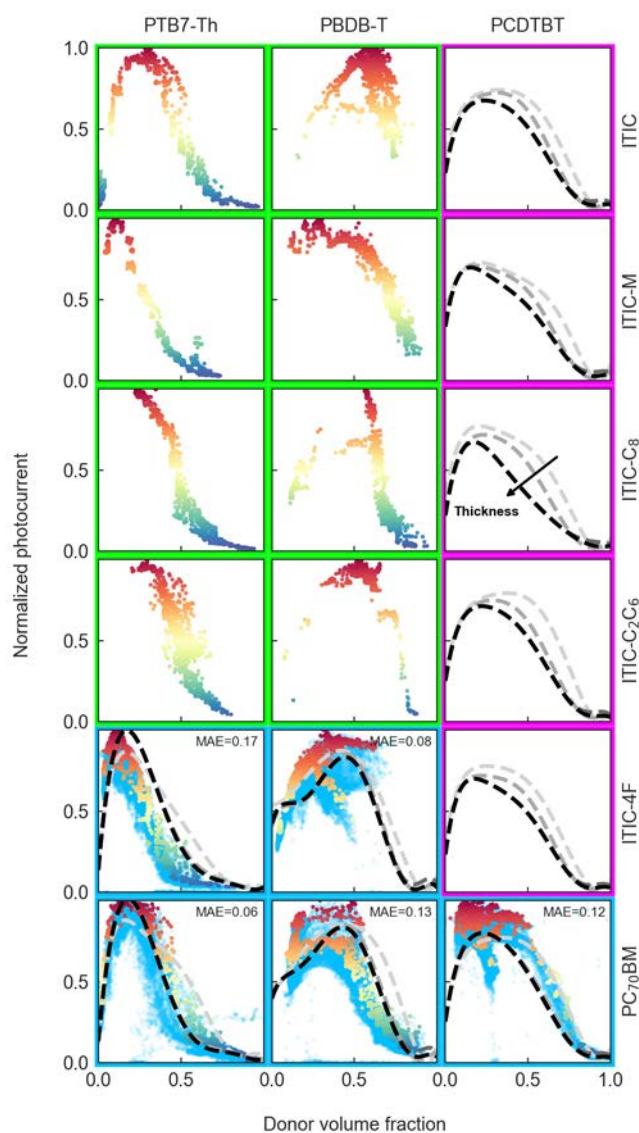
Figure 4 | Combinatorial matrix of binary OPV blends. Combinatorial matrix of photocurrent phase diagrams for a set of high-performing polymer donors (PTB7-Th and PBDB-T) and acceptors, including traditional fullerenes ($PC_{70}BM$) as well as a family of novel NFAs (ITIC and its derivatives: ITIC-M, ITIC-C_8, ITIC-C_2C_6 and ITIC-4F). The photovoltaic performance is assessed by quantifying the photocurrent under white light illumination (*y*-axis) as a function of the donor polymer loading (*x*-axis) and the active layer thickness (whose dependence is implicit in the *y*-axis dispersion). Datasets are highlighted in green (training), blue (validation) and magenta (prediction) in correspondence with the type of D:A combinations when in use with random forest (RF) models. The mean absolute error (MAE) of the RF model in reproducing the photocurrent upper shell of 1,000 values (depicted in colored rainbow scale, to be distinguished from the remaining experimental data points in blue) is shown for the validation datasets.

Therefore, we tested alternative ML approaches such as the random forest (RF) algorithm to improve the predictive capability of the AI models. The RF ensemble is initially trained using the same OPV binaries previously explored by the Bayesian machine scientist, which are highlighted with green frames in Figure 4. The validation (testing) datasets are highlighted in blue while the purely predictive scenarios are framed in magenta color. Thus, Figure 4 accordingly depicts a combinatorial matrix of the scattered J_{sc}-vol% dependences obtained in distinct D:A pairs following the high-

throughput experimentation approach, as well as the RF model predictions (dashed lines) at different active layer thickness values (colored from grey to black). Therein, we include organic semiconductors out of the pristine training materials set such as PCDTBT as donor polymer and two additional acceptors, namely a fluorinated ITIC derivative (ITIC-4F) and the workhorse fullerene, $PC_{70}BM$.

As part of the RF model validation process, we first perform a leave-one-out cross-validation (LOO-cv) of the RF ensemble including the 8 training datasets (green frames in Figure 4), as detailed in 0, Supporting Information. Based on the extrapolation reliability found (*ca.* 65% of success rate), we further validated the RF model by comparing the predicted trends with the experimental results obtained in D:A pairs out of the training set selection, i.e. binaries for which either one or the two materials have not been used within the training step (blue frames in Figure 4). This trait is precisely the main feature desired for highly predictive models.

Interestingly, our results indicate that the RF model extrapolates well (MAE < 0.20) in all validation binaries explored both the position of the J_{sc} maximum and its modulation in the composition (and thickness) diagram. The results obtained are equally consistent when validating a larger combinatorial matrix including data for high performing donor polymers such as PBDB-T-2Cl (PM7) and PBDB-T-2F (PM6), Figure S18, Supporting Information. It is worth highlighting that regardless of the molecular nature of the materials blended, the only model inputs for the extrapolation are the corresponding optoelectronic descriptors used in the training of the RF algorithm. In this particular case, we hand-picked the HOMO/LUMO energy levels reported from cyclic voltammetry (CV) measurements only as well as the corresponding mobilities from the same reference (whenever possible), as detailed in Section IV, Supporting Information.

Undoubtedly, the predictive power of the RF model is remarkable given its simplicity. From a chemical and fundamental point of view, the dissimilarities between the materials employed in the training and both PCDTBT and $PC_{70}BM$ (as the most distinct validation species in Figure 4) are important. The type of moieties in the backbone and grafted side chains (for the donor polymers), as well as the chemical structure and topology (for the acceptors) are significantly different. Despite these acute differences, the RF model draws well the J_{sc}-vol% dependence experimentally found in the validation datasets. On the other hand, the predictive capability of the RF model (magenta panels in Figure 4) is extremely useful to evaluate *a priori* the J_{sc}-vol% diagram of any OPV binary, including their tolerance against blending ratio fluctuations. This latter fact has important consequences in the upscaling of any novel D:A pair and is largely acknowledged in the OPV industry. Indeed, our results are very promising considering the limited number (8) of D:A material combinations employed in our first tentative model training. We thus believe that the predictive power of our method can be significantly enhanced when the training dataset is further extended or other material-specific descriptors are included, such as the molecular structures.
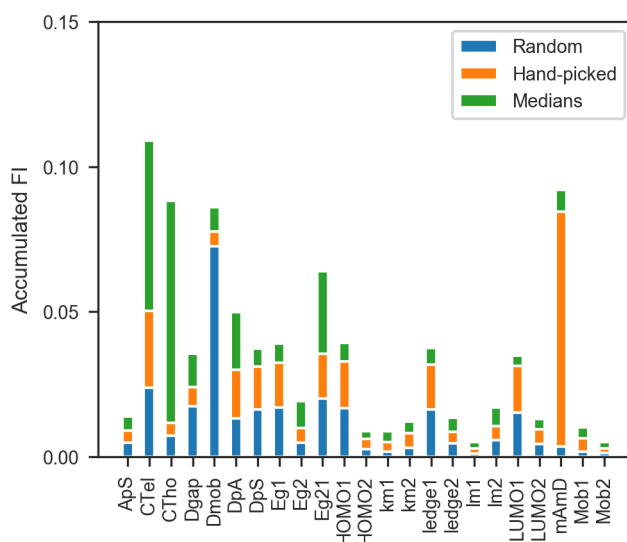
Figure 5 I Accumulated feature importance depending on the choice of descriptor values. Since the HOMO and LUMO energy levels as well as the charge carrier mobilities are took from the literature, we explore the effect that the actual value of the descriptors has on the FI drawn by the RF ensemble. We generally observe that descriptors related with energy level alignment (CT_e, CT_h, $E_{gap,d-a}$) as well as those related with the mobility imbalance ($\Delta\mu = |\mu_d - \mu_a|$, $\mu_{imb} = \mu_a/\mu_d$) show the highest accumulated FI.

AI models such as the RF ensemble also provide the so-called feature importance (FI), a magnitude that serves to identify and rank quantitatively those characteristics that mostly govern the experimental observables, i.e. the J_{sc}-vol% dependence. Accordingly, we first perform subsequent FI analysis using three distinct selections of optoelectronic descriptors. These differ on how the actual values are picked from the literature database (>80 references accessed): either randomly, by a consistent manual selection or calculated from the statistical medians of the scattered data. This analysis is performed to evaluate the sensitivity of the model against the consistency of the input descriptors. The accumulated analysis of the FI in each model (Figure 5) indicates that parameters related to the HOMO/LUMO energy level alignment, such as CT_e, CT_h or $E_{gap,d-a}$, as well as those related with the mobility of the blended species ($\Delta\mu$ and μ_{imb}) are, statistically, the most important descriptors in defining the J_{sc}-vol% dependence. These findings are in good agreement with the current understanding of the performance-composition space in OPV, as the existence of unbalanced charge carrier mobilities between the blended species has so far been considered as one of the key features that molds and displaces the J_{sc}-vol% diagram in binary blends[26]. Nevertheless, we actually observe that the actual selection of values for the descriptors has a large effect on the FI distribution, thus highlighting the requirement for great consistency among the experimental data selected or measured. In this regard, feature selection approaches might help in identifying those combinations of descriptors that return more robust models against experimental noise.

In particular, by performing a greedy MAE feature selection procedure we identify several two-parameter combinations that yield highly accurate RF models, even showing in some cases lower MAE than those models trained with a larger list of descriptors (0, Supporting Information). Among them, we would like to highlight the pair formed by $E_{gap,d}$ and $E_{gap,a}$, whose LOO-cv in 15 distinct D:A binaries is depicted in Figure 6. This model, based on E_{gap}s, is remarkably robust against experimental fluctuations and it extrapolates moderately well in some unseen blends, including all-polymer binaries (0, Supporting Information). Moreover, successful model equations are drawn by the Bayesian machine scientist when employing these two descriptors only (Section V, Supporting Information). Finally, we observe that model training using the consistently extracted solid-state optical band gaps from Tauc plots results as well in successfully validated RF models (0, Supporting Information). Hence, $E_{gap,d}$ and $E_{gap,a}$ (either electronic or optical) unify the main learning characteristics previously found by the 23-parameter model yet in a more physically intuitive approach and providing comparable predictive accuracy. Nevertheless, model predictions in workhorse D:A pairs such as P3HT:PC$_{60}$BM are not successful, which we believe is a consequence of the limited extension of the training datasets employed and the absence of highly semi-crystalline donor material systems in our training dataset.

In spite of such limitations, we believe that the simplicity and accuracy of this two-parameter model are virtues of striking importance for several reasons: (i) for theoretical material screening, as E_{gap} is a byproduct of density functional theory (DFT) calculations; (ii) for combinatorial material synthesis, as organic semiconductors are usually subjected to CV to quantify the HOMO-LUMO energy levels as part of a routine set of electrochemical characterizations; (iii) because E_{gap} is a magnitude sufficiently unrelated to processing; and (iv) due to that we observe a similar predictive accuracy when using solid-state optical band gaps in the model training, which can be easily accessed by UV-vis absorption spectroscopy measurements in thin films.

These features are especially advantageous when dealing with small batches of novel materials. In this case, RF models may help researchers to tailor more effectively the optimal device features (i.e. active layer thickness and composition) and explore *de facto* the full photovoltaic potential of the new molecular species. The here employed training dataset initially formed by 15 D:A binaries is in constant growth; therefore, the conclusions extracted by the RF model will be progressively refined blend after blend. For this reason, we make accessible our combinatorial screening database in a public CSIC repository, which is open to contributions from any researchers as part of a joint OPV materials screening project.
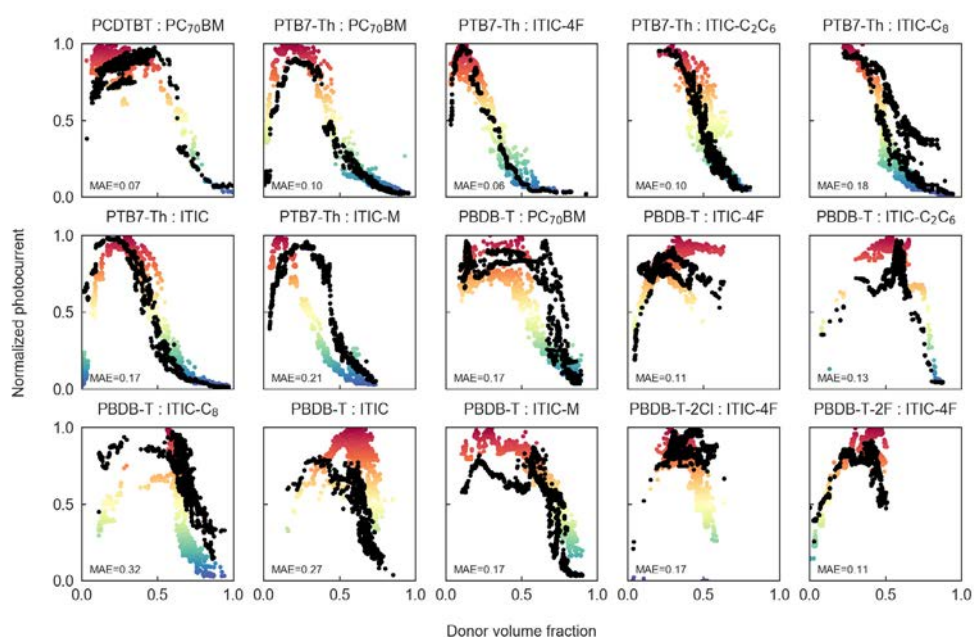
Figure 6 | Leave-one-out cross-validation (LOO-cv) of the two-parameter random forest (RF) model. By performing a greedy mean absolute error (G-MAE) feature selection procedure we identify the corresponding donor and acceptor electronic band gaps ($E_{gap,d}$ and $E_{gap,a}$) as one of the most descriptive paired features in two-parameter RF models. The corresponding LOO-cv predictions (black dots) performed in 15 experimental datasets show excellent agreement with the experimental normalized J_{sc} distributions (rainbow colored), with a MAE of 0.16 (±0.07). The RF models are evaluated at the same grid of thickness-composition values as the experimental measurements.

2. Conclusions

In this work, we have shown the synergic use of high-throughput experimentation and AI algorithms for the prediction of the J_{sc}-vol% space in binary bulk heterojunction organic solar cells. The generation of combinatorial libraries via blade coating and their subsequent imaging by Raman spectroscopy and LBIC mapping enables the efficient exploration of the complex performance landscape in such devices. The subsequent training of a Bayesian machine scientist is demonstrated to be useful in filling the corresponding space, which serves to evaluate the sensitivity of the selected binary upon variations of composition, active layer thickness and other intrinsic optoelectronic descriptors. We finally validate RF models that are able to predict the J_{sc}-vol% dependence with excellent accuracy in unseen binary blends (i.e. blends that are not in the training materials set). We identify descriptors related with the HOMO/LUMO energy level alignment of the donor and acceptor materials, as well as their mobility imbalance among the most important features in shaping the J_{sc}-vol% predictions. Interestingly, simple intuitive models of only two features, namely the electronic (or solid-state optical) band gaps of the blended species, reproduce with large accuracy the J_{sc}-vol% dependence.

3. Acknowledgements

4. Authors Contribution

X.R.-M. measured, modeled and analyzed combinatorial data. E.P.-S.-J. manufactured and measured discrete and graded organic photovoltaic devices. Z.F. and M.H. synthesized the acceptor materials ITIC-C_8 and ITIC-C_2C_6. R.G. implemented the artificial intelligence algorithms. X.R.-M. drafted the paper and prepared the figures. M.C.-Q. designed the experiments and led the project. All the authors discussed the results and commented on the manuscript.

5. References

1. Inganäs, O. Organic Photovoltaics over Three Decades. *Adv. Mater.* **30**, 1800388 (2018).

2. Yan, C. *et al.* Non-fullerene acceptors for organic solar cells. *Nat. Rev. Mater.* **3**, 18003 (2018).

3. Cheng, P., Li, G., Zhan, X. & Yang, Y. Next-generation organic photovoltaics based on non-fullerene acceptors. *Nat. Photonics* **12**, 131–142 (2018).

4. Hou, J., Inganäs, O., Friend, R. H. & Gao, F. Organic solar cells based on non-fullerene acceptors. *Nat. Mater.* **17**, 119–128 (2018).

5. Li, G., Chang, W.-H. & Yang, Y. Low-bandgap conjugated polymers enabling solution-processable tandem solar cells. *Nat. Rev. Mater.* **2**, 17043 (2017).

6. Liu, C., Wang, K., Gong, X. & Heeger, A. J. Low bandgap semiconducting polymers for polymeric photovoltaics. *Chem. Soc. Rev.* **45**, 4825–4846 (2016).

7. Liu, Q. *et al.* 18% Efficiency organic solar cells. *Sci. Bull.* **65**, 272–275 (2020).

8. Vandewal, K., Tvingstedt, K., Gadisa, A., Inganäs, O. & Manca, J. V. Relating the open-circuit voltage to interface molecular properties of donor:acceptor bulk heterojunction solar cells. *Phys. Rev. B* **81**, 125204 (2010).

9. Vandewal, K., Tvingstedt, K., Gadisa, A., Inganäs, O. & Manca, J. V. On the origin of the open-circuit voltage of polymer–fullerene solar cells. *Nat. Mater.* **8**, 904–909 (2009).

10. Mihailetchi, V. D., Xie, H. X., de Boer, B., Koster, L. J. A. & Blom, P. W. M. Charge Transport and Photocurrent Generation in Poly(3-hexylthiophene): Methanofullerene Bulk-Heterojunction Solar Cells. *Adv. Funct. Mater.* **16**, 699–708 (2006).

11. Hachmann, J. *et al.* The Harvard Clean Energy Project: Large-Scale Computational Screening and Design of Organic Photovoltaics on the World Community Grid. *J. Phys. Chem. Lett.* **2**, 2241–2251 (2011).

12. Sahu, H., Rao, W., Troisi, A. & Ma, H. Toward Predicting Efficiency of Organic Solar Cells via Machine Learning and Improved Descriptors. *Adv. Energy Mater.* **8**, 1801032 (2018).

13. Sahu, H. *et al.* Designing promising molecules for organic solar cells via machine learning assisted virtual screening. *J. Mater. Chem. A* **7**, 17480–17488 (2019).

14. Lopez, S. A., Sanchez-Lengeling, B., de Goes Soares, J. & Aspuru-Guzik, A. Design Principles and Top Non-Fullerene Acceptor Candidates for Organic Photovoltaics. *Joule* **1**, 857–870 (2017).

15. Sun, W. *et al.* Machine learning–assisted molecular design and efficiency prediction for high-performance organic photovoltaic materials. *Sci. Adv.* **5**, eaay4275 (2019).

16. Sahu, H. & Ma, H. Unraveling Correlations between Molecular Properties and Device Parameters of Organic Solar Cells Using Machine Learning. *J. Phys. Chem. Lett.* **10**, 7277–7284 (2019).

17. Nagasawa, S., Al-Naamani, E. & Saeki, A. Computer-Aided Screening of Conjugated Polymers for Organic Solar Cell: Classification by Random Forest. *J. Phys. Chem. Lett.* **9**, 2639–2646 (2018).

18. Pettersson, L. A. A., Roman, L. S. & Inganäs, O. Modeling photocurrent action spectra of photovoltaic devices based on organic thin films. *J. Appl. Phys.* **86**, 487 (1999).

19. Sievers, D. W., Shrotriya, V. & Yang, Y. Modeling optical effects and thickness dependent current in polymer bulk-heterojunction solar cells. *J. Appl. Phys.* **100**, 114509 (2006).

20. Deledalle, F. *et al.* Understanding the Effect of Unintentional Doping on Transport Optimization and Analysis in Efficient Organic Bulk-Heterojunction Solar Cells. *Phys. Rev. X* **5**, 011032 (2015).

21. Müller, C. *et al.* Binary Organic Photovoltaic Blends: A Simple Rationale for Optimum Compositions. *Adv. Mater.* **20**, 3510–3515 (2008).

22. Wolfer, P. *et al.* Identifying the optimum composition in organic solar cells comprising non-fullerene electron acceptors. *J. Mater. Chem. A* **1**, 5989 (2013).

23. Zhang, Y. *et al.* Thermally Stable All-Polymer Solar Cells with High Tolerance on Blend Ratios. *Adv. Energy Mater.* **8**, 1800029 (2018).

24. Wen, Z. *et al.* Effects of various donor:acceptor blend ratios on photophysical properties in non-fullerene organic bulk heterojunctions. *Chinese Chem. Lett.* **30**, 995–999 (2019).

25. van Bavel, S. S., Bärenklau, M., de With, G., Hoppe, H. & Loos, J. P3HT/PCBM Bulk Heterojunction Solar Cells: Impact of Blend Composition and 3D Morphology on Device Performance. *Adv. Funct. Mater.* **20**, 1458–1463 (2010).

26. Firdaus, Y. *et al.* Key Parameters Requirements for Non-Fullerene-Based Organic Solar Cells with Power Conversion Efficiency >20%. *Adv. Sci.* **6**, 1802028 (2019).

27. Kiy, M., Kern, R., Beierlein, T. A. & Winnewisser, C. J. Systematic studies of polymer LEDs based on a combinatorial approach. in *Organic Light Emitting Materials and Devices X* vol. 6333 633307 (2006).

28. Langner, S. *et al.* Beyond Ternary OPV: High-Throughput Experimentation and Self-Driving Laboratories Optimize Multicomponent Systems. *Adv. Mater.* **32**, 1907801 (2020).

29. Sánchez-Díaz, A., Rodríguez-Martínez, X., Córcoles-Guija, L., Mora-Martín, G. & Campoy-Quiles, M. High-Throughput Multiparametric Screening of Solution Processed Bulk Heterojunction Solar Cells. *Adv. Electron. Mater.* **4**, 1700477 (2018).

30. Harillo-Baños, A., Rodríguez-Martínez, X. & Campoy-Quiles, M. Efficient Exploration of the Composition Space in Ternary Organic Solar Cells by Combining High-Throughput Material Libraries and Hyperspectral Imaging. *Adv. Energy Mater.* **10**, 1902417 (2020).

31. Glaser, K. *et al.* Rapid experimental optimization of organic tandem solar cells: 200 absorber layer thickness combinations on a 4×4 cm 2 substrate. *J. Mater. Chem. A* **6**, 9257–9263 (2018).

32. Pascual-San-José, E. *et al.* Blade coated P3HT:non-fullerene acceptor solar cells: a high-throughput parameter study with a focus on up-scalability. *J. Mater. Chem. A* **7**, 20369–20382 (2019).

33. Guimerà, R. *et al.* A Bayesian machine scientist to aid in the solution of challenging scientific problems. *Sci. Adv.* **6**, eaav6971 (2020).

34. Rodríguez-Martínez, X. *et al.* Quantifying local thickness and composition in thin films of organic photovoltaic blends by Raman scattering. *J. Mater. Chem. C* **5**, 7270–7282 (2017).

35. Lin, Y. *et al.* An Electron Acceptor Challenging Fullerenes for Efficient Polymer Solar Cells. *Adv. Mater.* **27**, 1170–1174 (2015).

36. Fei, Z. *et al.* An Alkylated Indacenodithieno[3,2- b]thiophene-Based Nonfullerene Acceptor with High Crystallinity Exhibiting Single Junction Solar Cell Efficiencies Greater than 13% with Low Voltage Losses. *Adv. Mater.* **30**, 1705209 (2018).

37. Zhang, S. *et al.* Side Chain Selection for Designing Highly Efficient Photovoltaic Polymers with 2D-Conjugated Structure. *Macromolecules* **47**, 4653–4659 (2014).

38. Tang, Y. *et al.* A New Wide Bandgap Donor Polymer for Efficient Nonfullerene Organic Solar Cells with a Large Open-Circuit Voltage. *Adv. Sci.* **6**, 1901773

(2019).

39. Li, S. *et al.* Energy-Level Modulation of Small-Molecule Electron Acceptors to Achieve over 12% Efficiency in Polymer Solar Cells. *Adv. Mater.* **28**, 9423–9429 (2016).

40. Zhao, W., Li, S., Zhang, S., Liu, X. & Hou, J. Ternary Polymer Solar Cells based on Two Acceptors and One Donor for Achieving 12.2% Efficiency. *Adv. Mater.* **29**, 1604059 (2017).

41. Zhang, S., Qin, Y., Zhu, J. & Hou, J. Over 14% Efficiency in Polymer Solar Cells Enabled by a Chlorinated Polymer Donor. *Adv. Mater.* **30**, 1800868 (2018).

42. Blouin, N., Michaud, A. & Leclerc, M. A Low-Bandgap Poly(2,7-Carbazole) Derivative for Use in High-Performance Solar Cells. *Adv. Mater.* **19**, 2295–2300 (2007).

43. Chan, K. K. H., Tsang, S. W., Lee, H. K. H., So, F. & So, S. K. Charge injection and transport studies of poly(2,7-carbazole) copolymer PCDTBT and their relationship to solar cell performance. *Org. Electron.* **13**, 850–855 (2012).

44. Fan, Q. *et al.* Chlorine substituted 2D-conjugated polymer for high-performance polymer solar cells with 13.1% efficiency via toluene processing. *Nano Energy* **48**, 413–420 (2018).

45. Zhao, W. *et al.* Molecular Optimization Enables over 13% Efficiency in Organic Solar Cells. *J. Am. Chem. Soc.* **139**, 7148–7151 (2017).

46. Shi, Z. *et al.* Engineering the interconnecting layer for efficient inverted tandem polymer solar cells with absorption complementary fullerene and nonfullerene acceptors. *Sol. Energy Mater. Sol. Cells* **180**, 1–9 (2018).

47. Bracher, C. *et al.* The effect of residual palladium catalyst on the performance and stability of PCDTBT:PC70BM organic solar cells. *Org. Electron.* **27**, 266–273 (2015).

48. Cui, C., Wong, W.-Y. & Li, Y. Improvement of open-circuit voltage and photovoltaic properties of 2D-conjugated polymers by alkylthio substitution. *Energy Environ. Sci.* **7**, 2276–2284 (2014).

49. Li, Z. *et al.* High-photovoltage all-polymer solar cells based on a diketopyrrolopyrrole–isoindigo acceptor polymer. *J. Mater. Chem. A* **5**, 11693–11700 (2017).

50. Pan, M.-A. *et al.* 16.7%-efficiency ternary blended organic photovoltaic cells with PCBM as the acceptor additive to increase the open-circuit voltage and phase purity. *J. Mater. Chem. A* **7**, 20713–20722 (2019).

51. Ding, Z. *et al.* Polymer solar cells with open-circuit voltage of 1.3 V using polymer electron acceptor with high LUMO level. *Nano Energy* **32**, 216–224 (2017).

52. Wang, J. *et al.* Ultra-narrow bandgap non-fullerene organic solar cells with low voltage losses and a large photocurrent. *J. Mater. Chem. A* **6**, 19934–19940 (2018).

53. Pedregosa, F. *et al.* Scikit-learn: Machine Learning in Python. (2012).

54. Pranculis, V. *et al.* Charge Carrier Generation and Transport in Different Stoichiometry APFO3:PC61BM Solar Cells. *J. Am. Chem. Soc.* **136**, 11331–11338 (2014).

55. Ho, C. H. Y. *et al.* Using Ultralow Dosages of Electron Acceptor to Reveal the Early Stage Donor-Acceptor Electronic Interactions in Bulk Heterojunction Blends. *Adv. Energy Mater.* **7**, 1602360 (2017).

56. Liu, X. *et al.* High-Performance All-Polymer Solar Cells with a High Fill Factor and a Broad Tolerance to the Donor/Acceptor Ratio. *ACS Appl. Mater. Interfaces* **10**, 38302–38309 (2018).

Predicting the photocurrent-composition dependence in organic solar cells

Xabier Rodríguez-Martínez[1], Enrique Pascual-San-José[1], Zhuping Fei[2], Martin Heeney[2], Roger Guimerà[3,4] and Mariano Campoy-Quiles[1*]

[1] Institut de Ciència de Materials de Barcelona (ICMAB-CSIC), Esfera UAB, Campus Universidad Autónoma de Barcelona, 08193, Bellaterra, Barcelona, Spain.

[2] Department of Chemistry and Centre for Plastic Electronics, White City Campus, Imperial College London, London W12 0BZ, U.K.

[3] Institució Catalana de Recerca i Estudis Avançats (ICREA), 08010, Barcelona, Spain.

[4] Department of Chemical Engineering, Universitat Rovira i Virgili, 43007, Tarragona, Spain.

* e-mail: mcampoy@icmab.es

Section I. Materials and methods

a. Device fabrication

All devices were manufactured with inverted architecture (glass/ITO/ZnO/active layer/MoO_3/Ag). Pre-patterned and non-patterned ITO substrates (purchased from Ossila, 100 nm thick and 20 Ω square^{-1} sheet resistance), were cleaned by sequential ultrasonication in acetone, Hellmanex 10% solution in water, isopropanol and finally 10% NaOH water solution. A dispersion of ZnO nanoparticles (N-10, Avantama) was blade coated onto cleaned ITO substrates in air conditions using an automatic coater (ZAA 2300, Zehntner) and a lamination piece of equipment (ZUA 2000, Zehntner). The ZnO casting parameters were 50 μm blade gap, 50 μL casting volume, 4 mm s^{-1} blade speed and 40 °C yielding a thickness of 40 nm. A 100 °C post-deposition thermal annealing was carried out for 10 min in air. The ZnO coated substrates were then transferred into a nitrogen-filled glovebox for the deposition of the active layers.

All photovoltaic materials were used as received and dissolved in chlorobenzene with a total solid concentration of 15 mg mL^{-1} and stirred overnight at 80 °C. PBT7-Th and PCDTBT were purchased from Ossila. PBDB-T, PBDB-T-2Cl, PBDB-T-2F, ITIC, ITIC-M and ITIC-4F were purchased from 1-Material. ITIC-C_8 and ITIC-C_2C_6 were synthesized following previous publications of one of our groups and are further detailed below[36]. $PC_{70}BM$ was purchased from Solenne. On the one hand, discrete 1D-thickness graded samples (Figure S1a) were manufactured using premixed inks of donor and acceptor materials weighted in controlled fractions in a single vial, resulting in devices with fixed composition. D:A mixing ratio solutions extending from 1:0 to 0:1 were individually prepared to screen the composition space for PTB7-Th:ITIC and PBDB-T:ITIC-C_2C_6. The casting conditions were 100 μm blade gap, 70 μL casting volume and 90 °C casting temperature. The blade was intendedly decelerated from 90 mm s^{-1} to 5 mm s^{-1} resulting in a thickness-graded active layer (ca. 50-200 nm)[29,32]. On the other hand, 2D-thickness-composition graded samples (Figure S1b) were manufactured following the same

processing parameters as 1D devices excepting the blade speed, which in this case was kept fixed at 5 mm s^{-1} and two drops of 40 µL each of the neat material inks were cast. Finally, 10 nm of MoO$_3$ and 100 nm of Ag were thermally evaporated at a rate of 0.1 and 1 Å s^{-1}, respectively. Note that each 1D sample contains 24 devices, 12 of them with different thickness values (two per side), with a pixel active area of 8 mm^2.
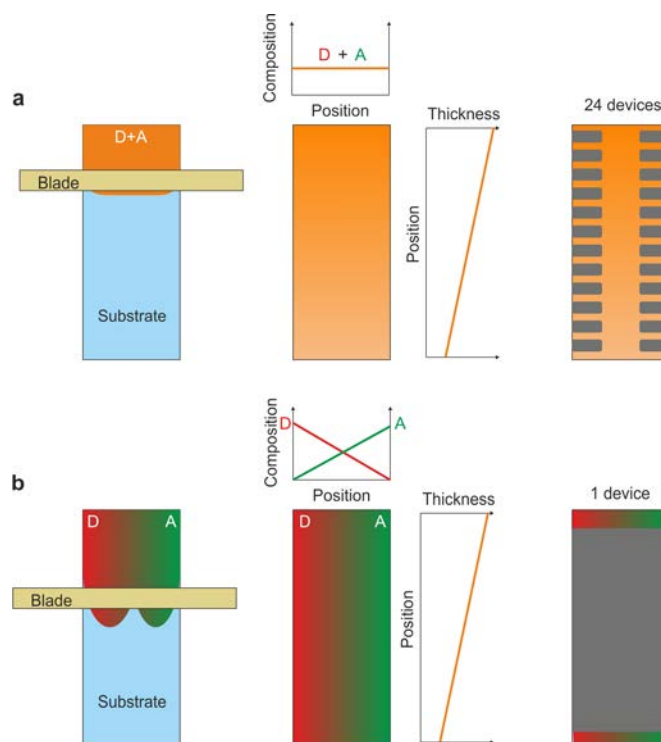

Figure S1. The two processing schemes for organic solar cells comprising lateral gradients in their active layer. (a) By decelerating the applicator during the coating of the active layer we generate a thickness gradient for inks of fixed D:A ratio. This approach, in combination with pre-patterned ITO substrates and their dedicated evaporation masks, allows the high-throughput screening of the thickness-performance dependence in 24 discrete devices. (b) To simultaneously screen very efficiently the composition, two drops of the pristine D and A inks coalesce during the coating leading to an orthogonal distribution of D:A ratio and active layer thickness. In this case, a single large-area device is obtained, which is then mapped by LBIC and Raman spectroscopy imaging.

b. Device characterization

J-V characteristics of 1D devices were automatically extracted by using a Keithley source meter and an Arduino based multiplexer/switcher that allows measuring 24 devices in less than 6 minutes. As a lighting source, a SAN-EI Electric, XES-100S1 AAA solar simulator was used to ensure a homogenous illumination in a 10 cm x 10 cm area. The solar simulator was previously calibrated with a certified silicon solar cell (NREL).

2D gradient large-area devices were characterized using a WITec alpha 300 RA+ confocal setup, connected to a current amplifier to extract photocurrent maps of the solar cell. The samples were excited using a 10X objective (NA 0.25) coupled to 488 nm solid-state laser (with its power set to 3 mW to avoid photodegradation). Our optical configuration yields a ca. 10 μm laser spot in diameter once focused on the active layer. Light beam induced current (LBIC) with monochromatic light was measured simultaneously along with Raman. However, to extend the electromagnetic spectrum of the excitation source, we coupled the built-in lamp of the WITec alpha 300 RA+ piece of equipment and employed it to map the photovoltaic response under white light illumination (Figure S2). The use of white light yielded a spot size of ca. 150 μm in diameter. The device photocurrent was acquired in short circuit conditions. Data analysis (D:A mixing ratio and thickness from Raman spectra) was performed using homemade MATLAB routines described elsewhere[34].
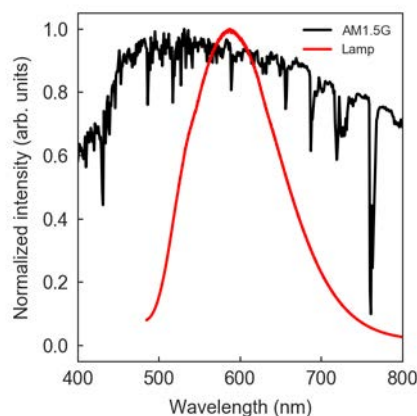

Figure S2. Normalized emission spectrum of the built-in lamp in the WITec alpha 300 RA+ setup measured upon reflection on a silver mirror (solid red line). For comparative purposes, the reference AM1.5G irradiance spectrum is also shown (solid black line) to indicate the notorious mismatch in regions far from the visible region of the electromagnetic spectrum.

c. Synthesis and characterization of ITIC-C₂C₆
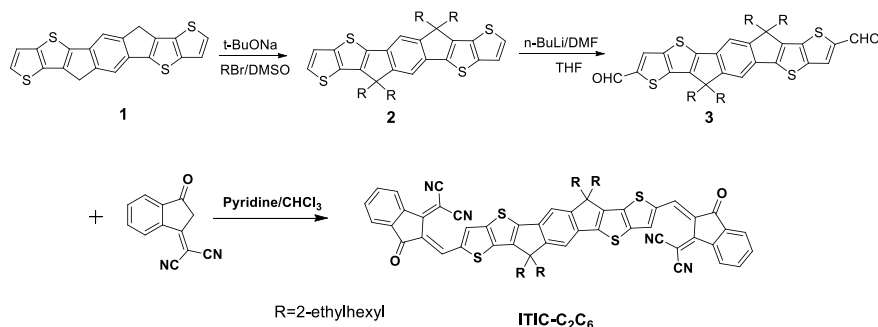
Scheme S1. The synthetic route of ITIC-C₂C₆.

5,11-Dihydro-5,5,11,11-(2-ethylhexyl)-*s*-indaceno[1,2-*b*:5,6-*b'*] dithieno[3,2-*b*]thiophene (2):

To a suspension of 5,11-dihydro-*s*-indaceno[1,2-*b*:5,6-*b'*] dithieno[3,2-*b*]thiophene (**1**) (0.70 g, 1.85 mmol) in anhydrous DMSO (40 ml) was added sodium *tert*-butoxide (1.06 g, 11.11 mmol) in parts. The reaction mixture was heated at 80 ℃ for 1 h, followed by the addition of 1-bromohexadecane (2.14 g, 11.11 mmol) dropwise. After complete addition, the resultant mixture was heated at 80 ℃ for overnight, then poured into ice-water and extracted by THF/hex (2/1, v/v, 100 mL) for 3 times. The combined organics were dried by MgSO4, filtered and concentrated under reduced pressure. This residue was purified by column chromatography on silica (eluent: hexane) to give a yellow oil (0.72 g, 47%). ^{1}H NMR (400 MHz, CDCl$_3$) δ 7.35 (d, 2H), 7.34-7.29 (m, 4H), 2.11-2.06 (m, 8H), 0.99-0.73(m, 32H), 0.70-0.45 (m, 28H); ^{13}C NMR (100 MHz, CDCl$_3$): δ 152.2, 145.4, 143.8, 141.0, 136.6, 134.2, 125.5, 120.3, 113.9, 53.8, 35.0, 34.9, 33.7, 29.1, 28.5, 28.4, 28.0, 27.0, 26.8, 22.9, 22.8, 22.7, 14.2, 13.8, 10.7, 10.6, 10.2.

6,6,12,12-Tetra(2-ethylhexyl)-6,12-dihydrothieno[3,2-b]thieno[2'',3'':4',5']thieno[2',3':5,6]-s-indaceno[2,1-d]thiophene-2,8-dicarbaldehyde (3):

A solution of n-BuLi (2.1 mL of a 1.6 M solution in pentane, 3.36 mmol) was added dropwise into **2** (0.70 g, 0.85 mmol) in THF (40 mL) at -78 ℃. After stirred at this temperature for 20 min, the mixture was allowed to warm to RT for 1.5 h. Then the mixture was cooled to -78 ℃ , and anhydrous DMF (0.3 mL) was added in one portion, and the mixture was allowed to warm to RT slowly and stirred overnight. Water (100 mL) was added, and the mixture was extracted with DCM (3 × 200 mL). The combined organics were dried by MgSO$_4$, filtered and concentrated under reduced pressure. The residue was purified by silica gel chromatography (eluent: DCM/hexane = 3/2, v/v) to afford an orange oil (0.50 g, yield: 67%). ^{1}H NMR (CDCl$_3$, 400 MHz,) δ (ppm): 9.96 (s, 2H), 8.00 (s, 2H), 7.48 (s, 2H), 2.16-2.10 (m, 8H), 0.99-0.73 (m, 32H), 0.70-0.44 (m,

257

28H); ^{13}C NMR (CDCl$_3$, 100 MHz,) δ (ppm): 182.9, 153.7, 150.4, 146.2, 143.9, 141.3, 140.8, 137.0, 130.2, 115.1, 54.2, 54.1, 43.2, 43.1, 42.6, 35.3, 35.1, 35.0, 33.8, 33.4, 28.5, 28.4, 28.0, 27.1, 27.0, 2687, 26.7, 22.8, 22.7, 22.6, 14.2, 13.8, 10.8, 10.6, 10.1.

{(2Z)-2-[(8-{(E)-[1-(Dicyanomethylidene)-3-oxo-1,3-dihydro-2H-inden-2-ylidene]methyl}-6,6,12,12-tetra(2-ethylhexyl)-6,12-dihydrothieno[3,2-b]thieno[2'',3'':4',5']thieno[2',3':5,6]-s-indaceno[2,1-d]thiophen-2-yl)methylidene]-3-oxo-2,3-dihydro-1H-inden-1-ylidene}propanedinitrile (ITIC-C$_2$C$_6$):

To a mixture of 3-dihydro-1H-inden-1-ylidene)malononitrile (165 mg, 0.85 mmol) and compound **3** (150 mg, 0.17 mmol) in CHCl$_3$ (20 mL) was added pyridine (0.5 mL). After addition, the mixture was heated to 80 °C and stirred for overnight, and then poured into water (30 mL) and extracted with DCM (3 × 20 mL). The combined organics were dried by MgSO$_4$, filtered and concentrated under reduced pressure. The residue was purified by silica gel chromatography (eluent: DCM/hexane = 2/1), followed by recrystallization from DCM/MeOH to afford a shining golden solid (143 g, yield: 68%). ^{1}H NMR (CDCl$_3$, 400 MHz,) δ (ppm): 8.99 (s, 2H), 8.71 (d, 2H), 8.21 (s, 2H), 7.96 (d, 2H), 7.79-7.76 (m, 4H), 7.54 (d, 2H), 2.29-2.16 (m, 8H), 0.96-0.71 (40H), 0.70-0.46 (m, 20H); ^{13}C NMR (CDCl$_3$, 100 MHz,) δ (ppm): ^{13}C NMR (100 MHz, CDCl$_3$) δ (ppm): 188.3, 160.5, 154.8, 153.7, 147.9, 147.4, 143.2, 140.1, 139.3, 138.4, 137.7, 137.3, 136.9, 135.2, 134.5, 125.3, 123.8, 122.4, 115.6, 114.7, 69.2, 54.3, 43.1, 43.0, 42.8, 35.4, 35.2, 33.7, 33.5, 28.6, 28.4, 28.1, 27.2, 27.0, 26.8, 22.8, 22.7, 22.6, 14.2, 13.8, 10.8, 10.2.

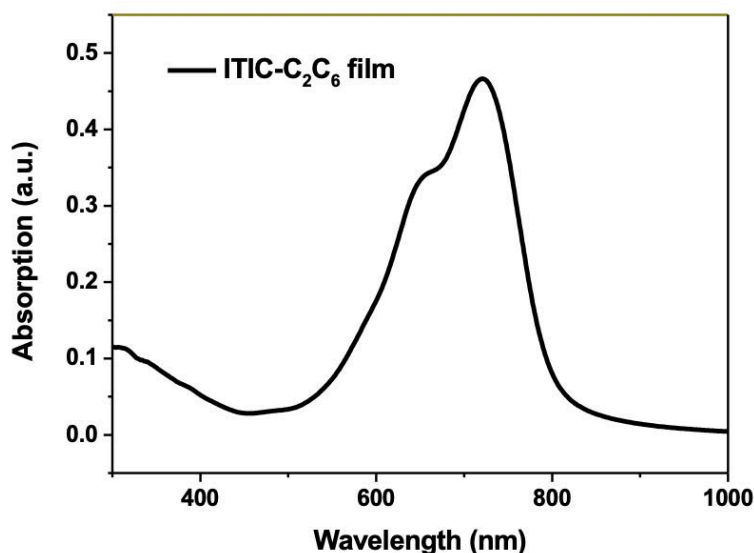**Figure S3. UV-Vis absorption spectrum of an ITIC-C$_2$C$_6$ film. The main absorption peaks locate at 656 nm and 721 nm. The absorption edge locates at 800 nm, corresponding to an optical band gap of 1.55 eV. PESA data for ITIC-C$_2$C$_6$ shows an ionization potential of 5.71 eV, which compared to ITIC-C$_8$ (IP = 5.68 eV from PESA and HOMO = -5.63 eV from CV) allows setting the HOMO level of ITIC-C$_2$C$_6$ at -5.66 eV.**

Section II. Comparison of Edisonian and high-throughput experimentation approaches

a. Sampling the thickness-composition space by means of active layer thickness gradients

For comparative purposes against the high-throughput screening methodology results, we prepared multiple solar cell devices in which the D:A blend ratio was varied in discrete samples and controlled steps throughout the entire compositional range, including in some cases neat active layers (i.e. homojunctions). This is the classical approach for D:A blend ratio screening, also known as Edisonian experimentation: the preparation of individual devices, each from a compositionally homogenized ink that results from the overnight stirring of controlled D:A weights in a single vial.

However, to accelerate the corresponding active layer thickness screening, the devices were blade coated to include an active layer thickness gradient spanning from ca. 50 nm to 200 nm for each composition step. This approach, combined with pre-patterned 25x75 mm^2 ITO substrates, enabled us to screen up to 12 different active layer thickness values for each D:A composition step, thus speeding up and making more efficient (in time and resources) the screening process.

Figure S4 depicts the solar cell device parameters (J_{sc}, V_{oc}, FF and PCE) obtained in PTB7-Th:ITIC (upper row) and PBDB-T:ITIC-C_2C_6 (lower row) batches, which are those included in Figure 2 in the main manuscript. We first observe that V_{oc} is fairly constant throughout the entire D:A composition diagram. Conversely, the FF varies more abruptly with the composition, showing its maximum close to 30-40 vol% of donor in both cases. Nevertheless, J_{sc} is still a good probe for PCE as they both show very similar upper-shell data distributions (green dashed lines) and peak performance positions in the D:A composition space.
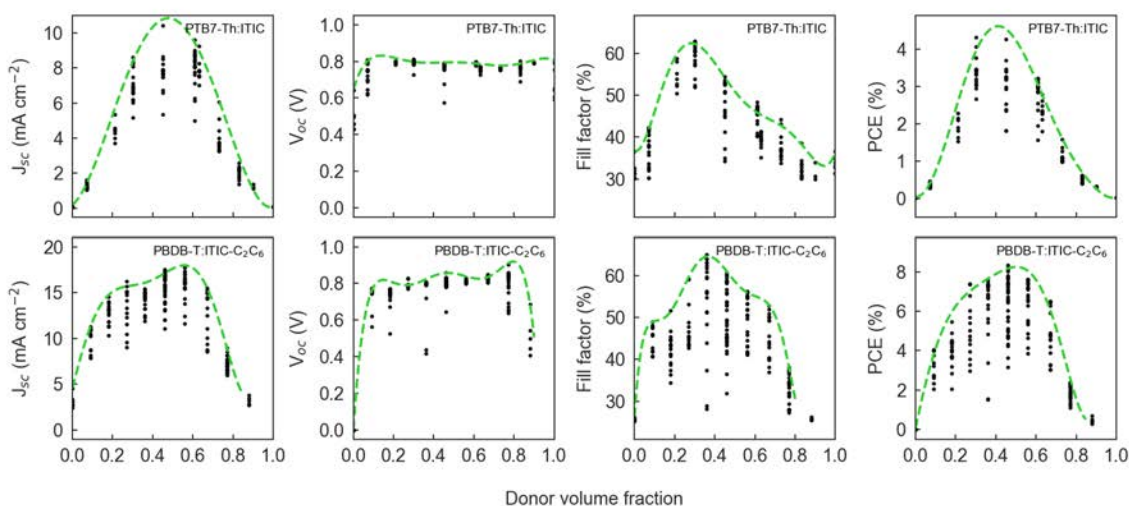

Figure S4. Solar cell device parameters (J_{sc}, V_{oc}, FF and PCE) for discrete composition step batches of PTB7-Th:ITIC (upper row) and PBDB-T:ITIC-C_2C_6. Since the devices were processed to show an active layer thickness gradient to accelerate its corresponding screening, the observed dispersion in the _y_-axis is exclusively ascribed to such deliberate thickness variation.

b. Analysis of the time and material cost savings in high-throughput experimentation

Despite the significant savings in time and resources offered by the (1D) thickness graded devices compared to the traditional discrete sampling approach, the use of bidimensional (2D) thickness-composition graded devices extends even further the abovementioned savings. A detailed time and material cost analysis of the corresponding discrete and 1D/2D graded devices is listed in Table S1. According to our estimations and compared to 1D graded devices, 2D combinatorial devices offer a 2,000-fold higher density of data points per sample (12 discrete pixels per 1D sample vs 24,000 data points per 2D sample) as well as an eleven-fold reduction in the usage of raw semiconducting materials to perform the J_{sc}-vol% dependence exploration. As a result, by following the 2D high-throughput screening approach the experimental time required per data point is below 90 seconds and the consumption of raw semiconducting material is as low as a few tens of nanograms per data point (Table S1).

Table S1. Time and material cost analysis for discrete sampling, 1D thickness-graded devices and 2D thickness-composition graded devices (high-throughput experimentation) in the full exploration of the J_{sc}-vol% space for a given OPV binary.

	Discrete sampling	1D thickness gradient	2D thickness-composition gradients
No. samples	66 [a]	11 [b]	1
No. data points per sample	1	12	24,000
No. data points (total)	66	132	24,000
Manufacturing time (h)	93.2 [c]	16.5	5.9
Measuring time (h)	0.55 [d]	1.12 [c]	9
Data analysis (h)	1	2	13
Total time (h)	94.8	19.6	27.9
mg of semiconductor	79.2	13.2	1.2
Time required per data point (h)	1.44	0.15	0.0012 (86 s)
mg required per data point	1.2	0.1	5E-05 (50 ng)

[a] From, to neat films in 10 vol% steps + 6 homogeneous thickness steps
[b] From, to neat films in 10 vol% steps + 12 thickness steps as gradient
[c] Assuming 11 batches with co-evaporation of 6 samples per batch
[d] J-V curve takes 30 s to be measured

c. Reproducibility evaluation of the high-throughput experimentation approach

We tested the reproducibility of the developed high-throughput experimentation approach by fabricating two batches of thickness-composition graded devices for the same D:A pair (PBDB-T:ITIC-C$_8$) in different days. Their corresponding large area maps of active layer thickness, donor volume fraction and normalized photocurrent are depicted in Figure S5. The spatial correlation of all three magnitudes in both batches is accordingly illustrated in Figure S6 and it demonstrates that the high-throughput experimentation approach is parametrically highly reproducible and self-consistent in terms of normalized photocurrent.
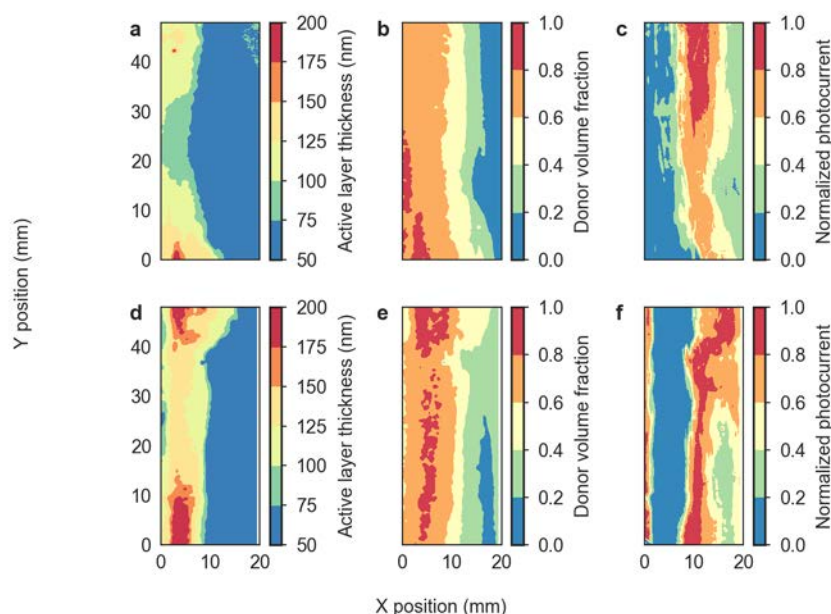
Figure S5. Batch-to-batch comparison of PBDB-T:ITIC-C$_8$ combinatorial devices. Active layer thickness maps (a,d) and composition images (b,e) were acquired by properly deconvoluting the spatially-resolved Raman spectra.[34] The normalized photocurrent images (c,f) were acquired in a subsequent step by mapping of a 150 µm white light spot throughout the active area of the device in the same Raman imaging setup.

Figure S6. The one-to-one comparison of the PBDB-T:ITIC-C$_8$ batches demonstrates that (a) a similar region of the composition vs. active layer thickness diagram is accessed, and (b) that in terms of normalized photocurrent the overall trend is overlapping in both cases.

261

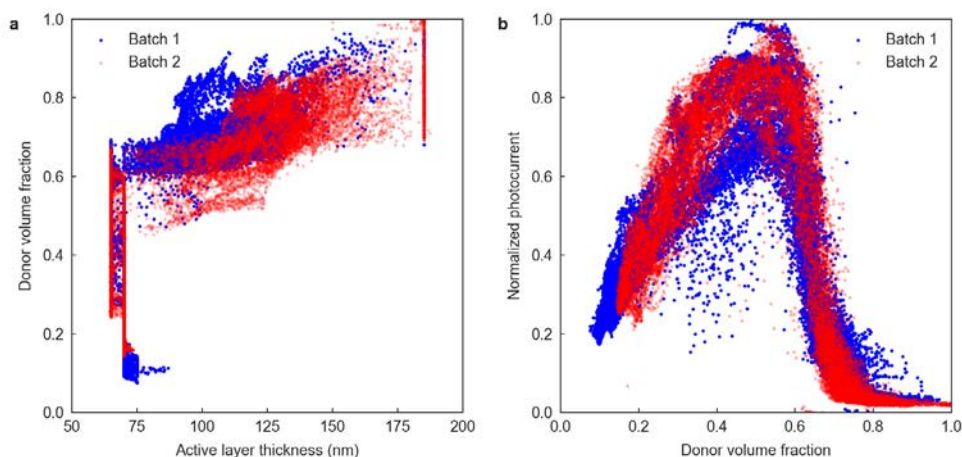## Section III. Ellipsometric characterization: normalized absorption coefficients and Tauc plots

The absorption coefficients (α) were deduced from the corresponding extinction coefficients (κ), extracted by means of variable angle spectroscopic ellipsometry (VASE) using a Semilab GES5E rotating polarizer ellipsometer. Modeling of the ellipsometry data was performed using the Winelli II piece of software package from SOPRALAB.

For the determination of the solid-state optical band gaps using the Tauc plots, we depict the magnitude $(\alpha\, h\nu)^{1/r}$ vs $h\nu$ (photon energy in eV), where $r = 2$ for indirect allowed transitions. By consistently extrapolating the linear regime of the absorption onset we determine the corresponding optical band gaps.
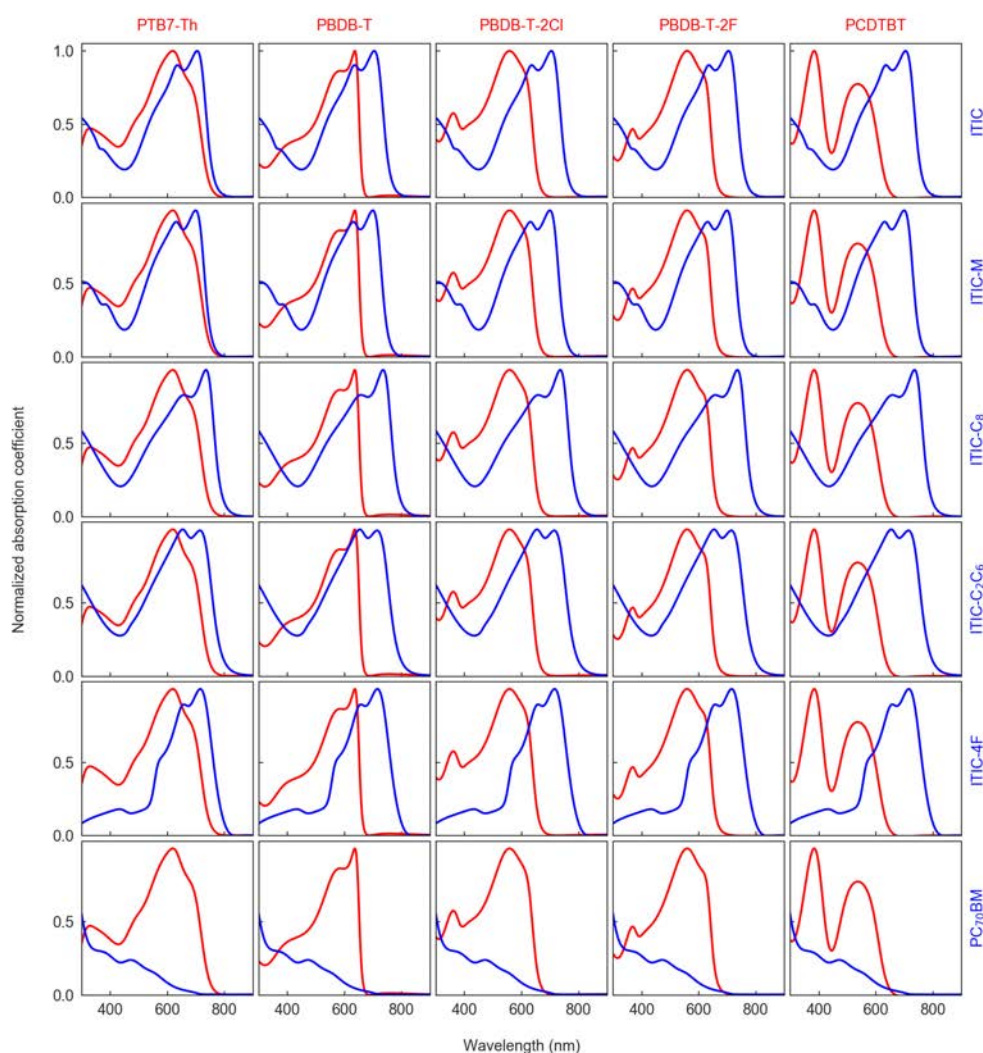

Figure S7. Combinatorial matrix of normalized absorption coefficients corresponding to the D:A binary OPV systems screened in the main manuscript. Data for donors and acceptors are depicted in red and blue colors, respectively.
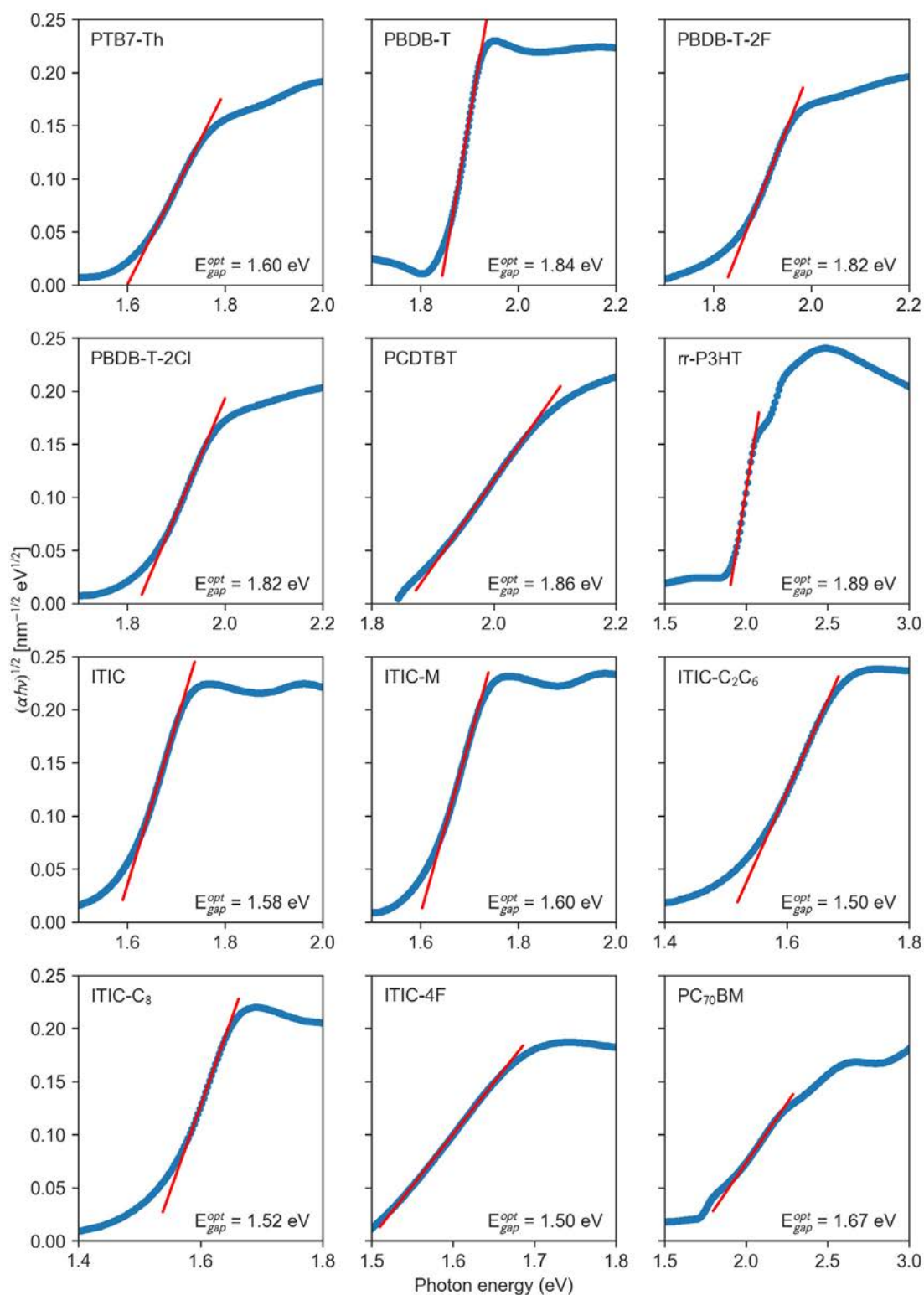
Figure S8. Tauc plots used to determine the solid-state optical band gap of the semiconducting materials studied.

263

Section IV. Listing of the optoelectronic descriptors used in the AI modeling

Donor and acceptor materials are characterized by a set of fundamental and intrinsic optoelectronic descriptors formed by 7 different magnitudes. While the optical descriptors (κ_{max}, λ_{max} and λ_{edge}) are deduced from their corresponding complex refractive indices determined by variable-angle spectroscopic ellipsometry (VASE) (Figure S7), the electronic descriptors (HOMO, LUMO, E_{gap} and $\mu_{h,e}$) are extracted from a variety of literature references. Note that E_{gap} is simply computed as the LUMO-HOMO difference, thus corresponding to the electronic band gap. Therefore, each D:A pair has 14 fundamental optoelectronic descriptors ascribed (7 per material). Below, we detail the values attained in each of the three distinct sets of descriptors selected for the training of AI algorithms.

In the first set (Table S2), we randomly select HOMO and LUMO energy levels from our literature database. We also randomize the selection of the corresponding mobilities. Therefore, we do not carefully select the data to be consistently ascribed to a unique characterization technique (i.e. cyclic voltammetry (CV) or ultraviolet photoelectron spectroscopy (UPS); or space-charge limited current (SCLC) devices or time-of-flight (TOF) measurements).

Table S2. Fundamental optoelectronic features used as a random selection of (electronic) descriptors. κ_{max}, λ_{max} and λ_{edge} were deduced from the ellipsometric measurements shown above.

	Material	κ_{max}	λ_{max} (nm)	λ_{edge} (nm)	HOMO (eV)	LUMO (eV)	E_{gap} (eV)	$\mu_{h,e}$ (cm^2 V^{-1} s^{-1})	Ref.
Donors	PTB7-Th	0.91	625	720	-5.24	-3.66	1.58	1.80E-04	[37,38]
	PBDB-T	1.37	637	651	-5.33	-3.53	1.80	1.08E-04	[39,40]
	PBDB-T-2F	0.79	568	642	-5.47	-3.65	1.82	2.97E-04	[41]
	PBDB-T-2Cl	0.84	567	639	-5.51	-3.57	1.94	2.13E-04	[41]
	PCDTBT	0.95	549	610	-5.50	-3.60	1.90	9.00E-06	[42,43]
Acceptors	ITIC	1.60	706	734	-5.64	-3.92	1.72	1.10E-04	[36]
	ITIC-M	1.68	702	729	-5.58	-3.98	1.60	1.10E-04	[39]
	ITIC-C$_2$C$_6$	1.86	718	756	-5.66	-3.91	1.75	*6.90E-04*	*
	ITIC-C$_8$	1.68	737	763	-5.63	-3.91	1.72	6.90E-04	[36]
	ITIC-4F	1.13	724	756	-5.69	-4.07	1.62	5.05E-04	[44,45]
	PC$_{70}$BM	0.40	479	585	-6.10	-3.90	2.20	1.00E-03	[46,47]

* For ITIC-C$_2$C$_6$, the corresponding HOMO and LUMO values are reported in Section A. The mobility is considered to be the same as ITIC-C$_8$.

In the second set (Table S3), we hand-pick those articles in which both reported HOMO and LUMO levels were measured by means of CV whenever possible. To further increase the consistency, we also index the value for the carrier mobility reported in the same work (if possible), typically measured by SCLC measurements on single carrier devices.

Table S3. In this selection of optoelectronic descriptors, both HOMO and LUMO energy levels are extracted from references using CV measurements whenever possible. Mobility values correspond preferentially to those reported in the same works as CV measurements. κ_{max}, λ_{max} and λ_{edge} were deduced from the ellipsometric measurements shown above.

	Material	κ_{max}	λ_{max} (nm)	λ_{edge} (nm)	HOMO (eV)	LUMO (eV)	E_{gap} (eV)	$\mu_{h,e}$ (cm^2 V^{-1} s^{-1})	Ref.
Donors	PTB7-Th	0.91	625	720	-5.30	-3.17	2.13	2.40E-04	48,49
	PBDB-T	1.37	637	651	-5.33	-3.29	2.04	3.00E-04	36
	PBDB-T-2F	0.79	568	642	-5.54	-3.61	1.93	5.00E-04	50
	PBDB-T-2Cl	0.84	567	639	-5.52	-3.55	1.97	5.20E-04	50
	PCDTBT	0.95	549	610	-5.50	-3.60	1.90	6.20E-05	42,51
Acceptors	ITIC	1.60	706	734	-5.64	-3.92	1.72	1.10E-04	36
	ITIC-M	1.68	702	729	-5.58	-3.98	1.60	1.10E-04	39
	ITIC-C_2C_6	1.86	718	756	-5.66	-3.91	1.75	*6.90E-04*	*
	ITIC-C_8	1.68	737	763	-5.63	-3.91	1.72	6.90E-04	36
	ITIC-4F	1.13	724	756	-5.71	-4.15	1.56	4.50E-04	50
	PC$_{70}$BM	0.40	479	585	-5.96	-3.90	2.06	5.70E-04	50,52

* For ITIC-C_2C_6, the corresponding HOMO and LUMO values are reported in Section A. The mobility is considered to be the same as ITIC-C_8.

In the third set (Table S4), and according to the large dispersion of HOMO/LUMO energy levels as well as mobility values found after accessing more than 80 distinct literature references (Figure S9), we take the median values of each of the electronic descriptors indexed. This is thought to evaluate the sensitivity of the AI algorithms upon usage of third-party measurements.
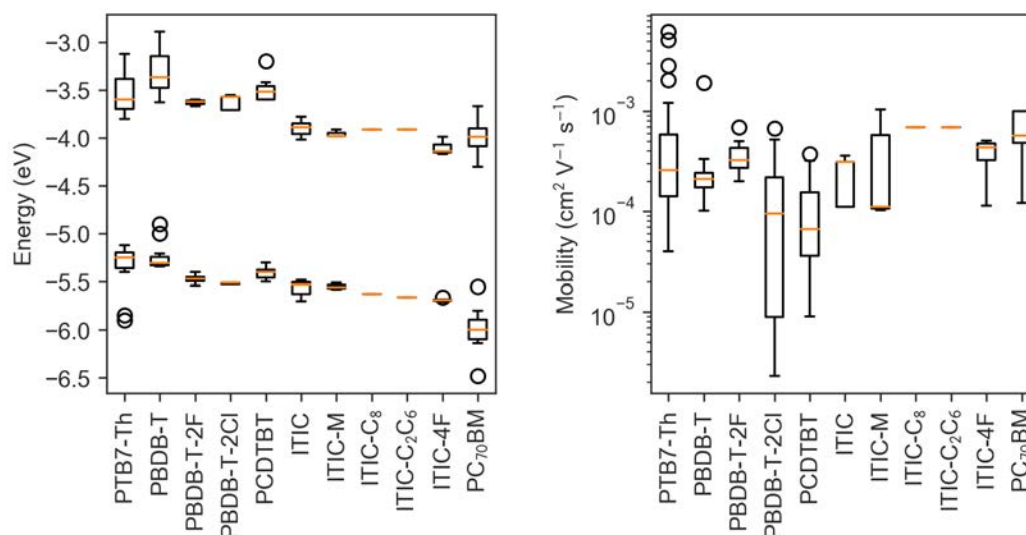

Figure S9. Left panel shows boxplots of the HOMO and LUMO levels for the materials used in this work as collected from the available literature. Right panel illustrates boxplots of the reported mobility extracted by means of SCLC devices in neat and blend films. More than 80 references were indexed in total.

Table S4. Fundamental optoelectronic descriptors obtained as median values after data mining of more than 80 distinct literature references. κ_{max}, λ_{max} and λ_{edge} were deduced from the ellipsometric measurements shown above.

	Material	κ_{max}	λ_{max} (nm)	λ_{edge} (nm)	HOMO (eV)	LUMO (eV)	E_{gap} (eV)	$\mu_{h,e}$ (cm^2 V^{-1} s^{-1})	No. refs.
Donors	PTB7-Th	0.91	625	720	-5.25	-3.60	1.65	2.58E-04	22
	PBDB-T	1.37	637	651	-5.30	-3.37	1.93	2.10E-04	15
	PBDB-T-2F	0.79	568	642	-5.47	-3.62	1.85	3.25E-04	7
	PBDB-T-2Cl	0.84	567	639	-5.51	-3.57	1.94	9.41E-05	5
	PCDTBT	0.95	549	610	-5.40	-3.52	1.88	6.65E-05	10
Acceptors	ITIC	1.60	706	734	-5.53	-3.89	1.64	3.13E-04	8
	ITIC-M	1.68	702	729	-5.56	-3.98	1.58	1.10E-04	3
	ITIC-C$_2$C$_6$	1.86	718	756	-5.66	-3.91	1.75	*6.90E-04*	*
	ITIC-C$_8$	1.68	737	763	-5.63	-3.91	1.72	6.90E-04	1
	ITIC-4F	1.13	724	756	-5.69	-4.14	1.55	4.32E-04	5
	PC$_{70}$BM	0.40	479	585	-6.00	-3.99	2.01	5.70E-04	17

* For ITIC-C$_2$C$_6$, the corresponding HOMO and LUMO values are reported in Section A. The mobility is considered to be the same as ITIC-C$_8$.

From the above lists of fundamental descriptors, an additional series of features is correspondingly derived as detailed in Table S5. These are built from the fundamental magnitudes and might refer to either the neat materials or to their corresponding blend. This second list of derived descriptors contains 9 elements, thus making a total of 23 descriptors per D:A pair (14 + 9). Therein, we identify 8 non-dimensional magnitudes, namely $\kappa_{max,d}$ (*km1*), $\kappa_{max,a}$ (*km2*), D$_{\%S}$ (*dps*), A$_{\%S}$ (*aps*), D%A (*dpa*), CT$_e$ (*ctel*), CT$_h$ (*ctho*) and μ_{imb} (*mamd*).

Table S5. Optoelectronic descriptors derived from any of the fundamental lists of material features provided above.

		Label (*var*)	Definition	Mathematical relationship
Electronic	**Blend**	E$_{gap,d-a}$ (*eg21*)	Energy gap difference	$E_{gap,d-a} = \left\| E_{gap,d} - E_{gap,a} \right\|$
		Δ_{gap} (*dgap*)	Effective band gap	$\Delta_{gap} = LUMO_a - HOMO_d$
		CT$_e$ (*ctel*)	Charge transfer efficiency for electrons	$CT_e = \dfrac{\left\| LUMO_d - LUMO_a \right\|}{k_B T}$
		CT$_h$ (*ctho*)	Charge transfer efficiency for holes	$CT_h = \dfrac{\left\| HOMO_d - HOMO_a \right\|}{k_B T}$
		$\Delta\mu$ (*dmob*)	Difference in mobility	$\Delta\mu = \left\| \mu_d - \mu_a \right\|$
		μ_{imb} (*mamd*)	Mobility ratio	$\mu_{imb} = \dfrac{\mu_a}{\mu_d}$
Optical	**Neat**	D$_{\%S}$ (*dps*)	Spectral overlap with the sun irradiance	$D_{\%S} = 1 - \dfrac{2500 - \lambda_{edge,d}}{2500}$
		A$_{\%S}$ (*aps*)	Spectral overlap with the sun irradiance	$A_{\%S} = 1 - \dfrac{2500 - \lambda_{edge,a}}{2500}$
	Blend	D%A (*dpa*)	Absorption complementarity	$D\%A = 1 - 2\dfrac{\lambda_{edge,a} - \lambda_{edge,d}}{\lambda_{edge,a} + \lambda_{edge,d}}$

Section V. Training and visualization of the Bayesian machine scientist

In the first run of the Bayesian machine scientist we take the 8 non-dimensional optoelectronic descriptors derived from the fundamental values listed in Table S2 (random selection of features from the literature). For the feeding of the algorithm we randomly select 1,000 data points from the high performing crust of photocurrent values in the corresponding J_{sc}-vol% space of each binary (8 D:A blends in the first run). Note that the upper crust of the J_{sc}-vol% space corresponds to the region where thickness and local morphology are more optimal for the OPV performance. By using a selection of values from the upper crust only, the computational cost is lowered while preserving the meaningful features of the phase space during the training. In addition, the machine scientist is biased to return zero normalized photocurrent (NP) at zero thickness and/or neat films, which gives physical sense to the most plausible model equation eventually found by the algorithm. Such equation returns a mean absolute error (MAE) of 0.07 ($\pm$0.02) when trained with the 8-element combinatorial matrix formed by PTB7-Th and PBDB-T blended with ITIC, ITIC-M, ITIC-C_8 and ITIC-C_2C_6 (Figure S10), which includes 8,000 experimental data points in total.
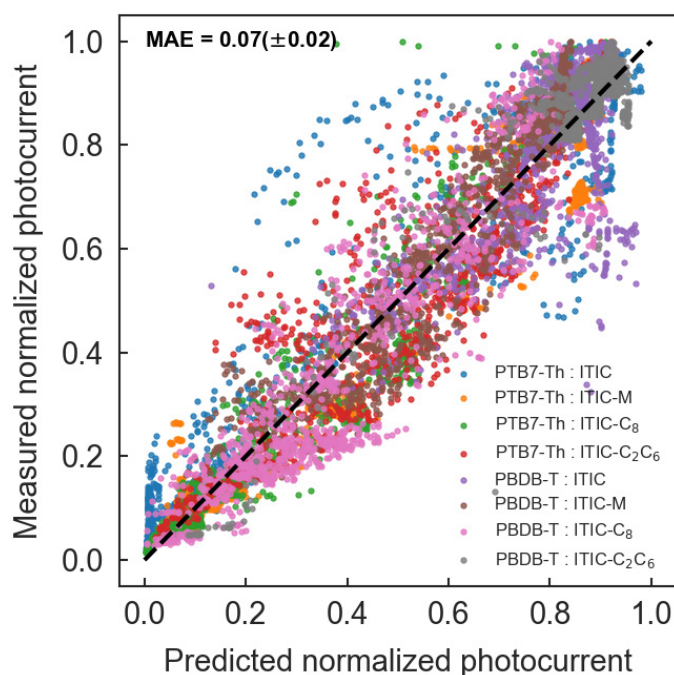

Figure S10. Correlation plot for the normalized photocurrent after training of the Bayesian machine scientist using 8 combinatorial datasets (8,000 experimental data points in total), namely PTB7-Th and PBDB-T individually blended with ITIC, ITIC-M, ITIC-C_8 and ITIC-C_2C_6. The mean absolute error (MAE) found corresponds to 0.07 ($\pm$0.02).
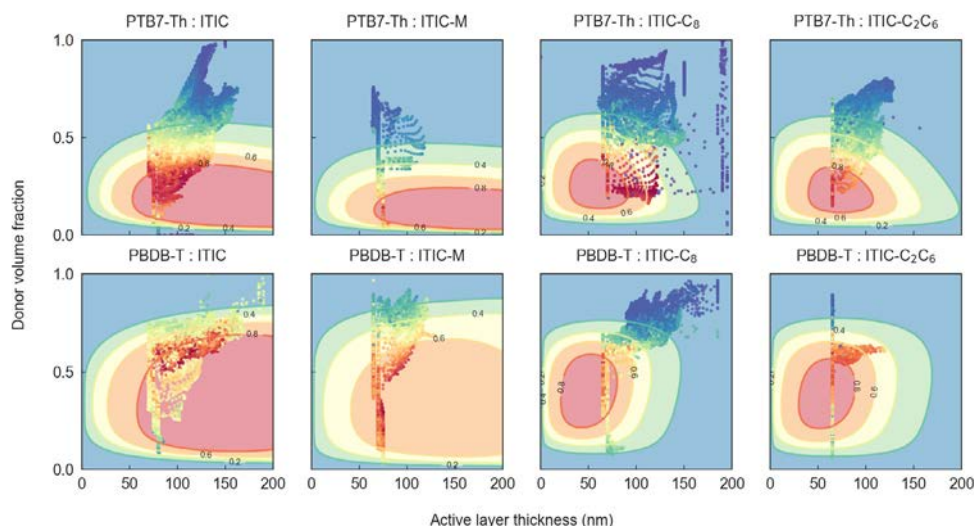
The equation found by the Bayesian machine scientist reads:

```
NP = sin(((((tan(((((tan(tanh((exp((((((((((((((aps / dps) / km2) **
((_a6_ / ctel) ** (_a3_ / ctho))) / _a9_) * ((DVF ** (tanh(DVF) /
(ctho + (DVF + km2))))) ** ((_a8_ + ALT) * dpa))) + (_a7_ * ALT))
+ ((DVF * _a3_) / (_a4_ + dpa))) + aps) + ((_a1_ + DVF) / dpa)) /
_a3_) + (aps * (_a5_ * (ctel + ALT))))) * (km1 + ctel)))) * ((DVF
/ mamd) + (((ALT ** dps) * (mamd + ((_a3_ + (_a7_ ** _a7_)) **
_a0_))) + _a9_))) / km2) * _a2_) / tan(dps))) + _a2_) / ((km2 **
km2) ** pow3(DVF))) * dpa)),
```

This equation includes two variables, namely the active layer thickness (ALT, in nm) and the donor volume fraction (DVF); and ten free parameters, valued as:

```
'_a0_' = 841.0242941013105,
```

```
'_a1_' = 0.9250910180810115,
```

```
'_a2_' = 0.006865810969620029,
```

```
'_a3_' = 0.20851084069638415,
```

```
'_a4_' = -1.0786072008599603,
```

```
'_a5_' = -1.6604993723756856,
```

```
'_a6_' = 7.989472231285854e+34,
```

```
'_a7_' = 0.10003869806486294,
```

```
'_a8_' = 77.87116793766913,
```

```
'_a9_' = -0.11596721509342561.
```

From the ensemble of plausible equations found by the machine scientist, the algorithm quantifies the importance of the features according to their rate of appearance. For example: a descriptor showing a feature importance (FI) of 0.50 implies that such parameter appears in 50% of the most plausible model equations found by the algorithm. Since the machine scientist finds quite complicated mathematical relationships, it ends up using most variables most of the times, thus leading to an uninformative classification of variables:

```
'km1' = 0.89, 'km2' = 1.00, 'aps' = 0.96, 'ctel' = 0.93, 'ctho' =
0.87, 'dpa' = 0.87, 'dps' = 0.93, 'mamd' = 0.87.
```

Nevertheless, and as shown in Figure S11, the model equation demonstrates capability to complement the experimental high-throughput exploration and fill the corresponding photocurrent phase space with mild patterns.

Figure S11. Contour plots for the normalized photocurrent model equation found by the Bayesian machine scientist. In this case, the scattered data includes all the experimentally accessed data points obtained in each combinatorial D:A device.

Contrary to its remarkable descriptive power, the model equation does not extrapolate well in unknown D:A pairs. In this regard, we illustrate in Figure S12 the predicted photocurrent phase space in four different binary validation datasets, namely PTB7-Th:ITIC-4F, PBDB-T-2Cl:ITIC-4F, PBDB-T:PC$_{70}$BM and PCDTBT:PC$_{70}$BM. The equation clearly mismatches the experimental normalized photocurrent both in absolute values and overall trends. Therefore, the machine scientist cannot be employed as an accurate predictive model out of the training set, at least when the training set is limited to the aforementioned 8 distinct D:A blends.
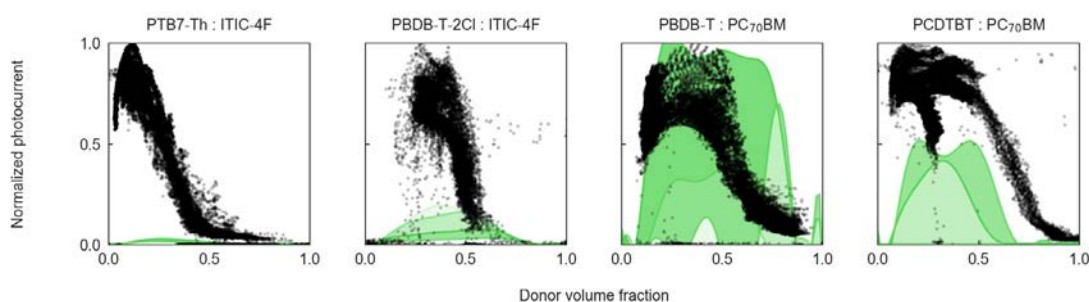
Figure S12. Model predictions drawn by the Bayesian machine scientist in four D:A pairs out of the training set. The experimental scattered data (black dots) are not properly reproduced by the robot (green curves and shaded areas) within the explored phase space diagram, i.e. from neat films up to 200 nm in active layer thickness.

269

We then employed the median values of the E_{gap}s to train a second Bayesian machine scientist algorithm including this time all the experimentally accessed D:A pairs (15 combinations). For this task, and in order to reduce the computational cost, we selected 500 data points from the high-performing crust of photocurrent values in each of the binary blends explored, thus making up a total of 7500 data points for the training step. After several weeks of training, the resulting 8-parameter, most plausible model equation reads:

```
NP = (-(-(tan((sin((((tanh((((cosh(((sinh(((DVF / _a1_) ** _a1_))
** (Eg1 + DVF)) * ((-(sqrt(Eg1)) + (Eg1 / pow2(_a6_))) * ((_a1_ *
_a3_) * (_a3_ * (_a4_ ** sin(fac(Eg1))))))))) ** (((Eg1 ** _a7_) *
((_a4_ + _a4_) + (((_a0_ + ALT) / _a7_) + ((Eg1 + ALT) + ((Eg1 *
(_a7_ + Eg1)) * (((Eg2 * Eg2) * Eg2) + (cos(((_a2_ + cos((Eg1 **
(Eg2 + Eg2)))) / (_a7_ / fac(Eg2)))) / cos(Eg1)))))))) ** (_a7_ *
(_a3_ * DVF)))) + sin(_a0_)) * ((ALT * (_a6_ / _a7_)) /
(sin(((((_a5_ * Eg2) + _a2_) ** Eg2) + ((Eg2 + (Eg1 ** (_a1_ **
(sqrt((DVF / (((ALT + ALT) / _a0_) + (_a3_ / Eg1)))) / (Eg2 **
DVF))))) * _a4_))) + (_a5_ + (pow2((Eg2 / Eg1)) * Eg2)))))) +
(_a5_ * (ALT / log((_a4_ * exp(_a1_)))))) * Eg1) /
(sqrt((tan(sinh(DVF)) ** exp(tan(sinh(DVF))))) + ((ALT + ((-(ALT)
+ _a2_) / Eg1)) * (_a2_ ** _a6_)))))) / (_a1_ ** fac(Eg2)))))) /
(((DVF ** _a4_) ** (_a5_ * fac(Eg1))) * Eg1))
```

where

'_a0_': 620.2945177575979,

'_a1_': '0.958014069387981,

'_a2_': 3443.5970433103516,

'_a3_': 1.2935329423986563,

'_a4_': 107.62433512234023,

'_a5_': -0.000594846647808181,

'_a6_': -0.971457385756211,

'_a7_': -4.2876008724962595

Interestingly, the MAE obtained in this run (Figure S13) is comparable to our previous exploration using a larger set of input descriptors, thus suggesting that the E_{gap}s alone are highly descriptive features for the J_{sc}-vol% dependence.
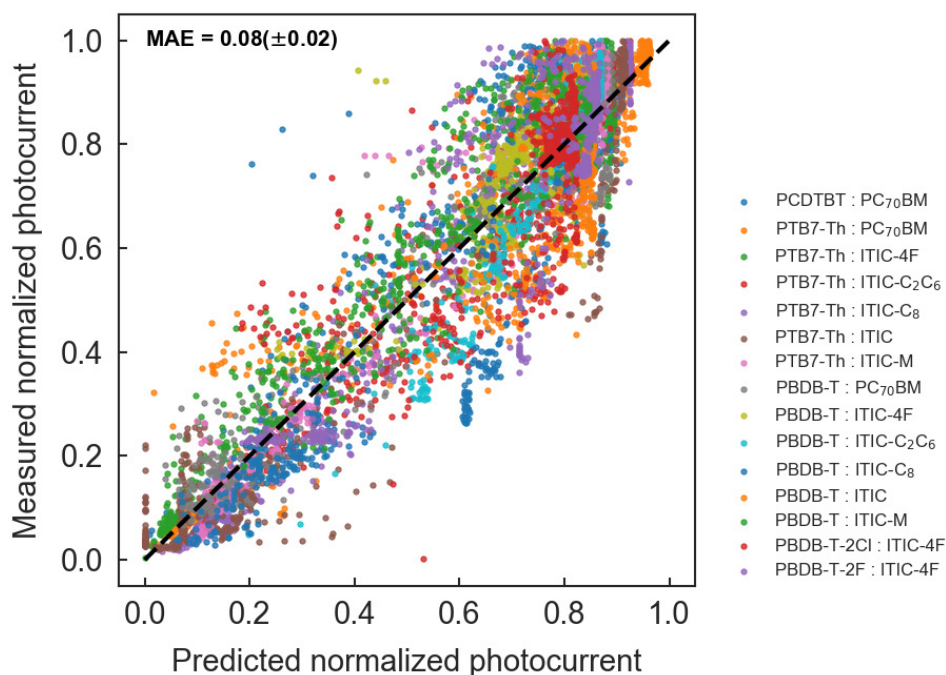
Figure S13. Correlation plot for the normalized photocurrent (NP) obtained after training the Bayesian machine scientist using 15 combinatorial datasets (7500 experimental data points in total), and two material descriptors only, namely the electronic band gaps of donor (*eg1*) and acceptor (*eg2*). The mean absolute error (MAE) found corresponds to 0.08 (±0.02).

By evaluating the abovementioned model equation in a grid, we build largely descriptive contour plots that serve us to follow the mild oscillations of the photocurrent in the thickness-composition space (Figure S14). Finally, we extrapolate the model to four different and unseen D:A pairs to evaluate the predictive capability of the equation found (Figure S15). We observe that the model fails at matching the optimum composition in blends including semicrystalline polymers such as P3HT, similarly to what we observe in the RF model extrapolations (Figure S22).
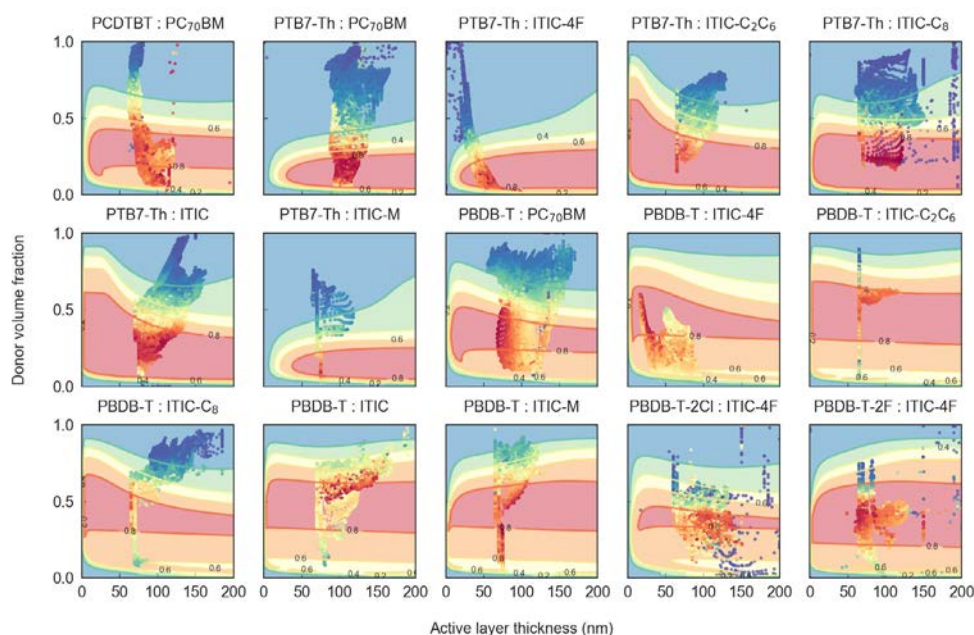
Figure S14. Contour plots for the normalized photocurrent obtained upon training the Bayesian machine scientist using data for 15 distinct D:A combinations (500 data points each) and two input descriptors only, namely the corresponding electronic band gaps of the donor and the acceptor materials. The scattered data shown corresponds to all the data points experimentally generated in each D:A combination, which largely exceed the 500 data points selected for the training step.
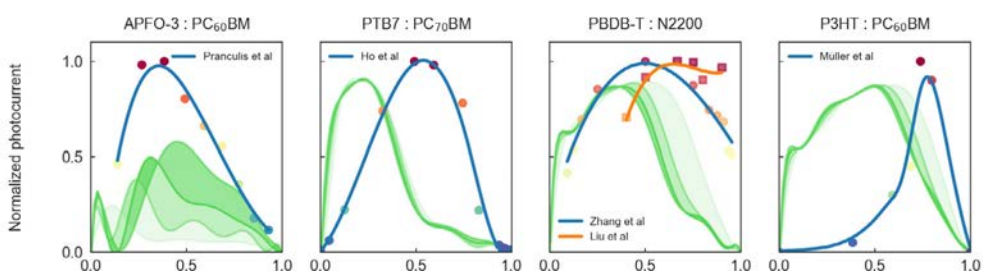

Figure S15. Extrapolations of the model equation found by the Bayesian machine scientist in unseen D:A pairs. Note that the only input parameters are the electronic band gaps of donor and acceptor materials. The active layer thickness dependence on the photocurrent distribution is illustrated by the darkness of the shaded green areas (the darker, the thicker, up to 200 nm).

Section VI. Training of the random forest machine-learning algorithm

a. Random forest ensemble optimization

The RF machine-learning (ML) model is implemented in Python 3.7.3 using the open-source toolbox Scikit-Learn[53] v0.22.2. The RF regressor is first optimized in terms of number of trees in the forest (*n_estimators*) employed by looking for a sweet spot between learning performance and computational cost. The learning performance is evaluated by averaging the mean absolute error (MAE) and mean squared error (MSE) in subsequent leave-one-out cross-validations (LOO-cv) of the 15 experimental binary OPV datasets generated in this work. Our results (Figure S16) show that when all fundamental and optoelectronic descriptors (23 elements) are employed in the training of a RF model, a moderate value of *n_estimators* = 100 yields converged MAE with very limited computational cost (few seconds of training time per LOO-cv). Herein, *n_estimators* is set to 100 by default in our RF training procedures.
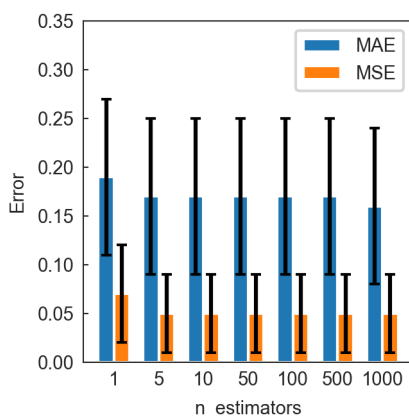
Figure S16. Exploration of the influence of the number of trees in the forest (*n_estimators*) in subsequent LOO-cv runs of 15 combinatorial datasets. The values and error bars depicted account for the mean and standard deviation of the MAE and MSE in the 15 runs performed at each *n_estimators* step.

b. Leave-one-out cross-validations and extrapolation capability

The first tentative LOO-cv included 8 datasets and the full list of optoelectronic descriptors (23). Our (arbitrary) criterion for successful extrapolation required the MAE to be below 0.20 in the validation datasets, which is a figure comparable to our experimental error (10-15%) in the determination of active layer thickness and composition[34]. Based on that threshold error, the RF model yields *ca*. 65% (5/8) accuracy in the present LOO-cv case example (Figure S17). Nevertheless, by extrapolating a single RF model trained with all 8 datasets we obtain a MAE < 0.20 in 7 out of 7 D:A binaries out of the training set (Figure S18). Note that the MAE is computed with respect to the upper shell of 1,000 values in the corresponding J_{sc} vs. active layer thickness and composition phase space (colored rainbow data in Figure S18). By further extending the training dataset to 15 distinct D:A blends, the LOO-cv returns an average MAE of 0.17 (±0.08), as depicted in Figure S19.
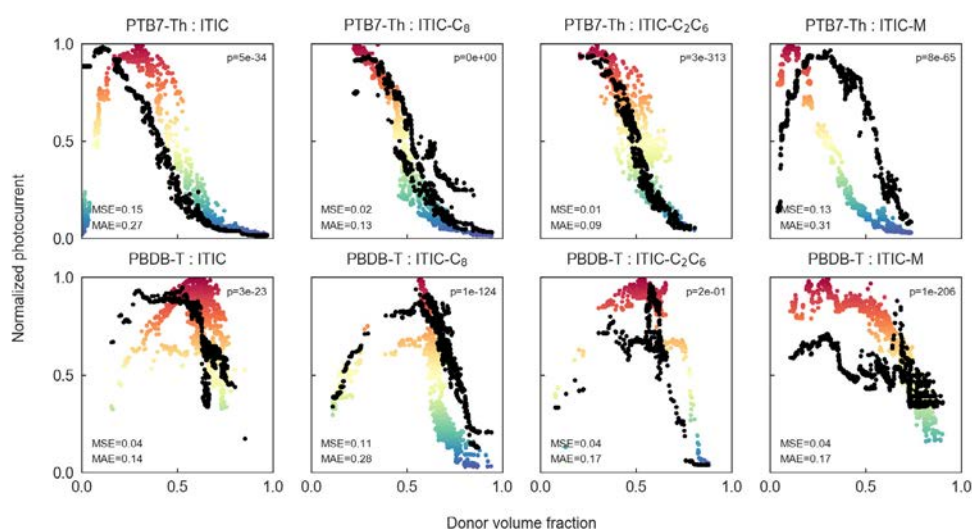

Figure S17. LOO-cv of the RF model trained with 23 descriptors and 8 datasets, namely PTB7-Th and PBDB-T donors blended with ITIC, ITIC-C$_8$, ITIC-C$_2$C$_6$ and ITIC-M. The extrapolation of the RF model is over imposed (black dots) on the actual experimental measurements (in color scale). The corresponding Spearman's rank correlation coefficients (ρ), MAE and MSE obtained in each LOO-cv run are also included.
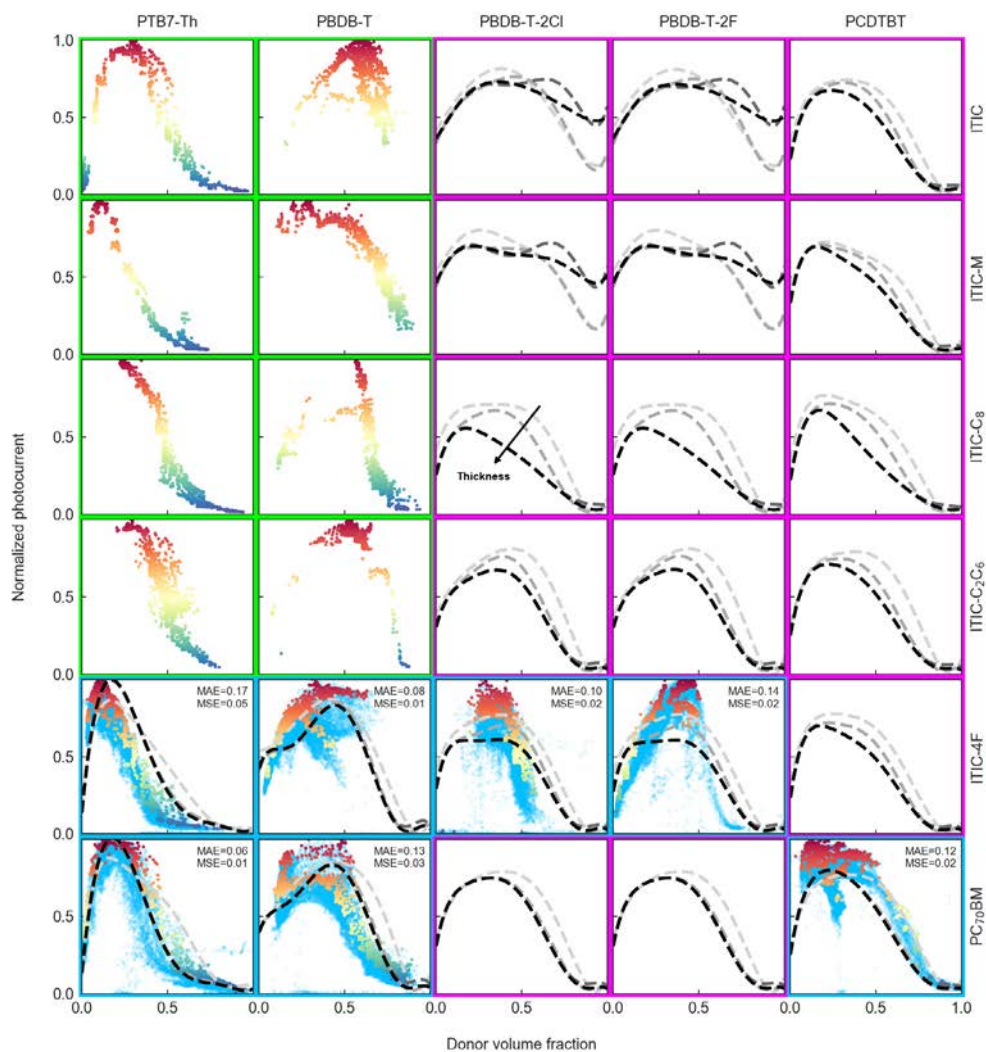
Figure S18. Full combinatorial matrix of the normalized J$_{sc}$ phase diagram of five donor polymers and six different small molecule acceptors built using a RF model trained with 8 datasets (highlighted in green) and 23 optoelectronic descriptors. Subplots highlighted in blue are used to test the predictive capability of the model (they were not used for training in the present case). Magenta panels remark those binaries in which there are not experimental data available, thus they are purely predictive cases. The RF model predictions are depicted as dashed lines corresponding to four different active layer thickness values: 50 nm (lightest grey), 100 nm, 150 nm and 200 nm (black).
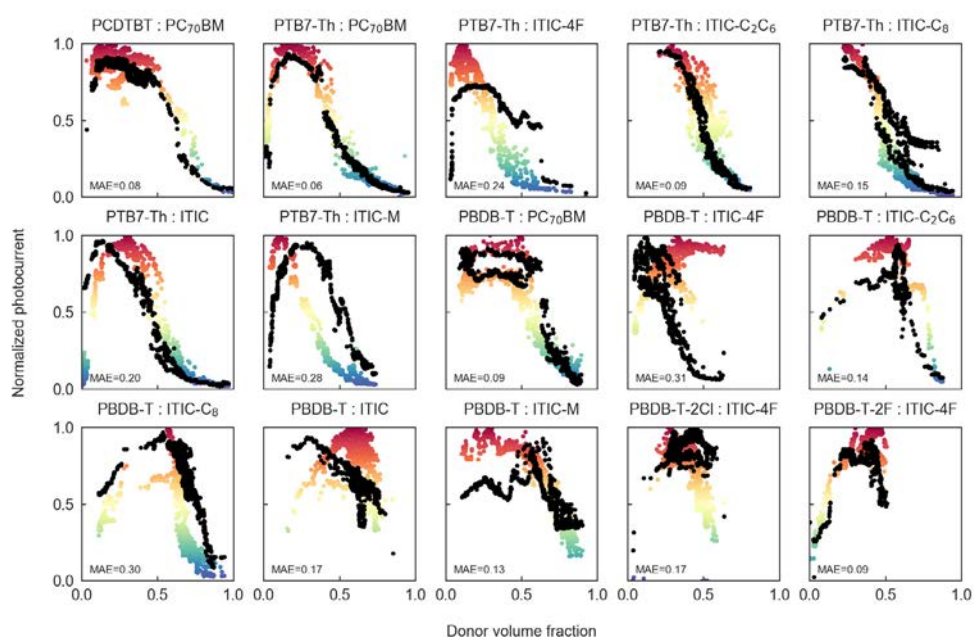
Figure S19. LOO-cv of the RF model trained with 23 descriptors and 15 datasets. The extrapolation of the RF model is over imposed (black dots) on the actual experimental measurements (in color scale). The average MAE obtained is 0.17 (±0.08).

c. Feature selection

Feature selection in ML algorithms such as RF consists of identifying those descriptors that best describe the given set of observables. This is useful to improve the accuracy of the model while avoiding overfitting and reducing the computational cost. Thus, feature selection generally results in simpler and more generalized models which might enable the understanding of their underlying learning structure to perform an intuitive interpretation, i.e. providing some physical sense to the model predictions in terms of normalized J_{sc} for a variety of material systems. The here proposed initial list of optoelectronic descriptors is notably large (23) yet insignificant with respect to the number of observables used in training: 1,000 data points per D:A pair. Note that all experimentally accessed D:A datasets (15 OPV binaries) are employed in the feature selection procedure to maximize the parametric variability *seen* by the model, thus making up a total of 14,000 data points for the training step (in subsequent LOO-cv runs). This implies that overfitting is not expected to arise; therefore, in our case feature selection is performed to identify the most relevant descriptors and to provide physical intuition to the learning algorithm.

Feature selection in ML does not follow a unique recipe or searching protocol. Conversely, it constitutes a route open to distinct approaches and statistical criteria depending on the type of problem (classification vs regression, categorical vs numerical features) and the information collected *a priori* about the target features in the explored datasets. In this work, we adopted a greedy mean absolute error (G-MAE) feature selection procedure. This approach starts by considering the simplest RF model (i.e.

276

excluding any feature in the modeling) and progressively screens the MAE of models of increased complexity. In our case, the G-MAE exploration was subsequently performed by LOO-cv of 15 datasets using each of the optoelectronic descriptors selections detailed in Section IV. We then averaged the MAE obtained for each combination of descriptors to build a G-MAE matrix (Figure S20). In this way, we also consider the variability of the input descriptors took from the literature. By following this protocol, we identify a series of RF models of two features only that minimize the MAE to *ca.* 0.15, which is a lower figure compared to that obtained using the full list of 23 descriptors (Figure S19).

Among the most successful parametric combinations, we generally observe that descriptors related to the HOMO energy level of the donor such as *dps* or *ledge1* (as well as *homo1* itself) result in accurate models. Regarding acceptor material descriptors, $E_{gap,a}$ (*eg2*) appears as the most successful feature in RF model training. Also, the combination of μ_{imb} (*mamd*) with features related to the HOMO of the donor lead to models with low MAE.

With all that, one of the most interesting parametric combinations identified is that formed by the donor and acceptor materials band gaps, $E_{gap,d}$ and $E_{gap,a}$. The intuitive understanding of such model is remarkable since it indicates that the RF model requires only the electronic band gaps of the mixed components to predict the J_{sc}-vol% phase space. Thus, the complementary absorption between donor and acceptor, determined by their respective band gaps, is likely to be enough for the RF ensemble to shape the normalized J_{sc} phase space of the corresponding blends.

Figure S22 illustrates the RF model extrapolations obtained in binary OPV systems out of the training set formed by the 15 D:A combinations explored in this work, using the electronic band gaps as the only input descriptors. The experimental datasets shown in Figure S22 were extracted from literature[21,23,54–56] and include several examples of polymer:fullerene blends as well as a representative example of an all-polymer binary blend, namely PBDB-T:N2200. Notably, in two of the blends explored (APFO-3:$PC_{60}BM$ and PBDB-T:N2200) the RF model is close to reproducing the position of the normalized J_{sc} maximum. Nevertheless, the model clearly fails in predicting the J_{sc}-vol% dependence of workhorse D:A pairs such as P3HT:$PC_{60}BM$. This might be indicative of limited extrapolation capabilities when the morphology of the blended materials widely differs with respect to the systems explored in the training step, namely mostly amorphous vs. semi-crystalline polymers as donors. However, further extension of the training dataset to such semi-crystalline systems could enhance the predictive power of the RF model.
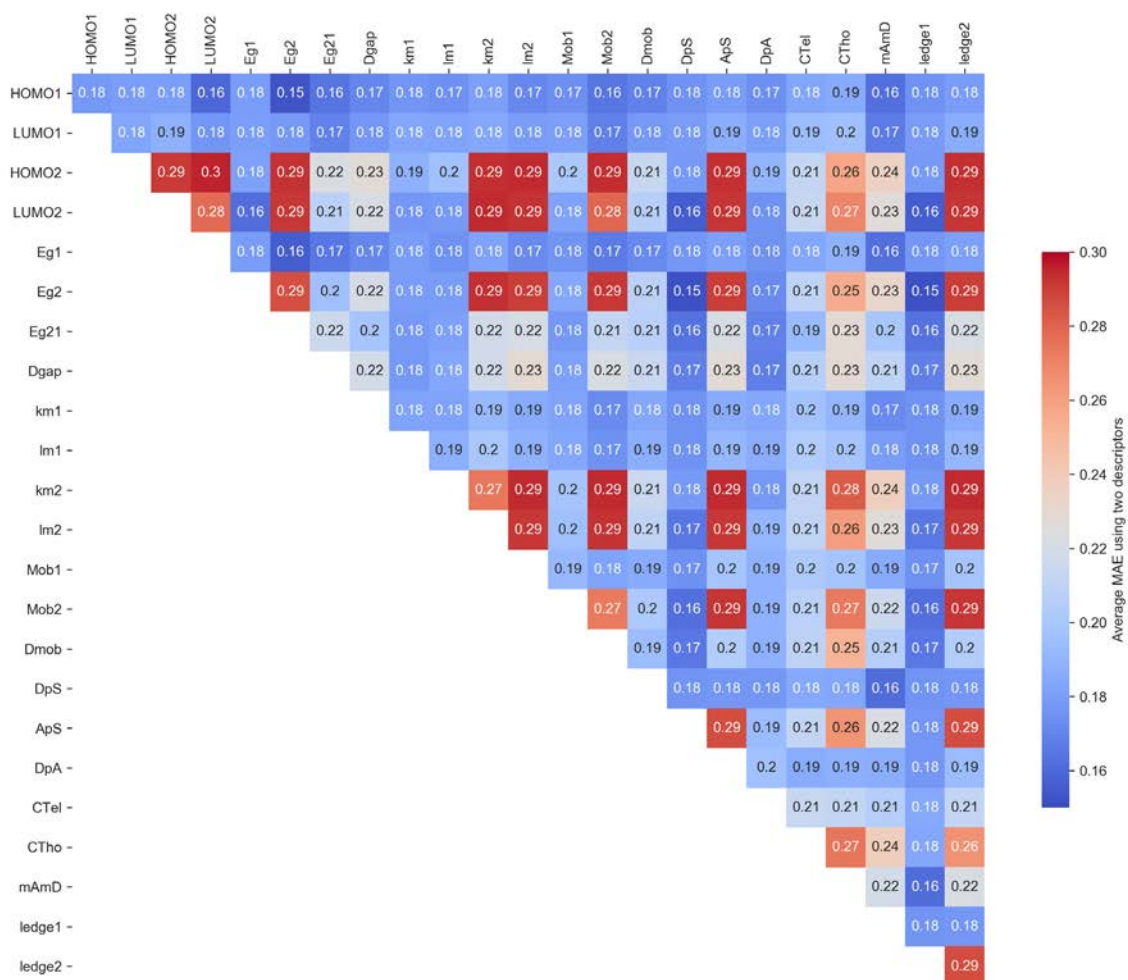
Figure S20. G-MAE matrix of RF models trained with combinations of two descriptors only using 15 experimental datasets. The MAE values were obtained by averaging the MAE in 15 successive LOO-cv runs for each of the optoelectronic descriptors selections detailed in Section IV. The diagonal components correspond to the MAE obtained in one-parameter RF models. The donor volume fraction (DVF) and the film thickness (FT) are included implicitly in all models.
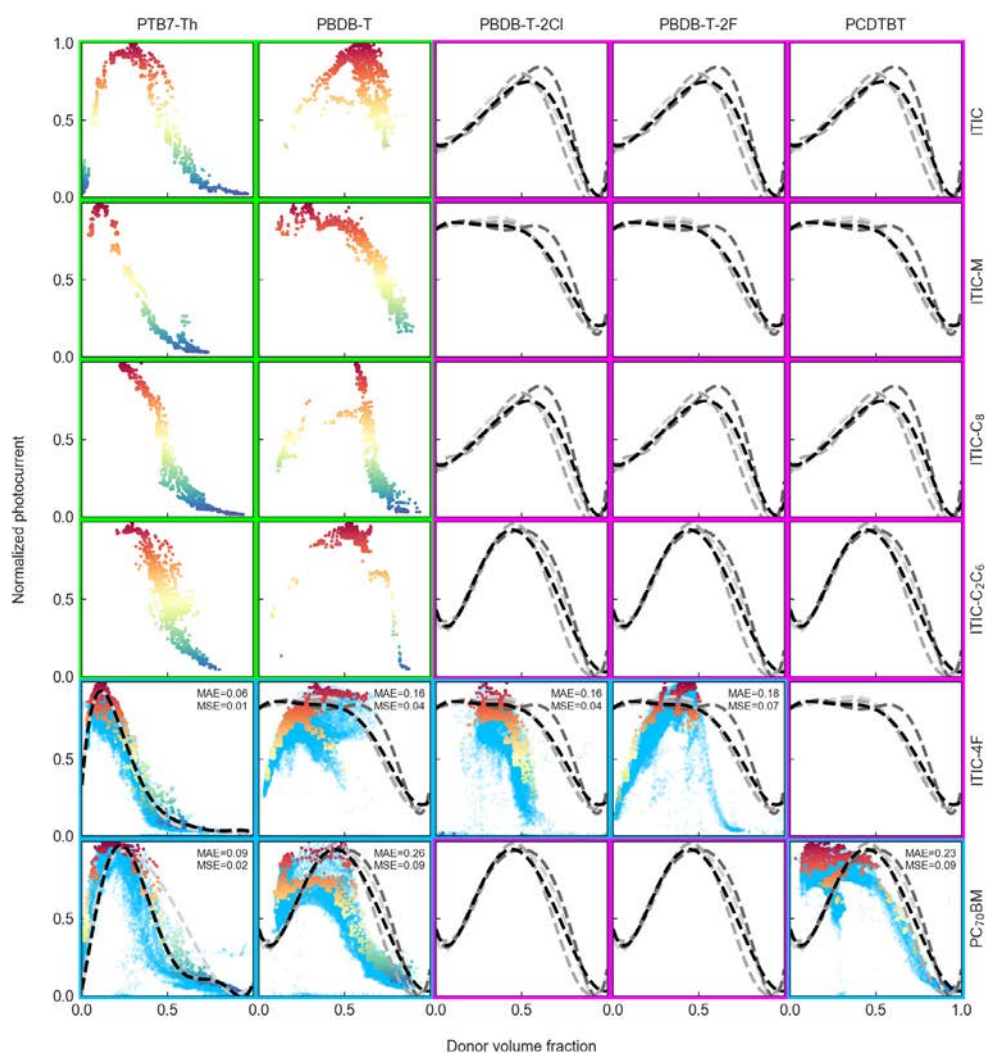
Figure S21. Full combinatorial matrix obtained after RF model training with 8 datasets (green frames) and 2 descriptors only, namely *eg1* and *eg2*. By constraining the extension of the training dataset, the MAE raises up to 0.16 (±0.07).
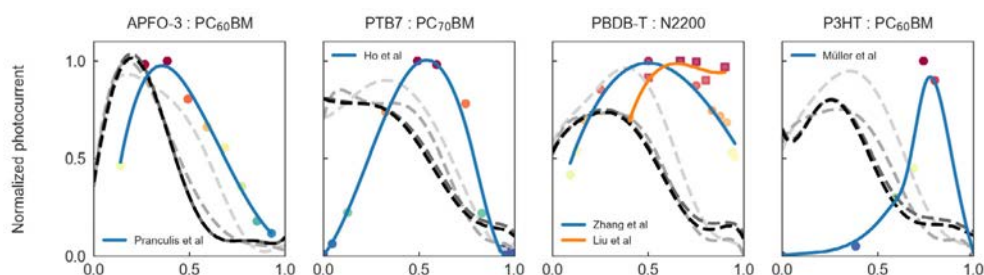

Figure S22. RF model extrapolations in binary OPV blends out of the initial training set. For the training of the RF, only two features were considered, namely *eg1* and *eg2*, apart from DVF and FT. The full list of D:A blends explored in this work (15) was employed in the training step. The scattered experimental datasets depicted were extracted from literature.[21,23,54–56] In the conversion from wt% to vol%, an average density for the polymers and fullerenes of 1.1 g mL^{-1} and 1.6 g mL^{-1} was considered, respectively.

d. Sensitivity analysis of the input descriptors in the two-parameter model

In this work, the HOMO, LUMO (thus E_{gap}) and mobility values are not consistently measured in the neat materials; they are, instead, took from a variety of literature references. Since there might be large quantitative differences between characterization methods (Section IV, Supporting Information), it is interesting to evaluate how critical these values are for the successful training of a RF model.

For that purpose, we trained a RF ensemble using the median values obtained in our HOMO/LUMO data mining study (Figure S9). As shown in Figure S23, the median values obtained in the corresponding distributions are still largely descriptive inputs for the RF algorithm. The model returns a MAE of 0.16 (±0.07), a figure which is in excellent agreement with our previous models using hand-picked literature values from CV measurements only (Figure 6).

Finally, since Tauc plots (Figure S8) can be employed to quantify the solid-state optical band gap of thin film materials, we further validated a RF model using such descriptors for the donor and acceptor materials only ($E_{g,opt,d}$ and $E_{g,opt,a}$). This approach is thought to keep the experimental consistency in our work since the complex refractive indices of the here studied materials were all measured in our group using the same experimental setup (a Semilab GES5E rotating polarizer ellipsometer). With all that, the results shown in Figure S24 indicate once again great modeling consistency as the MAE slightly raised to 0.18 (±0.07).
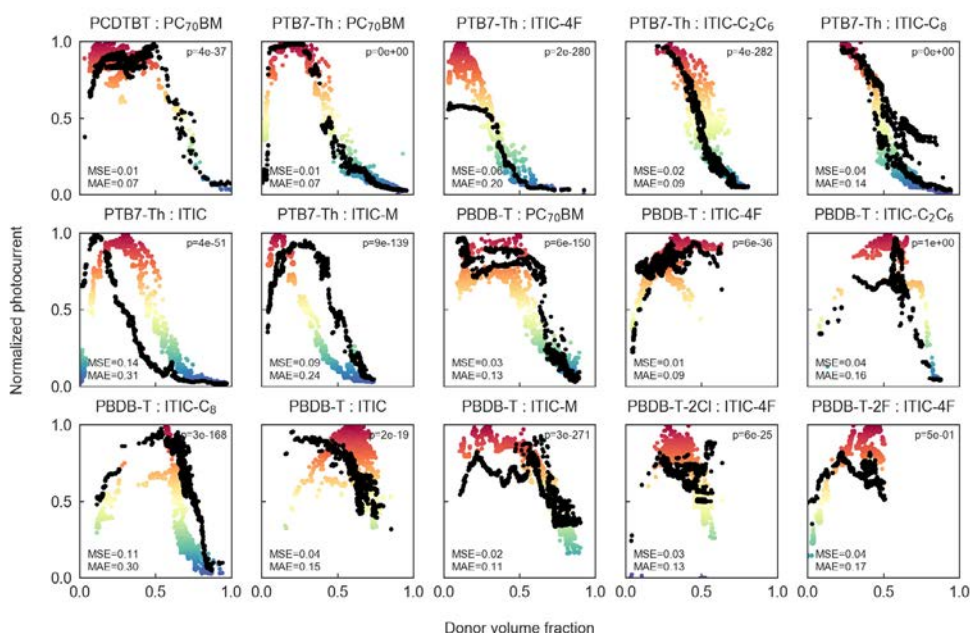

Figure S23. LOO-cv of a 2-parameter RF model trained using the median values of the electronic band gaps found in the literature. The resulting MAE reads 0.16 (±0.07).
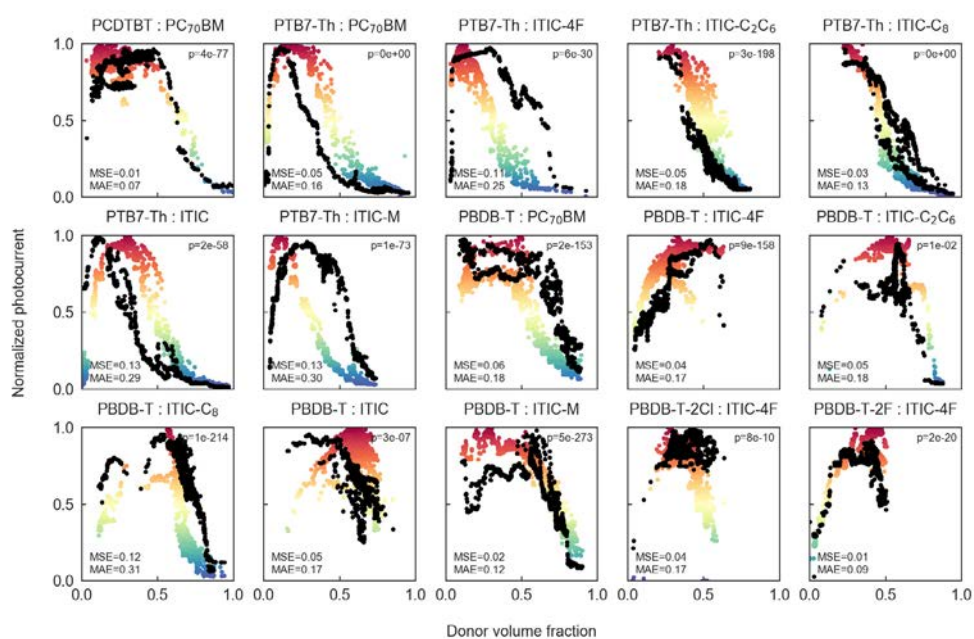
Figure S24. LOO-cv of a 2-parameter RF model trained using as input descriptors the corresponding solid-state optical band gaps of the materials, as obtained from the Tauc plots shown in Figure S8. The average MAE obtained equals 0.18 (±0.07).